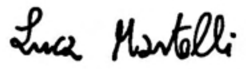

Luca Martelli

Dipartimento di Storia, Disegno e Restauro dell'Architettura
Sapienza Università di Roma
luca.martelli@uniroma1.it

He obtained a Single Cycle Master's Degree of Building Engineering-Architecture from the Faculty of Civil and Industrial Engineering of 'Sapienza' University of Rome in 2019. He took the State examination for professional practice as a senior civil and environmental engineer in the 1st Session of 2020. He took the State examination for professional practice as a senior architect in the 2nd session of 2020. He enrolled in the Order of the Engineer of the Province of Rome in 2020. In November 2020, he was appointed as a PhD student at the Department of History, Representation, and Restoration of Architecture (Dipartimento di Storia, Disegno e Restauro dell'Architettura – DSDRA) of 'Sapienza' University of Rome.
He has been a member of the Italian Union for Graphical Representation (Unione Italiana Disegno – UID) since 2022.
His main concentrations are: the study of the historical evolution of design drawing; the shadow representation theory in design for environmental comfort and Bioclimatic Architecture; architectural and urban survey.

Sapienza Università di Roma
Dipartimento di Storia, Disegno e Restauro dell'Architettura
Dottorato Innovativo Internazionale in
Storia, Disegno e Restauro dell'Architettura
International PHD Course in
History, Representation and Restoration of Architecture
Curriculum in Disegno / Representation - SSD ICAR/17

Luca Martelli

The Contribution of Radar Antenna in Data Acquisition

Tesi di Dottorato di Ricerca - Ciclo XXXVI - gennaio 2024

Luca Martelli

From the Integrated Survey of Architecture and Territory to its Representation. The Contribution of Radar Antenna in Data Acquisition

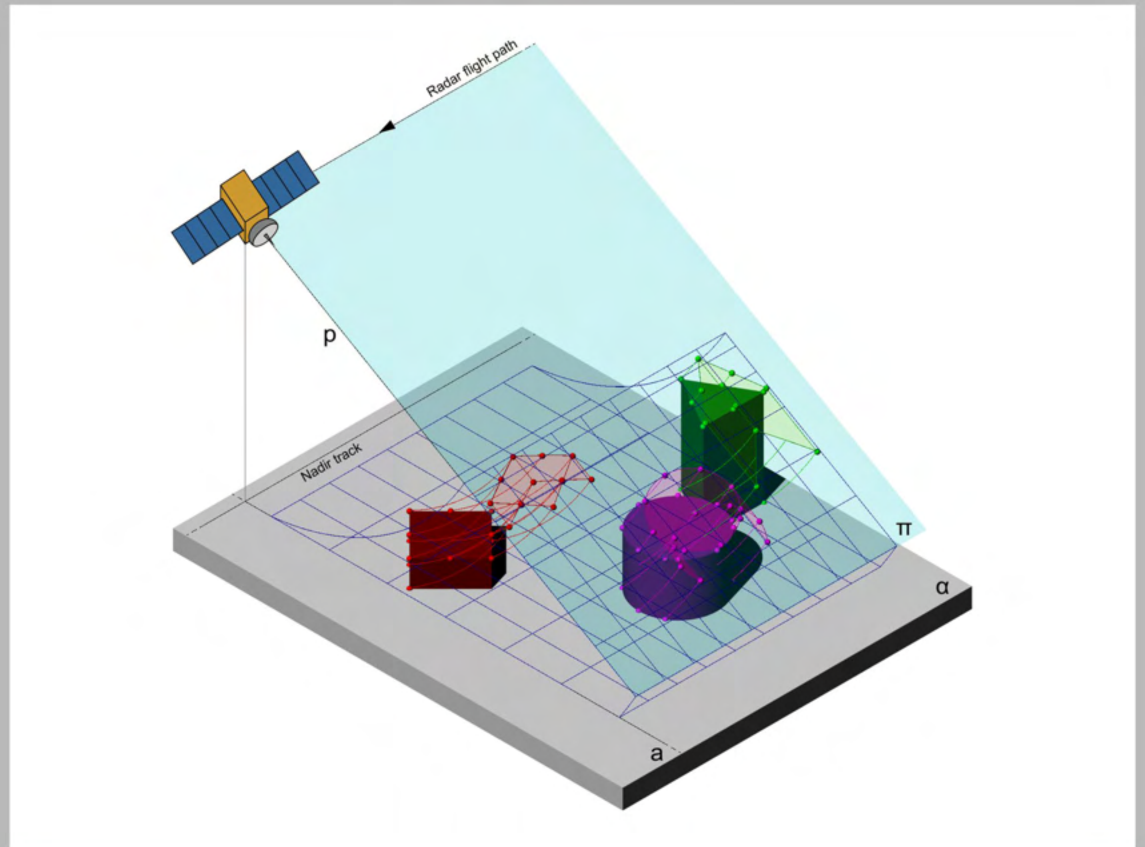

Dipartimento di Storia, Disegno e Restauro dell'Architettura
SAPIENZA
UNIVERSITÀ DI ROMA
Dottorato Innovativo Internazionale in Storia, Disegno e Restauro dell'Architettura
International PHD Course in History, Representation and Restoration of Architecture
Curriculum in Disegno / Representation - SSD ICAR/17

Abstract
The introduction of open-access data repositories about Territory has highlighted the issue of organising surveys at different dimensional scales in a systemic view. It is common practice to integrate data such as satellite photographs and DEMs (Digital Elevation Models) with other data obtained from terrestrial laser scanning, photogrammetry, topography and so on. In the Italian Scientific Disciplinary Area for Civil Engineering and Architecture SSD ICAR/17, the study of applications of optical radiation is an established fact, but much rarer is the discussion about the use of radio waves. In recent years, imaging radars (Radio Detection And Ranging), active sensors based on the recording of microwave energy pulses emitted by them and then reflected by bodies in their field of action, have become widespread. In relation to the purposes of integrated surveying, the overriding peculiarities of radar imaging are: A) the coherence of radar radiation, since microwaves are emitted in phase and then their phase shift is registered during reception; B) the different interactions between the target and the radar beam that scans it, depending on the microwave frequency band used and polarisation; C) the possibility of using these sensors even in total absence of light and in most atmospheric conditions; D) the execution of progressively more complex processing, starting from the two-dimensional images derived from the scans, to obtain DEMs or even point clouds. In this research: 1) we critically analyse methods for recording and processing radar images useful for integrated surveying of Territory and Architecture; 2) we employ some of these methods in two case studies concerning historical military architecture, in order to verify their effectiveness and precision; 3) we study representa tion apparatuses suitable for the restitution of radar data.

Sapienza Università di Roma - Dipartimento di Storia, Disegno e Restauro dell'Architettura
Dottorato Innovativo Internazionale in Storia, Disegno e Restauro dell'Architettura
International PHD Course in History, Representation and Restoration of Architecture
Curriculum in Disegno / Representation - SSD ICAR/17

Dott. Luca Martelli

From the Integrated Survey of Architecture and Territory to its Representation.
The Contribution of Radar Antenna in Data Acquisition

Tesi di Dottorato di Ricerca - Ciclo XXXVI - Gennaio 2024

Sapienza Università di Roma - Dipartimento di Storia, Disegno e Restauro dell'Architettura
Dottorato Innovativo Internazionale in Storia, Disegno e Restauro dell'Architettura
International PHD Course in History, Representation and Restoration of Architecture
Coordinatore prof. Piero Cimbolli Spagnesi
Curriculum in Disegno / Representation - SSD ICAR/17
Responsabile prof. Graziano Mario Valenti

Dottorando
Luca Martelli

Tutors
Prof. Fabio Lanfranchi; Prof. Laura Carnevali.

Cotutors
Dr. Gianfranco Fornaro; Dr. Simona Verde.

Stampato e riprodotto in proprio presso il

Abstract

The introduction of open-access data repositories about Territory has highlighted the issue of organising surveys at different dimensional scales in a systemic view. It is common practice to integrate data such as satellite photographs and DEMs (Digital Elevation Models) with other data obtained from terrestrial laser scanning, photogrammetry, topography and so on. In the Italian Scientific Disciplinary Area for Civil Engineering and Architecture SSD ICAR/17, the study of applications of optical radiation is an established fact, but much rarer is the discussion about the use of radio waves. In recent years, imaging radars (Radio Detection And Ranging), active sensors based on the recording of microwave energy pulses emitted by them and then reflected by bodies in their field of action, have become widespread. In relation to the purposes of integrated surveying, the overriding peculiarities of radar imaging are: A) the coherence of radar radiation, since microwaves are emitted in phase and then their phase shift is registered during reception; B) the different interactions between the target and the radar beam that scans it, depending on the microwave frequency band used and polarisation; C) the possibility of using these sensors even in total absence of light and in most atmospheric conditions; D) the execution of progressively more complex processing, starting from the two-dimensional images derived from the scans, to obtain DEMs or even point clouds. In this research: 1) we critically analyse methods for recording and processing radar images useful for integrated surveying of Territory and Architecture; 2) we employ some of these methods in two case studies concerning historical military architecture, in order to verify their effectiveness and precision; 3) we study representation apparatuses suitable for the restitution of radar data.

***Key words**: Integrated Survey; Differential Interferometry SAR; Point Clouds; Radar Imaging; Remote Sensing.*

L'introduzione di banche dati ad accesso libero riguardanti il Territorio ha posto l'accento sul tema dell'organizzazione, in una visione sistemica, dei rilevamenti a diverse scale dimensionali. È pratica comune integrare dati come le fotografie satellitari e i DEM (Digital Elevation Model) con gli altri dati ottenuti da scansioni laser terrestri, fotogrammetria, topografia e così via. Nel panorama del SSD ICAR/17, lo studio delle applicazioni delle radiazioni ottiche è un dato acquisito, ma assai più rara è la trattazione sull'uso delle onde radio. Nel corso degli ultimi anni si sono diffusi i radar (Radio Detection And Ranging) per la generazione d'immagini, sensori attivi basati sulla registrazione degli impulsi di energia a microonde da loro emessi e poi riflessi dai corpi nel loro campo d'azione. Ai fini del rilievo integrato, le peculiarità preminenti della produzione d'immagini tramite radar sono: A) la coerenza della radiazione radar a microonde, poiché queste ultime sono emesse in fase, per poi registrare il loro sfasamento durante la ricezione; B) le differenti interazioni tra il bersaglio e il fascio radar che lo scandisce, a seconda della banda di frequenza di microonde adoperata e della polarizzazione; C) la possibilità di usare questi sensori anche in totale assenza di luce e nella maggior parte delle condizioni atmosferiche; D) l'esecuzione di elaborazioni via via più complesse, partendo dalle immagini bidimensionali ottenute dalle scansioni, per arrivare a ricavare DEM o persino nuvole di punti. In questa ricerca: 1) analizziamo criticamente dei metodi di registrazione ed elaborazione di immagini radar utili al rilievo integrato territoriale e dell'Architettura; 2) impieghiamo alcuni di questi metodi in due casi di studio concernenti l'architettura storica militare, allo scopo di verificarne l'efficacia e la precisione; 3) studiamo apparati di rappresentazione idonei alla restituzione dei dati radar.

***Parole chiave**: Rilievo integrato; Interferometria SAR Differenziale; Nuvole di punti; Radar Imaging; Telerilevamento.*

Dedicated to my family.

Contents

Introdution

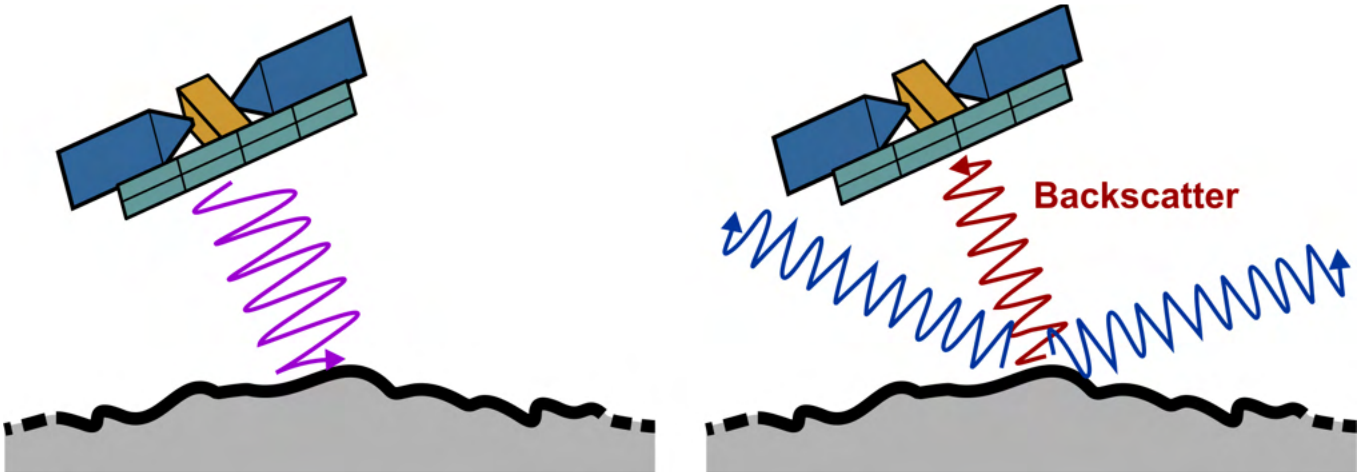

1/ Graphical illustration of backscatter in the case of a satellite radar, according to Ager 2013.

Radar stands for 'RAdio Detection And Ranging'. This acronym emphasises the usefulness of such a device, designed to detect the presence of a target and measure its distance from the platform or the from the trasmitting antenna[1]. The concept behind radars is relatively simple but, in most cases, their practical application is very complex[2].
Being able to determine the distance and movement of targets, throughout history these instruments have proved useful not only for military purposes but also for numerous civil applications such as air traffic control, monitoring the speed of vehicles on the road and observing atmospheric phenomena[3].
Radars are also used as an active graphic mapping technology, in which microwave energy pulses are emitted from an antenna and reflections from bodies capable of interacting with this signal - called backscatterers - are received by the same or other antennas and encoded into images (fig. 1).
The antenna of a imaging radar emits individual pulses of microwave radiation. This radiation is emitted at a Pulse Repetition Frequency (PRF) in the order of thousands pulses per second or more. The signal scatters in every direction and a small part, called radar backscatter, returns to the antenna. The instrument measures the characteristics of the echoes, including the round-trip time from the antenna to the scene and back, the strength of the reflection and the return phase of the wave.
The distance between sensor and target is easy to calculate, as it is given by the product of the pulse velocity, equal to the speed of light, times the round-trip time divided by two. As already mentioned, a radar can also determine whether the return signal wave is at its peak, at its trough or somewhere in between (fig. 2).
We often refer to the radar data associated with these pulse measurements as the 'fast-time dimension', while the information associated with the movement of the sensor along its path is called the 'slow-time dimension'. As far as remote sensing is concerned, one of the most important attributes of radars when it comes to image mapping lies in their ability to generate their own illumination as active

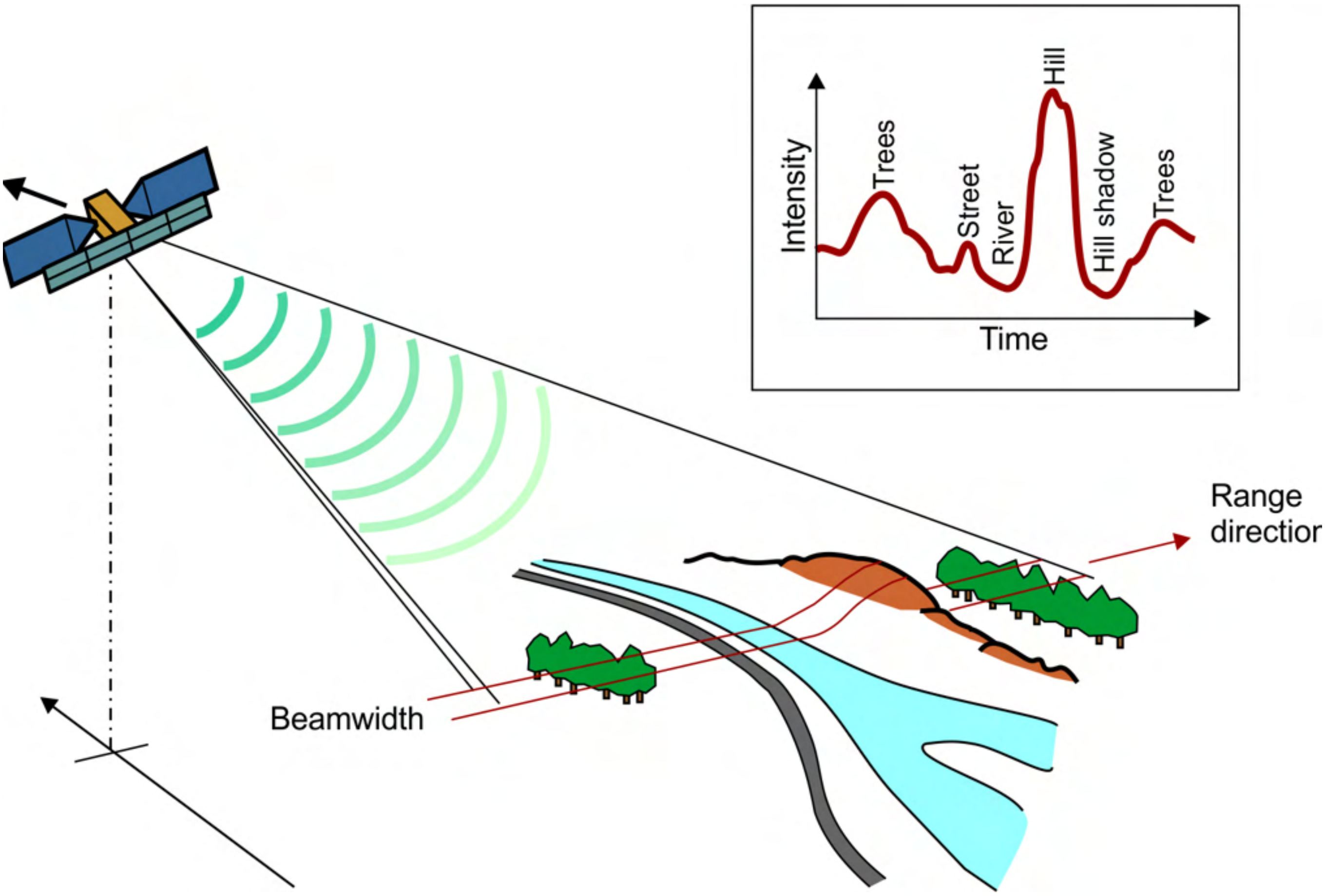

2/ Variation of the measured return signal based on the target scanned by satellite radar, according to Ager 2013.

sensors (fig. 3), thus being able to operate independently of the presence of sunlight, both during the day and at night.
Another of the most important features of radars when it comes to imaging applications is that the relatively long wavelengths of their signals can penetrate clouds, dust, and even volcanic ash. Furthermore, they can map images independently of most weather conditions that may affect the scene during scanning. Most of Earth's surface is covered by water, with large amounts of water vapour condensing into clouds over vast regions of land, so today radars are a key remote-sensing technology when atmospheric phenomena prevent data acquisition by other means.
The wavelengths of radar signals for imaging are much longer than those of visible light and are typically longer than those of the frequencies in K-band (between 18 and 27 GHz), as the latter are reflected by water vapour and other atmospheric particles. In fact, high-frequency microwave bands are used in the radar Doppler pulses of meteorological instruments to detect atmospheric disturbances. The most frequently used frequency bands for image generation are the X-band (between 8 and 12 GHz), the C-band (between 4 and 8 GHz) and some of the bands with the longest wavelengths; the wavelengths of the L-band (between 1 and 2 GHz) and the Ultra-High-Frequency (UHF) radars (between 300 and 1.000 MHz) are so long that they can penetrate foliage and can sometimes be deployed to map the territory beneath tree ca-

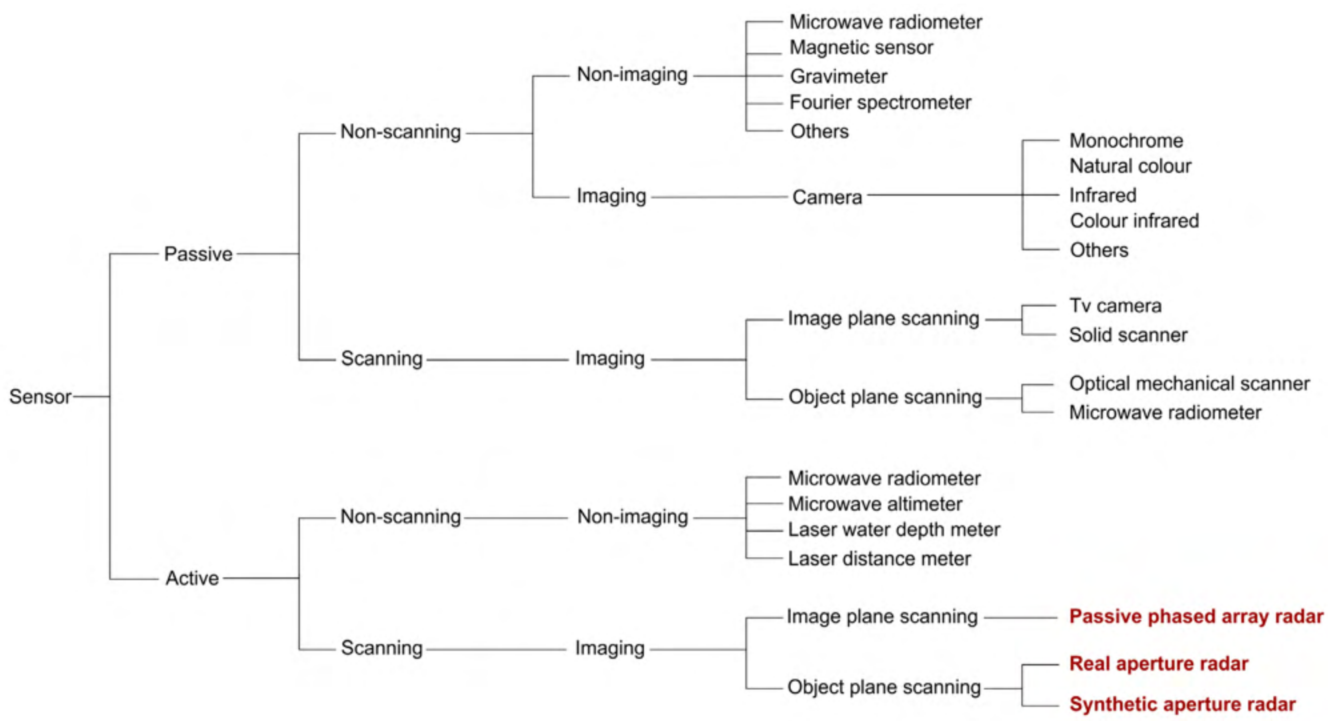

3/ Positioning of radars inside a classification of active and passive sensors, according to Planetek Italia 2022.

nopies of forests.

Unlike passive optical sensors, radars do not operate with fixed lenses, so they are flexible with regard to resolution and spatial coverage. Therefore, depending on how it is set up, a single system can acquire low resolution data from large areas, medium resolution data from medium areas, and high resolution data from small areas.

Distance weakens the intensity of the signals returning from the bodies to the radars and can increase the noise in the image being recorded. Consequently, a very long antenna must be used to perform remote sensing with a Real Aperture Radar (RAR). A particular technique called Synthetic Aperture Radar (SAR) improves resolution without using extremely long antennas. This allows high-resolution images of Earth's surface to be acquired even from orbital platforms, without distance affecting definition.

It should be noted that, depending on the type of transmitter used, illumination of a pulse radar system may be incoherent, partially coherent or (fully) coherent. The concept of coherence in fact expresses the phase relationships between transmitted and received pulses. Oscillations and electromagnetic waves are said to be coherent if their phase laws remain constant, while they are said to be incoherent if there are statistically distributed phase shifts. In the case of coherent radars, the antenna emits pulses of microwave energy whose characteristics are controlled and consistent from pulse to pulse.

Because of this peculiar coherence, data acquired with a SAR sensor are characterised by two components, one associated with the intensity of the received echo and one associated with its phase.

These two components can be processed into a Single Look Complex (SLC), where the data associated with the intensity and the data associated with the phase are graphically represented as complex numbers for each pixel.

The intensity component, after undergoing a process known as 'SAR focusing', forms an intelligible image, but only apparently comparable to a photograph.

As far as the phase component of the signal is concerned, it should be noted that during transmission, the microwaves in the radar beam depart from the antenna aligned in space and time, i.e. they depart 'in phase'. The phase component of a SAR image appears as an unintelligible image, resembling the so-called 'television snow' effect, but in reality it contains measurements of how much the received echo waves have gone 'out of phase' after interacting with the scattering elements constituting the scene. Phase is in fact associated with target distance, but is not immediately readable due to the fact that it is ambiguous in intervals of 2π. This information is of considerable interest, since phase differences between different channels or different acquisitions can provide information on numerous physical characteristics of the scanned scene, including data about its geometry.

Both components of a complex image do not correspond to a geographical or cartographic projection but are mapped on a virtual plane, according to an acquisition geometry radically different from photography and involving rollover operations as well as projection and sectioning. This is because the radar measures distances along a direction inclined with respect to the vertical. This operation must necessarily be performed from a lateral position and an oblique orientation in relation to the scene, in order to avoid ambiguities during the interpretation of return signals.

Within certain limits, the geomorphic and radiometric distortions to which SLCs are subject can be corrected, as long as information about the topographic configuration of the scanned area is already available.

The greatest potential of SAR sensors, however, lies in multichannel techniques, where several scans of the same area are used together. The three main SAR multichannel approaches are polarimetry, interferometry, and tomography.

Polarimetry is based on the fact that microwaves and radio waves in general can be polarised. A transmitted radar pulse can be horizontally polarised or vertically polarised: horizontally polarised waves travel parallel to the surface of Earth; vertically polarised waves travel perpendicular to the surface of Earth. At the same time, the radar can be configured to measure only the horizontally polarised or vertically polarised portion of the echo. The polarisation of the backscatter from a target depends on the geometry of the target. For example, for a backscatter signal with a large horizontally polarised portion, there is a high chance that the target has a predominantly horizontal geometric configuration. Thus, the difference in phase angle between the different polarisations may also facilitate a classification of the detected features into categories of geometric configurations.

In SAR interferometry, a minimum of two images of the same area are scanned while calculating the phase angle difference for each detected point. If the distance between the sensor and the body was different between the scans associated with the two images, the difference will cause a phase shift. This occurs both when the kinematic configuration of the radar changes between the two images, but also when the kinematic configuration of the surveyed terrain changes. A change in phase equal to one revolution angle (360°) or a multiple thereof, however, is indistinguishable from the absence of phase shift. For this reason, direct measurement is only possible for small changes in the radar-target distance, while larger variations require additional operations to resolve this ambiguity.

There are two main application modes of interferometry:

- In across-track interferometry, two passes are made with a SAR device along slightly different paths. The recorded phase differences can be used to construct a Digital Elevation Model (DEM).
- In differential interferometry, the two passes are taken at different time instants and can be used to accurately study and measure the elevation changes in the scanned surface that occurred in the time interval between the two surveys[4].

In SAR tomography, many scans of the same territory area (which may also have been taken diachronically) are used, all acquired from different trajectories, at different locations and in a quantity that must be in the tens. With an automated process, it is possible to order and interrelate the SLCs derived from these surveys, in order to then generate tomographies of the portion of territory under examination and, finally, reconstruct a three-dimensional model from these sections. Similarly to interferometry, SAR tomography also makes it possible to study and measure the displacements of backscatterers that occur between one survey and the next[5].

The periodic nature of SAR remote-sensing from satellite platforms, combined with the independence of radar illumination from other sources (such as the sun) and the relative insignificance of atmospheric agents to a considerable range of microwaves, cyclically generates a useful data set that is archived by national and international space agencies. In addition to secreted data and privately purchasable data, some space agencies provide their SAR products free of charge to scientific institutions or even release them into the public domain[6].

Among the various, numerous fields of application (environmental monitoring, space exploration, civil protection, etc.), the use of imagery and multi-channel techniques associated with SAR is finding use in different types of survey activities, for example:

- in cartographic modelling[7];
- in preliminary investigations for archaeological surveys[8];
- in non-invasive structural surveys, mainly of civil works such as bridges and viaducts[9] but recently also of historic buildings[10].

Remote-sensing by means of SAR encompasses several potentials for integrated land and architectural surveying. As aerospace projects for Earth observation by means of SAR increase, the likelihood of a given site being scanned from new angles and with a greater variety of frequency bands increases. The global coverage of satellite radars also allows data to be obtained on difficult-to-access and inaccessible areas, such as cliffs, overhangs and rocky coastlines. Digital archives of space missions make it possible to compare scans made over a particular area over the years.

Among the most significant examples of this type of use is the Horizon 2020 Project 'HERACLES: Heritage Resilience Against Climate Events on Site', which made use of data from the COSMO-SkyMed mission of the Italian Space Agency (Agenzia Spaziale Italiana – ASI). This initiative focused on the monitoring of historical architectural heritage in the context of climate change and integrated surveys aimed not at representation, but at conservation and restoration [11].

The purpose of this research was therefore to verify the usefulness of collecting and processing radar images within integrated surveys dedicated to representation. The information obtainable through these devices can support other direct and indirect surveying techniques within an integrated survey. Three objectives were set:

1. To critically discuss radar technologies for recording images and geometric data, in order to then select the most suitable ones for Landscape and Architectural Surveying purposes and, therefore, to identify applications in relation to the different dimensional scales.
2. Having chosen two case studies, to support established direct and indirect survey methods with an elaboration of SAR images acquired by satellite radar sensors. In addition to verifying the actual usefulness and accuracy of radar-derived information, we assessed the importance of the role of these data within our applications.
3. To examine the procedures for generating, processing and correcting radar images from the point of view of Architectural Drawing, and to study suitable representative systems for returning the data obtained.

On the one hand, therefore, the research dissected the literature on imaging radars (in particular satellite SARs), analysing their acquisition and processing techniques from the point of view of descriptive geometry and graphic communication.

On the other hand, integrated surveys were conducted on two sites belonging to the territories of the former State of the Presidi in Tuscany: the Spanish Fortress of Porto Santo Stefano in the municipality of Monte Argentario and Talamone Town Walls in the municipality of Orbetello. In addition to standard direct, topographic, and instrumental survey methods – LIght Detection And Ranging (LIDAR) acquisitions from a terrestrial laser scanner and from aircrafts, Structure from Motion (SfM) photomodelling –, products obtained from COSMO-SkyMed mission of ASI and TanDEM-X mission of the Deutsches Zentrum für Luft- und Raumfahrt e.V. (DLR) were collected and processed. Specifically, the products collected consist of 160 SLCs concerning the area of the Tuscan coastline and two DEM tiles concerning the territories belonging to the State of the Presidi. Thanks to the consultancy and processing techniques of the Institute for Electromagnetic Sensing of the Environment of the National Research Council (Istituto per il Rilevamento Elettromagnetico dell'Ambiente del Consiglio Nazionale delle Ricerche – IREA-CNR), four tomographic point clouds were obtained, which, in addition to providing information on the displacements of the two historical buildings that are the subjects of this study, were an aid in the process of integrating the radar data collected with conventional surveying techniques.

This work lasted approximately two years and consisted of fifteen stages:

1. The first stage, which took place between July 2021 and November 2021, focused on the preliminary definition of

the literature review and the formulation of initial methodological hypotheses. At the same time, research institutes dedicated to *surveying the environment using radar sensors were sought out.*

2. In the second stage, which took place between November 2021 and January 2022, contacts were established with Dr. Gianfranco Fornaro and Dr. Simona Verde at IREA-CNR. Through the co-supervision of Dr. Fornato and Dr. Verde it was possible to: begin a process of updating the literature review; choose ASI's COSMO-SkyMed mission as the source of the radar acquisitions to be used in the research; undertake an initial selection of case studies for the present research.
3. In the third stage, which took place between January 2022 and February 2022, the literature review was expanded through constant consultation with IREA-CNR and following the massive online open course 'Synthetic Aperture Radar: Hazards' by Prof. Franz J. Meyer of the University of Alaska Fairbanks. The shortlist of possible case studies for the research was narrowed down to three forts in the former Presidio State: Fort Filippo in Porto Ercole, in the municipality of Monte Argentario; the Spanish Fortress in Porto Santo Stefano, in the municipality of Monte Argentario; the Aldobrandesque Fortress of Talamone, in the municipality of Orbetello.
4. In the fourth stage, which took place between March 2022 and May 2022, the literature review was further integrated by following Planetek Italia s.r.l.'s telematics training courses. Moreover, thanks to the support of Dr. Simona Verde of IREA-CNR, it was possible to identify 160 SLCs of the COSMO-SkyMed mission to be requested from ASI, in order to build SAR tomographic clouds to be integrated with standard survey techniques. In addition to submitting the request for these SLCs to ASI, an information technology system was set up for the delivery of these complex images and for data interchange with IREA-CNR. A preliminary inspection was also carried out at the forts considered in the third stage.
5. In the fifth stage, which took place between May 2022 and July 2022, ASI approved the research proposal regarding this thesis. A second survey was carried out at the Spanish Fortress in Porto Santo Stefano, followed by a first survey campaign using a terrestrial laser scanner (LIDAR), in which 48 point clouds were acquired.
6. The sixth stage, which took place between 4 July and 7 July 2022, focused on a further expansion of the literature review by attending the Fraunhofer Institute for High Frequency Physics and Radar Techniques FHR's '13th International Summer School on Radar/SAR'.
7. During the seventh stage, which took place between July 2022 and September 2022, the delivery of SLCs by ASI was completed. Two DEMs useful for research were also identified, which were recorded during TanDEM-X mission of DLR and had a ground resolution of 12m. Digital Terrain Models (DTMs) and point clouds obtained through aircraft LIDAR scans with a ground resolution of 2 m, carried out during the 2008-2009 Extraordinary Remote Sensing Plan (Piano Straordinario di Telerilevamento Ambientale – PST-A), were also selected from the National Geoportal of the Italian Ministry of the Environment. Following considerations on the research schedule, the size of the buildings, and the time required for survey operations, the list of case studies was reduced to the Spanish Fortress of Porto Santo Stefano and the Aldobrandesque Fortress of Talamone.
8. In the eighth stage, which took place between September 2022 and November 2022, new survey campaigns with terrestrial laser scanners (LIDAR) were carried out at the Spanish Fortress in Porto Santo Stefano and the Aldobrandesque Fortress in Talamone. With regard to the Spanish Fortress, 69 point clouds were then aligned. The delivery of DTMs and LIDAR point clouds from aircraft by the Italian Ministry of the Environment was also completed.
9. In the ninth stage, which took place between November 2022 and March 2023, the research proposal for the two DEMs of the TanDEM-X mission identified in the seventh stage was submitted to DLR. An initial processing of the 160 SLCs of the COSMO-SkyMed mission into tomographic clouds was started by IREA-CNR, through the use of NASADEM (with a ground resolution of 30 m). A telematic training course for Unmanned Aerial Vehicles (UAV) pilots was also completed, aimed at obtaining the skills to carry out an SfM survey of Talamone Town Walls as a whole (instead of just the Aldobrandesque Fortress).

10. In the tenth stage, which took place between March 2023 and April 2023, the first SfM survey campaigns of Talamone Town Walls were carried out and the LIDAR point clouds were merged.
11. In the eleventh stage, which took place between April 2023 and May 2023, the SfM survey campaigns of Talamone Town Walls continued. The processing of the first tomographic clouds with NASADEM was completed by IREA-CNR. In addition, the LIDAR point clouds of the Italian Ministry of the Environment were converted from a system of geographic coordinates and ellipsoid height (EPSG: 6706) to a reference system of cartographic coordinates and geoid height (EPSG: 6707). In addition, the LIDAR point cloud alignment operation continued for the Spanish Fortress of Porto Santo Stefano and the processing of data about Talamone Town Walls, acquired with UAVs, began.
12. In the twelfth stage, which took place between May 2023 and June 2023, the SfM survey campaigns of Talamone Town Walls were continued. The application for the two DEM tiles of TanDEM-X mission was approved by DLR. One of the DEM tiles in question was then forwarded to IREA-CNR for the processing of a second set of tomographic clouds. In the meantime, the operation of alignment of the LIDAR point clouds for the Spanish Fortress of Porto Santo Stefano and the processing of data about Talamone Town Walls, acquired with UAVs, continued.
13. In the thirteenth stage, which took place between June 2023 and July 2023, survey operations were completed at both the Spanish Fortress of Porto Santo Stefano and Talamone City Walls. IREA-CNR completed the processing of the second set of tomographic clouds obtained through the use of the DEM from TanDEM-X mission. The operation of integrating the data obtained through acquisitions and processing with satellite radar with the data collected through standard survey techniques therefore begun. The drafting of this text also begun.
14. In the fourteenth stage, which took place between July 2023 and August 2023, the integration of the acquired data continued and the writing of the text of this doctoral thesis continued, especially with regard to Chapters 1 and 2.
15. In the fifteenth phase, which took place between September 2023 and October 2023, the data graphic renstitution took place. In addition, drafting, revision and layout of this PhD thesis were completed.

Notes

1. Skolnik 1981, p. 2.
2. Skolnik 1990, p. 1.1.
3. Skolnik 1981, pp. 8-13.
4. Ager 2013, pp. 21-25; Moreira, Prats-Iraola, Younis, Krieger, Hajnsek, Papathanassiou 2013, pp. 16-30.
5. Moreira, Prats-Iraola, Younis, Krieger, Hajnsek, Papathanassiou 2013, pp. 30-32.
6. Planetek Italia 2022.
7. Strozzi, Werner, Wiesmann, Wegmüller 2012, pp. 277-281.
8. Lasaponara, Masini, Pecci, Perciante, Pozzi Escot, Rizzo, Scavone, Sileo 2016, pp. 55-62.
9. Fornaro, Reale, Verde 2013, pp. 677-681.
10. Kavoulaki, Psaroudaki, Politaki, Lortal, Katsaveli, Pangalou, Pouli, Demadis, Grammatikakis, Eriksson, Soldovieri, Padeletti, 2017, pp. 96-97.
11. Kavoulaki, Psaroudaki, Politaki, Lortal, Katsaveli, Pangalou, Pouli, Demadis, Grammatikakis, Eriksson, Soldovieri, Padeletti, 2017, pp. 39-44.

Sintesi

Tra le loro varie applicazioni, i radar sono usati anche come tecnologia attiva di mappatura grafica, nella quale impulsi di energia a microonde vengono emessi da un'antenna e i riflessi dati da i corpi in grado di interagire con questo segnale vengono ricevuti dalla stessa antenna o da altre antenne, per poi essere codificati in immagini. Lo strumento misura le caratteristiche degli echi, incluso il tempo di andata e ritorno dall'antenna alla scena e viceversa, la forza della riflessione e la fase di ritorno dell'onda. La distanza tra sensore e bersaglio è data dal prodotto della velocità dell'impulso, pari alla velocità della luce, per il tempo di andata e ritorno diviso due. Uno degli attributi più importanti dei radar sussiste nella capacità di generare autonomamente la propria illuminazione in quanto sensori attivi. Inoltre, le lunghezze d'onda relativamente lunghe dei segnali a microonde possono penetrare nubi, polveri e persino la cenere vulcanica, permettendo anche di mappare immagini indipendentemente dalla maggior parte delle condizioni meteorologiche.

La distanza indebolisce l'intensità dei segnali che ritornano dai corpi ai radar e può aumentare il rumore dell'immagine registrata. Di conseguenza, per effettuare il telerilevamento con un Radar ad Apertura Reale è necessario utilizzare un'antenna molto lunga. Una particolare tecnica chiamata Radar ad Apertura Sintetica migliora la risoluzione senza utilizzare antenne estremamente lunghe.

I dati acquisiti con un sensore radar ad apertura sintetica sono caratterizzati da due componenti, una associata all'intensità dell'eco ricevuta e una associata alla fase di quest'ultima, le quali vanno a costituire le cosiddette immagini complesse, mappate su un piano virtuale.

Le maggiori potenzialità dei sensori radar ad apertura sintetica risiedono nelle tecniche multicanale: polarimetria, interferometria e tomografia.

Un impulso radar trasmesso può essere polarizzato orizzontalmente o verticalmente: le onde polarizzate orizzontalmente viaggiano parallelamente alla superficie della Terra; le onde polarizzate verticalmente viaggiano perpendicolarmente alla superficie della Terra. Allo stesso tempo, il radar può essere configurato per misurare solo la porzione di eco polarizzata orizzontalmente o verticalmente. La differenza dell'angolo di fase tra le diverse polarizzazioni può agevolare una suddivisione dei corpi rilevati per categorie di configurazioni geometriche.

Nell'interferometria radar ad apertura sintetica si scandiscono un minimo di due immagini della stessa porzione di territorio, calcolando la differenza dell'angolo di fase per ciascun punto rilevato. Se la distanza tra il sensore e il corpo è stata differente tra le scansioni associate alle due immagini, la differenza causerà uno scostamento di fase. Esistono due modalità applicative principali dell'interferometria: l'interferometria trasversale eseguita contemporaneamente da più punti su un piano trasversale alla traiettoria della piattaforma, attuata dunque da percorsi leggermente differenti; l'interferometria differenziale attuata da istanti temporali differenti.

Nella tomografia radar ad apertura sintetica vengono adoperate molte scansioni dello stesso ambito territoriale, tutte eseguite da traiettorie e giaciture differenti, in istanti diversi e in una quantità che dev'essere nell'ordine delle decine. Con un processo automatizzato, è possibile ordinare e interrelare fra loro le immagini complesse derivate da tali rilevamenti, per poi generare delle tomografie della porzione di territorio in esame e, infine, ricostruire da tali sezioni un modello tridimensionale.

All'aumentare dei progetti aerospaziali per l'osservazione della Terra mediante radar ad apertura sintetica, si accrescono le probabilità che un dato sito venga scandito da nuove angolazioni e con una maggior varietà di bande di frequenza. La copertura globale dei radar satellitari permette inoltre di ottenere dati anche sulle aree difficilmente accessibili e gli ambiti impervi, come i dirupi, gli strapiombi e le coste rocciose.

La finalità del presente lavoro è consistita quindi nel verificare l'utilità della registrazione e dell'elaborazione di immagini radar all'interno di rilievi integrati dedicati alla rappresentazione.

Da un lato, quindi, la ricerca ha sviscerato lo stato dell'arte sui radar per la generazione di immagini, analizzandone i processi di acquisizione ed elaborazione sotto il profilo della geometria descrittiva e della comunicazione grafica. Dall'altro, sono stati condotti dei rilievi integrati su due temi appartenenti ai territori dello storico Stato dei Presìdi toscani: la Fortezza spagnola di Porto Santo Stefano e la Cinta muraria di Talamone. In aggiunta ai metodi standard di rilevamento diretto, topografico e strumentale, sono stati raccolti ed elaborati prodotti radar che, grazie alla consulenza e alle elaborazioni dell'IREA-CNR, hanno dato origine a nuvole di punti tomografiche ausiliarie.

Luca Martelli

1. Mathematical and geometrical foundations of radar operation

1.1 Determination of geometric data about targets

To understand how radars detect objects in space and provide information about sensed bodies, it is appropriate to dwell very briefly on the components common to all these instruments (fig. 1.1). Essentially, a radar system needs the following parts[1]:

- an antenna for transmission, fixed or mobile, emitting electromagnetic radiation generated by an oscillator of some kind;
- an antenna for reception, also fixed or mobile. The functions of transmission and reception can also be performed by the same antenna thanks to a possible duplexer, which will intervene each time the radar switches from a transmission event to a reception event and vice versa: in this case we will speak of a monostatic radar. In bistatic radars there is one antenna for transmission and one for reception. In multistatic radars, there is one antenna for transmission and several antennas for reception;
- an energy detector or receiver.

A portion of the transmitted signal is intercepted by one or more reflective objects (the targets) and re-radiated in all directions. This re-radiated energy is of primary interest for radar operation. In fact, the receiving antenna picks up the returned energy and channels it into the receiver, where it is analysed to detect the presence of the target and derive its position in space, as well as its relative speed. The nature of this echo signal thus provides information about the detected object.

In fact, by measuring the time it takes for the radiated energy to travel to the target and return, it is possible to calculate the range of the target to the sensor.

In addition, the use of a directive antenna (an antenna with a narrow beamwidth) to detect the angle of arrival of the echo signal makes it possible to determine the positioning angle of the target with respect to the sensor.

Radars are able to detect the presence of objects in space and collect up-to-date information on some of their geometric and physical characteristics over an interval of time. For example, radars designed to continuously detect the movement of an object are also capable of continuously indicating the rate of change of its position. Under certain conditions, these devices can even derive the path (or trajectory) of the target and predict its next position[1].

If there is relative motion between the radar sensor and the target, the deviation in carrier frequency of the reflected wave (Doppler shift) is a measure of relative (radial) velocity and can be used to distinguish moving objects from stationary objects. The Doppler shift is the apparent deviation in frequency caused by relative motion between the source of a wave and a receiving apparatus (fig. 1.2). One of the best-known examples of this phenomenon is the whistle of a running train, whose constant pitch appears higher when the convoy approaches a stationary listener and lower when it moves away[2].

The deviation in the frequency of the return signal due to Doppler shift allows the discernment of moving targets of interest (such as an aircraft) from unwanted stationary targets (such terrestrial and marine background clutter). This applies even if the stationary return signal should be several orders of magnitude higher than that of the moving target. All radar echoes are certainly affected by Doppler shift and imaging radar systems are no exception. The Doppler shift represents precisely the frequency band that makes azimuth focusing possible. In fact, the final azimuth resolution is proportional to the inverse of the Doppler band.

It is also possible to consider the detection of an object independently from data collection about it, but practical applications where one wants to detect the presence of targets without having information about their positions in space and their characteristics are rather rare. Although the detection of a target can be considered as independent the extraction of data about it, there is a relationship between the two opera-

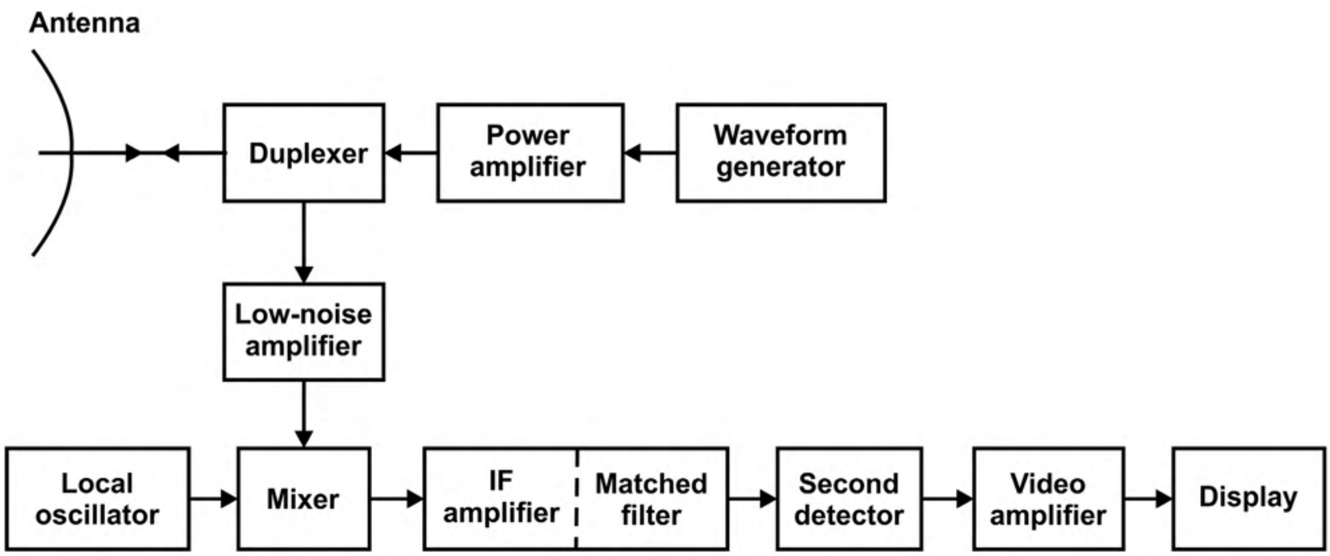

1.1/ Block diagram, according to Sklolnik 1990, of a simple example of a monostatic radar system, equipped with: a single antenna dedicated to both transmission and reception; a power amplifier transmitter; a superheterodyne receiver.

tions. The collection of useful information about the target is one of the most important utilities of radar systems and, in addition to the above-mentioned essential components, for optimal processing this operation requires the use of a matched filter or its equivalent. The data that can be acquired about an object is not only limited to the distance between it and the sensor. In fact, the more target information is known prior to radar detection operations, the more efficient object detection will be. We can refer to some elementary examples: when the position of the target in space is already known, the antenna can be directly pointed in the appropriate direction, saving time or energy that would otherwise be consumed in scanning empty spaces;
when the relative velocity of the target is known, the receiver can be pretuned to the optimal reception frequency, avoiding the search for the frequency band on which the Doppler shift might occur.
Most common radar systems are capable of providing the position of a target along its range direction and azimuth direction. The rate of change of the target position can also be measured by the variations, along the passage of time, in the values of its range and its angle with respect to the sensor, thus allowing it to be tracked. Indeed, in many radar applications, one cannot claim to have detected a target until its spatial tracking has been performed.
Resolution is the parameter that defines the quality of the radar, whether it is for detection or remote-sensing. The definition of resolution, in the broadest sense, is the level at which a sensor can discern two closely spaced targets with similar properties (geometry, colour, speed, etc.).
However, angular resolution, a problematic subject for remote-sensing, is defined as the minimum angular separation between two bodies that can be distinguished by a sensor.
If equipped with sufficient resolution in one or more dimensions (relative to the distance between the scanned body and the sensor), a radar system can therefore detect the size and shape of a target. In the early years of development of radar imaging, however, these instruments failed to find application in remote-sensing at great distances. In fact, from a technological point of view, the construction of antennas large enough to guarantee an acceptable angular resolution (which can be azimuthal or angular in elevation), even from considerable distances, represented a great practical difficulty. The first imaging radars had azimuth resolutions of the order of hundreds of metres. Technological development gradually allowed this problem to be addressed, and then solved it effectively with

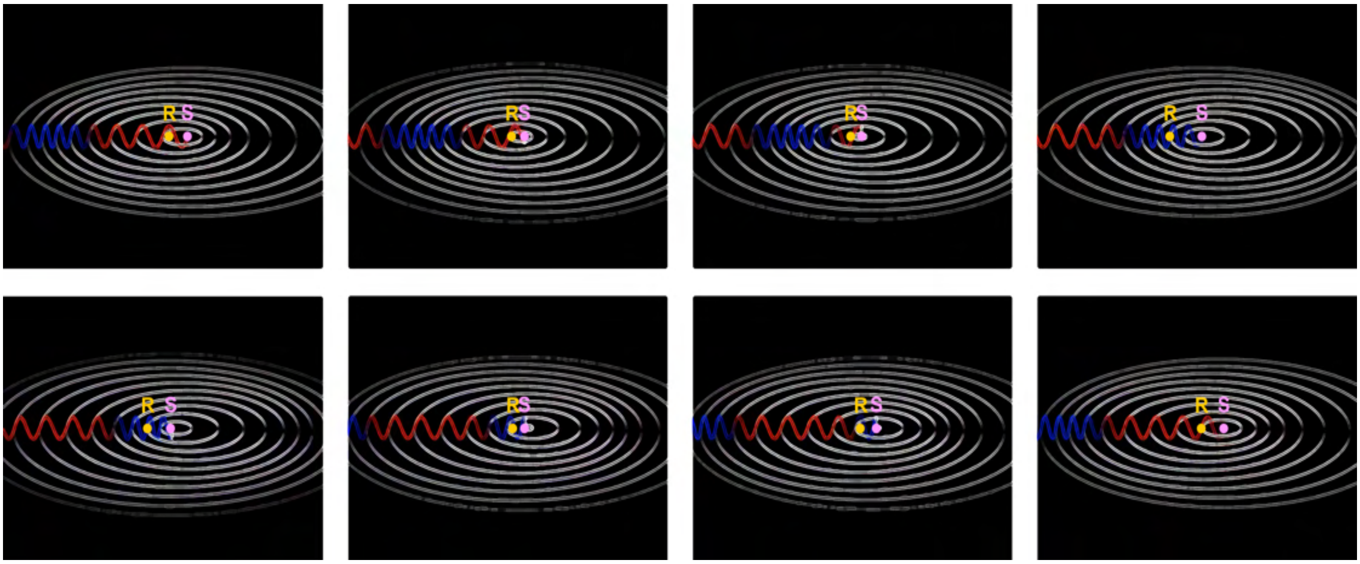

1.2/ Graphical exemplification, according to Gallis 2004, of the Doppler effect due to relative motion between the source of a wave and a receiving apparatus. In this example, relative harmonic motion exists between wave source S and receiver R. S radiates the waves with a constant frequency over time but, due to the relative displacement, the distance between S and R changes cyclically. Consequently, the time taken by each wave front to reach R also changes cyclically, causing an apparent frequency shift in the latter.

the introduction of Synthetic Aperture Radars (SAR)[3], which we will discuss later in Chapter 2.
The polarisation of radars, one of the multichannel processing techniques that we will review in Chapter 3, makes it possible to ascertain any symmetry conditions in a target.
In principle, a radar can also measure the roughness of a target surface and report some information about its dielectric properties. In fact, the way a microwave signal of wavelength λ interacts with a scattering medium (such as the Earth's surface or tree canopies that make up a forest) depends on the dielectric properties of that medium. These properties govern how much of the incoming radiation is scattered from the surface of the medium, how much signal penetrates into it, and how much energy is always dispersed into it by absorption.
Some of the geometric data obtainable from most radar systems regarding the targets they can detect are listed and briefly discussed below.

1.1.1 Range

Radar systems of current conception and good design can derive much more information from the signals reflected by bodies than just the distance between sensors and targets. However, measuring the latter remains one of the most important and characteristic functions of these instruments. The most commonly used radar waveform is a sequence of short, rectangular-shaped pulses, modulating a sinusoidal carrier wave. The shorter the pulses, the more accurate the measurement of the target's distance from the sensor. A short pulse has a wide spectral width (bandwidth).
Electromagnetic radiation is a form of energy with the properties of a wave. To illustrate the concept with a schematic analogy, electromagnetic waves propagate through time and space in a manner similar to the waves of an aquatic body (fig. 1.3) but, except for polarised light, they oscillate in all directions perpendicular to their direction of travel (the wave front of a transverse wave).
Such waves have two notable measurable characteristics (fig. 1.4): wavelength and frequency (or period). The wavelength λ is the distance between two successive crests. The frequency f is the number of oscillations (cycle) completed in a period of 1 s and is therefore expressed in cycles/s. The period T of the wave is related to the frequency f by the relation $T = 1/f$.

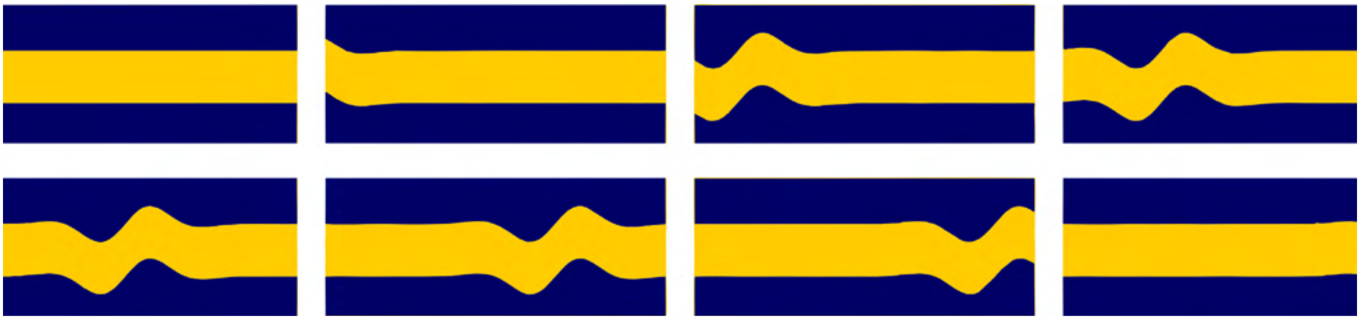

1.3/ Graphical illustration of the behaviour, in time and space, of a transverse wave front travelling through a medium. Source: Gallis 2004.

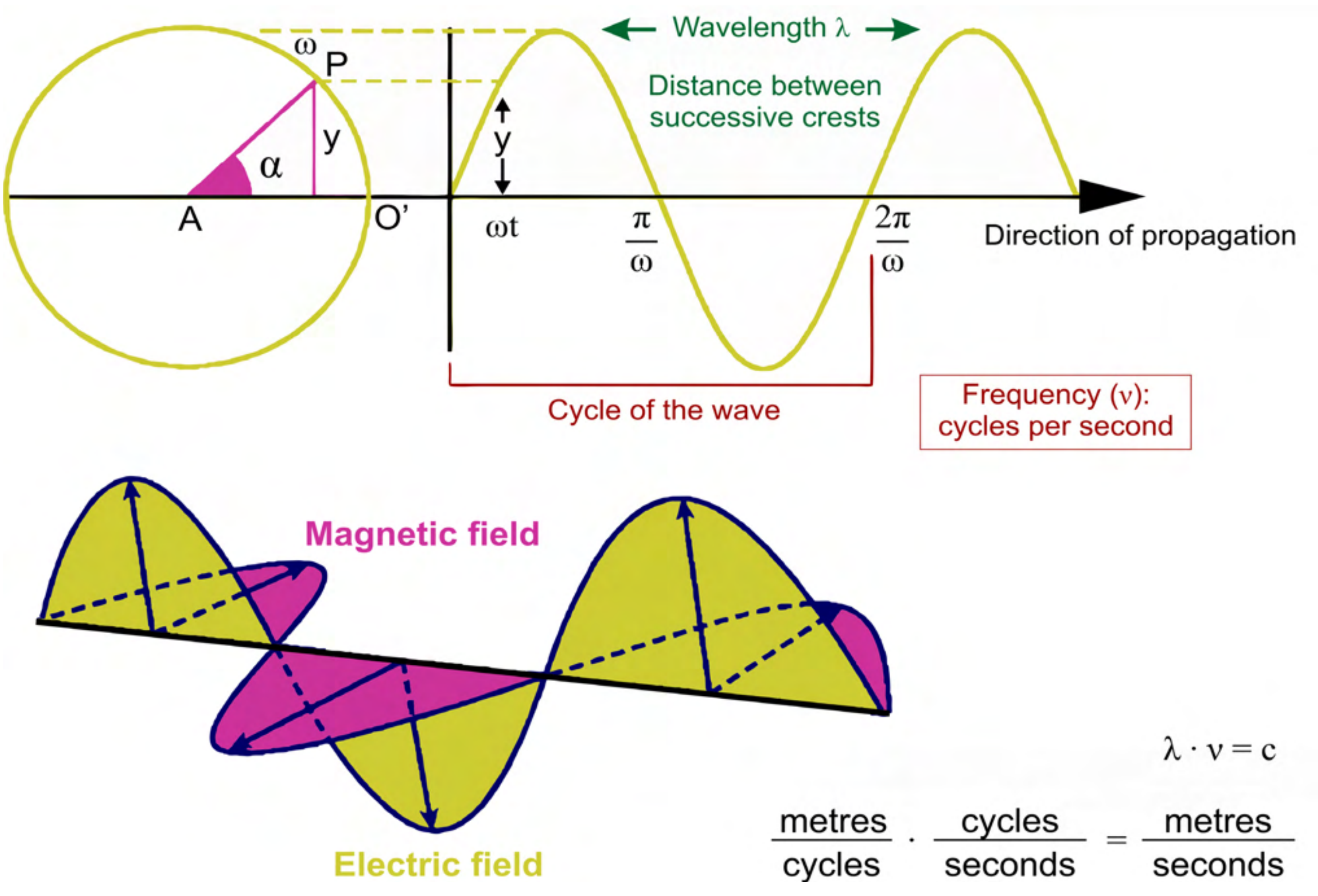

1.4/ Example of an electromagnetic wave, showing both magnetic and electric fields, together with wavelength and frequency definitions. Source: Emery, Camps 2017.

In vacuum, electromagnetic waves travel at a constant speed c, the speed of light (c = 299,792,458 m/s), the product of wavelength λ by frequency f, as written in Expression (1.1).

$$\lambda \cdot f = c \approx 300{,}000\ km/s \qquad (1.1)$$

The range R of the target from the sensor is determined by measuring the time TR taken by the pulse to reach the body and return to the system, as stated in Expression (1.2)

$$R = \frac{cT_R}{2} \qquad (1.2)$$

The factor 2 appears in the denominator due to the two-way propagation of the radar wave[4].
Once a pulse has been transmitted, sufficient time must pass before the system emits the next one for any echo to return and be correctly detected. Therefore, the rate at which pulses can be transmitted should be derived from the maximum distance at which possible targets are expected to be found. Should the pulse repetition rate be too high, echoes from some targets may arrive after the next pulse has been transmitted, causing ambiguity in the distance measurement. Simply put, the echo from the furthest expected target must arrive before the transmission of the next pulse. The farthest target is determined by the footprint of the antenna beam on the ground Echoes abnormally picked up by the radar after the transmission of the pulse following the one that generated them are called unwanted second-time-around echoes. Echoes picked up with a delay of several transmission/reception cycles relative to the pulse that generated them are called multiple-time-around echoes. The bodies associated with unwanted second-time-around and multiple-time-around echoes are interpreted as being much less distant from the sensor than in reality, thus compromising detection.
The range beyond which targets return unwanted second-time-around echoes is called the maximum unambiguous range Runamb and is stated in Expression (1.3).

$$R_{unamb} = \frac{c}{2 \cdot PRF} \qquad (1.3)$$

where PRF = Pulse Repetition Frequency (PRF), expressed in Hz.
If the maximum unambiguous range Runamb is interpreted as a function of PRF, it is possible to plot a graph (fig. 8).

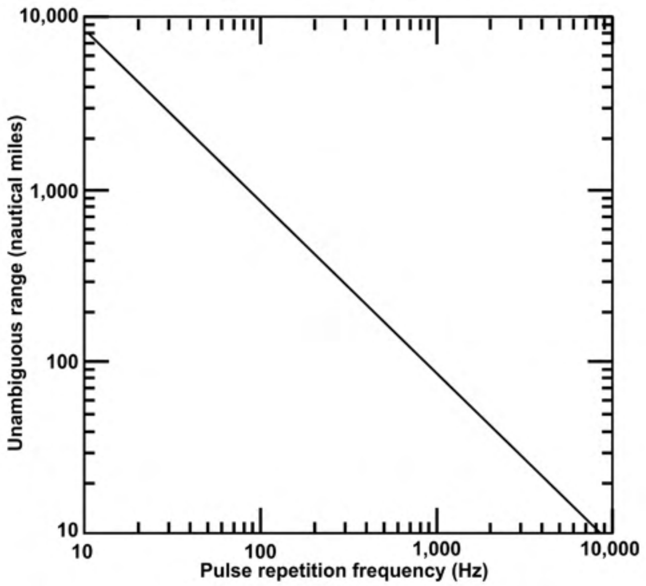

7/ Diagram, according to Skolnik 1981, of the maximum unambiguous range Runamb as a function of thePulse Repetition Frequency (PRF).

A radar, therefore, measures the distances to all bodies that are included in its Field of View (FOV) and whose backscattered signal is detectable, i.e. greater than the noise inevitably produced by the device during its operation. The system can distinguish two targets if the distance between them is greater than the range resolution[5].
If we consider a situation where a radar must detect a large body, such as a building or bridge, the range resolution determines ability of the instrument to unambiguously sample different portions of the scanned structure as distinct elements. A regular sampling of the structure to be surveyed is achieved by acquiring a range profile, where the corresponding spatial unit is called radar bin.
A range profile is the amplitude diagram of the return signal, represented as a function of the range of the detected backscatterers (figg. 9, 10). In this diagram the ordinates are expressed in decibels, while the abscissae can be expressed in radar bins or in equivalent distance equivalent distance, which can be obtained by multiplying the rank of the bins by range resolution, as stated in Expression (1.4).

$$distance = N_{bin} \times range\ resolution \qquad (1.4)$$

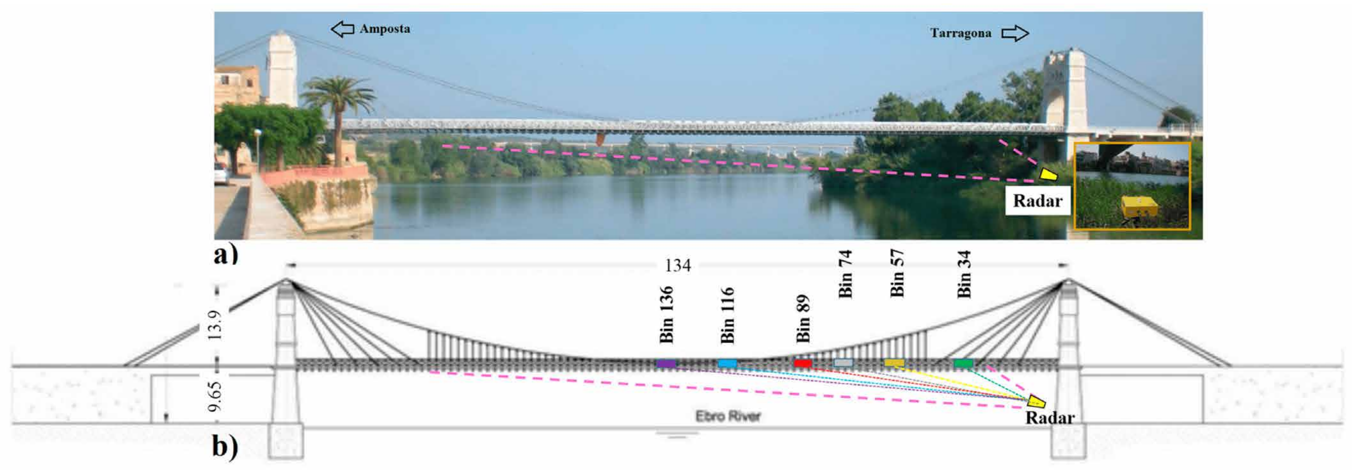

1.6/ Example of an interferometric radar scan on a civil structure, with the objective of detecting the displacements of a bridge deck. The object of the survey is a cable-suspended bridge over the River Ebro, near the town of Amposta, Catalonia. (a) Photograph of the Amposta bridge with an approximate indication (dotted pink lines) of the section illuminated by the sensor during the scan. A photo of the interferometer used, taken during the acquisition, is shown in the box at the bottom right of the figure. (b) Elevation of the deck with the radar bins selected to estimate deck deflections shown above. Source: Luzi, Crosetto, Fernández 2017 / licensed under CC BY 4.0 (http://creativecommons.org/licenses/by/4.0/). © 2017 by Luzi, Crosetto, Fernández. Licensee MDPI, Basel, Switzerland.

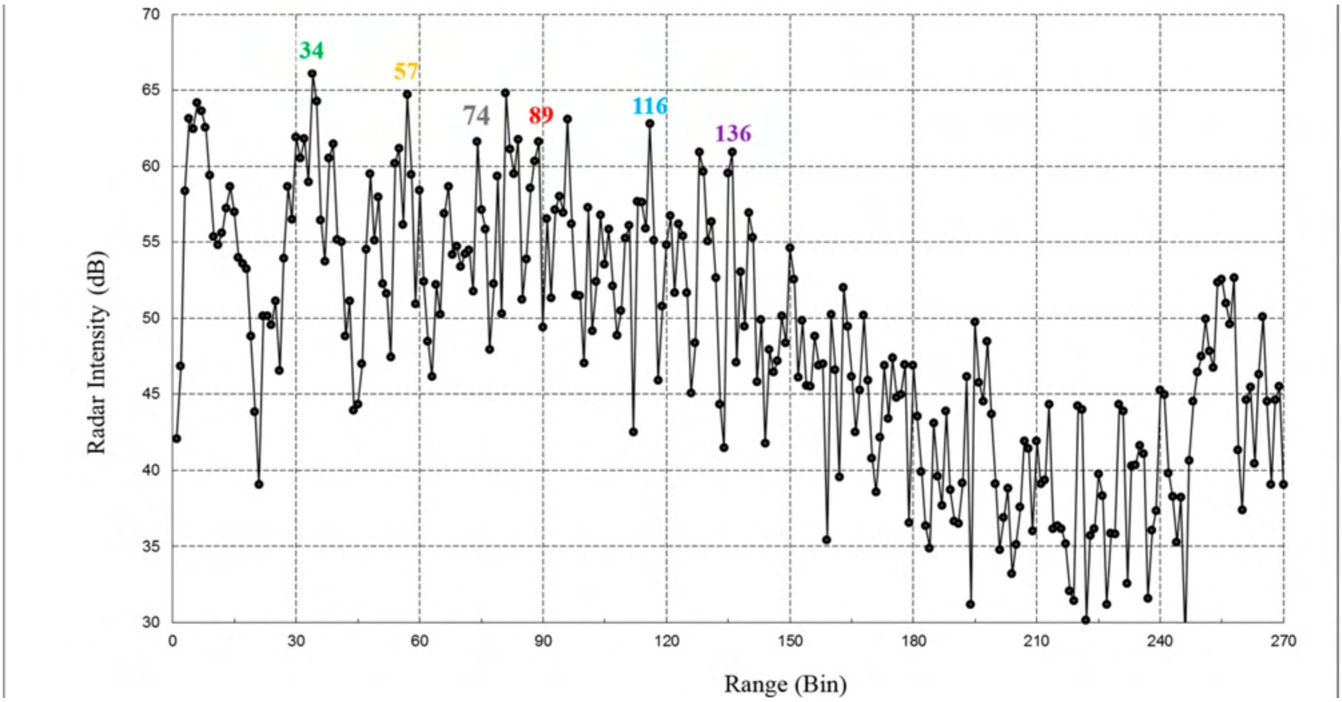

1.7/ Range profile obtained from interferometric radar scanning of the Amposta bridge (fig. 1.6). The ordinates correspond to the amplitude of the received radar echo, which is represented as a function of the radial range of the detected targets. The abscissae are expressed in radar bins, each corresponding to 0.5 m range resolution. The coloured numbers indicate the bins selected to estimate the deflections in the bridge deck. Source: Luzi, Crosetto, Fernández 2017 / licensed under CC BY 4.0 (http://creativecommons.org/licenses/by/4.0/). © 2017 by Luzi, Crosetto, Fernández. Licensee MDPI, Basel, Switzerland.

Particularly prominent peaks in the range profile correspond to the portions of the structure characterised by the best reflection. The location and size of the bins is governed by the FOV of the transmitting and receiving antennas and the range resolution. The signals received by the instrument are split into a sequence of bins, based on the return time of the transmitted signal, which is proportional to the distance between the sensor and the body. By controlling the strength of the signal received in each bin, the system can split the echoes between the different bins, corresponding to the different ranges. Radars can perform this operation while scanning at the required azimuth and elevation angles. More bins allow more accurate estimates of ranges. A pulse of short duration could be detected and mapped in only one or two bins associated with the range bins, rather than being distributed over many bins. However, a pulse of longer or wider duration allows more energy to be transmitted and gives the receiver more time to integrate the energy, allowing it to detect detect bodies at greater distances[6].

To ensure fine range resolution and long range detection, radars perform an operation called pulse compression. The most commonly used signal for a generic radar system is a simple pulse modulated waveform, however other types of modulation can also be used. In fact, the carrier wave of the pulse can be frequency modulated or phase modulated, allowing the echoes to be compressed in time after reception. This results in the benefits of high range-resolution, without the need for a short pulse. By passing through a matched filter, the output becomes a compressed pulse, whose duration corresponds approximately to the reciprocal of the spectral amplitude of the modulated long pulse. Thus, pulse compression enables the resolution of a short pulse (wide-bandwidth) to be achieved by using the energy of a long pulse.

Continuous waveforms (CWs) with phase or frequency modulation can also be used to accurately measure the range between the sensor and a body. It is also possible to measure the range of a single target by comparing the phase difference between two or more frequencies of this type of waveform. Another application of modulated CWs is their use to distinguish the return signal from the transmitted signal and to discern target echoes of interest from stationary clutter by taking advantage of Doppler frequency shift.

On the other hand, unmodulated CWs do not allow ranges to be measured directly. In this case, however, it is still possible to measure the latter by applying both frequency modulation and phase modulation.

The measurement of range with CWs is widely used in aircraft radar altimeters and various sensing instruments[7].

1.1.2 Radial velocity

Radial velocity. Through successive measurements of the range, the radial velocity of the target relative to the sensor can be derived. The Doppler frequency shift of the echo returned by a moving body also allows a radial velocity measurement. However, in many radars the recognition of Doppler frequency is highly ambiguous, thus reducing its usefulness as a radial velocity measurement tool. When practicable, it is often preferred over successive distance measurements along range direction, as it can achieve a more accurate figure in a shorter time interval. Any measurement of a velocity, whether by range or Doppler frequency shift, must be made within a certain time interval. The longer the scan time, the more accurate the velocity measurement can be. In addition, a longer scan tends to let the radar signal prevail over the noise, which favours the accuracy of the measured data.

Although the Doppler frequency shift is used to measure radial velocity in some very different applications (such as speed cameras and satellite radars for surveillance), it is much more widely used as a basis for distinguishing moving targets from stationary clutter echoes[8].

1.1.3 Direction angles

The target direction with respect to the orientation of the

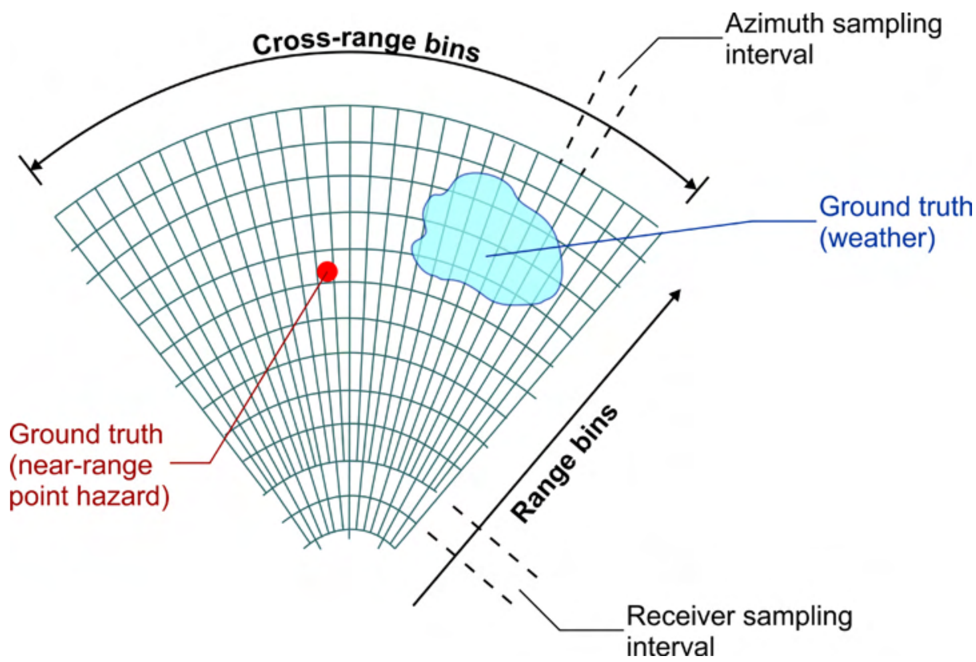

1.8/ Graphical exemplification of a case of dividing the FOV into range bins and cross-range bins. Note the degradation of azimuth resolution, proportional to the angular difference with the angle-off-boresight. Source: Zhang Yan, Li Zhengzheng, Cheong Boonleng, Cai Jingxiao, Ramesh Nepal, Suarez Hernan, Blake William, Andrews Joel, Yong Teoh, 2013.

radar sensor is derived by detecting the angles from which the return wavefront originates. Usually, this is done with a directive antenna with a narrow radiation pattern. In fact, assuming that the atmosphere does not disrupt the straight-line propagation of electromagnetic waves, the Line Of Sight (LOS) direction of the antenna corresponds to the direction of the target when the picked-up signal is at its maximum intensity. This hypothesis of no alteration on the return signal attributable to atmospheric phenomena must also be taken into account for other methods of measuring target angles.
Another method for determining the direction of the incident waveform is to measure the phase difference between two separate receiving antennas, as is done with the radar interferometry technique.
Signal phase-comparison with monopulse radars is also based on measuring the phase of the signals of two separate antennas. The signal amplitude-comparison with a monopulse radar, on the other hand, determines the target direction by comparing the amplitudes of the echoes achieved by two divergent wave beams, but radiated by a single antenna.
If we adhere to the definition of a radar measurement as data obtained from the comparison of an echo with the outgoing signal that originated it, the angles of the incoming signal (also called, briefly, angles of arrival) do not strictly constitute radar detection information in the same way as range and radial velocity. This is because, in principle, only the LOS needs to be considered to determine the target direction. Nevertheless, the measurement of target lying angles relative to sensor orientation is an integral part of most radar scanning operations.
The accuracy of the angle-of-arrival measurement depends on the size of the antenna aperture. The wider the antenna, the narrower the emitted beam width and thus the better the accuracy of the data[9].
As with range, the target direction angles are also subdivided by the system into azimuth azimuth radar bins and elevation elevation radar bins (fig. 11). The subdivision of the FOV of the RADAR into these angular bins, however, is not uniform,

unlike with range bins. Both azimuth angular resolution and elevation angular resolution, on the other hand, tend to maximise around the spatial units corresponding to the angles closest to the location of the boresight vector, i.e. with the bins closest to the axis along which the antenna radiates signal power at the highest possible level (often corresponding to the axis of symmetry of the antenna). Conversely, as the angular difference with the angle-off-boresight increases, azimuth resolution and angular resolution in elevation degrade proportionally.
Similar to the range profile, there is the cross-range profile, i.e. the diagram of the amplitude of the received signal represented as a function of azimuth[10].

1.1.4 Size

If the radar system has sufficient resolution, it can measure the extent or size of the target. For example, when the bodies to be detected are of the order of tens of metres in size, the resolution must be a few metres or less. Obtaining resolutions of this order of magnitude along the range is relatively simple, whereas, if we limit ourselves to conventional antennas and typical radar scanning ranges, angular resolution is severely disadvantaged.
However, by use of resolution in the Doppler frequency domain, it is possible to resolve the target along the directions transverse to the LOS (i.e. azimuth angle and elevation angle) with a definition comparable to that of the range direction. For this to happen, there must be relative motion between the constituent parts of the target and the radar sensor. This is the basis for the excellent azimuth resolution achievable with a Synthetic Aperture Radar (SAR), which utilises a relative motion between target and sensor, caused by the translation of the platform on which the latter is installed. In the Inverse Synthetic Aperture Radar (ISAR), on the other hand, the relative motion is given by the movement of the target[11].

1.1.5 Shape

A high-resolution radar, capable of obtaining the profile of a target either along the range direction or transverse to it (such as SAR and ISAR systems), also provides the size and shape of the target.
The shape of a body can also be obtained by means of tomography, in which a two-dimensional image of a three-dimensional object is reconstructed by measuring the signal size and amplitude at different scanning angles. In these applications, the sensor can rotate around an immobile object, or the radar system can be stationary while the object rotates around its own axis. With the coherent tomographic radar method, (which is a different technique from Synthetic Aperture Radar Tomography, illustrated and used later in this study) therefore, resolution along the range direction no longer plays a vital role in acquisition.
As mentioned earlier, a comparison of backscattered fields in different polarisations can yield quantitative data regarding possible symmetry conditions of targets. Since radars are active sensors that generate their own illumination source, they are among the few remote-sensing instruments that allow full control over the polarisation of the signal during both the emission path and the reception path, guaranteeing an application with maximum efficiency. Polarisation describes the orientation of the plane of oscillation of a propagating signal. In linearly polarised systems, the orientation of this plane of oscillation is constant along the propagation path of the electromagnetic wave (fig.12).
Harnessing the full potential of this technique requires the definition of a polarisation matrix from the following data: measurements of the phase and amplitude of the return signal in two mutually orthogonal polarisations, plus a cross-polarisation component. Theoretically, the data collected via the multi-channel polarisation analysis technique should allow bodies to be distinguished on the basis of their geometry but, from a practical point of view, this is not a simple operation.
A remarkable characteristic of the shape of any target is surface roughness. This feature can be of particular interest in land surveying because, for example, it changes according to the different echoes associated with different types of terrain[12].
Rough surface bodies scatter the incident electromagnetic energy in a diffuse manner; smooth surface bodies scatter the signal with a specular reflection. By studying the nature of the backscatter as a function of the incident angle, it is therefore possible to derive information on how rough the target surface is (fig. 1.10).
Surface roughness is a relative measurement parameter and depends on the wavelength of the illuminating signal. A surface that appears rough at a certain wavelength may appear smooth when illuminated with longer-wavelength radiation.

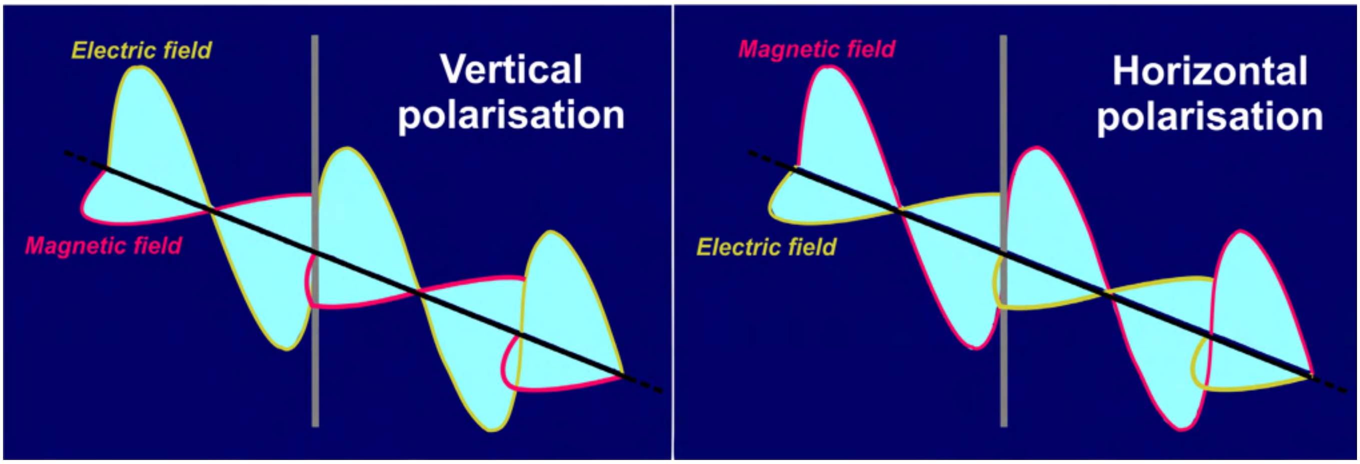

1.9/ Graphical illustration of the vertical and horizontal polarisation of an electromagnetic wave. Source: Ager 2013.

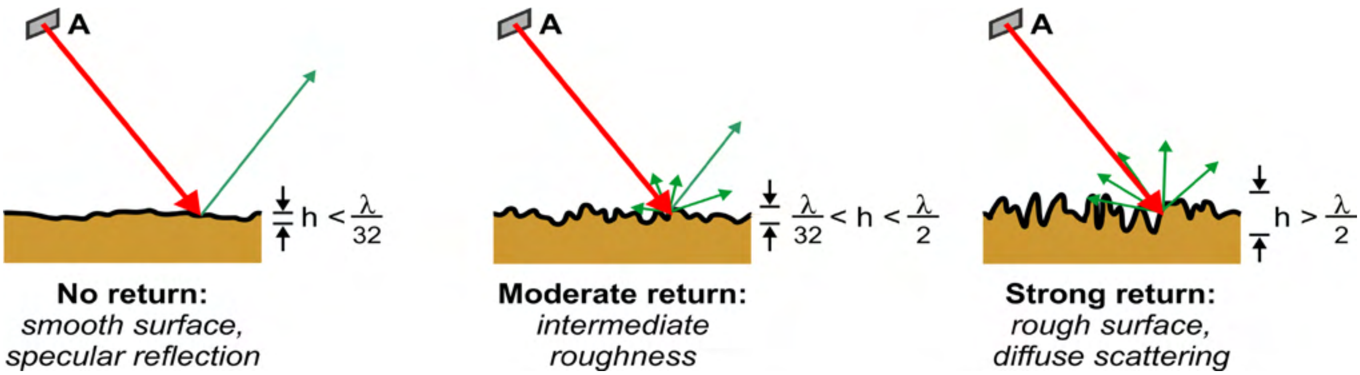

1.10/ Graphical exemplification of the relationship between the surface roughness of the target and the signal wavelength according to the Fraunhofer criterion: (a) smooth surface; (b) moderately rough surface; (c) considerably rough surface. Source: Meyer 2019.

Therefore, another method to quantify surface roughness is to vary the frequency of the illuminating radiation and observe the transition from specular scatter to diffuse scatter.
A direct method of obtaining roughness data is to study the scatter from a body, adopting a resolution that is appropriate to the body's roughness scale[13].

1.1.6 Other target measurements

Just as it is possible to determine the radial velocity of a body through Doppler shift, it is also possible to measure the tangential (cross-range) component of velocity of the target velocity vector. In fact, this can be derived from a spatial Doppler frequency shift, which expands or compresses the apparent antenna radiation pattern. This is similar to the phenomenon where the radial component of velocity can expand or compress the waveform of a radar signal reflected from a moving target over time, thus producing a temporal Doppler frequency shift. Tangential velocity detection requires a wide-baseline antenna, such as an interferometer.
Another useful set of information that can be collected by

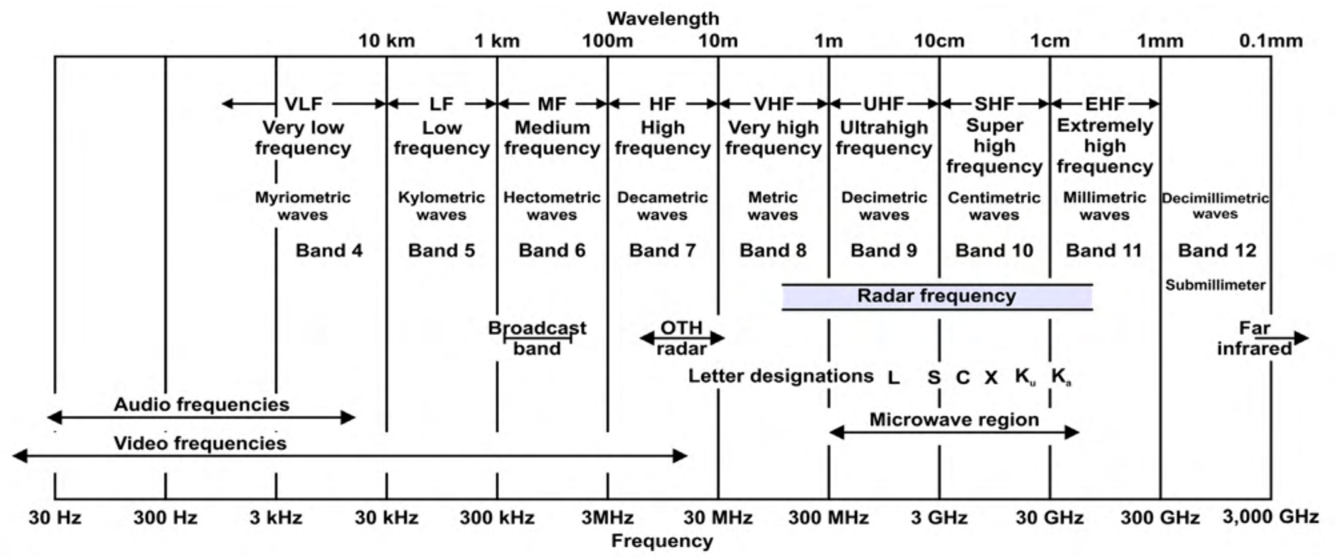

1.11/ Positioning, according to Skolnik 1981, of radar and microwave frequencies in the electromagnetic spectrum.

observing the variation in amplitude of the return signal over time concerns changes in the radial projection of a complex target. Usually, a change in the radial projection of a target is followed by a change in its equivalent Radar Cross Section (RCS) or radar signature σRCS. Assuming for simplicity that the radiation is isotropic, the equivalent RCS of a target is the ratio of the power density scattered back PRX at the radar receiver to the incident radar power density PTX per unit solid angle (referring to an equivalent sphere of radius r0) at the target, as stated in Expression (1.5).

$$\sigma_{RCS} = \lim_{r \to \infty} 4\pi \cdot r_0^2 \cdot \frac{P_{R_x}}{P_{T_x}} \qquad (1.5)$$

Furthermore, the RCS of the target depends not only on the frequency and polarisation of the waves transmitted by the antenna, but also on the form and composition of the target.

Finally, the vibrations to which a body is subjected can induce a distinctive modulation in the radar echo, which can be detected by a spectral analysis of the return signal[14].

1.2 Radar frequencies

To date, conventional radars have generally been designed to operate at a frequency range of approximately 220 MHz to 35 GHz. However, these thresholds are not to be considered categorical, as RADARs operating at frequencies outside this range can also be built (and have been built). Skywave Over-the-Horizon (OTH) radars can be set at frequencies below 4 or 5 MHz, and groundwave High-Frequency (HF) radars can go as low as 2 MHz; conversely, millimetre-wave radars capable of operating at 94 GHz have also been built.

We can therefore say that most radars operate using microwaves, albeit with some notable exceptions (fig. 1.11).

In telecommunications engineering, letter designations are used to indicate the general frequency band in which a radar sensor operates. Originally, the letters used to identify the bands (P, L, S, X and K) were introduced during World War II for reasons of military secrecy. Once the need for secrecy ceased to exist, the scientific community maintained the use of this nomenclature, but developed variations of it in relation to the disciplines related to the fields of application and identified, as new regions of the electromagnetic spectrum were introduced in radar operations, new bands with other letters and acronyms. An example of the slight alterations undergone is the renaming of the P-band, now known as the Ultra-High-Frequency (UHF) waveband[15].

Afterwards, this band classification was officially ratified by the Institute of Electrical and Electronics Engineers (IEEE) with the IEEE Std 521-1976[16] Standard, and was then uni-

INTERNATIONAL TABLE				
Band designation	**Nominal frequency range**	***Specific frequency ranges for radar based on ITU assignments (see NOTE 1 and NOTE2)***		
		Region 1	**Region 2**	**Region 3**
HF	3 MHz to 30 MHz	(NOTE 3)		
VHF	30 MHz to 300 MHz	None	138 MHz to 144 MHz 216 MHz-225 MHz (see Note 4)	223 MHz -230 MHz
UHF	300 MHz to 1000 MHz (Note 5)	420 MHz to 450 MHz (Note 4) 890 MHz to 942 MHz		
L	1 GHz to 2 GHz	1215 MHz to 1400 MHz		
S	2 GHz to 4 GHz	2300 MHz to 2500 MHz		
		2700 MHz to 3600 MHz	27000 MHz to 3700 MHz	
C	4 GHz to 8 GHz	4200 MHz to 4400 MHz (Note 6)		
		5250 MHz to 5850 MHz	5250 MHz to 5925 MHz	
X	8 GHz to 12 GHz	8.5 GHz to 10.68 GHz		
K_u	12 GHz to 18 GHz	13.4 GHz to 14 GHz		
		15.4 GHz to 17.7 GHz (Note 7)		
K	18 GHz to 27 GHz	24.05 GHz to 24.25 GHz	24.05 GHz to 24.25 GHz 24.65 GHz to 24.75 GHz (Note 8)	24.05 GHz to 24.25 GHz
K_a	27 GHz to 40 GHz	33.4 GHz to 36 GHz to 36 GHz		
V	40 GHz to 75 GHz	59 GHz to 64 GHz		
W	75 GHz to 300 GHz	76 GHz to 81 GHz		
		92 GHz to 100 GHz		
mm (Note 9)	110 GHz to 300 GHz	136 GHz to 148.5 GHz		
		151.5 GHz to 155.5 GHz		
		231.5 GHz to 235 GHz		
		238 GHz to 248 GHz (Note 10)		
THz	300 GHz to 1000 GHz	300 GHz to 3000 GHz		

Tab. 1.1. Standard RADAR-Frequency Letter-Band Nomenclature. Source: IEEE Std 521-2019 Standard[20].

versally used in radar applications. After a few intermediate steps over the years, consisting of IEEE Std 521-1984[17] and IEEE Std 521-2002[18], the IEEE Std 521-2019 Standard is currently in force (Table 1.1), which continues to consider almost the same band division system formalised in 1976, but with some modifications and additions concerning the lower frequencies[19]. Although other classification systems have been proposed over time, contemplating subdivisions of the electromagnetic spectrum into substantially different intervals, albeit always encoded with letters, none of these has met with the same success.

Identifying bands with letters and acronyms remains a conveniently telegraphic way of identifying the frequency range within which a radar system operates. At the same time, this

Band	Frequency Range (GHz)		Wavelength Range (cm)	
HF	0,003	0,03	10.000	1.000
VHF	0,03	0,3	1.000	100
UHF	0,3	1	100	30
L	1	2	30	15
S	2	4	15	7,5
C	4	8	7,5	3,75
X	8	12	3,75	2,5
K_u	12	18	2,5	1,67
K	18	27	1,67	1,11
K_a	27	40	1,11	0,75
V	40	75	0,75	0,40
W	75	110	0,40	0,27
mm	110	300	0,27	0,01
THz	300	1000	0,01	0,001

Tab. 1.2. Frequency and wavelength thresholds of radar bands identified by IEEE Std 521-2019 Standard[21]

nomenclature continues to be advantageous in the military field, as it can generically subsume within their band the frequencies on which a device is set, thus indicating its application characteristics without revealing its precise domain of operation. In this way, the exact limits of a radar frequency operating range can just be communicated when strictly necessary.

In practical terms, the actual extent of the bands represented by the letters and acronyms is managed by the International Telecommunications Union (ITU), which assigns specific frequency domains for radiolocation (radar) use according to geographical regions of application, called ITU Regions. ITU Regions are established by the ITU Agency through Regulations and, for some of the radar bands identified by IEEE Standards, the actual frequency ranges may vary from region to region.

For example, although the IEEE Std 521-2019 Standard identifies the nominal extent of the C-band as between 4 and 8 GHz, in practice it is considered that a C-band radar may operate in two sub-intervals: the first, common to all ITU Regions, is from 4,200 MHz to 4,400 MHz; the second is from 5,250 MHz to 5,850 MHz in ITU Region 1, but in the other two ITU Regions it ranges from 5,250 MHz to 5,925 MHz.

Although the identification of frequencies by numerical values is necessary to make accurate assessments, letter designations can be used when a more concise nomenclature is required[22].

Consistent with what was stated at the beginning of this Chapter, we can invert (1.1.) to derive the wavelength λ by dividing the speed of light c by the frequency f, which results in Expression (1.6).

$$\lambda = \frac{c}{f} \qquad (1.6)$$

This unequivocally means that it is possible to express every frequency band identified by the IEEE Standards as a wave-

length range (table 1.2). The wavelengths generally used by radars are considerably longer than those of visible light.
When choosing the frequency band for a radar survey, the wavelength of the carrier must usually be of the same order of magnitude as the structures to be scanned. As we have already mentioned at the beginning of this chapter and as we will go into in more detail in Chapter 2, the characteristics of electromagnetic interaction with the surface of the target (especially the geometric and dielectric properties of the latter) play a preponderant role in the selection of the appropriate frequency band. Several scanning performance characteristics depend on these properties, such as penetration into a certain medium, the dynamic range covered by the radar backscatter for a certain scene, or the transmitted bandwidth required for higher resolution.
For example, the sensitivity to surface roughness increments as the carrier wave frequency increases. In the RCS of scenes in natural contexts, under the same conditions, carrier waves of lower frequencies typically cover greater dynamic ranges than carriers of higher frequencies.
These frequency-band factors therefore have a substantial effect on the detection results and the radar images acquired. Under the same environmental conditions, significantly different radar images can be obtained from the same scene, depending on the frequency band used (fig. 1.12).
Radars for remote-sensing radars operate at frequencies ranging from a few tens of MHz, i.e. Very-High-Frequency (VHF) waves, to a few tens of GHz, i.e. the W-band. More specifically, in the design of imaging radars, there is a tendency to avoid wavelengths shorter than the K-band, as these are reflected by water vapour and other atmospheric particles. When electromagnetic radiation passes through the atmosphere, it interacts with particles suspended in it, such as aerosols and clouds. The capacity of the atmosphere to allow this radiation to pass through it is defined as its electromagnetic transmissivity or opacity and varies with the wavelength of the radiation (fig. 1.13, fig. 1.14). The gases constituting Earth's atmosphere absorb radiation at certain wavelengths of the electromagnetic spectrum but, at all other wavelengths, they are more or less traversed.
The intervals of the electromagnetic spectrum that are absorbed by atmospheric gases such as water vapour (H_2O), carbon dioxide (CO_2) and ozone (O_3) are called absorption bands. In contrast to absorption bands there are specific wavelength ranges for which the atmosphere is transparent, i.e. where there is little or no absorption. These wavelength bands are called 'atmospheric windows' because they allow radiation to easily pass through the atmosphere and reach Earth's surface. The atmosphere is almost opaque to electromagnetic radiation for part of the mid-infrared and for all of the far-infrared. In the microwave domain, on the other hand, most radiation travels through the atmosphere unimpeded, allowing radar pulses to reach Earth's surface.
Most remote-sensing instruments on airborne or space platforms have to operate in one or more atmospheric windows, taking readings and measurements within specific frequency (and thus wavelength) ranges. The atmosphere may in fact have an effect on the propagation of the radar signal, inducing strong attenuation, as well as delays and phase modulations in the echoes received by the sensor. Lower microwave frequencies (approximately C-band and below) are affected by the ionosphere, while higher frequencies (Ku-band and above) are attenuated by the troposphere.
Although most remote-sensing systems are designed to analyse radiation reflected from bodies, some sensors - especially those on meteorological satellites - directly measure radiation absorption phenomena in the atmosphere, such as those associated with CO_2 and other gases. High-frequency microwave bands, on the other hand, are used in meteorological instruments with Doppler radar to detect rainfall and storms.
The bands most typically used for imaging are the X-band, the C-band and some of the longer wavelength bands. As a general rule, the lower-frequency bands (approximately below the C-band, 4-8 GHz) are used to penetrate volumetric structures such as forests, snow, ice, dry soil; the higher-frequency bands (C-band and above), on the other hand, normally have little or no penetration capability into natural surfaces and, therefore, are used for surface remote sensing. The extension of the wavelengths in the L-bands and UHF waves is such that they penetrate through foliage and sometimes allow the radar pulses harnessing them to reach below tree canopies of forests.
Currently, radar design on space platforms focuses on the C-, L-, and X-bands, achieving a reasonable balance between penetration, sensitivity to surface roughness, geometric resolution and technological maturity. In the near future, the field

Luca Martelli

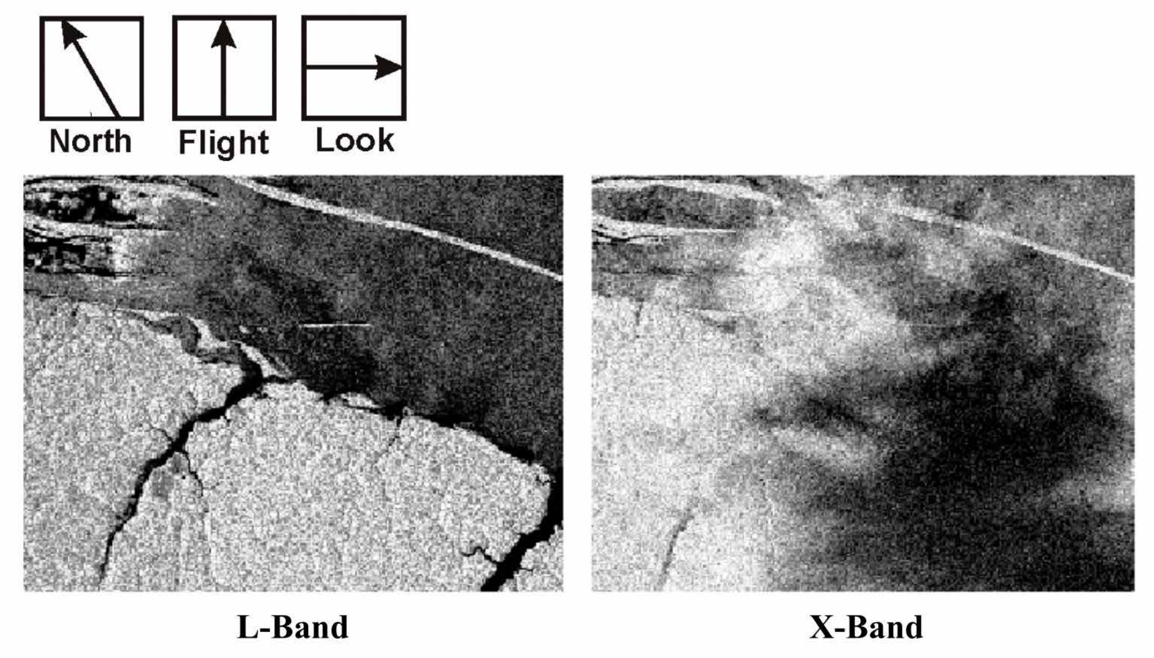

1.12/ Pair of images captured by the Spaceborne Imaging Radar-C/X-band Synthetic Aperture Radar (SIR-C/X-SAR) on 16 April 1994 over the Brazilian Rain Forest near Manaus. In both images the rain forest (bottom left section) and the Rio Negro river (top right section) are visible. The two radar images were acquired simultaneously at L-band (left) and X-band (right), in both cases with VV polarisation. The dark area in the bottom right section of the image associated with the X-band was caused by raindrops in the atmosphere, which attenuate X-microwaves. Each of the scanned areas measures approximately 16 km × 12 km and has its centre of gravity at the coordinates 1°30'S, 48°54'W. Source: Alpers, Melsheimer 2004 / Immagine di pubblico dominio [Image under Public Domain].

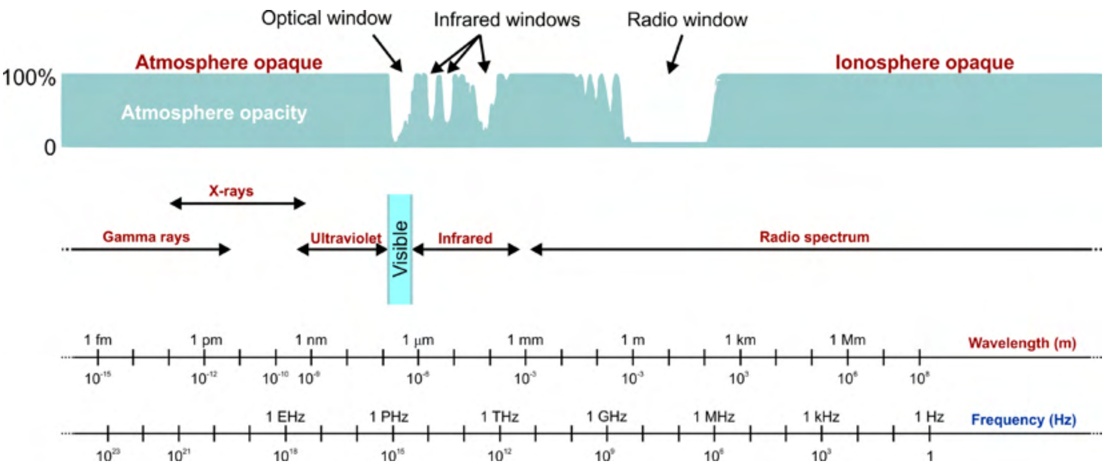

1.13/ Diagram of Earth's atmospheric opacity. Atmospheric opacity can be represented, in terms of percentage, both as a function of wavelength and as a function of the frequency of incident electromagnetic radiation. Source: Long, Ulaby 2014.

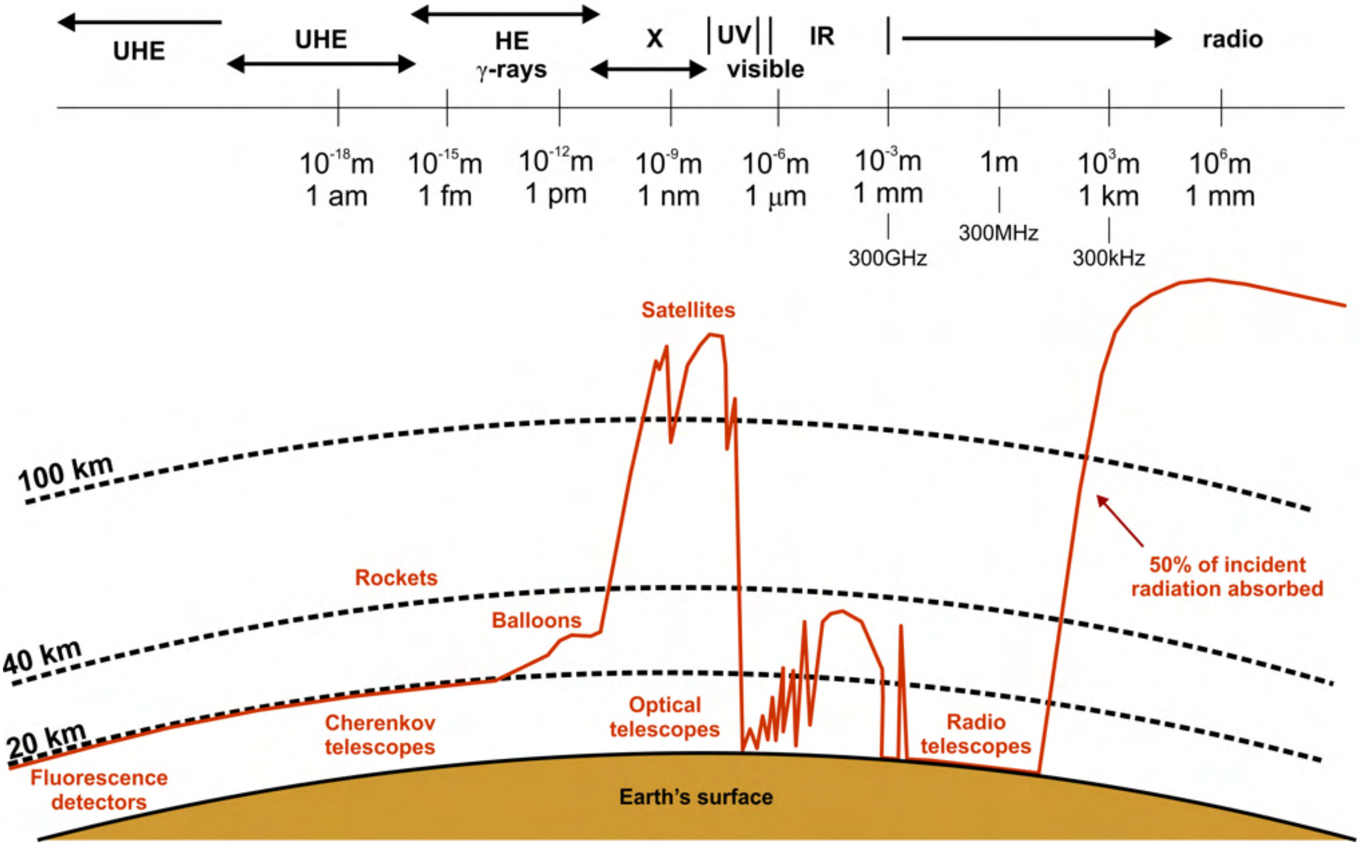

1.13/ Nella pagina precedente, Diagram of Earth's atmospheric opacity. Atmospheric opacity can be represented, in terms of percentage, both as a function of wavelength and as a function of the frequency of incident electromagnetic radiation. Source: Long, Ulaby 2014.
1.14/ In questa pagina,Diagram of atmospheric transparency as a function of electromagnetic wavelengths. The solid line indicates the altitude at which a sensor can detect half of the incoming radiation. Of all the photons coming from the planetary surface, only those of optical and radio frequencies can be measured directly from Earth's orbit. The electromagnetic pulses associated with the other wavelengths are, at least partially, absorbed by the atmosphere. Source: Satalecka 2010.

of applications will extend to the UHF waveband on the one hand, and the Ku and Ka bands on the other[23].

1.3 Radar classifications based on sensor position and orientation during scanning

Over the years, the evolution of radar technology has enabled various applications in increasingly diverse environments. There are numerous taxonomies of radars, many of which overlap with each other precisely because of this variety of operating modes and uses.

Although the first of the objectives of our research is to study the geometry and acquisition modes of imaging radar systems, with a particular focus on SAR systems for satellite remote-sensing, we feel it necessary to first identify these specific categories by framing them according to criteria based on the spatial location and orientation of the sensor during scanning.

If we consider the contents of the Preliminary Document for the 'Carta del Rilievo architettonico' ('The Architectural Survey Charter') presented and approved at the conference Il rilievo dei beni architettonici per la conservazione, held in Naples from 15 to 17 April 1999[24], we can place most of the applications as a series of cases included in a set identifiable between the following examples of two borderline cases:

- systems where the sensor, the platform and the survey station are merged or otherwise connected and all present in situ. In this type of situation, the operators of radar scans tend to coincide or collaborate with the team that intends to survey the site or artefact being acquired. These are therefore operations that we can legitimately liken to instrumental surveying. An example for this type of situation could be the cyclic in situ monitoring of a glacier, using a portable imaging terrestrial radar interferometer (fig. 1.15);
- systems where the sensor is mounted on a mobile platform, which is located at a considerable distance from one or more sensing stations and which may possibly need an infrastructure of repeater elements to remain connected to them[25]. In these eventualities, operators of RADAR scans tend to act independently and to distribute the acquired information in the form of open data in the public domain , or in any case accessible to scientific institutions upon evaluation of an application, or upon payment formulas. Except in exceptional cases, therefore, the role of the surveyors of the territorial sphere or architectural episode thus scanned (or yet to be scanned) focuses on the search and selection of already archived material (i.e. commissioning the operators for an acquisition that can only be planned by RADAR specialists). For this case, an example might be the use of images acquired by synthetic aperture satellite RADAR [SAR] with signals in the X-band, in order to carry out preliminary remote sensing of a partially buried archaeological site, to be supplemented later by instrumental in situ survey campaigns[26].

From these two borderline cases, it can be deduced that the role of the detector and its design possibilities change depending on the spatial and organisational set-up of the entire radar system, ranging from the smallest and most transportable of assembled instruments to planetary-scale space missions.

The way in which scanning results are archived and distributed is also not negligible. In the first borderline case, in fact, the information is collected, processed, transmitted and stored ad hoc for the survey being conducted and, within the limits of its competence, the surveyor has the power to intervene in the process in all its phases; in the second borderline case, on the other hand, the data of interest to the surveyor are part or will be part of a vast pre-existing catalogue, managed by the operators of the radar system through procedures aimed at serving a wide user base.

1.15/ Portable Real Aperture Radar (RAR) interferometer during a scan of the Rhone glacier in the Valais region of Switzerland, performed on 6 September 2007. Source: Strozzi, Werner, Wiesmann, Wegmüller, 2012. © 2012 IEEE.

As already mentioned, one can find numerous examples of radar equipment that present varying degrees of hybridisation between these two modalities, such as the active sensors mounted on Italian National Coast Guard aircraft for long-range detection of hydrocarbon and other oily substance pollution at sea. In this case, the data collected are then transmitted to the various institutional Environmental Monitoring Agencies, giving rise to indirect collaboration and exchange of information, but still subject to coordination exercised by one or more local authorities[27].

1.3.1 Classification of RADARs according to sensor housing platform

Keeping in mind that the sensor is a single part of a larger

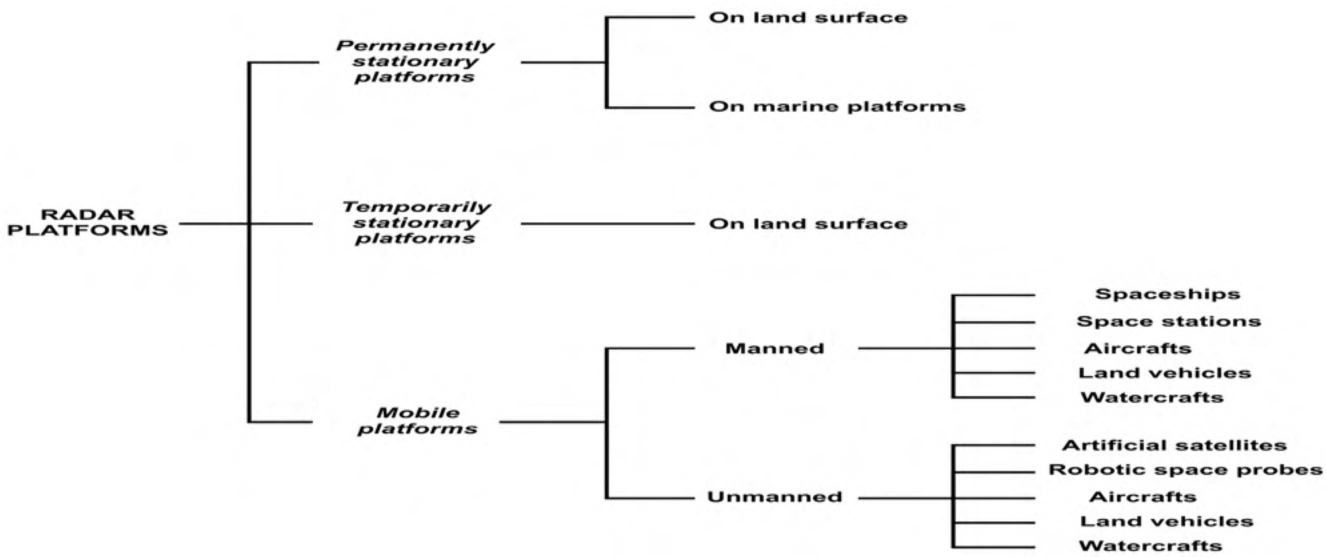

1.16/ Schematic classification of the main types of radar platforms, with reference to their relative motion with respect to the Earth.

system, made up of numerous other components (such as signal conditioners, data recorders and memories), main radar equipment can also be classified schematically according to the type of platform on which the antenna or antennas are installed, with reference to its relative motion with respect to the Earth or, in the case of space probes, with respect to another celestial body (fig. 1.16):
permanently stationary platforms require the sensor to be installed on a purpose-built base or otherwise erected in situ. In this case, the other components such as the information recorders and the control station with operators may or may not be near the antenna. Radar stations are normally constructed on land (fig. 1.17), but some examples have also been built on marine platforms (fig. 1.18);
temporarily stationary platforms (fig. 1.18) generally consist of tripods or detachable bases, which can be fixed or even just placed on the ground for a limited period of time, without requiring construction work (fig. 1.19);
mobile platforms may have a crew, a pilot or no operator on board (such as remote-controlled vehicles and drones). Although the movement of the platform relative to the ground is essential for proper scanning, there may be situations in which the carrier does not have to operate continuously. Mobile platforms can include land vehicles (even those without engines), watercraft, aircraft – both aerodines (fig. 1.20) and aerostats –, space shuttles (fig. 1.21), space stations, space probes and artificial satellites.
The above classification only takes into account the motion or stillness conditions of the platform, which are a physically different thing from the motion or stillness conditions of the sensor, i.e. the antenna(s). This difference does not have substantial consequences on the functioning of radar technology in the strict sense, but rather on the operational aspects and the scaling relationship between the instrument and the portion of space to be scanned.
There are, in fact, fixed platforms housing antennas which, in order to scan, perform rotations around a vertical axis or translations along a rail fixed to the ground.
In the first case, the azimuthal direction of the scan corresponds to the angular direction of the rotation, while the LOS (and therefore the radial direction, along range direction) is a straight line belonging to one of the infinite number of planes passing radially through the antenna's vertical v (fig. 1.22a)[28].
In the second case, the azimuthal direction is to be considered rectified and corresponds to the translation of the antenna, while the range direction will always be parallel to the LOS and will belong to one of the infinite number of planes orthogonal to the path taken by the sensor (fig. 1.22b). Usually

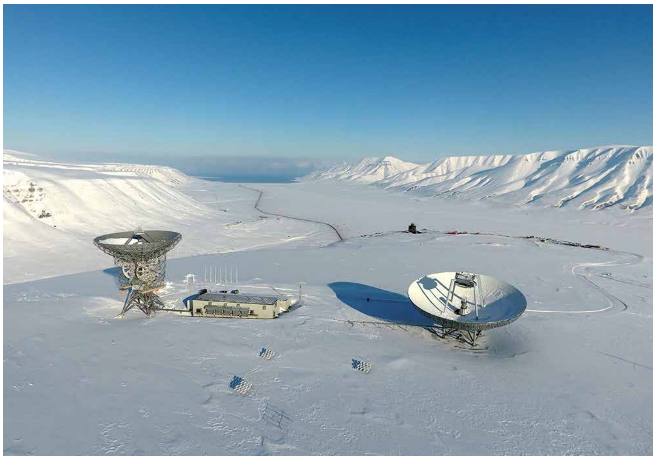

1.17/ *EISCAT Svalbard Radar (ESR) near Longyearbyen, Spitzbergen Island, Svalbard Archipelago, Norway. The site is located above the Arctic Circle and is close to the North Pole. The facility has two antennas: a 32-metre mechanically fully steerable parabolic dish antenna and a fixed parabolic antenna, aligned along the direction of the local geomagnetic field. The sensors are computer-controlled, but can be controlled by the other facilities of the European Incoherent Scatter Scientific Association (EISCAT). Source: European Incoherent Scatter Scientific Association, 2016. Fotografia di Craig Heinselman.*

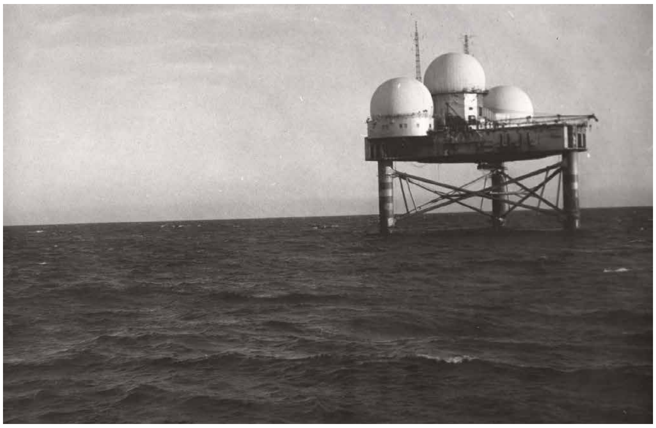

1.18/ *RADAR Station Texas Tower No. 4, built by the US Navy [U.S. Navy] in 1957 south of Woods Hole and destroyed in 1961. Photograph preserved in New York Bight, at the family of Captain David M. Whipp, C&GS. Source: National Oceanic and Atmospheric Administration, 2019 / Image under Public Domain.*

1.19/ *A portable Real Aperture Radar (RAR) interferometer in front of the Rhone Glacier in the Valais region of Switzerland. The photo allows an approximate comparison of the size of the instrument with the human scale. Source: Werner, Strozzi, Wiesmann, Wegmüller 2008. © 2008 IEEE.*

radars designed for remote-sensing, which we will discuss in more detail later, use a movement pattern similar to the latter case, where however the movement during scanning operations is performed by the entire platform rather than by the antenna alone. Furthermore, in cases of scanning vast areas with high-altitude or even space platforms, the curvature of Earth's surface can no longer be neglected and requires the adoption of more complex geometric schemes.

1.3.2 Radar platforms dedicated to remote-sensing

In addition to the above classifications, it is now worthwhile to circumscribe the field of remote-sensing in order to better identify the SAR systems dedicated to it, the subject of our study.

Since antiquity, the awareness that a view from above corresponded to a privileged observation point for controlling the territory has prompted human beings to seek out and construct high-altitude positions. It is sufficient to think of wartime motivations or the need to select areas suitable for settlements, oversee crops and livestock, monitor the surroundings. The range of optical, measuring, surveying and graphic capture instruments that have flanked or even replaced the human eye in this type of situation has expanded with technological evo-

1.20/ Experimental SAR, mounted on aerodyne and operated by pulses at the L frequency band. (a) Aircraft sensor platform, consisting of a Gulfstream-3 jet. The Radar is embedded in a pod located under the fuselage. (b) Details of the pod, with the antenna on the outer surface and the other components inside. Source: Jones, Holt 2018 / licensed under CC BY 4.0 (http://creativecommons.org/licenses/by/4.0/). © 2018by Jones, Holt. Licensee MDPI, Basel, Switzerland.

1.21/ Photograph of the Spaceborne Imaging Radar-C/X-Band Synthetic Aperture Radar (SIR-C/X-SAR) sensor at the Jet Propulsion Laboratory. The radar is placed in the payload bay of the orbital space shuttle Endeavour (STS-59). In the background, an area of the Pacific Ocean northeast of Hawaii. The antenna of the SIR-C/X-SAR, consisting of a triangular support structure and flat panels [flat antenna panels], is capable of collecting data within three frequency bands simultaneously: C-band, L-band and X-band. When this picture was taken, in 1994, six NASA astronauts spent a week and a half in Earth orbit in support of the SIR-C/X-SAR mission. Source: National Aeronautics and Space Administration, 1998 / Image under Public Domain. Credits: NASA/JPL.

lution, arriving, in the contemporary age, at artificial apparatuses capable of fixing images on sensitive supports (as in the case of aerophotogrammetry) or even registering the electromagnetic energy reflected or emitted by bodies on Earth's surface (by means of passive or active sensors mounted on aircraft or satellite platforms), translating it into digital images. This is how remote-sensing originated, i.e. the science of acquiring, processing and interpreting information about objects, areas and phenomena located around Earth's surface, without coming into direct contact with them[29]. In addition to military applications, the research fields that took immediately advantage of the potential offered by remote-sensing (Geology, Climatology, Environmental Monitoring, Civil Engineering, Archaeology, etc.) obviously also include Land and Architectural Representation, particularly with regard to integrated surveying.

Usually radar platforms dedicated to remote-sensing are aircraft or space-based (in the latter case mainly satellite-based). Let us therefore consider the example of a spatial radar (fig. 1.23), simplifying its acquisition geometry and thinking that its platform is travelling along a path belonging to the plane of the sheet of paper on which it is drawn. The platform follows the velocity vector vs described by the arrow (the s in

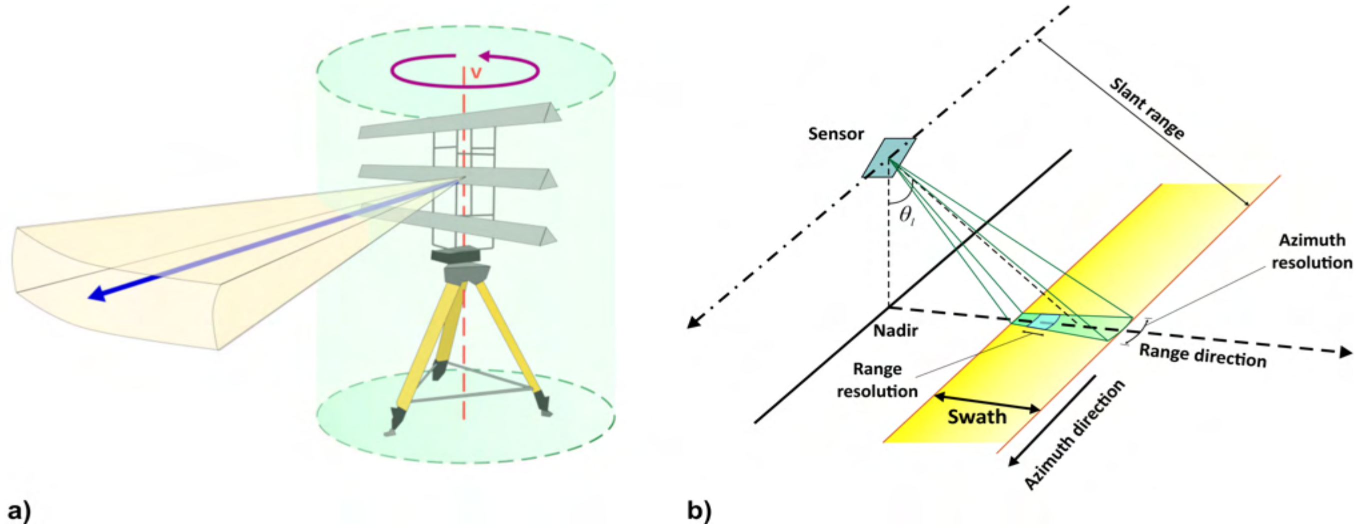

1.22/ Comparison of the acquisition geometries of the stationary radar with antenna rotating on a vertical axis v (a) and the radar with antenna in translatory motion (b). In the case of the sensor with the antenna in translatory motion, the azimuthal direction can be considered as rectified.

the subscript stands for spacecraft), , illuminating the targets on the bold horizontal line below, which locally represents the scanned terrain (assumed flat) neglecting the curvature of the planet. The shaded triangle in the figure represents the vertical cross section of the radar beam emitted by the antenna, with an aperture angle Θaz. The bold grey line then represents the section of the illuminated area on the planetary surface, corresponding to the instantaneous footprint of the radar antenna. The trajectory of the platform defines the along-track dimension, which is measured by the radar with its slow timescale sensitivity. With each new pulse transmission, a new sampling is made. The dashed segment joining the sensor and the midpoint of the section of the instantaneous footprint represents an average of the LOS direction of the acquisition. The plane normal to the velocity vector vs is called boresight or broadside. The boresight vector is given by the intersection of this plane and the vertical section of the radar beam, as explicitly illustrated. The angle between the boresight vector and the LOS is called squint angle, denoted as θsq in the figure. The mean LOS constitutes the (slant) range direction. Echo delays are measured by the radar with its fast timescale sensitivity, during a time interval between two successive antenna reception events. The projection of the range component on the straight line passing through the centre of the emission and perpendicular to the along-track direction is the cross-track direction of the scan. For small squint angles, the extent of a range can be confused with its cross-track direction component[30].

1.3.3 Nadir-looking and side-looking radars

In this subsection we will analyse an important classification of radar systems, concerning many remarkable aspects of acquisition geometry in remote-sensing operations with aircraft and space platforms.

Radar equipment can in fact be divided into two distinct categories, based on the orientation of the LOS projection on the broadside plane:

- nadir-looking radars (fig. 1.24a), which have the projection of the LOS on the broadside plane congruent with the boresight vector;
- side-looking radars (fig. 1.24b), for which there is a looking angle θl between the projection of the LOS on the broadside plane and the boresight vector. In this case, the angle between the LOS and the line perpendicular to the tangent at the point of intersection between the scanned planetary surface and the LOS itself is called incidence

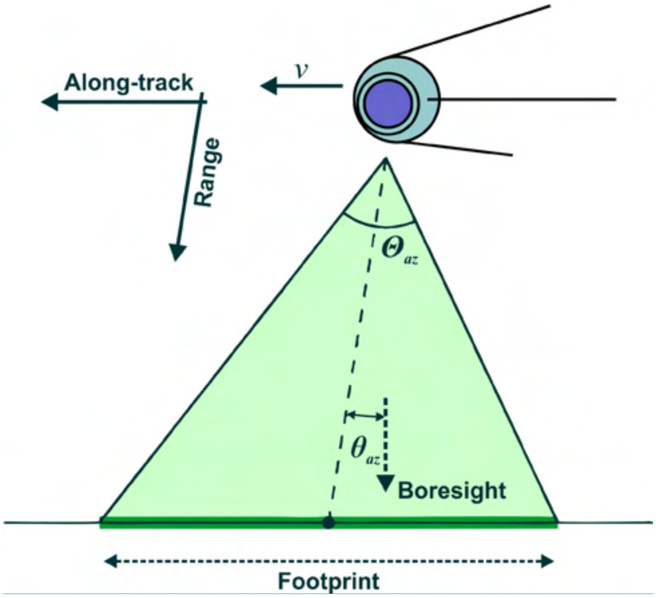

1.23/ Simplified side view, of a spaceborne radar. In this schematisation, the platform trajectory defines the along-track coordinate, measured with the slow timescale sensitivity of the system. Antenna pointing defines the LOS coordinates or slant range, measured with the fast timescale sensitivity of the system. Source: Emery, Camps 2017.

angle θi. In the case of the hypothesis of scanning a sufficiently contained surface without topographic relief, thus being able to schematise it as a plane, incidence angle θi is equal to looking angle θl. For satellite systems, the earth's curvature comes into play so that, even in the absence of topography, there is a small difference between θl and θi.

As the platform moves following velocity vector vs, the intersection between the radar wave ray emanating from the sensor and the planetary surface identifies a strip, also called a swath. In the generic cross-section with respect to vs and thus the along-track direction, this strip is characterised by a swath width.

Altimeters, scatterometers and sounders generally operate with nadir-looking geometries. Nadir-looking microwave sensors usually receive very strong echoes and, as a result, typically use less power than side-looking radars. However, nadir-looking radars cannot distinguish two backscatterers A and B equally spaced from the nadir point in the plane orthogonal to the azimuth, because a single wavefront illuminates both points at the same time. The echoes from both targets return to the sensor simultaneously (fig. 1.25a). This causes an ambiguity in the distance calculation for any symmetrical arrangement of equidistant points, called right-left ambiguity. The solution for right-left ambiguity with nadir-looking sensors requires the use of two radar beams, which can be achieved in two ways:

- by using two separate antennas;
- through the use of a single antenna, but supported by analogue or digital beamforming. Nadir-looking radars possibly having a squint angle are usually called forward-looking radars or backward-looking radars.

In the case of side-looking microwave sensors, the radar illumination is emitted from only one side of the platform and there cannot be left-right ambiguity. Neglecting topography effects, the distance is always increasing from near to far range, whereas in nadir-looking radars it is an even function with respect to the centre of the beam (fig. 1.25b).

As we will see later, the oblique LOS inherent in this type of acquisition geometry results in the generation of images that are only apparently similar to photographs, since their capture is not governed by projectivity relationships. When scanning with side-looking radars, the presence of slopes, height differences or superfetations of any kind in the imaged area causes various types of geometric distortions in radar images. We will examine these distortions in Chapter 2.

In side-looking observations, the backscattering energy from the planetary surface tends to be lower. Therefore, side-looking radars generally require more transmission power than their nadir-looking counterparts[31].

Real Aperture Radar (RAR) and Synthetic Aperture Radar (SAR), which we will study in Chapter 2, typically adopt side-looking geometries.

1.4 Radar profilers and imaging radars

Radars for remote-sensing can also be classified according to the size of the measurements they take.

Radar profilers generate profiles of ranges or Doppler maps. Altimeters are a classic example of this type of instrument. In the diagrams drawn by altimeters, the ordinates correspond to the height of the surface and are measured considering: the

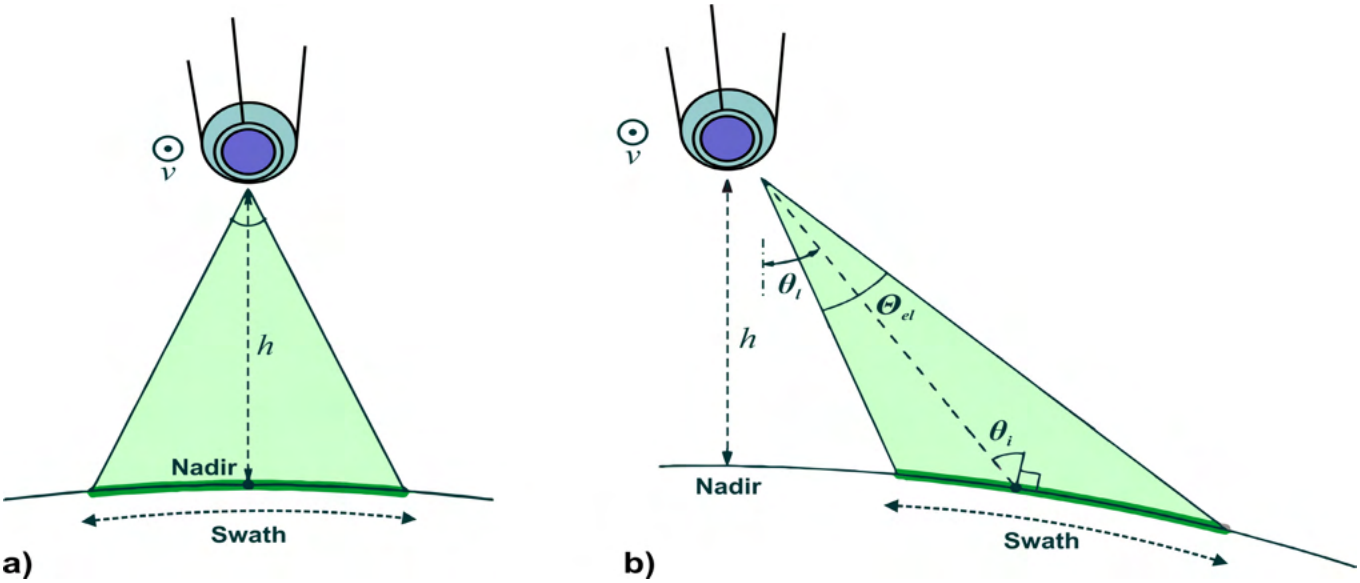

1.24/ Graphical exemplification in elevation of nadir-looking and side-looking acquisition geometries. (a) In the case of a nadiral radar, the cross-section of the wave beam is ideally symmetrical with respect to the boresight vector and the LOS, the directions of which are coplanar with the path of the platform and its projection on the planetary surface. (b) In the case of the side-looking radar, the projection of the platform path onto the planetary surface does not fall within the strip and the cross-section of the wave beam is asymmetrical. Source: Emery, Camps 2017.

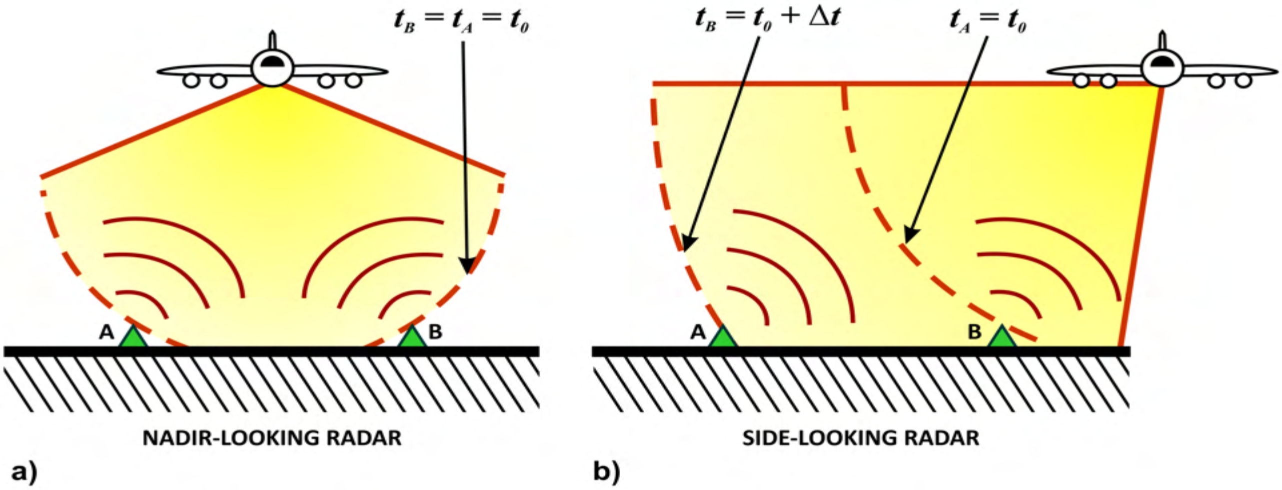

1.25/ Comparison between nadir-looking geometry and side-looking geometry in relation to a hypothetical case of two targets A and B placed at the same altitude. (a) A and B are at the same distance from the antenna, so the echoes return to the nadir-looking radar at the same time and the sensor cannot distinguish the two bodies from each other. (b) The distance between A and the antenna is greater than that between B and the antenna, so the echo of A will develop with a delay Δt relative to the echo of B, allowing the laterally oriented radar to distinguish the two returning signals.

1.26/ One of the radar antenna arrays of the Multichannel Coherent Radar Depth Sounder (MCoRDS), mounted under the wing of NASA's P-3 aircraft. The MCoRDS employs panels under the wings and fuselage of the aircraft, for a total of 15 antennas that can transmit and receive signals in order to map the polar ice and the rock bed below. Source: National Aeronautics and Space Administration, 2013a / Image under Public Domain. Crediti: NASA / George Hale.

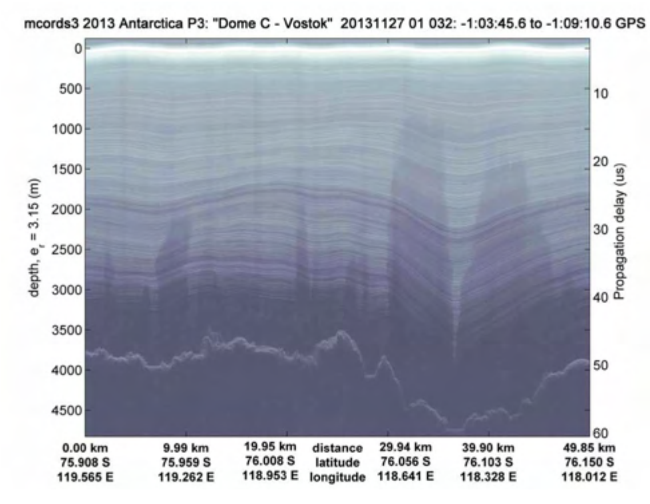

1.27/ Diagram of the ice surface, internal stratification and bedrock (jagged line at the bottom of the image) in the section between the National Aeronautics and Space Administration's Dome C observatory and Lake Vostok. Survey carried out by the MCoRDS with the flight of 27 November 2013. Source: National Aeronautics and Space Administration, 2013b / Image under Public Domain. Crediti: CReSIS / Theresa Stumpf.

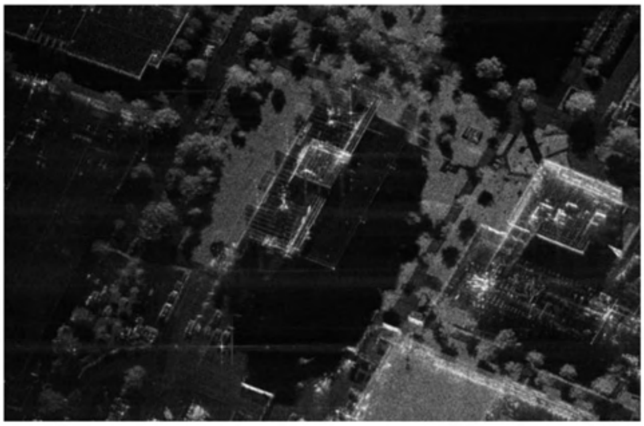

1.28/ Radar image of the Kirtland Air Force Base Building near Albuquerque, New Mexico, acquired by Sandia National Laboratories using a synthetic aperture sensor operating in Ku.-band. Source: Sandia National Laboratories, 2023a. Courtesy of Sandia National Laboratories, Radar ISR.

position of the satellite, the range values given by the return pulses and the morphological characteristics of the scanned surface. The abscissas correspond to the position of the satellite along its along-track position, projected onto Earth's surface.

Radar sounders, such as the Multichannel Coherent Radar Depth Sounder (MCoRDS) of the National Aeronautics and Space Administration (NASA) (fig. 1.26), work similarly to altimeters, with the difference that the waves penetrate the surface and generate an image of the lower layers. The profiles obtained at different depths result in two-dimensional images (fig. 1.27). Again, the values at the ordinate are measured taking into account the distance from the sensor, while the values at the abscissa correspond to the positions of the satellite along its along-track positions.

In the case of both the altimeter and the sounder, Doppler processing techniques (such as synthetic aperture) can be used to improve the resolution in the along-track dimension.

Other types of two-dimensional images can be obtained by harnessing fast-time sampling and the angular component, or slow-time sampling of radar scans, such as in the case of meteorological radars or side-looking radars (fig. 1.28), whether they use real apertures or synthetic apertures[32].

Notes

1. Skolnik 1990, pp. 1.1-1.6.
2. Skolnik 1981, pp. 1-3.
3. Ager 2013, p. 27.
4. Skolnik 1981, pp. 1-3; Skolnik 1990, pp. 1.1-1.6.
5. Emery, Camps 2017, p. 43-46.
6. Luzi, Crosetto, Fernández 2017, pp. 2-8.
7. Skolnik 1981, pp. 1-3; Skolnik 1990, pp. 1.10-1.11.
8. Skolnik 1990, pp. 1.11-1.12.
9. Ibidem, p. 1.12.
10. Zhang, Li, Cheong, Cai, Ramesh, Suarez, Blake, Andrews, Yong 2013, pp. 1-8.
11. Skolnik 1990, p. 1.12.
12. Ager 2013, p. 25; Skolnik 1990, pp. 1.12-1.13.
13. *Ibidem*.
14. Emery, Camps 2017, pp. 209-301; Skolnik 1990, p. 1.13.
15. Skolnik 1981, pp. 7-8; Skolnik 1990, pp. 1.13-1.15.
16. The Institute of Electrical and Electronics Engineers 1976, pp. 1-8.
17. The Institute of Electrical and Electronics Engineers 1984, pp. 1-8.
18. The Institute of Electrical and Electronics Engineers 2003, pp. 1-10.
19. The Institute of Electrical and Electronics Engineers 2020, pp. 1-15.
20. *Ibidem*.
21. Skolnik 1981, pp. 7-8; Skolnik 1990, pp. 1.13-1.15.
22. The Institute of Electrical and Electronics Engineers 2020, pp. 1-15.
23. Ager 2013, p. 21; Emery, Camps 2017, pp. 62-66.
24. The Preliminary Document Verso la "Carta del Rilievo architettonico": testo di base per la definizione dei temi (Towards the 'Architectural Survey Charter': basic text for the definition of the themes) was drafted by an international research group, consisting of: Antonio Almagro, Gianni Carbonara, Stella Casiello, Dino Coppo, Cesare Cundari, Gaspare de Fiore, Mario Docci, Mario Fondelli, Tatiana Kirova, Emma Mandelli, Paola Rota Rossi Doria, Ciro Robotti, Jean Paul Saint-Aubin, Francesco Starace.
The aim of the research was to propose to the scientific community a basis for reflection on the principles and criteria to be pursued in architectural surveying. The Document developed by the working group was presented and approved at the first conference Il rilievo dei beni architettonici per la conservazione (The survey of architectural heritage for conservation), held in Naples between 15 and 17 April 1999. It was then disseminated internationally and proposed for final discussion at the second conference Il rilievo dei beni architettonici per la conservazione, held in Rome between 16 and 18 November 2000. On that occasion, starting from the Preliminary Document, a second Document was drafted and approved, the Dichiarazione sul rilevamento architettonico (Declaration on Architectural Surveying), which framed the field of intervention more succinctly, defining its aims, procedures and methodologies, and also setting criteria for graphic representation. In any case, in the final vote at the second conference in November 2000, the Preliminary Document was fully recognised as a supplementary and explanatory text to the Declaration. Cf. Cundari 2013, pp. 521-526.
25. Planetek Italia 2022.
26. Lasaponara, Masini, Pecci, Perciante, Pozzi Escot, Rizzo, Scavone, Sileo 2016, pp. 55-62.
27. Ministero dell'Ambiente e della Tutela del Territorio e del Mare 2015.
28. Strozzi, Werner, Wiesmann, Wegmüller 2012, pp. 1-5; Werner, Strozzi, Wiesmann, Wegmüller 2008, pp. 1-4.
29. Dainelli 2011, p. 3.
30. Emery, Camps 2017, pp. 340-341.
31. *Loc. cit.*, pp. 342-344.
32. *Loc. cit.*, pp. 341-342.

Sintesi

Essenzialmente, radar necessita dei seguenti componenti: un'antenna per la trasmissione; un'antenna per la ricezione; un rilevatore di energia o ricevitore. Nei radar bistatici sono presenti un'antenna per la trasmissione e una per la ricezione. Nei radar multistatici sono invece presenti un'antenna per la trasmissione e più antenne per la ricezione.
Una porzione del segnale trasmesso viene intercettata da uno o più oggetti riflettenti (i bersagli) e reirradiata in tutte le direzioni. Misurato il tempo impiegato dall'energia irradiata per viaggiare fino al bersaglio e ritornare, è possibile calcolare la distanza dello stesso bersaglio rispetto al sensore.
La distanza R del bersaglio dal sensore è determinata misu-

rando il tempo TR impiegato dall'impulso per arrivare al corpo e ritornare al sistema: R=cTR/2, dove c è la velocità della luce.
L'uso di un'antenna direzionale (un'antenna con un'ampiezza di raggio ridotta) per rilevare l'angolo di arrivo del segnale di ritorno permette di determinare l'angolo di posizionamento del bersaglio rispetto al sensore.
Se sussiste un moto relativo tra il radar e il bersaglio, lo scostamento nella frequenza portante dell'onda riflessa (effetto Doppler) è una misura della velocità (radiale) relativa e può essere usata per distinguere gli oggetti in movimento dagli oggetti stazionari.
La risoluzione del sensore adottato è uno dei fattori principali per gli scopi del telerilevamento. La definizione di risoluzione, nel senso più ampio del termine, è quella del livello al quale un sensore può discernere due bersagli molto ravvicinati e aventi proprietà simili (geometria, colore, velocità, etc.). La risoluzione angolare è definita come la minima separazione angolare tra due corpi che possono essere distinti da un sensore.
Tra le informazioni che un radar può ricavare su un bersaglio, le più importanti sono: la distanza radiale; la velocità radiale; gli angoli di direzione azimutale e d'elevazione; le dimensioni; la forma; la sezione radar equivalente o firma radar, cioè il rapporto tra la densità di potenza retroddifusa al ricevitore radar e la densità di potenza radar incidente per unità di angolo solido (facendo riferimento a una sfera equivalente) sul bersaglio.
Nell'Ingegneria delle Telecomunicazioni, per indicare la banda generale di frequenza nella quale opera un sensore radar si usano denominazioni basate su lettere e acronimi. Questa suddivisione in bande è stata ratificata ufficialmente dall'Istituto d'Ingegneria Elettrica ed Elettronica (IEEE) con lo standard IEEE Std 521-1976. Attualmente è in vigore lo Standard IEEE Std 521-2019.
Nella scelta della banda di frequenze per un rilevamento radar, solitamente la lunghezza dell'onda portante dev'essere dello stesso ordine di magnitudine delle strutture da scandire. I radar per il telerilevamento funzionano a frequenze che vanno da poche decine di MHz, cioè le onde a frequenze-molto-alte (VHF), ad alcune decine di GHz, ossia la banda W. Nella progettazione dei sistemi RADAR per la generazione di immagini si tende a evitare lunghezze d'onda minori della banda K (18-27 GHz), poiché queste vengono riflesse dal vapore acqueo e da altre particelle atmosferiche.
Classificando i radar in base alla piattaforma del sensore, si individuano: le piattaforme permanentemente stazionarie; le piattaforme temporaneamente stazionarie; le piattaforme mobili. Esistono inoltre piattaforme fisse alloggianti antenne che, per effettuare la scansione, compiono rotazioni attorno a un asse verticale oppure traslazioni lungo una rotaia solidale col terreno.
Solitamente le piattaforme dei radar dedicati al telerilevamento sono aeromobili o spaziali. Prendiamo ad esempio un radar montato su piattaforma spaziale per descriverne brevemente il sistema di riferimento: la traiettoria della piattaforma definisce la coordinata lungo il percorso, misurata con la sensibilità alla dimensione a tempo lento del sistema. Il puntamento dell'antenna definisce la coordinata della linea di mira o distanza radiale inclinata, misurata con la sensibilità alla dimensione a tempo rapido del sistema. L'area illuminata dal raggio radar è detta impronta istantanea dell'antenna.
I radar possono essere suddivisi in due categorie basate sull'orientamento della proiezione della linea di mira sul piano trasversale: i radar nadirali e i radar orientati lateralmente.
I radar nadirali non possono distinguere due elementi retrodiffondenti a uguale distanza dall'antenna, perché un singolo fronte d'onda illumina ambo i punti nel medesimo istante. Gli echi da entrambi i segnali ritornano al sensore simultaneamente, provocando un'ambiguità nel calcolo della distanza.

Luca Martelli

2. Acquisition geometry of side-looking radars

2.1 Basic principles of image acquisition with side-looking radars

Radar images generated by side-looking microwave sensors appear at first glance very similar to the much more familiar images captured by those instruments operating in the visible or infrared part of the electromagnetic spectrum. The concepts outlined in Chapter 1, however, anticipated that the principle underlying the acquisition of a radar image is fundamentally different from these two examples.

Sensors dedicated to the visible and infrared spectrum use a lens or mirror system to project radiation from a scene onto a 'two-dimensional array of detectors', which could be an electronic array or, in early remote-sensing instruments, a chemically impressionable film. Two-dimensionality can also be achieved by using scanning systems or by moving a single line array of detectors[1].

In this technical approach to image capture, which can be described in the terms of Geometric Optics and is also typical of the most common cameras, the detectable shapes in the bodies in a scene determine by projection, onto the focal plane of the instrument, the shapes constituting the image that will later be captured (fig. 2.1). At the same time, the forms originated by projection of the same shape are in homographic correspondence, therefore the images captured by the instrument are referred to each other projectively. This is possible because, during the process of capturing the respective projections on the focal plane, the double ratios[2] between the ordered groups of four aligned points and lines from bundles identifiable in the scene remain unaltered, allowing the homography relationship (also known as projectivity) to subsist[3].

With this approach in the acquisition geometry, the resolution of the images depends on the distance between the sensor and the scene to be captured. The closer the instrument, the higher the resolution and the smaller the details those can be distinguished in the images obtained; as the instrument moves further away from the scene, however, the resolution degrades and only the largest objects will still be recognisable in the images captured.

The angular resolution of an optical system is primarily limited by both the aperture diameter and the turbulence of the wave propagation medium (in this case Earth's atmosphere). Quantitatively, the angular resolution r of an aperture of size l is given by the ratio between the wavelength λ to be conside red and this assigned size, as stated in Expression (2.1).

$$r = \frac{\lambda}{l} \qquad (2.1)$$

The human eye is an everyday example of an optical system and its resolution r is limited by the diameter of the pupil. In the case of an average illumination with a wavelength of 5 x 10-4 mm, the pupil diameter varies between 1 and 8 mm, resulting in an angular resolution power of approximately 2 arcmin to 10 arcsec. An average angular resolution power of 1 arcmin corresponds to a ground resolution of 3 m for an observation distance of 3 km. In the case of optical instruments with a larger diameter roughly associated with a factor of 100, a resolution power in the order of 10 cm[4] results for an altitude of 100 km.

However, compared to what has just been summarised, side-looking radars for imaging employ quite different systems to capture scenes, except for a possible analogy between the angular resolution of optical sensors and that used by real aperture microwave antennas. This leads to profound differences between radar images and those in the visible and infrared range. There are two different methods by which radars can be used to record images, leading to a classification of these sensors into two broad categories corresponding to them: Real Aperture radars (RAR) and Synthetic Aperture RADARs (SAR). We will elaborate on the differences between these two types later in this chapter.

Typically, as the aircraft or space platform carries the sensor along its trajectory, radar images are acquired in strips, also known as sweeps swaths.

The cross-track direction is the direction perpendicular to the trajectory followed by the platform and, in radar image acquisitions, corresponds to the range direction. With both RAR and SAR, return signals are distinguished by exploiting the time delay between echoes that are back-scattered from different bodies on the scanned surface.

The along-track direction is the direction parallel to the motion of the platform and, in radar imaging operations, is identified with the azimuthal direction.

During the radar image return process, one of two systems must be used to separate targets in the cross-track direction and the along-track direction:

- the angular size method, characteristic of real aperture sensors. As we will see later, only the azimuth mapping of RARs has similarities with normal cameras;
- the Doppler history method peculiar to synthetic aperture sensors. By exploiting time delay time delay and Doppler history results, SAR images are characterised by resolutions that are independent of the distance between the instrument and the scene it is scanning. This prerogative becomes crucial for the realisation of spatial SARs without the need to construct an extremely large antenna.

Also distinguishing radar images from images captured by passive sensors operating in the visible and near-infrared range of the electromagnetic spectrum is the acquisition geometry.

Optical systems, not relying on the measurement of distances, do not suffer from from left-right ambiguity when they acquire in a nadiral orientation.

Instead, we know that imaging radars, in order to avoid ambiguities, use antennas that illuminate the planetary surface obliquely. In this side-acquiring geometry, the antenna usually emits a fan-like beam that illuminates an elongated elliptical-shaped area, the instantaneous footprint, on the area to be scanned (Fig. 2.2). Generally, the area illuminated transverse to the path of the platform defines the swath that will make up the radar image. Within this radar beam, the sensor transmits a very short effective pulse of electromagnetic energy. The further a point lying on the illuminated surface has a cross-track coordinate away from the platform (and hence the radar), the more its echo will arrive proportionally late.

Therefore, by dividing the reception time into increments with equal time units, i.e. into time bins, the scanned surface can be divided into a series of bins associated with the range bins. In the azimuthal direction, the spacing is related to the Pulse Repetition Frequency (PRF), or rather the space travelled by the platform moving at speed v in the time between two pulses, i.e. 1/PRF.

As the platform moves, a set of range bins is scanned sequentially, allowing the spatial surface to be acquired section by section. In the radar image, the brightness associated with each pixel depends mainly on the Radar Cross Section (RCS) value discussed in the previous chapters and stored in the corresponding time bin. As we shall see later, the real distinction between RAR and SAR lies in the different ways in which azimuth resolution is handled.

In the technical lexicon of radar remote-sensing with side-looking geometry, the term range is used to denote two different measurements (fig. 2.3):

- the slant range, corresponding to the range of the radar. This specification is due to the fact that the Line Of Sight (LOS) and the Field Of View (FOV) of the radar are in an oblique orientation. The slant range is the length of the segment connecting the radar with the single backscatterer;
- the ground range, i.e. the distance between the ground projection of the platform track – called nadir track – and the ground projection of the individual backscatterer. If we schematise the territory locally as a horizontal plane, the ground range of a backscatterer corresponds to the projection, on the cross-track direction, of the ground projection of its slant range from the sensor.

Resampling radar images from the slant range to the ground range is a complex procedure that, as we will illustrate later, requires special attention to the topography of the scanned terrain.

Let us now schematise the generic section of the planetary surface transverse to the platform track as an arc of circumference. The point section of the nadir track corresponds to the point of tangency between the arc of the circumference given by the spatial profile and a horizontal line, which is perpendicular to the junction of the platform track section with the nadir track section itself. As we have already seen in Chapter

1, the looking angle θl corresponds to the angle between this junction and the LOS.
Still maintaining the schematisation of the contour of Earth's surface (or the surface of another planet) as an arc of a circle, the incidence angle θi is defined as the angle between the perpendicular to the tangent of the arc in the target and the propagation vector of the radar wave (having as its direction the conjunction between the radar and the target itself).
If we adopt a more abstract schematisation, considering neither the elevation nor the curvature of the planet and treating the spatial profile as a horizontal straight line, the looking angle θl is equal to the incidence angle θi . However, it is vital to remember that this approximation is only valid in the case of a flat terrain scanned by a radar from an airborne platform with a low-altitude trajectory. In the case of systems with spaceborne platforms in fact, it is indispensable to take into account the curvature of the planetary surface, since this always involves an angle of incidence greater than the angle of observation. What is more, if elevation variations are present, the local angle of incidence in mapped radar images may vary from pixel to pixel.
Let us consider, for sake of simplicity, the case of a hillside illuminated by a side-looking radar sensor and highlight the local normals at different points on the land contour (fig. 2.4). If we make a comparison with a hypothetical flat, horizontal spatial profile, it is clear that at points on the side of the hill facing the radar, the local normal takes a steeper slope towards the radar. Therefore, the local incidence angle θi on the side of the hill facing the sensor will be smaller than a point at the same distance on the ground range but on a flat terrain.
A commonly used concept in military literature is the depression angle, which is, always considering the generic cross-section perpendicular to the platform track, the angle between the LOS and the horizontal line passing through the radar sensor. It is immediately apparent that the depression angle is the complementary of the looking angle θl, thus a small observation angle results in a large depression angle and vice versa.
Also derived from military literature is the grazing angle, i.e., again adopting the schematisation of the land surface in a horizontal straight line, the angle between the latter and the LOS of the radar. In this case, it clearly follows that the grazing angle is the complement of the incidence angle θi[5].

2.1.1 Factors influencing the resolution of a radar

We have already mentioned that the resolution of an image is defined as the minimum distance between two neighbouring bodies to be detected so that they can be effectively distinguished. We will now discuss in detail the problem of resolution in side-looking radars.
We will first examine an example of ground resolution for a simple radar and observe that it cannot provide good resolution. Next, we will discuss how this problem can be solved and therefore study an equation that is independent of the distance between the sensor and the scene.
Let us consider a radar pulse transmitted by a side-looking antenna and reflected by two bodies on the planetary surface. The pulse is emitted at the speed of light c for a very short time interval, so it has a length equal to c times the duration of the pulse. This long pulse hits the first body and is reflected by it, and then continues towards the second body. The front part of the impulse begins to be reflected, while the back part of the impulse continues towards the second body. In this case, the two targets are sufficiently spaced apart in space to generate two distinct reflections (fig. 2.5a).
If the two backscatterers were closer together, the two echoes would be mixed with each other and the radar would not be able to distinguish the two bodies (fig. 2.5b)[6].
Let us analyse the problem in more detail, so that we can properly introduce its solution. Let us consider two point targets spaced by a length xr in the direction of the slant range. From Expression (1.2) in Chapter 1, since radar waves propagate at the speed of light c, the corresponding echoes will be separated by a time difference Δt, which is written in Expression (2.2),

$$\Delta t = \frac{2x_r}{c} \qquad (2.2)$$

where factor 2 is due to the outward and return propagation of the signal, as described above. Normally, radar waves are not transmitted continuously. Rather, these instruments generally transmit short bursts of energy, identifiable as radar pulses. Let us consider a Cartesian graph with the instants of time t as abscissae and the voltage levels of the received signals as ordinates. Two bodies can be distinguished if the leading edge of the pulse returned by the second target, which is furthest from the sensor, is received later than the trailing edge of the pulse returned by the first target (fig. 2.6). In other words, the two reflected pulses must not be overlapped at any time.

Therefore, the limit of the smallest possible time difference for the separation of two targets by the radar receiver equals the length τ of the effective pulse duration. Therefore, the slant range resolution will be as stated in Expression (2.3).

$$\frac{2x_r}{c} = \tau \Rightarrow x_r = \frac{c\tau}{2} \qquad (2.3)$$

Now consider two point targets separated from each other by a length xg in the direction of the ground distance. Their respective return pulses will be separated by a difference Δt, which we can write Expression (2.4),

$$\Delta t = 2x_g \frac{\sin(\theta_i)}{c} \qquad (2.4)$$

where θi is the local incidence angle. As in the previous case, two backscattering point elements can be distinguished if the leading edge of the pulse returned by the second target (which is, again, the more distant of the two from the radar) is received later than the trailing edge of the pulse returned by the first target. Thus, the ground range resolution of the radar will be given by Expression (2.5).

$$2x_g \frac{\sin(\theta_i)}{c} = \tau \Rightarrow x_g = \frac{c\tau}{2\sin(\theta_i)} \qquad (2.5)$$

This is due to the fact that the ground range resolution is equivalent to half of the instantaneous footprint of the radar beam on the surface of the area being scanned. An important observation is appropriate at this point: Expression (2.5) implies that the ground range resolution varies as a function of the incidence angle θi locally. This means that slopes in the scene to be scanned affect the ground range resolution in radar images. Please note: in SAR, actually, one never refers to the ground range resolution but always only to the slant-range. Thus, for slopes facing the sensor, the resolution in the ground direction is worse than for slopes facing the opposite side.

Occasionally, the effective pulse length is expressed in terms of the system bandwidth B. As we shall see later, for pure sinusoidal pulses this can be posited to a good approximation in Expression (2.6).

$$\tau = \frac{1}{B} \qquad (2.6)$$

As explained in Chapter 1, a pulsed radar determines the range by transmitting a pulsed signal and measuring the round trip time travelled by the latter. Often, when designing a signal pattern for a radar sensor, there may be an important requirement to convey as much energy as possible in each pulse, in order to achieve a more favourable Signal-to-Noise Ratio (SNR). This is possible by increasing the peak of the transmitted power or by using a longer pulse. However, the peak power is usually severely limited by the available power sources, especially in the case of space-based sensors. On the other hand, as can be observed from Expression (2.5), increasing the pulse length means worsening the ground range resolution. Even a pulse of very short duration, such as one millionth of a second, has a significant impact on the radar image and, in fact, would result in a slant range resolution of 150 m.

Usually, a good compromise between these two options is the use of modulated pulses, since these remain characterised by a wide bandwidth even when the pulse is very long. After pulse compression, which we have already discussed in Chapter 1, radar achieves a short effective pulse length, thus increasing the resolution[7].

There are various ways to modulate the radar pulse, but the most common technique consists of linearly varying the frequency of the signal during its transmission. In technical lexicon, this waveform is called a chirped pulse (fig. 2.7), because a sound wave of this shape sounds like a chirp of a bird. Since chirp modulation is the most widely used, we will use it in the following example to explain how signal modulation can be used to improve ground range resolution.

Consider Expression (2.6), which can be inverted into Expression (2.7).

$$B = \frac{1}{\tau} \qquad (2.7)$$

Substituting Expression (2.7) into (2.3) gives Expression (2.8)[8].

$$X_{r_{chirp}} = \frac{C}{2B} \qquad (2.8)$$

For chirped pulses , after compression, B is the frequency variation within the pulse and this means that they do not require inconveniently short durations to develop wide bandwidths and finer ground range resolution. More precisely, in a chirped pulse the signal frequency is altered linearly as a function of time. If the frequency is changed from f0 to f0 + Δf, the effective bandwidth B becomes as stated in Expression (2.9).

Expression (2.9) is independent of the pulse duration τp . It is therefore possible to produce a pulse with a long duration (hence high energy) and a wide bandwidth (hence fine resolution). For such a signal, the instantaneous frequency is written as in Expression (2.10).

$$f(t) = f_0 1 + \frac{B}{\tau_p} t \quad \text{for} \quad \frac{-\tau_p}{2} \le t \le \frac{\tau_p}{2} \qquad (2.10)$$

The corresponding signal amplitude is stated in Expression (2.11).

$$A(t) \sim \Re\left\{\exp\left[-i2\pi \int f(t)\,dt\right]\right\} = \cos\left[2\pi\left(f_0 t + \frac{B}{2\tau_p} t^2\right)\right] \qquad (2.11)$$

$\Re(x)$ denotes the real part of x. Note that the instantaneous frequency is the derivative of the instantaneous phase. A pulse signal such as that in Equation (2.11) has a physical pulse length τp and a bandwidth B. Basically, with the chirped pulse, the range resolution depends only on the frequency variation of the pulse and is independent of the pulse duration and the distance between the sensor and the scene. In the case of sine pulse T·B =1, whereas for the chirped pulse T·B >>1. In extremely simple terms, the higher the T·B product, the higher the compression gain after the matched filter. Typically, several hundred time bandwidth products are used in radar systems.

Recalling what was stated earlier in this Section, it might seem, apparently, that a pulse such as the one in the form expressed in Equation (2.11) cannot be used to discern backscatterers placed between them at a distance less than the physical length of the pulse itself. It is certainly correct that echoes from two bodies so close that they are separated in the range direction by a much smaller gap than physical length of the pulse will overlap in time. Indeed, if the modulated pulse and thus the radar echoes have a constant frequency, it will not be possible to discern the two bodies. But if, on the other hand, the frequency is modulated as described in Expression (2.10), the echoes given by the two targets will have different frequencies at any instant of time and can therefore be separated by filtering the frequencies.

In their practical realisation, radar systems include a matched filter that compresses the return pulses from the different targets. If we consider an example where a signal in the form described in Equation (2.11) is transmitted, the echo received by a single point backscatterer placed at range R is a scaled replica of the transmitted signal itself, delayed by a time of t = 2R/c. Mathematically, for this type of point backscatterer, the output of the matched filter is described as a convolution of the return signal with a replica of the transmitted signal. Paying attention to the limits of integration, for large time bandwidth products results into Expression (2.12).

$$V_0(t) = \tau_p E_r \exp(i\omega t)\exp(-i4\pi R/\lambda)\,\frac{\sin[\pi B(t-2R/c)]}{\pi B(t-2R/c)} \qquad (2.12)$$

ω = 2πf0 and Er = electric field received by the RADAR from a point source.

This compressed pulse has half the power width of about 1/B and its peak occurs at the instant t = 2R/c so ground range resolution using a modulated pulse of the type described in Equation (2.11) is a function of the chirped bandwidth and not the physical length of the pulse.

For SAR systems dedicated to remote-sensing, whether from an aircraft or space platform, the use of physical pulse lengths of several tens of microseconds is the norm. With regard to bandwidths bandwidths, those of several hundred megahertz are common among aircraft platform systems, while those of tens of megahertz have become less rare among space platform systems. In fact, commercial space radars currently have a maximum pulse bandwidth between 300 and 400 MHz, which results in resolutions of approximately 0.5 m. Interestingly, some aerospace companies are considering significantly increasing the bandwidth of signals to be transmitted with next-generation systems.

We have therefore identified the first major difference betwethrough the path of the sensor (i.e. any plane belonging to the sheaf of planes passing through the trajectory itself of the radar). It is therefore on this virtual plane, radial with respect to all possible rollover arcs, that the radar image is mapped.

From the flat figures formed by the targets on the (ideally flat) land surface to their counterparts on the mapped radar image, nonlinear geometric distortions occur.

This effect can be better understood if we consider an example where point backscatterers in the scene form elementary figures such as a segment or a circle (fig. 2.17). Following radar mapping on the virtual plane, the segment becomes a curve and the circle becomes an asymmetrical ovoid figure.

Obviously, in reality, the terrain to be scanned is never perfectly flat and the backscatterers can also be found at altitudes very different from those given by the elevation of the terrain, especially in the case of illuminating structures of considerable size compared to the resolution of the radar, such as tower buildings (fig. 2.18). Differences in elevation of the detected targets affect the slant ranges between them and the sensor, thus altering the mapping order of the backscatterers along the slant range direction, compared to the original locations along the ground range resolution.

At this point we can dispel any doubts about the substantial difference between photographic images and radar images.

Considering ourselves in the regime of Geometric Optics, the projectivity relationship between a scene and a photograph of it exists because the numerous projection and section operations performed with the passive optical sensor do not alter the values of the double ratios of the figures.

In the case of the active microwave sensor, however, in addition to the projection and section operations, there are also rollover operations from the constituent planes of the scene to the virtual plane of the radar image. These operations take as their rollout axis the path taken by the sensor, which is not, however, the common straight line of all the planes on which the targets to be mapped lie, but just the common straight line of all the possible destination planes of the rollovers. It is therefore a non-linear mapping that alters the values of the double ratios between the figures constituting the scene and their counterparts on the radar image, excluding any projectivity relationship.

The combination of the phenomena just described causes three peculiar types of geometric distortions in radar images, which we will elaborate on later in this chapter: foreshortening, layover and radar shadowing.

2.5 Geometrical distortions due to tilting

Let us summarise what was observed in the previous paragraph. If we assume a scene consisting of an ideally flat terrain with no planetary curvature, a side-looking radar in straight flight maps each individual target illuminated by its beam by turning it on a virtual plane. This virtual plane is identifiable as a generic plane belonging to the sheaf of planes passing through the trajectory of the platform and the sensor, adopting as its rollover axis the path of the instrument itself.

Differently from the acquisition geometry of passive optical sensors, which only contemplates projection and section operations and therefore preserves the values of the double-ratios during the mapping of the photographic image, the acquisition geometry of side-looking radars also foresees operations of rollover of figures between planes not belonging to the same sheaf. Such operations alter the values of the double-ratios and therefore exclude any projectivity relationship between the scene and the mapped radar image. While homography relations occur between a scene and its photograph, therefore, no such relations can exist between a scene and its radar image.

Due to this peculiar acquisition geometry, any unevenness, superfaction or slope present on the spatial surface scanned by the sensor results in geometric distortions in the acquired data. These distortions are particularly evident in radar images mapped from particularly rugged terrain.

However, if for a pixel on a radar image the elevation h assumed by the sensor at the time of its scanning and the incidence angle θi at the corresponding real point belonging to the scene are known, it is possible to calculate the correct position of the pixel in question. For example, thanks to a Digital Elevation Model (DEM) of the scanned area a radar image can be re-mapped into a format similar to that of an optical image, allowing the registration of the pixels that compose it. However, this does not mean that all geometric distortions in a radar image can be corrected[20].

In the following we list and briefly discuss the three most relevant types of geometric distortion in radar images: foreshortening, layover and radar shadowing.

en radar imaging and passive sensor imaging. The cross-track resolution, in the case of radars, is independent of the distance between the scene and the sensor but is rather a function of the bandwidth of the system[9].

2.1.2 Notes on the radar equation for remote-sensing

The quality of a radar image is also highly dependent on the corresponding SNR. Using an analogy, it can be considered similar to the relationship that exists between the brightness of a scene photographed with a camera and the sensitivity of the film or digital sensor. In the case of radar imaging systems, we have to consider the SNR as the effect of thermal noise on instrument sensitivity. In addition to the echo given off by the target, the received signal also inevitably contains noise resulting from the fact that all objects, at temperatures above absolute zero, emit radiation across the entire electromagnetic spectrum. The noise component present within the spectral bandwidth B of the sensor travels with the signal and, inevitably, the receiver electronics also generate noise that contaminates the signal[10].
The idealised power budget required to establish a radar link (transmitter-target-receiver) is defined by the radar equation.
Before discussing the radar equation, however, it is essential to explain in a simplified manner the concept of antenna gain. First of all, let us assume that the electromagnetic wave propagates under ideal conditions – without dispersion – and that we have an isotropic radiator, i.e. a source that emits radiation uniformly in all directions. If the radiator emits high-frequency energy, it propagates spherically and, as radius R increases with distance, there are concentric spherical surfaces of area 4πR2 gradually increasing and uniform power density but gradually decreasing around the device (fig. 2.8).
As the spheres expand, the energy distributed over each of them remains the same, so the power density on the individual spherical surface is inversely proportional to the square of the corresponding radius. We therefore calculate the non-directional power density Su as stated in Expression (2.13).

$$S_u = \frac{P_s}{4\pi \cdot r_0^2} \qquad (2.13)$$

Ps is the transmitted power and r0 is the range from the transmitter antenna to the target. If we now think of reducing the area of the generic spherical surface to a spherical zone around a straight line in a particular direction, maintaining a constant transmit power, the power density is concentrated in the area of the spherical zone (fig. 2.9).
The power redistributes to be radiated mainly in the direction of the line we have chosen, resulting in the antenna gain. We can therefore write the directional power density Sg as in Expression (2.14).

$$S_g = S_u \cdot G = \frac{P_s}{4\pi \cdot r_0^2} \cdot G \qquad (2.14)$$

G is precisely the antenna gain[11].
When bodies reflect the signal transmitted by the sensor, they in turn scatter a signal in a way that is vaguely comparable to that of an antenna, so it can be said that each target also has its own gain.
In the case of remote-sensing radars, a scene can be schematised as consisting of a distributed continuum and without discrete scatterers, allowing us to assume the absence of integration gains (fig. 2.10).
The radiating power of a radar antenna, which for simplicity of exposition we assume to be monostatic, is called Equivalent Isotropic Radiated Power (EIRP) and can be written as in Expression (2.15).

$$P_{Tx} = G \cdot P_{peak} \qquad (2.15)$$

G is the gain of the transmitter antenna in the LOS and Ppeak is the peak power developed by the power amplifier after the echoes have been received by the antenna. Considering the free-space losses in the forward path from the radar to the scene, the surface power density in the vicinity of the scene can be expressed as in Expression (2.16).

$$\xi_{Tx} = \frac{P_{Tx}}{4\pi \cdot r_0^2} \qquad (2.16)$$

$$B = \left|\left(f_0 + \Delta f\right) - f_0\right| = |\Delta f| \qquad (2.9)$$

r0 is the distance between the radar and the scene. The power of the signal at the receiver can be calculated by performing a surface integral over the area illuminated by the radar – which determines one of the contributions present in a single sample in the echoes –, integrating the length of the transmitted pulse along range δr and the width of the instantaneous footprint of the antenna δa along the azimuthal direction (fig. 2.11).
The areola on the ground contributing to a single echo sample

and on which the integration of the power received by the radar must be performed can be approximated by the Expression (2.17).

$$A_{illum} \approx \frac{c \cdot \tau_p}{2 \cdot \sin(\theta_i)} \cdot \frac{r_0 \cdot \lambda}{L_a} \qquad (2.17)$$

τp is the duration of the transmitted pulse and La is the length in the azimuth direction of the antenna. The first factor at the right-hand member in Expression (2.17) is the ground range resolution given by the envelope of the impulse, while the second factor is the projection, on the spatial surface to be scanned, of the width of the instantaneous footprint of the antenna in the azimuthal direction. The scene is characterised by its own equivalent Radar Cross Section (RCS) σ0 and, given the above premises, the surface power density in the vicinity of the radar antenna can be calculated as in Expression (2.18).

$$\xi_{Rx} = \xi_{Tx} \cdot \frac{A_{illum} \cdot \sigma_0}{4\pi \cdot r_0^2} \qquad (2.18)$$

Received power is a function of the effective area of the receiver antenna Ae,Rx which, when collected, becomes PRx as stated in Expression (2.19).

$$P_{Rx} = \xi_{Rx} \cdot A_{e,Rx} = \xi_{Tx} \cdot \frac{A_{illum} \cdot \sigma_0}{4\pi \cdot r_0^2} \cdot \frac{\lambda^2 \cdot G}{4\pi} \approx \frac{\lambda^3 \cdot G^2}{(4\pi)^3 \cdot r_0^3} \cdot \frac{c \cdot \tau_p}{2 \cdot \sin(\theta_i)} \cdot \frac{\sigma_0}{L_a} \cdot P_{peak} \qquad (2.19)$$

The thermal noise power at the end of the receiver chain can then be written as in Expression (2.20).

$$N = k_B \cdot T_0 \cdot B_{eq} \cdot F_{Rx} \qquad (2.20)$$

kB = 1.38064852 ×10-23 J/K is the Boltzmann constant, T0 = 290 K is the reference temperature (i.e., approximately, the room temperature), Beq is the equivalent noise bandwidth of the receiver and FRx is the noise figure at the receiver . The noise figure is the expression in dB of the noise factor FN = (SI /NI) / (SO/NO) and is therefore written as in Expression (2.21).

$$F_{Rx}(dB) = 10\log_{10}(F_N) = 10\log_{10}\left(\frac{S_I/N_I}{S_O/N_O}\right) = \left(\frac{S_I}{N_I}\right)_{dB} - \left(\frac{S_O}{N_O}\right)_{dB} \qquad (2.21)$$

SI is the available power of the input signal, NI is the available power of the input noise, SO is the available power of the output signal and NO is the available power of the output noise.

By changing the arrangement of terms and identifying the noise bandwidth as the available transmitted bandwidth of the radar, the SNR becomes as stated in Expression (2.22).

$$SNR = \frac{P_{Rx}}{N} = \frac{\lambda^3 \cdot G^2}{(4\pi)^3 \cdot r_0^3 \cdot k \cdot T_0 \cdot F_{Rx}} \cdot \frac{\delta r_g}{L_a \cdot PRF} \cdot \sigma_0 \cdot P_{avg} \qquad (2.22)$$

The Pulse Repetition Frequency (PRF) allows us to scale the peak power Ppeak to the average power Pavg transmitted by the radar.

Typically, the sensitivity of a radar dedicated to remote-sensing is measured with Noise Equivalent Sigma Zero (NESZ) and corresponds to the value of σ0 for a signal-to-noise ratio of 0 dB, as written in Expression (2.23).

$$NESZ = \sigma_0(SNR = 0\ dB) = \frac{(4\pi)^3 \cdot r_0^3 \cdot k \cdot T_{eq} \cdot F_{Rx} \cdot L_a \cdot PRF}{\lambda^3 \cdot G^2 \cdot P_{avg} \cdot \delta r_g} \qquad (2.23)$$

As might be expected from the above definition, the lower the NESZ, the better the sensitivity of the system. NESZ is one of the primarily binding requirements in the design of any radar for remote sensing. High values of NESZ result in noisy radiometry and inaccuracy in the determination of target position, compromising the quality of final measurements. Normally, a spaceborne platform radar should have a NESZ of less than -20 dB.

It should be noted that, due to the technological limitations of components, the noise bandwidth is usually greater than the transmit bandwidth.

Another common technique to characterise a microwave sensor for imaging is to determine the territorial surface backscatter radar signature σN , which returns SNR = 1. This is called the noise equivalent backscatter cross section, which is why there is an N in the subscript. It expresses the weakest territorial surface echo that can be detected and, therefore, can be used to define the maximum range of surface units that can be mapped by the instrument[12].

2.2 Real Aperture Radar

The RAR sensor dedicated to imaging adopts a side-looking acquisition geometry. As already noted, in such a configuration, the antenna usually emits a fan-shaped beam which illuminates a highly elongated elliptical area on the land surface (fig. 2.2). The illuminated area, transversal to the plane identified by the platform track and the nadir track, obviously translates with a motion parallel to that of the platform, thus tracing the swath of the radar image.

For an antenna of width W operating at a wavelength λ, the

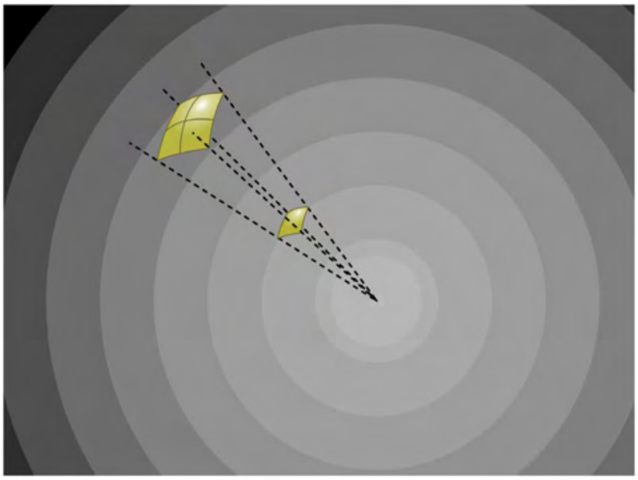

2.1/ According to Emery, Camps 2017, assuming that the electromagnetic wave propagates under ideal conditions, an isotropic radiation radiates uniformly in all directions. The energy propagates as concentric spherical surfaces of uniform non-directional power density. As the radius increases, the non-directional power density decreases.

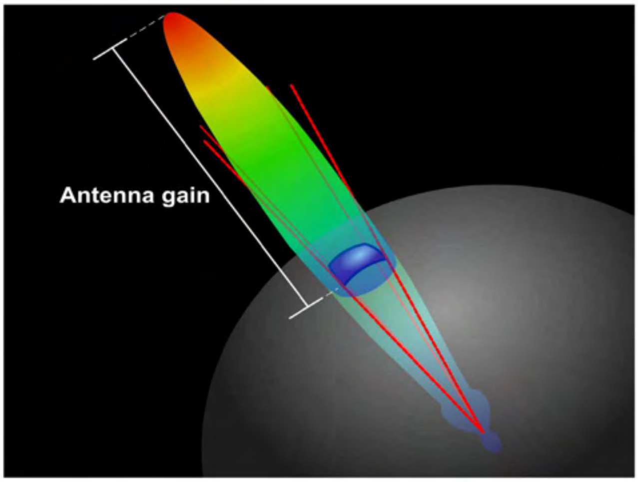

2.2/ According to Emery, Camps 2017, as the spherical area of uniform non-directional power density in a spherical zone around a straight line in a particular direction decreases, the power density is concentrated in the area of the spherical zone. The power redistributes to be radiated mainly in the direction of the chosen line, resulting in antenna gain.

angular aperture of the beam in the plane identified by the platform track and the LOS is given by Expression (2.24).

$$\theta_r \approx \frac{\lambda}{W} \quad (2.24)$$

The length of the instantaneous footprint length of the antenna on the land surface or swath width S is written in Expression (2.25).

$$S \approx \frac{h\theta_r}{\cos^2(\theta_1)} = \frac{\lambda h}{W \cdot \cos^2(\theta_1)} \quad (2.25)$$

h is the altitude of the sensor above the planetary surface, θl is the angle of observation (i.e. the angle from the centre of the illuminating ray to the vertical passing through the RADAR) and it is assumed that θr is very small. It should be remembered that Equation (2.25) does not take into account the curvature of Earth and that this effect should not be ignored. If the aperture of the beam emitted by the antenna is large, it is necessary to use the law of cosines to calculate the swath width S.
A RAR sets its acquisition process on the resolution given by the antenna beam in the along-track direction. This implies that the resolution of the RAR in the along-track direction is determined by the size of the antenna as well as the distance from the scene. Given an antenna length L, in the along-track direction the amplitude of the antenna beam is as written in Expression (2.26).

$$\theta_a \approx \frac{\lambda}{L} \quad (2.26)$$

It follows that, at a distance R from the sensor, the radar beam width develops an instantaneous footprint having an along-track dimension equal to xa as stated in Expression (2.27).

$$x_a \approx R\theta_a \approx \frac{\lambda R}{L} \approx \frac{\lambda h}{L \cdot \cos\theta_1} \quad (2.27)$$

For example, for h = 950 km, λ = 24 cm, L = 11 m and θl = 25° you have xa = 22.87 km. Even if you had a particularly short wave with λ = 1.67 cm and an altitude as low as h = 220 km, you would roughly have xa = 368.53 km, which is a relatively poor resolution even for remote sensing. In RARs, if the two targets are simultaneously included in

the footprint along the azimuthal direction, they cannot be distinguished, so the minimum distance for them to be distinguishable (i.e. the definition of resolution) is indeed the extent of the footprint[13].
It can therefore be said that, as far as along-track direction is concerned, RARs have similarities with passive optical sensors. In fact, active microwave remote sensing systems are also subject to diffraction limiting laws of optics and, in this respect, we can say that the antenna plays a similar role with respect to RAR as the lens does with respect to the camera. However, as the wavelengths of the visible part of the electromagnetic spectrum are small (λ ~ 1 μm), in the case of passive optical sensors it is possible to achieve resolutions of a few metres with orbital altitudes and aperture size in the order of a few tens of centimetres[14]. If we wanted to achieve the same resolution as an average human eye in the visible range with any RAR, we would need antennas of colossal dimensions: for example, a wavelength of 5 cm, corresponding to a frequency of 5 GHz and therefore within the C-band, would require an antenna with a diameter of 175 m. Sensors with such large apertures can neither be installed on aircraft for high-altitude flights nor launched into space.
However, if higher radar frequencies are exploited (usually the X-band or higher), it is possible to achieve acceptable azimuth resolutions from the altitudes attainable by aircraft. It is therefore for this reason that RARs are not normally used for remote-sensing with space platforms, with the exception of altimeters and scatterometers, which do not require high resolution data.
With regard to the application of the radar equation in real aperture sensors, the backscattering surface of the signal towards the sensor is given by the physical length L of the antenna in the along-track direction and the projection lg of the pulse length on the ground in the cross-track direction (fig. 2.2). We have seen that Expression (2.27) allows us to calculate the dimension xa of the radar beam emanating from the antenna in the along-track dimension. If the pulse has duration τp in time and the signal is incident on the ground at an angle θi , the pulse length projected onto the ground surface results into Expression (2.28).

$$l_g = c\frac{\tau_p}{2\cdot\sin(\theta_i)} \quad (2.28)$$

In the case of RAR, therefore, the radar equation is written:

$$P_r = \frac{P_t G_t G_r \lambda^2}{(4\pi)^3 R^4}\frac{\lambda R}{L}\frac{c\tau_p}{2\cdot\sin(\theta_i)}\sigma_0 \quad (2.29)$$

In Chapter 1 we defined the equivalent RCS (σRCS) of a target as the ratio of the scattered back power density at the radar receiver to the incident radar power density per unit solid angle of the target. For a real aperture RAR scan, therefore, the normalised RCS is written in Expression (2.30).

$$\sigma_0 = \lim_{R\to\infty}\frac{4\pi\cdot r_0^2}{A_0}\frac{|E_r|^2}{|E_i|^2} \quad (2.30)$$

A0 is the illuminated area on the land surface, Er is the reflected electric field and Eiis the incident electric field.
The above reasoning proves that when a RAR maps a large area, the received power decreases as the range to the third power. We can therefore calculate the length of a physical design antenna by rewriting Expression (2.27) in the form of Expression (2.31).

$$P_r = \frac{P_t\cdot W^2\cdot L\cdot c\cdot\tau_p\cdot\sigma_0}{8\pi\cdot\lambda\cdot R^3\cdot\sin(\theta_i)} \quad (2.31)$$

Expression (2.31) is the radar equation in the case of detecting a target distributed over a continuum by means of a real aperture sensor. From Expression (2.31) it is clear that the received power increases as the square of the antenna width; however, increasing the antenna width reduces the swath width. Lengthening the antenna means increasing the received power only linearly, while at the same time improving the resolution of the true-aperture RAR along-track direction. For this reason, RAR sensors are usually designed with the longest antennas of those practically installable on the respective platforms.
To summarise, in achieving along-track resolution a RAR adopts an imaging system that bears similarities to passive optical sensors. The resolutions achievable in practice are usually worse than what is generally required for remote-sensing operations, so RARs are not commonly used in this type of application[15].

2.3 Synthetic Aperture Radar

Synthetic Aperture Radar (SAR) is an expression referring to a particular implementation of an active microwave imaging sensor that utilises the relative motion of the platform relative to the target and a specialised signal processing mode to map images. Prior to the conception of SAR, the main active microwave imaging sensors operated with the real aperture system were known as Side-Looking Aperture Radars (SLARs). The technique of SAR began its development in the early 1950s. Carl Wiley of the Goodyear Aircraft Corporation is generally credited as the first person to theorise the use of Doppler frequency analysis of signals from a moving coherent radar in order to improve the resolution along-track resolution. In 1952, he noticed that two targets at different along-track coordinates were at different angles relative to the velocity vector of the platform (in that case, aircraft), resulting in different Doppler frequencies. In other words, he discovered that there is a one-to-one correspondence between the along-track co-ordinates of a backscatterer and the Doppler effect on the signal reflected by the backscatterer to the radar. By exploiting this effect, targets can be separated in the along-track direction based on their different Doppler frequencies. In fact, Wiley postulated that an analysis of the frequencies of the recorded signals could allow a finer resolution in the along-track resolution than was obtainable with the SLAR conventionally used at the time. The technique researched by Wiley originally circulated in the scientific literature under the name 'Doppler beam sharpening' but later became known as Synthetic Aperture Radar (SAR) and was not widely used until the mid-1980s.

Essentially, this technique allows a much longer antenna (hence the term 'synthetic aperture') to be synthesised from a sequence of scans made with a shorter antenna moving along its path. Since antenna length is intrinsically linked to the resolution of a radar sensor, the much longer 'virtual' antenna synthesised with Wiley's technique allows the acquisition of high-resolution images even from space-based platforms, using practical-sized components for orbital-level operations. A reasonably short L length antenna is mounted on a platform moving at a velocity v along its flight path. As it moves, it constantly transmits short radar pulses and receives echoes from bodies on the ground. Each radar pulse illuminates an instantaneous footprint of length S on the planetary surface. In accordance with Equation (2.25), in remote-sensing applications using RAR or SLAR on a space platform, the limited length L of the antenna results in instantaneous footprints that typically measure several kilometres, thus allowing only poor resolution. In order to apply the synthesised aperture technique proposed by Wiley, we must first ensure that, as the antenna beam scans the terrain as it travels, a body P on the spatial surface is illuminated by several consecutive pulses (fig. 2.12). Assuming several kinematic configurations, the antenna should illuminate the target P from point x1 (the first time P is detected within FOV of the radar) to point x2 (the last kinematic configuration where P is still within the FOV of the radar). Once the data has been acquired, a post-processing procedure is applied to combine all scans between x1 and x2 into a single dataset that appears to have been detected with a much longer antenna. The length of this longer (virtual) antenna is called the 'synthetic aperture', as if it were the result of a linear array of shorter antennas. The length LSA of this synthetic aperture can be written as in Expression (2.32).

$$L_{SA} = \frac{\lambda}{L} \cdot R_0 \approx \theta_a \cdot R_0 \qquad (2.32)$$

It equals the instantaneous footprint length S illuminated by the real (smaller) antenna installed on the platform[16].

Now that we have introduced the concept at an intuitive level, we will argue the above from a more analytical point of view. The main difference between real aperture and synthetic aperture active microwave sensors lies in the way the azimuth resolution is handled. Our previous remarks on range resolution and the radar equation for a real aperture system continue to apply here. However, the along-track imaging approach and the along-track resolution are somewhat different between the cases of RAR and SAR. As the radar moves along its path, it transmits energy pulses and records reflected signals (fig. 2.13). During the processing of radar data, the position of the platform is taken into account when adding the signals to integrate the energy for the along-track direction. The distance between the backscatterer and the radar changes as the latter moves along its path. The minimum distance obviously occurs when the point backscatterer in question ends up lying on the broadside plane of the platform of the radar, i.e. when this point is crossed by that perpendicular to the nadir track which is at the height of the projection of the centre of the antenna on the planetary surface (fig. 2.12).

The phase of the radar signal is written $\phi(s) = -4\pi R(s)/\lambda$. The variation of the distance between the radar and the target means that, after the distance is reduced, the phase of the signal changes depending on the position of the platform along its path. The (varying) range between the sensor and the generic backscatterer can be expressed as in Expression (2.33).

$$R(s) = \sqrt{R_0^2 + v^2 s^2} \quad (2.33)$$

R0 is the minimum distance between the target and the radar, v is the speed of the radar platform and s is the instant of time along the flight path (measured by the slow-time dimension) having for instant zero the instant corresponding to the minimum distance R0 . With a good approximation for radar remote-sensing situations we can state that vs << R0 and, although this is not always true for very high resolution radars, the basic principle remains the same. Since R0 >> vs, the first-order approximation of (2.33) is valid and we can schematise the range between the sensor and the target as a function of the values in the slow-time dimension as in Expression (2.34).

$$R(s) \approx R_0 + \frac{v^2}{2R_0} s^2 \quad (2.34)$$

The phase of the signal after distance reduction, as shown in the second exponential in Equation (2.12) then becomes as stated in Expression (2.35).

$$\phi(s) = -\frac{4\pi R(s)}{\lambda} \approx -\frac{4\pi R_0}{\lambda} - \frac{2\pi v^2}{R_0 \cdot \lambda} s^2 \quad (2.35)$$

The instantaneous frequency of this signal is written in Expression (2.36).

$$f(s) = \frac{1}{2\pi} \frac{\partial \phi(s)}{\partial s} = -\frac{2v^2}{R_0 \cdot \lambda} s \quad (2.36)$$

Relation (2.36) is the expression of the linear frequency associated with a chirped pulse. To determine the bandwidth of this signal, we need to know the maximum time available for integration of the signal. This integration time is given by the time interval in which the backscatterer is within the beam emitted by the antenna. For an antenna of physical length L, the horizontal Half Power Beam Width (HPBW)[17] is θa = λ/L, so the target at the minimum distance R0 is illuminated for a time written in Expression (2.37).

$$s_{tot} = \frac{\lambda \cdot R_0}{L_v} \quad (2.37)$$

The radar takes half of this time to reach the minimum distance R0 and half to move away from it. Therefore, the bandwidth of the signal shown in Equation (2.36), which is the Doppler bandwidth of the SAR signal is stated in Expression (2.38).

$$B_D = \frac{2v}{L} \quad (2.38)$$

By passing this signal through a matched filter, as in the case described earlier in Section 2.1, the resulting compressed signal will have a width in time of 1/BD . Since the platform moves at a velocity v, this results in a along-track resolution written in Expression (2.39).

$$\Delta_a = \frac{V}{B_D} = \frac{L}{2} \quad (2.39)$$

The result just obtained shows that the azimuth surface resolution (or along-track surface resolution) for a SAR is equal to half the length of the physical antenna and is independent of the distance between the sensor and the ground. At first glance, this outcome appears rather paradoxical: a smaller antenna implies a better resolution. However, the phenomenon can be interpreted in the following way: the smaller the physical antenna, the larger its instantaneous footprint. This allows a longer scanning time for each point on the surface, thus synthesising a longer antenna – or rather a linear arrangement of antennas –. This synthetic antenna array results in a greater Doppler bandwidth and thus a finer resolution of the spatial surface. Similarly, if the distance between the radar and the planetary surface increases, the physical footprint of the antenna also increases, resulting in a longer scanning time interval and greater Doppler bandwidth, which counterbalances the increase in distance.

Current space-based SAR sensors can achieve resolutions ranging from approximately 0.5 m to 20 m, depending on design features and acquisition modes. The most recent developments in antenna design and image processing have made it possible, through the concept of digital beamforming, to map radar images obtained from the scanning of large strips. As seen above, an imaging RADAR transmits a series of pulsed electromagnetic waves. Therefore, the Doppler history of a backscatterer is not measured continuously but sampled cyclically. According to the Nyquist sampling theorem, in order to obtain an accurate recording of the Doppler history, it is necessary that the sampling takes place at least twice as often as the frequency in the Doppler bandwidth. Therefore, the Pulse Repetition Frequency (PRF) must be greater than the value written in Expression (2.40).

$$PRF \geq 2\left(\frac{B_D}{2}\right) = \frac{2v}{L} \quad (2.40)$$

We should note that, within Expression (2.40), we have used half of the Doppler bandwidth as the highest frequency in the Doppler signal. This is due to the fact that the Doppler frequency varies linearly from -BD/2 to +BD/2. Therefore, although the total bandwidth of the signal is BD, the highest frequency within the bandwidth is only BD/2.

According to Expression (2.40), every time the sensor moves half the length of the antenna, at least one sampling (i.e. at least one pulse) must occur. For example, for an imaging system with a platform speed v = 7 km/s and an antenna length L = 10 m, the minimum PRF corresponds to 1.4 kHz.

In remote-sensing operations, the need to illuminate a certain swath size sets an upper limit to the value of the PRF. Conversely, we can also state that the need to adequately sample the signal bandwidth limits the swath width that can be scanned (fig. 2.14).

Generally, during image processing, the SAR processor acts in two stages:

1. data are range compressed, then correlated with a range reference function. To visualise the concept, this operation can be thought of as producing as many fan-shaped radar beams as there are range bins for scanning (fig. 2.15). In the range, the width at HPBW of such a fan beam depends on the resolution along the slant range resolution and the angle of incidence. In the azimuth, the HPBW of the main lobe is always approximately equal to the HPBW of the main lobe of the true aperture antenna;
2. Azimuth compression involves correlating the data with an azimuth reference function (Doppler function) along the synthetic aperture length LSA. This step involves the development of the synthetic aperture. Consequently, in this step, the azimuth width is reduced to the azimuth HPBW of the multiple fan beams, relative to the synthetic aperture length LSA . This results in a resolution in the ground resolution equal to, approximately, half the length L of the real antenna.

The dataset resulting from the aperture synthesis process is usually referred to as a SAR image and, for the same distance from the scanned scene, has a much higher resolution than images acquired with a RAR image or a SLAR image. The concept of aperture synthesis underlies all contemporary radar systems, although over time various technical modifications have been introduced to maximise both image resolution and scan coverage[18].

2.4 Study of geometric relations between the scene and the mapped radar image

On the basis of the arguments discussed above, we can state that, although there is a superficial similarity with photographs taken at high altitude and at a sensitive inclination with respect to the nadiral attitude, the images obtained with side-looking radars are mapped with a substantially different acquisition geometry than that of passive optical sensors.

Along the range direction, the echoes received from the backscatterer on the scanned surface by a side-looking radar are distributed and sorted according to the time of arrival, either along the slant range or azimuth direction. Along the azimuthal direction, the scan follows the succession of pulses dictated by the PRF.

For the slant range direction, echoes from targets at the same elevation on the scanned surface arrive at the radar most rapidly from the side of the swath facing the sensor, which is referred to as the near-range of the swath. As one runs along the cross-section of the swath, the return signals arrive progressively later and later, up to the side of the strip in the opposite direction from the sensor, identifiable with what is called the far-range distance of the swath. As we have already observed when studying resolution in radars, in order for the sensor to distinguish two backscatterers, their mutual range separation must be at least half the length of the transmitted pulse.

In the case of SARs, the analogy between the handling of angular resolution in passive optical sensors and that in RARs is also broken.

2.4.1 Non-projective nature of the geometric relationships between the scene and the mapped radar image

The core of the difference between the mapping systems of

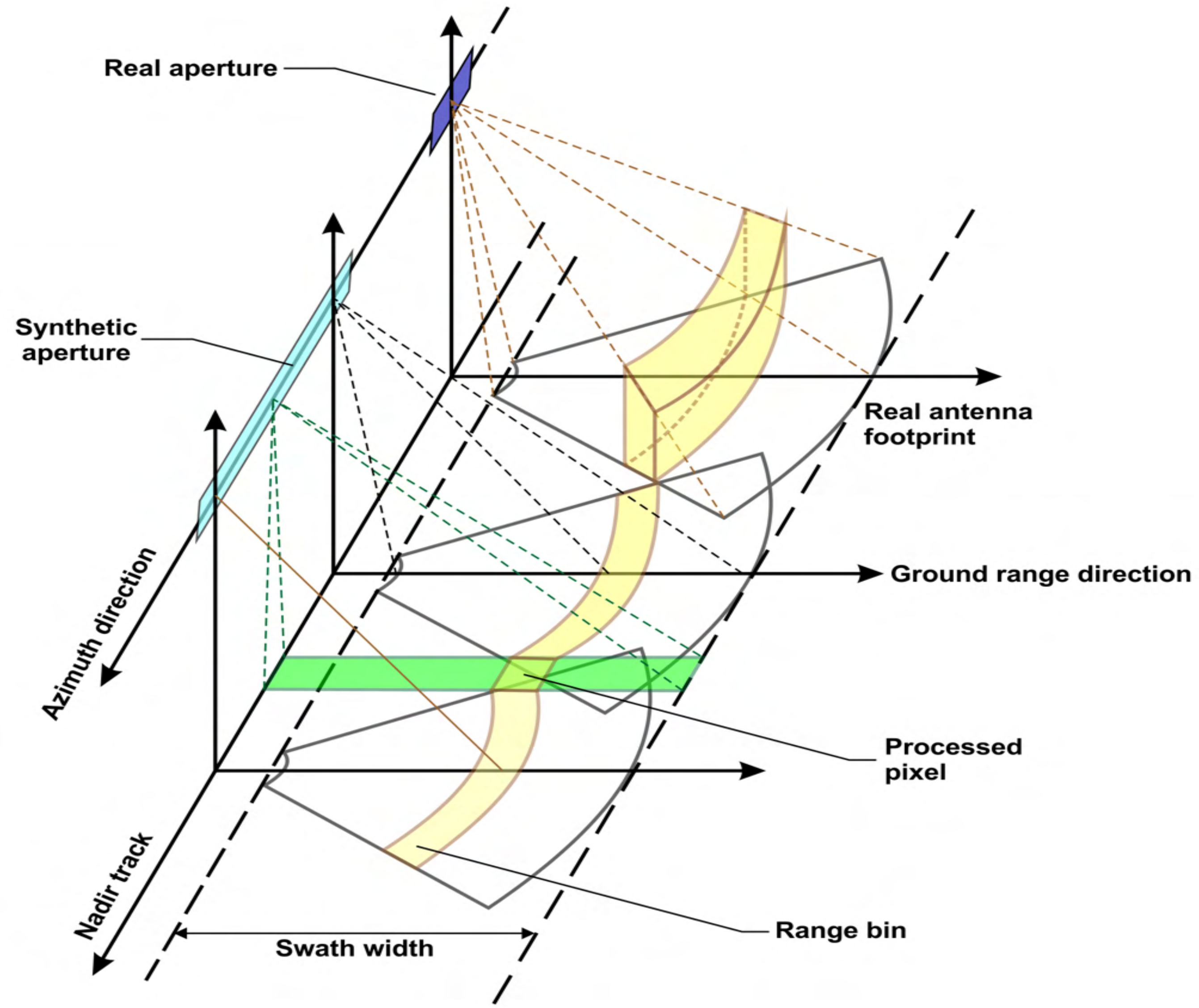

2.4/ Three-dimensional diagram of the acquisition geometry of SAR, according to Keydel 1992.

passive optical sensors and side-looking radars lies in whether the latter are based on time delays or Doppler history.

From a geometric-spatial point of view, the mapping of radar images can be interpreted as a set of rollovers of the detected backscatterers, from the spatial surface or otherwise from the scene, onto a virtual target plane (fig. 2.16a). These rollovers take as their axis the rectified trajectory of the sensor and, with respect to this path, occur from cross-section to cross-section. The virtual target plane is any plane belonging to the sheaf of planes passing through the radar path. It is therefore a radial plane with respect to all the circumferential arcs traced by the respective rollovers operated by the microwave sensor.

In other words, any plane belonging to the sheaf of planes passing through the trajectory of the sensor can be used to map the radar image, since the slant range of the recorded targets are equal on each of them and identifiable with the radii of the rollovers. The along-track coordinates of the targets are recorded transversely from section to section, so they too are equal in all planes of the sheaf of planes passing through the sensor trajectory.

This complex of operations, however, is in no way assimilable to rollover prospectivity, since the source planes containing the targets detected by the sensor do not necessarily belong to the sheaf of planes passing through the radar rectified path, to which the virtual target plane belongs instead.

In other words, the operations performed during the mapping of the radar image cannot be traced back to rollover perspectivity, because the rectified path of the sensor does constitute the axis of all the rollovers performed in space, but it is not the common straight line of all the planes on which the figures to be mapped and the mapped figures lie. A notable example of a plane not passing through the radar rectified trajectory is in fact the ideally flat spatial surface (assumed at the beginning of this argument) on which the targets lie, which therefore does not even belong to the sheaf of planes passing through the sensor path.

We can support this reasoning by using a graphic exemplification. Let us assume, for simplicity's sake, that a side-looking radar is travelling along the horizontal line s and is scanning a perfectly horizontal plane α, located below s (fig. 2.16a). Let the height h between α and s be fixed at 120 m

Let us consider four points on α, which we call A, B, C, D and which lie on a line a perpendicular to the nadir track of the radar platform. Let A, B, C, D be equidistant from each other, say 30 m. Let the distance along a between A and nadir track be 30 m, obviously so that A is included in the FOV of the sensor. Respecting the enumeration order as one moves away along a, B will be at 60 m from the nadir track, C will be at 90 m and D will be at 120 m.

We perpendicularly section the paths and the scene on α with a plane ω, passing through α and thus through A, B, C, D. The point image S of the path s in the plane ω is the radar kinematic configuration at the minimum distances SA, SB, SC, SD from A, B, C, D.

Let us observe the scene in elevation, in the section corresponding to the plane ω (fig. 2.16b). Let us [turn] the points A, B, C, D around S on any straight line p belonging to the bundle of straight lines passing through S, thus determining the rollover points A', B', C', D'. If we measure the segments between A', B', C', D' we will have |A'B'| = 10.734 m, |B'C'| = 16.118 m, |C'D'|= 19.964 m.

Let us calculate the double ratios (A B C D) and (A' B' C' D'):

$$(ABCD) = \frac{(ABC)}{(ABD)} = \left(\frac{\overline{|AC|}}{\overline{|BC|}}\right) / \left(\frac{\overline{|AD|}}{\overline{|BD|}}\right) = \left(\frac{60m}{30m}\right) / \left(\frac{90m}{60m}\right) \simeq \frac{2}{1,5} \simeq 1,333$$

$$= \frac{(A'B'C')}{(A'B'D')} = \left(\frac{\overline{|A'C'|}}{\overline{|B'C'|}}\right) / \left(\frac{\overline{A'D'|}}{\overline{|B'D'||}}\right) = \left(\frac{26,852m}{16,118m}\right) / \left(\frac{46,816m}{36,082m}\right) \simeq \frac{16,660}{12,975} \simeq 1,284 \qquad (2.41)$$

The inequality between the double ratio (A B C D) of the four points on a and the double ratio (A' B' C' D') of the four rollover points on p categorically excludes the existence of any homography or projectivity relationship between the two groups of four points each[19].

As a side note to the result just obtained, it is important to note that along a we have |AB| = |BC| = |CD| and along p we have |A'B'| < |B'C'| < |C'D'|. This confirms that, with the radar mapping process on the virtual plane, the distances between targets decrease as one scrolls towards the near-range of the swath, while they lengthen as one scrolls towards the far-range.

It is possible to reiterate the reasoning by continuing to place equidistant points on line a until it intersects with p. It will then be seen that the segments between the rollover points on p tend to increase in length as one moves away from S.

The alteration of the values of the double ratios and thus the absence of homography relations between the groups of four points belonging to the scene and the respective groups of four points mapped onto the radar image prove that the latter is not the result of rollover prospectivity.

2.4.2 Spatial representation of the geometric relationships between the scene and the mapped radar image

The reasoning we outlined earlier can be reiterated in space for each cross-sectional plane of the platform's flight path, in relation to each along-track co-ordinate value.

The rollovers of the individual illuminated targets in each cross-sectional plane, performed around each point of the trajectory of the radar, can all be considered to be performed on straight lines belonging to a single virtual plane, passing

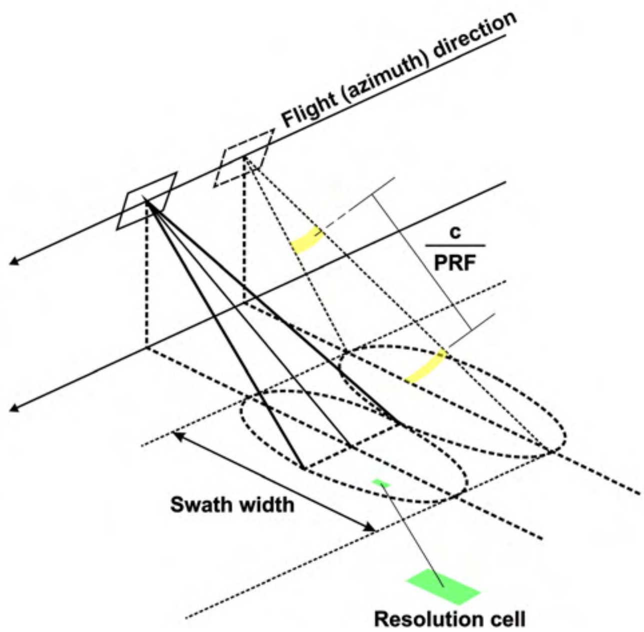

2.5/ The coordinate system and illumination geometry in the case of a SAR, according to Ottl 1992. The higher the PRF required for proper sampling, the smaller the swath width.

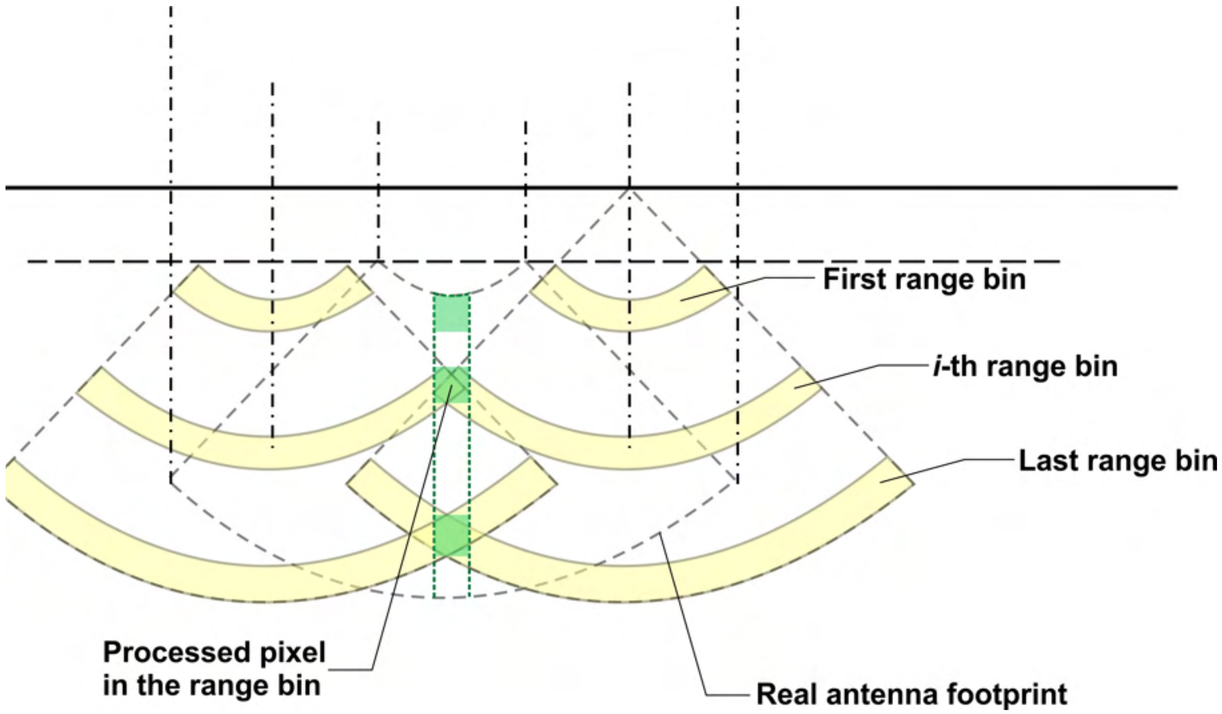

2.6/ Two-dimensional diagram of the acquisition geometry of SAR, according to Keydel 1992, with exemplification of the distribution of the FOV of the sensor into range bins for individual kinematic configurations.

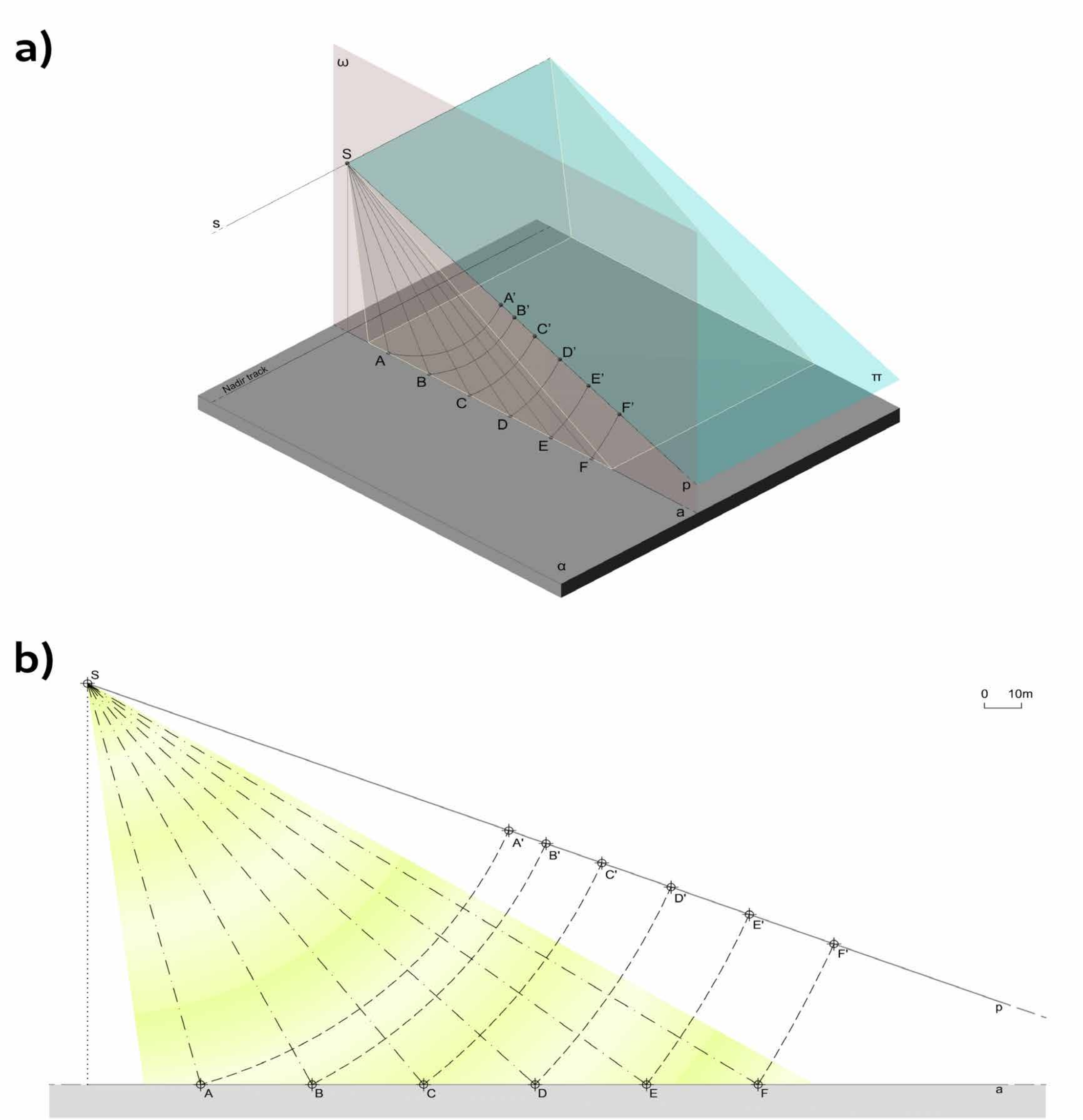

2.7/ Exemplification of the non-projective nature of the radar image mapping system in space (a) and on a section obtained from a generic plane transverse to the trajectory (b). Let A', B', C', D' be the respective rollover points of A, B, C, D around the point image S of the platform path s on a generic transverse plane ω. Between the lengths of the segments AB, BC, CD on the straight line a, belonging to the plane α of the ideally flat and horizontal scanned surface, there exists a relation of equality. Between the lengths of the segments A'B', B'C', C'D' on the line p, belonging to a generic plane π of the bundle of lines passing through the trajectory s of the platform, there exists a relation of inequality. The double ratios between the segments on a are different from the double ratios between the segments on p. Therefore there cannot exist a relation of projectivity between the scene on α, to which the straight line a belongs, and the radar image, identifiablein the plane π, to which the straight line p belongs.

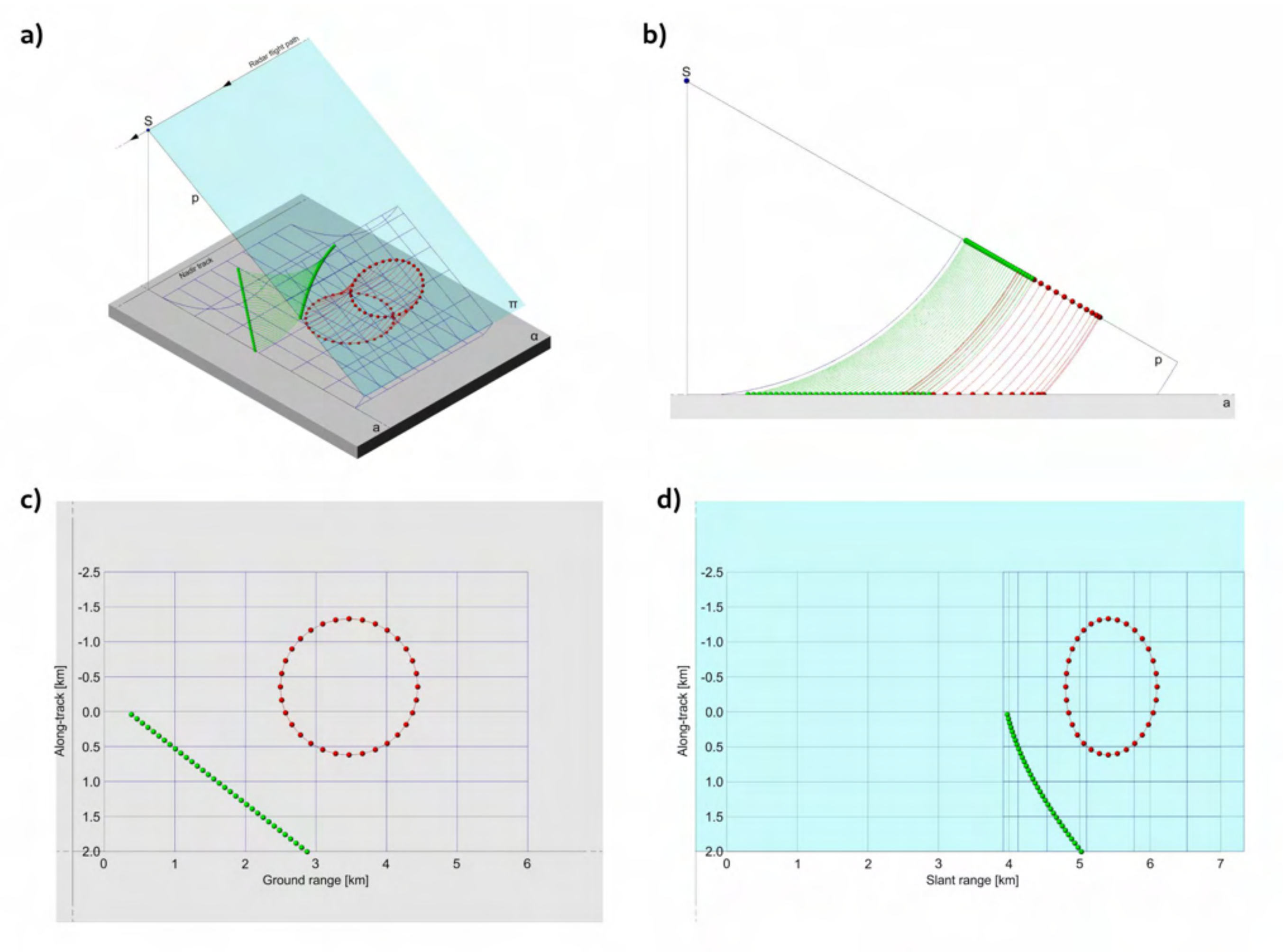

2.8/ Mapping on a radar image of a scene consisting of plane figures: (a) representation in space; (b) representation in cross-section with respect to the radar trajectory; (c) plan of the scene on the horizontal α plane; (d) true shape of the radar image mapped on the generic π plane (the virtual plane), which belongs to the sheaf of planes passing through the path of the RADAR in flight. Since α does not belong to a sheaf of planes having the radar trajectory as a united line, the double ratios between the groups of four points identifiable in the scene and their counterparts obtained from the overturning on the virtual plane do not coincide. Thus between the figures on the scene and the figures in the radar image there is no projective relationship, but instead a non-linear distortion has been applied. This effect, in radar remote-sensing lexicon, is called foreshortening.

2.5.1 Foreshortening

The slopes facing the sensor appear compressed in relation to the slopes looking the other way (fig. 2.19). Let us consider the cross-section of a scene with a symmetrical mountain in the terrain plane xgyg (fig. 2.20) and assume that the radar maps its base, denoted A, and its summit, denoted B. The respective tilts of A and B on the virtual plane, around sensor S,

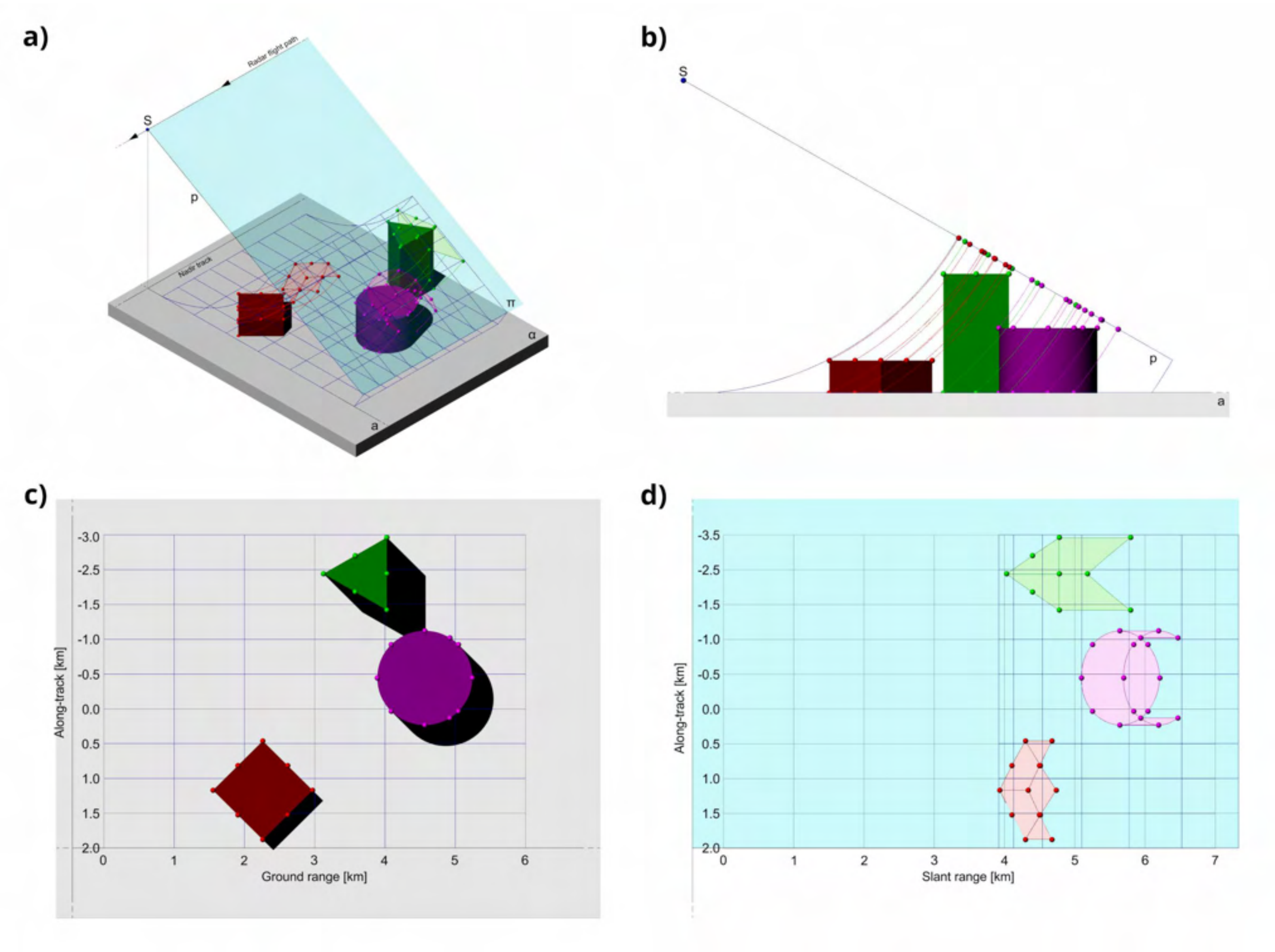

2.9/ Mapping on a radar image of a scene consisting of solids, hypothetically scanned with a SAR with radius amplitude θa = 60°: (a) representation in space; (b) cross-sectional representation with respect tothe radar trajectory; (c) planivolumetric plan of the scene in the horizontal α plane; (d) true shape of the radar image mapped on the generic π plane (the virtual plane), which belongs to the sheaf of planes passing through the radar path in flight. Targets at the same distance on the ground range from the nadir track but at different altitudes may exchange order when mapped: this effect is called layover. Furthermore, those point elements that are not illuminated by the beam emitted by the antenna cannot be detected by the radar: this also applies to those that constitute bodies. In the latter case, RADAR shadows are generated.

will be A' and B'. However, segment A'B' is shorter than segment AB. Therefore, when |yA - yB | > |SB'| - |SA'| and therefore |AB| > |A'B'|, the radar image appears foreshortened. The foreshortening factor F is written approximately in Expression (2.42).

$$F = \sin\left(\theta_1 - \alpha\right) \qquad (2.42)$$

θl is the looking angle of the radar system and α is the angle of the slope on the surface. α is positive (α+) when the slope is facing the sensor (foreslope) and is negative (α-) when the

slope is facing the opposite side backslope).
The foreshortening factor F reaches its maximum if $\theta l \rightarrow \alpha$.
Foreshortening is typical of mountainous areas with moderate heights.
When $\theta l < \alpha+$, foreshortening switches to layover, a situation that occurs for example when areas with steep slopes are illuminated with small incidence angles θi[21].

2.5.2 Layover

In the extreme case where a slope is greater than the angle of incidence θi, layover occurs, i.e. a distortion where the order of two targets in the radar image is reversed from their original positions along the ground range direction. Layover can also be said to occur when the looking angle θl is smaller than the foreslope $\alpha+$ ($\theta l < \alpha+$). In such a situation, a hill, for example, would appear to overhang the land area in front of it (fig. 2.21).
Let us consider the cross-section of a scene on the ground plane xgyg with a strong inclination to the foreslope, having angle $\alpha+$ significantly greater than the looking angle θl (fig. 2.22). Again, the respective rollover pointsof base A and summit B on the virtual plane, around sensor S, will be A' and B'. However, although $yA < yB$ we have $|SA'| > |SB'|$. In other words, the oblique radial distance of the base A to the antenna is greater than that between the top B and the same antenna, so the mapping order will be reversed and in the resulting radar image the mountain will appear to overhang.
Since the layover is a consequence of the height of the targets in relation to the rest of the scanned surface, it is typical of mountainous areas but also occurs in urban areas with noticeably tall buildings.
Overrunning cannot be corrected after acquisition but only avoided by setting an incidence angle θi greater than any angle $\alpha+$ expected in the slopes facing the sensor before scanning[22].

2.5.3 Radar shadowing

Analytically, radar shadowing can be interpreted as a phenomenon opposite to foreshortening. When the sum of looking angle θl and the modulus of the backslope $\alpha-$ exceeds the right angle, i.e. $|\theta\ |l\ + |\alpha\ |- > 90°$, the slopes looking in the opposite direction to the sensor are shadowed.
The shadows are caused by bodies in the scene that intercept the radar beam and prevent the illumination of areas behind them from the sensor. This effect manifests itself, for example, in those images from the Seasat Mission where mountainous reliefs with a backslope $\alpha-$ greater than about 10° were scanned (fig. 2.23).
Let us consider the cross-section of a scene on the ground plane xgyg with a steep backslope (fig. 2.24). The respective rollover points of the top B and base C on the virtual plane, around the sensor S, will be B' and C'. However, the segment AB of the slope facing the sensor intercepts the radar beam, overshadowing the triangle whose vertices are B, C and the projection D of point B on the line yg (constituting, in this simplified case, an ideally flat terrain). When mapping the radar image, therefore, the segment B'D' between the tilts B' and D' will be totally interpreted as having zero reflectivity
Although they cause gaps in data acquisitions, radar shadowing can be utilised to study the topographical conformation of the terrain, in a similar way to the solar illumination shadows of optical images[23].

2.6 Advanced geometric models for radar scans from high altitude and space platforms

As noted earlier, it is only possible to ignore terrestrial curvature in radar scans from low-altitude aircraft platforms. Typically, the assumption of an ideally flat land surface is implicitly accompanied by the assumption of a straight-line path by the platform, as these models have similar orders of accuracy. It should be noted that actual aircraft trajectories are usually not straight and cannot be straight even on the basis of deliberate choices, due to turbulence and possible forced deviations from the planned path.
For radar scans from high-altitude aircraft or space platforms, the assumption of a flattened land surface can only be used for preliminary and simplified analyses.
Let us consider the cross-section of a scene scanned by side-looking radar installed on an aircraft flying at low altitude (fig. 2.25a). The aircraft flies at altitude h above its nadir track on the ground. The radar antenna has an elevation aperture Θel. Under the assumption of a perfectly flattened Earth surface, the looking angle θl between the antenna LOS and the

Luca Martelli

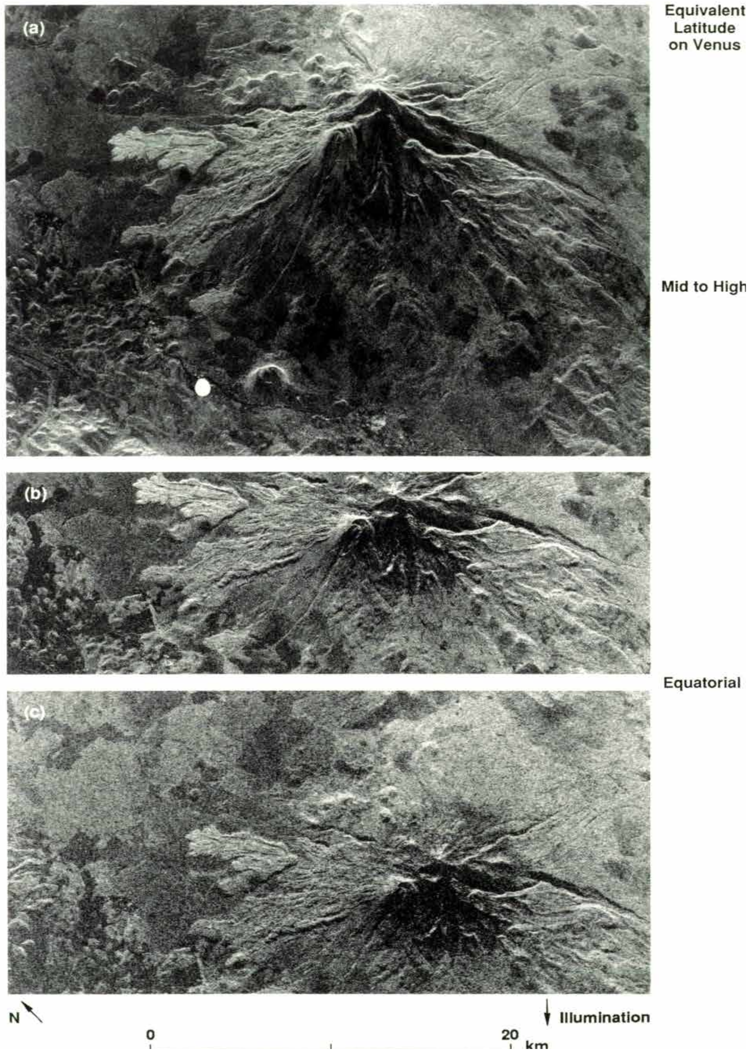

2.10/ S AR images of Mount Shasta in California, acquired by Shuttle Imaging Radar-B (SIR-B) in the L-band, with looking angles of 28° (a), 51° (b) and 57° (c). Mount Shasta is a potentially active volcano that rises approximately 3,000 m above the surrounding Californian terrain. As the sensor was pointing towards the lower side of the respective image during each scan, the volcano appears tilted towards the upper side at different degrees in each scan. Note the progressive stretching of the three Radar images as one scrolls from the upper to the lower side. Source: Ford, Blom, Crisp, Elachi, Farr, Saunders, Theilig, Wall, Yewell 1989 / Image under Public Domain.

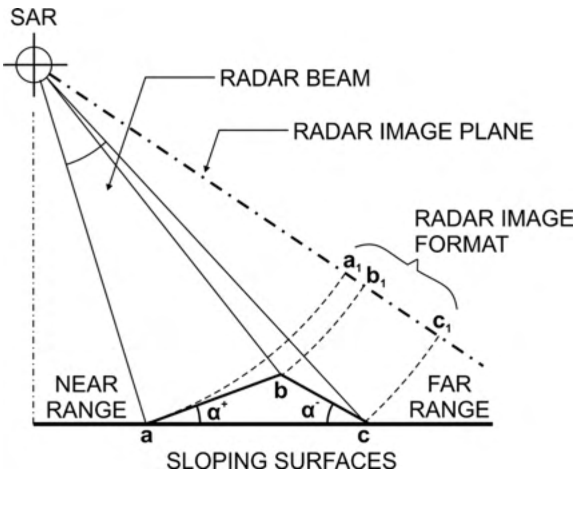

2.11/ Example diagram about foreshortening, according to Keydel 1992. Foreshortening of the declivity segment AB, the ends of which are tipped on the virtual plane of the radar at points A' and B', in relation to the declivity segment BC, the ends of which are tipped at points B' and C'. θl is the viewing angle looking angle, α+ is the foreslope, α- is the backslope.

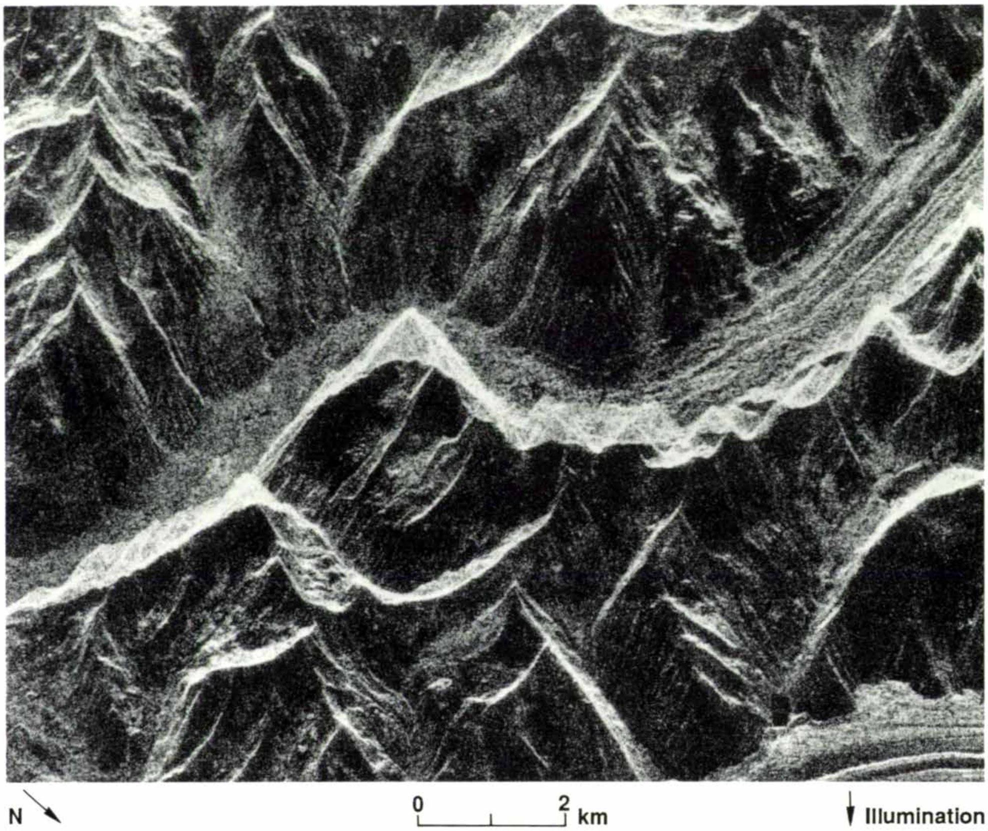

2.12/ Example of layover in a SAR image of the Alaska Range, scanned during the Seasat Mission. Since the sensor was pointing towards the underside of the image and the mountain ranges have a steep slope, this resulted in an layover effect of the mountain top (bottom) on the glacier at its foot (centre of the image). The glacier can be easily identified by the ice tongue on the right. Note the progressive stretching of the radar image as one scrolls from the upper to the lower side. Source: Ford, Blom, Crisp, Elachi, Farr, Saunders, Theilig, Wall, Yewell 1989 / Image under Public Domain.

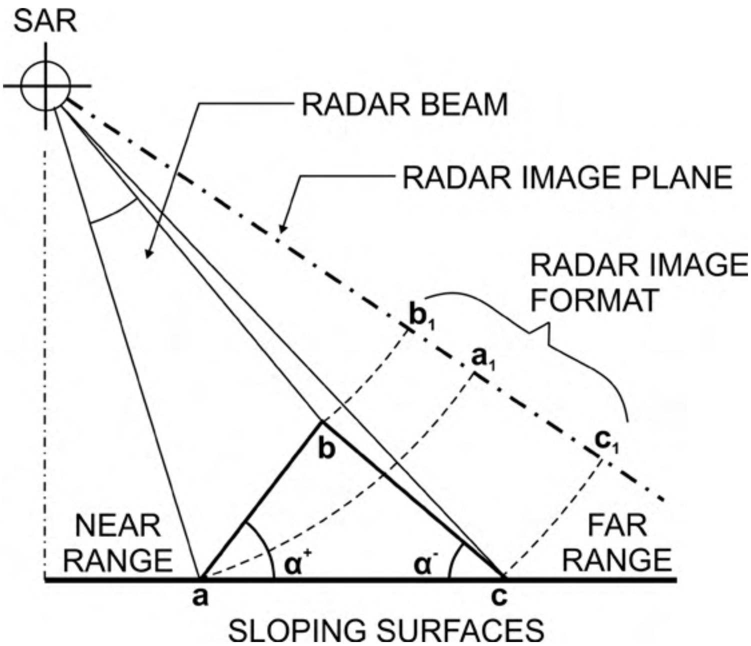

2.13/ Schematic example of overriding layover, according to Keydel 1992. Layover of the declivity segment AB, the ends of which are inverted in reverse order (B'A') in the plane of the radar image. The looking angle θl is smaller than the foreslope α+.

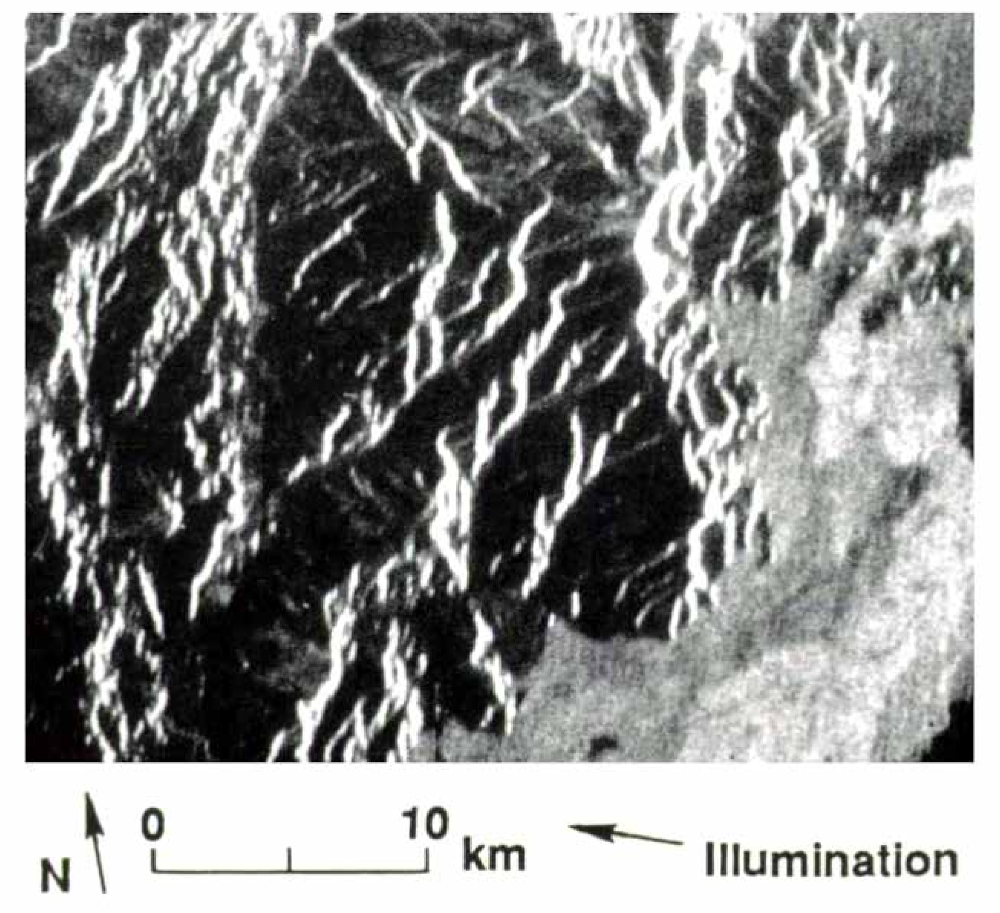

2.14/ SAR image of the Lava Field of the Craters of the Moon in Idaho, acquired during the Seasat Mission. Since the sensor was pointing towards the left side of the image and the mountainous reliefs have a steep slope on the opposite side, this resulted in numerous radar shadows. Note the progressive stretching of the radar image as one scrolls from the right to the left side. Source: Ford, Blom, Crisp, Elachi, Farr, Saunders, Theilig, Wall, Yewell 1989 / Image under Public Domain.

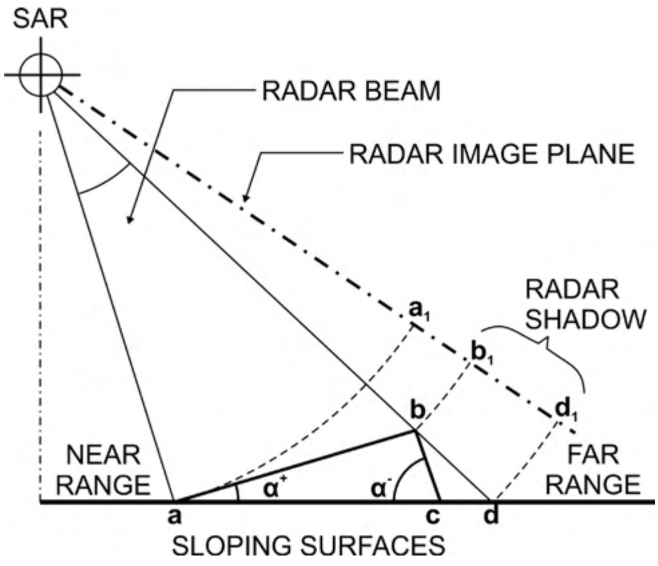

2.15/ Example diagram of radar shadowing, according to Keydel 1992. Radar shadowing of the surface section consisting of segments BC and CD, having points B' and D' tilted to the image plane.

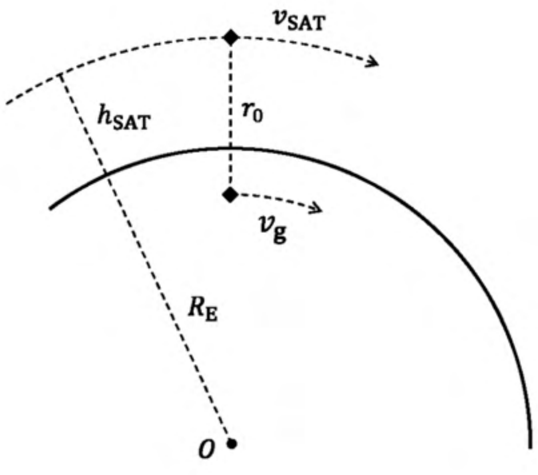

2.16/ Patterns of acquisition geometry with side-looking radar under the flattened land surface assumption (a) and under the spherical planetary surface assumption (b). The flattened land surface model is only useful for scans from low-altitude airborne platforms, while more complex models are required for airborne surveys from higher altitudes or space platforms. Source: Emery, Camps 2017.
2.26/ Illustration of space platform velocity vs and ground velocity vg in a quasi circular orbit geometry, according to Emery, Camps 2017.

nadir vector coincides with incident angle θi , i.e. the angle between the direction of signal propagation and the local normal with respect to the point on the surface intercepted by the LOS. If the curvature of the planetary surface is neglected, the slant range and the ground range always constitute the hypotenuse and cathetus, respectively, of a right-angled triangle, allowing the acquisition geometry to be approached simply by applying the Pythagorean Theorem as stated in Expression (2.43).

$$y_{gr}(p) \rightarrow r_0(p) = \sqrt{h^2 + \left[y_{gr}(p)\right]^2} = \frac{h}{\cos\left[\theta_i(p)\right]} \qquad (2.43)$$

p denotes a point on the ground, ygr and r are the coordinates along the ground range direction and the slant range direction respectively. The swath of the radar beam can be written as Expression (2.44).

$$S_w = h\cdot\left[\tan\left(\theta_l+\frac{\Theta_{el}}{2}\right)-\tan\left(\theta_l-\frac{\Theta_{el}}{2}\right)\right]\approx\frac{h}{\cos(\theta_i)\cdot\sin(\theta_i)}\cdot\Theta_{el} \qquad (2.44)$$

The radar beam swath grows proportionally to the height of the sensor.
For high-altitude aircraft and space platforms, however, the assumption of a flattened planetary surface allows only approximate evaluations and a more elaborate geometric model is consequently required. The calculation of the coverage of a satellite scan, for example, cannot be performed by neglecting the curvature of the planetary surface, as this would result in incorrect values of the orbital cycles required to cover the area of interest. One can then consider the radar as moving in a Keplerian orbit, using a local spherical surface to approximate the scene to be scanned.
The above model is not necessarily the one adopted for the analysis and operations of a real mission, which typically involve the use of data on the actual topographical configuration of the planet and real orbits, but it is objectively useful for approximate coverage estimation and performance analysis.
If we consider the cross-section of the scene without the assumption of a flattened Earth surface (fig. 2.25b), the first obvious difference is that the equality between looking angle θl and incidence angle θi is lost. On the other hand, the greater the slant range, the greater the rate at which the incidence angle θi increases. Consequently, the slant radial distances [slant ranges] appear compressed in comparison to their counterparts determined under the flattened planetary surface assumption. The oblique radial distance constitutes one side of an obtuse triangle that can be solved with the cosine law, as in Expression (2.45).

$$r_0 = R_p\cdot\cos(\theta_i) - \sqrt{R_p^2\cdot\cos^2(\theta_i) + h\cdot\left(2\cdot R_p + h\right)} \qquad (2.45)$$

RP is the radius of the planet (e.g. the Earth) at the latitude of the scene to be scanned. The incidence angle θi can always be calculated using the cosine law as a function of the slant range, as in Expression (2.46).

$$\theta_i = \arccos\left[\frac{\left(R_P + h\right)^2 - r_0^{\,2} - R_P^{\,2}}{2\cdot r_0\cdot R_p}\right] \qquad (2.46)$$

The width of the swath [swath] can be written in the approximation of Expression (2.47).

$$S_w \approx \left[R_P \cdot \cos(\theta_i) - \sqrt{R_P{}^2 \cdot \cos^2(\theta_i) + h \cdot (2 \cdot R_P + h)}\right] \cdot \frac{\Theta_{el}}{\sin(\theta_i)} \qquad (2.47)$$

An additional consequence of the curvature and rotation of the Earth is that the velocity of the instantaneous footprint of the radar beam on the land surface, called ground velocity, is less than the velocity of a space platform. In the case of a space platform, in fact, if no manoeuvres are required to steer the antenna, both the radar and the instantaneous footprint of its beam cover similar angular spans of the circumference with which it is possible to approximate the cross-section of the Earth's surface (fig. 2.26).
The ratio of ground and spacecraft velocities decreases as the altitude of the orbits increases, as incidence angle θi and as orbital inclinations increase. For nearly quasi circular orbits, the ground speed can be approximated as in Expression (2.48).
vs is the velocity of the space platform, Trot is the period of rotation of the Earth, θlat is the latitude of the point considered on Earth's surface, and φincl is the inclination of the orbit. The second term of the right-hand member of Expression (2.48) approximates the effect of the planet rotation and the plus or minus sign is used to distinguish descending passes and ascending passes, respectively.
Compared to the flattened Earth surface hypothesis, for which it is assumed that the velocity of the ground and that of the space platform are equal, in this model the ground velocity varies with the radial distance from the radar range, decreasing in the case of a flat scene[24].

2.7 Radiometric distortions

The phenomena governing scene mapping by means of active microwave sensors involve a number of peculiar anomalies, also related to the acquisition geometry. Since, in general, the type of side-looking radar used in remote-sensing is the SAR, we feel it is appropriate to review the abnormalities that mainly concern this type of instrument.
A SAR sensor typically measures three basic characteristics of the received echo: the backscatter, usually represented as the normalised RCS σ0 ; the time delay; and the Doppler shift. The first characterises the generic target radiometrically,

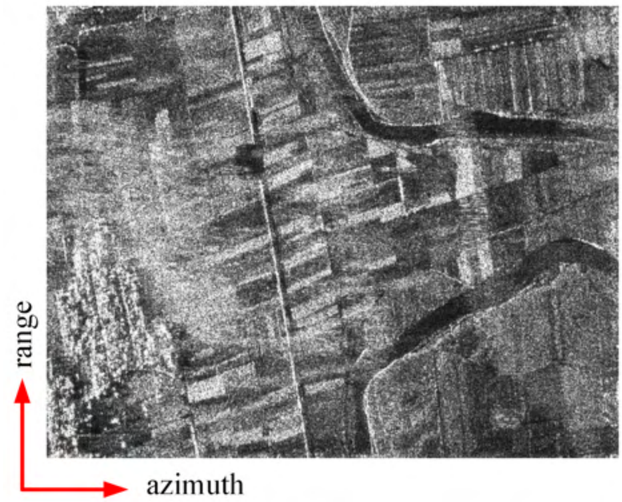

2.17/ SAR image segment particularly prone to range ambiguities. Source: Yu Kun, Zhu Shengqi, Lan Lan, Yang Biao, 2023 / licensed under CC BY 4.0 (http://creativecommons.org/licenses/by/4.0/). © 2023 by Yu Kun, Zhu Shengqi, Lan Lan, Yang Biao. Licensee MDPI, Basel, Switzerland.

while the other two allow the return signal to be associated with its correct location in the radar image to be mapped.
Below we list and briefly describe the most common types of radiometric abnormalities found in SAR images.

2.7.1 Range ambiguities and azimuthal ambiguities

As we stated earlier, a SAR maps a spatial surface by recording echoes from linear segment to linear segment, by means of successive pulses. The length of the echo, i.e. the swath width of the scene being scanned and mapped, is determined by the width (in the cross-sectional area with respect to the path of the platform) of the beam emitted by the antenna or a data window (i.e. a restriction programmed to record only a portion of the scanned swath). The leading edge of each echo corresponds to the near-range of the swath; the trailing edge of the echo corresponds to the far-range of the swath.
The exact timing of echo reception depends on the range between the sensor and the planetary surface to be mapped. Physically, it is possible that the timing of the pulses or the extension of the return signals allow the manifestation of

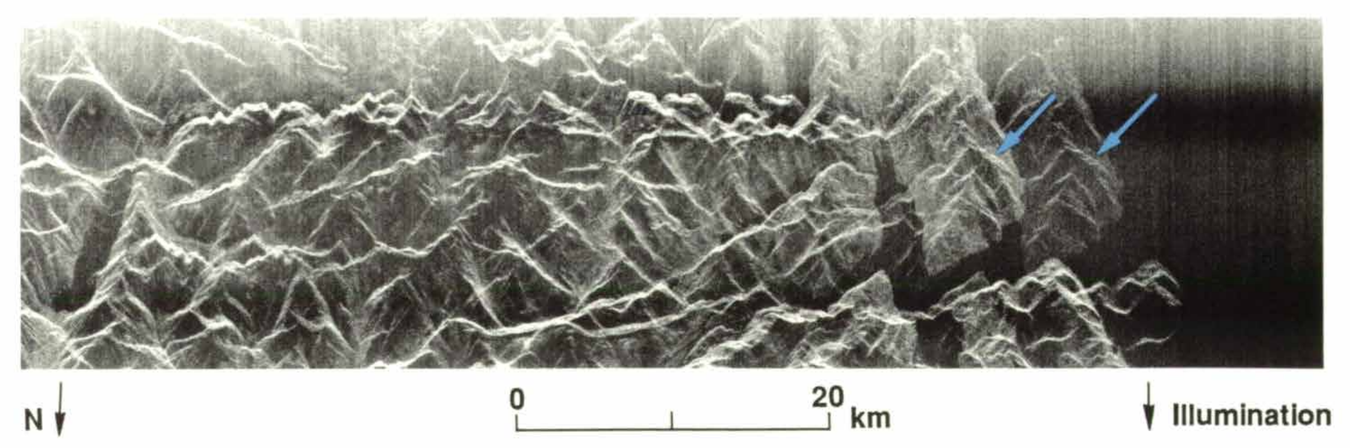

2.18/ RADAR image of a mountainous area near Juneau, Alaska, acquired by Shuttle Imaging Radar-B (SIR-B) in the L-band and affected by azimuthal ambiguities due to inadequate processing. Source: Ford, Blom, Crisp, Elachi, Farr, Saunders, Theilig, Wall, Yewell 1989 / Image under Public Domain.

unwanted second time-around-echoes. In other words, this is the situation in which the trailing edge of a first return signal is superimposed on the leading edge of the next return signal, causing the image portion associated with the near-range of the second echo to be superimposed on the far-range portion of the first echo (fig. 2.27). This type of anomaly is called range ambiguity.

The time extension of a radar echo is given by Expression (2.49).

$$T_e \approx 2\frac{R}{c}\theta_r \tan(\theta_1) = 2\frac{h\lambda}{cW}\frac{\sin(\theta_1)}{\cos^2(\theta_1)} \qquad (2.49)$$

To avoid unwanted second-time-around-echoes and multiple-time-around echoes, this time interval should be shorter than the time interval separating two pulses (i.e. 1/PRF). This condition is written in Expression (2.50).

$$PRF < \frac{cW}{2\,h\lambda}\frac{\cos^2(\theta_1)}{\sin(\theta_1)} \qquad (2.50)$$

The design of a radar must not only avoid unwanted second-time-around and multiple-time-around echoes, but also select instrument parameter values – especially the PRF – so that the entire echo only occurs within the inter-pulse period. In other words, no echo must be picked up by the radar while it is transmitting a pulse.

Expression (2.50) sets an upper limit to the PRF. As already stated, designers of SARs must balance the system parameters to maximise the swath width and, at the same time, ensure a sufficiently high PRF to adequately sample the signal Doppler spectrum.

The possibility that the return signal of a backscatter element is sampled at the PRF, along the azimuth direction, gives rise to another type of ambiguity present in SAR imagery. In such a situation, the azimuth spectrum of the backscatter of a target is repeated in the frequency domain by multiples of the PRF. Generally, the azimuth spectrum is not a band-limited signal, it is rather weighted by the antenna pattern in the azimuth direction. Parts of the azimuthal spectrum may be aliased and associated high-frequency data may therefore appear in the lower part of the spectrum. Graphically, these azimuthal ambiguities appear as artefactual images of a target repeated at regular intervals along the azimuthal direction (fig. 2.28).

To reduce azimuthal ambiguities, the PRF of a SAR must be above the lower limit set by Expression (2.40). To reduce both radial distance ambiguities and azimuthal ambiguities, the PRF must therefore simultaneously satisfy the conditions set by Expression (2.40) and Expression (2.50). We can therefore restate these conditions in a single inequation, as stated in Expression (2.51)

$$\frac{cW}{2\,h\lambda}\frac{\cos^2(\theta_1)}{\sin(\theta_1)} > \frac{2v}{L} \qquad (2.51)$$

Then we can write the lower limit for the antenna size in Expression (2.52).

$$LW > \frac{4vh\lambda}{c}\frac{\sin(\theta_1)}{\cos^2(\theta_1)} \qquad (2.52)$$

It is important to note that Inequation (2.52) is only valid under particular conditions, where the processor of the SAR commits the full Doppler bandwidth to processing and where a swath is mapped covering the full width (in the cross-sectional area with respect to the platform path) of the beam emitted by the antenna. It is not necessarily the case that this situation occurs every time a SAR is scanned.

It may happen, for various reasons, that SAR images are only processed up to a partial portion of the maximum resolution achievable by the instrument, or that the swath width is intentionally limited by recording only that section of the signal falling within a so-called data window. When one of these situations occurs, limiting the size of the antenna according to the condition in Expression (2.52) is counterproductive. If the swath width is artificially limited and the resolution is simultaneously lowered, antennas significantly smaller than the limit set by Inequality (2.52) can be used with very good results[25].

2.7.2 Artifacts due to spurious signals from radar filter side lobes

When a target with a strong backscatter is represented on the radar image as a very bright element and the latter is surrounded by a dark area, another type of anomaly may occur. During image mapping, it may happen that the brightness of the brightest cell oversteps its boundaries and prevails over the dark background given by the surrounding cells, generating faintly visible artefacts.

This type of abnormality does not only affect radar sensors and is also common in optical systems, where they are connected to the side lobes of the point spread function. However, in optical instruments, the characteristics of the 'feet' depend on the characteristics of the image-generating optics, i.e. the hardware.

In the case of SAR, these artefacts are generated by spurious

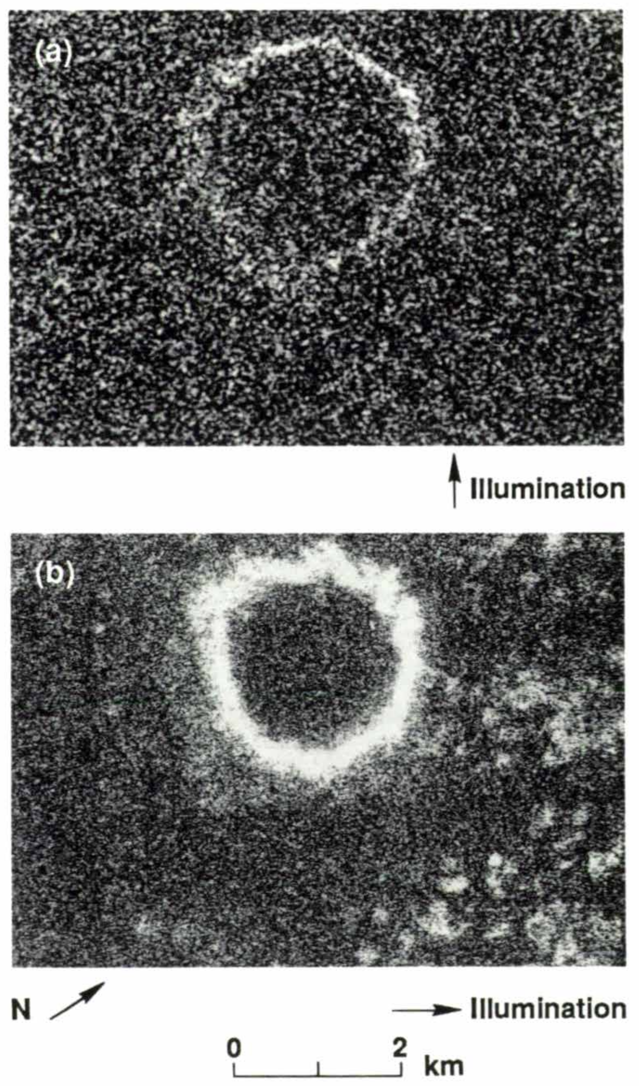

2.19/ RADAR images of a crater on the Iraqi-Jordanian border, both subject to speckle phenomena of varying magnitude. Image (a) was acquired in 1984, during the course of the Shuttle Imaging Radar-B Mission (SIR-B) and highlights the ridge of the crater rim. Image (b) was acquired in 1981, during the course of the Shuttle Imaging Radar-A (SIR-A) Mission. The narrower sensitivity range of the SIR-A sensor did not allow it to detect the crater rim ridge in more detail. Source: Ford, Blom, Crisp, Elachi, Farr, Saunders, Theilig, Wall, Yewell 1989 / Image under Public Domain.

signals given by the side lobes of the processing filters. The characteristics of side lobes depend mainly on the technical characteristics of the filters in question. These anomalies can be mitigated by eliminating part of the side lobes through appropriate weighting of the signal spectra during compression by the matched filter. For remote-sensing optical systems, a procedure similar to this technique exists, called apodization of the telescope aperture[26].

2.7.3 Signal attenuation and speckle

In SAR images, especially those involving extended targets rather than point targets, the variation in brightness is not gradual but is instead characterised by a grainy texture, called speckle (fig. 2.29). Even when mapped from a scene that is prone to constant backscatter, the resulting image will have statistical variations in brightness on a pixel-by-pixel basis, but with a constant average over several pixels. This effect is characteristic of all coherent imaging systems that have a very narrow spectral width and is caused by the interference of numerous backscatters within a resolution cell. If the sensor is moved a short length, the composite amplitude of the received signal will be an independent sampling of the backscatter of the target. In principle, each of these independent samplings provides additional data on the target, but their mutual interference is actually handled as an artefact. In years past, speckle was even considered as a noise source with multiplicative character, i.e. one that could not be mitigated by increasing the transmitted power. This consideration is inaccurate, as it is precisely the coherent nature of the system that gives radars the potential to achieve resolutions in the same order as the wavelength adopted[27].

A similar phenomenon occurs when optically observing a scene illuminated with lasers, as these too are characterised by a coherent nature.

In a medium-resolution SAR image, the backscatter given by a single resolution cell – which has an extent of about 10 m × 10 m – is the coherent sum of thousands of individual scattering events (fig. 2.30)

Let us imagine that a SAR sensor is mapping a homogeneous surface, such as a smooth plain. Let us assume that the individual scattering events within a resolution cell are all characterised by approximately the same intensity. Due to their

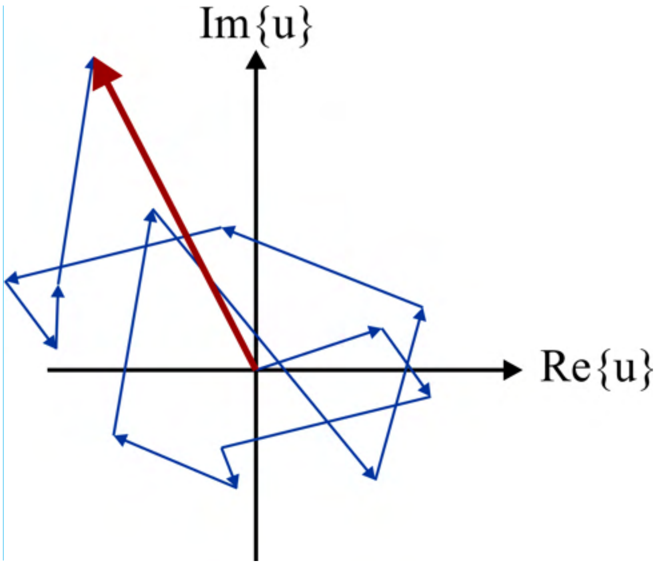

2.20/ Cartesian diagram, representing an example of speckle as a coherent sum (bold black vector) of several individual scattering events (grey fillet vectors) within a resolution cell. The abscissa and ordinate represent, respectively, the values of the real component ℜ{u} and the imaginary component ℑ{u} of the intensity I. Source: Meyer 2019.

different positions within the resolution cell, the phases of the return signals of the individual scatterers will vary randomly, so that the backscatter given by an area corresponding to a certain pixel will be the sum of thousands of random vectors. Since the arrangement of the scatterers in different cells of the same resolution is not identical even in homogeneous scenes, both the amplitude component and the phase component of the sum vector will vary randomly from pixel to pixel, resulting in the typical granular irregularity described earlier (fig. 2.29). If the number of individual scattering events is high, the distribution of intensities in a SAR image follows an exponential distribution in the form of Expression (2.53).

$$\mathrm{PDF}\left(\mathrm{I} \mid \sigma_0\right) = \frac{1}{\sigma_0}\exp\left\{-\frac{\mathrm{I}}{\sigma_0}\right\} \qquad (2.53)$$

PDF ($I \mid \sigma 0$) is the Probability Density Function (PDF) depending on the intensity $I = \Re\{u\}2 + \Im\{u\}2$ of the image in a pixel ($\Re\{u\}$ and $\Im\{u\}$ are, respectively, the real and imaginary components of the backscatter vectors) and the (true) normalised equivalent normalised RCS σ0 of the scanned

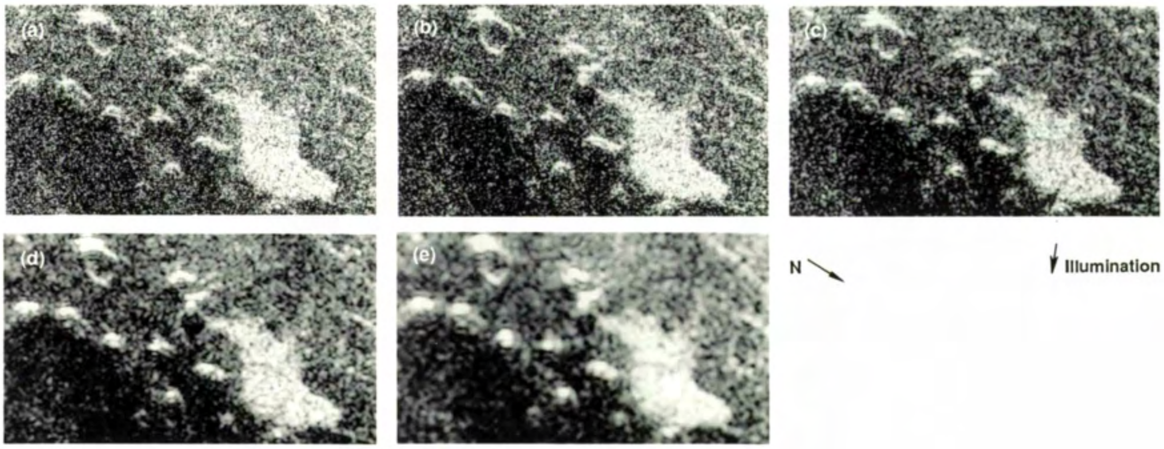

2.21/ Radar images of SP Lava Field of the San Francisco Volcanic Field, Arizona, acquired during the Seasat Mission. The amount of speckle in each image is a consequence of the number of looks N used in the eventual mediation. Images (a), (b), (c), (d) and (e) have N values of 1, 2, 4, 8 and 16, respectively, resulting in the corresponding resolutions of 86 m, 120 m, 172 m, 240 m and 344 m.
Source: Ford, Blom, Crisp, Elachi, Farr, Saunders, Theilig, Wall, Yewell 1989 / Image under public domain [Image under public domain].

target. The distribution in Expression (2.53) is often called speckle distribution. It is a valid description for distributions of anomalies detected between homogeneous targets in SAR images of medium resolution. As already mentioned, the shape of the speckle distribution depends on the (true) normalised RCS σ0 of the scanned target. σ0 , let us remember, describes the portion of RADAR energy transmitted by the antenna that is scattered back from the target to the sensor and is a normalised version of the parameter determined by Expression (1.5). Therefore, the brighter a portion of the image, the more intense the abnormalities characterising it will be. The graph of speckle statistics changes depending on the value of σ0 , so we can draw an abacus that gathers a trend for each value of σ0 that we wish to consider (fig. 2.31). In the drawn abacus, we can see how the speckle distribution PDF (I | σ0) expands as σ0 increases and begins to approximate a uniform distribution for very high values of σ .0
Compared to classical noise sources, which are often constant over the entire SAR image, the speckle phenomenon is also characterised by its dependence on pixel brightness. It is difficult to counteract since, in order to model PDF (I | σ0), it is necessary to know the true normalised equivalent normalised RCS σ0 of the target.

A number of different approaches have been developed to mitigate speckle, but none are currently free of side effects nor can they be considered convenient in any situation. For example, to reduce brightness fluctuations in the radar image, one can incoherently average signals in succession or adjacent pixels, i.e. sum their power values. Adopting this method means obtaining a more accurate radiometric measurement and an image with fewer irregularities, but at the cost of a deterioration in resolution.
Another more elaborate approach to mitigate speckle is to combine radar images acquired with neighbouring frequencies and then incoherently averaging them. By doing so, the exact interference patterns lead to independent signals but with the same statistical properties, thus resulting in a less irregular result once incoherent averaging is applied. It is due to a similar phenomenon that a scene illuminated with white light of the visible spectrum is not characterised by speckle. In most SARs for imaging, the reduction of irregularities is performed by averaging the brightness of the pixels along the azimuth or along the range or along both of these directions. The averaged number of statistically independent pixels is called number of looks N. The mathematical connection between the signal standard deviation SN and the mean signal power $\bar{P}$ is written in Expression (2.54).

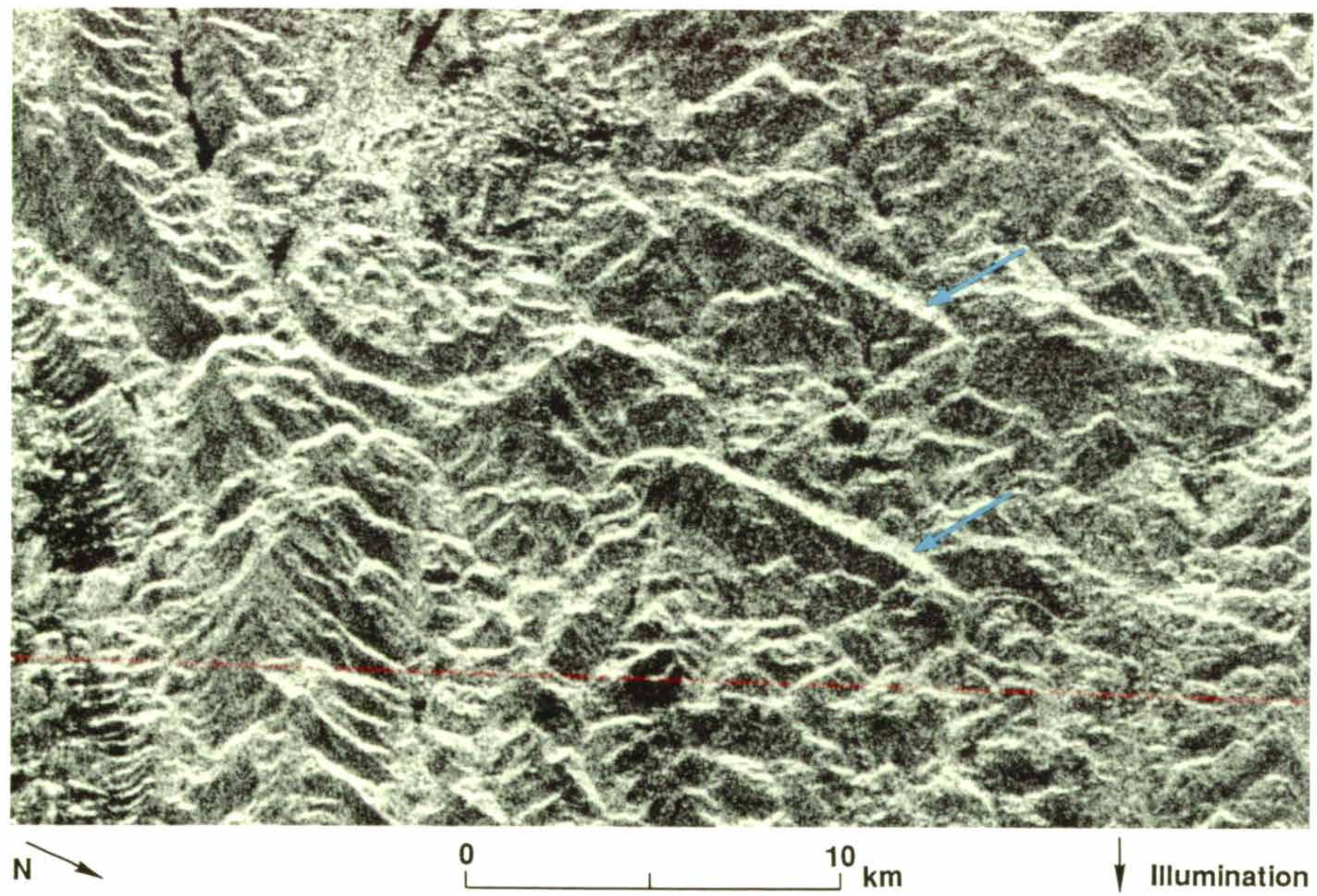

2.22/ Radar image of the Appalachian Mountains in Kentucky, acquired during the Seasat Mission and subject to a radial distance window range gate. Both the data in the corrected phase and the data in the offset phase occupied the same synthetic aperture. The artefacts indicated by the arrows are the most obvious, but all data in the same azimuthal band of the image are replicated. Source: Ford, Blom, Crisp, Elachi, Farr, Saunders, Theilig, Wall, Yewell 1989 / Image under Public Domain.

$$S_N = \frac{1}{\sqrt{N}} \bar{P} \qquad (2.54)$$

The higher the number of looks N, the better the image quality from a radiometric point of view but, at the same time, the worse the spatial resolution of the image. It should also be borne in mind that, for approximately $N > 25$, large increases in the number of looks result in only a small reduction in signal fluctuation. This modest improvement in radiometric resolution should be weighed against a consistent deterioration in spatial resolution (fig. 2.32).

For example, if we were to average 10 cells of resolution in an image obtained from 4 observations ($N = 4$), the magnitude of the speckle will be reduced by approximately 0.5 dB but, at the same time, the resolution of the radar image will be lowered by a certain order of magnitude. The evaluation of the convenience of this loss of resolution in exchange for a reduction in speckle must be made in relation to the objectives of the scanning operations and the type of scenes to be mapped. Another possibility, if one has a large number of images of the same area, is to mediate incoherently along the images.

In this way, spatial resolution is preserved, but the disadvantage is that several images are required (usually acquired at different times, so stationarity of the observed scene is also required).
In addition, much effort has been put into the development of effective speckle filters over the past decade, resulting in various filtering techniques[28].

2.7.4 Effects of range gate misalignment

Like all active microwave sensors, SARs have the advantage of constituting their own illumination source. However, integrating the illumination of a backscatterer and the associated echo reception is a very complex problem. The receiver must be timed to acquire the return signal from the same portion of the spatial surface illuminated by the radar beam: the time interval underlying this receiver calibration is called the 'range gate'.
While the alignment of the target illumination is a temporal problem, the alignment of the echo associated with the target is a geometric problem, which means that the relationship between these two data varies with the altitude assumed by the sensor. Often, during an acquisition, the range gate must be changed several times in a second to adapt the scan to changes in altitude.
In situations where the altitude of the SAR is not perfectly known, the alignment of the antenna pattern and the range gate may also be imperfect, possibly causing two different types of artefacts:

- the former consists of a black shading of the radar image, as its margins are determined by the edges of the range gate;
- The second, which is much easier to equivocate, is a repetition of data that can result from a cross-track shift in the ground range coordinates (fig. 2.33). This deviation occurs if the range gate is out of phase and is not properly accounted for during data correlation[29].

2.8. Interactions between the target and the radar signal

As with all side-looking radars, SAR transmits microwave signals from an oblique location and measures the backscattered portion of the signal in the direction of the sensor, in order to analyse the scanned spatial surface. Mathematically, this calibrated measurement is described by the RCS or radar signature σRCS which, in Chapter 1, we had already seen defined as the ratio between the backscattered power density PRX and the incident power density PTX per unit solid angle (referring to an equivalent sphere of radius r0) on the target. It is also possible to define the RCS σRCS as the ratio of the scattered back signal strength IRX to the incident signal strength ITX per unit solid angle, as stated in Expression (2.55).

$$\sigma_{RCS} = \frac{I_{RX}}{I_{TX}} 4\pi \cdot r_0^{\,2} \qquad (2.55)$$

Interpreting the RCS of a specific target located on the scanned land surface is not always a straightforward and linear operation, as it is influenced by several scene characteristics and sensor parameters. Among the scene parameters governing the RCS, the most important are the surface roughness hrough and the dielectric properties of the scanned body, the latter quantified by its relative complex dielectric constant εr .
While hrough describes how much of the scattered radar energy is redirected towards the sensor, the dielectric properties determine whether signals can penetrate the backscattering surface and, if so, how deep they can reach. Both hrough and εr are functions of the wavelength λ adopted by the sensor and, within certain limits, the polarisation of the signal. This explains why the technical char   to interpret the equivalent RCS of real objects, measured in a SAR image[30].

2.8.1 Dielectric properties and radar signal penetration depth

The dielectric properties of a medium determine how it interacts with a microwave signal of wavelength λ. The medium in question can be the surface of a planet such as the Earth, a glacier or the canopy of a forest. The dielectric properties establish:

- the proportion of the signal that will scatter in space once it hits the surface of the medium;
- how much radiation will penetrate the medium;
- how much energy dissipates in the medium.

The greater the wavelength λ to which the sensor is set, the greater the depth to which the radar signals emitted by the sensor penetrate (fig. 2.34). This concept is related to the dependence of the dielectric constant εr on the length λ of the incident wave and is also what gives a certain frequency band a greater penetration capacity than higher frequency bands. For example, the L-band has a higher susceptibility to body penetration than the C-band and X-band.

For areas covered by vegetation, this implies that most signals in the X-band spread out once they hit the tree canopies, while the C-band and, even more so, the L-band can pass through them and map the space under the canopies. Therefore, if data concerning a tree mass (e.g. tree structure, biomass, etc.) is to be detected with a SAR, systems using longer wavelengths should be used. Similarly, users wishing to detect flooding under vegetation canopies should adopt SAR sensors employing the longer wavelengths as the data source for their observations. In addition to the wavelength λ of the sensor, the penetration depth of a SAR signal through the canopy of a vegetation canopy is also influenced by the density of the canopy. For example, signals in the C-band can often map the terrain beneath the trees of forests in the northern hemisphere, as these are quite sparse, but cannot fully penetrate the structures formed by rainforest canopies, which are denser and more layered.

The rule of greater penetration due to the longer wavelength λ remains valid for uncovered surfaces such as alluvial soils or the upper layers of glaciers: X-band signals propagate after impacting the surface, while the C-band and even more so the L-band can penetrate deep into the medium.

The dry, well sorted granular materials are those most easily penetrated by radar radiation, down to depths of several times the wavelength of the signal emitted by the antenna.

To quantify the depth of penetration δp into an uncovered surface, it is necessary to know the parameter εr about the dielectric properties of the medium that constitutes that surface. Given εr , δp can be approximated as in Expression (2.56).

$$\delta_{\mathrm{p}} \approx \frac{\lambda \sqrt{\varepsilon_{\mathrm{r}}{}'}}{2\pi \cdot \varepsilon_{\mathrm{r}}{}''} \qquad (2.56)$$

εf' is the real component – corresponding to the permectivity [permettivity] of the medium [medium] – and εf'' is the imaginary component – called the loss factor of the medium [medium] – of the relative complex dielectric constant εr.

To establish an initial reference value, we can take into account the fact that vacuum has a dielectric constant of 1.0. Metals have a very high dielectric constant, in the case of conducting materials even tending towards infinity. Most other natural materials have dielectric constants between 2 and 10, with very low dissipation factors (between 0.01 and 0.1). Water with dissolved ions has a much higher dielectric constant (around 80) due to its polarisability, generating significant effects in radar images of wetlands.

In addition to the density of the material and the wavelength adopted by the sensor, the components εf' and εf'' also depend considerably on the moisture content of the medium. With reference to a specific material, e.g. a loam with a particular composition, the dielectric properties can be graphed as a function of water content for different wavelengths λ used by radar sensors (fig. 2.35). Looking at these diagrams, it can be seen that both εf' and εf'' increase as the moisture content of the material increases, leading to a reduction in the penetration depth δp consistent with what is described by Expression (2.56).

Obviously εf' and εf'' also depend on the frequency f = c/λ of the signal emitted by the sensor. As the frequency increases, and therefore as the wavelength λ decreases, εf' decreases and εf'' increases, so that there are higher values of δp for SAR set at low frequencies (corresponding to longer wavelengths). Using again the previous example with loam and assuming a volumetric humidity of 0.35, we can calculate in an approximate way the penetration depth δp according to Expression (2.56) and graph the dependence of δp on the wavelength λ of the scan (fig. 2.36). We thus find an almost linear increase in the penetration depth δp as wavelength λ emitted by the sensor increases[31].

2.8.2 Backscatter from surfaces

The predominant phenomenon in the interaction between radar signals and surfaces is reflection, with a spatial sensitivity in the order of wavelength λ.

In order to describe more realistic situations of interaction between scattering surfaces, one must start with an ideal reflection model where one assumes (fig. 2.37a):

- to illuminate an infinitely large layer of material on the surface with microwave radiation;
- an angle of incidence angle θi null;
- energy diffusion only in the direction perpendicular to the surface layer.

If the surface layer has a finite length relative to the order of magnitude of the wavelength λ, one of three possible cases can be reached.

In the case of an infinitely small and isolated scatterer (fig. 2.37b), the target behaves isotropically and diffuses the received energy in all directions.

In the case of areas of small extension (figg. 2.37c, 2.37d), the surfaces bear a response characterised by directivity, which becomes more and more pronounced as the extension of the surface target increases. Consequently, most of the reflected energy follows the angle of reflection, but some is scattered in other directions.

In general, the aperture angle aperture angle of the scattering pattern can be approximated as in Expression (2.57).

$$\theta_s \approx \frac{\lambda}{L_s} \qquad (2.57)$$

Ls is the width of the surface segment of illuminated material. Relation (2.57) is analogous to Expression (2.26) concerning the aperture θa of an antenna, and the scattering patterns given by the surfaces are reminiscent of the radiation patterns of antennas. Furthermore, this model assumes that the radiation spreads homogeneously and is invariant with respect to rotation (if the incidence angle was non-zero, the scattering patterns to be drawn would have to be rotated accordingly). The power returned by the segment can be considered as a function of the local refractive index of the ground, as with the Fresnel coefficients for reflection.

We can represent any surface as a complex of facets of various lengths and locations. The refractive index of the ground beneath a segment may vary, modulating the scattering pattern of the individual facet. Adopting the schematisations of geometric optics, the scattering pattern of the scene will be given by the superposition of the scattering patterns of the individual facets composing it (fig. 2.38). Although the facet model has its limitations, especially in cases where the problem needs to be investigated down to the microscopic scale or a more refined study of the electromagnetic interaction between radar waves and the surface is required, it allows an explanation of the relationship between surface hrough and brightness in the radar image[32].

2.8.3 Surface roughness

With a few exceptions (especially dry snow and dry sandy soils), most uncovered or sparsely vegetated terrain allows microwave radiation very little penetration, so that usually in SAR remote-sensing surveys surface scattering predominates within the acquisition.

Surfaces that are very smooth with respect to the wavelength λ scale scatter the impacting radiation in a specular direction and, therefore, this form of scattering is called 'specular reflection'. Scattering from a smooth surface has no component in the direction of transmission, so the resulting tone in the associated portion of the image will be black (fig. 2.39).

Rougher surfaces cause the random scattering of more radar energy until it reaches a diffuse Lambertian distribution. As the roughness increases, more energy is backscattered towards the sensor, resulting in a brighter portion of the image for rougher surfaces.

The scattering behaviour of radar waves by rough surfaces can be quantified through the use of models that correlate surface roughness to radar backscattering. Before discussing such models, however, it is appropriate to review methods for a quantitative description of surface roughness.

The roughness of the backscattering surface is the key element defining the RCS in the scene. For narrow-band imaging systems such as SAR, the criterion for determining whether a surface should be detected as rough or not must necessarily be set in relation to the wavelength of the sensor. If the roughness scale of a randomly rough surface is constructed using the standard deviation of the height h from an average height of the surface of that body, then the threshold value of h for which the surface in question will be interpreted as rough by our SAR can be established.

A divide between a smooth surface (characterised by an almost specular reflection of the signal) and a rough surface – as well as between the corresponding scattering phenomena – is loosely suggested by the Rayleigh criterion. According to this criterion, a surface is considered to be rough if the Root-Mean-Square (RMS) of the height of the microrelief is greater than the hrough,R value, which is one-eighth of the wavelength of the sensor divided by the cosine of the angle of incidence, as written in Expression (2.58).

$$h > h_{rough,R} = \frac{\lambda}{8 \cdot \cos(\theta_i)} \qquad (2.58)$$

$h_{rough,R}$ is the root mean square deviation of the height, λ is the wavelength and θi is the angle of incidence. Since this criterion does not consider an intermediate category of surfaces between fully smooth and fully rough, it was modified in 1971 in the Peake and Oliver criterion to include factors defining the upper and lower values of the RMS surface smoothness or roughness. The Peake and Oliver criterion states a smoothness threshold in Expression (2.59).

$$h < h_{\text{smooth PO}} = \frac{\lambda}{25 \cdot \cos(\theta_i)} \qquad (2.59)$$

It also states a roughness threshold in Expression (2.60).

$$h > h_{\text{rough,PO}} = \frac{\lambda}{4{,}4 \cdot \cos(\theta_i)} \qquad (2.60)$$

Another important schematisation is that of the Fraunhofer criterion, which defines a surface as rough if its height deviations h exceed the value hrough,F, as stated in Expression (2.61).

$$h > h_{\text{rough ,F}} = \frac{\lambda}{32 \cdot \cos(\theta_i)} \qquad (2.61)$$

It is important to note that Expressions (2.58), (2.59), (2.60) and (2.61) depend on the wavelength of the signal and indicate that surfaces with fixed height h variations could be qualified as rough in the X-band but not in the C or L bands. Such formulae can be used as a guide in the interpretation of SAR images, provided one keeps in mind their limitations in modelling natural surfaces. In addition, the use of several slightly different formulae reveals the difficulty of deriving a behavioural model for a complex surface, even though they allow one to identify the ranges in which the transition from smooth to moderately rough to strongly rough will occur.

Aside from the description used, it appears from the expressions just studied that a given surface appears rougher as the wavelength decreases and, independently of wavelength, a given surface appears smoother as the angle of incidence increases (fig. 2.40).

Variations in local angles of incidence for different types of surfaces result in characteristic radar brightness curves, quantified as values of the normalised equivalent RCS σ0 as a function of the incidence angle θi (fig. 2.41). Clearly, a smooth surface produces a sharp peak when the radar illumination is perpendicular to it (i.e. when θi = 0), while a very rough surface scatters the signal equally in all directions, without relying particularly on the incidence angle. For small incidence angles θi, typically below 20°-25°, smooth surfaces may be brighter than rough surfaces: not taking into account the looking angle θl may lead to misinterpretations of the roughness of a radar image[33].

2.8.4 Backscattering by volumes

When backscatterers are located in a resolution cell beyond a surface layer, this is a volume scatterer. In addition to reflection, a certain amount of refraction also occurs in the interaction between the microwave signal and a target, especially in the case of homogeneous volumes. Volume scattering occurs in two distinct categories of media: inhomogeneous media and homogeneous media (fig. 2.42).

During the scan, the SAR flies along its trajectory v and laterally illuminates the volume scatterer. The extension of a resolution cell along the slant range through the volume has the shape of a circular corona. It can be assumed that within each resolution cell there is a suitable number of scatterers.

A forest is a good example of an inhomogeneous volume scatterer. Other examples of inhomogeneous volume scatterers are natural vegetation and crops.

Homogeneous volume scatterers are snow, ice, sand or dry soil. The scattering patterns of volumetric targets cannot be defined as easily as in the case of simple artificial targets or surfaces. They also depend on parameters such as heterogeneity, local orientation of dielectric properties, humidity or varying refractive indices.

The attenuation experienced by the radar signal as it travels within the volumetric target depends on the wavelength λ and the properties of the medium [medium]. Typically, longer wavelengths are more penetrating than shorter ones and dense materials are more attenuating than diffuse ones[34].

The ability of radar waves to penetrate volumes gives radars valuable capabilities in the field of remote-sensing and surveying in general: the characterisation of a structure by identifying the distribution of a diffuse element. In the field of Architectural and Land Survey, these features have already been experimented with Ground Penetrating Radars (GPR). These are sensors on a moveable ground platform or which can be applied and moved along walls, whose waves penetrate the surface and generate an image of the lower layers (fig. 2.43). Similarly to radar sounders, they generate profiles at different depths, mapping two-dimensional images (whose ordinate values are measured taking into account the distance to the sensor, while the abscissa values correspond to the along-track position)[35]. In the case of remote-sensing, this translates into the potential of identifying the three-dimensional distribution of a backscatterer. This property is expected to play a major role in radar missions aimed at gathering information on the structures of the biosphere and cryosphere and thus monitor the evolution of climate processes[36].

2.8.5 Multiple radar signal reflections: double bounce, triple bounce and urban areas

With regard to the detection of artificial targets and urban areas, there are geometric categories of scenes that are particularly relevant, covering multiple reflections such as double bounce and triple bounce.

Double bounce is characterised by a double reflection due to the interaction of the radar signal with a dihedral-like target (fig. 2.44). In the case of urban areas, the double bounce manifests itself together with the layover effect already discussed in this chapter. As a consequence of this, not only do the buildings in the radar images appear spread out over the terrain, but their radar signatures present bright pixels at the base and top of these structures. For example, horizontal bright lines along the buildings mapped in a radar image usually correspond to double (or triple) reflections of the building vertical edge when it collides with the radar LOS. This means that the radar signature allows the location of the building to be distinguished from the path of the sensor platform. Double bounce reflections are also characteristic of sparse forest areas.

More complex targets such as bridges usually have a more complex reflection patterns, which may include three or more bounces (fig. 2.44). Trihedral-shaped targets, called corner reflectors, are commonly used for the calibration of radar systems.

In the case of remote-sensing an urban area, the interpretation of radar images becomes more challenging due to the typically more complicated reflection patterns, overlapping signals from buildings and structures, and the greater geometric and dielectric complexity of individual targets[37].

Notes

1. Van Zyl, Kim 2011, pp. 2-3.

2. Let us consider three points A, B, C of an oriented line r. The ratio of the measures of the two segments AC and BC, bounded by the first and third points respectively, is called the simple ratio of the three points in the order A B C and is written (A B C) = |AC| / |BC|. By changing the successione of these three points, the value of the simple ratio also changes.
The simple ratio can also exist between three oriented straight lines belonging to an oriented bundle and is defined as the ratio of the sines of the two angles determined by the first and third straight lines, the second and third lines respectively.
Let us now consider four points A, B, C, D placed in a certain order on an oriented line r, for example in the order A B C D. The ratio of the two simple ratios (A B C) and (A B D), formed by the first two points with the third and fourth, is called the double ratio of the four points in the order considered and is written (A B C D) = (A B C) / (A B D) = (|AC| / |BC|) / (|AD| / |BD|). Obviously, changing the order in which the four points succeed each other also changes the value of the double ratio.
Similarly, the double ratio can also exist between four oriented straight lines in an oriented bundle and is defined as the ratio of the two simple ratios formed by the first two rays with the third and fourth.
Double ratios enjoy the following properties: (1) a double ratio does not change if two elements are exchanged with each other and the other two are exchanged at the same time; (2) exchanging the last two (or the first two) elements mutates a double ratio into its inverse; (3) the exchange of the two internal elements (or of the external elements) changes the double ratio into its complementary to the complementary to the unit; (4) the double ratio of four points, of which the last at infinity is equal to the simple ratio of the first three points.
The double ratio never changes for operations of projection and section, thus constituting a remarkable metric-projective property of an ordered group of four aligned points or lines of a bundle.
For an in-depth discussion of the simple ratio and the double ratio cf. Docci, Maestri 1992, pp. 21-29; Masotti Biggiogero 1980, pp. 14-22.

3. Docci, Maestri 1992, pp. 33-36.

4. Keydel 1992, p. 1-1.

5 Van Zyl, Kim 2011, pp. 1-6.

6. Ager 2013, p. 28.

7. Van Zyl, Kim 2011, pp. 6-8.

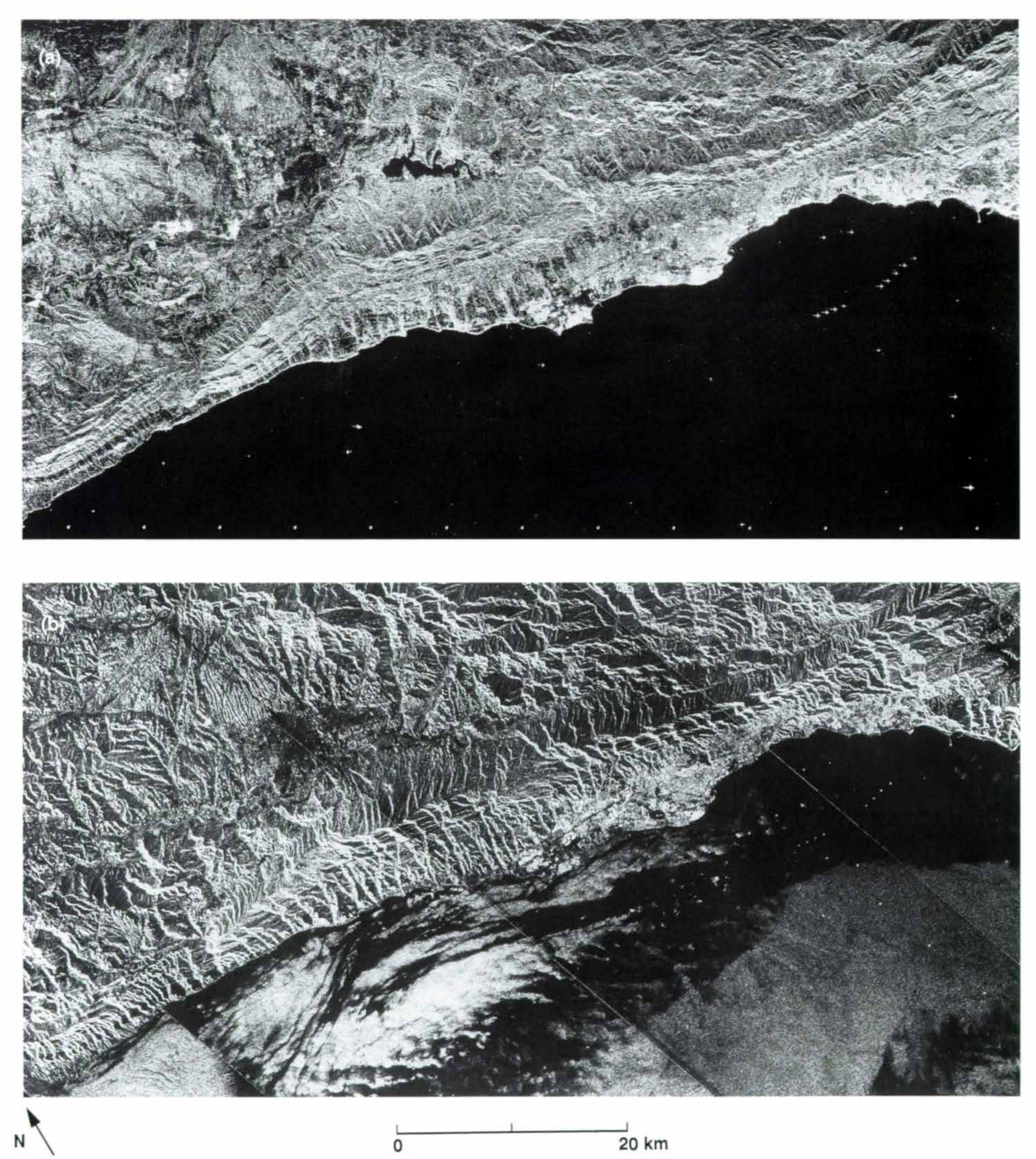

2.23/ Accentuation of roughness and topography: SAR imagery of the Santa Ynez Mountains in California. (a) Image acquired during the Shuttle Imaging Radar-A (SIR-A) Mission with an incidence angle of about 50°. At this location, roughness effects dominate the image. (b) Image acquired during the Seasat Mission with an incidence angle of about 20°. With such a small angle, the topography is more pronounced as the slopes are closer to this small value. Source: Farr 1993 / Public domain image [Image under Public Domain].

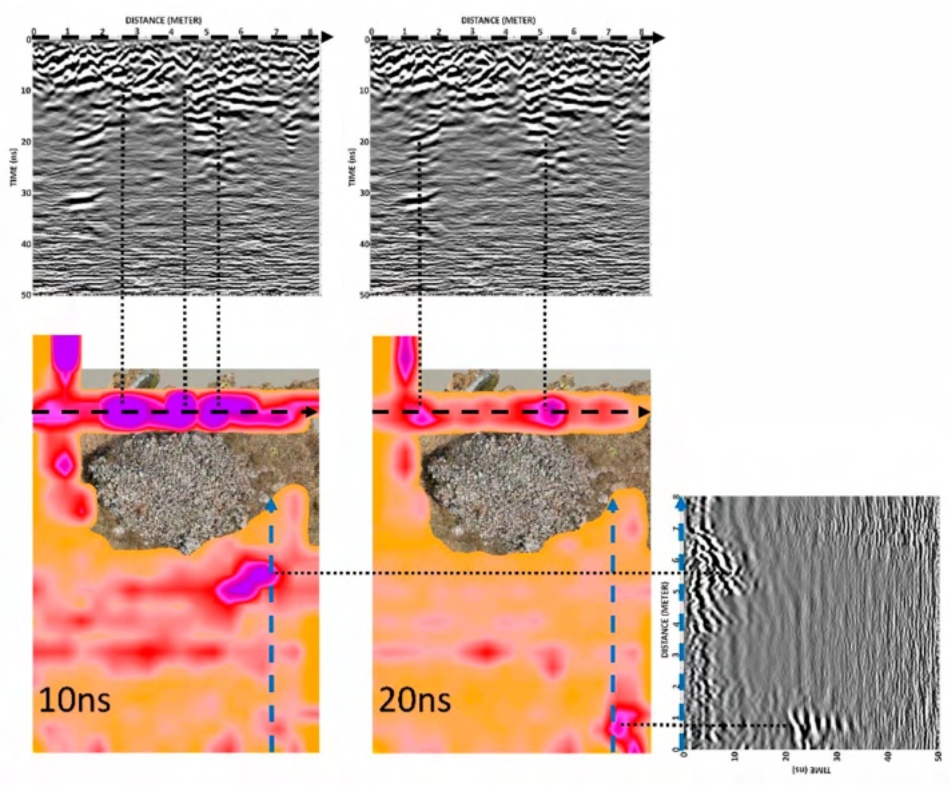

2.24/ Vertical profiles (in greyscale) of the stratification of the archaeological site of prehistoric mounds in Parabita (Lecce, Italy), obtained with a Ground Penetrating Radar (GPR) along the sections highlighted with dashed black lines on the photo-plane. The two dimensions of the vertical profiles correspond to the position of the platform and the signal return time in nanoseconds, while the brightness of the individual pixels corresponds to the intensity of the return signal. On the photo-plane of the archaeological site, depth maps were also superimposed as a function of platform position and return time (in the red to purple colour scale). Source: Persico, Colica, Zappatore, Giardino, D'Amico 2022 / licensed under CC BY 4.0 (http://creativecommons.org/licenses/by/4.0/). © 2022 by Persico, Colica, Zappatore, Giardino, D'Amico. Licensee MDPI, Basel, Switzerland.

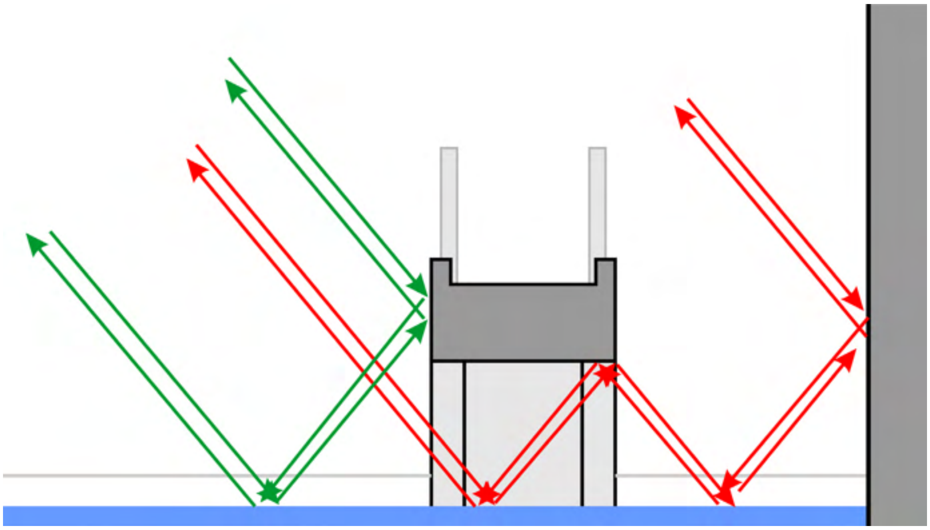

2.25/ Examples of reflection geometries in an urban environment. The reflection of the radar signal on one side of the footbridge and then on the water surface, or vice versa, causes a double bounce (green arrows). The reflection of the radar signal on the intrados of the footbridge, then on the water surface and finally on the retaining wall of the reservoir, or vice versa, causes a triple bounce. Meteoric water collected on horizontal closures and pavements can also constitute a temporary reflection surface.

8. Ager 2013, pp. 28-29.
9. Van Zyl, Kim 2011, pp. 8-10.
10. *Loc. cit*. pp. 10-11.
11. Schrank, Evans, Davis 1990, pp. 6.2-6.7.
12. Emery, Camps 2017, pp. 307-310.
13. Van Zyl, Kim 2011, pp. 11-12.
14. Keydel 1992, p. 1-1.
15. Van Zyl, Kim 2011, pp. 12-13.
16. Meyer 2019, pp. 22-24; Van Zyl, Kim 2011, pp. 13-14.
17. The Half Power Beam Width (HPBW) is the angle at which the relative power of the antenna is more than 50% of its peak power in the radiated effective field. It is a concept closely related to antenna gain and represents that part of the emission characterised by maximum coherence and functionality. Usually, the width at HPBW is also a measure of antenna resolution. In fact, two backscatterers at the same range are said to be resolved in angle by the radar if they are separated by a distance equal to at least the HPBW. For more details cf. Schrank, Evans, Davis 1990, pp. 6.7-6.8.
18. Keydel 1992, pp. 1- 1-1 -2; Ottl 1992, pp. 4- 1-4 -5; Van Zyl, Kim 2011, pp. 14-16.
19. Docci, Maestri 1992, pp. 33-36.
20. Meyer 2019, p. 24.
21. Emery, Camps 2017, pp. 344-347; Keydel 1992, pp. 1 -9-1 -10; Van Zyl, Kim 2011, pp. 19-20.
22. Emery, Camps 2017, pp. 344-347; Keydel 1992, pp. 1 -10-1 -11; Van Zyl, Kim 2011, pp. 19-20.
23. Emery, Camps 2017, pp. 344-347; Keydel 1992, pp. 1 -10-1 -11; Van Zyl, Kim 2011, pp. 19-20.
24. Emery, Camps 2017, pp. 347-350.
25. Van Zyl, Kim 2011, pp. 16-17.
26. *Loc. cit.*, pp. 17-19.
27. Emery, Camps 2017, pp. 305-306; Van Zyl, Kim 2011, p. 20.
28. Ford, Blom, Crisp, Elachi, Farr, Saunders, Theilig, Wall, Yewell 1989, pp. 91-94; Meyer 2019, pp. 24-25; Van Zyl, Kim 2011, pp. 20-21.
29. *Loc. cit.*, p. 99.
30. Meyer 2019, p. 25.
31. Farr 1993, p. 55; Meyer 2019, pp. 25-26.
32. Emery, Camps 2017, pp. 314-318.
33. Farr 1993, pp. 48-54; Meyer 2019, pp. 26-27.
34. Emery, Camps 2017, pp. 321-322.
35. Bonanno 2007, pp. 198-200; Persico, Colica, Zappatore, Giardino, D'Amico 2022, pp. 1-12; Pizzurro 2007, pp. 222-227.
36. Emery, Camps 2017, p. 322.
37. *Loc. cit.*, pp. 311-314.

Sintesi

Tipicamente, mentre la piattaforma aeromobile o spaziale trasporta il sensore lungo la propria traiettoria, le immagini radar vengono acquisite in strisciate, note anche come spazzate. La direzione trasversale rispetto al percorso è la direzione perpendicolare alla traiettoria seguita dalla piattaforma e, nelle operazioni di cattura delle immagini radar, corrisponde alla direzione radiale. La direzione lungo il percorso è la direzione parallela allo spostamento della piattaforma e, nelle operazioni di generazione delle immagini radar, s'identifica con la direzione azimutale.

Durante il processo di restituzione dell'immagine radar, per separare i bersagli nella direzione trasversale al percorso e nella direzione lungo il percorso si deve impiegare uno tra i due seguenti sistemi:

- il metodo della dimensione angolare, caratteristico dei sensori ad apertura reale. Solo la mappatura azimutale dei radar ad apertura reale presenta delle analogie con le normali fotocamere;
- il metodo della cronologia Doppler, peculiare dei sensori ad apertura sintetica. Sfruttando il ritardo temporale e i risultati della cronologia Doppler, le immagini di questi radar si contraddistinguono per risoluzioni indipendenti dalla distanza tra lo strumento e la scena che sta scandendo.

Il termine distanza è usato per indicare due misure differenti:

- la distanza radiale inclinata, corrispondente alla distanza radiale del radar. Questa specificazione è dovuta al fatto che la linea di mira e il campo d'azione del radar sono in una giacitura obliqua. La distanza inclinata è la lunghezza del segmento che connette il radar con il singolo elemento retroddifondente;
- la distanza a terra ossia la distanza tra la proiezione a terra della traiettoria della piattaforma – detta percorso nadirale – e la proiezione a terra del singolo elemento retrodiffondente. Se schematizziamo localmente il territorio come un piano orizzontale, la distanza a terra di un elemento retrodiffondente corrisponde alla proiezione, sulla direzione trasversale alla traiettoria della piattaforma, della proiezione a terra della sua distanza inclinata

dal sensore.
Il budget idealizzato di potenza necessaria per stabilire un collegamento radar è definito dall'equazione radar. Nel caso dei radar per il telerilevamento, una scena si può schematizzare come costituita da un continuum distribuito e senza che sia composta da elementi diffondenti discreti, consentendoci di ipotizzare l'assenza di guadagni da integrazione.
Differentemente dal caso di un radar reale, un radar ad apertura sintetica può appunto sintetizzare un'antenna di lunghezza molto più lunga da una sequenza di scansioni compiute con un'antenna più corta che si sta muovendo lungo il proprio percorso. Poiché la lunghezza dell'antenna è intrinsecamente legata alle capacità di un sensore radar, l'antenna "virtuale" molto più lunga sintetizzata permette l'acquisizione di immagini ad alta risoluzione anche da piattaforme spaziali, usando componentistica di dimensioni pratiche per le operazioni a livello orbitale.
Le operazioni compiute durante la mappatura dell'immagine radar non possono essere ricondotte alla prospettività di ribaltamento, perché il percorso rettificato del sensore costituisce sì l'asse di tutti i ribaltamenti effettuati nello spazio, ma non è la retta unita di tutti i piani sui quali giacciono le figure da mappare e le figure mappate. L'alterazione dei valori dei birapporti tra le quaterne di punti appartenenti alla scena e le rispettive quaterne di punti mappate sull'immagine radar comporta che non sussistano relazioni di omografia. Si tratta di una mappatura non lineare che altera i valori dei birapporti tra le figure costituenti la scena (sia figure piane che solidi) e le loro controparti sull'immagine radar, escludendo qualsiasi relazione di proiettività. L'insieme dei fenomeni appena descritti causa tre tipi peculiari di distorsioni geometriche: lo scorciamento, dove i pendii rivolti verso il sensore appaiono compressi rispetto ai pendii che guardano dall'altra parte; lo scavalcamento, dove l'ordine di due bersagli nell'immagine radar è invertito rispetto alle loro posizioni originarie lungo la direzione della distanza a terra; le ombre radar, causate da corpi nella scena che intercettano il raggio radar e impediscono l'illuminazione delle aree ad essi retrostanti rispetto al sensore.
I radar sono suscettibili anche alle seguenti distorsioni radiometriche: ambiguità lungo la distanza radiale e ambiguità azimutali; artefatti dovuti a segnali spuri conseguiti dalle risposte estremali dei filtri radar; attenuazione del segnale e chiazzatura; effetti di disallineamento della finestra della distanza radiale.

Luca Martelli

3. Information provided by the Processing of Synthtic Aperture Radar images

3.1 Backscatter and target modelling

In radar images, backscatterers can be defined as those having dimensions of the same order of magnitude as the wavelength used by the sensor.

In radar images, backscatterers can be defined as those having dimensions of the same order of magnitude as the wavelength used by the sensor. Succinctly, we can roughly define the complex reflectivity in a radar resolution cell as the coherent superposition of the reflectivities of the individual scatterers within the cell itself[1].

Generally, three different categories of targets can be distinguished in relation to the resolution cell (fig. 3.1):

- point targets;
- extended targets;
- distributed targets.

The point target is identified as a single dominant scattering element within a resolution cell. Both the amplitude and phase detected by the sensor in the corresponding pixel of the radar image will be dominated by the response of this point element, which spreads over several consecutive resolution cells following the system impulse response.

In reality, the cell where a single scatterer stands out will always include contributions from smaller scatterers, which will cause a slight deviation from the ideal point target response. Within the resolution cell, the scattering element with the most stable radar echo over time also tends to become the one that prevails over the others. However, a point target is always characterised at any instant by only one frequency in the Doppler spectrum, allowing the use of spectral estimation techniques for enhanced resolution imaging.

An extended target can be identified as a single scattering element present and dominant over smaller ones in several resolution cells. The reflectivity pattern of the extended target is characterised by a certain coverage both in space and in the Doppler domain. Buildings are a remarkable case of extended scatterers.

A distributed target is completely characterised by a small number of statistical descriptors and cannot fit within the definition of a single scatterer. Distributed targets are normally modelled by superposition of several scattering elements with similar Radar Cross Sections (RCSs), arranged in no particular order within a resolution cell. Due to the coherent superposition of the echoes returned by them, the amplitude and phase characterising the reflectivity of the cell appear random. Depending on whether the coherent signal of the distributed scatterer is the result of constructive (i.e. echo enhancing) or destructive (i.e. echo attenuating) interference, the resolution cell involved will appear lighter or darker respectively, causing a speckle effect. A distributed target has an echo spectrum covering the entire Doppler instantaneous domain. Moreover, its signal is hardly stable over time, since it is sufficient for one of its small scatterers to move relative to the others for the phase of the entire resolution cell to change.

One of the most important aspects to evaluate when studying a scene detected with Synthetic Aperture Radars (SAR) is the density of single scatterers that compose it.

Time series analyses of radar images are carried out to detect physical changes that have occurred in a scene scanned several times during a certain period of time. Targets that typically show sufficient consistency over time allow the generation of a multi-temporal stack. Generally, there are two approaches: one based on distributed targets (fig. 3.2a) the other based on point targets (fig. 3.2b)[2].

3.2 Main features of remote-sensing satellites

An artificial satellite is a receiver-transmitter specialised in wireless telecommunications, launched by a vector rocket and placed in orbit around the Earth. Artificial satellites enable global coverage and periodic repeat scans.

Launching a satellite requires time-consuming procedures for design and preparation, with a high expenditure of economic resources at all stages of development: production, launch into orbit, maintenance, and continued operation. In addition, there is always a certain probability that some sensors will fail after launch and this, together with the high cost of repair and re-launch, makes the risk of failure quite high.

With regard to the distance of the satellite from Earth's surface, satellite platforms can be classified into four groups (fig. 3.3):

1. Low Earth Orbit (LEO) satellites, between 160 and 1,400 km of distance, which complete their orbit in about 90 minutes. These are the most common scientific satellites, but are also used for telecommunications and military applications. In this case, it depends on the application of the satellite, but the orbit is almost circular.
2. Medium Earth Orbit (MEO) satellites, between 10,000 and 15,000 km of distance, consisting mainly of Global Navigation Satellite System (GNSS) satellites and spy satellites, with orbital periods ranging from 2 to 24 hours.
3. Satellites in GEostationary Orbit (GEO), around 36,000 km of distance.
4. Highly Elliptical Orbit (HEO) satellites, placed beyond 36,000 km of distance to minimise the impact of terrestrial radiation on their instruments.

As far as the typological classification of orbits is concerned, two main types can be distinguished: geosynchronous orbits and polar orbits. In addition to these two, there is another particular type: the elliptical orbit or eccentric orbit. We will briefly describe these three categories below:

- Geosynchronous orbits (fig. 3.4) – When a satellite reaches a distance of approximately 36,000 km from Earth's surface, its orbit corresponds to the rotation of the Earth. Since the satellite moves at the same rotational speed as the planet, it appears from the Earth itself to be bound to a specific longitude. A satellite with a geosynchronous orbit contained in Earth's equatorial plane is defined as having a 'geostationary orbit' and, therefore, its projection on Earth's surface always remains at the same point. A geostationary orbit is extremely valuable for meteorological monitoring, because satellites that adopt it constantly provide observations on the same portion of the planet. Telecommunication and navigation satellites also make use of geostationary orbits.
- Polar orbits (fig. 3.5) – At orbital altitudes lower than Earth, a satellite following a highly inclined orbit moves from pole to pole. Polar orbits make it possible to generate global coverage and the frequency with which they allow a satellite to return to an already surveyed point can be daily or monthly. A special case of polar orbit is the 'heliosynchronous orbit', which allows the satellite to cover each spot of the Earth at a fixed local time or at fixed intervals: this type of orbit is of great importance for passive sensors, since these measure the reflection of sunlight from the Earth. Satellites with passive sensors must be adjusted to the rhythm of day and night; in other words, acquisitions must take place at the same local time so that, from Earth's surface, the altitude of the sun above the horizon is always the same. Taking a particular site on the planet surface as a fixed reference, the polar orbit tracts flying over it are divided into:
    - ascending pass, when the space platform is moving approximately from the South Pole towards the North Pole;
    - descending pass, when the space platform is moving approximately from the North Pole to the South Pole.

      The division into ascending passes and descending passes plays an important role for side-looking radars, as it indicates the scanning side of the sensor at the time of an acquisition.
- Elliptical or eccentric orbits (fig. 3.6) – In this type of orbit, the instantaneous velocity of the satellite varies depending on its position along the orbital path. When the satellite is in the part of the orbit closest to the Earth, it moves faster, because Earth's gravitational force is stronger. Conversely, when the satellite is at the furthest point of the orbit from the Earth, it moves at the slowest speed. An elliptical orbit can be useful for communication satellites, because it allows them to travel over a specific portion of the Earth for most of the orbit and lose contact with that region for a short time (i.e. when the satellite is over the other side of the Earth).

While polar orbits make it possible to cover the entire surface of Earth, non-polar orbits do not generate global coverage and make it possible to return to an area that has already been covered with time intervals ranging from a few hours to a few weeks.

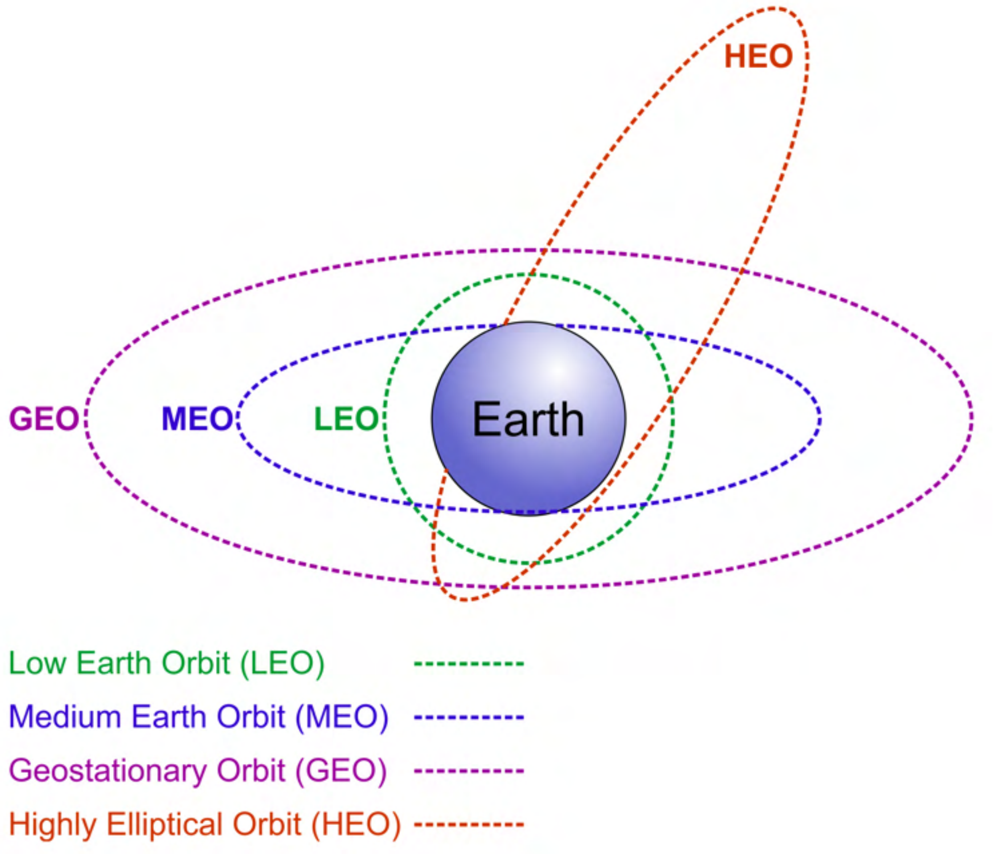

3.1/ Schematic subdivision of satellite platforms into categories based on orbital distances, according to Planetek Italia 2022: Low Earth Orbit (LEO), between 160 and 1.400 km; Medium Earth Orbit (MEO), between 10,000 and 15,000 km; GEostationary Orbit (GEO), around 36,000 km; Highly Elliptical Orbit (HEO), places over 36,000 km.

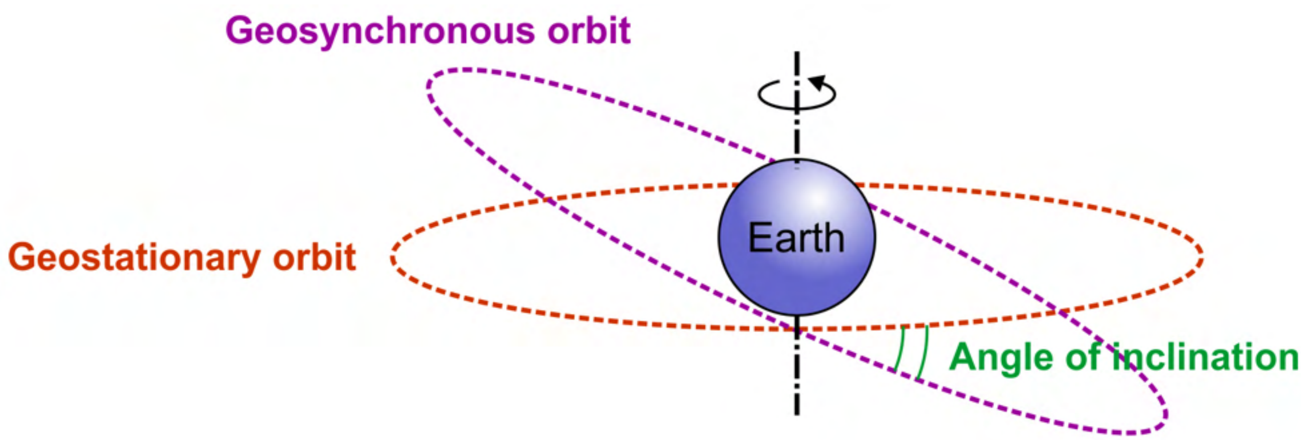

3.2/ Schematic example of geosynchronous orbits and geostationary orbits, according to Planetek Italy 2022. The geostationary orbit is a special case of a geosynchronous orbit having a zero inclination angle with respect to Earth's equatorial plane.

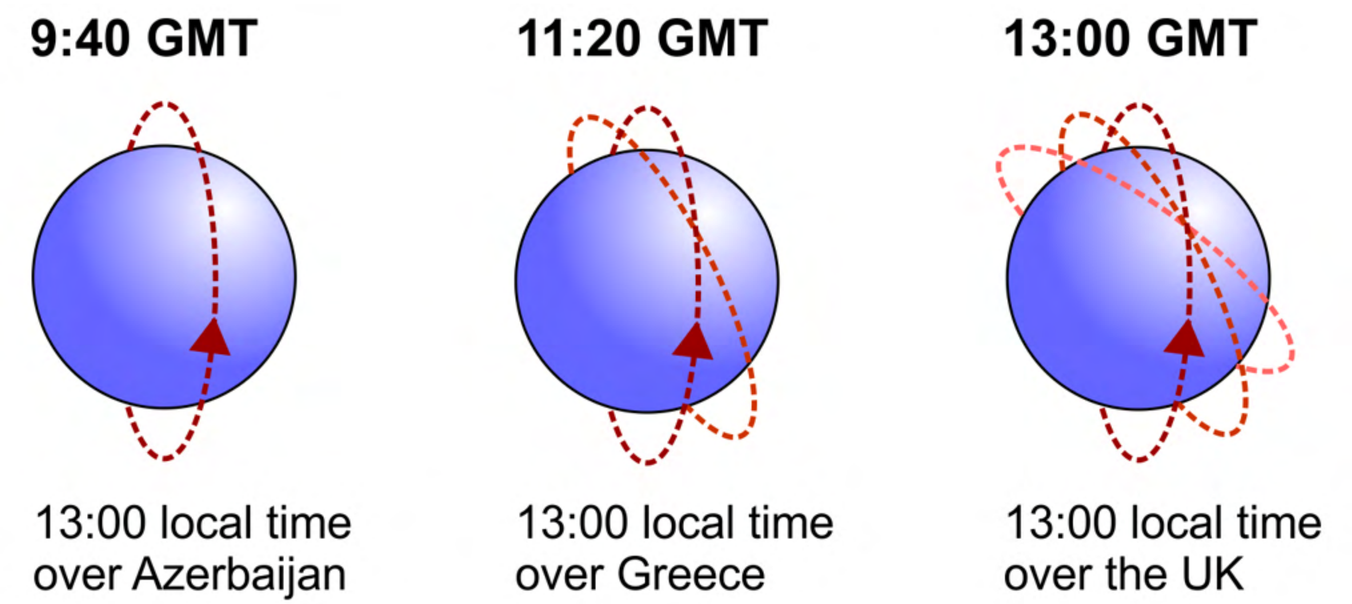

3.2/ Schematic illustration of the heliosynchronous orbit, a special case of polar orbit, according to PlanetekItalia 2022. The platform follows a highly inclined orbit moving from pole to pole and covers each spot of the Earth at a fixed local time or at fixed intervals.

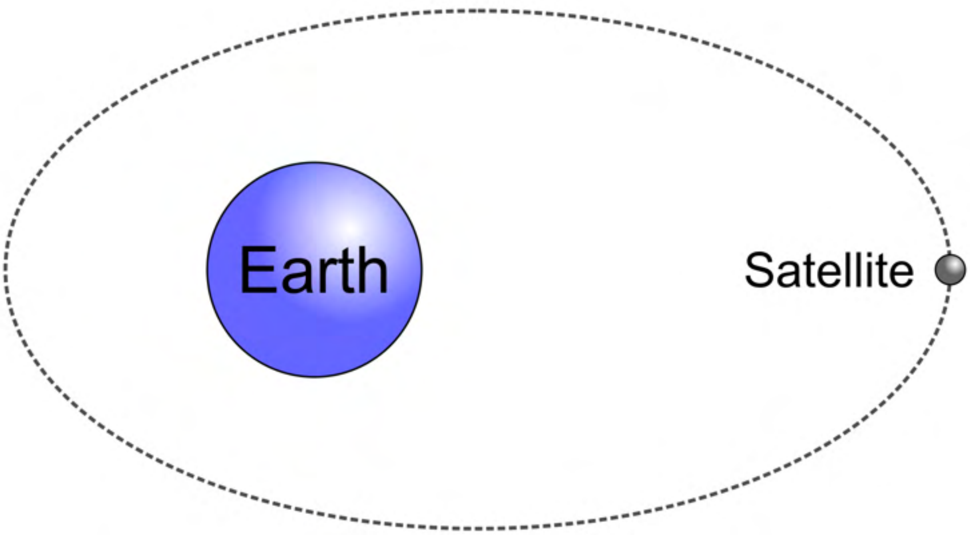

3.3/ Schematic example of an elliptical or eccentric orbit, according to Planetek Italia 2022. The instantaneous velocity of the platform varies depending on its position along the orbital path. When the
satellite is in the part of the orbit closest to the Earth, it moves faster because Earth's gravitational force is stronger. Conversely, when the satellite is at the farthest point of the orbit from Earth, it moves at the slowest speed.

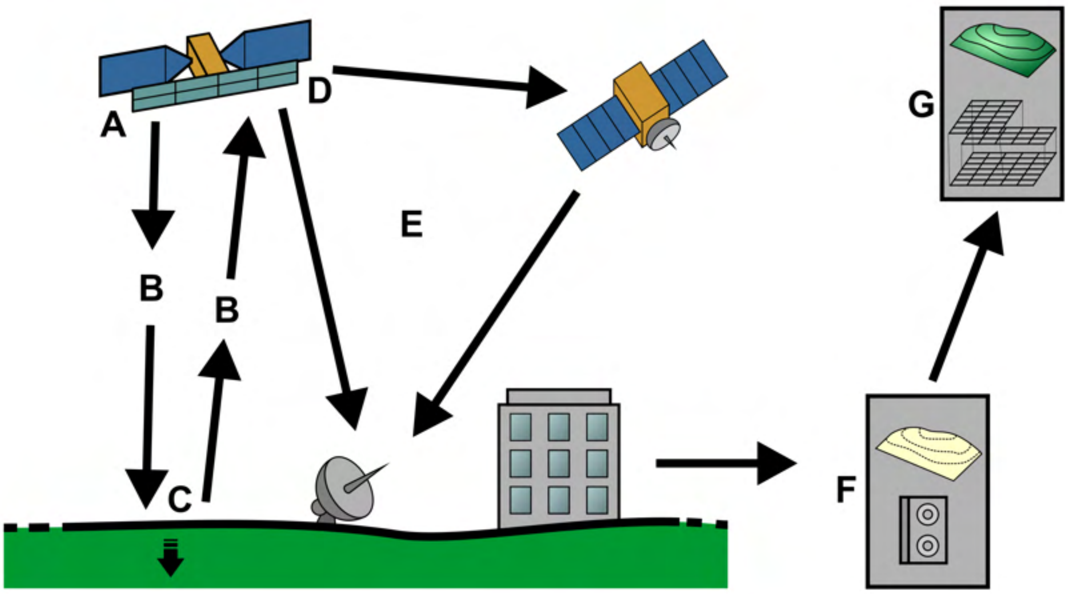

3.4/ Schematic representation of the space segment and ground segment of a satellite remote-sensing system, according to Planetek Italia 2022. (A) Emanation of illuminating radiation; (B) interaction between the radiation and the ground signal; (C) interaction with the target; (D) recording, via sensor, of the energy returned by the target; (E) transmission, reception and processing; (F) interpretation and analysis; (G) application.

The time between a first and second pass of an artificial satellite over a certain area of Earth's surface is called Revisit Time (RT) and depends on:

- the type of orbit of the satellite;
- the position of the target;
- the swath of the sensor.

The closer the site to be surveyed is to the poles or the lower the angle of elevation, the more frequently the satellite will pass over the same point on Earth[3].

Four types of resolution must be taken into account for satellite remote-sensing:

- Spatial resolution, i.e. the spatial area covered by a pixel in a satellite image. Generally, the higher the spatial resolution, the smaller the area covered by a single pixel.
- Temporal resolution, i.e. the length of time it takes for a satellite to re-scan an area already covered at the same angle. It depends on the capabilities of the satellite and the sensor, the intersections and overlaps in the satellite path, and the latitude of the satellite. Some satellites have a higher temporal resolution than others because:
  - they are able to electronically steer their own sensors;
  - the intersections and overlaps of their orbits augment with increasing latitude in the southern and northern hemispheres.

  The areas at higher latitudes are scanned more frequently than the ones at the equatorial zone, due to the increase in intersections and overlaps as the orbital paths form tighter meshes near the poles.
- Spectral resolution, which describes the ability of a sensor to finely detect ranges of wavelengths. Instruments identify different wavelength ranges along the electromagnetic spectrum, identifiable in the frequency bands already discussed in Chapter 1. The narrower the wavelength domain, the finer the spectral resolution. Different spectral channels with finer resolution allow remote-sensing of multiple aspects of Earth's surface.
- Radiometric resolution, which describes the ability of a sensor to distinguish differences in energy (or radiation). The better the radiometric resolution, the greater

the sensitivity of the sensor to small differences in detected energy. It is determined by multiple factors, the main ones being:

- Saturating radiance value, i.e. the brightest value that the sensors can measure.
- How radiance measurements are quantified, i.e. converted into a digital bit stream. The main sensor types are: 16 bits and 4,096 levels as in the MODerate resolution Imaging Spectroradiometer (MODIS) and the Multi-angle Imaging SpectroRadiometer (MISR); 10 bits and 1,024 levels as in the Advanced Very-High-Resolution Radiometer (AVHRR); 8 bits and 256 levels as in the Landsat Thematic Mapper; 6 bits and 64 levels as in the Landsat Multispectral Scanner.

3.2.1 Overview of the satellite remote-sensing system: space segment and ground segment.

Any satellite communication network can be divided into two parts (fig. 3.7):

- the space segment, i.e. that portion of the satellite communication network consisting of orbiting satellites;
- the ground segment, which comprises all the ground elements of a satellite system and is responsible for communication with satellites. It includes all the hardware and software components needed to send and receive data from a satellite.

The satellite remote-sensing part of the space segment can be summarised in seven steps:
(A) emanation of illuminating radiation;
(B) interaction between radiation and Earth's atmosphere;
(C) interaction with the target;
(D) recording, via sensor, of the energy returned by the target;
(E) transmission, reception, and processing;
(F) interpretation and analysis;
(G) application.

The electromagnetic waves of the illuminating radiation interact with the atmosphere and the target, eventually being recorded by the sensor. The recorded data is then transmitted back to Earth and processed to be converted into useful information. Between phase (D) and phase (E) there is the process of recording data on board the satellite, before it is transmitted to a ground station. Another satellite, part of the Tracking and Data Relay Satellite System (TDRSS), is involved in the transmission part.

As already mentioned, there are various types of sensors, but in remote sensing applications the ones we are most interested in are those for image production, i.e. those that create satellite scenes. Traditionally, magnetic tape recorders were used to store data on board satellites; today, almost all current satellites use recorders with solid-state memories. The advantage of recorders with solid-state memories is that they are made entirely of solid materials, in which the only moving parts are electrons; consequently, information can only be changed by voltage changes in the transistors. Storage capacities can reach hundreds of gigabytes. The data recorder can store data acquired from areas other than the Ground Receiving Station (GRS) and send it when the latter is in the satellite Field Of View (FOV).

Data storage is followed by transmission: the images acquired and stored on board must be transmitted to a GRS when the satellite becomes visible from the latter. There are two methods for transmitting the data acquired by the satellite to an Earth station:

- direct transmission to the ground station GRS, either instantaneously if the latter is along the satellite Line Of Sight (LOS) or later using on-board recording.
- Indirect transmission via a Tracking and Data Relay Satellite System (TDRSS), i.e. a system of geostationary satellites (approximately 36,000 km of altitude) with a longer FOV of both remote-sensing satellites and GRSes. This mode is more flexible, as it allows data to be sent first from the satellite equipped with the sensor to the relay satellite and then from the latter to the GRS. TDRSSes operate independently of sensor-equipped satellites and can receive and transmit more types of data than just images. Some examples of space missions that make use of TDRSSes are Landsat and Sentinel. Two notable examples of TDRSSes are that of the National Aeronautics and Space Administration (NASA) and the European Data Relay System (EDRS).

As far as the ground segment is concerned, the basic configuration of a GRS for receiving and processing remotely sensed data includes four main steps:

(a) the antenna system (reception of signals from satellite

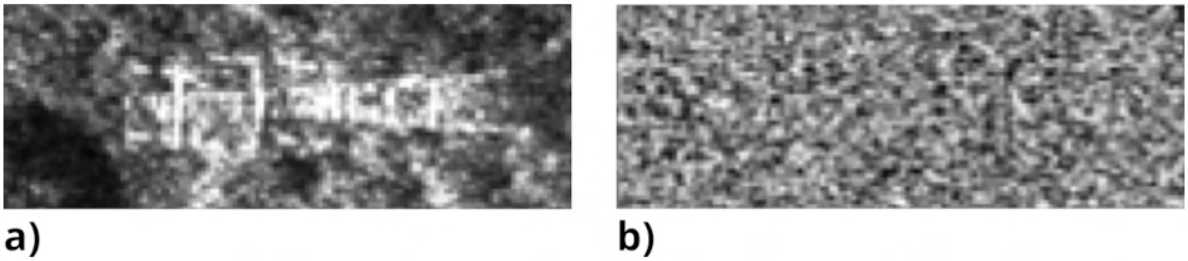

3.5/ Portion of Single Look Complex (SLC) obtained by scanning a plot of land on which an electricity pylon (the orientation of the pylon is rotated 90 degrees counterclockwise with respect to the base of the image). Image associated with signal amplitude (a) and image associated with signal phase shift (b). Source:Wu, Wang, Chen, 2023 / licensed under CC BY 4.0 (http://creativecommons.org/licenses/by/4.0/). © 2023 by Wu, Wang, Chen. Licensee MDPI, Basel, Switzerland.

subsystems);
(b) reception and processing procedure (decoding and transformation of the received signal at the various levels for further processing);
(c) software (creation of registration requests, scheduling of data processing and correction sessions in accordance with individual satellite characteristics);
(d) licences to operate with specific satellites (access to and processing of data).

In the context of satellite communications, a downlink (DL) is the connection from a satellite to a GRS. Antennas receive data usually in the S-frequency band for telemetry or in the X-frequency band for imagery. Reception is either directly from the satellite for remote-sensing or via a satellite of a TDRSS. The DL speed ranges from 100 to 500 Mbit/s[4].

It is important to remember that a SAR does not use lenses and passive sensors to capture the scene through a projection and sectioning process and map it onto a matrix of pixels, as digital cameras do. A SAR only takes into account raw measurement data regarding the time of travel and return, amplitude and phase of the emitted and reflected signal, which are then manipulated with signal processing algorithms into images and other products.

The raw measurement data is processed with a received backscatter phase history, which contains the echo measurements and timing data necessary for more advanced processing. A backscatter phase history file is not an image and cannot be displayed, but is processed in a pixel-based matrix form called Single Look Complex (SLC). The SLC is a key product of radar, used to generate amplitude images of the signal and many other radar processing that cannot be produced simply based on amplitude data alone. It is important to note that some products resulting from more advanced processing, such as subsidence maps and Digital Elevation Models (DEMs) require more than one SLC.

A radar SLC is different from a conventional image in that, while the latter has only one brightness value for each pixel, the former has two values for each pixel. These values can be schematically associated with the amplitude and phase of the measured backscatter. For each pixel, the backscatter amplitude data contain information comparable to traditional brightness, while the backscatter phase data contain very precise information on the timing of the acquisition, necessary for advanced processing.

The image associated with the amplitude of the return signal is easy to interpret (fig. 3.8a), while the image associated with the phase of the signal would seem to consist of random elements (fig. 3.8b). This fact, however, is misleading, as phase measurements are precise and of great value, as they allow for very complex interpretations and processing such as those adopted in the technique of Persistent Scatterers Interferometry (PSI)[5], which we will discuss later in this chapter.

Obviously, data resulting from an aperture synthesis process are typically called 'Synthetic Aperture Radar image' (SAR image) and, all things being equal (especially observation distance), have a much higher resolution than those acquired with Side-Looking Aperture Radar (SLAR)[6].

The SAR sensor of the satellite acquires the raw data and

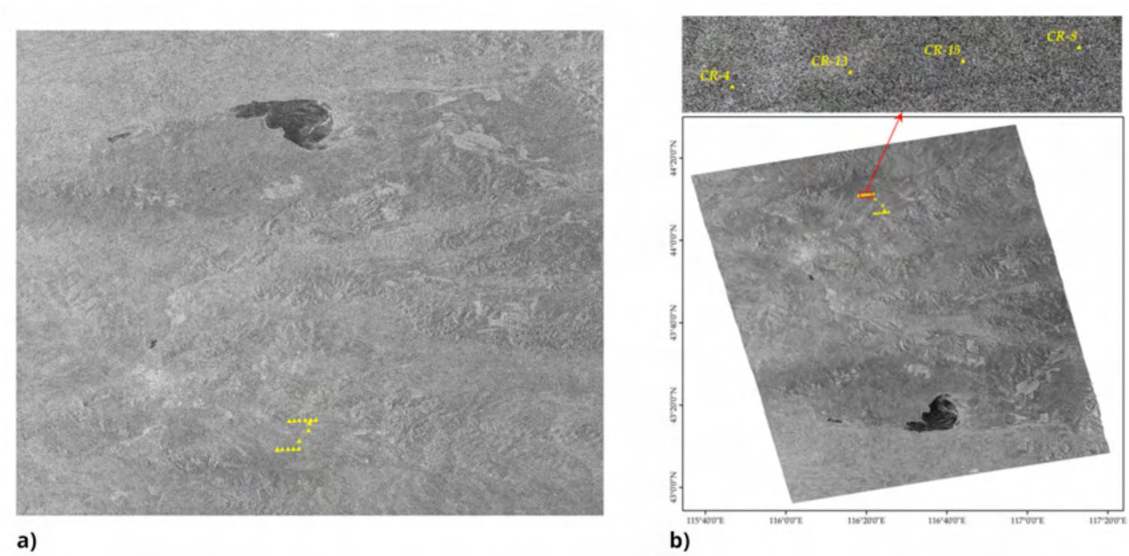

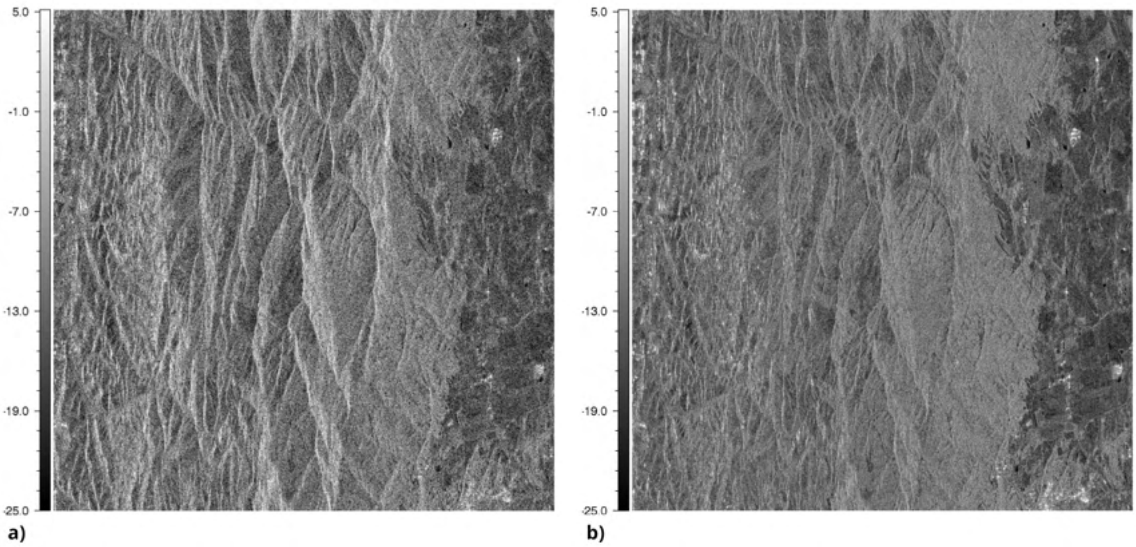

3.6/ Example of the results of a geometric correction process for images from the C-SAR/01 mission (Cband signal). The yellow triangles in the figure represent the theoretical positions of trihedral reflectors for geocoding. (a) Image taken from an SLC of a scan performed on 22 November 2023 at the Xilinhot test site. (b) The same image of the Xilinhot test site after the geometric correction process. Source: Jiao, Zhang, Liu, Wang, Huang, 2023 / licensed under CC BY 4.0 (http://creativecommons.org/licenses/by/4.0/). © 2023 by Jiao, Zhang, Liu, Wang, Huang. Licensee MDPI, Basel, Switzerland.

3.7/ Measurement of the backscattering r coefficient in the same SAR image before (a) and after (b) the application of a radiometric distortion compensation algorithm induced by the topographic terrain configuration. Source: Imperatore, Di Martino, 2023 / licensed under CC BY 4.0 (http://creativecommons.org/licenses/by/4.0/). © 2023 by Imperatore, Di Martino. Licensee MDPI, Basel, Switzerland transmits it to the GRS. This raw data is characterised by resolutions related to the duration of the chirped pulse and the extent of the footprint in azimuth (similarly to the case of RAR). After downloading by GRS, the processing (matched-filtered compression along range and synthetic antenna compression) leading to the high-resolution images is performed[7]. Succinctly, the elements that influence the acquisition of a SAR image are:

- the characteristics of the radar sensor;
- the interaction between Earth's atmosphere and the signal, which in the case of microwaves is minimal (if at all) but can still cause appreciable alterations;
- the combination of the morphological configuration of the scanned territory and the acquisition geometry of SAR systems;
- other secondary factors.

The acquisition geometry of SAR images causes not only the geometric distortions reviewed in Chapter 2, but also radiometric distortions. For certain applications anyway, such as the implementation of interferometry, radiometric correction and geocoding are not necessary. In addition to altering the mapping order of the resolution cells in topographically inclined areas, the oblique angle of the illuminating radar energy adds topographical shading to the true RCS of the surface, giving the slope facing the sensor a radiometrically 'overexposed' appearance. Both of these effects hinder the use of SAR in many applications: radiometric modulations often mask the true radar reflectance of the scanned scene; moreover, geometric and radiometric distortions make it more difficult to detect changes in the scene along the passage of time because, when combining images from multiple scanning locations, incidence angle-dependent artifacts θi lead to classification errors. The correction of geometric and radiometric distortions is strongly recommended if SAR data are analysed as a collection of acquisitions obtained at various incidence angles or processed together with images of another nature. The RCS in one pixel of a calibrated SAR image is stated in Expression (3.1).

$$\sigma = \sigma_0\left(\theta_i\right) \cdot A_\sigma\left(\theta_i\right) \qquad (3.1)$$

σ0 is the normalised (incidence angle-dependent) normalised RCS, θi is the local incidence angle and Aσ is the area of the surface covered by a pixel. Thus, in accordance with Expression (3.1), two images acquired from different locations will be different due to the dependence of σ0 and Aσ on θi , even when no appreciable changes occur on the scanned portion of the area. Therefore, to perform tasks such as a reliable study of SAR images in a Geographic Information System (GIS) or a change analysis on a series of images associated with the signal amplitude and acquired from different scanning locations, geometric and radiometric distortions must be removed. To recover the true RCS σ0 from the measured radar data σ, the geometric dependence on σ must be removed by correcting Aσ (θi). The process of adjusting Aσ (θi) is called Radiometric Terrain Correction (RTC). RTC includes both geometric terrain correction (geocoding) and radiometric compensation. It is normally performed with the following steps:

- Geometric correction of the terrain (geocoding) is carried out in order to remove geometric distortions in the image (fig. 3.9). A DEM is required to adjust the position of topographically inclined pixels. For areas between ±60° of geographic latitude, it is common practice to use NASADEM, a public domain DEM produced by NASA based on a primigenial model acquired in 2000 during the Shuttle Radar Topography Mission (SRTM) and then refined with scans from subsequent missions. However, geocoding does not allow for correct mapping of areas subject to layover and radar shadows, which remain blank.
- Radiometric normalisation of terrain (fig. 3.10), performed to remove geometry-dependent radiometric distortions, consists of a pixel-by-pixel estimation and compensation of Aσ (θi) using a DEM.

Once normalised, SAR data are largely free of geometric aberrations, thus reducing radiometric differences between images acquired from different geometries. Consequently, image data calibrated through RTC lead to improved processing when combined with information obtained from other remote-sensing methods and in change analyses with multi-location scans[8].

From a visual point of view, once the correction process is complete, SAR images lose much of that deceptive resemblance to photographs and become more like maps where numerical data are represented by shades in a grey scale.

3.2.2 NASA scale of satellite data processing levels

Satellite SAR data are available at different stages (or levels) of processing, ranging from raw data directly acquired from satellites to refined information display products. Major space agencies retrieve data from satellites, process it to make it functional for a wide range of o fic purposes, open data, etc.). The variety of types of SAR data provided by a space agency is related to the kind of applications envisaged. Extracting and utilising these different layers of information are often not straightforward and linear operations. Furthermore, amplitude, phase and polarisation information are often differentially relevant depending on the scientific target audience. For this reason, space agencies share their imagery at different processing levels, each increasingly simplified and designed to emphasise different components of the SAR information space.

Unfortunately, there is no single coherent classification system for processing stages that is shared by all space agencies and, very often, the formats in which the data are distributed are different. One of the most commonly used terminologies is that of the National Aeronautics and Space Administration (NASA), consisting of the following levels:

- Level 0 – raw data corresponds to the least manipulated level and consists of the decoded but unfocused scans, i.e. before the application of Wiley's synthetic aperture processing. Unlike optical sensors, visualising the raw data of a SAR system does not provide much useful information about the detected scene. The raw data only become an interpretable image after aperture synthesis processing. Of course, the raw data are the basis for all higher levels of processing, so they are an essential type of information for any SAR data archive. However, outside the data processing community, raw products encounter little use. Although raw data is essential for any SAR sensor, not all satellite operators publicly share this type of information. For some sensors, satellite data security laws prohibit the publication of raw data, but in most cases, providers of remote-sensing services prefer to keep it confidential to protect proprietary information about their processing routines.
- Level 1 – the first stage consists of the first forms of data that can be visualised as images along the scale of possible processing. To this category belong complex images SLCs and detected amplitude images. SLCs are SAR data at full native resolution (single look), having both amplitude and phase information stored for each pixel (complex). Complex images (SLC images) are typically provided in the original tilted observation geometry, so they are neither geocoded nor have undergone RTC. Unlike most optical sensors, the native resolution of SAR sensors is often very unbalanced between the azimuthal and range direction. This is why images very often appear geometrically distorted when inspected with graphics processing software. While SLC images arrive with radiometric calibration factors already applied, in these full-resolution products speckle remains unmitigated. For polarimetric data, SLC products are provided for each polarimetric channel. Backscatter phase information in SLC images is an essential prerequisite for processing with Interferometric Synthetic Aperture Radar (InSAR), which is used to map a topographic surface or the deformation of a surface. In addition, SLC products are the basis for images processed at a higher level, such as amplitude-associated images, polarimetric products and geocoded images. Amplitude-associated products are fully-focused SAR images, which have, however, been stripped of the phase information of the return signal and are usually spatially averaged with other multi-looked (spatially averaged) images to reduce speckle. Although useful for a range of mapping and monitoring applications, images of the detected amplitude are provided in different states of geocoding. Most SAR systems provide amplitude products that have been left in the original acquisition geometry, so the geocoding operation becomes a task for the user, who often has to perform it manually. In other cases, the information needed to link the image coordinate system to the geographical coordinates is included in the file containing the image. Typically, the products associated with the amplitude of the return signal are georeferenced or geocoded with an ellipsoidal approximation of Earth, so distortions caused by the topographic configuration of the scanned surfaces are not corrected within them. In their original form, the functions of scanned amplitude images are limited to data visualisation and inspection. These products acquire relevance in cartography, change detection, environmen-

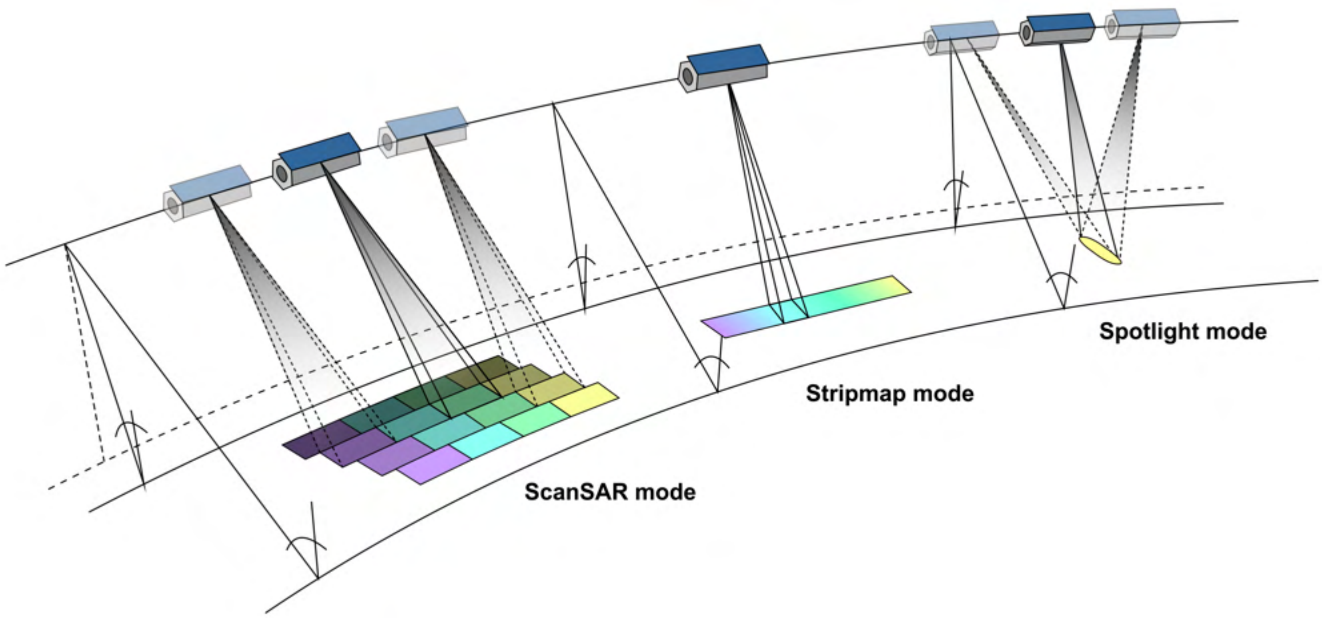

3.8/ Graphical exemplification, according to Moreira, Prats-Iraola, Younis, Krieger, Hajnsek, Papathanassiou 2013, of different operating modes for SAR satellite systems, used to increase the swath width (ScanSAR mode) or improve azimuth resolution (Spotlight mode) in comparison to the Stripmap mode.

tal risk monitoring and other disciplines only after an end user has applied the steps of geocoding and terrain correction.

- Level 2 – this stage corresponds to the Level 1 information that has been converted into geophysical quantities through a computer algorithm known as 'retrieval'. These are all those products projected onto the land surface, organised in regular grids and transformed into physical variables such as the calibrated RCS (as contemplated in the RTC process), the deformation along the LOS or polarimetric decomposition variables. Although Level 2 products are only distributed by a few space agencies at the moment, an increasing number of future sensors will offer products at advanced processing levels. Calibrated radar images can be used for cartography, land-use classification, detection of land changes and the study of environmental hazards. This category also includes interferometric data, which can be used in disaster damage estimation, land surface deformation analysis and much more.
- Level 3 – are Level 2 data of controlled quality that have been mapped onto a space-time grid.
- Level 4 – are Level 3 data that have been combined with models or other tools.

Distribution formats are very heterogeneous. Some Level [0] and Level [1] products are distributed in GeoTIFF files (Sentinel, TerraSAR-X), HDF[5] files (COSMO-SkyMed), or CEOS files (ALOS[2]). CEOS is a specific format designed for Earth Observation. Level [2] and higher data are still in a research and development phase, so they can be distributed in raster images such as GeoTIFF, alphanumeric sheets containing coordinates such as KMZ or special file types such as HDF[5]. At the same time, however, Level [2] and higher products are easier to use and manage than lower-level products, proving useful in a range of applications that is still expanding[9].

3.3 Modes of acquisition and accuracy of Synthetic Aperture Radars

Contemporary SAR systems are capable of operating in different mapping modes by controlling the antenna radiation pattern. In the case of a planar antenna, this is done by dividing it into sub-apertures and controlling the phase and amplitude of each sub-aperture via Transmit/Receive Modules. Typically, a SAR employs a few hundred transmit/receive modules, the settings of which are controlled by software. The most basic operating mode of all is the Stripmap mode, where tthe swath moves at the same velocity of the satellite, thus mapping a single continuous strip[10]. Stripmap mode has some advantageous properties such as a fixed azimuth of detection (which typically extends a few seconds along the orbit), a good antenna antenna pattern and good radar mapping coordinates. Other SAR image generation modes allow the balance between azimuth resolution and scanned cell extent to be changed by steering the antenna pattern in azimuth or elevation (fig. 3.11). These parameter tradings are due to the fundamental limitations of a single-channel SAR system. Any system manoeuvred to violate these limits will produce ambiguities in the image, such as those studied in Chapter 2. However, these limitations can be circumvented through multi-channel digital beamforming techniques[11].

3.3.1 High Azimuth Resolution Mode: Spotlight mode

In Spotlight modes, while the sensor is moving, the antenna is steered linearly along the azimuth to illuminate almost the same spot on the ground for a longer period of time when compared to Stripmap mode. The longer illumination time results in an improved synthetic aperture length and, consequently, better resolution. However, Spotlight mode does not map a continuous strip but, rather, individual patches along the radar flight path (fig. 3.11).

The simplest Spotlight mode is the 'staring' one: the centre of rotation of the antenna pattern coincides with the centre of the mapped scene, thus maximising both illumination time and azimuth resolution. The dimensions of the scene coincide approximately with the instantaneous footprint of the radar antenna (fig. 3.12a).

In order to overcome the poor extension of fixed gaze spotlight scenes, a 'sliding Spotlight' mode was developed. The centre of rotation is placed at a greater distance, usually outside the scene to be scanned, so the steering rate is lower than in staring mode. In comparison to Staring mode, targets are illuminated for a shorter time interval than the duration of the acquisition, which allows a more extensive scanning of the scene along the azimuth direction. In the sliding Spotlight mode, the counterpart for this greater extension of the scannable scene is a worsening of the azimuth resolution (fig. 3.12b).

As a consequence of the azimuth steering, the Doppler Centroid (DC) – i.e. the Doppler frequency of the scan at the mean squint angle θsq[12] – varies linearly as a function of the along-track coordinate in the scene. This variation is less than the azimuthal bandwidth of the scene, but must be accommodated by the central image mapping unit that is part of the radar. Spotlight mode allows an improvement in azimuth resolution without reducing the size of the antenna. This results in the Pulse Repetition Frequencies (PRF) of Spotlight scans being only marginally higher than those of Stripmap mode scans. This increase is committed to accommodate the migration of the DC in the scene extension.

TerraSAR-X, from the Deutsches Zentrum für Luft- und Raumfahrt e.V. (DLR), was the first operational mission for civil purposes to include a SAR sensor capable of acquiring images in both the staring and sliding Spotlight modes, achieving azimuth resolutions of 25 and 50 cm respectively[13].

3.3.2 Wide Swath Modes: ScanSAR and TOPS

If a wider swath is required than in Stripmap mode, there are ScanSAR and TOPS modes, which are executed in short scan intervals or 'bursts'. The available scan integration time is invested in different subswaths.

In ScanSAR mode, antenna elevation patterns are steered at different elevation angles corresponding to multiple subswaths (fig. 3.11). Each subswath is illuminated by multiple pulses for a shorter time than in stripmap mode. The timing is adjusted so that time-varying elevation patterns cyclically repeat the mapping of several continuous subswaths[14].

The number of sub-swaths is counterbalanced by the amount of illumination time available and this has consequences for the azimuthal resolution of the final image. Specularly in the case of the Spotlight mode, this degradation of azimuth resolution does not imply a consistent worsening of the PRF in comparison with the Stripmap mode, since the instantaneous Doppler bandwidth is that imposed by the antenna size (fig. 3.13a).

A further condition on the duration of the scan intervals is imposed by the continuity of the images mapped in consecutive bursts. Depending on the azimuth position in the terrain, targets are detected with different portions of the azimuth pattern and this has two consequences:

- The DC of the targets varies linearly as a function of the azimuth coordinate.
- An amplitude modulation of the mapped images, corresponding to the integration sequence and called 'scalloping', appears in the final products. Scalloping is usually modest, on the order of 1-2 dB, but results in inhomogeneities that affects both the radiometric and interferometric quality of radar images.

Taking the example of TerraSAR-X, its ScanSAR mode has a swath width of about 100 km, with an azimuth resolution of 15 m.

To overcome the problem of azimuth inhomogeneity in the Sentinel-1 Mission, the Terrain Observation by Progressive Scans (TOPS) mode was introduced. It subdivides the scanning in discrete elevation sections and then executes bursts typical of the ScanSAR mode, but contemplates backwards to forwards steering opposite to spotlight. The illumination time is reduced with respect to stripmap, that is the same area on the ground is acquired in a shorter time, thus allowing moving the beam in range to extend the swath. In this way, scalloping is reduced, usually around 0.5 dB. Inhomogeneity is less, in exchange for higher DCs (fig. 3.13b)[15].

3.4 Circular Synthetic Aperture Radar

A specific mode exclusive to SAR systems on aircraft platforms consists of surveys with circular flight paths. Targets in the scene are scanned 360°, which allows both very high resolution mapping and angular distinction. On isotropic targets, the impulse response of a circular SAR has polar symmetry with the best resolution obtainable from SAR resolution, i.e. $\delta x \leq \lambda/4$. This resolution value appears to be independent of the transmitted bandwidth. This theoretical result would require an infinitely thin isotropic target, which does not exist in reality. In any case, images acquired with a circular SAR are characterised by a very high resolution with reduced blurring and a greater level of detail.

The swath, instead of being along a strip, has a circular shape generated by the rotation of the footprint on the ground. The resulting survey is spatially variable, highly sensitive to the topographical configuration of the terrain and also to motion compensation. This sensitivity to the topographic configuration of the terrain is a key element of the tomographic potential of circular SAR scans[16] (Fig. 3.14).

3.5 Calibration of synthetic aperture radar images

The signal round-trip time intervals associated with the pixels of a calibrated image are accurately consistent with the SAR acquisition geometry model. The calibration of SAR images is based on three aspects:

- obtaining from the sensor radiometric values close to the actual radar intensity of the scanned scene;
- ensuring high-fidelity spatial detection of backscatterers;
- achieve an accurate representation of the complex ratios between polarimetric channels.

Let us begin with the first aspect. Since propagation dissipations can be estimated on average with great accuracy, the radiometric fidelity of a SAR system sensor depends on a good characterisation of the antenna pattern, SAR pointing and the electronic components of the transmitter and receiver (transmitted and transfer power functions, receiver gain, anomalies and deviations). For the radiometric calibration of SAR systems, external targets with high RCS are used, usually transponders (fig. 3.15). In order to assess the average elevation configuration of the sensor, scans are performed over homogeneous areas (e.g. for higher frequency bands, surveys of rainforests are arranged). Typical absolute radiometric fidelity values of a SAR systems are above 30%, i.e. 1 dB.

Let us now turn to the second aspect. The determination of the accurate position of the target relative to the image pixel depends very much on the knowledge of the acquisition geometry, the delays of the radar signals and echoes due to interaction with the atmosphere, and the electronic payload of the radar platform.

A good knowledge of the radar observation geometry is based on a precise knowledge of the orbit ephemeris and the antenna pointing behaviour, thus the behaviour of the space platform on which it is mounted.

Delays in the propagation of radar signals through the atmosphere can be estimated using meteorological models.

The internal delays of the radar electronics can be verified with the help of external targets, usually in the shape of a trihedron (fig. 3.16), whose position must be known with a very high level of accuracy, normally higher than the range

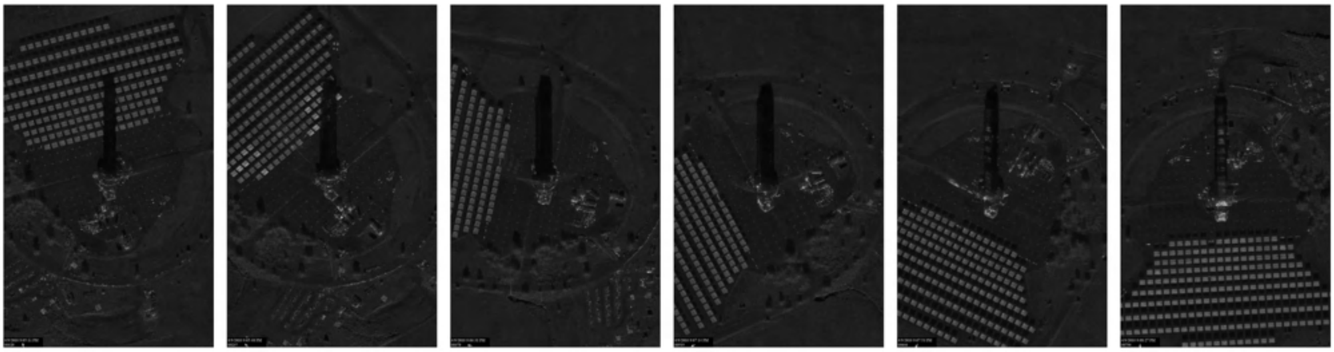

3.9/ Photograms of a movie obtained from a VideoSAR processing performed from a circular SAR scan of the solar tower at Sandia National Laboratories. The VideoSAR algorithms provide continuous acquisition and processing of the data recorded in the phase history of the return signal. The time interval between individual images is at the operator's discretion and independent of the length of the radar aperture. Source: Sandia National Laboratories, 2023b. Courtesy of Sandia National Laboratories, Radar ISR.

resolution of the system. The next step in the calibration process involves the evaluation of the relative accuracy of the SAR system in detecting the position of the targets between multiple scans, which is of paramount importance for interferometric applications. Relative accuracy depends on the separation between available efemerides, i.e. the distance between kinematic configurations assumed by the radar during each acquisition (known as the baseline), which should typically be kept to values better than a fraction of the wavelength adopted by the sensor.

Regarding the third aspect, an accurate representation of polarimetric ratios reveals accurate radiometric and interferometric information in relation to one channel to another. Polarimetric calibration requires accurate characterisation of the transmitter and receiver, including antenna patterns and horizontally and vertically polarised receiver channels in terms of geometry, imbalances and crosstalk (i.e. noise due to the presence in a given channel of signals relevant to another adjacent channel)[17]. In addition, polarimetric calibration also involves the estimation and compensation of Faraday rotation - i.e. the rotation of the signal polarisation plane - caused by the propagation of radar signals through the ionosphere[18]. Typical values of these ratios are below 30% in terms of amplitude deviation and a few degrees in terms of phase.

3.6. Polarimetry with Synthetic Aperture Radar

The field of SAR research underwent a significant leap in the early 1980s with the introduction of multi-channel techniques such as polarimetry and interferometry. Although the effectiveness of both of these advanced techniques had been demonstrated long before, radar polarimetry only became an operational research tool with the introduction of the Airborne Synthetic Aperture Radar (AIRSAR) system of the National Aeronautics and Space Administration/Jet Propulsion Laboratory (NASA/JPL), also during the early 1980s. The functionality of radar polarimetry from space was tested with the two Spaceborne Imaging Radar C-band and X-band (SIR-C and SIR-X) SAR sensors used for scans from the space shuttle Endeavour in April and October 1994, respectively[19].

As already mentioned in Chapter 1, radar waves and other forms of electromagnetic radiation consist of electric and magnetic fields, one perpendicular to the other. The polarisation of an electromagnetic wave concerns the orientation of the electric field and describes the lie of the plane of oscillation of the signal being propagated. In linearly polarised systems, the lie of this plane of oscillation is constant along the propagation path of the electromagnetic wave. In other systems, such as circularly or elliptically polarised SARs, the orientation of the plane of oscillation changes, describing geometric shapes such as circles or ellipses.

If the wave electric field is oriented vertically with respect to the planetary surface, the wave is said to be vertically polarised; similarly, if the wave electric field is oriented horizontally with respect to the spatial surface, the wave is said to be

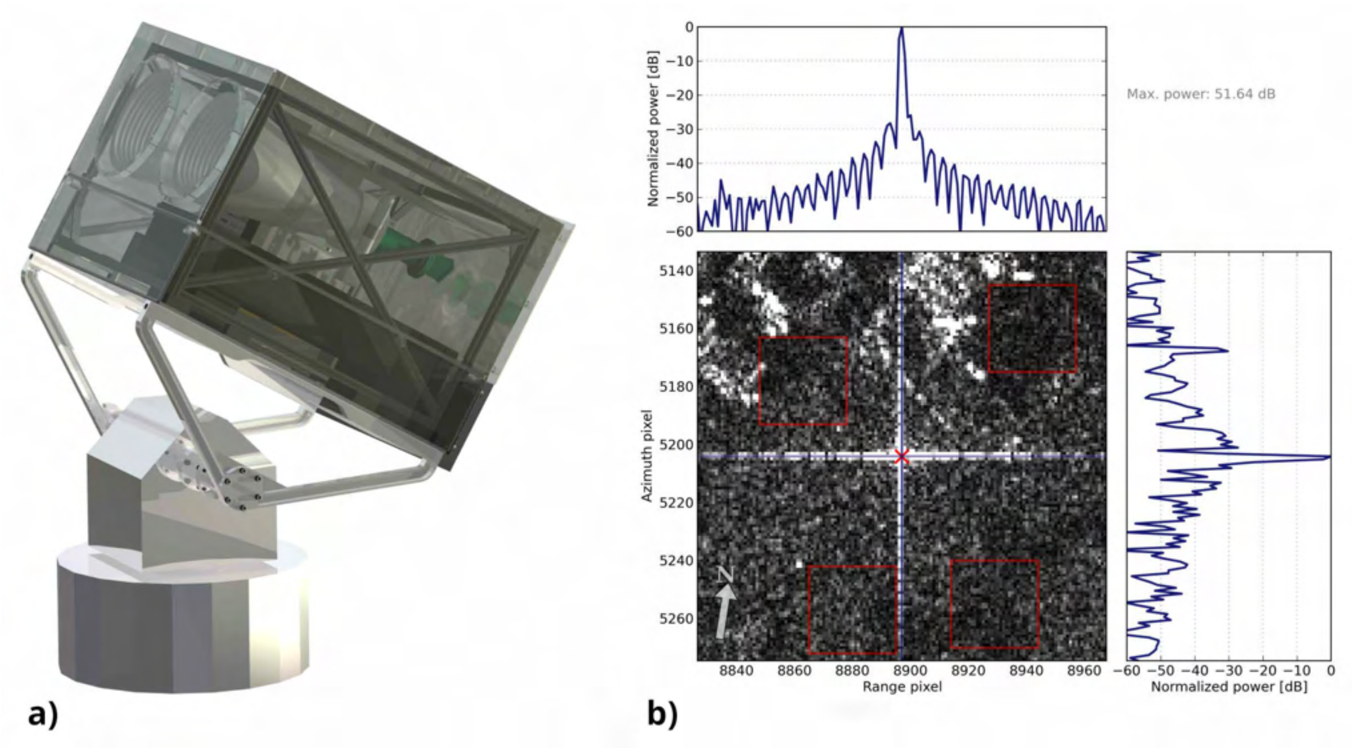

Fig. 3.10/ Calibration of sensor sensitivity against the radiometric values of a real scene. (a) Rendering of DLR's Kalibri transponder, dedicated to the C-band, mounted on a hinged support for biaxial orientation. (b) Portion of a SAR image with associated echo diagrams received from the Kalibri transponder, recorded during a scan over Oberpfaffenhofen Airport in Germany, carried out on 7 April 2013. The pixel relative to the resolution cell where the transponder was positioned is in the centre of the image portion, highlighted bya blue crosshair and a red oblique crosshair. The target-to-clutter ratio recorded obviously leans very favourably towards the transponder. The four red squares indicate the areas that were sampled to estimate the magnitude of stationary background echoes in the scene. Source: Döring, Schmidt, Jirousek, Rudolf, Reimann, Raab, Antony, Schwerdt 2013 / licensed under CC BY 4.0 (http://creativecommons.org/licenses/by/4.0/). © 2013 by Döring, Schmidt, Jirousek, Rudolf, Reimann, Raab, Antony, Schwerdt. Licensee MDPI, Basel, Switzerland.

horizontally polarised. Most of contemporary SAR sensors are linearly polarised and transmit vertically or (also) horizontally polarised waveforms.

Since radars emit coherent radiation, polarisation is controllable and the instrument can be configured to emit the signal at a certain polarisation (vertical or horizontal) and record echoes at the same or the other polarisation. The appearance of the final radar image will vary depending on the polarisation used to illuminate the area to be scanned and the physical structures of the reflective bodies detected. For example, tall, slender objects scatter vertically polarised energy more strongly than horizontally polarised energy, while overhead power line cables reflect the horizontally polarised signal more strongly.

Although the polarisation of an electromagnetic wave can assume a range of positions, imaging radars normally only use vertical pulses, horizontal pulses or combinations of these two polarisations (fig. 3.17).

For example, a radar might transmit horizontal pulses and record the horizontally oriented portion of the backscatter: this system is called HH, indicating horizontally oriented transmission and reception.

Many conventional satellite-based SARs have single-polarised sensors, which support only one linear polarisation.

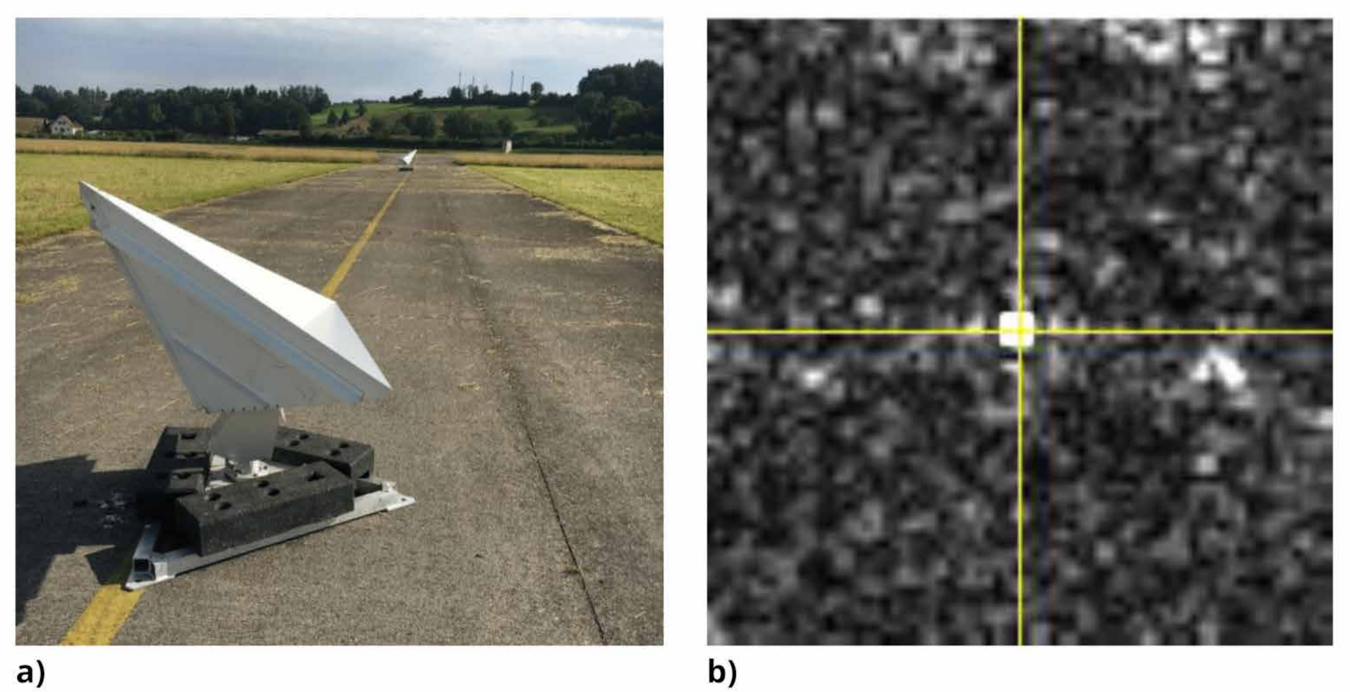

3.11/ Calibration of the Sentinel-1B satellite SAR satellite and quality control of Sentinel-1A/B products. (a) 1.5 m trihedron reflectors at a test site near Torny-le-Grand, Switzerland. (b) Radar image portion mapped by Sentinel-1A, framing a 1.5 m trihedron reflector. The local incidence angle was 45.7°. The yellow crosshair indicates the predicted phase centres (peak intensities) from calculations based on the radar technical parameters and perturbation corrections (such as delays from interaction with the atmosphere) obtained from models. CopernicuSentinel data (2016). Source: Schubert, Miranda, Geudtner, Small 2017 /licensed under CC BY 4.0 (http://creativecommons.org/licenses/by/4.0/). © 2017 by Schubert, Miranda, Geudtner, Small. Licensee MDPI, Basel, Switzerland.

These technologically outdated sensors operate mainly in the HH system (horizontally polarised transmission, horizontally polarised reception) and the VV system (vertically polarised transmission, vertically polarised reception).

When a pulse of a particular polarisation strikes a body, however, it is also possible for a portion of the energy to be backscattered by 90°. Nevertheless, it is possible to organise transmission and reception cycles in such a way as to combine different polarisations. Transmission could be oriented horizontally, but reception could be set vertically, thus resulting in the HV system referred to as 'cross-polarisation' cross-polarisation. Conversely, the VH system, also of cross-polarisation, involves a vertically oriented transmission combined with a horizontally set reception (fig. 3.18).

Traditionally, there are monopolarised radars capable of transmitting the signal in one polarisation and receiving the backscatter directly in the other (as in an HV system where the signal is transmitted horizontally and the echo is received vertically) but, in practice, this type is not very widespread and has been supplanted by dual-polarised and quad-polarised radars (fig. 3.19).

To give an example, cross-polarisation is often useful in the detection of ships in the seas and oceans because, under certain conditions, it suppresses the radar signature of the open ocean (constituting clutter) and derives noticeably bright radar signatures from ships. On the other hand, HH polarisation can sometimes be used to record ship wakes, precisely because it preserves the radar signature of the seas and oceans. Dual-polarised (HH, HV) scans, therefore, can be used together for more in-depth monitoring of maritime traffic.

The technical characteristics of some satellite radars, such as RADARSAT-2, even allow the polarisation to change betwe-

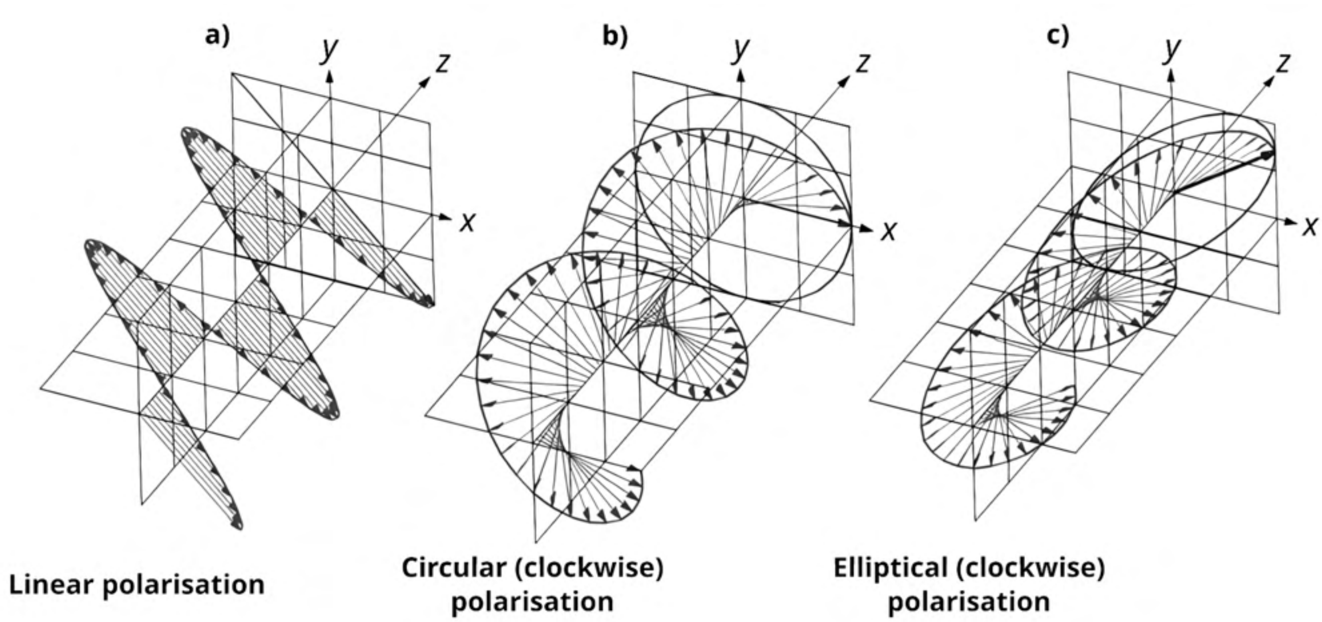

Fig. 3.12. Graphical exemplification, according to Japan Aerospace Exploration Agency 1997, of the main types of polarisation of the electromagnetic signal. (a) Linear polarisation; (b) Clockwise circular polarisation; (c) Clockwise elliptical polarisation.

en pulses, resulting in the type of scan known as quad-polarised. An example would be when the antenna alternately emits horizontally (H) and vertically (V) oriented waves, thus recording HH, HV, VV, and VH data. Normally, radar images obtained from cross-polarisation during the same survey are quite similar, so a quad-polarised scan usually produces three distinct images.

The polarimetric radar images can be merged into a composite image in false colours, so that they can be distinguished by polarisation type (fig. 3.19f). This approach is useful to better identify targets on the scanned portion of the terrain. For example, to accentuate differences between polarimetric channels during a comparison, HH, VV, and HV data are often combined into a single false-colour image. S_{HH}, S_{VV}, and S_{HV} are complex scattering amplitudes and their subscripts horizontal (H) or vertical (V) indicate associated received and transmitted polarisation. They are the elements of a 2 × 2 complex scattering matrix that describes the transformation of the two-dimensional transmitted plane wave vector into the received wave vector by the scatterer. Usually, in single false-colour images $|S_{HH}|$ corresponds to red, $|S_{VV}|$ corresponds to blue, and $|S_{HH}|$ corresponds to green[20].

3.6.1 Influence of signal polarisation on radar image mapping

To recapitulate, knowing the polarisation with which a SAR image was acquired is important, especially for particular environments such as urban areas, as signals with different polarisations interact differently with illuminated bodies, affecting the radar brightness of the pixel recorded in a specific channel.

The main objective of methods for the interpretation and decomposition of scattering is to break down the polarimetric signature of a distributed target, generally given by the superposition of different scattering contributions within a resolution cell.

The application of radar polarimetry is implicitly based on the idea that depolarisation[21] of radar waves allows a greater understanding of the scattering mechanisms of the scanned scene. The depolarisation of microwave radiation is a phenomenon that can be described in relation to the amplitude and phase values measured in a signal between different po-

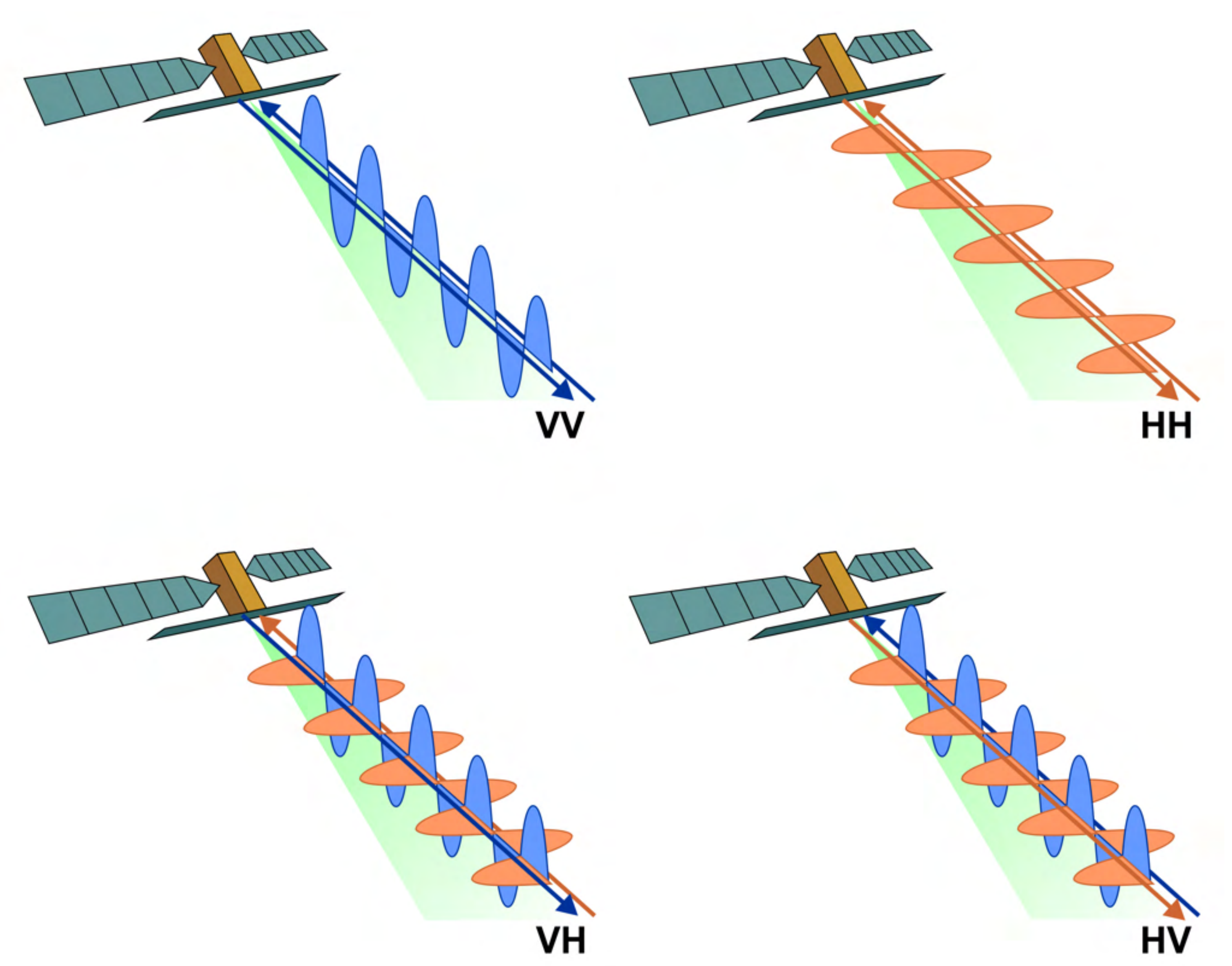

3.12/ Graphical illustration of the polarisations of the forward and return signal in the VV, HH, VH and HV schemes.

larisations. In order to study the scattering process with a polarimetric radar, it is therefore necessary to mathematically characterise the interactions between polarisations unambiguously[22], but an analytically in-depth treatment would transcend the objectives of this research. The Freeman-Durden decomposition of polarimetric data, while starting from a mathematically rigorous backscatter interpretation method, associates the outgoing and returning signal polarisations with certain categories of geometric configurations of the scanned scene[23]. This allows us to illustrate schematically how signal polarisation intervenes in the radar image mapping process, depending on the geometric configuration of the scanned bodies.

Let us assume, for the sake of simplicity, that a scene can be described as a combination of three types of scatterers (fig. 3.20):

- scatterers with a rough surface;
- double-bounce and multiple-bounce scatterers;

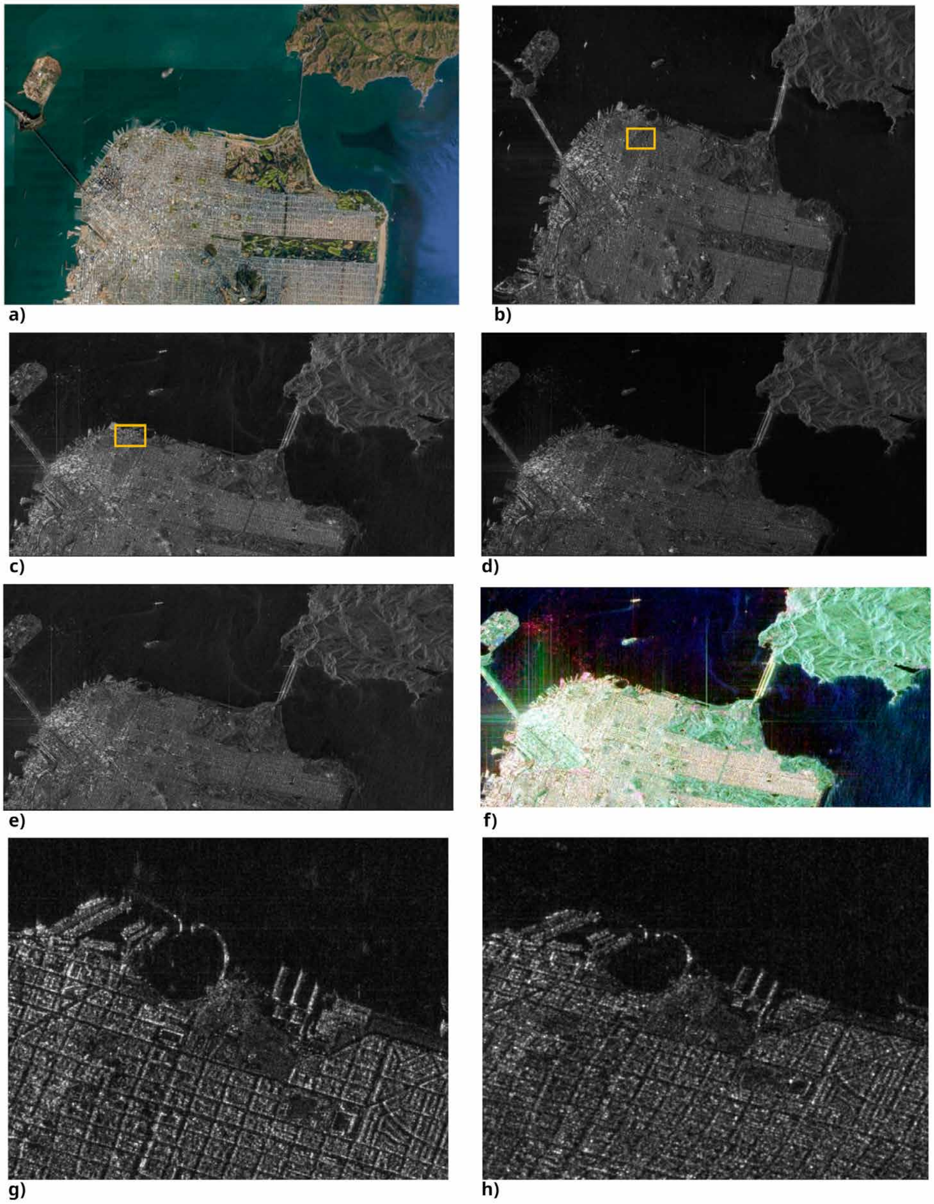

3.13/ Images of a polarimetric SAR remote-sensing test site located in San Francisco. Radar scans were performed from 27 March 2019 to 29 April 2020 with the Gaofen-3 satellite and C-band signals. (a) Opticalsatellite image; (b) intensity-associated component of a radar image with HH polarisation; (c-e) intensityassociated components of medium-resolution images with single-channel HH, HV, and VV polarisations, respectively; (f) false-colour composite image of medium resolution, obtained from the combination of the three previous images (|SHH| corresponding to red, |SHV| corresponding to green, and |SVV| corresponding to blue); (g-h) components associated with the intensity of portions of high-resolution radar images with HH polarisation, corresponding to the area highlighted in yellow in images b and c of this figure. Source: Qu, Qiu, Wang, Lei, Ding 2022 / licensed under CC BY 4.0 (http://creativecommons.org/licenses/by/4.0/). © 2022 by Qu, Qiu, Wang, Lei, Ding. Licensee MDPI, Basel, Switzerland

- volumetric scatterers.

The category of scattering scatterers distributed over a surface consists of lawns and fields with low vegetation, bare ground, roads and other paved or asphalted surfaces.

Double-bounce and multiple-bounce scatterers include any type of construction and artificial structure (including poles fixed into the ground), tree trunks, and other vertical structures that deflect a signal already reflected a first time, sending it back to the sensor.

Finally, vegetation canopies belong to the category of volumetric scatterers, as signals bounce back several times when propagating within vegetation structures.

These scattering types do not contribute equally to all three polarimetric channels. With regard to scattering power, each polarimetric channel has a greater susceptibility to certain scattering types according to schematic criteria (Tab. 3.1).

These general criteria make it possible to compare the RCS between different polarimetric channels and even to programme an automatic classification of scatterers (fig. 3.21), if data with all relevant polarisations are available (usually data from quad-polarised scans)[24].

Following the above criteria:

- a strong scattering in |SVV| is typical of rough surfaces (bare ground, moving water, etc.);
- a strong scattering in |SHH| indicates the predominance of double-bounce or multiple-bounce echoes (usually corresponding to artificial structures, tall vegetation, etc.);
- spatial variations in |SHV| indicate the distribution of volumetric backscatter elements for the scene, such as forest canopies and soil easily penetrated by microwaves, such as sand or other types of dry, porous soil.

Recently, polarimetric decomposition techniques have proved functional for separating and removing the contribution of local vegetation (constituting clutter) from the backscatter and for enabling the estimation of the moisture content of the scanned terrain[25].

3.7 Interferometry with Synthetic Aperture Radar

Radar measures the amplitude and delay of detected echoes. As already illustrated, delay information can be extracted from the phase of the received signal with subwavelength accuracy. However, the accuracy of distance detection during phase measurement in a normal SAR image is achieved with numerous difficulties, as the latter appears to be confused with other components. In particular, the phase pattern resulting from the coherent combination of the scatterers in the resolution cell (in a uniformly distributed phase) severely complicates the operation.

The differential distance-measuring potential, typical of and unique to SAR systems, is called SAR interferometry and lends itself to a number of applications concerning the scanned portion of the terrain, such as three-dimensional mapping of its topographical configuration, detection and measurement of displacements within it or monitoring of its vertical deformations.

All contributions common to the two acquisitions are compensated in the phase difference but, for example, the atmospheric phase is different between the two images and remains as a disturbing contribution. In the case of speckle this can result in decorrelation, because the contribution is random in relation to the two acquisitions. The differential phase of at least two SAR images must be mapped at two different times or from two different positions. The two images in question are called 'interferometric pair', while the time separation interval or geometric distance between them are called temporal and spatial baselines, respectively. In the field of satellite remote-sensing, it is customary to distinguish between the two products of the interferometric pair, a 'master' image and a 'slave' image, but this choice of terminology is currently controversial and not universally recognised, since both products are required to generate the desired output. A more scientifically accepted description (and one that we will adopt here) is the one which identifies a first acquisition and a second acquisition[26]. The combination of two SAR images can be mathematically expressed as in Expression (3.2).

$$i(r,x) = s_1(r,x) \cdot s_2^*(r,x) \qquad (3.2)$$

i is called the interferogram of the images s1 and s2 .

When both invidual scans are performed simultaneously, the operation is called single-pass interferometry. Single-pass interferometry systems are expensive, as they require at least two receiving channels and this is a very costly constraint for space operations. Currently, there are only two ways to perform single-pass interferometric acquisition:

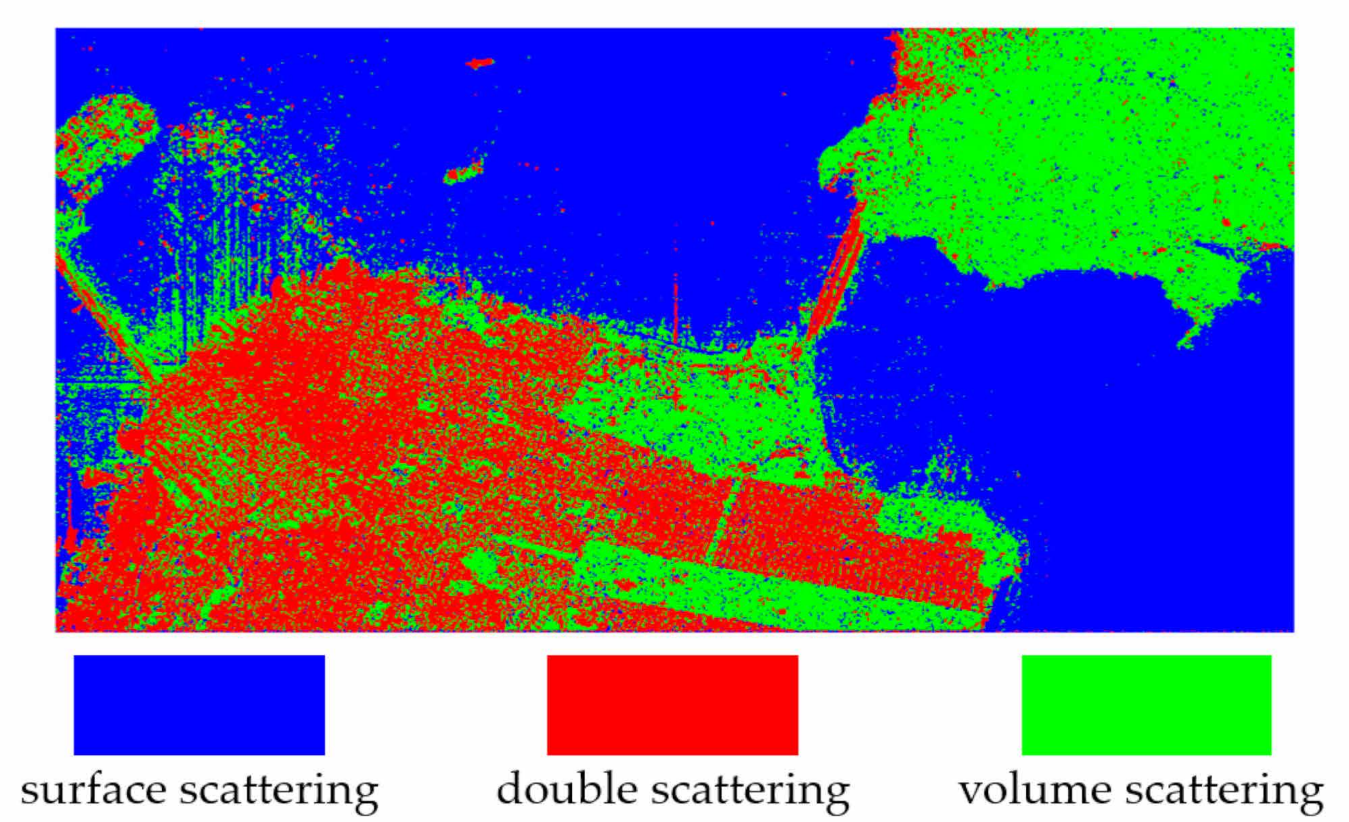

3.14/ Classification of backscatterers in the San Francisco urban environment previously examined by polarimetry (fig. 3.19). The three categories of targets adopted in this classification are those identified by the Freeman-Durden decomposition. Source: Qu, Qiu, Wang, Lei, Ding 2022 / licensed under CC BY 4.0 (http://creativecommons.org/licenses/by/4.0/). © 2022 by Qu, Qiu, Wang, Lei, Ding. Licensee MDPI, Basel, Switzerland.

- Building a boom that makes two radars integral with each other and in fact materialises the geometric baseline in the form of a constraint, as in the case of the Space Shuttle Endeavour during the Shuttle Topography Mission (SRTM) in February 2000.
- Using two close-formation satellite radars belonging to the same constellation at the same time, such as DLR's twin sensors TerraSAR-X and TanDEM-X. The alternative to a synchronised pair of scans with two receivers is to acquire the second image with the same sensor after a certain number of orbital cycles. This operation is called repeat-pass interferometry and is obviously influenced by the changes that occur in the scene during the time interval between the two detections. In this case, the geometric baseline can be mathematically deduced from the tolerances in both the space platform orbit control and our knowledge of the platform orbit.

The phase of the interferogram is called the interferometric phase and is stated in Expression (3.3).

$$\phi_i(r,x) = \angle\{i\} = \angle\left\{s_1(r,x) \cdot s_2^*(r,x)\right\} \qquad (3.3)$$

where the operator $\angle\{\cdot\}$ extracts the angle between 0 and 2π from the input complex number.

As already stated, the interferometric phase contains information of subwavelength accuracy by the radar, concerning the differential measurement of the radial distance obtained by two scans. Once the complex value is known, however, it is only possible to determine the main angle in the complex pla-

ne between [-π, π], while information on the 'number of turns' leading to the exact value of δr is lost. This phenomenon is called phase wrapping. However, the interferometric phase is not always directly observable due to the wrapping of ϕ_i, which poses a major problem in determining unambiguously the phase changes caused by the different acquisition positions and locations between the two surveys.
Jumps between 0 and 2π are called fringes, due to the characteristic visual effect induced in the wrapped interferograms, and they typically correspond to areas of phase continuity. In this case, the fringes represent slopes rather than sudden drops, due to the topographic configuration of the scanned scene. In an interferogram, phase is difficult to represent graphically, as it is always ambiguous with respect to integer multiples of 2π. Conventionally, two criteria for representing interferometric phase can be adopted:

- the greyscale bar criterion, for black corresponds to 0 and white corresponds to 2π;
- the counterclockwise colour wheel criterion for which, approximately, red corresponds to 0 and 2π, blue to π/2, cyan to π and yellow to 3π/2.

Of the two criteria, the colour wheel is objectively the best, as it graphically translates the continuity of values between multiples of a round angle. For example, π/8 and 19π/20 are two values that are very close, but the greyscale criterion would make them appear very far apart (fig. 3.23). The continuity becomes much more evident once the unwrapping of the interferometric phase is performed, i.e. once the exact phase value has been estimated (including 'full 2π turns'). With a colour scale representation, the hues are redistributed and the fringes are eliminated (fig. 3.24)[27].

3.7.1 Geometric models of interferometry

The characteristic accuracy of interferometry, having a level of detail of an order of magnitude less than the adopted wavelength, allows different estimates to be made regarding the scanned scene depending on the position and location assumed during the survey.
In the case of single-pass interferometry, two synchronised radars or two antennas on the same platform are used; in the latter case, there are two ways to scan:

- the Single-antenna-transmit mode, where one antenna emits the signal and both receive the echoes;

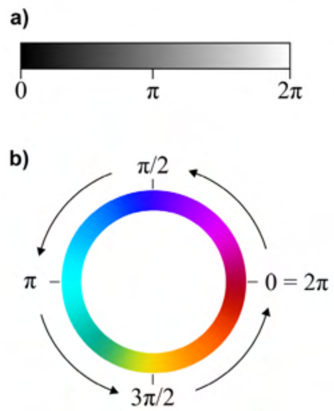

3.15/ Graphical representations of the interferometric phase with greyscale bar criterion (a) and counterclockwise colour wheel criterion.

- the Ping-pong mode, where each antenna transmits its own signal and receives the respective echoes, thus doubling the physical baseline.

When performing interferometric detection of a stationary scene, the two images are acquired from slightly different positions and with different looking angles θl . Triangulation of the delays from the two scan points to the target allows the localisation of the latter in space, i.e. the estimation of information regarding the altitude of the scene (fig. 3.23).
Phase difference between the two images can be written as a function of the altitude of the backscatterer, as stated in Expression (3.4).

$$\phi_i = m \cdot \frac{2\pi}{\lambda} \cdot \left(r_{0,2} - r_{0,1}\right) \qquad (3.4)$$

m is a constant introduced to consider whether the two images were acquired by the radar using the same flight path in both cases or not:

- in the case of a single-pass system, m=1 is set;
- in the case of a repeat-pass system, m=2 is set;
- in the case of a single-pass system with a sensor in Ping-pong mode, m=2 is still set.

Adopting the schematisation of parallel rays[28], the range can be approximated as in Expression (3.5).

$$\phi_i \approx m \cdot \frac{2\pi}{\lambda} \cdot b \cdot \sin\left(\alpha - \theta_1\right) \qquad (3.5)$$

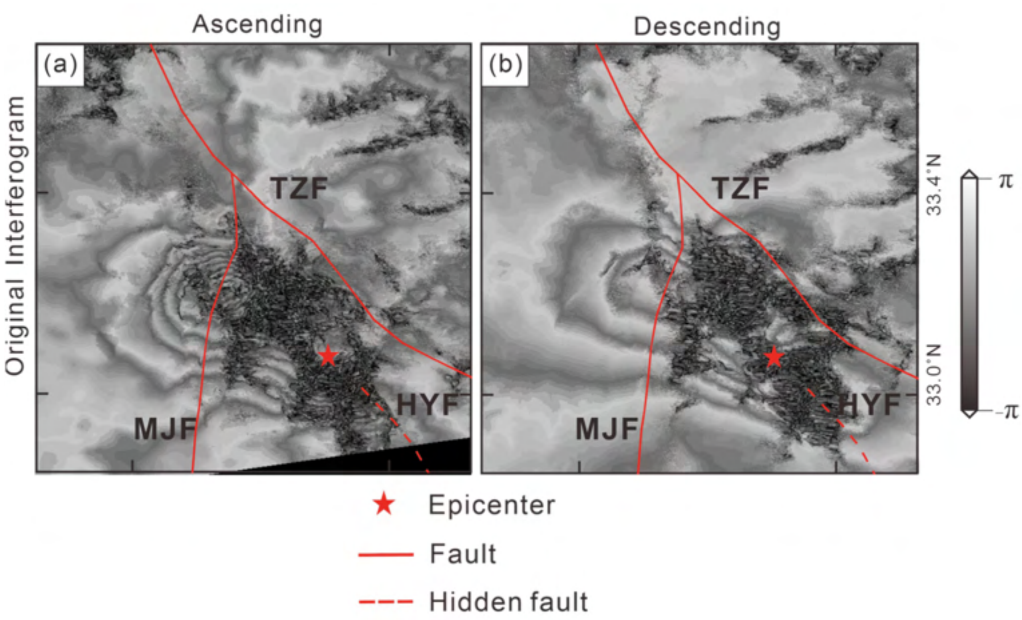

3.16/ Greyscale interferometric phasing of interferometric pairs obtained from Sentinel-1 sensor data on earthquake-induced deformation in the Jiuzhaigou area in 2017, near the fault system of the eastern part of the Kunlun Mountains in southern Central Asia. (a) Interferogram from scans along ascending passes; (b) Interferogram from scans along descending passes. Source: Peng, Huang, Wang 2023 / licensed under CC BY 4.0 (http://creativecommons.org/licenses/by/4.0/). © 2023 by Peng, Huang, Wang. Licensee MDPI, Basel, Switzerland.

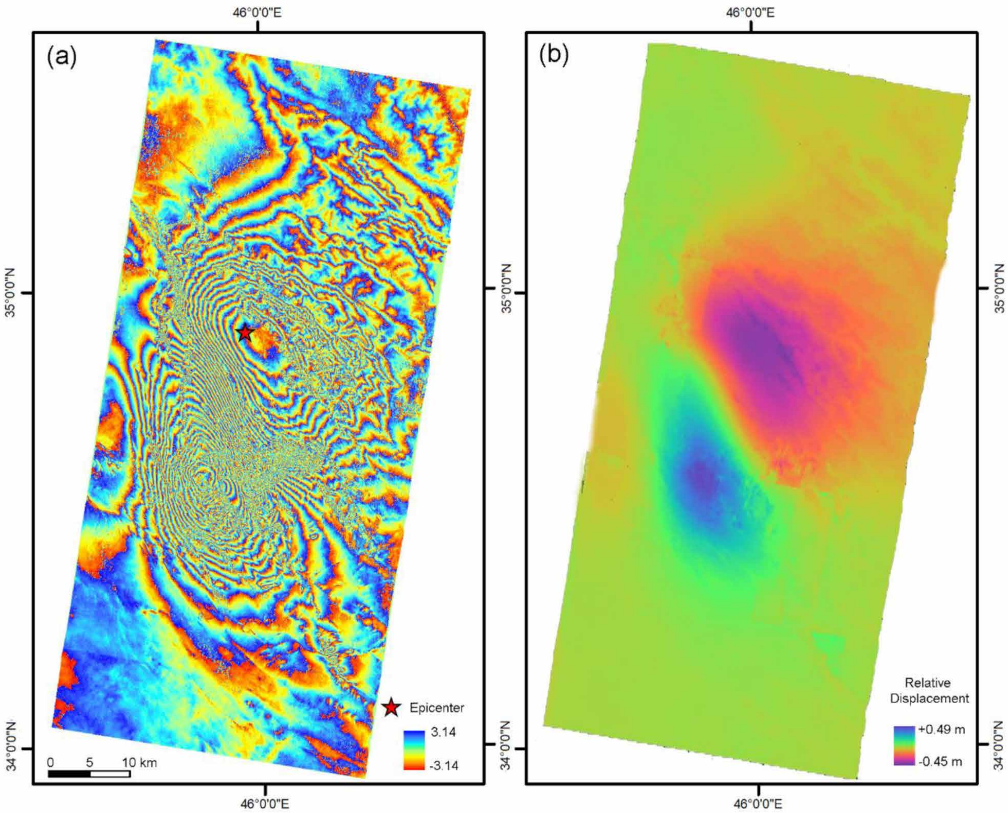

3.17/ Wrapped (left) and unwrapped (right) colour interferometric phases of interferometric pairs obtained from Sentinel-1 sensor data regarding earthquake-induced deformation in Southern Halabjah (Sarpol-eZahab, Iraqi Kurdistan) on 12 November 2017. Source: Gunce, San 2018 / licensed under CC BY 4.0 (http://creativecommons.org/licenses/by/4.0/). © 2018 by Gunce, San. Licensee MDPI, Basel, Switzerland.

The last two factors constitute the projection of the baseline onto the radar LOS, also known as the parallel baseline. The altitude of the scattering element can be written directly as in Expression (3.6).

$$h = H \cdot \left[1 - \cos\left(\theta_1\right)\right] \quad (3.6)$$

Expression (3.6) is accurate but rarely useful in practice. For real systems, an assessment of the actual radial distances of the scene through geocoding is preferable. For quick analyses, however, the angular information in Expression (3.5) is too detailed to be interpreted by eye. By also adopting the flat-Earth approximation, we can express the interferometric phase as a function of the altitude of the scatterer statedi in Expression (3.7).

$$\phi_i \approx m \cdot \frac{2\pi}{\lambda} \cdot \frac{b_\perp}{\left[r_0 \cdot \sin\left(\theta_i\right)\right]} \cdot h \quad (3.7)$$

$b_\perp$ is the baseline projection perpendicular to the LOS, i is the angle of incidence and h is the altitude of the backscatter element. Neglecting the curvature of Earth, the sensitivity of the interferometric phase to the topographic configuration can be calculated as stated in Expression (3.8).

$$\frac{\partial \phi_i}{\partial h} \approx m \cdot \frac{2\pi}{\lambda} \cdot \frac{b_\perp}{\left[r_0 \cdot \sin\left(\theta_i\right)\right]} \quad (3.8)$$

$b_\perp \approx$ b-cos(a-θl) is the projection of the baseline perpendicular to the LOS and θ_i is the incident angle. It appears from Expression (3.8) that the greater the perpendicular baselines, the greater the sensitivity to changes in the topographic configuration of the scanned surface. On a theoretical level this deduction is correct, but not very applicable in a realistic situation due to two side effects:

Increasing the cross-track baseline increases geometric decorrelation, also known as angular decorrelation. In other words, the mapped images become increasingly different from each other, worsening the phase quality of the interferogram.

The frequency of the fringes increases, complicating the unwrapping of the interferometric phase.

Given a resolution cell, we can linearise the interferometric phase as a function of altitude h, as in Expression (3.9).

$$\phi_i \approx \frac{\partial \phi_i}{\partial h} \cdot h = 2\frac{\pi \cdot h}{h_{amb}} = m \cdot 2\frac{\pi}{\lambda} \cdot \frac{b_\perp}{r_0 \cdot \sin\left(\theta_i\right)} \cdot h \quad (3.9)$$

The parameter h_{amb}, called the height of ambiguity, describes any cross-track interferometric observation and approximates the topographic altitude, which causes a cyclic change in the interferometric phase. In light of what has been said above, the altitude of ambiguity h_{amb} is related to both the sensitivity of the interferometer and the complexity of phase unwrapping. The higher h_{amb}, the lower the sensitivity in the interferometric scan with respect to the topographic configuration and the lower the difficulty unwrapping the phase.

In repeat-pass interferometry (fig. 3.26), on the other hand, the two SAR images are acquired from the same position and the phase offset is given by the movement of areas or targets belonging to the scanned scene.

To observe the displacements, the two radar images must be mapped at two different times. For a case like this, the interferometric phase is written as in Expression (3.10).

$$\phi_i = m \cdot 2\frac{\pi}{\lambda} \cdot \delta r_{LOS} = m \cdot \frac{2\pi}{\lambda} \cdot v_{LOS} \cdot \delta t \quad (3.10)$$

δr_{LOS} is the displacement along the Line of Sight (LOS), v_{LOS} can be interpreted as an equivalent radial velocity describing the movement of the scene as linear and δt is the time interval between the two radar scans, called temporal baseline.

Moving targets (such as land vehicles, vessels and aircraft) or sea currents and ice blocks in the ocean must be detected in very short time intervals (a few seconds or less). These scans require two or more antennas mounted on the same platform with a certain separation distance along the trajectory. Such sensors constitute single-pass interferometers, called along-track interferometric systems.

Along-track interferometry can also be used to estimate fast movements of natural surfaces, such as those of ice blocks scattered in the ocean.

Slower movements such as those of glaciers, ice sheets or lava flows require time intervals of several hours or even several days, so they are normally detected with repeat passes of the same satellite.

In the case of repeat passes, the cross-track baseline between scans is usually non-zero, which adds a topographic component to the interferometric phase, which is a disturbing factor in the estimation of the displacements that occurred between the two acquisition instants. A standard technique for removing the topographic contribution is to use two consecutive

interferograms to form a differential interferogram, where the topographic contribution cancels out. This method is known in scientific literature as Differential Interferometry Synthetic Aperture Radar (DInSAR).
In the case of very slow displacements such as land subsidence, deformations in man-made structures, seismic and volcanic activities, the time intervals for surveys typically take days to years. Many images are needed to isolate the deformation signal (which may be very weak because of very noticeable fringes, like in earthquakes) from the disturbing components (topographic phase, atmosphere, noise). Therefore, a substantially larger number of radar images than two tends to be required. A series of images to be combined with an interferometric process is called an 'interferometric stack'. The processing of an interferometric stack can extract information from several pairs of radar images to derive very accurate data on the temporal evolution of the scanned scene[29].

3.7.2 Consistency, effective number of scans and decorrelation sources

The Interferometric Synthetic Aperture Radar (InSAR) model just presented implicitly assumes that the radar images s_1 and s_2 differ only in a phase term proportional to the ranging difference in the two scans. In reality, both the sensor and the backscatter of the scene during the two acquisitions introduce additional differences in the data, which reduce the similarity between the two radar images and worsen the quality of the interferometric phase. A measure of the similarity of the interferometric pair is given by the interferometric coherence γ, which is essentially a correlation factor of the image pair that can be calculated by statistical estimation. The coherence magnitude tends to 1 for a small interferometric phase variance, but tends to 0 when the interferometric phase variance is large.
Multilook filtering is a standard procedure to improve the quality of the interferometric phase, offset by a decrease in geometric resolution. Averaging over N samples, if these are independent, only results in an improvement of a factor N in the variance. Factors with spectral weighting or oversampling establish correlation between samples and the actual number of independent samples Ne could be smaller than N.
Through statistical calculations, the accuracy of the interferometric phase can be represented as a function of interferometric coherence γ, resulting in curves associated with the number of scans (fig. 3.27).
Decorrelation sources degrade the coherence between scene scans and the quality of the interferometric measurement. We can write interferometric coherence as the product of several decorrelation factors, as stated in Expression (3.11).

$$\gamma \approx \gamma_{\mathrm{SNR}} \cdot \gamma_{\mathrm{amb}} \cdot \gamma_{\mathrm{proc}} \cdot \gamma_{\mathrm{geo}} \cdot \gamma_{\mathrm{temp}} \qquad (3.11)$$

The separation of contributions is related to the different physical sources. The subscripts of the factors indicate the effects of noise, ambiguities, processing errors, geometric changes, and temporal changes, respectively. We discuss the individual factors below.
The first cause of decorrelation γSNR is obviously noise, which is independent in the two images. The greatest contribution to this factor is made by the thermal noise of the receiver, while other minor contributions are caused by phenomena such as quantisation noise provoked mainly by different effective dynamic ranges. If the SNR between the two images is different, the value of γSNR can be expressed as in Expression (3.12).

$$\gamma_{\mathrm{SNR}} \approx \left[\left(1+\mathrm{SNR}_1^{-1}\right)\cdot\left(1+\mathrm{SNR}_2^{-1}\right)\right]^{-1/2} \qquad (3.12)$$

Assuming identical Signal-to-Noise Ratio (SNR) between the two scans, i.e. SNR_1=SNR_2, Relation (3.12) contracts into Relation (3.13).

$$\gamma_{\mathrm{SNR}} \approx \frac{\mathrm{SNR}}{1+\mathrm{SNR}} \qquad (3.13)$$

In both Expression (3.12) and Expression (3.13), the SNR can include additional types of noise in addition to those just enumerated.
The second factor γ_{amb} in the right-hand member of Relation (3.11) describes the impact of range and azimuth ambiguities. These ambiguities, assuming they are inconsistent in the two images, appear uncorrelated in the interferogram. The azimuth ambiguities could be correlated between the two images if the baseline is small and, at the same time, the PRF and acquisition pointing are the same, but small variations in the PRF can cause decorrelation. The third source of decorrelation γ_{proc} is given by proces-

sing, thus taking into account phase and localisation errors that may arise during interferometric processing. In airborne SAR, the decorrelation associated with processing can be caused by significant residual displacement errors in the platform. In space missions, processing errors arise from co-registration errors, in turn provoked by pointing errors, orbit knowledge, and information on the topographic configuration of the scene.

The fourth factor γ_{geo} in the right-hand member of Relation (3.11) describes the impact of the change in observation position and location, which gives rise to a different result of the coherent superposition of the scatterers over the scanned territory[30]. This geometric decorrelation factor can be decomposed into two surface components and a purely volumetric component[31], as stated in Expression (3.14).

$$\gamma_{geo} = \gamma_r \cdot \gamma_D \cdot \gamma_{vol} \qquad (3.14)$$

Subscripts r, D and vol stand for range, Doppler, and volume respectively. If instantaneous Doppler scaling is ignored, the wavelength of the radar carrier is projected onto dimensions of a different geometric resolution of the SAR images. The received echoes can be interpreted as a sample of the scene spectrum in the projected wave number. For elevation, the difference between the projected wave numbers of the interferometric pair is known as spectral shift, which can be approximated as in Expression (3.15).

$$\Delta k_r = \frac{2\pi}{\lambda} \cdot \left[\frac{1}{\sin(\theta_{i1})} - \frac{1}{\sin(\theta_{i2})} \right] \qquad (3.15)$$

k_r is the range wave number, while the angles θ_{i1} and θ_{i2} refer to the local incident angle for the pixel considered. Relation (3.15) can be interpreted as a deviation in the range frequency domain of the shape statedi in Expression (3.16).

$$\Delta B_r = c \cdot \frac{\Delta k_r}{2\pi} \qquad (3.16)$$

Which typically increases for larger (perpendicular) baselines and defines the portion of the spectrum that manifests as noise in the interferogram. Knowing exactly the position and orientation of the scan, the decorrelation factor of the spectral deviation can be contained to a value of 1 by filtering the common portion with a bandpass filter, though reducing the spatial resolution of the interferogram.

The Doppler term γ_D is analogous to the spectral offset in the azimuthal plane only, where the variation in wave number, caused by the two different squint angles θ_{sq1} and θ_{sq2}, is stated in Expression (3.17).

$$\Delta k_a = 4\frac{\pi}{\lambda} \cdot \left[\sin(\theta_{sq2}) - \sin(\theta_{sq1}) \right] \qquad (3.17)$$

ka is the azimuth wave number and the factor 4π is due to the two-way propagation of the signal. As in the case of spectral deviation, the Doppler decorrelation term can be limited to 1 – within the accuracy possibilities of the pointing system – through common band filtering of the spectral medium, though reducing the available resolution of resultant interferograms.

Volumetric decorrelation γ_{vol} is due to the change in radar signatures of volumetric structures when mapped from different viewing angles. Volumetric decorrelation increases as penetration into the media increases and as cross-track baselines increase. Volumetric decorrelation cannot be neutralised during processing and can only be mitigated by carefully choosing the cross-track baseline of the scan (normally by reducing its extent).

The fifth and last factor γtemp in the right-hand member of the relation (3.11) is due to temporal effects. Temporal decorrelation is caused by the dynamics of the scene developing over time, due to changes in the structure, dynamic state or dielectric properties of the scene. Temporal decorrelation is a fundamental limitation of repeat-passes interferometry and can only be mitigated by minimising the temporal baseline between scans. Similar to the case of geometric decorrelation, temporal decorrelation changes scale with carrier frequency and is therefore more influential for short wavelengths. Although temporal decorrelation is considered simple noise in many interferometric measurement cases, it can provide valuable information as a radar signature of a physical change in the scene[32].

3.7.3 Interferometric processing

In a typical algorithm for interferometric SAR processing that takes the geometry of a scan s1 as a reference, the first step consists of coregistering the image s2 into the geometry s1. This task is typically performed in the case of both aircraft and space platforms using trajectories, timing values and ex-

ternal topographical information of the scene (such as NASADEM) as data.
The second step is band-pass filtering of both images to the common range and azimuth bands in the scene, in order to reduce spectral decorrelation (thus trying to achieve γ_r - $\gamma_D \rightarrow$ 1) and thus increase total coherence.
At this point, the interferogram is computed and, as anticipated, the current resolution of the interferogram is proportional to the common bandwidth of the observation.
Normally, the next step consists of removing the synthetic phase component generated by the computation with whatever scene information (external to the processing) is available to us. In the case of an acquisition with cross-track interferometry, the so-called "flattening" usually consists of the removal of the interferometric phase estimated from an ellipsoid or from the available DEM. This phase is also known as '(flat) Earth removal', where the term 'flat Earth' clearly refers to the fringe removal introduced by the Earth ellipsoid and can be used in a broad sense to refer to the removal of any interferometric phase expected a priori.
Once 'flattened', the interferogram is 'multilooked' to the desired averaging factor. As seen above, multilooking consists of low-pass filtering followed by possible downsampling to adjust the final bandwidth of the resulting interferograms. Low-pass filtering can be performed either in the time domain or in the frequency domain. The step before unwrapping is the computation of the interferogram phase using Expression (3.3). After this operation, the interferometric phase is wrapped in an interval of 2π.
Phase unwrapping consists of finding the most probable solution in a matrix of multiples of 2π, varying in each pixel of the interferogram. One could constrain the solution to spatial continuity and preservation of signal energy, but this would be a flawed position of the problem. From vector field theory, the solution must satisfy the condition stated in Expression (3.18).

$$\nabla \times \nabla \phi_i = 0 \qquad (3.18)$$

where ϕi represents the unwrapped phase of the interferogram. Unwrapping errors typically arise due to high fringe frequency, due to low SNR, or due to spatial discontinuities in the interferogram. Unwrapping errors can be identified and corrected by a second observation (or even further observations beyond the second one) of the same interferometric phase with a different sensitivity, which can be achieved by changing baselines or wavelengths (operations that are, however, impracticable with satellite radar sensors). With a sufficient difference in sensitivity, the phase jumps will be spatially arranged differently, providing reliable information for a reliable estimate[33].

3.5.4 Differential Synthetic Aperture Radar Interferometry

The interferometric phase between two SAR images acquired at different times includes information on the dynamics of the scanned scene. The general approach of DInSAR can be described as a combination of the effects of single-pass interferometry and repeat-passes interferometry. Any differences found in the scene, be it the cross-track baseline [cross-track baseline] or ground displacements, will be a contribution to the interferometric phase. Keeping us in a general case, the interferometric phase of any repeat-passes acquisition can be expressed as the sum of a topographic and a differential component, as stated in Expression (3.19).

$$\phi_i = \phi_{topo} + \phi_{diff} \qquad (3.19)$$

The topographic component will increase as the transverse baselines increase and the differential component will account for any dynamic changes in the scan.
When we described single-pass interferometry and repeat-pass interferometry we had used a simplified model, attributing the differential phase in its entirety to the displacements in the scene, though this situation is difficult to find in reality. Even after error-free calibration, unwrapping, and removal of the topographic contribution, the differential interferometric phase will be contaminated by atmospheric propagation and noise, as stated in Relation (3.20).

$$\phi_{diff} = \phi_{disp} + \phi_{atm} + n \qquad (3.20)$$

Atmospheric term ϕatm is due to uncompensated delays and defocusing introduced by radar wave propagation through the ionosphere and troposphere, while n represents a phase noise process. As explained in Chapter 1, the troposphere tends to affect shorter wavelengths, usually from the C-band upwards. Residual atmospheric fringes are normally caused by changes in the local water vapour pressure, resulting in residual delays in the centimetre scale.

The differential interferometric fringes follow the measured displacement in the LOS of the radar. If several acquisitions are used with different LOSes, the different displacement projections can be used to estimate more than one component of the scene displacement (fig. 3.28).
Displacement estimation is performed on the equivalent slant range planes of the acquisitions. If and only if we have ascending and descending LOSes simultaneously, the angle of incidence θi can be used to further decompose the ground displacements (e.g. into northing and easting) and vertical components. The accuracy of the estimation of the two-dimensional components will depend on: the accuracy of the interferometric phase; the variance of thermal and atmospheric noise; the angle between the LOS vectors. In fact, the more the LOS vectors tend to be orthogonal, the less noise scaling will occur during inversion. The two different LOSes can be realised in many different ways, the most common of which are: ascending and descending passes; left and right oriented acquisitions; different squint angles θsq; along-track separation in bistatic scans.
Being sensitive to deformations in the magnitude of wavelength, DInSAR can also be used to detect changes in the dielectric properties of volumes through changes in the backscatter phase centre of volumetric targets. An example of this application is the model for the relationship between differential interferometric phase and differential soil moisture. Other similar examples are given by changes in the humidity of forests and structures consisting of snow and ice.
DInSAR has been used extensively for over two decades to detect strong radar signatures from deformations such as landslides, volcanic eruptions, or earthquakes. However, when performed from only two images, DInSAR is limited in accuracy by errors in the removal of topographic and atmospheric configuration information. If, however, one has a stack of numerous interferograms, it is possible to estimate the contaminating effects of DInSAR] measurements, such as atmospheric influences and errors in the DEM used. In this method it is expected that atmospheric phase errors are uncorrelated between consecutive passes and will therefore be averaged out if a large number of scans are combined.
Stack-based DInSAR is an analysis of areas that remain coherent along the image time series. Depending on the composition of the scene, one can opt to consider it as consisting of distributed areas or point targets.
Normally, distributed areas are detected using interferometric coherence, the averaging of which consolidates the robustness of the detection but reduces the geometric resolution of such areas. A combination of amplitude and coherence-based detections can enlarge the zone subject to measurement and, in such a case, the unwrapping of the phase of the scanned area is an aid in identifying false positives. Such an unwrapping operation must be performed on a three-dimensional wide-mesh grid set to the values of azimuth, range, and time. Then, it must be considered as a two-dimensional unwrapping of each interferogram. Once the differential unwrapped phase is obtained, the different components of the differential phase can be estimated in terms of pixels by calculating the values of the DEM errors, the atmospheric phase screen, and the linear and non-linear components of the deformation. The interpretation of a scene as distributed areas lends itself to the monitoring of large areas, including rural areas with slow time correlation losses.
The schematisation of the scene as persistent point scatterers assumes the presence of a dominant backscatterer in the resolution cell and achieves high accuracy in locating targets with any baseline, even one of great extent. This type of interpretation finds application in urban environments, especially in the monitoring of man-made structures such as civil works and buildings, but is also suitable for very stable natural surfaces (such as rocky spires). The Persistent Scatterers Interferometry (PSI) approach allows for full-resolution detection based on the backscatter amplitude of these targets[34].
In addition to interferograms, another type of processed data typical of DInSAR are time series diagrams, which allow the estimated displacements of targets between scans to be represented as graphs (fig. 3.29). Conventionally, these diagrams have the instants of acquisitions arranged on the abscissa and the estimated values of the displacements arranged on the ordinate.

3.8 Synthetic Aperture Radar Tomography

Synthetic Aperture Radar Tomography (TomoSAR) is a recent technological advancement that enables the use of interferometric methods in multidimensional mapping operations. By exploiting scans with multiple spatial baselines and separation along time (temporal baselines), TomoSAR techniques allow the realisation of a synthetic fine beam radar scanner along the vertical direction. Such a system allows full three-dimensional reconstruction as well as long-term deformation monitoring in complex scenes (referred to as four-dimensional imaging, since it records changes along time as well as in the three spatial dimensions).

Focusing for three-dimensional mapping allows the study of the scattering structure of the scene along the vertical direction, which is neither possible with conventional two-dimensional SAR nor InSAR. This is an important feature for those applications where scattering is distributed at multiple height levels, e.g. forests and glaciers. The fine vertical scanning capabilities of TomoSAR also lend themselves to the study of complex man-made scenes, such as urban areas and infrastructures, where geometric distortions such as layover frequently arise and lead to interference caused by the response of multiple scatterers, related to different structures on the ground, mapped in the same pixel[35] (fig. 3.30).

To describe the operation of TomoSAR, it is useful to start with a three-dimensional localisation model that assumes the presence of a single scatterer within a resolution cell (fig. 3.31).

Normally, this situation does not arise in surface areas subject to layover such as urban areas, nor in complexes consisting of volumetric targets with media that are semi-transparent to electromagnetic radiation such as forests, snow masses, and ice sheets. As discussed in Chapter 2, due to the particular acquisition geometry of side-looking radars (and therefore SARs), targets at the same range distance from the sensor cannot be separated and are mapped in the same resolution cell. If therefore InSAR is used on scenes where layover phenomena or volumetric targets of semi-transparent matter are present, each resolution cell will contain numerous scatterers, so the interferometric phase will be the result of a weighted average of the heights of the targets within the slant range resolution cell.

The typical layover effect substantially compromises scans over urban areas, especially very high-resolution systems such as the ones in recent TerraSAR-X and COSMO-SkyMed missions, due to its distribution over a large number of pixels. This problem can be overcome with TomoSAR, by making different passes over the same area to realise a synthetic aperture in elevation, resulting in a resolution within the slant range resolution cell along direction re. Assuming that the maximum cross-track baseline in the tomographic aperture is be, the resolution in elevation obtained via SAR tomographic processing is stated in Expression (3.21).

$$\delta r_e \approx r_0 \cdot \theta_e \approx \frac{\lambda \cdot r_0}{2 \cdot b_e} \qquad (3.21)$$

Factor 2 in the denominator is again given by the radar signal round-trip. Predictably, the tomographic resolution gets finer as the cross-track baseline increases, which, in order to achieve resolutions of a few metres, should usually take on values one to two orders of magnitude smaller than orbital altitude. When projected in the vertical direction, the vertical resolution of a TomoSAR acquisition can be roughly written as in Expression (3.22).

$$\delta h \approx \frac{\lambda \cdot r_0}{2 \cdot b_e \cdot \cos(\theta_i)} \qquad (3.22)$$

The minimum value of the cross-track baseline between passes defines the sampling of the tomographic aperture. To ensure that the sampling rate is high enough to avoid indistinguishability of signals once they have been sampled (a phenomenon known as aliasing), the cross-track baseline must be less than the value stated in the left-hand member of Expression (3.23).

$$b_{min} \leq \frac{\lambda \cdot r_0}{2 \cdot h_V \cdot \cos(\theta_i)} \qquad (3.23)$$

hv is the expected maximum height in the scene to be scan ned. Should the actual maximum height in the scene be greater than hv, aliasing phenomena (i.e. undersampling distortions) will occur. On the other hand, assuming an excessive safety margin when setting the value of hv results in costly oversampling of the tomographic aperture. In the context of TomoSAR, a greater number of passes corresponds to better resolution, so if a better cubic volume of resolution without unwanted artefacts is to be achieved, the complexity of the entire geometric configuration of the acquisition must be increased.

To give a numerical example, the first experimental demonstration of TomoSAR, carried out in 1998 with the DLR's E-SAR aircraft system, employed 13 passes uniformly interposed from separation distances of 20 m, achieving an ele-

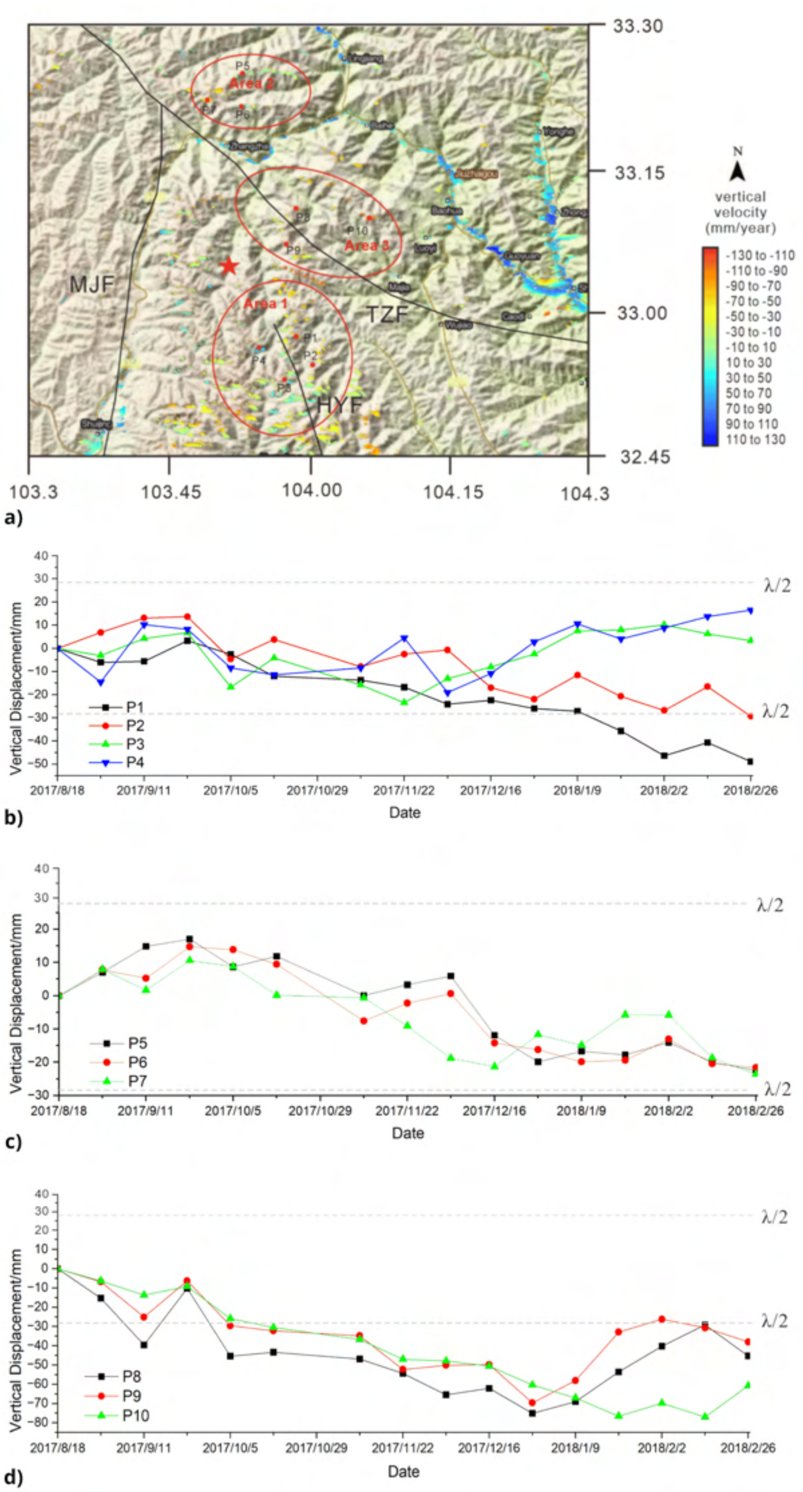
33.30
33.15
33.00
32.45
103.3
103.45
104.00
104.15
104.3
MJF
TZF
HYF
Area 1
Area 2
Area 3
N
vertical velocity (mm/year)
-130 to -110
-110 to -90
-90 to -70
-70 to -50
-50 to -30
-30 to -10
-10 to 10
10 to 30
30 to 50
50 to 70
70 to 90
90 to 110
110 to 130
a)
Vertical Displacement/mm
λ/2
P1
P2
P3
P4
2017/8/18
2017/9/11
2017/10/5
2017/10/29
2017/11/22
2017/12/16
2018/1/9
2018/2/2
2018/2/26
Date
b)
P5
P6
P7
c)
P8
P9
P10
d)

3.18/ Interferometric study of the Jiuzhaigou earthquake with time series placed between 18 August 2017 and 26 February 2018. (a) Vertical mean velocity map, the scatterers examined are highlighted with dots from P1 to P10, divided into three regions. (b) Time series diagram of the deformation in region 1 (targets P1, P2, P3, P4). (c) Time series diagram of the deformations in region 2 (targets P5, P6, P7). (d) Time seriesdiagram of the deformations in region 3 (targets P8, P9, P10). In all three diagrams, the dashed grey lines represent the ambiguity threshold. Source: Peng, Huang, Wang 2023 / licensed under CC BY 4.0 (http://creativecommons.org/licenses/by/4.0/). © 2023 by Peng, Huang, Wang. Licensee MDPI, Basel, Switzerland.

vation resolution of 2.9 m towards the middle of the altitude range considered in the scan.

One of the most interesting applications of TomoSAR is the generation of images of volumetric structures, such as forests and ice. For scenes of this type, low frequencies are especially suitable, due to their significant penetration capabilities. To give a few examples, SAR tomograms can be used to study the topographical configuration of the terrain beneath tree canopies, to assess the structures of arboreal expressions and to detect objects hidden by foliage[36].

By solving the problem of layover, besides, SAR tomography techniques provide a valuable tool for carrying out three-dimensional reconstructions and long-term slow displacement studies, useful for structural safety and monitoring the state of preservation, even in the case of individual buildings and civil engineering works[37].

3.6.1 Simplified position of the geometric problem in Synthetic Aperture Radar Tomography

As already stated several times, a single SAR image is mapped in the azimuthal x and range coordinates r.

In case of backscattering given by a single surface having local slopes smaller than the local angle of incidence, the image generation process is injective. A radar image produced from this situation can be easily corrected and adapted to any geographical or cartographic reference system.

As anticipated, however, in case of scenes consisting of volumetric scatterers and surfaces with highly inclined or even vertical locations (such as urban areas), SAR imaging mapping becomes non-injective and three-dimensional reconstruction becomes necessary.

TomoSAR allows backscatter densities to be resolved in the coordinates of the third direction of the native radar reference system, the elevation s also known as slant-height. This direction is orthogonal to the virtual plane passing through the azimuth direction and the direction along the range.

TomoSAR also applies the concept of aperture synthesis to the elevation s-direction addition to the azimuthal x-direction, taking advantage of multiple passes made by the sensor at different orbital positions to construct a virtual array arrangement of antennas (fig. 3.32). Similarly to the technical improvement between Real Aperture Radar (RAR) and SAR discussed in Chapter 2, aperture synthesis in elevation allows the antenna beam width to be reduced in that direction as well, thus realising a radar scanner capable of three-dimensional reconstructions even in space[38].

By stacking all coherent multilook radar images and performing tomographic processing, profiles can be derived for each x-r pixel along the s-direction. These profiles may be continuous in the case of scenes consisting of forests or they may consist of only a few discrete scatterers which, in the case of scans of urban areas, usually correspond to targets on the ground, facades and roofs.

We now propose a simplified description of the geometric modelling implemented with TomoSAR. Let us suppose that we have N kinematic configurations of antennas, possibly realised with repeat passes of a single satellite sensor on orbits S1, ..., SN, characterised by spatial offsets that allow different mapping positions (fig. 3.33). We adopt a Cartesian reference system to describe this geometric arrangement: x, r, z are respectively the azimuth axis, the range axis and the altitude axis; s is the elevation axis and has a direction orthogonal to the xr plane.

In Born's weak-scattering approximation regime, the expression for the focused data in the x', r' coordinate sampling performed by the generic n-th antenna is stated in Relation (3.24).

$$\hat{\gamma}_n(x',r') = \iint dx\,dr\, f(x'-x, r'-r) \int ds\, \gamma(x,r,s)\, e^{-j\frac{4\pi}{\lambda}R_n(x,r,s)} \qquad (3.24)$$

λ is the operating wavelength, j represents the projected wave

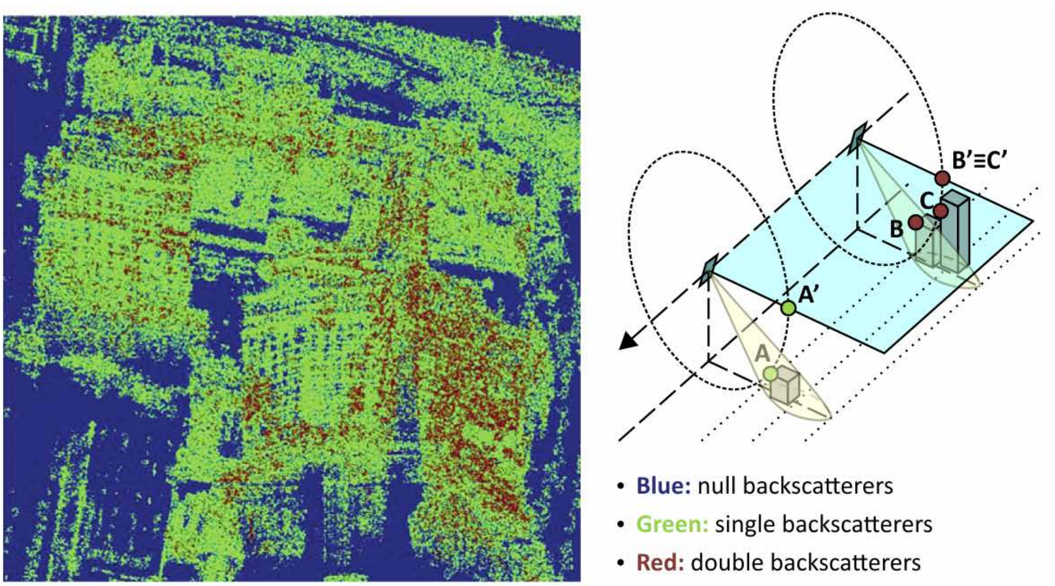

3.19/ Single and multiple backscatterers. (a) Elements identified from a tomographic processing of radar images of the Bellagio Hotel in Las Vegas; blue dots represent null backscatterers; green dots represent single backscatterers; red dots represent double backscatterers present in the same resolution cell. (b) Graphical exemplification of the mapping of the backscatterers on the virtual plane of the radar image. Source: Fornaro, Pauciullo, Reale, Zhu, Bamler 2012. © 2012 IEEE.

number, Rn (x, s, r) represents the n-th (n = 1, ..., N) distance from the generic point target, γ is the function modelling the scattering properties of the volumetric scene, and f is the Point Spread Function (PSF) along the azimuthal direction and the range. Expression (3.23) describes how the SAR image is the result of an integration along the elevation direction that maps the backscattering properties of a three-dimensional scene in the azimuth - (slant) range plane.

In three-dimensional graphic mapping, focusing along the azimuth and range directions as well as image registration are performed as the first processing step. To simplify the notation, we assume that the azimuthal (Doppler) and range (transmitted) bandwidths are sufficiently wide to allow an approximation of the Point Spread Function (PSF), obtained after focusing, as a generalised two-dimensional Dirac function. Under these assumptions, for a pixel at coordinates x, r the signal sample hn measured by the n-th antenna can be written as in Expression (3.25).

$$h_n = \int_{I_s} \gamma(s)\, e^{-j\frac{4\pi}{\lambda}R_n(s)}\, ds \qquad (3.25)$$

Is is the extension of the scene in the s-direction of the elevation. At this point a procedure, called deramping compensation with respect to the reference point O, is applied in order to compensate for a quadratic phase distortion caused by the Fresnel phase approximation (fig. 3.34).

As stated in Expression (3.26), this procedure involves a multiplication by the distance of the reference point, which is normally adjusted on the basis of the pixels available on an external DEM.

$$g_n = h_n e^{-j\frac{4\pi}{\lambda}R_n(0)} = \int \gamma(s)\, e^{-j\frac{4\pi}{\lambda}[R_n(s) - R_n(0)]}\, ds \approx \int \gamma(s)\, e^{-j2\pi\xi_n s}\, ds$$
$$\zeta_n = \frac{2}{\lambda}\frac{b_n}{r} \qquad (3.26)$$

ζn is the spatial frequency along the direction of elevation, while bn is the cross-track baseline of the n-th antenna with respect to the master antenna (i.e. the first kinematic reference configuration in the antenna array). The last approximation in Expression (3.26) is the result of an expansion of the difference Rn (s)-Rn (0) and the association of a non-essential dependent term 2s in the unknown backscattering function. Expression (3.26) shows that the relation between the received signal (for n=1, ..., N) and the unknown backscattering function is a Fourier transform.

Collecting the various gn in a data vector g, sampling γ(s) in sm (m=1, ..., M) and collecting the samples in a vector γ, the problem to reconstruct the unknown samples of γ(s) consists in inverting the linear system in Expression (3.27).

$$g = \begin{bmatrix} e^{-j2\pi\zeta_1 s_1} & \dots & e^{-j2\pi\zeta_1 s_M} \\ \dots & \dots & \dots \\ e^{-j2\pi\zeta_N s_1} & \dots & e^{-j2\pi\zeta_N s_M} \end{bmatrix} = A\gamma \qquad (3.27)$$

A is an N × M matrix, called a model matrix or sensing matrix, whose column vectors are N-dimensional. The generic column vector of A is written in Expression (3.28).

$$\begin{aligned} &a_m{}^T = [e^{-j2\pi\xi_1 s_m}, \dots, e^{-j2\pi\xi_N s_m}] \\ &m = 1, \dots, M \end{aligned} \qquad (3.28)$$

amT vectors are called steering vectors and are associated with the elevations sm (m= 1, ..., M), i.e. the angle sm/r (r>>2a). In general, M is set to a value that is at least equal to N (but a higher value is usually preferred), in order to preserve the spatial details of the backscattering reconstructed from the measurements[39].

3.8.2 A brief review of three-dimensional tomographic mapping methods.

In an ideal situation, the schematisation of the elevation profile leads to a linear system such as Expression (3.27). However, we can schematise a more realistic situation as in Expression (3.29).

$$g = A\gamma + \varepsilon \qquad (3.29)$$

where the vector ε represents noise.

The spectral estimation problem of profile reconstruction along the s-direction can be approached as an inversion of the linear system of Relation (3.29). This inversion must be implemented carefully, since:

1. Fourier transform samples are not equispaced at the spatial frequency ζn along the direction of elevation.
2. The number N of samples of the Fourier transform could be small.
3. The SNR may be low for the majority of the pixels to be processed.
4. The data may contain non-Gaussian phase noise due to uncompensated atmospheric delays and unmodelled displacements.
5. In order to perform their detections correctly, satellite-based SARs have torus-shaped spatial tolerance ranges within they have to orbit, called orbital tubes. Many of the current microwave satellite sensors (like the ones of Sentinel and TerraSAR-X missions) have orbital tubes with narrow cross-sections, which therefore allow only small baselines, hence poor resolution in elevation. Others, like the sensors of COSMO-SkyMed mission, have generally much broader tubes and much better elevation resolutions.

Several methods have been proposed to address these problems, each characterised by a different balance between simplicity, computational efficiency in processing, reduction of sidelobes and super-resolution capabilities. Each of these techniques, therefore, could lend itself to certain types of applications rather than others. It is not possible for us to describe the individual approaches in analytical detail here, so we will limit ourselves to a qualitative comparison based on interactions with various types of scenes.

Non-parametric methods, such as beamforming, Singular Value Decomposition (SVD) and Capon adaptive beamforming are characterised by a certain flexibility in scenarios with an elevation backscattering profile, especially with regard to distributed scatterers (thus with the consistent presence of speckle), but also including the case of pointlike backscattering. However, for the three-dimensional mapping of forested volumes, linear methods such as SVD and nonparametric Capon beamforming are suitable for handling cases of irregular baselines.

For three-dimensional mapping applications as well as the monitoring of areas characterised by layover, on the other hand, super-resolution methods for multiple scatterers, such

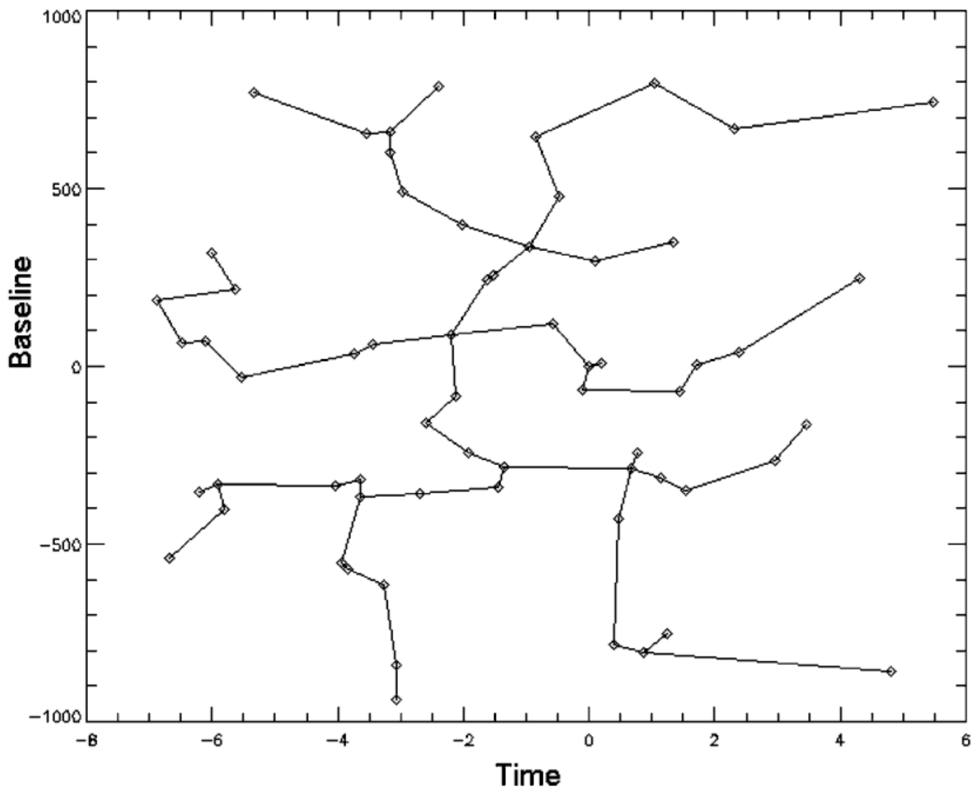

3.20/ Diagram constructed by the algorithm based on the minimum spanning tree, on a plane with the temporal baseline as abscissa and the spatial baseline as ordinate. The points represent the individual scans, while the segments represent the best possible interferograms identified by the programme. Source: Fornaro, Serafino 2006. © 2006 IEEE.

as Multiple Signal Classification (MUSIC), might achieve better results. These techniques, however, require the backscattering order to be known in each pixel before they can be applied[40].

3.8.3 Differential Synthetic Aperture Radar Tomography

Differential SAR Tomography is also called four-dimensional SAR focusing mapping, as it records a time variable in addition to the three spatial coordinates. It is a natural extension of TomoSAR for graphically mapping and monitoring targets with displacements.

The measurement of backscatter takes place on a virtual plane in the dimensions of elevation s and velocity, also known as the tomo-Doppler plane. For each pixel along the azimuth and range dimensions, the presence of peaks in the elevation-velocity plane identifies backscatterers – which may interfere in the same resolution cell if more than one peak is present –, positioned at certain heights and moving at certain speeds.

This time, therefore, let us assume that the scans S1, ..., SN seen during the formulation of the geometric problem of three-dimensional tomographic reconstruction were taken at different time instants t1, ..., tN. Assuming that the target P positioned at an elevation s is characterised by a deformation d(s,tn), after deramping compensation we will have the following stated in Expression (3.30).

$$g_n \approx \int \gamma(s)\, e^{-j2\pi\zeta_n s - j\frac{4\pi}{\lambda} d(s,t_n)} ds \qquad (3.30)$$

Relation (3.30) extends Equation (3.26) to the presence of motion. The exponential strain signal can be expanded in Fourier harmonic series, leading to Relation (3.31).

$$g_n = \iint \gamma_{4D}(s,v)\, e^{-j2\pi\zeta_n s - j2\pi\eta_n v} dv ds$$

$$\zeta_n = \frac{2}{\lambda}\frac{b_n}{r} \qquad \eta_n = \frac{2t_n}{\lambda} \qquad (3.31)$$

v is the Fourier variable associated with ηn; v is measured in ms-1 and takes on the meaning of a velocity or, rather, a spectral velocity. For a linear deformation, the spectral velocity v coincides with the deformation velocity while, for more complex motions, v identifies the harmonic velocity associated with the motion. The inversion of Expression (3.29) leads to the estimation of the backscatter distribution in the elevation-velocity plane. Each of the methods described for the three-dimensional case can be applied by extending the definition of the steering vector, as stated in Expression (3.32).

$$a_m^T = [e^{-j2\pi\xi_1 s_m - j2\pi\eta_h v_m}, \dots, e^{-j2\pi\xi_N s_m - j2\pi\eta_N v_m}] \qquad (3.32)$$
$$m = 1, \dots, M$$

M is the product of the number of bins in elevation and the grid velocities used for the schematisation of the surface integral in Relation (3.31).

Beyond the separation of elevation and velocities, four-dimensional SAR imaging also allows the separation of time series of scatterers subject to layover[41].

It can even be combined with specific non-uniform deformation models, thus going beyond the four dimensions. An example is the detection of thermal deformations in buildings in association with the distribution on the baseline of temperature, in order to obtain synoptic analyses in five dimensions (three spatial coordinates, one temporal coordinate, one variable associated with thermal deformation). The extension of the functionalities of four-dimensional graphical mapping to the monitoring of thermal expansion has shown that a high degree of correlation between the distributions on the baseline, mainly thermal and temporal, can lead to problems of ambiguity in detection. In any case, an unmotivated increase in the dimensionality of the mapping reduces the detection performance of the scatterers[42].

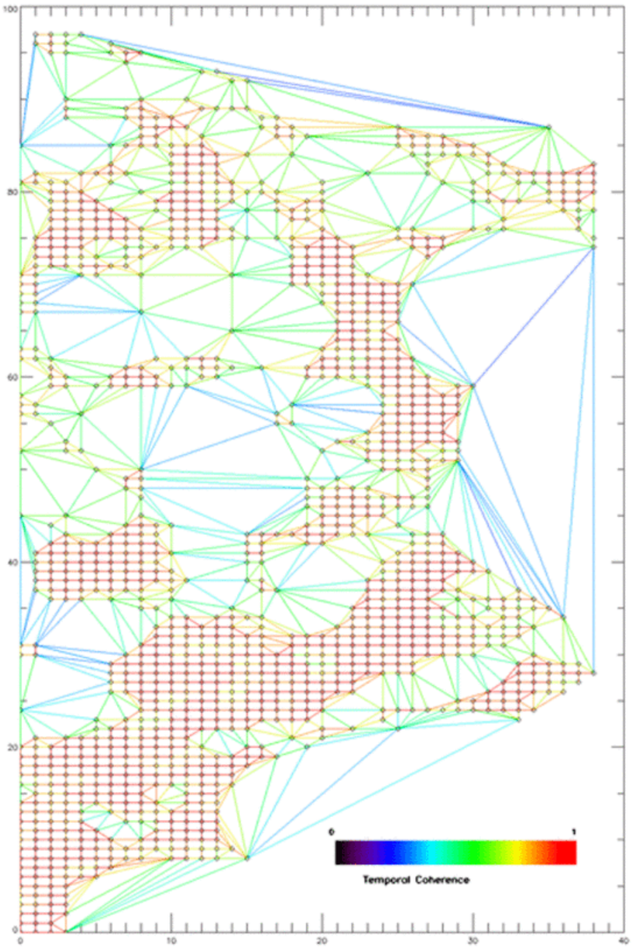

3.21/ Automated integration grid of regions subjected to the spatial differentiation procedure. The colours communicate the temporal coherence values of the regions, represented as points. Source: Fornaro, Serafino 2006. © 2006 IEEE.

3.8.4 Examples of multidimensional remote sensing with Tomographic Synthetic Aperture Radar

In 2006, the Institute for Electromagnetic Sensing of the Environment of the National Research Council (Istituto per il Rilevamento Elettromagnetico dell'Ambiente del Consiglio Nazionale delle Ricerche – IREA-CNR) presented a method for multidimensional imaging using simple tomographic processing based on an estimate of backscattering distribution in the elevation-velocity plane. This is in order to identify, from C-band scans, up to two possible mutually interfering backscatterers in the same pixel. Before the actual tomographic process is applied, the data undergoes an atmospheric calibration. More specifically, in order to minimise the effects of spatial and temporal decorrelation, a minimum spanning tree strategy is applied, where an algorithm automatically connects the acquisitions in a plane where the dimensions are the temporal and spatial baselines.

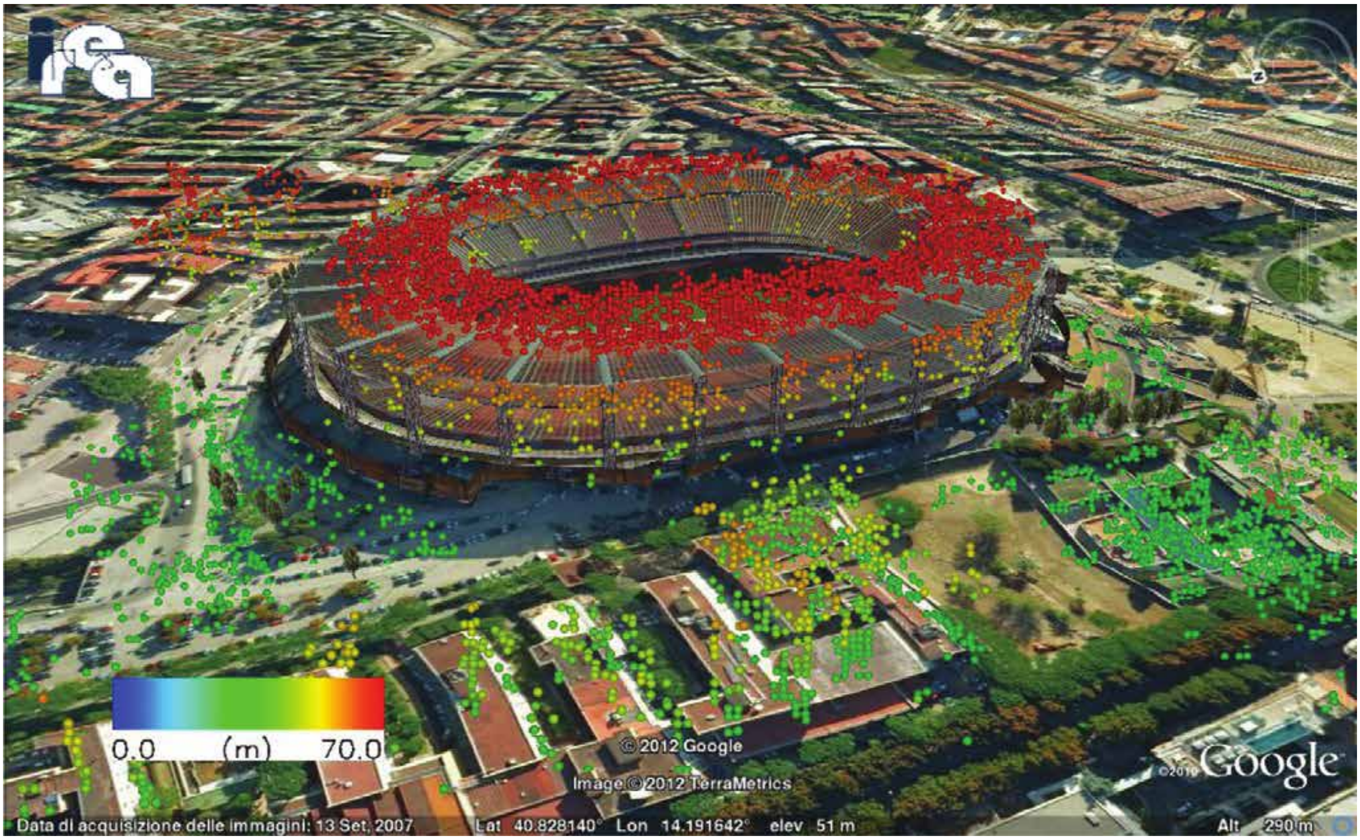

3.22/ Three-dimensional reconstruction of the San Paolo Stadium in Naples, Italy. The point cloud, here represented within Google Earth™, is the result of a five-dimensional TomoSAR processing, starting from radar images acquired by ASI's COSMO-SkyMed mission. The colour map is set to the estimated altitude values of the individual targets identified. Source: Fornaro, Pauciullo, Reale, Zhu, Bamler 2012. © 2012 IEEE. Google™ and Google Earth™ are trademarks of Google LLC and this thesis is not endorsed by or affiliated with Google in any way.

On this plane, the programme considers the individual scans as points having certain temporal baseline and spatial baseline values as coordinates, and then connects these points with segments of the shortest possible length, which represent the interferograms obtainable with the least possible temporal decorrelation and spatial decorrelation (fig. 3.35). Then, in order to separate the atmospheric contribution from the data, as well as to estimate the topographic configuration and deformations lost after various stages of filtering, an analysis is performed using a spatial fi ltering technique, which is performed in the multitemporal and multibaseline analysis stage through spatial differentiation. First, the algorithm dedicated to this operation performs a retrieval of topographic configuration and deformation contributions at a coarse resolution scale, since a grid of stable and strong backscattering elements does not lend itself to mediation performed directly on a spatial domain of spatial scale. However, this method also works at finer resolutions and can therefore be performed a second time to arrive at associated information at more detailed scales of representation. This approach thus leads to the identifi cation of regions where the multitemporal, multibaseline signal is sufficiently reliable with respect to local variation. These regions must be linked to each other before moving on to the integration stage, in order to achieve an extensive reconstruction of the residual signals related to topographic configuration and deformations (i.e. not only to obtain measurements of local variations, however reliable). The programme then performs an iterative spatial integra-

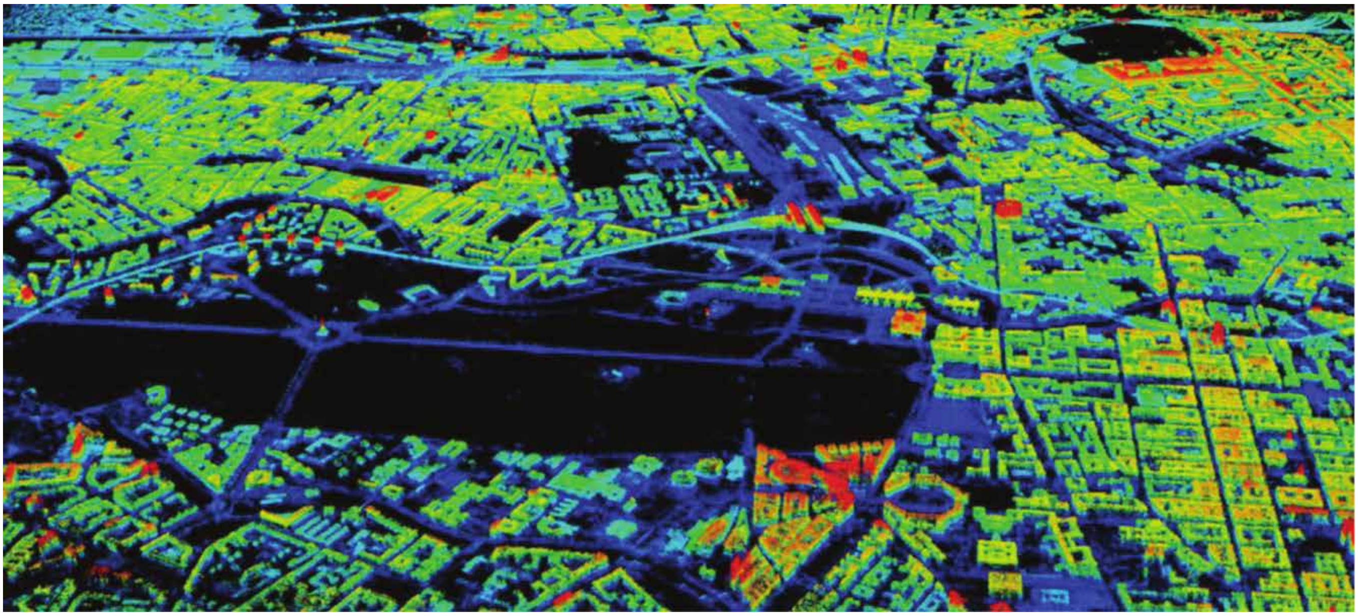

3.23/ Three-dimensional reconstruction of the urban environment at the Großer Tiergarten Park in Berlin. Fusion of two point clouds generated by processing with five-dimensional TomoSAR from data acquired by the TerraSAR-X satellite along ascending passes and descending passes. The colour map is set to the estimated altitude values of the individual targets detected. Source: Fornaro, Pauciullo, Reale, Zhu, Bamler2012. © 2012 IEEE.

tion operation, where shorter segments correspond to better temporal coherence and greater effectiveness of the spatial differentiation in terms of filtering out the atmospheric contribution, thus improving the reliability of the estimate. In this way, the error propagation effects caused by the less reliable gradient segments, typical of global integration processes, are mitigated. Graphically, this automated operation is represented by a spatial integration grid where the points represent the regions and the segments the best possible connections between them, while the colours make explicit the temporal coherence values of the various features (fig. 3.36)

The approach then addresses the problem of tomographic reconstruction in two steps:

1. Estimation of the parameters of the scatterers, i.e. position in space and deformation.
2. Selection of a number of scatterers in a detection framework, with the caution of achieving high detection performance for a given false alarm rate[43].

In 2011, IREA-CNR published new results concerning the possibility of resolving, for the first time, the layover phenomena arising on vertically developed structures such as buildings. The tomographic processing was carried out on the basis of a set of scans of the Las Vegas area, performed in the context of Terra-SAR X mission. In this demonstration case, the results concerning the Mirage Hotel were particularly relevant.

In order to deal with the increased sensitivity of X-band radiation to small changes in targets, such as those caused by thermal expansion, the technique was extended to also measure this component in a five-dimensional domain (three spatial coordinates, one temporal coordinate, one variable associated with thermal deformation). In fact, although already detected at the C-band by the European Remote-Sensing (ERS) satellite and Enviromental Satellite (Envisat) missions, this effect is much more evident at the X-band, due to an increase in sensitivity associated with shorter wavelengths. In order to also account for the thermal expansion component, the deformation model – typically consisting of a linear time term – was extended with a new term measured in mm/K, which is linearly related to the temperature of the area at the instants of acquisition.

Another significant example of a method for multidimensio-

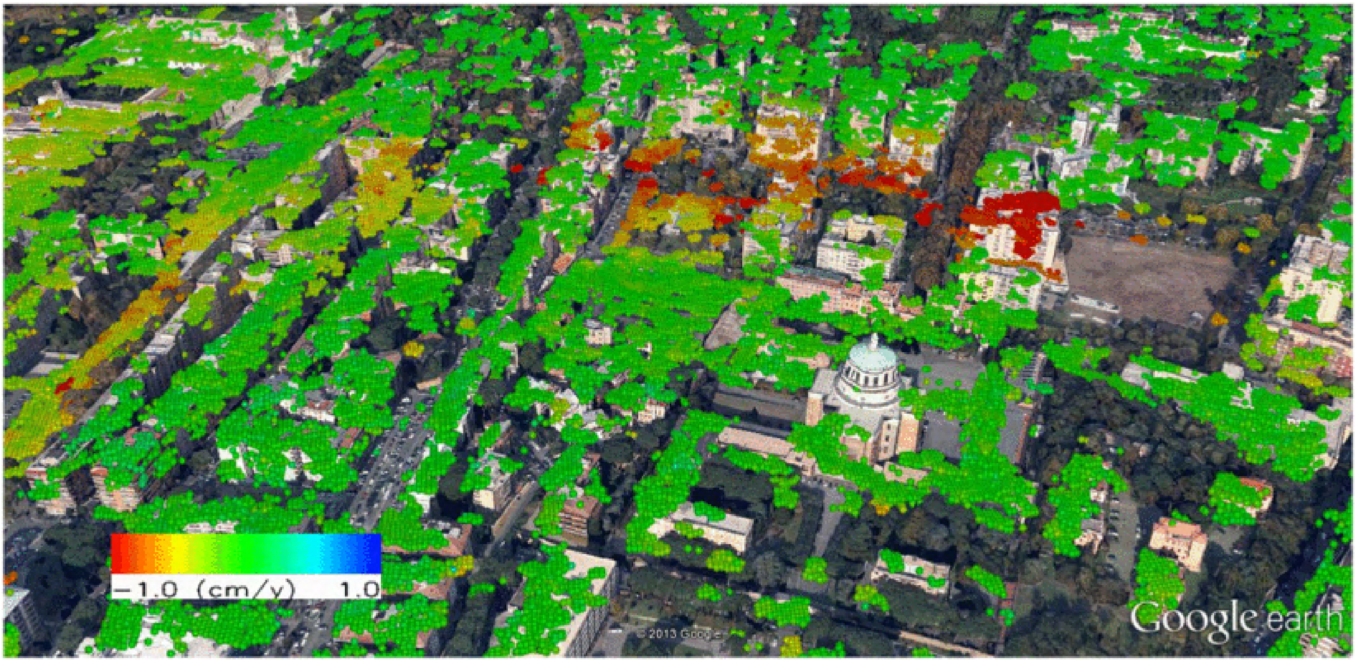

3.24/ Three-dimensional visualisation, in Google Earth™ environment, of the scatterers detected through four-dimensional tomographic processing in the Grotta Perfetta area in Rome, Italy. The colours were set according to the estimated values of average deformation velocity (in cm per year). Source: Fornaro, Pauciullo, Reale, Zhu, Bamler 2012. © 2012 IEEE. Google™ and Google Earth™ are trademarks of Google LLC and this thesis is not endorsed by or affiliated with Google in any way.

nal SAR remote sensing is that based on the 'Tomo-GENESIS' system, presented by DLR in 2011. Tomo-GENESIS was developed from an earlier system dedicated to interferometric processing called 'GENESIS' – already used in Shuttle Radar Topography Mission (SRTM) and TanDEM-X mission –, following an extension of the latter to the concept of TomoSAR. The layover phenomena in SAR images obtained from scans of urban areas is considered as attributable to two general cases:

- buildings with different heights in layover with the ground;
- taller buildings in layover with the ground and the roof of a lower building.

Both situations suggest that pairs of double backscatterers, in mutual interference in a single resolution cell, are more frequent at lower elevation values above ground than at higher values in the same coordinate.
From a stack of SAR images, therefore, the Tomo-GENESIS system retrieves the following information: the number of scatterers in a pixel; the amplitude and phase; the topographical configuration and the motion parameters of each scatterer detected, such as the linear deformation velocity and the extent of thermal expansion-induced seasonal motions.
The Tomo-GENESIS system can boast the following features: the possibility of making estimates for the description of non-linear motions characterised by multiple components; the so-called super-resolution capability, reaching resolutions on the ground of less than 3m; the integration of processing based on Persistent Scatterers Interferometry (PSI) and Tomographic Synthetic Aperture Radar (TomoSAR); an algorithm for the integration of data obtained in point clouds.
In 2012, IREA-CNR and DLR made a joint presentation of the results obtained in a series of experimental applications, ch aracterised by initial radar images acquired with different satellite scanning modes and thus different ground resolutions.
One of the tests concerned the five-dimensional graphic mapping of the kinematic configurations assumed, as a result of

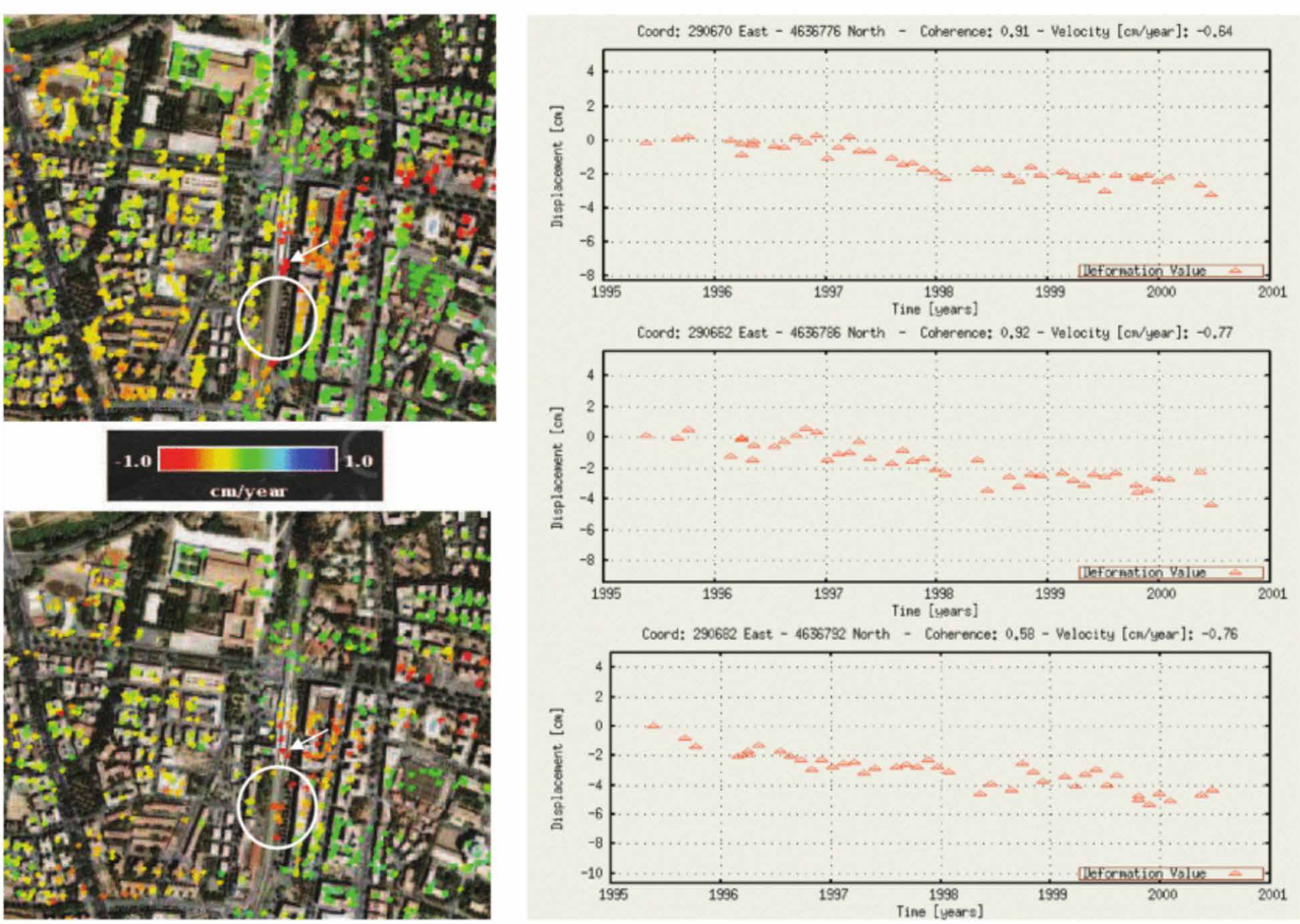

3.25/ Basckscatterers detected with the four-dimensional TomoSAR technique in an urban area in the southern part of Rome, Italy. Data acquired by the ERS-1 and ERS-2 satellites between 1995 and 2000. (a) The identified targets superimposed on a Google Maps™ image, coloured according to the estimated average deformation velocity. (b) From top to bottom: time series of the estimated displacements along the LOS of the sensor, associated with the deformations of the dominant and non-dominant double scatterers and a single scatterer in the area indicated by the arrow in figure a). Source: Fornaro, Reale, Serafino 2008.

thermal deformations, by the scatterers detected in San Paolo Stadium in Naples, Italy. The source materials were 28 radar images acquired by COSMO-SkyMed satellite constellation along descending passes in the standard Stripmap mode (with a spatial resolution of approximately 3m), carried out from February 2010 to February 2011. From the tomographic processing, a three-dimensional point cloud was derived where, at each point, the value of the estimated deformation over time and the relative value of the estimated thermal dilation of materials were associated. In this case, the colouring of the individual point was associated with the estimated altitude value for the corresponding backscatterer identified (fig. 3.37).

Again for the purpose of five-dimensional graphical mapping,

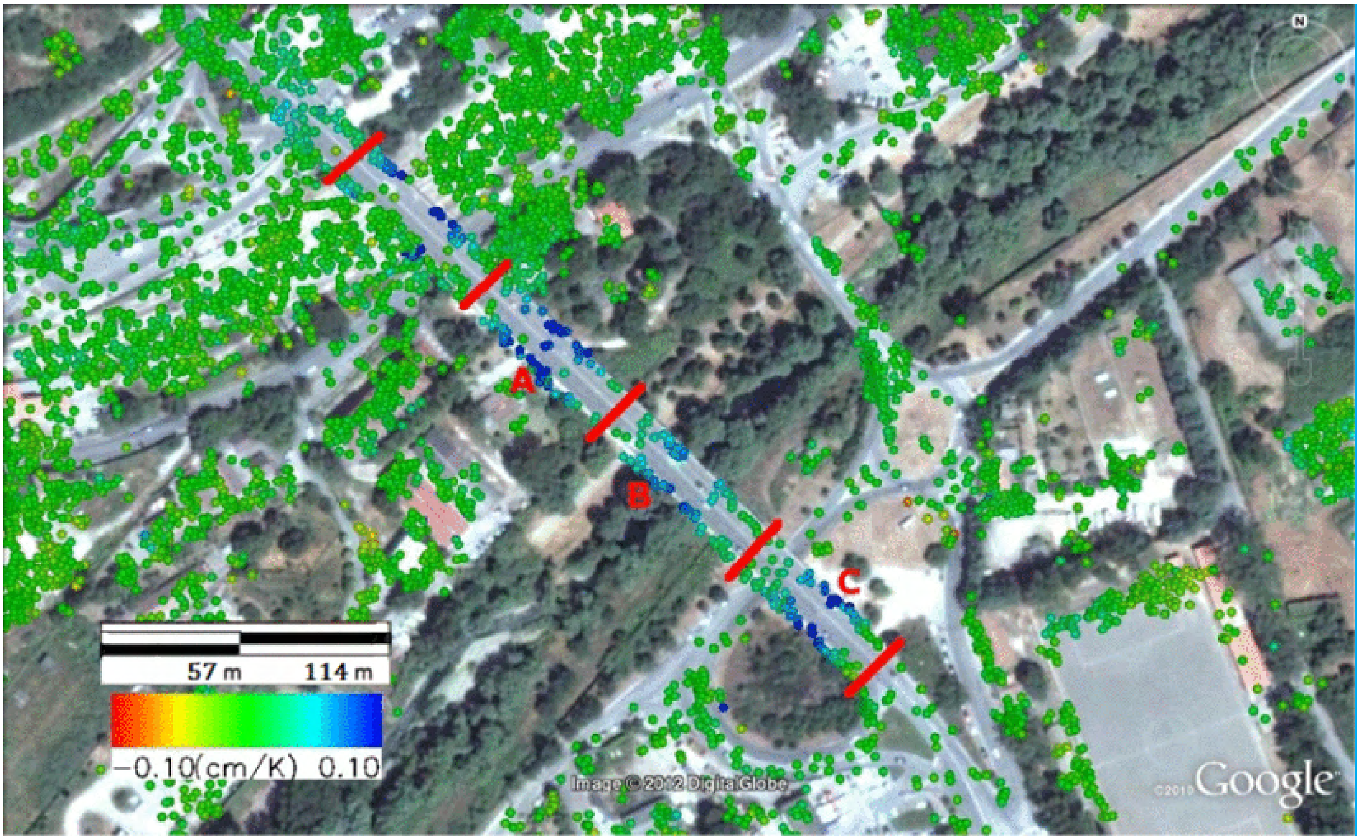

3.26/ Average deformation velocities of the targets identified on the Musumeci Bridge in Potenza, Italy, estimated through five-dimensional processing with TomoSAR. The point cloud was superimposed on a Google Maps™ image. The colour map is set according to the estimated thermal coefficient for each backscatterer. Three targets were highlighted with the letters A, B, C, of which the time series of inelastic deformations were diagrammed (fig. 3.40). Source: Fornaro, Reale, Green 2013. © 2013 IEEE. Google™ and Google Maps™ are trademarks of Google LLC and this thesis is not endorsed by or affiliated with Google in any way.

another test assumed an urban area of the city of Berlin as the test site. In this case, the source material was provided under advantageous conditions and consisted of 173 radar images acquired by TerraSAR-X satellite in Spotlight mode (with a spatial resolution of approximately 1m). 94 of these SLCs were scanned along ascending passes, while the remaining 79 images were acquired along descending passes. The resulting tomographic cloud in this case counted 40 million backscatterers, with such a density that even a building object of architectural scale, such as the Victory Column in the centre of the Großer Tiergarten Park, could be identified. Again, the colouring of individual points was associated with the estimated value of altitude for the relevant target identified[44] (fig. 3.38).

However, in addition to the estimated value of the altitude of the individual backscatterer, in the case of four-dimensional graphical mappings the colouring of the points in the tomographic clouds can also be associated with the estimated average deformation rate over the time interval considered[45] (fig. 3.39). For each identified target, moreover, the estimated values of the displacements along the LOS of the radar sensor can be graphed in time series[46] (fig. 3.40), analogously to what has been seen in the case of DInSAR.

Similarly, in the case of five-dimensional graphical mapping, the individual point can be coloured according to the thermal coefficient of the inelastic deformation estimated for the corresponding target (fig. 3.41). In addition to the displacements

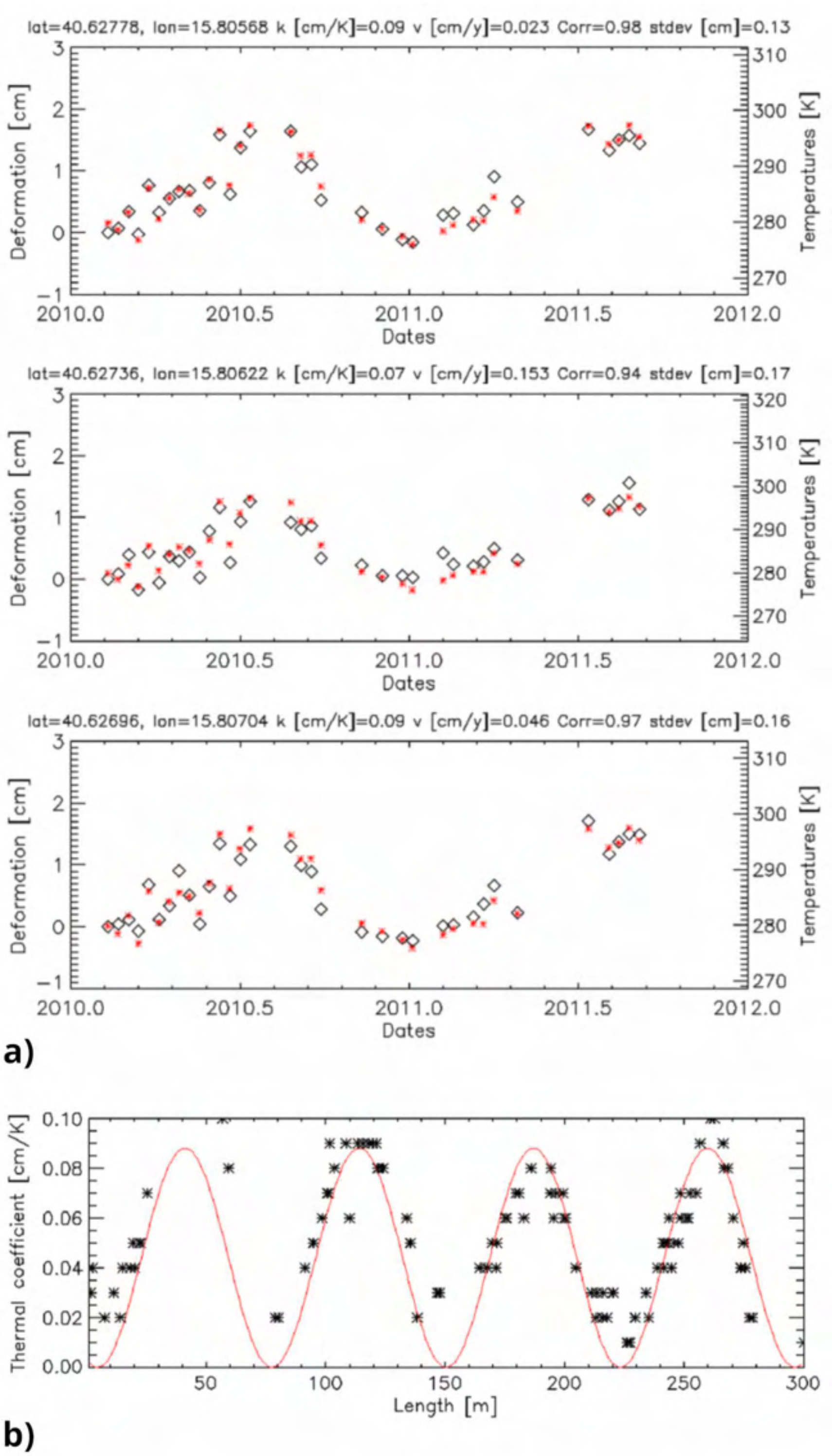

3.27/ Study of the thermal deformations of the Musumeci Bridge in Potenza. (a) Time series of the deformation (in cm) of the three backscatterers A, B, C belonging to the bridge and highlighted in the point cloud (fig. 3.41): top, target A; middle, target B; bottom, target C. The individual radar measurements are depicted as black diamonds, while the red stars represent the deformations associated with the daily mean temperature distribution. Above each diagram are shown from left to right: the latitude and longitude coordinates of the analysed backscatterer; the estimated thermal coefficient (in cm per kelvin); the average strain rate (in cm per year); the measured correlation coefficient between the radar time series, the thermal component and the standard deviation of their difference. The axis on the right represents the average daily temperatures associated with the deformations represented by the red stars. (b) Time series of the estimated values of the thermal coefficient for the southern flank of the bridge. The diamonds represent the distribution of the estimated values of the thermal coefficient, while the red solid line is a sinuisoidal function estimated from these values. Source: Fornaro, Reale, Green 2013. © 2013 IEEE. Google™ and Google Maps™ are trademarks of Google LLC and this thesis is not endorsed by or affiliated with Google in any way.

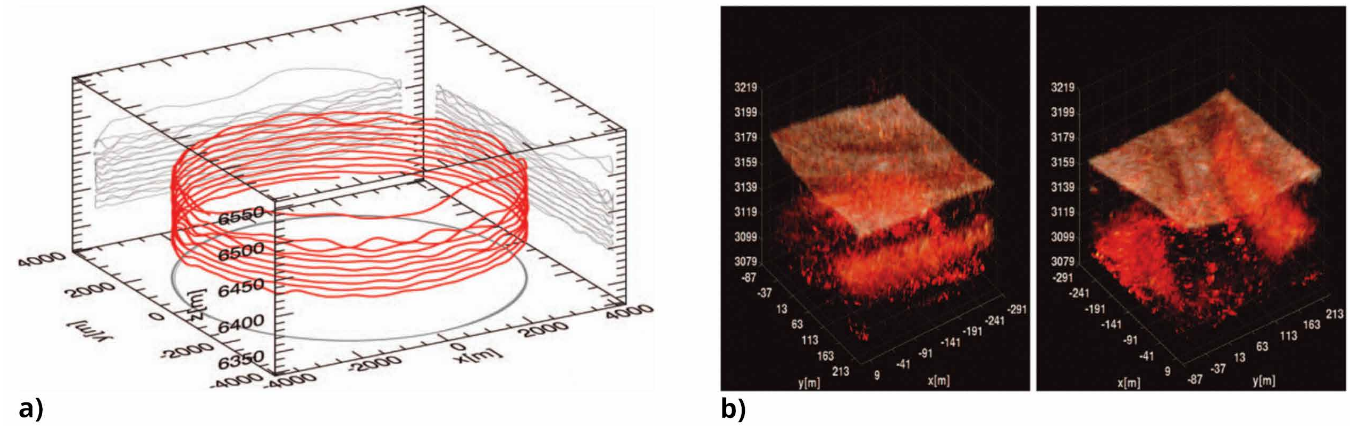

3.28/ Remote-sensing with holographic SAR of the Findel Glacier on Monte Rosa, Switzerland, performed in March 2015 with DLR's F-SAR sensor mounted on an aircraft platform. (a) Geometric diagram of the circular flight paths made by the platform around the glacier. (b) Three-dimensional representation of the holographic SAR tomogram, from two different viewpoints. Both the upper surface of the glacier and the rock bed on which it rests have been reconstructed. Source: Ponce, Prats, Scheiber, Reigber, Hajnsek, Moreira, 2015. © 2015 IEEE.

along the LOS of the radar sensor, it is also possible to plot the estimated values of the inelastic deformation and thermal coefficient for the individual backscatterer in time series[47] (fig. 3.42).

3.6.5 Holographic Synthetic Aperture Radar

By coupling the circular SAR acquisition mode with tomographic aperture, a combination of tomography and a 360° scanning trajectory around the scene is achieved, called holographic SAR (fig. 3.43). This results in three-dimensional imaging capabilities and the highest ground resolution obtainable in a fraction of a wavelength. However, the effectiveness of both methods is related to the stability of backscattering of targets between different illumination locations, limiting their range of applications in real scenes, where the scatterers tend to be anisotropic. This means, however, that holographic SAR can be used to study the anisotropic properties of the bodies which constitute a scene[48].

Notes

1. Emery, Camps 2017, pp. 302-304.
2. Meyer 2022.
3. Planetek Italy 2022.
4. Loc. cit.
5. Ager 2013, p. 30.
6. Meyer 2019, p. 23.
7. Planetek Italy 2022.
8. Meyer 2019, pp. 37-38.
9. *Loc. cit.*, pp. 30-34; Meyer 2022.
10. Moreira, Prats-Iraola, Younis, Krieger, Hajnsek, Papathanassiou 2013, p. 13.
11. Emery, Camps 2017, p. 384; Moreira, Prats-Iraola, Younis, Krieger, Hajnsek, Papathanassiou 2013, p. 134.
12. The Doppler Centroid (DC) corresponds to the centre frequency in the Doppler spectrum of the acquired data and is related to the azimuthal centre of the radar beam. Appropriate algorithms identify the azimuthal energy of the signal in the azimuthal frequency domain detected by the sensor. This is necessary so that the signal energy in the Doppler spectrum can be correctly captured by the azimuth compression filter, ensuring the best possible Signal-to-Noise Ratio (SNR) and azimuth resolution. The DC can be expressed as the Doppler frequency of the scan at the mean squint angle, in symbols: $fDC = - [(2 - vs)/\lambda] - \sin(\theta sq)$. Cf. Emery, Camps 2017 p. 382; European Space Agency 2012.
13. Emery, Camps 2017, pp. 384-385.
14. *Loc. cit.*, p. 385; Moreira, Prats-Iraola, Younis, Krieger, Hajnsek,

Papathanassiou 2013, p. 13.
15. Emery, Camps 2017, pp. 385-387.
16. *Loc. cit.*, pp. 388-389.
17. *Loc. cit.*, pp. 389-391.
18. *Loc. cit*., p. 327.
19. Van Zyl, Kim 2011, p. 23.
20. Ager 2013, p. 25; Meyer 2019, pp. 27-28.
21. The depolarisation of a radiation exists in the reduction or cancellation of its degree of polarisation, normally due to scattering processes or disordered reflections or refractions. Cf. Istituto dell'Enciclopedia Italiana Treccani 1996.
22. Emery, Camps 2017, pp. 325-326.
23. Freeman, Durden 1998, pp. 963-973.
24. *Ibidem*; Meyer 2019, pp. 27-28; Qu, Qiu, Wang, Lei, Ding 2022, pp. 8-23.
25. Moreira, Prats-Iraola, Younis, Krieger, Hajnsek, Papathanassiou 2013, pp. 14-19.
26. Emery, Camps 2017, p. 401.
27. Meyer 2022.
28. Parallel-ray approximation is only valid if the range has a magnitude several orders of magnitude greater than the baseline. This is a typical scenario for space borne SAR interferometric systems.
29. Emery, Camps 2017, pp. 403-408.
30. *Loc. cit.*, pp. 408-410.
31. Moreira, Prats-Iraola, Younis, Krieger, Hajnsek, Papathanassiou 2013, pp. 19-30.
32. Emery, Camps 2017, pp. 410-413.
33. *Loc. cit.*, pp. 413-417.
34. *Loc. cit.*, pp. 417-422; Fornaro, Lombardini, Pauciullo, Reale, Viviani 2014, pp. 42-43.
35. Fornaro, Lombardini, Pauciullo, Reale, Viviani 2014, pp. 41-43.
36. Emery, Camps 2017, pp. 422-427; Moreira, Prats-Iraola, Younis, Krieger, Hajnsek, Papathanassiou 2013, pp. 30-32.
37. Fornaro, Lombardini, Pauciullo, Reale, Viviani 2014, pp. 41-43.
38. Fornaro, Pauciullo, Reale, Zhu, Bamler 2012, pp. 9-10.
39. Fornaro 2013, pp. 8 - 1-8 - 5.
40. Fornaro, Lombardini, Pauciullo, Reale, Viviani 2014, p. 46; Fornaro, Pauciullo, Reale, Zhu, Bamler 2012, p. 10.
41. Fornaro 2013, pp. 8 - 12 - 13.
42. *Loc. cit.*, pp. 8 - 13 - 14; Fornaro, Lombardini, Pauciullo, Reale, Viviani 2014, p. 49.
43. Fornaro, Serafino 2006, pp. 3497-3504.
44. Fornaro, Pauciullo, Reale, Zhu, Bamler 2012, p. 13.
45. Fornaro, Pauciullo, Reale, Green 2014, p. 2783.
46. Fornaro, Reale, Serafino 2008, pp. 477-478.
47. Fornaro, Reale, Green 2013, pp. 679-681.
48. Emery, Camps 2017, pp. 422-427; Moreira, Prats-Iraola, Younis, Krieger, Hajnsek, Papathanassiou 2013, pp. 30-32.

Sintesi

Si distinguono tre differenti categorie di bersagli in rapporto alla cella di risoluzione radar: il bersaglio puntuale; il bersaglio esteso; il bersaglio distribuito.
Le piattaforme satellitari, incluse quelle per i sensori radar, possono essere classificate in quattro gruppi: satelliti in bassa orbita terrestre; satelliti in media orbita terrestre; satelliti in orbita terrestre geostazionaria; satelliti in orbita ellittica alta. Si possono distinguere due tipi principali di orbite satellitari: le orbite geosincrone e le orbite polari. A questi due tipi si aggiunge il caso particolare dell'orbita ellittica. Per il telerilevamento satellitare si deve tenere conto inoltre di quattro tipi di risoluzione: la risoluzione spaziale; la risoluzione temporale; la risoluzione spettrale; la risoluzione radiometrica.
Per essere utilizzabili, i dati grezzi che le stazioni di terra ricevono dai radar ad apertura sintetica satellitare devono essere sottoposti a un processo di focalizzazione, ricavando così un'immagine complessa costituita da: una componente intellegibile associata all'ampiezza del segnale; una componente non intellegibile associata allo scostamento del segnale. Successivamente, le immagini complesse devono essere sottoposte a un processo di correzione radiometrica del terreno rappresentato, costituita da: una fase di correzione geometrica allo scopo di rimuovere le distorsioni geometriche dell'immagine; una fase di normalizzazione radiometrica, per rimuovere le distorsioni radiometriche dipendenti dalla geometria.
Una delle classificazioni più usate per i dati radar ad apertura sintetica è quella della National Aeronautics and Space Administration (NASA), composta da quattro livelli che vanno dai dati grezzi ai dati corretti di qualità controllata e combinati con informazioni esterne.
La modalità di base con cui i radar ad apertura sintetica satellitari effettuano le scansioni in strisciate è detta motalità Stripmap. Molti di questi sistemi possono usare modalità alternative per incrementare l'apiezza della spazzata, come la ScanSAR e la TOPS, oppure per migliorare la risoluzione

azimutale, come la Spotlight a sguardo fisso e la Spotlight a scivolamento. Una modalità di acquisizione esclusiva dei radar ad apertura sintetica su piattaforme aeromobili è quella circolare, dove le traiettorie corrispondono a una serie di giri attorno al bersaglio.

La calibrazione delle immagini radar ad apertura sintetica si basa su tre aspetti: 1) ottenere dal sensore valori radiometrici vicini all'intensità radar reale della scena scandita; 2) garantire un'individuazione spaziale degli elementi retrodiffondenti ad alta fedeltà; 3) conseguire una rappresentazione accurata dei rapporti complessi tra i canali polarimetrici. Questi processi di calibrazione si effettuano mediante la scansione e lo studio delle retrodiffusioni di bersagli noti costituiti da trasponder e riflettori a triedro.

L'applicazione della polarimetria si fonda sull'idea che la depolarizzazione delle onde radar consenta una maggiore comprensione dei meccanismi di diffusione della scena scandita e, quindi, della geometria dei corpi che la costituiscono. Un radar ad apertura sintetica può essere impostato per emettere onde polarizzate con una certo orientamento e riceverne in un altro (generalmente in giaciture verticali od orizzontali). Lo studio comparato di immagini a differenti polarizzazioni permette di ricostruire, con un consistente margine di attendibilità, le configurazioni geometriche dei bersagli.

L'interferometria permette la misurazione differenziale delle distanze attraverso un minimo di due scansioni da punti di osservazioni differenti. Queste scansioni possono essere eseguite: in una singola battuta, usando più di un'antenna; in battute ripetute, usando più volte la stessa antenna. L'approccio dell'interferometria differenziale può essere descritto come una combinazione tra il metodo a singola battuta e quello a battute multiple. Esso si presta a un certo numero di applicazioni riguardanti la porzione di territorio scandita, quali la mappatura tridimensionale della sua configurazione topografica o l'individuazione di spostamenti al suo interno.

Sfruttando molteplici scansioni effettuate da più punti di osservazione e in più istanti, le tecniche con radar ad apertura sintetica tomografico permettono la realizzazione di uno scanner con raggio sintetico fine lungo la direzione verticale, risolvendo il problema dello scavalcamento e della sovrapposizione di più elementi retrodiffondenti nella medesima cella di risoluzione. In questo modo è anche possibile realizzare nuvole di punti tridimensionali, dove i punti corrispondono ai bersagli, associando informazioni sugli spostamenti e le deformazioni termiche riscontrati.

Luca Martelli

4. Communicational aspects of radar images and their products

4.1 Images and radar products as representations of events that cannot or must not be perceived directly

Radar imaging and remote-sensing satellite imaging are normal tools of expression, used in many forms and manifestations[1].

Originally, as early as the first experiments in the first quarter of the 20th century, the purpose of radar was to detect and locate bodies that could not be perceived by the human eye directly or with optical instruments, either due to long distances or adverse environmental or meteorological conditions. Guglielmo Marconi recognised the potential of short waves in radio detection and, in a 1922 speech to members of the Institute of Radio Engineers, cited the example of a device that would enable the crew of a ship to detect another vessel hidden by fog or bad weather[2]. Thus, radars were designed to represent bodies that could not be perceived at a given time, in order to anticipate and possibly prevent a probable harmful event, which could be an accident (as in Marconi's example) or an air raid. Indeed, the evolution of military technology and historical transformations in the art of warfare have, since the introduction of bows and arrows, increased the distance of enemies in conflict[3].

The function of many types of radar, even today, is to enable an exogenous cognitive process. Firstly by transmitting a signal, then by recording and communicating a completely invisible event, i.e. the reflection of the emitted signal by a backscatterer, radar make it possible to learn of the presence of a potentially perceptible object when it cannot be (in the case of impediments to vision) or must not be (in the case of the object in question being dangerous) directly perceived. All remote sensing instruments allow Earth's surface to be monitored and surveyed in a (virtually) continuous manner even though, albeit extremely more powerful than the human eye, these sensors still have 'perceptive' limits, related to the resolution capabilities of the images they produce. The threshold of detectability and measurability sets the boundary between what is documented by the radar data (and thus historically occurred) and what is not recorded (or is simply captured as 'noise' or 'artefact' of the material medium) and thus does not have the possibility of accessing the dimension of what happened[4].

Imaging radars, which were developed in a relatively more recent historical period, also continue to have this function. Indeed, they are used both in the field of warfare and for the purpose of monitoring the context of catastrophic situations. However, since these devices are able to provide an intelligible representation of certain aspects of targets that cannot be directly perceived by the human eye, such as dielectric properties or deformations that have occurred over a very long period of time, they are becoming increasingly important in various scientific and civil applications (fig. 4.1). In the case of remote-sensing from airborne or space platforms, this also means being able to access the representation of an object that is difficult to reach because it is in a distant location or too large to be observed directly by the human eye.

Indeed, images mapped with side-looking radars are also part of that vast field of infographic techniques that have constituted a far-reaching reconfiguration in the relations between the observing subject and the modes of representation. The generation of images of a scene by means of microwave pulses is one of those techniques that are repositioning vision in a separate plane of the human observer, in the same way as images obtained through magnetic resonance imaging and multispectral acquisitions[5]. Vision, perception, and experience are always generally mediated, configured and articulated by a series of technical-material Apparates, which historically transform and continuously reorganise what Walter Benjamin calls the 'Medium of perception', i.e. the intermediate space, the environment, the 'perceivable milieu'[6].

Thus, imaging radars are always technical devices that perform 'switching' operations, transforming the invisible echoes of their signals into perceivable events associated with target information. These data may concern obvious characteristics of the scanned bodies, such as geometric shape in the case of Synthetic Aperture Radar (SAR) polarimetry, but they may also concern properties that cannot be experienced directly, as in the case of very slow motions.

In the vast majority of cases, especially with regard to remote-sensing, imaging radars also perform 'compression' and 'expansion' operations. From a spatial point of view, the only case in which radar sensing should theoretically not require compression or expansion operations is that of a perfectly 1:1 scale restitution. From the temporal point of view, moreover, the only application of radar scanning that does not involve compression or expansion operations would be that strictly theoretical one of a representation ideally executed in real time. The expression 'strictly theoretical' has been used because there is in fact no analogue or telematic video communication system capable of performing a restitution without using a signal transmission time, no matter how short it may be.

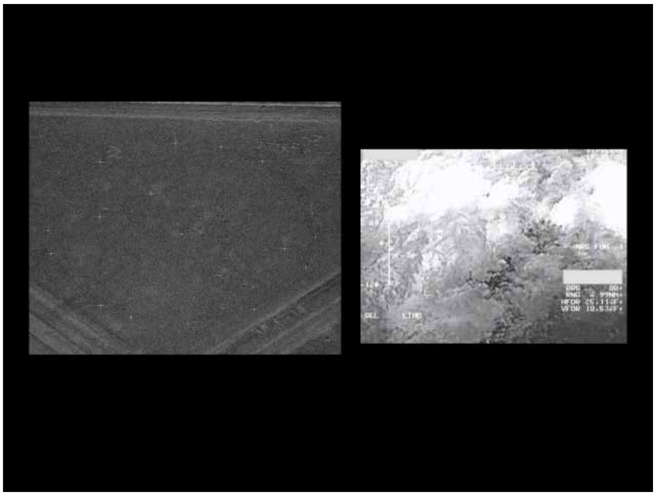

4.1/ Frame from composite videoclip obtained by juxtaposing a "VideoSAR" processing on the left and footage taken with an infrared camera on the right. Both acquisitions were taken at the same time interval from the same aircraft platform. The clouds, which reflect infrared rays, are transparent to the microwave radiation of the Synthetic Aperture Radar (SAR) and this allows for the graphical representation of the terrain. Source: Sandia National Laboratories, 2023b. Courtesy of Sandia National Laboratories, Radar ISR.

4.2 Informational and communicational aspects of radar images

Every type of remote-sensing document belongs to the category of 'perceptual synthesiser' because it brings the scanned events to human perception. This description is already very appropriate for Single Look Complexes (SLCs) produced by SAR, since they are precisely a synthesis of two 'direct documents', i.e. two products on which radiation is directly imprinted through electrotechnical and computer processes, without the intermediation of human thought[7]:

- the first direct document is the intelligible image associated with the received echo amplitude;
- the second direct document is the unintelligible image associated with the returned echo phase shift.

Clearly, a SLC of a territory, no matter how much it may be subjected to processes of geometric correction, radiometric correction and georeferencing, cannot be considered as a cartographic object, precisely because it is not the result of a critical data sorting operation conducted by a human being. Rather, it is treated as a block of data resulting from technical procedures and processing carried out by computerised algorithms[8].

However, it is important to remember that the character of communicational codification substantially enters into effect as soon as computerised equipment is interposed between survey and restitution, thus achieving image processing. Indeed, in addition to their pre-eminently 'informational' character, the two components of any SLC already have a 'communicational' character given by the grey scales chosen to represent amplitude and phase deviations (fig. 4.1). This communicational character becomes particularly evident when scientific literature associates the pixels that make up these images with the term 'brightness', linking the concept of reflectance of targets to microwaves (invisible to the human eye) with the concept of reflectance to light (of which the human being has direct experience). A body with a very strong backscatter is matched by a very white pixel, establishing a parallelism between microwave illumination and optical wave illumination. This is a convenient 'natural metaphor', i.e. a translation of characteristic features of natural appearance[9].

Another aspect of radar images that requires careful study concerns radiometric and geometric distortions related to the

4.2/ Radar image of the barrier at the driveway entrance to Kirtland Air Force Base near Albuquerque, New Mexico, acquired by Sandia National Laboratories using a synthetic aperture sensor operating in Ka-band. Given the image apparent resemblance to a photograph, the lighter pixels, even arranged like four-pointed stars, would suggest a bright reflection, such as that typical of a highly polished metallic object. In reality, bodies with such a strong radar reflection "only" have a geometric configuration and dielectric properties such that they backscatter a large portion of the signal transmitted by the sensor. Source: Sandia National Laboratories, 2023a. Courtesy of Sandia National Laboratories, Radar ISR.

very nature of their acquisition. In Chapter 2 we illustrated how between the radar image and the scene from which it was derived, the projectivity relationship is lost, due to the tilting of the target from the ground to the virtual mapping plane, caused by the side-scanning geometry. Although SLCs are very often intelligible they, behind their apparent realism, often conceal numerous obstacles to interpretation, as they do not respect the concepts of projection and section, which are not only at the basis of human graphic representation methods but which also take up the operating principles of human vision. If we interpret imaging radars [imaging radars] as 'innervations' that transform the sensorium of the human body, following Walter Benjamin's thought, SLCs just after the focusing operation – i.e. the process that makes raw data intelligible through the synthesis of the radar aperture, as conceived by Carl Wiley – present anomalies, generate 'short circuits' that disorient the user[10].

Without appropriate geometric and radiometric corrections that make it more familiar to human vision, a radar image loses much of its usefulness. It is precisely for this reason that interventions through the introduction of external data, such as geocoding with Digital Elevation Models (DEM)[11], become indispensable. In this way, the projectivity relationship with the scene is partially reintegrated.

We cannot use the definition of "projective manipulation" introduced by Giovanni Anceschi neither in the case of distortions arising during acquisition, nor in the case of corrections, since the projective character is not modulated but lost during acquisition and reconstructed during correction[12].

It is interesting to note at this point that the partial reintegration of the projectivity relationship between radar images and the scene is possible because, in the field of telecommunications engineering, the former are primarily treated as data blocks. William John Thomas Mitchell has placed some emphasis on the distinction – present in English but not in Italian, French or German – between 'pictures' and 'images': the former are considered material entities that owe their historically concrete existence to a set of supports, media and devices; the latter are considered immaterial entities (figures, motifs, forms) that can cross time and manifest themselves in one medium or another without losing their identity[13]. Indeed, the expression "radar image" would seem to suggest a form of digital information that can pass from the memory of one computer to that of another without losing its application potential. However, this particular form of data has no functionality outside of digital devices and their supports. We cannot derive from the print of a radar image in a book the value of the phase shift measured in a particular pixel. On the contrary, even within the digital environment, the raster preview obtained from a SLC has a very small number of functions compared to those of the data block containing the backscatter information of the depicted scene. However, a more circumstantial category to which we can ascribe the radar image and any product derived from it is that of the 'technical image' (technische Bilder), introduced by Vilém Flusser in 1995. This is a type of image that translates into digital terms linear and discrete sequences of signs, the 0s and 1s of the binary digital code[14].

Raw data and SLCs derived from them are therefore rather flexible 'conservative fixations' of radar scans. They keep the recorded data 'in power' within the human perceptual present, in ways that are sometimes closer to those of a spreadsheet than to those of a photograph (although both types of digital image, photographic and radar, are based on the concept of a numerical matrix)[15].

The concept of a block of data inevitably recalls the problem of the degree of schematisation adopted during their recording. In the case of the collation of a set of records, the 'object of the representation' always possesses a determined 'surface attitude'. In the case of radar images, the surface arrangement of the representation object, placed at a certain distance from the sensor and thus associated with a certain signal return time, is characterised by 5 parameters: 3 dependent on the radar device – angle of incidence θi of the transmitted signal, wavelength λ of the transmitted signal, polarisation of the transmitted signal – and 2 dependent on the portion of the object surface detected by the individual resolution cell of the microwave sensor – dielectric constant of the surface ε, roughness hrough of the surface –. As with the schematisation of the entire spectrum of visible colours into a more limited range of hues, which can be viewed on screens and printed on paper in the cases of photography and video recording, a similar problem arises mutatis mutandis for radar images. With respect to this starting configuration, which in principle possesses a continuum of ε and hrough values, the fixation of a virtual imprint of zones, features, points constituting the radar image - be it a complex image or an interferogram - within a colour scale (which may be bichromatic or polychromatic, but must always be unidirectional), always requires an obligatory selection at the measurement stage, an 'attributive reduction'[16].

4.3. Perceptual synthesis using multichannel synthetic aperture radar techniques

For SAR, especially those dedicated to remote sensing, the definition of 'perceptual synthesiser' becomes even more fitting when multi-channel processing techniques are taken into account. By processing several SLCs together, polarimetry, interferometry, and tomography make numerous sets of information synoptically available to the detector, the result of scans on a large spatial scale and at multiple instants of time, even over decades-long intervals[17].

The composite images that can be obtained from differently polarised signals received from the same scene are precisely the result of overlapping scans performed at several instants. It is precisely this comparison of several digitally fixed and stored signals that allows the classification of targets according to the polarisation of their echoes and, thus, to posit a certain type of geometric configuration for each category[18].

Interferometric Synthetic Aperture Radar (InSAR) analyses the differences between two or more scans with the aim of detecting the topographic configuration of a land surface or its deformation in the time interval between acquisitions, or both types of information[19]. In the case of single-pass interferometry, where scans are carried out simultaneously from two different observation points, the perceptual synthesis in relation to the human scale only takes place spatially. In the case of repeat-pass interferometry, on the other hand, where scans are performed at multiple instants of time, the interferometric radar assumes the role of a perceptual synthesiser not only spatially, but also temporally.

As a technological advancement deriving from InSAR, Synthetic Aperture Radar Tomography (TomoSAR) also starts from the analysis of a large number of scans, typically performed at different times, which may be separated by longer or shorter time intervals. Excluding the unlikely case (due to issues of economic resources and execution complexity) of a series of scans intended for tomography and performed simultaneously by a large number of sensors, any processing with TomoSAR subtends to be a perceptual synthesis over time. Even when the tomographic process is limited to an exclusively three-dimensional reconstruction, in fact, the result of the processing still derives from the selection of the targets that have returned the most stable echoes among the scans considered. With four-dimensional TomoSAR, of course, the measurement of deformation over time becomes graphically explicit and takes on a synoptic character, either through a three-dimensional point cloud, with a colour map representing the average speed of deformation occurring in the individual target detected, or through diagrams representing the various estimates of the kinematic configurations assumed by the same target along the sensor Line of Sight (LOS). Similarly, the five-dimensional tomographic processing dedicated to thermal deformations allows the colour map of the point cloud to be set up based on the average values of the thermal coefficients estimated for the targets along time, as well as diagrams of the nonelastic deformations for each target[20].

The greater the degree of perceptual synthesis associated with the products obtained with multi-channel processing techniques, the greater becomes the weight of the communicative aspect.
The matrix of polarimetric and interferometric processing is always given by a variable number of (relatively) direct documents, identifiable in each SLC with amplitude of the signal and the component associated with the signal deviation. The operations of collection and selection of these starting materials already represents a critical operation conducted by a human being. During the various processing operations, the informational character certainly remains significant and even increases, but at the same time, precisely because a new set of information is introduced, more or less arbitrary choices are required to encode and communicate it.
In the case of polarimetry, an important example is the encoding in false colours to identify the types of polarised backscatter in composite images (fig. 4.3). Although the choice of such colours is usually conventionally fixed according to the type of composite image to be obtained, there is no doubt that a communicational character underlies this convention[21].
As far as interferometry is concerned, a very significant example is the problem of identifying interferometric phase fringes using greyscales and colour scales. In Chapter 3, in fact, we discussed how representing the continuum of the interferometric phase with a greyscale hinders the perception of continuity between a value shortly before a multiple of 2π and a value shortly after such a multiple of 2π, since it creates jumps from white to black at each corner turn. The circular colour scale solution is certainly much more functional, but it too is the result of a communicational choice[22]. Nothing prohibits us, to associate the values 0 and 2π with blue instead of red[23] (fig. 4.4).
It is also important to note that Differential Interferometry Synthetic Aperture Radar (DInSAR) allows time series diagrams of estimated target displacements. Such diagrams are not direct documents, but 'generated documents', as they represent discrete values through a notational system.
The products of TomoSAR are also all generated documents. The data from polarimetric and interferometric images, although subject to further transfer and overlay and fusion processes, still retain the substantial characteristics of the direct document and continue to present themselves as conservative fixations of events imperceptible to human eye. With TomoSAR processing, on the other hand, information moves to a more abstract level and must therefore be communicated with a notational system. Data are extrapolated from a large set of SLCs, which are then sorted and transformed in order to obtain a three-dimensional reconstruction of the backscatterers, possibly accompanied by other information regarding displacements over time or even the thermal coefficients of

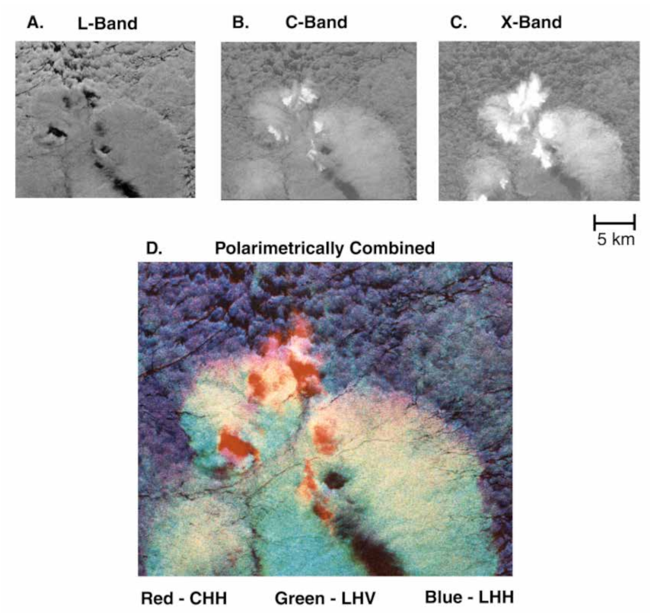

4.3/ SAR images of a rain cell captured by the Spaceborne Imaging Radar-C/X-band Synthetic Aperture Radar (SIR-C/X-SAR) on 10 April 1994 near Ontong Java Atoll, Solomon Islands. The images were acquired in (a) L-band, (b) C-band and (c) X-band, each with VV-polarisation and an incidence angle of about 50°. The composite image (d) was obtained from the polarisation combinations selected from Lband and C-band to highlight different scattering components in the rain cell. The choice of colours was made in order to accentuate certain features as much as possible: the combination L-band and HH polarisation (LHH) highlights echoes from the ocean subjected to low altitude winds; the combination Lband and HV polarisation (LHV) accentuates echoes from high altitude winds in the rain cell; the combination C-band and HH polarisation (CHH) isolates ice particles in the rain cell. Source: Holt 2004 / Public domain image [Image under Public Domain].

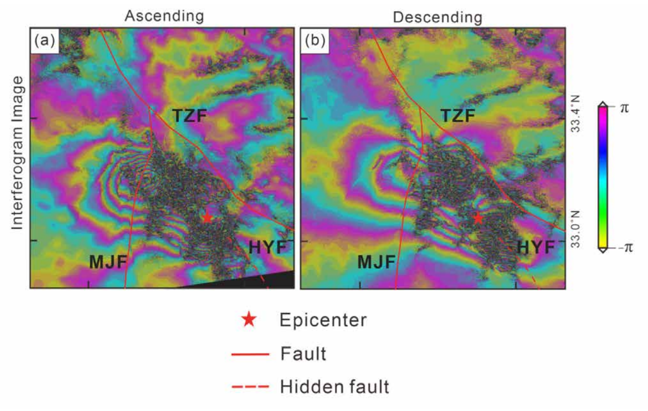

4.4/ Colour-scale interferometric phase pairs obtained from Sentinel-1 sensor data on earthquakeinduced deformation in the Jiuzhaigou area in 2017, near the fault system of the eastern part of the Kunlun Mountains in southern Central Asia. Multiple phase values of π were associated with the colour red. (a) Interferogram from scans along ascending passes; (b) interferogram from scans along descending passes.
Source: Peng, Huang, Wang 2023 / licensed under CC BY 4.0 (http://creativecommons.org/licenses/by/4.0/). © 2023 by Peng, Huang, Wang. Licensee MDPI, Basel, Switzerland.

nonelastic deformations[24].
Typically, this information is represented as three-dimensional point clouds and time series diagrams, especially in the case of buildings and urban surveys. Point clouds have above all a spatially synoptic character, as they represent several backscatterers simultaneously. Like interferometric time series, tomographic time series have a temporally synoptic character, as they represent the characteristics assumed by the same target during scans performed at different times.
Recorded data from a TomoSAR system are certainly among generated documents and can plausibly be classified as 'heteromorphic constructs', i.e. digital. Indeed, they identify profiles and graphical trends, both spatially and temporally, and are thus characterised by an aspectual figurativeness. It is quite easy to find such attributes in diagrams indicating the evolution of elevation displacements of a backscatterer. Similarly, point clouds obtained through tomographic processing transform a phenomenally complex reality into units by performing a quantitative survey (fig. 4.5). This quantitative survey, let us remember, is the conceptual prerequisite for any measurement.
It is possible to comfort the classification of TomoSAR just proposed with a counterexample. 'Homeomorphic', i.e. analogue constructs, are based on structural figurativeness and infer an articulation of the represented phenomenon. For the sake of argument, if tomographic products were homeomorphic constructs, in case we wanted to obtain a TomoSAR analysis of a building with bearing masonry walls, the various automated processes would have to recognise a hierarchical structure of some kind in the scanned scene and distinguish the perimeter masonry from the interior partitions, or subdivide the building into shear walls, infill walls and partitions[25].
Compared to polarimetric and interferometric images, the essence of generated documents typical of time series diagrams and tomographic products also has another implication, corresponding to a greater communicative malleability. Whereas polarimetric and interferometric images are characterised by a rather limited interactivity due to their character as direct documents, both time series from Differential Interferometry Synthetic Aperture Radar (DInSAR) and time series from TomoSAR are rather versatile. In order to be handled the former require a high level of scientific training and a great deal of technological and economic resources, while the latter can be used as simple spreadsheets. Tomographic point clouds also present this type of versatility and lend themselves to various manipulations by a non-specialist users, who can even insert them in their favourite telematic mapping service and intervene on their notational system, changing the symbols representing the backscatterers or the colour scale to their liking.
On the basis of the distinction between 'hot' and 'cold' media introduced by Marshall McLuhan[26], the acquisition of greater interactivity and versatility vis-à-vis a casual or in any case non-specialised user would seem to suggest a 'cooling' between one level of processing and the next, a reduction in definition (where the term definition is not to be confused with the resolution of radar images, but corresponds to the amount of information 'administered' by the medium to the user). Compared to polarimetric and interferometric images, differential interferometric and tomographic time-series diagrams focus the user's attention on a few targets at a time or even just one at a time, but because of this, they engage the user more. Tomographic point clouds are also considerably 'cooler' than

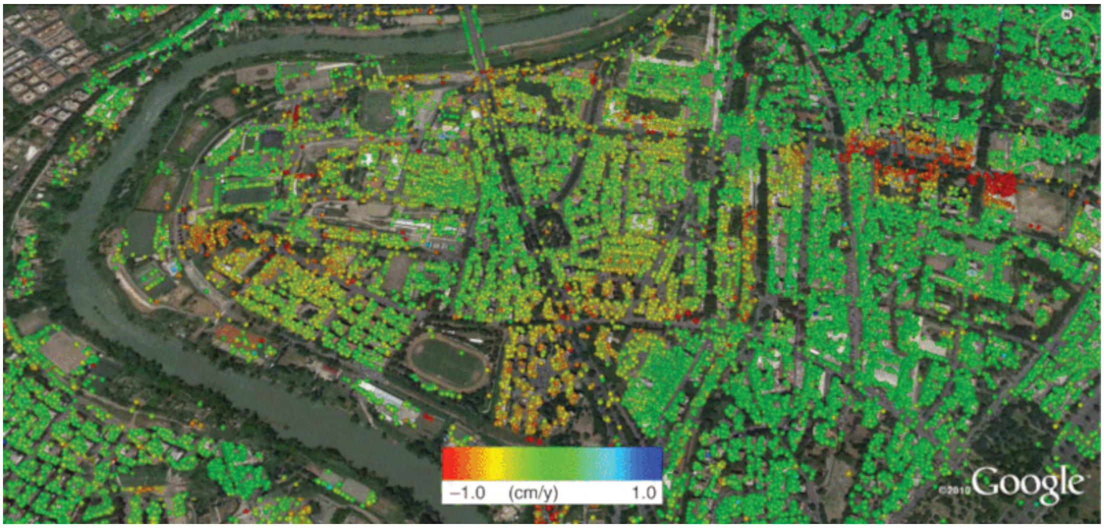

4.4/ Point cloud reconstructed with TomoSAR from 29 scans performed by the COSMO-SkyMed mission satellites over Rome, Italy. The points represent the backscatterers identified by the tomographic processing and are coloured according to the average speed of displacement (note the subsidence phenomenon due to the consolidation of an alluvial deposit near the Tiber river). The point cloud was imported into the digital three-dimensional environment of Google Earth™. Source: Fornaro, Lombardini, Pauciullo, Reale, Viviani 2014 © 2014 IEEE. Google™ and Google Earth™ are trademarks of Google LLC and this thesis is not endorsed by or affiliated with Google in any way.

SLCs, polarimetric images and interferometric images, as they are the result of selecting the most stable backscatterers over time. As already mentioned, however, this allows the non-specialist user to better navigate the data, especially since the three-dimensional reconstruction provided by the point cloud is digitally 'navigable'.

4.4 Communicational classifications of the various forms of synthetic aperture radar data

Below we propose some classifications of SAR products from a communicational perspective, useful for comparing the various forms that can be taken by acquired and processed data.

4.4.1 Classification according to the processing level scale

A first classification of SAR images and products derived from them can be conducted on the basis of the processing level scale of satellite data adopted by the National Aeronautics and Space Administration (NASA) specifying, for each level, the corresponding document type:

- To Level 0 belong the 'raw' data, i.e. those that have not yet undergone the focusing process of the aperture synthesis and are therefore in an unintelligible form. These are direct documents.
- Level 1 corresponds to focused, native-resolution data, based (also independently) on the signal amplitude and signal deviation components of SLCs. These forms of information also belong to the category of direct documents.
- To Level 2 belong geometrically and radiometrically corrected and georeferenced data. Physical parameters generally correspond to each pixel of these products. These are direct documents that, however, alongside their predominantly informational character, also have a substantial communicational character.
- Level 3 corresponds to those data meeting the criteria of Level 2, which have been subjected to a quality check and have been framed in a space-time grid. To this level belong interferograms and time series obtained with DInSAR. This level therefore includes both some direct and some generated documents (specifically, heteromorphic constructs).
- To Level 4 belong those data that fulfil the criteria of

Level 3 and have also been combined with models or other instruments. This is the case with point clouds and tomographic time series. All products related to this level are generated documents that can be identified as heteromorphic constructs.

Confirming the transition from direct to generated documents from Level 2 to Level 4 are the versatility and ease of use of these products, which grow with these steps[27].

4.4.2 Classification according to levels of iconicity

For a second classification we can resort to a "taxonomy of empirical cases" identifiable in the various forms of SAR data. For this purpose we can reacall the 'levels of iconicity' theorised by Abraham André Moles and later reinterpreted by Giovanni Anceschi.

The component associated with signal amplitude and the component associated with signal phase shift are direct documents constituting SLCs. Both of these components are characterised by very mimetic modes of cognitive use. It is therefore appropriate to assimilate them to the genre of 'retouched photographs', where, however, the term photograph is not intended to circumscribe the nature of the source document, but to emphasise its mimeticity, perhaps illusory. The classification of signal amplitude images at this level of iconicity is quite straightforward, due to their deceptive resemblance to photographs. On the other hand, images relating to signal deviation are more affected by the switching operations performed by radar instruments, but they also act by mimesis of the captured phenomena (forms not perceptible to human beings, but nonetheless materially existing), although they seem to resemble the 'television snow effect' most of all.

Polarimetric images and interferograms are also ascribable to retouched photographs, although the greater weight of their communicative character reduces their mimeticity compared to a SLC.

On the other hand, time series diagrams, whether for displacements or thermal deformations, are easily classified as 'perfect abstractions', as they adopt totally conventional graphical notations, which do not recall at all the figure of what they are supposed to represent.

Conceptually, point clouds are more ambiguous to classify since, depending on how they are captured and processed, they can have characteristics typical of retouched photography, 'line simplification' and 'constructive drawing'. In fact, if captured with a certain level of detail, point clouds can even be mistaken for realistic three-dimensional models at a first, superficial glance, thus with a mimesis typical of retouched photographs. However, it is undeniable that point clouds are the result of a quantitative simplification operation performed by the scanning tool, thus coming close to drawing strokes simplifications, but not in a totally congruent manner. The latter, in fact, are characterised by qualitative schematisations that must give them descriptive functions. At the same time, point clouds are certainly characterised by strongly operational functions (just think of their usefulness in measurements) typical of construction drawings[28].

4.4.3 Classification according to levels of figurativeness

A third classification based on Rudolf Arnheim's 'perceptual approach' is also possible. This approach to the ordering of "levels of figurativeness" identifies two poles and a midpoint: we have "replicas" at the figurative pole; "stylised objects" at the midpoint; "non-mimetic forms" at the abstract pole[29].

Given, however, that radar images and all that follows from them are the product of a commutation obtained by machines, instead of the notion of mimesis (appropriate to the case of a human enunciator, a draughtsman), it is better to adopt the notion of recognition on the scale proposed by Algirdas J. Greimas: in this way, the ordering of levels is referred to the instance of the enunciator, i.e. the end user (who is always human). We thus have:

- documents with 'high iconicity', i.e. prone to replication, such as SLCs and their amplitude and phase-shift components, polarimetric images, interferometric images, very dense point clouds;
- documents with 'normal iconisation', i.e. stylised objects such as sparse point clouds;
- documents 'based on abstract codes', tending towards non-mimetic form, such as time series diagrams representing displacement and thermal deformation estimates for each identified target.

Notes

1 Anceschi 1992, p. 4.
2 Skolnik 1981, pp. 8-9.
3 Pinotti, Somaini 2016, p. 253.

4 Anceschi 1992, p. 8; Pinotti, Somaini 2016, p. 253-256.
5 Crary 2013, pp. 3-4.
6 Pinotti, Somaini 2016, p. 90.
7 *Loc. cit.*, pp. 17-18.
8 *Loc. cit.*, p. 51.
9 *Loc. cit.*, p. 20-22.
10 Pinotti Somaini 2016, p. 135.
11 Meyer 2019, pp. 37-38.
12 Anceschi 1992, pp. 60-70.
13 Pinotti, Somaini 2016, p. 45.
14 *Loc. cit.*, pp. 148-149.
15 Anceschi 1992, pp. 20-22.
16 *Loc. cit.*, pp. 70-72.
17 *Loc. cit.*, pp. 20-22.
18 Moreira, Prats-Iraola, Younis, Krieger, Hajnsek, Papathanassiou 2013, pp. 14-19.
19 Meyer 2019, p. 38.
20 Fornaro, Pauciullo, Reale, Zhu, Bamler 2012, pp. 12-14; Fornaro, Reale, Serafino 2008, pp. 477-478; Fornaro, Reale, Verde 2013, pp. 679-681.
21 Ager 2013, p. 25; Meyer 2019, pp. 27-28.
22 Meyer 2022.
23 Peng, Huang, Wang 2023, p. 8.
24 Fornaro, Pauciullo, Reale, Zhu, Bamler 2012, pp. 12-14; Fornaro, Reale, Serafino 2008, pp. 477-478; Fornaro, Reale, Verde 2013, pp. 679-681.
25 Anceschi 1992, pp. 17-18.
26 Underlying the distinction between 'hot' and 'cold' media introduced by McLuhan is the concept of definition, to be understood as the amount of data transmitted to the user. A warm medium extends a human sense to 'high definition', filling the user with information so rich that it does not require any form of integration. Cold media, on the other hand, propose data to their recipients that must be completed, integrated from a perceptual, interpretative and social point of view. It follows, therefore, that the cold form conveys information at a lower definition than the hot form, but is nevertheless more engaging for the user. Cf. Pinotti, Somaini 2016, pp. 194-197.
27 Anceschi 1992, pp. 17-18; Meyer 2022.
28 Anceschi, pp. 26-38.
29 *Loc. cit.*, pp. 46-49.

Sintesi

I radar sono stati concepiti per rappresentare corpi non percepibili in un determinato momento, al fine di anticipare e possibilmente prevenire un probabile evento dannoso, il quale può essere un incidente oppure un bombardamento aereo. La funzione di molti tipi di radar, ancora oggi, è consentire un processo conoscitivo esogeno. Trasmettendo un segnale per poi registrare e comunicare un evento del tutto invisibile, cioè la riflessione del segnale emesso da parte di un elemento retrodiffondente, essi consentono di venire a conoscenza della presenza di un oggetto potenzialmente percepibile quando non può essere (nel caso di impedimenti alla visione) o non deve essere (nel caso l'oggetto in questione sia pericoloso) percepito direttamente.

Le immagini mappate con i radar orientati lateralmente fanno parte di quel vasto campo di tecniche di infografica che hanno costituito una riconfigurazione di ampia portata nelle relazioni fra soggetto osservatore e modi di rappresentazione. I radar per la produzione di immagini sono sempre apparecchiature tecniche che compiono operazioni di «commutazione», trasformando gli echi invisibili dei loro segnali in eventi percepibili associati a informazioni sui bersagli. Nella stragrande maggioranza dei casi, specialmente per quanto riguarda il telerilevamento, i radar per la generazione di immagini eseguono anche operazioni di «compressione» ed «espansione». Accanto al loro carattere preminentemente «informazionale», le due componenti delle immagini complesse hanno già un carattere «comunicazionale» dato dalle scale di grigi scelte per rappresentare l'intensità e gli scostamenti di fase.

Senza adeguate correzioni geometriche e radiometriche che la rendano più familiare alla visione umana, un'immagine radar perde molte delle proprie utilità. Proprio per questo sono indispensabili degli interventi tramite l'introduzione di dati esterni, come la geocodifica con i Digital Elevation Model. In questo modo la relazione di proiettività con la scena viene parzialmente reintegrata.

Né nel caso delle distorsioni che insorgono durante l'acquisizione, né nel caso delle correzioni si può usare la definizione di «manipolazione proiettiva» introdotta da Giovanni Anceschi, poiché il carattere proiettivo non viene modficato ma perduto durante l'acquisizione e ricostruito durante la correzione. È interessante notare che la parziale reintegrazione della relazione di proiettività tra immagini radar e scena è

possibile perché, nel campo dell'ingegneria delle telecomunicazioni, le prime vengono trattate innanzitutto come blocchi di dati.

Una categoria alla quale possiamo ascrivere l'immagine radar e qualsiasi prodotto da essa derivato è quella della «immagine tecnica» (technische Bilder), introdotta da Vilém Flusser nel 1995. Si tratta di un tipo di immagine che traduce in termini digitali delle sequenze lineari e discrete di segni.

Per varie ragioni, il radar ad apertura sintetica rientra nella definizione di «sintetizzatore percettivo»: uno dei motivi riguarda le immagini complesse, che sono date dalla combinazione di una componente associata all'intensità del segnale e una associata allo scostamento di fase. Il termine «sintetizzatore percettivo» diventa ancora più calzante se si prendono in considerazione le tecniche di elaborazione multicanale. Elaborando più immagini complesse assieme, polarimetria, interferometria e tomografia rendono sinotticamente disponibili per il rilevatore numerose serie di informazioni, frutto di scansioni su vasta scala spaziale e in più istanti di tempo, anche lungo intervalli decennali.

Maggiore il grado di sintesi percettiva associato ai prodotti ottenuti con le tecniche di elaborazione multicanale, maggiore però diventa il peso dell'aspetto comunicazionale. Durante le varie elaborazioni il carattere informazionale rimane certamente significativo e addirittura incrementa ma, al tempo stesso, proprio perché vengono introdotte una nuova serie di informazioni, si rendono necessarie delle scelte più o meno arbitrarie per codificarle e comunicarle.

Le immagini complesse e i loro componenti, i prodotti polarimetrici e gli interferogrammi sono «documenti diretti», cioè il risultato della "impressione" delle radiazioni attraverso processi elettrotecnici e informatici.

I diagrammi delle serie temporali derivanti dall'interferometria differenziale radar ad apertura sintetica e dalla tomografia radar ad apertura sintetica non sono documenti diretti, ma «documenti generati», poiché rappresentano valori discreti attraverso un sistema notazionale. Stessa cosa si può dire delle nuvole di punti tomografiche.

Luca Martelli

5. The Territorial Context of the Former State of the Presidi of Tuscany

5.1 The Environmental System of the Tuscan Coastline

From a territorial point of view, the Presidia of Tuscany initially comprised that part of the Republic of Siena that Philip II of Spain kept under his dominion in 1557, according to the instructions given to Don Juan de Figueroa, castellan of Milan, for negotiations with Cosimo I de' Medici, Duke of Florence. The primigenial territorial nucleus consisted of the communities of Orbetello, Talamone and Ansedonia, located along the stretch of Tyrrhenian coast at the height of the Grosseto Maremma, as well as the community of Porto Ercole, located in the south-eastern part of the Argentario Promontory In 1596, the fortified town of Porto Longone was added to these territorial areas, together with its district on Elba, the largest island of Tuscan Archipelago.

In 1634, Niccolò Ludovisi, whose family was enfeoffed to Spain, took over as Prince of Piombino. Consequently, the Principality of Piombino,located on the Promontory of the same name to the east of the Island of Elbawas managed by the Spanish Crown in addition to the State of the Presidia

Porto Santo Stefano, another locality situated in the north-eastern portion of the Argentario Promontory, was initially a simple maritime landing place substantially devoid of a stable population but, shortly after 1622, it was endowed with its own fortress while remaining under the jurisdiction and command of the Governor of Orbetello This situation continued throughout the existence of the Presidium State and even beyond, untilGrand Duke Leopold II of Lorraine established the municipality of Monteargentario in 1842, which included both Porto Santo Stefano and Porto Ercole[1].

The complex territorial structuring of the Presidium State was clearly the result of the progressive addition of all the annexations just enumerated, but also of the particular articulation of these territorial areas, as well as their morphological, environmental and landscape biodiversity and variety.

The lower Maremma is in fact a series of diversified environments, where mountainous areas alternate with flat or hilly areas.Low, sandy coasts are followed by rocky ones and vice versa. Compared to other areas in Italy, the Maremma has suffered relatively few traumas, even though its current state is the result of a series of profound interventions: from the reclamation of marshy land to territorial and urban planning aimed at encouraging tourist development[2].

The Island of Elba has a varied landscape, characterised by rocky coastal environments and Mediterranean mountainous relief, such as Monte Calamita and Monte Capanne, but also by the dune system in the Gulf of Lacona. Like the other islands of the Tuscan Archipelago, in terms of flora Elba presents various typically Mediterranean scenarios: broadleaf and sclerophyll woods, plantation pine forests, garigues, scrubland and rocky outcrops[3].

The Piombino Promontory, dominated by Monte Massoncello and embraced by the Val di Cornia, is characterised by a coastal rocky complex of particular naturalistic and landscape interest, since it is connected to the residual wetlands of the backdunes. The latter represent testimonies of marshy landscapes that were destroyed following land reclamation works, such as the former Rimigliano Lake, which was transformed into agricultural land[4].

For these reasons, we consider it useful to describe the environmental context of the territory that once belonged to the former State of the Presidi by identifying four areas:

- the Agro orbetellano, comprising Orbetello, Talamone and Ansedonia;
- the Monte Argentario area, including Porto Santo Stefano and Porto Ercole, plus the islands of Giglio and Giannutri;
- the former district of Porto Longone, today Porto Azzurro, on the island of Elba;
- the area of the former Principality of Piombino.

Consistent with the choice of the case studies of the Spanish Fortress of Porto Santo Stefano and the Talamone town wall for the present research, we will focus mainly on the Orbetello countryside and Monte Argentario.

5.1.1 The Orbetello countryside

The territory of the municipality of Orbetello is characterised by a very varied geomorphology, depending on the location considered. The context of its structural genesis corresponds to the formation of the Apennine chain, caused by the collision between the European Plate and the African Plate. Like the rest of southern Tuscany, in fact, the Orbetello countryside went through several deformation phases that occurred from the Triassic to the Neogene, over an interval of about 220 million years. These deformation cycles were associated with two main tectonic processes that determined the current geological structure of Tuscany:

- a first compressional phase which, on the one hand, caused a stacking of strata of the Ligurian and Tuscan Units on the Units of the Umbria-Marches Series during the Oligocene-Miocene temporal phase; on the other hand, it caused the uplift of the Apennine chain during the Miocene-Pleistocene temporal phase;
- a second distensive phase that, from the Upper Miocene to the Upper Pleistocene, transformed the arrangement and structure of the units stacked in the previous stage, forming numerous basins filled with neogeneic sediments.

Before being completely exhausted, the first cycle of compression and stacking caused depressions, in which lake and marsh basins were created. In fact, along the entire coastline, the most depressed places are scattered and contain lakes communicating with the sea - such as the Lagoon of Orbetello and the Lake of Burano - or small swamps and freshwater reservoirs, largely mineralised by sulphur and carbonic acid - such as the Lagaccioli di Capalbio, of karstic origin: Lago Acquato, Lago Secco, Lago di San Floriano and Lago del Cutignolo -. The end of the compressional phase immediately corresponded with the beginning of a cycle of marine transgression, i.e. a shift of the coastline inland. This transgression led to a neo-autoctonous, i.e. a sedimentary succession that was deposited on top of the stratifications of mineral materials that had arrived and sedimented in turn in earlier times (allochthonous). Evidence of this phenomenon is evident in the plains of the Agro-Orbetellano, which are covered by sea sand or shell tuffs; in other cases, however, they are covered by terrestrial deposits left by rivers. This phase of transgression, analogous to a regression cycle (i.e. the shifting of the coastline towards the sea) that occurred in the Pliocene, has such characteristics and dynamics that it cannot be directly attributed to changes in sea level (attributable to the state of the ice caps or to possible alterations in the oceanic basins), assuming instead a lowering of the previously uplifted Apennine chains.

During the Miocene and Pliocene distensive phase, in addition to the manifestation of direct faults and sedimentary accumulations in various basins, widespread magmatism also occurred, gradually moving from west to east. The mountainous part of the Agro-Orbetellano is mostly reduced to stratiform rocks, mostly limestone and in the rest of the cases sandstone or clay, more or less altered in their structure and transformed into plutons by the serpentine masses and metal seams that penetrated it. The orographic structure of the lower Maremma, characterised by the limestone hills, is manifested along the Tuscan coast by the relief systems of Monte dell'Uccellina (affected by karst phenomena) and Monti orbetellani. Similarly, Monte Argentario and the island of Giannutri are also made up of Tuscan limestones. It is precisely these limestone formations that represent the recharge zones of the carbonate aquifers of Monte dell'Uccellina, Monte Argentario and the areas of Orbetello and Capalbio. The freshwater that feeds the Orbetello Lagoon and the Chiarone spring near Capalbio in fact comes from the Orbetello Mountains[5].

In the northern area of the municipality of Orbetello we find the hills of the Maremma Regional Park, covered by lush Mediterranean scrub. The mountainous area slopes down to the west towards the beach and the sea, and to the east towards the cultivated plain created from land that was originally marshy and then reclaimed.

Descending southwards, the hills end first in the Talamone Promontory and then in the Talamonaccio Promontory. In particular, the rocky coast near Talamone and Fonteblanda is subject to evident erosion phenomena. The material constituting the Talamone plateau, the last southern spur of Monte dell'Uccellina, is a siliceous cement breccia similar to that found in the mountains of the Grosseto Maremma and, at times, intersected by quartz layers or strands. The same breccia of Talamone, towards the base, is mantled by a kind of schi-

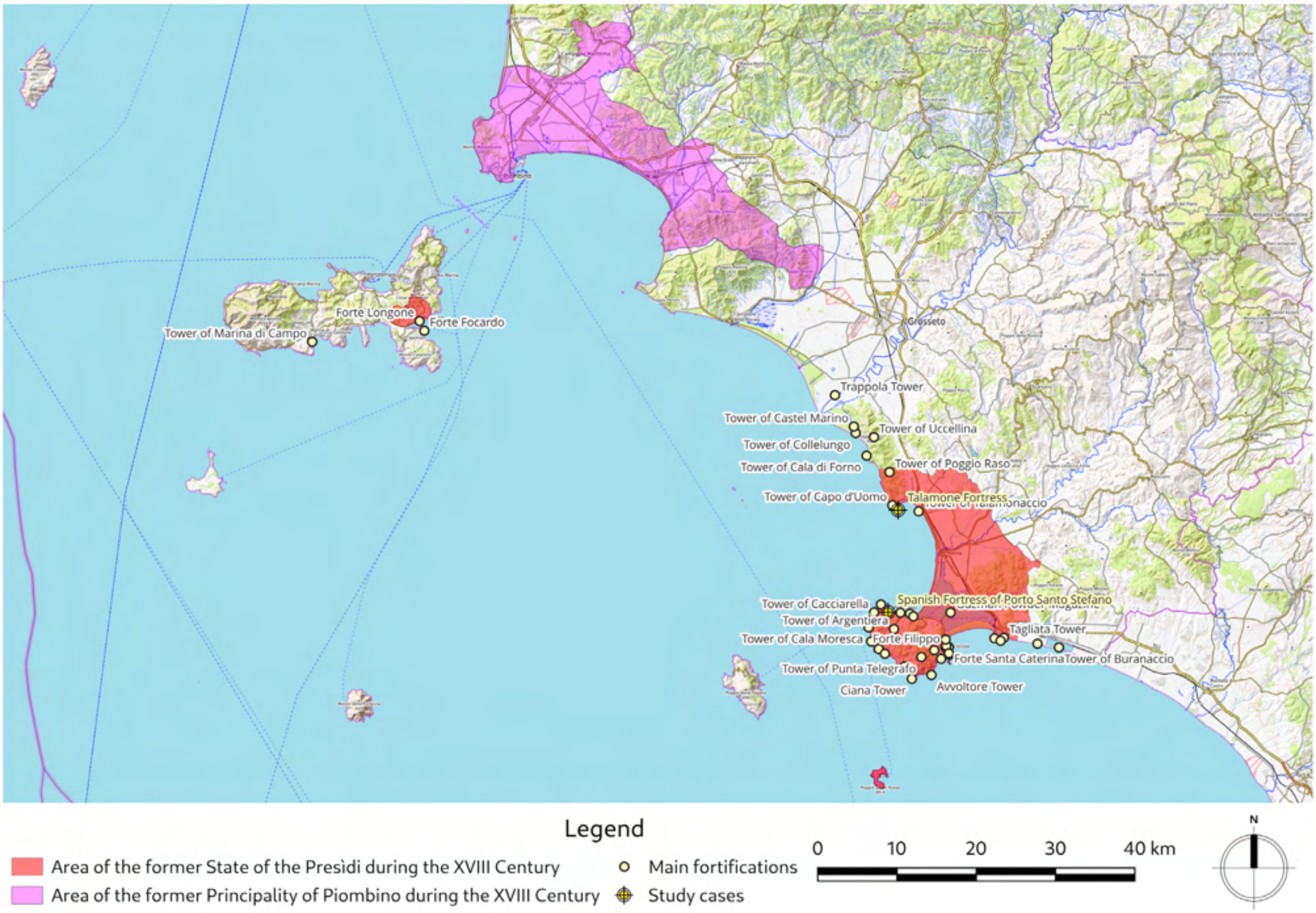

5.1/ Area of the former State of the Presidi and sites of the main works of its defence system. Source: Della Monaca, Roselli, Tosi, 1996. Map data from opentopomap.org / licensed under CC-BY-SA (https://creativecommons.org/licenses/by-sa/3.0/).

stous marl, which sometimes appears as jasper with minute crystals of hyaline quartz. In addition to hosting a series of garrigue and Mediterranean scrub areas, the surroundings of Talamone and Fonteblanda are also characterised by important habitats of Community interest, such as some residual wetlands with respect to reclamation works and lowland forests of considerable naturalistic value, such as the Campo Regio Woods. The latter are a formation dominated by Fraxinus oxycarpa and occupy an important place in the Tuscan Naturalistic Repertoire as the 'riparian ash woods of the Camporegio fossil interdunal blades'. Today, the reclaimed plain behind Talamone is in a critical situation, since the drainage system created during the reclamation works is undersized with respect to current water flows. In fact, this system collects water from almost the entire local plain, thus exposing itself to the risk of the transport of pollutants towards the remaining wetlands around Talamone and Fonteblanda. Continuing southwards, close to the coastline, the landscape is made undulating by sand dunes of remote origins and covered by Mediterranean scrub, while inland the morphology of the land is flat. The soils in this area are rich in minerals and take on a reddish or dark colour. Towards the east, the topographical configuration increases in altitude and the land becomes covered with olive, beech and chestnut trees. From these hills it is possible to embrace the Orbetello Lagoon, the coast and the Tyrrhenian Sea as far as Monte Argentario and Giglio Island. Returning towards the coastthe plain is characterised by other residual marshy areas, which are home to nature reserves rich in flora and fauna. The main plant species include rows of eucalyptus trees, pines, rushes, reeds, tamarisks and lentisk bushes. Some of the beetles found in these places are: the green cetonia; the rhinoceros beetle; the cerambix; the flying deer; several species of ladybirds. There are also a few species of hemipterans such as the green-livered pyrrhocore, while among the lepidopterans we find the swallowtail and the pear saturnia. Among the land reptiles, we encounter the marsh tortoise, several species of grass snakes, as well as the green and yellow columbine. The scrubland is also home to the Hermann's tortoise, weasel, fox, beech marten, hedgehog and green lizard. In this area, the marshes are home to the rare marsh harrier, the penduline tit nests in the eucalyptus trees and pheasants take refuge in the pine forests.

The Orbetello Lagoon in front, on the other hand, is the habitat of white egrets, black-winged stilts, common stilts, voltolins plus various species of seagulls and, in autumn, it is possible to watch the migration of cormorants, lapwings, coots and greater flamingos[6]. The Lagoon was formed thanks to the formation of two tombolos, which connected the mainland to Monte Argentario - formerly an island just a few kilometres from the coast - and thus gave rise to the largest wetland area on the Italian west coast, consisting of an area of about 2,700 ha. There are very few examples of such lagoons in the world and, as far as Italy is concerned, this is a unique case. The wetland is bordered to the north-west by the Tombolo di Giannella and to the south-east by the Tombolo di Feniglia, both formed following the last glacial oscillation, around 5,000 years ago. Approximately in the centre of the Lagoon is the town of Orbetello, located above a third tombolo, even older and yet never reaching Monte Argentario, although it was connected to the latter by a bridge called "La Diga", built in 1842[7]. On the outskirts of the Orbetello Lagoon, in Monte Argentario, near the knoll of Ansedonia and in the part of the Tuscan coast near the Tombolo di Feniglia, there are massive, cavernous rocks. At the same time, the three tombolos are covered by ancient sandstone impasti caused by the marine regression cycle discussed above. Enveloped in these slurries are shells of molluscs absent in the lagoon and typical of the sea, such as Ostrea jacobea and Arca pilosa. A further confirmation of the influence of tectonic phenomena coeval with the cycle of maritime transgression comes from the fact that most of the Argentario Promontory and the islets in its surroundings are made up of soils of materials that later became plutons[8].

What today we improperly call a lagoon is actually a coastal pond, since its brackish waters are in communication with the sea through three small canals, whose modest flow rates allow such an interchange with the sea water that it only affects the areas bordering the canals themselves and not the entire body of water. One of these watercourses is located at the eastern end of the Tombolo di Feniglia and is named Taglio di Ansedonia after the nearby promontory of the same name. The other two watercourses are located at the ends of the Tombolo di Giannella: to the west we have the Canale di Nassa, also known as the Canale di Santa Liberata; to the north-east we have the Canale di Fibbia, a simple hydraulic work that connects the lagoon with the mouth of the nearby Fiume Albegna, where the Spanish built the 'Saline Sadun'.

The profile of any cross-section of the Tombolo di Giannella or the Tombolo di Feniglia has the central part colonised by Mediterranean scrub, while near their shores there are pioneer plants typical of the Italian coasts, such as prickly sparto, eringio, beach santolina and Pancratium maritimum. The banks of the Orbetello coastal pond, on the other hand, are mainly surrounded by halophilous, i.e. salt-loving, essences: glasswort, statice, bulrush and, in places where the presence of salt is less, marsh reed (Phragmites australis). A few centimetres above sea level and a few metres from the banks, we find the typical Mediterranean scrub, including mastic, phillyrea, myrtle, alaterno, heather and sarsaparilla. Between the Tombolo di Giannella and the Tombolo di Feniglia, the former has its beaches subject to erosion and is more anthropised, although it has maintained its spontaneous vegetation in its natural areas. The latter, on the other hand, hosts a fixed dune ecosystem and, after a long period of sporadic anthropisation due to pastoralism, was purchased by the Italian State in 1910 and then entrusted to the Forestry Corps, which carried out a reforestation process favouring the domestic pine, which was then widely used for these purposes[9].

At present, the "Duna Feniglia" Protection Forest Reserve occupies a 474 hectare strip of flat land between the Orbetello Lagoon to the north and the Tyrrhenian Sea to the south, which connects the Colle di Ansedonia with the Argentario Promontory through a junction near Porto Ercole. In addition to the stone pine, there are other essences of the Mediterranean maquis such as the saltwort, which grows on the banks of the coastal pond and psammophilous plants on the Tyrrhenian coast. Cork trees, junipers and oaks also abound. In the area of the Reserve closest to Ansedonia there has been a population of fallow deer for years, which live under the supervision of the Forestry Corps. This protected area is also the habitat for other mammals such as hares, roe deer, badgers, wild boar and porcupines. The Reserve is criss-crossed by a path accessible from the entrance of the Tombolo di Feniglia on the Porto Ercole side, a path that runs along the Lagoon for 200 m and winds for another 700 minside the pine forest

Contributing to the conservation of the Orbetello Lagoon was the foundation, in 1971, of one of the first World Wide Fund for Nature (WWF) Oases in Italy.1965, the nesting of the northern part of the stretch of water- known as Stagnone dei Lombardi - by the stilt-bird, a species of bird considered extinct in Italy, was discoveredTherefore, by virtue of a Decree of the President of the Republic, the area was placed under the protection of WWF Italy. In 1977, the presence of over 10,000 wintering ducks led to the recognition of the area as a Zone of International Importance according to the Ramsar Convention, covering an area of 800 hectares, to which were added 30 hectares of land and areas permanently covered by water in state concession to WWF Italy. Within this area, a State Nature Reserve of 80 ha known as 'Laguna di Orbetello Ponente' was also established, the management of which was also entrusted to WWF Italy by Decree of the Ministry of Agriculture and Forestry of 08/08/1980. To all these forms of protection was added, in 1998, the institution of the Provincial Nature Reserve, which considerably enlarged the protected area to an area of 1,582 ha, but partially modified its boundaries and excluded the mouth of the Albegna river and the Tombolo di Giannella[10], to favour the so-called 'open waters' of the coastal pond[11].

However, over the years the WWF has managed to purchase some areas on its own initiative, such as the Patanella Woods, thus expanding the protected area. The Bosco di Patanella is the only forest that has remained almost intact in the lagoon area. It consists mainly of cork oaks, domestic pines and maritime pines, accompanied by an undergrowth of Mediterranean scrub and the massive presence of heather (Calluna vulgaris), a heather that here finds the southern limit of its distribution in Italy. Under the Bosco's pines, specimens of two particular types of orchid can grow: the small Spirante spiralis, which flowers in autumn; the Limodorum abortivum, which flowers in spring and can reach a height of 80 cm. The particular microclimate of the Patanella Forest also favours the proliferation of many species of epigeous fungi. Many sylvids nest in the forest: the Sardinian warbler, the little tern, the long-eared owl, the hobby hawk, the green woodpecker, the long-tailed tit, the titmouse, the jay and the tufted cuckoo. The shores of the coastal pond along the forest, on the other hand, are the habitat of the gazetteer, heron and kingfisher, while common terns have nested on one of the artificial islets in the stretch of water. In winter, the Pond's shoreline is frequented by flamingos, spoonbills, white egrets and lesser mergansers.

Currently, the Orbetello Lagoon is home to over three hundred different bird species, with concentrations of between 15,000 and 20,000 individuals between the autumn and winter seasons The coastal pond is an environment teeming with simple organisms, which form the basic diet of higher animals, so fish and birdlife find an ideal habitat for their growth here. The fish species present in the lagoon are those typical of brackish and marine environments: among the fish we find mullet, bass, eel, gilthead bream, sole, gobies and dairy fish, which provide a food source for fish-eating birds. As already mentioned, the coastal pond communicates with the Tyrrhenian Sea through three watercourses: theTaglio di Ansedonia, at the eastern access to the Tombolo di Feniglia; the Canali di Fibbia and di Nassa at the ends of the Tombolo diGiannella

Further south, the Colle di Ansedonia interrupts the continuity of the coastline, forming a small promontory between Lake Burano, the Lagoon of Orbetello and the Tdi Feniglia. It can be considered as a relief located at one end of the Orbetello Mountains, which descend from the north by the Colle di Sant'Angelo and the Colle di Capalbaccio (also known as the Colle delle Tombe) to the sea. The predominant rock at the knoll of Ansedonia consists of limestone, which barely preserves the appearance of the original stratification, presenting itself mostly in massive structures, of a bigia hue and crystalline grain penetrated by metalliferous veins. This rock, which in many places is covered or interbedded with a calcareous breccia, tends to be criss-crossed by large cracks and is often pierced by boll-shaped cavities or branched cells containing abundant traces of red iron oxide.

In this rock massif, on the side of the Torre della Tagliata, a very wide and very long rift was formed, known to the local population as the 'Queen's rift' and constituting the opening to the sea of the ancient channel known today as the Etruscan Tagliata. The rift has internal walls corresponding exactly, between concave and convex, to the same limestone breccia cliff. The Regina's rift must therefore be the natural effect of an earthquake or some other kind of cataclysm, due to which the sector of the Ansedonia Promontory facing south-east was ripped open, on top of which stretches ofthe walls of the ancient city of Cosastill be seen. Near the rift there is another ancient artificial opening made to pierce the cliff and penetrate at water level into the sea, not far from the Torre della Tagliata. In the past, it was assumed that this opening was used for bathing purposes, as the seats carved into the stone at the site suggest.

After Ansedonia, the coastline continues with a dune conformation, while the hinterland consists of hills covered with sparse vegetation. Further south-eastthe brackish basin behind Lake Burano, which in 1977 was recognised as an Area of International Importance according to the Ramsar Convention. In addition to being part of the residual areas of the Maremma marshlands and characterised by a system of coastal dunes, it is also a staging area for various species of migratory birds, especially anseriformes and caradriiformes. Already the site of a wildlife refuge, also managed by WWF Italy, Lake Burano has been granted a State Nature Reserve of the same name by Decree of the Ministry of Agriculture and Forestry of 13/08/1980. Similarly to the case of Talamone, the drainage of the plain around the lake is no longer sufficient for contemporary water flows, thus exposing the lake to the danger of contamination by pollutants transported by water[12].

5.1.2 Monte Argentario, Giglio Island and Giannutri Island

The Argentario Promontory is entirely occupied by the mountain of the same name, which has three peaks. The highest of these peaks, located near Porto Ercole, reaches a height of 635 m and is known as Punta Telegrafo, in memory of a communication tower built under the French government and originally named Ancien Sémaphore Saint-André, but now ruined[13]. With a significant difference in height from Punta Telegrafo, the second highest peak is Punta Ronconali, the most central of the three and having its summit covered by large, steep cliffs, dismantled and dismantled by the passage of time. The third peak is Monte dell'Argentiera, above which rises the tower of the same name, between Porto Santo Stefano and the Torre di Santa Liberata. The branches that descend to the coast are small spurs that form a sheer drop to the sea for most of the perimeter of the Promontory, so the latter has deep valleys, sinuses and bends occupied by isolated cliffs on all sides. One of the largest Argentario valleys opens up towards the northern coast of the latter, taking the form of a sinus and ending in the left horn under Monte di San Pietro, which dominates several creeks, particularly that of Porto Santo Stefano, the deepest. An even more extensive valley descends from Punta Telegrafo towards the east, bifurcating into two sinuses: the first between Capo dell'Avvoltore and Forte Stella; the second between Forte Stella and Monte Filippo, ending in the deep cove of Porto Ercole.

The historically most frequented centres of the Argentario are Porto Santo Stefano to the north and Porto Ercole to the south-east, which were initially formed near these inlets on the side of the Promontory facing the Tuscan coastline, as they could be used as safe harbours hidden from the open sea. Even today, other natural shelters for navigation include Cala Grande and Cala Moresca to the west, Cala Piatti and Cala della Maddalena to the south-west, Cala d'Isola Rossa and Capo della Piana to the south, and Capo dell'Avvoltore to the south-east. Around the coast of the Promontory there are some rocks detached from the cliffs of Monte Argentario, of which they were part before falling into the sea. Among these, the most relevant are the islet near Porto Ercole, those of Argentarola, Isola Argentina on the south side of the Promontory and Isola Rossa on the south-west side. On the side facing the islands of Giannutri and Giglio, the Argentario has a very jagged slope at the base and is interrupted by several spurs, which leave in the middle several sinuses forming the sites of various towers and defensive fortresses. Coves, crags and islets, present in large numbers, thus confer considerable landscape value to this entire area.

As far as geological and geomorphological structuring is con-

5.2/ Area of Orbetello countryside with borders of the former State of the Presidi and sites of the main works of its defence system. Source: Della Monaca, Roselli, Tosi, 1996. Map data from opentopomap.org / licensed under CC-BY-SA (https://creativecommons.org/licenses/by-sa/3.0/).

cerned, the distensive cycle that took place from the Upper Miocene to the Upper Pleistocene - after the collision between the Adriatic Plate and the Corsican-Sardinian Plate - was accompanied by phenomena of magmatism and erosion, which led to the emergence of the intrusive magmatic rocks that today make up the monzogranitic pluton of Giglio Island. On the side of the Promontory facing the Orbetello Lagoon and the continent, the sedimentary rocks show less alteration than those on the side facing the open sea, since in the former case massive formations are very rare or even absent. This situation is repeated in many areas of the Tuscan coastline. At the same time, the islands facing the Argentario are formed by crystalline rocks, granites and serpentines. These two geological aspects of the territory have led to the hypothesis that the configuration of the area including Giglio and Argentario is determined by two magmatic intrusions, located at the Island and deep near the Promontory. According to this conjecture, the intrusions of these plutons would have caused the uplift of sedimentary strata and the formation of a massif between two parallel fault systems. This massif, raised above the surrounding earth's crust, would be in correspondence with Monte Argentario. Subsequently, an extensive tectonic phase would have caused a sinking of the surface between Argentario and Giglio, thus creating a maritime channel. The evolution of the Island of Giannutri, on the other hand, was different. The island is a structural continuation of cavernous limestone from the Franco Promontory and corresponds to a raised massif of the Tuscan-Alpine Units, which has remained exposed[14].

In any case, the material constitution of the Argentario is characterised primarily by compact limestone rock, typical of the Apennines. However, the serpentine ophiolitic rocks underlying the stratiforms of the Monte or penetrating between them metamorphosed to such an extent that a significant part of this compact limestone was converted into blackish coloured granular and cavernous limestone and crystalline marble limestone, such as that covering Punta Telegrafo. In particular, the cavernous limestone is arranged in masses rather than layers, sometimes pearly, sometimes blackish-grey in hue, with cracks and veins inlaid with spathic limestone and metal sulphides, which run through it in thin, irregular ramifications. The oxidation of these sulphides probably led to the formation of gypsum (calcium sulphate), which is present in some of the mountain's corrugations, between the cavernous limestone or in veins between traces of breccia. This particularly candid gypsum occurs on the outer flanks of the Argentario, for example near Cala delle Colonne, Cala Piatti and Cala Grande. On the slopes and higher slopes of the Promontory there is also the aforementioned calcareous-siliceous breccia, similar to the verrucano of Monte Pisano.

The base of the granular limestone and the boiling limestone would appear to be a talc and siliceous schist, another typically Apennine rock The closer this marly schist is found to the ophiolitic rocks, the more it acquires a very fine grain and a characteristic madreporic shimmer. On the west coast of the Promontory and also in the upper part of the Monte, the stones listed above have undergone injections of considerable serpentine, gabbro and other magnesian rocks. More than in the rest of Argentario, these materials are very visibly accompanied by jasper and verrucano on the seashore on the side of Cala Grande, in the Spiaggia del Pispino and near the Salita della Carpina.

In fact, the third Apennine rock present on Argentario is macigno, a type of sandstone. The distribution of boulder on the Promontory diminishes in quantity, losing its mineralogical characteristics and its typical stratification as it approaches the serpentine masses, presenting instead sometimes jasper, sometimes reddish clayey schist speckled with quartz stones, sometimes a particular quality of dark red gabbro. The fragments of plutonised limestone, madreporic schist and quartz rock formed the aforementioned mass of verrucano, consisting of breccia bound together by a siliceous material. This type of breccia covers the rialto behind Porto Ercole, on top of which stands Forte Stella and alongside which quarries were opened for the extraction of the stones needed to make millstones and grindstones. As already mentioned, Monte Argentario is part of those relief systems associated with ancient formations, predating the appearance of the Apennines. In its structure, the predominant materials are Tuscan limestones, a fact that brings it into common with the other cases of limestone hills near the Maremma coast: Monte dell'Uccellina and the hinterland of Orbetello.

The island of Giannutri also consists of carbonate formations typical of the Tuscan limestone hill. Situated south of Argentario and south-east of Giglio, Giannutri is mountainous, has no water springs and is shaped like a half-moon with horns pointing eastwards, which delimit an open gulf. Its morphology is also the result of marine abrasion on a mild anticline, but it is still characterised by very gentle contours. However, its coastline is high, marked by cliffs with a maximum height of 10 m and several inlets.

The island of Giglio, on the other hand, consists essentially of a neo-Quaternary granitic pluton belonging to the Tuscan Magmatic Province. This pluton was exhumed by erosion to form an igneous mountain system, characterised by typical phenomena of erosion and meteoric alteration. After Elba, Giglio is the largest and most populated island in the Tuscan Archipelago. It is all mountainous and elongated in shape, with two opposite ends: one stretching north, the other south-east. Moreover, on its western side is a protruding promontory that forms one of the horns of a wide inlet known as the Golfo del Campese. A little further south, also on the western side, is the former mining site of Cala dell'Allume. The Island of Giglio is mainly covered by granite rocks, with a light ash-coloured bedrock dotted with frequent black patches of mica, especially where the granite occurs in the form of large cliffs.

The islands of Giannutri and Giglio, as well as islets such as Formica di Burano and those around Argentario, form an island system included in the Tuscan Archipelago Park. In fact, Giannutri and Giglio present endemic plant species of biogeographical interest (e.g.: the Linaria capraria on Giglio; the Limonium sommierianum, widespread on both islands), as well as habitats of conservation interest (such as the coastal garigues of Euphorbia dendroides and the coastal junipers of Juniperus phoenicea subsp. turbinata at Giannutri) and undisturbed cliffs where rare bird species nest (such asthe Corsican seagull at Giglio and the greater shearwater at Giannutri)

Similar to the stretches of Tuscan coastline along the mainland, Argentario and Giannutri are also affected by karst phenomena of the hypogean and epigeal type. Some of the caves derived from such karst phenomena are only accessible from the sea, such as the Grotta del Turco along the Costa della Cacciarella and the Grotta Azzurra at Cala dei Santi, both along the perimeter of the Argentario Promontory. There were also water springs on the Argentario slopes, some of which gushed from the less steep slopes, i.e. from the north-west and east sides. Originally, the richest of these springs was the Fonte di Sant'Antonio, which gushed out near the Nunziatella and flowed down into the Orbetello Lagoon, crossing Terra Rossa and skirting some ancient ruined aqueducts. We also note, near Porto Ercole, residual nuclei of mobile dune at Cala Galera and a wetland area behind the dunes along the rocky coastal slopes.

As far as flora is concerned, the northern and eastern slopes of Monte Argentario are mainly covered by ilex groves and, secondarily, by mixed woods. The latter may consist of sclerophyll and broad-leaved trees or, in the impluvial areas, of humid ilex groves with laurel, constituting important habitats of Community interest. In addition to the holm oak, therefore, tall trees typical of the area also include: elm, turkey oak, oak, ash, chestnut, sabina, carob and lesser palm. As for local shrubs, in addition to the laurel mentioned above, we have: lazarus, lentisk, albatross, myrtle, rosemary, nerion oleander, honeysuckle, various types of filaria and cytisus. Rare plant species also grow on the limestone cliffs of Monte Argentario, such as: the fern Phyllitis saggittata, on rocky outcrops with driftwood; the Centaurea paniculata var. litigiosa, an endemism exclusive to Monte Argentario. Around the cliffs, there are also various types of American agave and annual medicinal plants. Rare vegetable and animal species are linked to the thickets and garigues: among the former we can count the Cneorum tricoccon, a shrub found in Tuscany only on the slopes of Monte Argentario, on the Island of Giannutri and on the Island of Montecristo; among the latter the Sylvia sarda and the Sylvia conspicillata, nesting near the Argentario Promontory and the Island of Giglio. In any case, the local vegetation is in continuity with that of the Tombolo di Feniglia, which we recall is affected by the characteristic pine forest with a prevalence of Pinus pinea and the undergrowth of Mediterranean maquis, both under the protection of the 'Duna Feniglia' Protection Forest Reserve.

The current terrestrial fauna in the Monte Argentario woods, originating in the Orbetello countryside, has been able to colonise the Promontory precisely by crossing the Tombolo di Feniglia and the Tombolo di Giannella. Essentially it consists of hares, porcupines, roe deer and wild boars[15].

5.1.3 Former district of Porto Longone

Originally, the town of Porto Longone - today Porto Azzurro - was formed at the bottom of a breast bordering a beach along a vast gulf on the Island of Elba.

Situated south-west of the coastal town of Piombino on the Tuscan coast, Elba is the main island of the Tuscan Archipelago. The shape of a tripartite mountain massif, which advances with a branch to the west and, on its way eastwards, divides into two other branches. On the eastern side, one branch proceeds northwards to Capo Vita, the other southwards to Monte Calamita and the Cape of the same name. The three branches are connected by subordinate hills that, at the points of greatest depression, form deep, narrow valleys. The latter frame the frequent sea basins on the northern and southern sides of the island. Thus, Monte Capanne to the west and Monte Volterraio in the centre form the base, while Monte Calamita forms a front to the south and Monte Giove forms a front to the north. The highest point is on the summit of Monte Capanne, which rises 1,019 m above sea level. It is the highest and most massive of all those in the Tuscan Archipelago and alone constitutes the westernmost part of Elba, between Marciana Marina facing north and Marina di Campo on the opposite side. The island is not crossed by any rivers, except for small streams, many of which are fed by perennial, drinkable springs, except for those that gave their name to the town of Rio, where the saline-ferruginous waters of the same name flow.

Initially, the marina of Porto Azzurro was bordered to the east by Capo San Giovanni and to the west by Forte Focardo, built on the extreme tip of the inlet. Another military construction, Forte Longone, rises above the prominence of a promontory at the entrance to the gulf.

The Island of Elba is part of a macro-zone that has gone through all the phases of Tuscan geological history, even though it is located in the spatially most backward band of the Apennine orogeny. Three great underground plutons are recognised in this macrozone, the thrust of which determined the formation of the Poggio Ballone massif and the Colline Metallifere on the continent, as well as Monte Capanne on Elba. The chronological order in which the three magmatic bodies were formed is evident: the oldest pluton is Monte Capanne, which is totally exposed; the most recent pluton is the Colline Metallifere, as it is completely covered by sedimentary rocks; temporally, Poggio Ballone is placed between the other two, as magmatic rocks sometimes outcrop on its flanks.

The islands of the aforementioned macro-zone, orographically, show reliefs resulting from intense erosion on hard rocks, with the exception of Pianosa, where hill forms prevail on neo-Quaternary deposits. As already mentioned, large hilly areas are distributed over a large part of the Island of Elba: in the eastern sector, between Cavo and Capoliveri, we find Hill forms with gentle slopes, on Ligurian Units and Tuscan Units; the central sector of the Island, on the other hand, is prevalently constituted up to the slopes of Monte Capanne by rocks belonging to the Ligurian Units, interspersed with outcrops of neo-Quaternary magmatic rocks, which form steep slopes. At Capo Calamita and along its promontory, Palaeozoic rocks outcrop, which are part of landscapes that can be traced back to the Collina on siliceous soils. The western part of Elba shows typical volcanic mountain features, similar to the island of Montecristo. On Elba, there are also flat areas of modest size, typologically ascribable to the High Plain and associated with the Coast with dunes and cordons. A particular case of these plains is the Mola district, which has residual wetlands contextual to the system of the Island's backdune depressions[16].

As far as the geological constitution of the area is concerned, the eastern coast of the Island of Elba is formed by Verrucano, starting from Fornacelle up to Monte Calamita. In correspondence with Monte Arco, the verrucano alternates with large banks of saccaroid limestone and calciscrete. Porto Azzurro, Forte Longone, Capo San Giovanni and its adjacencies to the north (towards Monferrato) and to the west (almost as far as Acquabona) lie above such metamorphosed terrain that, although a sedimentary origin can be identified, it is difficult to determine whether it belonged to the macigno or verrucano formation. The Jurassic limestone is not well characterised on the Island of Elba: near Rio, the cavernous limestone abuts the verrucano, while west of Monte Fico and Monte Arco, between Acquabona and the Golfo Stella, limestone masses appear, cavernous in some places and saline in others. The most developed formation on the Island of Elba is cretaceous, represented by alberese and macigno, similar to the Tuscan coastline. The two rocks make up the bark of the mountains not only in the eastern part of the island, but also in its central part, going in the direction from north to south between Portoferraio and Capo di Fonza, running from east to west from Monte Orello to Sant'Ilario. In this area, limestone predominates, with the exception of Monte Orello, which is covered by alberese limestone.

There are three types of igneous rock on the island of Elba: serpentine, granite and ironstone. The serpentine rocks can be divided into three almost parallel series from north to south: the northernmost from the Valle di San Martino to Porto Azzurro; the second from the Grotte and Portoferraio to Capo Stella; the third from Marciana Marina to Marina di Campo and Ripa Nera. As for the granites, they are arranged in a west to east direction, starting from Monte Capanne in the east and continuing in large granite dykes, which cross the boulder mountains in the central part. These granite dykes end at Monte Calamita and at Capo San Giovanni (near the eastern beach of Porto Azzurro), in the form of large wedges or strands. As for the iron rocks, it has been hypothesised in the past that they are the product of iron injections, which are abundant in the eastern part of the Island of Elba. There, the oligist iron branches off into very large veins that intersect each other, forming a network from which, again according to the above-mentioned hypothesis, the mines of Rio and Capo Pero would have drawn before their closure (on Elba, in fact, there are historically numerous sites of vast mining and quarrying basins, now almost completely inactive). These seams just mentioned altered and plutonised the limestone and sandstone rocks near the Torre di Rio, Monte Calamita and Terra Nera. Iron injections often converted the compact limestone into saline marble and cavernous limestone: sometimes these turned into ilvaite, also known as yerite; sometimes they changed into some species of grovacca, amphiboles, absesto and talc. In other circumstances, the stratiform masses of verrucano are traversed by large strands of oligist iron, which in the upper schist divide into a multitude of veins as at Cavetta di Capo Pero. In other locations, such as Capo Calamita, the metamorphosed layers of boulder were penetrated by granite veins, which at Capo San Giovanni are so numerous that they form a network. This phenomenon is repeated in other places: in the Gulf of Procchio; in the marly soil of Enfola along the marina of Portoferraio; in the serpentine and red gabbro tip of the small Olmo Promontory, near Marciana Marina; in the eastern part of the island, between Marina di Campo and San Pietro, where an ophiolitic mass is interpenetrated by granite veins and veins[17].

Like other islands in the Tuscan Archipelago, Elba is characterised by a varied Mediterranean plant landscape. First of all, its mountains have the typical characteristics of Mediterranean mountain relief (e.g. Monte Capanne, Monte Calamita, Monte Capannello and Cima del Monte). Other vegetation features are: thickets and garrigue along the rocky coastal environments; rocky outcrops; broadleaf woods, such as the chestnut groves on the northern and western slopes of Monte Capanne; sclerophyll woods and high sclerophyll thickets, such as the mature ilex groves between Rio dell'Elba and Cavo; cork oak woods; plantation pine forests. Other important elements are the small wetlands of Mola and Schiopparello, as well as the coastal dune system of Lacona, the only case of a dune system in the entire Tuscan Archipelago together with that of Cala Giovanna on the island of Pianosa. Elba is also home to various plant species of phytogeographical or endemic interest, such as Limonium ilvae, Viola corsica and Centaurea ilvensis. At present, forest exploitation on Elba has waned to the point of being sporadic, and the ageing processes of the stands tend to turn the woods into transitional forests. This situation has mostly positive effects from a naturalistic point of view, but these are not always accompanied by desirable consequences from a management and ecological point of view. After centuries of exploitation, in fact, the woods on the Island of Elba were almost suddenly deprived of any form of supervision and control. Today they appear rather unstable from an environmental point of view, also in relation to the impact of their colonisation by wild boar and mouflon, introduced for hunting purposes since the 1960s[18].

5.1.4 Former Principality of Piombino

At the time of the existence of the former Principality of the same name, Piombino was a small maritime town with a roadstead and a navigable canal, as well as two fortresses and walls. In the early 20th century, however, most of the walls were demolished to facilitate urban expansion. The original historic core of the town is located on the southernmost tip of the Piombino Promontory, formerly known as the Promontory of Populonia. To the north-east of the historic centre is the Old Port of Piombino (originally known as Porto di Falesia and then Porto di Faliegi), while to the south-west is the stretch of sea separating the city from the Island of Elba, known as the Piombino Channel.

From a geological and geomorphological point of view, the

Piombino Promontory is in the same macrozone as the Island of Elba. Its formation therefore dates back to the period of the Apennine orogeny, but it occurred in one of the most distant areas among those involved in this phenomenon. We can therefore also find evidence of all phases of Tuscan geological history in the Promontorio di Piombino. The development of the valley bottoms and plains was governed by the general subsidence trend of the Tuscan coastline and the eustatic movements of the sea level in the Pliocene and Pleistocene. The Promontory, made up of Tertiary and Pre-Tertiary rocks, is an offshoot of the continent that emerged as an island and was connected to the latter by a bench cordon, which connected it to the area where San Vincenzo now stands. Sediments deposited by the rivers filled the space that was and still is created in the areas of greatest subsidence. Therefore, the alluvial deposits of the Cornia River contributed to the formation of the Promontory, so we can consider a part of the local plains as constituted by overflow basins. The rest of the plains is configured as High Plain areas, formed by recent or active conoid systems and travertine outcrops of late formation.

The hydrographic network is intricate, but has discontinuous stretches with frequent closed or semi-closed basins. If the relevant reclamation work had not been carried out, the tendency to sink would keep much of the Cornia coastal plain in a damp state. Extensive coastal dune systems are typical of subsiding coasts and, in these cases, tend to be accompanied by backdune wetlands. After land reclamation, few residual retrodunal wetland systems

remain on the Piombino Promontory, such as those at Rimigliano and near the Orti del Bottagone. At present, the effects of the subsidence process are amplified by an increasingly massive exploitation of groundwater for agricultural, industrial and civil purposes.

One of the highest points of the Piombino Promontory and the territory of the former Principality is Mount Massoncello, 286 m above sea level. The small mountain group located between Porto Baratti to the north and Piombino to the south is formed of grey and cerulean macigno, with thin layers of shale (bisciaio). Above this terrain are the remains of the ancient Etruscan city of Populonia and modern Piombino. As already mentioned, the rest of the former Principality is covered by alluvial soil, pebbles, gravel and other detritus dragged along the shoreline by the waters of the Fiume Cornia and the Fosso della Corniaccia, as well as by the ditches that descend from the Campiglia hills. In the Rimigliano Lido there is a recent tuffaceous conglomerate, where the arenes slowly agglomerated with shells by means of a calcareous binder.

Until the 1830s, a significant portion of the territories of the former Principality was marshy and included Lake Rimigliano and at least three marshes: the first, rather vast though of varying limits, was the Paulde di Piombino to the north of the town of the same name, fed by rivulets flowing down from Campiglia and the river Cornia; the second, smaller, was the Torre Mozza marsh, fed by the Valnera stream (now reduced to a ditch), which descended towards the coast between the mouth of the Fosso della Corniaccia and Torre Mozza; the third was the Palude dell'Altura, so called because it was located on land at a higher altitude than the surrounding countryside.

Interventions aimed at reclaiming the area were implemented from 1828, on the initiative of the last Grand Duke of Tuscany Leopold II of Lorraine, mainly using the method of land reclamation by filling. In 1831, Leopold II entrusted Cavaliere Commendatore Alessandro Manetti with the direction of the reclamation works in the Piombino district, which began in 1832. The hydraulic works directed by Manetti included: the alteration of the course, basins and mouth of the Cornia; the draining of the Palude dell'Altura; the destruction of the Rimigliano Lake and the conversion of its bottom into cultivable fields. The operation, which was repeatedly subject to delays and interrupted due to both technical difficulties and the geopolitical changes that led to the Unification of Italy, was only concluded after the Second World War, when the mouth of the Cornia, once inside the wetland, was taken to the sea at Torre del Sale.

The gradual reclamation of the Val di Cornia and the new conformation of the Piana di Piombino allowed the urban centre of the same name to industrialise and expand. What considerably accelerated the development of Piombino was the impulse given by the iron and steel industry, which benefited from iron from the mines on the Island of Elba. After a few attempts that began in 1864, Piombino's ferrous metallurgy sector gained considerable momentum in 1891 with the opening of the 'Magona d'Italia' plant, intended for the manufacture of tin-plated iron bands. Later, with the construction of the blast furnaces and steelworks of the Ilva Company and other plants, Piombino became one of the most important centres of the Italian iron and steel industry[19].

The local stretch of the Tuscan coastline includes both dune complexes (among the most important, those of Rimigliano and Sterpaia) and rocky complexes such as the Piombino Promontory, often connected with the residual wetlands of the backdune areas, constituting evidence of marshy coastal landscapes destroyed by land reclamation.An example of the latter category is the aforementioned Orti del Bottagone Marshes, an area of high naturalistic interest due to the presence of stretches of water and marshy habitats, both brackish (in particular salt marshes) and dulcic aquatic (especially reed beds). This area also serves as a resting and wintering area for various aquatic bird species. On the other hand, in the stretch of coast near the Gulf of Sterpaia, there is a pine forest on sand dunes that is unfortunately in a critical condition, as it is exposed to the spread of phytopathologies and above all to the consequences of coastal erosion. Like the Gulf of Sterpaia, the Gulf of Baratti and the southern stretch of the coastline near Rimigliano are also subject to erosion processes of their sandy coastal strips, often associated with the aforementioned subsidence phenomena, also favoured by the extraction of water from the coastal water tables. The latter, in particular, has accelerated as a result of the increase in demand related to accommodation activities. Along the Piombino Promontory there is an extensive stretch of rocky coastline of high naturalistic interest, on the one hand comprising an important area frequented by migratory birds, and on the other characterised in floristic terms by a residual station of Chamaerops humilis (dwarf palm) and the only station of the Asteriscus maritimus in the entire Peninsula, Punta Falcone. Moving inland, the Val di Cornia agricultural complex extends into the alluvial plains behind the coastal areas of Rimigliano and Sterpaia. However, the area has been the subject of significant interventions to protect natural resources, especially coastal ecosystems (an important example is the system of protected areas managed by Parchi Val di Cornia S.p.A.)[20].

5.2 Development of the settlement system in Prehistory and Protohistory

The following is a brief reconstructive outline of the peopling of the territory of the former State of the Presidia during Prehistory and Protohistory, in order to comprehensively describe the evolution of its settlement system from its origins. We will analyse the four territorial areas previously described - Agro orbetellano; Monte Argentario, Isola del Giglio and Isola di Giannutri; the former district of Porto Longone; the former Principality of Piombino - beginning with the Palaeolithic.

5.2.1 Palaeolithic

The oldest human frequentation in the Maremma dates back to 500,000 years ago - to the Lower Palaeolithic -and is attested by a few finds. Among these, the discovery of 799 lithic tools at Montauto di Manciano stands out. The first frequentations on the Island of Elba also date back to the Lower Palaeolithic.

As far as the Maremma is concerned, the sites with evidence dating back to the Middle Palaeolithic, more precisely to the Mousterian period, consisting of cave settlements and perhaps also open-air settlements, are much more numerous In such contexts, artefacts in flint, jasper and quartz have been found, mainly obtained using the Levalloisian chipping technique.working techniquemust have been handed down up to around 40,000 years ago among peoples dedicated to hunting, gathering, and coastal sea and lake fishing, as can be deduced from the Pleistocene terrace on the left bank of the Torrente Osa a few kilometres east of the town of Fonteblanda, perhaps also in the Grotta di Golino near Talamone and in the Grotta di Cala dei Santi, near the Argentario Promontory. In the latter, in fact, the Tyrrhenian fossil beach layer with the remains of malacological fauna and the overlying breccia fill with the remains of cold fauna - specifically, ibex from the glacial periods - contain artefacts in brown flint and jasper, as in the Grotta del Granduca near Punta degli Stretti.

On the Island of Elba, the discovery of open-air encampments attests to the frequentation of the central-eastern area in the Lower Palaeolithic period.

In the Grotta di Golino near Talamone, however, the deposits have a prevailing horizon referring to the Upper Palaeolithic, with finds consisting of micro-bullets of the Nouilles type, which can be ascribed to the evolved Cravettian period[21].

5.2.2 Neolithic

Compared to the Palaeolithic, evidence of frequentation in the lower Maremma during the Neolithic period is more nu-

merous, gathering in the upper Albegna valley and on the Argentario Promontory. Finds suggest that settlements were mainly distributed in the flat areas and on small plateaus, where there are traces of villages with obsidian artefacts - indicating intense trade - and pottery.
As already mentioned, on Monte Argentario the evidence associated with the Neolithic period is manifold: in the pine forest of the Valle degli Acquastrini, in the Valle dei Molini, at Capo d'Omo, at Punta del Pane, at Costa delle Olive, south of the Torraccia della Peschiera di Nassa, on the Piano del Pianone, at Poggio delle Piane, at Le Piane and Le Piane Alte, at Terra Rossa and east of Poggio Polveriera. The Island of Giglio and the Island of Giannutri were also affected by discoveries: as regards the latter, the sites of Grotta delle Capre and the overlooking Vigna Vecchia are worth mentioning. As far as the Island of Elba is concerned, the attestations are sporadic and of little importance, but they indicate a more stable frequentation and a rather articulated network of contacts[22].

5.2.3 Eneolithic

Finds concerning obsidian industry suggest its continuation into the Eneolithic or Copper Age as well, flanked however by evidence of the exploitation of metal knowledge. The presence of sites attributable to the Eneolithic in the Argentario Promontory was already known in 1843, the year of the discovery of skeletal remains in the Grotta di Cala dei Santi. This was followed by discoveries in the Grotta degli Ugazzi during 1860, then those inside the Grotta del Granduca at Punta degli Stretti.
Starting around 3000 B.C., the Rinaldone facies developed in the Maremma, one of the most significant cultural variants of the period, which extended into the early phase of the Bronze Age. In particular, to the material production of the Rinaldone culture belong numerous lithic arrowheads and a vascular type called 'flask vase'. In the Tuscan hinterland we come across numerous Rinaldonian sites: from the Fiora Valley to the Tuff Area, from the Rosellano area to the Colline Metallifere. As far as the Tuscan coastline is concerned, it has been recognised at Orbetello and at Gravicchio near Capalbio. In the latter locality there is in fact a burial ground with oven tombs (i.e. where the dead are placed in a crouched position) and grave goods consisting of typical flask-shaped vases, bowls and other artefacts in flint, jasper and copper. The same facies can be found in the Grotta dei Cervi and in a cave above Punta degli Stretti, both on the Argentario Promontory: in the latter, typical Eneolithic black lustre impasto pottery and a decorated olla were found. In addition, other finds of Rinaldonian origin have been discovered on the island of Giglio.
From around 2000 B.C. onwards, there was a population increase in the lower Maremma and numerous settlements, including pile-dwellings, developed. From a technological point of view, the use of the plough and storerooms of bread and metal objects became widespread. As far as the Island of Elba is concerned, the extremely rare evidence from the early and middle Bronze Age indicates that profound changes in the economic and social sphere were linked to the exploitation of cuproferous deposits.
In the lower Maremma, from around 1700 B.C., sheep-farming developed, places of worship were carved out of caves where water was present (especially in the Fiora Valley) and trade with the Aegean was interwoven, as attested by the discovery of Mycenaean pottery.
At the height of the Bronze Age, due to the phenomenon of transhumance from the mountain pastoral sites, the Apennine culture descended towards the coastal pastures. Settlements multiplied, spreading throughout the lower Maremma, leaving flint, obsidian and typical glazed and decorated pottery both on the mainland and on the islands. Along the Maremma coastline, we find the following sites: the Grotta dello Scoglietto at Monte dell'Uccellina; Scarceta, in the municipality of Manciano; and finally, near Ansedonia, the Torre della Tagliata area, the Grotta delle Settefinestre and the Grottino, in which burials with pottery have been found. Traces of numerous villages are scattered along the Tombolo della Gianella: near the Fossone; in front of the Casette di Fibbia; near the Santa Liberata beach; on the edge of the 'Laguna di Orbetello Ponente' Reserve; on the Peschiera di Nassa. In the area of the Murelli, along the Tombolo di Orbetello, there are the remains of another village, among which scrapers and siliceous tips have been found, as well as impasto pottery. On the Tombolo di Feniglia, excavation near Pertuso for the reopening of the Taglio di Ansedonia brought to light lustrous impasto vases with plastic cord decoration. Proceeding south-east, still along the Tombolo, as far as the southern end of the Taglio di Ansedonia, traces of small groups of huts with clay floors can be found.

Traces of the Bronze Age also appear very numerous on the Argentario Promontory: on the northern peak and on the western flat area of Poggio Pertuso; in the mines of Roccadoro; at Poggio delle Forche; at the Torre dell'Avvoltore; in the Grotta di Cala dei Santi; at the Fontanile delle Ficaie; at the Fontana della Ciana; at Punta delle Scorpacciate; at the Grottino della Punta di Cala dell'Olio; at Capo d'Omo; at Punta del Corallo; at the Argentiera Tower; at Cala dei Pozzoni; on the Pianone plain; at Punta degli Stretti; at Le Piane; at Terra Rossa. The various sites found on the Island of Giglio are also ascribed to the same period: on the high ground of Giglio Castello; near the Castellare del Campese; near the Pitocci; near the Porte; on the Poggio della Pagana; on the two high ground of Castelluccio; at Mortoleto; on the Punta di Campo Marino; near the Castellare del Porto; on the point north of the Port; at Punta Arenella. Fragments of vases found at Vigna Vecchia, on the island of Giannutri, would also seem to be attributable to the late Aeneolithic. On Elba, finds from the last centuries of the Bronze Age are numerous and frequent, especially on the western side of the island, i.e. Monte Capanne and Monte Giove. In that area, copper mining and working played a prominent role, as can be seen from the findings of 'hoards' of axes and ornamental objects. Other prevalent activities were sheep farming and trade with other Mediterranean peoples[23].

5.2.4 Protovillanovan

Suddenly, all coastal areas became depopulated, probably due to danger from the sea. Settlements were concentrated in a few highland positions, often already inhabited, but preferable as they were strategically safe. This led to the development of 'castellieri', which were further protected with fortified cliffs and multiple concentric circles of walls, all built dry-stone using crude megalithic techniques. Some examples of this type of settlement in the Orbetello countryside are: the castelliere of Monte Sant'Angelo, provided with several circles of walls and at the top, near the ruins of the church, a spoil with impasto pottery in the filling; the castelliere of Poggio di Capalbiaccio, the site of the discovery (near the ruins of the Tricoste Castle) of impasto pottery decorated with bundles of four grooves, flanked by large dots; the castelliere of Monteti, above Capalbio. On Monte Argentario there are the castellieri of Torre Argentiera, Torre di Capo d'Omo and Poggio Mandrioli, the latter probably equipped with double walls.

From around 1150 B.C. onwards, the rite of incineration was adopted and metal was once again hoarded, as attested by the findings at a rocky ravine at La Tradita - where a proto-Villanovan cremation tomb was found - and a quartz stone pertugio on the sea in the Campese pyrite mine on Giglio Island - a repository, possibly funerary, of bronze -. Other ripostigli have been found in various locations in the upper Albegna Valley

Giglio Island also has castellieri, called 'castellari' or 'castellucci' by the local populationthe Castellare del Campese, covered in hut plaster and fragments of impasto; the Castelluccio Nord, elliptical in shape, covered in hut plaster and with a tower on the southern side; the Castelluccio Sud, of which a large section of wall on the south-western edge of the hill has survived; the Castellare del Porto; a potential site of a castelliere at Mortoleto

Despite the presence of Protovillanovan attestations also on the island of Giannutri, the latter was too exposed and low to offer the necessary protection from the dangers of the sea, so it had to be completely abandoned.

should be noted, however, that the castling strategy just described, characterising the final period of Prehistory, did not achieve the defensive effects desired by the local populations[24].

5.3 Development of the settlement system in Antiquity

We now provide a summary overview of the development of the settlement system, during the Etruscan and Roman Ages, of the four territorial areas identified at the beginning of this Chapter.

5.3.1 Extruscan Age

Between the end of the Bronze Age and the Iron Age, the castellieri, located on naturally fortified areas, were abandoned in favour of places of similar conformation but allowing for greater expansion of the built-up area. This real upheaval of the settlement system, defined as proto-urbanisation, was at the origin of the major Etruscan cities and its most evident example was that of Vulci (located just outside Tuscan territory, currently in the province of Viterbo), resulting from the abandonment of the proto-historic centres of the Fiora Valley. Alongside the major centres, minor centres such as Poggio

Buco, Pitigliano, Sovana and Orbetello sprang up in the 8th and especially 7th century B.C., sometimes on the sites of previous protohistoric settlements. In this context, the town of Caletra stood on the site of today's Marsiliana and constituted a control point along the Albegna, since from that point the river was navigable to the sea. Caletra thus stood as a small power centre antagonistic toVulci

In the lower Maremma, the centre of greatest poleographic attraction became the lagoon city of Orbetello, whose ancient name we do not know, but which we can well identify archaeologically from the 7th century BC. Givenposition on the Tombolo of the same name and its particular environmental context, Orbetello could not be seen from the Tyrrhenian Sea and, at the same time, was almost inaccessible by land. This endolagunar defensive solution is reminiscent of the contexts and locations of other classical cities, such as the Greek Sibari, the Umbrian Ravenna and the Estruscan Spina, highlighting the rise of this settlement model.

This situation was moreoveranalogous to other centres in Etruria, whose cities were hidden from the open sea and perched on high elevations, maintaining only small sanctuaries and harbours on the coast to entertain their maritime relations, which were in any case intense. The only apparent exception would seem to be the case of Populonia, which arose early in the 8th century B.C. It was, however, located on the summit of the rugged promontory of the same name, thus far from the sea and the metallurgical activities of Porto Baratti below.

The entire promontory of Piombino, in fact, is rich in evidence of settlements, burial areas and production activities, as is the territory included in the present-day municipalities of Scarlino and Massa Marittima Populonia expanded its dominion to include much of the Colline Metallifere inland and part of the territory of Vetulonia, thus structuring a very complex political and economic system. The Tuscan Archipelago and in particular the Island of Elba, characterised by its strategic geographic position and mineral wealth, became coveted and contested prey for the major powers from the 8th-7th centuries BC. By placing the Tuscan Archipelago under its influence and securing the diversified opportunities it offered, Populonia strengthened its composite system based on agriculture, metallurgy and trade. Thus, stable Etruscan settlements arose on Elba, closely linked to Populonia and located in sites from which it was possible to control the sea ports (today's Marciana Marina and Portoferraio) and mining exploitation. Besides Populonia, other ancient settlements near the Colline Metallifere were Falesia, Vignale, Rondelli, Campiglia Marittima and Scarlino.

In the lower Maremma, only two small settlements arose close to the open sea, probably as sanctuaries and harbours: Tèlamonon the Hill of Talamonaccio and on the Poggio di Bengodi (opposite today's Talamone); Porto Ercole, with the sanctuary of the Molini, on the Argentario Promontory. We hypothesise that the coastal strip was left abandoned, as if under threat of potential danger from the sea.

All these changes in the settlement and economic system were accompanied by profound cultural and social changes. At the end of the Iron Age, incineration was replaced by inhumation(excluding the more inland areas of the Chiusi-Volterra culture), grave goods became richer and imported goods increased. This phenomenon reached its peak in the so-called Orientalizing period, between the end of the 8th century and the 7th century B.C., in which trade with the East and Greece was very intense. From the end of the 8th century, Greek colonisation brought remarkable technological innovations such as writing, the potter's wheel and new agricultural techniques.

To find vestiges of other Etruscan settlements that can be ascribed to the period between the 7th and 6th centuries B.C., we must go inland, behind the coastal lagoons and especially behind the first hills. These were small settlements of an essentially agricultural character along the valleys of Albegna, Castione, Radicata and Chiarone, probably ruled by local aristocracies. Notable examples are at San Donato, at Poggetti and Doganella, at Magliano, at Marsiliana, at Torrettina, at Polverosa, at Parrina, at Binetti, on Monte Nebbiello, at Radicata and at Serpentara.

With the beginning of the advanced phase of the Iron Age, a progressive expansion began in the territory and an increase in the number of settlements allocated around the primitive nuclei of Caletra, Orbetello and Pescia. The maximum area reached in this phase of expansion of anthropisation appears to have been reached in the first half of the 6th century B.C.. At that time, the formation process of Etruscan cities was being completed and Vulci showed strong economic and cultural growth. In fact, the urban centre was importing goods, exporting wine produced in its own countryside to the western Mediterranean, producing luxury goods, and was a transit point for the latter to inland and northern Etruria. Towards the end of the century, all the smaller settlements began to depopulate, both near the coast and inland. On the other hand, there was a demographic increase and a strengthening of the civic and defensive structures of the large urban communities, accompanied by a need for urbanism that induced the rural population to move to the towns of Vulci and Roselle, as well as Orbetello. This situation of stagnation of the rural areas, which lasted for the 5th century B.C., was similar not only to that of other territories in Etruria, but also to the state of many areas of Magna Graecia. Between the end of the Orientalising Age and the beginning of the Archaic Age, the major Etruscan cities tended to provide themselves with an outlet to the sea and to found port settlements, as evidenced by the harbour structures found in the historical centre of Orbetello and the traces of frequentation of the port of Tèlamonassociated with this historical period

After the battle of Cumae in 474 B.Cbetween the Etruscans and Syracusans, trade routes began to favour the Adriatic Sea. The loss of its primacy, with the consequent urgency to unlock the availability of resources in the territory and to open or strengthen trade with inner Etruria, may have been at the origin of Vulci's systematic elimination of the minor centres of the lower Maremma. Regarding the town of Caletra, in fact, no records remain after the second half of the 6th century B.C. and this suggests its destruction behind a military intervention by Vulci. Similarly, with reference to the period between the end of the 6th and the first half of the 5th century B.C., the total absence of evidence on other peripheral centres in the Fiora and Albegna valleys - such as Saturnia, Poggio Buco, Orbetello, Tèlamon, Pitigliano and Sovana - leaves room for the hypothesis that Vulci massively attacked these towns as well. The fall of Caletra corresponded with an increase in the scattered settlement in the countryside on the opposite bank of the River Albegna, in the vicinity of present-day Magliano in Toscana.

The restructuring of the territory of Vulci was completed with the formation and expansion of Kalousion, a large settlement in the lower valley of the Albegna (about 4 km from the river mouth), in the present-day locality of Doganella. Probably founded as a colony of the Agro Vulcente, Kalousion developed from the end of the 7th century B.C. until the 5th century B.C., when it was conquered by the Romans. This settlement was characterised by an atypically large extension (about 230 ha, almost twice the size of the city of Vulci), a city wall and a rather regular urban layout, characteristic of newly founded cities, within which cultivated fields and pastures were also included. Given the absence of local aristocracy in relation to this period, it is assumed that Kalousion society was egalitarian, unlike the major Etruscan cities. The exchange between the city and the countryside was governed by patronage relations, however beneficial to all involved, as the rural community could enjoy its surpluses, while the urban population profited from trade and crafts (ceramic kilns, metallurgical activities and cloth weaving). The acceleration in the expansion of the rural settlement of Kalousion was probably made possible by the reclamation of land and the development of agricultural organisation, while Tèlamon functioned as a sea port, useful for trade.

Also in the 5th century, the Island of Elba was affected by a phenomenon of militarisation, associated with the creation of a control system over local resources, coastal and insular supply basins, maritime traffic but also the circulation and distribution of goods. Consequently, highland fortresses became key elements of the Elban landscape in the Classical and Hellenistic Ages, not only tracing the role of their continental counterparts, but relating to them.

During the 4th century B.C., there was a gradual demographic increase in the countryside, with the appearance of small settlements and, more often, small necropolises, thus reconstituting the scattered settlement system that had been rarefied in the previous century. This phenomenon, however, did not represent a general recovery, as the economic conditions of the cities remained generally good, even though Etruria was threatened by many external dangers. As anticipated, the Syracusans and Carthaginians had controlled the routes and trade since the 5th century, as they had robbed the Etruscans of the maritime supremacy for which they were known in previous centuries. Moreover, the pressure exerted from the north by the Celts anticipated their migratory waves towards the south (which would only be definitively blocked by the Romans in 225 BC). At the same time, we must emphasise that the deep as well as physiological divisions between the Etruscan cities constituted a further element of internal weakness.

Also during the Hellenistic Age, therefore, hill fortresses arose in many territories of the lower Maremma, placed in strategic positions on the coast or on the internal borders. In the territory of Vulci, the fortified centres of the 4th century BC were either newly founded or built on the ruins of a fallen city, such as Saturnia, Tèlamon or Orbetello. During the second half of the 4th century, for instance, Orbetello was provided with walls and saw its settlement develop. The town had become a phrourion (i.e. a fortified port of call) located on the Etruscan coast and along a major trade route, which ran from Pyrgi and Tarquinia to Populonia, the Island of Elba, Corsica, Genoa and Enserune. Through this trade network, goods from Magna Graecia, Campania, Latium and Etruria were distributed. The markets involved in this flow enjoyed substantial economic prosperity until the middle of the 3rd century B.C. and the small sanctuary found behind Porto Ercole was probably associated with a secondary port of call pertaining to this shipping route[25].

5.3.2 Roman Age

The Etruscan territories of the lower Maremma were conquered by the Romans between the taking of Roselle in 294 and the subjugation of Vulci in 280 BC. The subjugated Etruscan cities had to submit to particularly punitive alliance treaties, which provided for the confiscation of vast portions of territory. Subsequent interventions by the Romans profoundly altered the settlement system, with consequences for the landscape. The foundations of the colonies of Cosa (273 B.C.), Saturnia (183 B.C.) and Heba (around 150 B.C.) entailed a redefinition of a large sector of the territory that had previously belonged to Vulci, which was carried out by means of centuriazione. The Romans also built two major road routes: the main north-south route consisting of the Via Aurelia and the Via Aemilia Scauri, work on which began in 241 B.C.; the Via Clodia, laid out in 181 B.C. in the area of Sovana. The communication works also included a minor road network and port infrastructure, in particular the portus Cosanus. The Roman road network was confirmed by milestones and mansionesfarms along the routes

The surviving, impoverished Etruscans had to retreat to the old cities or to the margins of the colonised territories. However, Etruscan culture survived until the 1st century B.C., as demonstrated by the large fictile pediment of the temple of Talamonaccio, dating back to more or less the middle of the 2nd century B.C., depicting in relief a scene from the Seven against Thebes.

The Latin colony of Cosa, whose site was located near present-day Ansedonia, took over as the demographic pole of the lower Maremma in place of Orbetello, which thus took the name Sub-Cosa or Succosa. Substantially, however, settlement trends did not change, as the phenomenon of urban centralisation in a site located on high ground and surrounded by powerful defensive works persisted, despite the fact that it was close to the Tyrrhenian Sea. Cosa was in fact an outpost on the stretch of the Tuscan coastline controlled by Rome and served as a bridgehead for the conquest of northern Etruria and Liguria. Its citizens were Romans, interested only in the limited strip of centred farmland that surrounded it, and therefore completely unrelated to the population of the Vulcan territory. As a frontier bulwark, therefore, Cosa's importance rapidly declined from the middle of the 2nd century B.C. since, after the conquest of Cisalpine Gaul, the Romans considered Etruria a pacified inland territory. It was thus destined for agrarian exploitation by the surviving local aristocracy and then, progressively, on behalf of the Roman senatorial class. The new reorganisation of land ownership entailed latifundist exploitation and the conversion of the countryside into specialised plantations entrusted to teams of slaves, organised in villae rusticae, each administered by its respective vilicus, often on behalf of a dominus not resident in the same place. As far as

northern Etruria is concerned, its conquest by Rome took place in the first decades of the 3rd century B.C. and had two main consequences: on the one hand, a restructuring of the road network, similar to what happened in the lower Maremma; on the other hand, an intensification of metallurgical activities, characterised by very high peaks until the 1st century B.C..Both of these phenomena caused an increase in the local demand for timber, which was followed by an early impoverishment of the woodland cover in the Val di Cornia area and the establishment of massive coal production. In particular, the latter left indirect but easily identifiable toponymic traces such as the place names 'Rimigliano' and 'Milia', dating back to the powerful Roman family of the Aemili Scauri, who were responsible for the construction of the consular road of the same name and economically involved in coal production. In the lagoons of the northern part of the Tuscan coastline, the

population remained intense and scattered from the Etruscan Age until the early Imperial Age, and then simplified and polarised into villages in Late Antiquity.
On the Island of Elba, the first phase of fortresses came to a violent end between the beginning and middle of the 3rd century B.C., due to an attack by the Carthaginians or more probably the Romans (the latter were in fact already subduing northern Etruria). Similarly to what happened on the mainland, the working of iron on Elba underwent an abrupt and disorganised acceleration, accompanied by considerable increases in the exploitation of local mines and woods. Towards the end of the 2nd century B.C., the abandonment of fortresses was matched by the foundation of new permanent settlements on the island's meagre plains and, consequently, ironworking activities were joined by agricultural activities.
After the upheavals caused by Hannibal Barca's descent, there was a phase of recovery in Etruria, in which small landowners were able to take advantage of the slavery techniques already widespread in the more developed regions of the Mediterranean, especially for the profitable cultivation of vines and olives. There is no certain evidence of an agricultural crisis in Etruria, but the most probable dynamic regarding the disappearance of small landowners in the area must have been that of a social class crisis, with the progressive decay of its members from the status of military to that of urban plebs. The Roman state guaranteed the absence of inland conflicts and pirate raids from the sea. This peace and the lushness of the cultivations constituted favourable conditions for the decentralisation of anthropisation and therefore, towards the last quarter of the 2nd century B.C., the settlement system in the lower Maremma began to expand over all the fertile plains and all the coasts, tracing the situation already seen during the Bronze Age. From being a source of danger, the Tyrrhenian Sea had become an opportunity to set up an export network, especially of wine - the main local product - but also of oil and other goods derived from collateral activities (such as amphora furnaces, linked to wine consumption, the brick industry and fishponds). In fact, the earnings from investments in the wine-growing sector were the basis of the wealth of the Sestii (who had found a flourishing market for their wine in Gaul, especially through the Rhone Valley) and the Domizii Enobarbi (at that time owners of such a vast number of latifundia in the Argentario Promontory, on the Island of Giglio and elsewhere, that they were able to raise an entire army with men in their employ), families who built the finest villae urbanae in the Cosanian countryside, later imitated by other large landowners during the last half-century of the Republic. At the beginning of the 1st century BC, the war between Marius and Sulla led to the destruction of several urban centres, including Saturnia and also the mansio of Telamon, with its sanctuary. During the Sillan Age or shortly afterwards, towns of Etruscan origin such as Succosa or Roman colonies such as Cosa met their end. There was thus an upheaval in demographic evolution, which sustantiated in an exodus from highland or otherwise fortified centres to the open countryside. The latter was populated according to radically different settlement needs, in function of a different socio-economic framework, dictated by changes in labour and production relations. As far
as Elba is concerned, in the 1st century B.C., mining activities reached their highest levels of production, only to decline sharply and then cease due to a series of concomitant factors: the Romans' acquisition of new mines in Spain, Noricum and Sardinia, which flanked those on Elba; the appearance of villas in the island's landscape; and the Roman Senate's prohibition of mining on Italic soil. At the end of the 1st century B.C., sumptuous seaside villas were built, such as the one at Linguella in Portoferraio, the one at Le Grotte and the one at Capo Castello. The only urban centre attested to dating back to the Roman era was the town of Fabricia (as it was called by 18th century scholars), found beneath the present-day centre of Portoferraio.
In the Orbetello countryside, the villas of the republican period stood on sites of great landscape interest, usually on slopes overlooking the sea, remodelled into large terraces by cryptoporticus and bastions. There were several villas at the foot of the hills overlooking the Orbetello Lagoon and, therefore, in relation to the Via Aurelia or its side roads, especially the one that connected with the Via Clodia from Subcosa to Saturnia: Villa delle Grotte, so called because of its cryptoporticus; the rustic Roman villa of the Sette Finestre, built on an artificially flattened and enlarged hill; the Villa delle Colonne or Sughereto di Ballantino; the villa above the Taglio d'Ansedonia; the Casalone del Rosi; the villas near the Provinca and Le Monache; Casal Marotti; the villa at Monte Alzato; the villa at Burano. Scattered settlement from the Ro-

man period also appeared early on the three tombolos, especially on the southern side of Giannella, near the Santa Liberata beach and the Peschiera di Nassa. As far as the Tombolo di Orbetello was concerned, anthropisation extended as far as Madonnella, while on the Tombolo di Feniglia it extended along the Pertuso, both at the east and west ends. In the Argentario Promontory the following areas were occupied: the northern sector of Poggio Pertuso; the Sgalera beach; Poggio delle Forche; the Valle degli Acquastrini; the site of the Argentiera Tower; the site of the Calvello Tower; the Olive Coast; the Piane Alte; the Piane sector west of Poggio di Terra Rossa; the Fattoria di Terra Rossa; the plain east of Poggio della Polveriera. On the two sides of Giglio Island stood, in suggestive opposing positions, a villa at what is now Giglio Porto and one on the site of Castellare del Campese.

Around 100 A.D., the crisis of the slave villas led to changes in ownership and cultivation, while seaside villas spread along the coast. According to epigraphic documentation, between Nero and Hadrian the imperial private estates took over much of the coast, at the expense of the ancient senatorial class. In the Agro orbetellano villages increased in number; villages sprang up near Talamone, near the Torretta locality, at Camarrone, near the mouth of the Albegna river (where the Torre delle Saline stands), at Parrina and at Tagliata. On the Tombolo di Giannella, anthropisation consolidated along the Santa Liberata beach and near the Peschiera di Nassa, and also spread to the Fossone and Villa Barabino. Along the Tombolo di Orbetello arose the Villa della Madonnella, overlooking the Laguna di Levante. On the Tombolo di Feniglia a dozen or so settlements arose between Taglio d'Ansedonia and Pertuso, plus nine villas overlooking the Laguna di Levante with their fishponds and placed at intervals of 300-500 m apart: this was a typical complex of villae marittimae intended exclusively for holidaying, lacking the corresponding villae rusticae and other activities apart from fish-farming - for the needs of a refined cuisine for the wealthy classes -and hunting in the woods behind, in accordance with a lifestyle that was spreading during the Early Empire

Manyvillae also sprang upin the Argentario promontory during this period, almost all of them close to the coast: between the northern sector of Poggio Pertuso to the beach of Sgalera; at Poggio delle Forche; at the Caves of Porto Ercole; near the site of the Tower of the Avvoltore, overlooking the Cala dei Santi; at the Fontanile delle Ficaie; near the Fountain of the Ciana; in the Valley of the Acquastrini; in the Valley of San Mamiliano; near the site of the Tower of Capo d'Omo; in the Cala di Porto Santo Stefano; in Bausani; on the Colle dei Muracci; near the site of the Calvello Tower; in the Cala del Pozzarello; in the Cala dei Pozzoni; near the Villa di Santa Liberata; at the Poggio delle Piane; in the Piane; near the site of the Torraccia della Peschiera di Nassa; in Terra Rossa; near the Fortino di Pian di Croci; in the Poggio della Polveriera. In the heights of the hinterland of the Promontory there were only modest isolated agricultural installations, with the exception of the settlement on the site of the Argentiera Tower, which must have had some specific function. On the Island of Giglio, villae were scattered along the coast and on the first slopes: on the Campese side, they were present at Punta Fenaio, at the Fontuccia orchards, near the site of the Castellare del Campese Tower, on the Faraglione del Campese, at the Pitocci, near La Vena; as regards the surroundings of Giglio Porto, there were findings at Punta Arenella, at Porto and near the Castellare. On the island of Giannutri, which was once again frequented, there were two villae overlooking the opposing gulfs of Spalmatoio and Cala Maestra: the first had port facilities, the second had stately quarters and extensive services. These buildings, probably forming a single residential complex, were connected by a road and had a lighthouse located on the small rise of Monte Mario, which stood between the two sites.

In the course of the Empire, the favourable conditions that allowed for the free expansion of the settlement system in pleasant but undefended positions disappeared. From the end of the 2nd century A.D., settlement in the countryside began to thin out and many villas were abandoned. The large plantations, still profitable in the 1st century A.D., were gradually abandoned in the course of the 2nd century A.D. and transformed into extensive production. There was a gradual return to the fallow (novale) tradition and the rotation of land between cereal and pastoral farming. Gradually, the original centurial mesh of the 3rd century B.C. and the rows of late-republican cultivation were replaced by untidy latifundia. As the name 'insula Matidiae' attributed to the Argentario suggests, at this point the ancient Cossan territory must have been incorporated into the imperial private estate. From the Severian Age onwards, the cultivated and inhabited strips of land began to gradually shrink between the hills that had become overgrown and the swamped coastline due to the lack of maintenance of land reclamation works. Urban centres were decaying: Cosa was reduced to a centre of limited civil life, while Heba and Saturnia were abandoned between the 3rd and 4th centuries AD. Only a few farms continued to survive in the shadow of the ancient villaeoften abandoned. The invasion of Alaric's Visigoths induced most of the population to abandon the areas near the Via Aurelia and the roads, infrastructures described in the 5th century AD by Rutilio Namaziano as impassable and too dangerous.

On the island of Giglio, on the other hand, given the considerable distance from the continent and the protection offered by the local forests, a settlement developed in continuity between Porto, the Vena and above all the Castellare del Campese During the sack of Alaric, therefore, the island was able to cope with the emergency and accommodate the fugitives from Rome. Only monastic communities took refuge on the more distant and inhospitable islands, as in the case of Capraia, documented by Rutilio[26].

5.4 Development of the settlement system in the Middle Ages

During the Middle Ages, there was an alternation of diametrically opposed settlement solutions, but with similarities to previous historical phases, such as the castellieri and the Roman villae. This 'seesaw' was a function of the historical factors that conditioned the environment, above all the advantages and disadvantages deriving from the sea, which could make the Maremma attractive or inhospitable from time to time.

5.4.1 From the Early Middle Ages to the Aldobrandeschi

The process of Christianisation of the communities in the Maremma was completed between the 5th and 6th centuries. The Byzantines resisted the Lombards by building fortresses in the coastal strip, such as at Cosa and Talamonaccio. This fragile defensive system, however, was unable to contain the invasion and, between the end of the 6th and the beginning of the 7th century, the Lombards occupied the entire lower Maremma. Due to the fall of the Roman Empire, the barbarian invasions and the reduction of trade, the population of Elba left the island, where only a few monastic communities remained. Around 610, the Tuscan Archipelago was taken from the Byzantines by the Lombards and, after the defeat suffered by the latter at the hands of the Franks, it passed to the Papacy through a donation.

During the 7th century, the Roman-based settlement system of the Cossano territory was disintegrating, while the presence of malaria in the area was recognised for the first time. The ruins of the villae were sometimes recovered by religious congregations to found the seats of their cenobia, and sometimes they were precariously occupied by communities of shepherds. At the turn of the
7th to 8th century, open settlements (curtes), small villages and a few scattered houses developed, far from the coast and tending to be sheltered on high ground. During this phase, the economy was basically sylvo-pastoral, with some modest areas devoted to agriculture. From the
surviving records, it can be deduced that very few settlements survived during the Early Middle Ages without, among other things, being certain that they were not occasional and limited in time. Hermitages and monasteries in general were more stable, since they were sheltered by woods and isolated on elevated areas, such as the monastery of Sant'Angelo (near the castelliere on the hill in front of Orbetello) and that of Binetti on the mainland, those on Monte Argentario and on the islands, such as the monastery of Punta Scaletta, which settled in the Villa of Cala Maestra on the Island of Giannutri. Probably, Succosa and the Cossan port near the Church of San Biagio had some function as Byzantine naval bases, especially for the routes to the Island of Elba and Luni. Talamonaccio instead became a Longobard settlement.

The name Orbitellum appeared for the first time in place of Succosa in 805, in the text of the donation, by Pope Leo III and Charlemagne, of all the territories of the former maritime Etruria to the Abbey of the Three Fountains, through the institution of Privilegium concessionis. In the relevant diploma, engraved on a copper plate, explicit reference is made to a 'fortress' called Orbitellum and 'surrounded by a pond'.

Populonia became a diocese in the 5th century, but was depopulated in the 9th century due to a pirate raid and, consequently, the episcope was transferred to Massa Veternensis (the name by which the Romans called the present-day Massa Marittima). At that time, the frequentation of the lagoon areas in the Piombino peninsula never stopped completely, but it became increasingly rarefied as the coastal and valley floor roads were abandoned. The first record of the town of Piombino is found in a diploma of Emperor Otto I of Saxony, dating back to 969. The importance of the Promontory of Piombino depended on its proximity to the Island of Elba and its mineral resources. At the height of the Middle Ages, the other settlements on the Piombino peninsula and the Colline Metallifere (Metal-bearing Hills) that assumed particular importance were: the mining castle of Rocca San Silvestro, near Campiglia; the urban centre of San Vincenzo, developed from the Torre di San Vincenzio alone, originally part of a watchtower system along the Tuscan coast, under the authority of the captaincy of Livorno; the castle of Sassetta in the Val di Cornia, subject to the power of various seigniories over time (such as the Pannocchieschi, who controlled it until the late 16th century); Suvereto, another village in the Val di Cornia that took its name from a nearby forest of cork oaks.

Following its own victory against the Saracen fleets in 874, Pisa was commissioned by the Pope to protect the Island of Elba, thus taking the opportunity to slowly begin to take possession of it. Under Pisan domination, mining, fishing, agriculture and trade, including the export of iron and granite flourished again. The island was also equipped with imposing defensive structures, such as the Tower of San Giovanni, the Fort of Volterraio and the Fort of Luceri - of which only ruins remain - in the municipality of Portoferraio.

Between the early and late Middle Ages,the entire territory of the southern Maremma was an ecclesiastical domain: Argentario became the property of the Roman Basilica of Saints Marcellinus and Peter; the Cosano territory was forfeited to the Abbey of the Three Fountains; the Abbey of San Salvatore in Amiata took possession of Talamone. In addition to the ruins of the monastic complexes from this period, we are also left with various toponymic traces associated with them.

In the 9th century, while the Papacy claimed the southern part of Maremma, the Aldobrandeschi family, feudal lords of Lombard origin, expanded their dominions into the northern area.growing economic and jurisdictional affirmation of the Aldobrandeschi reached a turning point in 989, when Countess Ermengarda stipulated a contract that secured her the ownership of several castles and courts in the Agro orbetellano, so much so that the Papacy was forced to reaffirm the abbatial dominion over Orbitellum on several occasions in the following decades. The town is in fact mentioned in the bull issued by Gregory VII (of Sovanese origins) in 1081, entrusting the Abbey of the Three Fountains to the Cluniac Order. In 1140, Innocent II in turn issued a bull by which he transferred jurisdiction over the Abbey and its territories to the Cistercian congregation, binding it strictly to the Apostolic See. For this reason many papal privileges were bestowed, including the confirmation of the rights over the properties described in the Carolingian diploma in favour of the Abbey of the Three Fountains. At

the same time, at the beginning of the 12th century, the Aldobrandeschi succeeded in unifying the entire Grosseto Maremma for a brief period, including Massa Marittima, which changed its name from Massa Veternensis to Massa Metallorum and retained its setting as a centre of mining activities in the following centuries.

In 1216, Bonifazio degli Aldobrandeschi, Count of Santa Fiora, took possession of Orbetello following a patrimonial division between heirs. Subsequently, a ruling by Gregory IX issued in 1230 removed the Orbetello population from the Sovanese diocesan jurisdiction and assigned it directly to the abbot of Tre Fontane. Consequently, the Counts Aldobrandeschi were forced to resort to the institution of the grant in emphyteusis, for which they had to pay a periodic tribute to the abbot and undertook to improve the conditions of the town. In 1262, the Count of Santa Fiora, Ildebrandino XII degli Aldobrandeschi, opposed the Sienese and regained dominion over Orbetello, whose rights were then donated by his mother Tommasia to his nephew Uberto, Cardinal of Sant'Eustachio. In 1269, Ildebrandino 'the Red', Count of Sovana and Pitigliano, stipulated an agreement with Abbot Elia, a Cistercian monk, in which the formal possession of Orbetello by the Abbey of the Three Fountains was confirmed, but the territory was granted as a fief to the Aldobrandeschi family upon payment of an annual fee. In 1286, this concession was ratified in favour of Countess Margherita degli Aldobrandeschi, who, however, married a member of the Orsini family, thus putting this family in charge of the Orbetello territory in 1293. In 1303, Boniface VIII declared Countess Margherita forfeited and the Orbetello feud was assigned to Pietro Caetani, the Pope's nephew.

The phenomenon of encastellation took place between the 11th and 12th centuries, with the construction of castra both on previous villages or curtes and newly founded ones. In the Agro orbetellano, castles were built on high ground for classical defensive reasons - hills and mountains offered the advantages of surveillance with privileged viewpoints and, often, sheer cliffs, difficult to climb - and to avoid the danger of malarial fever, which infested the plains. For similar reasons, the road network between one castle and another also consisted of paths at high altitudes, in order to avoid swampy areas and thus the risk of malaria. At the same time, parish churches and monasteries grew in importance, also becoming aggregating poles within the settlement system.

From the end of the 11th century, Pisa embarked on a phase of slow decline, marked in 1284 by the defeat suffered at the Battle of Meloria against the Genoese, who tried several times to wrest control of the Island of Elba from the Pisans. The latter in turn descended into a new state of economic decay, aggravated by pirate raids, famine and plague epidemics. All this led Elba into a demographic crisis until the end of the 14th century,during which the Principality of Piombino was also founded

The encastellation reached its maximum development at the beginning of the 13th century, encompassing all the centres still inhabited today, but also many others that were abandoned in the course of time In Maremma, for all the centuries of the Middle Ages, most of the population lived enclosed in castles, while a few other intermediate posts had an exclusively military character, such as watchtowers on the sea and control posts of strategic and customs interest. Often, precisely for these reasons, castles had to be enlarged and provided with new walls and quarterdocks surrounding a larger area. During the Late Middle Ages, expanding city states also came into the Maremma and entered into contention with feudal lords, abbeys and those local communities with ambitions of autonomy.

In the 13th century, much of the former Cosano territory was enfeoffed to the Aldobrandeschi, who occupied its strategic points and built their fortresses there, repeating what we have seen in protohistoric times. Thus arose the castle of Tricoste, the castle of Capalbio, the village of Ansedonia and, probably, a cassero at Talamone (whose identification with the present-day Rocca is still a matter of debate), the latter located on a different site from the ancient town of Telamone. At that time, the main sources of wealth of the Maremma settlements included saliferous production and cereal crops, particularly wheat, barley and spelt. These products were the subject of trade, both by land and sea, which was also conducted with the Sienese market. In any case, the Aldobrandeschi counts had reserved the right to control exports through special prohibition instruments, which they applied at their pleasure as feudal lords[27].

5.4.2 The period of Sienese domination

During the 12th century, the Commune of Siena began to expand in the Maremma, to finally assert itself in the 14th century. In fact, the Sienese Republic planned to conquer the entire Maremma territory and, to achieve this aim, committed imposing human and economic resources in military actions (small battles and raids), the purchase of castles, the construction of defensive works and the renovation of entire settlements, such as Talamone, Magliano and Roccalbegna. In particular, the Republic of Siena competed with Florence for ownership of the port of Talamone, finally succeeding in acquiring it in 1303. However, the port of Talamone was never able to develop due to geotechnical and static problems that compromised the structures built, to the wrong political-economic management by the Commune of Siena (based more on the exploitation of the territory than on its development) and, consequently, to the absence of productive plots of land in the surrounding area. The port of Grosseto did not have better luck as, during the 14th century, it was swept away by a flood that pushed the course of the River Ombrone away from the city. In addition to all this, the Black Death of 1347-48 decimated the population of the countryside and contributed greatly to driving the few urban agglomerations in the area into decline.

In an interval of about one hundred years, straddling the 13th and 14th centuries, the Maremma castles were thus subdued, besieged, conquered or even destroyed, as in the case of Scerpena, Capalbaccio and Ansedonia. The latter, especially, had become a refuge for thieves and was therefore destroyed by the Sienese in 1329. The Sienese also expanded into the Metalliferous Hills of the northern Maremma, subjugating Monterotondo Marittimo, Montieri, Massa Marittima, Gavorrano and Roccastrada.

In the meantime, the city of Orvieto also tried to secure an outlet to the Tyrrhenian Sea and, between the end of the 12th and the beginning of the 14th century, succeeded in exerting

5.3/ Pianta di tutto lo Stato di Siena (Map of the whole State of Siena). Hypothetical dating: 17th century. Archivio di Stato di Firenze (Florence State Archives). Archival collection: ASFi, Piante dello Scrittoio delle Fortezze e Fabbriche, 9. Catalogue ID #15508. Su concessione del Ministero della cultura / Archivio di Stato di Firenze (by courtesy of the Italian Ministry of Culture / Florence State Archives).

its influence especially in the valleys of the Fiora and Albegna Rivers, as far as Capalbio and Orbetello. Following a bitter battle in 1303, the Orvietani wrested control of a large part of the Orbetello countryside from the Abbey of the Tre Fontane. On 8 July 1304 the Commune granted all the citizens of Orbetello the same rights as the citizens of Orvieto in terms of freedom, franchise and immunity. Later, however, with the crisis of Orvieto's authorities, the Orbetellano Agro estate was divided between the Orsini of Pitigliano (who had antagonistic relations with the Orvietani for border reasons), the Baschi of Montemerano and the Republic of Siena. After the death of Countess Margherita degli Aldobrandeschi in Pitigliano, her daughter Anastasia inherited the Orbetigliano fief, which she brought as dowry to Guido Orsini. In 1335, the Orvietani regained their control over Orbetello and forced its citizens into a new act of submission.

At about the same time, Talamone was destroyed in 1337, only to be rebuilt in 1357 despite a threatening climate, between pirate raids on the one hand and a bush that was an ideal den of brigands on the other.

The serious state of decadence of the Orbetello countryside induced the Abbey of the Tre Fontane, still holder of the relevant title, to invest Ildebrandino, Nicola and Gentile Orsini, i.e. Anastasia's sons, as feudal lords. The feud comprised the Castle of Orbetello, the Lagoon with annexed fishing and salt exploitation rights, the town of Ansedonia with the port of Feniglia. In 1376, Guido Orsini had the priory church of Santa Maria Assunta enlarged, assisted by his nephews Guido and Bertoldo: the latter was in turn invested as feudal lord in 1401. In 1406, with the conquest by the Florentines of the State of Pisa, the latter was dismembered: Florence obtained control over the Pisan territories of San Vincenzo, Sassetta and Campiglia Marittima, in the Val di Cornia; the territories of Piombino, Suvereto and Follonica-Scarlino, as well as the municipalities of Elba, the Island of Pianosa and the Island of Montecristo went instead to constitute the Principality of Piombino.

At the beginning of the 15th century, the king of Naples, Ladislaus I of Anjou-Durazzo, began to manifest his expansionist plans towards the Sienese territories. The Orsini allied themselves with the Neapolitans against the Republic of Siena and the Maremma was shaken by the guerrilla warfare that resulted from this confrontation. In 1410, although the Sienese had conquered the village of Sovana, Bertoldo Orsini withdrew his support from the Neapolitans, who in retaliation invaded the Orbetello countryside and captured the count. As a result, Ladislaus I took possession of Orbetello, but was betrayed by the governor and the castellan, who managed to hand the town over to the Sienese. In need of further outlets to the sea, the Commune of Siena subdued the fortress and the village of Orbetello on 30 August 1414, avoiding an attempt by the Pope to prevent such conquests. In 1417, therefore, the entire Orbetello countryside became part of the territories of the Sienese Republic. Later, in 1452, the official investiture took place, which always provided for the payment of an annual fee to the Abbey of the Tre Fontane. Parallel to these events, in 1442, the Sienese built the Argentiera Tower on Monte Argentario, placed at the centre of the defensive walls of an ancient castelliere. During the period of Sienese domination, Orbetello underwent a rapid decline: from the initial population of about four hundred inhabitants in wealthy or even affluent conditions, by 1434 it had dwindled to only eighty people in serious poverty. In addition to all this, in 1454 conflicts between the Orsini, the Sienese and the Kingdom of Naples flared up again, bringing the Agro orbetellano into an even worse state of demographic and economic crisis. Meanwhile, disputes also continued between the Abbey of Tre Fontane and the Republic over the payment of annual tributes.

A few decades later, the Guelph government established itself in Siena, requisitioned the possessions of the Ghibelline Salimbeni family and used them to form the capital of the Monte di Pietà, which it founded on 4 March 1472 to lend the needy the funds necessary to rent pastures and grow grain. Also known as 'Monte dei Paschi di Siena', this institution survived economically thanks to charity and part of the citizens' taxes that were paid by the municipality, while profits were in turn redistributed to the citizens. Its physical seat was established in Palazzo Salimbeni, where the headquarters of the Monte dei Paschi di Siena bank still stands today. As already noted, however, the Monte di Pietà also tended more and more towards the exploitation of pastures and the extensive cultivation of cereals necessary for Siena's sustenance.

Similar to the examples of Talamone and the Torre Argentiera, small watchtowers were built on every promontory and strategic place to control the landing at the creeks below, whose function was mainly to prevent assaults by the Barbarians and

Turks. These military posts often corresponded to the positions of settlements already seen in the Bronze Age. Thus, ancient settlement solutions were traced, but with a highly differentiated characterisation. Despite the huge investments made, however, the Sienese Republic failed in its project to unify the Maremma and, probably, the dissipation of all the resources mobilised and the poor yield of the conquered lands contributed decisively to plunge it into a state of crisis that would lead to its own downfall in 1557[28].

5.5 The Establishment of the State of the Presidi under the Spanish Monarchy

The formation of the Tuscan Presidium State can be seen as the outcome of three concomitant historical events: the dynastic war between King Francis I of Valois of France and Charles V of Habsburg, Emperor of the Germanic Holy Roman Empire and King of Spain; the decline of the Republic of Siena; and the renewed Ottoman power[29].

5.5.1 The monarchical war between France and Spain in the first half of the 16th century

The clash between the dynasties of François I of Valois and Charles V of Habsburg markedthe entire European geopolitics of the 16th century.

In 1515, François I inheriteda difficult situation from his uncle Louis XII of Valois, who had suffered a defeat inflicted on him by the Holy League and had to leave Italian soil. With the Battle of Marignano on 14-15 September 1515and the Treaty of Noyon in 1516, however, the new French king succeeded in regaining the Duchy of Milan and the Duchy of Parma and Piacenza, and even obtained official recognition of these conquests from Spain

advent of Charles V of Habsburg was characterised by his sudden and fortunate inheritance, which took place between 1516 and 1519 andhad such a scope as to upset the political balance in the European framework. Indeed, the premature death of his father Philip the Fair in 1506 was followed by the insanity of his mother - Joan the Mad - and the deaths of his grandfathers, Ferdinand of Aragon and Maximilian of Austria, who died in 1516 and 1519. The Prince was thus crowned King of Spain and the Aragonese Kingdoms of Italy (the Kingdoms of Naples, Sicily and Sardinia) in 1516 with the name Charles I and King of Flanders and Emperor of the Holy Roman Empire in 1519 with the name Charles V. The French Monarchy thus found itself squeezed on all sides by the immense territorial extension subject to the young monarch and this inevitably led to a conflict of unprecedented proportions.

Having secured the alliance of Pope Leo X and England, Charles V drove the French army out of Italy, returning Parma and Piacenza to the Papal States and installing Lodovico il Moro's son, Francesco II Sforza, in Milan. The climax of these operations was the Battle of Pavia on 24 February 1525, at which the French were captured and Francesco I was taken prisoner to Madrid. A year later, the King of France regained his freedom, but had to lower himself to sign the Peace of Madrid, according to which he pledged to renounce Lombardy, Naples and Burgundy and promised not to carry out any further attacks against Charles V.

After the battle of Pavia, Charles V's allies also began to fear his power, so they switched to the side of the French and formed the League of Cognac in 1526, within which England, Pope Clement VII (Julius de' Medici, successor to Leo X), Francesco II Sforza (whose power in Milan had been reinstated by Charles V), the Republic of Venice and the Republic of Florence found themselves alongside the King of France. A further source of problems for the emperor were the Turks, who were advancing in the Balkans over Hungary at this time, pushing towards Vienna. Nevertheless, Charles V enjoyed success, especially in Italy, where he sent the small but devastating army of the Landsknechts. In 1527, after having routed the defence opposed by Giovanni delle Bande Nere, a member of the Medici family, the Landsknechts attacked and sacked Rome. The sack of Rome was followed by famine and pestilence, so Clement VII was forced to come to terms with the imperial forces and leave the League of Cognac. Taking advantage of the Pope's difficulties, the Florentine people drove the Medici out of the city for the second time, proclaiming the Republic again in May 1524 and allying themselves with the Emperor. At the same time, the great Genoese admiral Andrea Doria abandoned Francis I to enter the service of Charles V.

Worried by the Ottoman advance towards Vienna, in 1529 the Emperor entered into negotiations with France and signed the Peace of Cambrai, which stipulated that Francis I and Charles V would renounce Italy and Burgundy respectively.

In Italy, all of Clement VII's wishes were fulfilled: the Duchy of Milan returned to Francesco II Sforza; Andrea Doria was recognised as Lord of Genoa; the Republic of Venice returned Cervia and Ravenna to the Papal States; Charles V repudiated the alliance with the Florentine Republic and pledged to bring the Medici family back to Florence in exchange for an official coronation as King of Italy and Emperor of the Holy Roman Empire. Thus it was that Florence was besieged and forced to surrender in 1530.

Recognising that the Turks, although not directly involved, were playing a major role in the European chessboard, constituting a real threat to Charles V's Spain and his allies on the Italian peninsula, Francis I made an unscrupulous official alliance with Suleiman I the Magnificent, Sultan of the Ottoman Empire. In 1533, Suleiman I summoned Kayreddin the Redbeard, beylerbey of Algiers and skilful strategist, to appoint him grand admiral of the Ottoman navy. Kayreddin's raids on the Italian coasts began in 1534 and by 1537 he had already conquered several Venetian islands in the Aegean Sea, and then threatened the Tyrrhenian Sea by sailing into the Straits of Messina with a sizeable fleet of 150 galleys.

With the death of Francesco II Sforza, Charles V occupied the Duchy of Milan in 1535 and this provided a pretext for the French to resume hostilities with the Hispanics. Francis I thus invaded Italy, while Charles V penetrated France from Germany and Provence. However, the threat of the Turks, who were again assailing Austria from the Balkans and Italy from the Adriatic Sea, was becoming more and more concrete. In 1538, in fact, Kayreddin entered the Adriatic and sailed as far as Prevesa, in Epirus, nimbly avoiding the allied fleets, Imperial and Venetian, who pursued him everywhere. Despite the fact that the missed clashes between the navies were mainly the result of a devious ploy by Charles V, who did not want to contribute to increasing Venice's prestige in the event of victory, the Emperor decided to sign the truce of Nice, which was also realised in 1538 thanks to the mediation of Pope Paul III, who had succeeded Clement VII.

In 1542, relying on alliances with England and the Ottoman Empire, Francis I of Valois broke the truce. Due to their policy of balance, however, the English decided to approach Charles V of Habsburg and attacked France from the north. The Emperor was meanwhile worried about a new Turkish assault in Hungary, so in 1544 he agreed to the Peace of Crépy, proposed by the French King, who in turn was interested in freeing himself from military operations due to the unpopularity of his co-belligerents among the whole of Christendom. With the peace of Crépy, the Duchy of Milan remained with the Holy Roman Empire and Piedmont was left to the French, while Pope Paul III obtained for his son Pier Luigi Farnese the Duchy of Parma and Piacenza, in which the new Farnese dynasty was born. Despite the truce between Spain and France, Kayreddin again wreaked havoc in Italy with his 1543-44 expedition, in which he succeeded in conquering Talamone and Porto Ercole, as well as sacking the island of Elba and deporting its inhabitants as slaves.

Henry II of Valois, who succeeded Francis I in 1547, resumed hostilities against Charles V of Habsburg in 1552, fulfilling his father's directives. He in fact allied himself with the German Protestants and easily occupied the bishoprics of Metz, Toul and Verdun. Also in 1552, the Habsburg Monarchy suffered another bloody defeat at Themisvar in Hungary at the hands of the Turks. To these defeats was added a threatening naval expedition of the French on Naples, supported by the Ottoman fleet anchored on the island of Ponza, a military action that ended in nothing, as the Turks considered it satisfactory to have captured seven galleys led by the Genoese Admiral Andrea Doria. Meanwhile, Kayreddin continued his raids until 1553, brutally devastating the areas of Orbetello, the Argentario Promontory and the Tuscan Archipelago.

Thus, military operations continued by inertia and following entirely new directions, traced by a new and widespread religious commitment, caused on the one hand by a reaction to the unscrupulous diplomatic strategies of both monarchic dynasties, and on the other by the rise of Protestantism. Thus it was that the King of Spain signed the important Peace of Augsburg in 1555, with which the Protestants also gained concrete religious freedom. However, it was with the military truce of Vaucelles on 5 February 1556 that Charles V set out to end the war and his empire at the same time. With this agreement, the warring parties would commit themselves to desist from all military action for a minimum period of five years. Furthermore, while the French would maintain their conquests in Piedmont, the Spanish would secure complete hegemony over the Tuscan territories[30].

5.5.2 The End of Sienese Self-Determination and the Resto-

ration of Local Imperial Rights

In the 15th and early 16th century, some of the leading Italian jurists defined the Sienese Republic as a State no longer subject to the Holy Roman Empire for a long time and, therefore, holder of all supreme prerogatives by virtue of custom or acquisitive prescription of the same imperial rights. This 'libertas', to be understood therefore as independence and consequent fullness of jurisdiction, was also retrospectively analysed by the jurist Tiberio Deciani in the second half of the 16th century. He in fact compared the past status of the Commune of Siena, at the time already subject to the Empire, to that of Florence, Lucca and Genoa[31].

The self-determination of the Sienese Republic decayed with the sudden and resounding restoration of the old imperial rights by Charles Vof Habsburg. The interference already began in the first years of the Habsburg monarch's rule, since in 1520, after his own ascension to the imperial throne, he asked the Commune of Siena to confirm its submission to the Germanic Holy Roman Empire, a subjection already granted by the Republic on the occasion of the coronation of the King of Spain in 1516. These acts had not only a protocol value but also a political significance, as they aimed to limit French diplomatic influence, which in Italy had found a catalyst in the figure of Pope Clement VII, namely Cardinal Giulio dei Medici. An open nepotist, the Pontiff was in fact willing to grant the support of the Ecclesiastical State to that power between the two contenders (the French on one side and the Hispano-imperial on the other) that would best favour the ambitions of the Medici family.

To aggravate Siena's situation was the affair of the League of Cognac in 1526, since, despite the poor results of the anti-imperial alignment and the Republic's valid resistance against the French assault, eight papal galleys under the orders of the Genoese Andrea Doria succeeded in seizing Porto Ercole and Talamone.

From 1530, Charles V's meddling in Sienese affairs of state became more and more evident, intrusive and binding, for it was in that year that the imperial agent Don Lope di Soria arrived at the Commune, charged with uniting the citizens, who were divided into opposing factions. However, the misso did not demonstrate political stature up to the mark and the imposition of his decisions came about through the intervention of the imperial army commanded by don Ferrante Gonzaga, already victorious in 1530 over the Florentine resistance. Having recalled don Ferrante, the Emperor replaced don Lope di Soria with the Marquis Piccolomini del Vasto, well liked by the Sienese citizens, who however failed in his assigned task. Not even the task of reforming the government of the Republic conferred in 1541 on the minister Antoine Perrenot of Granvelle, who could avail himself of the lordship of Count Francesco Sfrondati of Cremona, was to no avail. Already in 1543, the Count from Cremona was replaced by the Spaniard Don Giovanni di Luna. In addition to sending agents in charge of preparing the municipal ordinances, the constraints imposed by Charles V on the Municipality of Siena also included the claim of financial subsidies, the direct appointment of certain important figures in the magistracy, and the allocation of military contingents in the territory of the Sienese Republic.

In the meantime, after Kayreddin Barbarossa had threateningly appeared in the Strait of Messina in 1537, both the State of Siena and the Holy Roman German Empire fortified their ports as soon as possible: 50 Spanish infantrymen under the command of Captain Carlo Mannucci were stationed at Porto Ercole; 100 infantrymen were sent to Grosseto under the leadership of Captain Enea Sacchini; another 500 infantrymen were sent to Orbetello under the orders of the local commissioner Alessandro Guglielmi. As already mentioned, despite the peace of Crépy signed by François I of Valois in 1544, the Ottoman admiral sacked the Island of Elba and deported part of its inhabitants as slaves. He then landed at Talamone and besieged its fortress, defended by a few men, who had to capitulate under the intense bombardment and following the raids carried out inside the walls by the Turks, and thus met with a massacre.

After the attack against Talamone, Kayreddin showed his intention to head for Porto Ercole, prompting the Commune of Siena to address a request for help to Cosimo I de' Medici, Duke of Florence. The latter immediately seized the opportunity to intervene in Siena's political affairs, also urged by the fact that Leone Strozzi, prior of Capua and a prominent member of the anti-Medicean party, was in the Turkish fleet. Cosimo I immediately sent 3,000 infantrymen commanded by Stefano da Palestrina and 100 celestial troops under the orders of Chiappino Vitelli, forces that the Republic convoyed towards Orbetello and Porto Ercole. The soldiers were not able to arrive at Porto Ercole in time, but they represented a sufficient deterrent to make Kayreddin desist from his intention to attack Orbetello, even though he had already made preparations for the assault. The Turkish admiral then merely raided the island of Giglio, taking 700 people from there into slavery.

In 1546, Cosimo I signalled to Charles V of Hapsburg the need to place the Island of Elba and its coastline in the hands of a prince capable of defending them, obtaining a promise from the Emperor that those lands would be assigned to him in exchange for a loan of 200,000 scudi. The Florentine Duke thus had the Fortress of Cosmopoli built on the island, corresponding to today's Portoferraio, surrounded by a circle of bastions leaning against two forts and so powerful as to resist, in 1553, the assault of a Franco-Turkish fleet commanded by the Ottoman corsair Dragut. The latter, although he had seized the rest of the island, had to give up his plan to drive out the Medici troops. In any case, the threat of a cession of Piombinese to Cosimo I aroused the protests of its legitimate master, Giacomo VI Appiani, as well as the resentment of the Republic of Genoa.

Between 1546 and 1552, during a lull in military operations, the rivalries between the opposing political factions in Siena intensified, which Don Giovanni di Luna proved unable to quell even with the help of the Spanish troops stationed in the territory of the Republic. He was thus removed from the Commune in 1546 and, after a second short-lived attempt by Minister Granvelle, in 1547 Charles V appointed Don Diego de Hurtado de Mendoza, a distinguished but authoritarian man of letters, as his representative. In addition to earning popular antipathy, the new imperial representative alienated Cosimo I de' Medici, who was still waiting in vain for permission to annex Piombino and Elba to his domains after paying the aforementioned sum of 200,000 scudi to the Empire.

In order to maintain power, Don Diego smuggled in increasing numbers of imperial troops, which only provoked an ever deeper and more widespread hostility towards the Empire. Relations between Siena and Charles V broke down definitively with the Commune's veto of Mendoza's proposal to build a new fortress on the Hill of San Prospero, with the advice of Gian Giacomo de' Medici, Marquis of Marignano, but at the expense of the city. Don Diego responded to the outbreak of discontent with repression, even resorting to the hanging of confessed offenders.

Thus, in 1549 an anti-Spanish insurrection broke out in Orbetello, skilfully heterodirected by the French but immediately repressed by Genoese and Neapolitan galleys on the surrounding coasts. This episode was followed by an anti-Spanish conspiracy in the city of Siena, still under French influence but orchestrated over a longer period of time and with the help of numerous citizens, led by Amerigo Amerighi. On 27 July 1552, taking advantage of an occasional absence of Don Diego de Mendoza, the city was conquered by the 'dominion bands' trained and led by Enea Piccolomini and Mario Sforza di Santa Fiora, supported later by mercenary troops hired with money provided by the King of France. After an attempted resistance, Hispano-Imperial and Florentine troops stationed in the Commune had to take refuge in the Fort of San Domenico. The last resistance organised by Don Diego de Mendoza - who had fled to Florence and was ambiguously protected by Cosimo I, who hoped to gain favours from both France and Spain - fell on the evening of 28 July, with the arrival of the first contingents of the regular army from France. Monsieur De Lanssac, the French ambassador in Rome and the main architect of the coup d'état, then ruled Siena for a short time, followed by Marshal Paolo De Termes, commander-in-chief of the French forces, who immediately increased the armed forces in the city to 3,000 military personnel. De Termes also sent 500 infantrymen and 100 cavalrymen against Orbetello, which did not fall, but provided a pretext to order Cosimo I to get Don Diego de Mendoza and the Spanish soldiers, who were still protected by the Duchy of Florence, out of his territories. With unscrupulousness, Cosimo I fulfilled the requests of the French representative by ordering the Hispano-imperials to head to the port of Livorno to leave Tuscany, but did not prevent them from going to Orbetello to join the local forces instead of embarking.

A new local geopolitical balance in the war between Spain and France thus emerged, on the one hand with the Medici troops associated with the Hispano-Imperial forces, on the other with the Sienese allied with the French. The King of France separated the civil Sienese power from the military one by appointing first Cardinal Fabio Mignanelli and then, as his lieutenant, Cardinal Ippolito d'Este, alongside Marshal De Termes, in charge of preventing an expected counter-offensive by the Emperor's followers. However, these figures,

authoritative as they were, were completely irrelevant.
The Spanish response was prompted by Don Pedro de Toledo, viceroy of Naples, who relied particularly on Cosimo I, his son-in-law, knowing his geopolitical ambitions and his considerable financial resources. Once again, however, the Florentine Duke maintained an ambiguous position, displeasing the French, the Sienese and the Hapsburgs. Military manoeuvres began in February 1553, but at first the Emperor's allies only achieved a series of defeats or local victories paid dearly, followed by a phase of stagnation in the conflict. Cosimo I tried to plot a conspiracy in Siena against the French, through his ambassador Leone Ricasoli, but those involved were discovered and imprisoned. Four of these conspirators were executed and their remains were exposed to public ridicule.

The imperial army deployed 20,000 men including infantrymen and cavalrymen accompanied by heavy artillery against the Fortress of Montalcino, defended by only 3,000 men including mercenaries and volunteers but equipped with a mighty wall, practically inaccessible on three sides In June 1553, after 80 days of siege, the Emperor's followers had to retreat while retaining their position at Orbetello, while Florentine troops continued to occupy Lucignano.

In August 1553, the French counter-attacked with the Ottoman fleet and occupied Corsica, which belonged to the Republic of Genoa, which was an ally of Spain. Although the conquest of the island provided a great strategic advantage, at that moment the French army needed a respite to consolidate in the newly obtained positions, especially considering that the Turkish navy had to return to its bases in the East. In any case, the seriousness of the seizure of Corsica allowed Cosimo I to obtain from Charles V the authorisation to conduct the war against Siena to the end, both because the Emperor was facing internal problems in Germany and because the Duke of Florence declared himself willing to bear all the costs of the conflict in exchange for an adequate territorial compensation, in other words in exchange for all the lands of the Sienese Republic. Before the resumption of hostilities, two coups were attempted in Siena, on 1 and 5 January 1554 respectively, which were followed by the return to the city of Piero Strozzi, sworn enemy of the Medici.

The military manoeuvres began between 26 and 27 January with a great nocturnal assault on Siena from different directions. Despite the city's unpreparedness, the population, led by Piero Strozzi, responded so promptly and decisively that they repulsed the Florentines and forced them into a long siege. While waiting, the Florentine army plundered the Sienese countryside and conquered towers, convents, farms and small castles. In the meantime, Charles V decided to put an end once and for all to the self-determination of the Sienese, and in fact, on 30 May 1554, the Habsburg Monarch stripped the Republic of Siena of every privilege granted to it by the previous emperors, declaring it to have fallen under the full authority of the Holy Roman German Empire and assigning it to his son Philip II as perpetual Vicariate. In order to alleviate the difficulties in supplying supplies, damage the besiegers and solicit the arrival of reinforcements, on 11 June 1554 Piero Strozzi forced the Florentine encirclement with 8,000 infantrymen and 1,000 cavalrymen to move the battle into the Volterrano and Pisan Plain, thus joining the French troops descending through the Garfagnana near Ponte a Moriano, in the Lucchese. Having reunited his own soldiers with the French, Strozzi confronted the Marquis of Marignano, who was pursuing him, and then even fought against Don Giovanni Gonzaga, commander of the imperial forces. Despite his profuse skill, these actions did not bring tangible results, partly due to the non-arrival of other reinforcements that were supposed to land in Viareggio. The condottiero therefore decided to return to Siena, but his intent was foreseen by the Florentines and the Hispano-imperials, who forced him into a clash at Marciano on 3 August, inflicting a heavy defeat. Despite the loss of Monteriggioni, the most important external fortress of the Commune of Siena, on 29 August, Strozzi again forced the Florentine blockade and returned to his own city on 17 September to bring the supplies he had collected to his fellow citizens. In spite of the strenuous defence of the French garrison commanded by Blaise De Montluc, the situation became increasingly dramatic for the starving Sienese, so much so that they went so far as to drive all those deemed useless out of the city and consume anything that could be considered even vaguely edible, including blades of grass. After a new surprise assault attempt on Christmas night 1554 and a violent bombardment on 11 January 1555 with artillery stationed on the knoll of Ravacciano, the long diplomatic negotiations for the Sienese surrender began between Piero Strozzi, who had taken refuge in Montalcino, and Cosimo I de' Medici. The lengthening of the negotiations beyond what

was necessary was caused by the tenacious resistance of the Sienese to the hypothesis of their submission to the Empire, by hopes of further French intervention and by devious court rivalries. Thus, the negotiations ended when Piero Strozzi decided to resign from all representative offices and the closing of the agreement was entrusted to Cardinal Ippolito d'Este. On
17 April 1555, in the presence of the Spanish official Francisco de Toledo, the Sienese plenipotentiaries stipulated the 'chapters' of the surrender with Cosimo I, which included an ambiguous and misleading promise about respecting the 'freedom' of the defeated Republic. In fact, the Duke of Florence wished to reach an agreement as soon as possible, so as to prevent the Emperor from examining the text and prejudicing future Medicean expansions by inserting some clause. Cosimo I therefore declared that he had sufficient power to conclude such pacts, proposing their ratification within two months. The reprimand of Charles V was not long in coming and he threatened not to validate the agreement, considering it unworthy of his kingship and the outcome of the war. However, Cosimo I managed to meet the Spanish Monarch's demands thanks to two unscrupulous political expedients: on the one hand, he conferred the major responsibilities over the government of Siena - to be exercised in the name of the Emperor - to his lieutenant Angelo Niccolini; on the other hand, he circumscribed the civic autonomy of Siena to a collegial magistracy with no effective decision-making powers, called the Balìa, whose twenty members - all originally from the Commune - were appointed by the Duke of Florence himself together with the Caesar's agent Francisco de Toledo. This solution was however temporary and on 19 June 1555, through a measure that repeatedly defined Siena as an 'imperial city', Charles V imposed Francisco de Toledo as Governor in place of Angelo Niccolini. The Sienese population in extreme distress, its total refusal to submit to the Florentines and the desperate need to secure the clemency of the Emperor were all favourable circumstances for the Spanish misso, who induced the Bailiff to draw up an act of formal renunciation of the agreement made with Cosimo I, as well as total and unconditional submission to the Holy Roman Empire. Charles V was thus able to renew the concession of the perpetual Vicariate of Siena to his son Philip II. After the death of Francisco de Toledo, Francesco de Mendoza y Bobadilla, Cardinal of Burgos, was appointed as new governor. What
delayed the complete surrender of the Sienese citizenship was the episode of the 'Republic of Siena withdrawn to Montalcino', which occurred on the initiative of around 650 of the most influential families of the city, who took refuge in the fortress of the same name immediately after the events of 17 April 1555. This government-in-exile, protected by French arms, was presided over by Piero Strozzi and other politicians elected before the surrender: the Capitano del Popolo Mario Bandini, the gonfaloniere Giulio Vieri and one of the Lords, Fabio Spannocchi, who had carried with them the seals and insignia of the Commune of Siena. They ordered the numerous settlements of the Sienese state still garrisoned by the soldiers of Henry II of Valois to lend their allegiance to the Republic of Siena, which had withdrawn to Montalcino, one of its primary aims being the recovery of the territories occupied by the Florentines and the Hispano-imperial forces, including the capital. The secessionists organised themselves in a rather structured manner: they constituted a General Council and some magistracies; they began to mint coins and entertain diplomatic relations, even attempting to obtain a temporary transfer of the archiepiscopal seat from the Pope.
In the meantime, the Medici troops laboriously continued their occupation of Porto Ercole, Talamone, Castiglion della Pescaia, Scarlino and Gavorrano, just in time to avoid the arrival of a new Ottoman fleet that sacked Porto Baratti and Piombino, and then headed for Corsica. Given the distribution of the Florentine forces over the Sienese State, at that point Cosimo I began a pressing diplomatic action to make Charles V of Habsburg fulfil his commitments, leaving him dominion over the territories of the Republic of Siena or at least compensating him for the military expenses, amounting to 1,200,000 scudi. However, the Duke of Florence was taken aback by the Emperor's abdication, formalised on 17 January 1556[32].

5.5.3 The division of the Habsburg dominions and the dismemberment of the Republic of Siena

Realising the difficulties and risks associated with the management of an entity as vast as his empire, Charles V decided to divide it in two: on the one hand the imperial dignity and dominions of the House of Austria, to be left to his brother Ferdinand I of Habsburg; on the other the Kingdoms of Flanders, Spain, Italy and the colonies in America, assigned to his son Philip II.

On 27 January 1556, Henry II of Valois agreed to take part in an alliance against the Hispano-Imperials and the Florentines, organised by Pope Paul IV together with the Duchy of Ferrara and the Republic of Venice, in support of Piero Strozzi and the Republic of Siena, which had withdrawn to Montalcino. However, on 5 February of the same year, the King of France signed the truce of Vaucelles with the Habsburgs, according to which the French renounced all claims to the Tuscan territories. In addition to incurring inevitable accusations of betrayal, Henry II of Valois subsequently adopted an even less transparent attitude, as he was exonerated by Paul IV from the obligations he had assumed with the agreement made together with the Hispano-imperials and continued to lend political and military aid to Montalcino, sending as his personal representatives first Jean Larquevêque de Parthenay, baron of Subise and former ambassador to Parma, then Blaise De Montluc, who had heroically defended Siena during the Medici siege. The French, however, imposed heavy conditions on the renewal of their support, demanding that the Sienese territories become a royal state totally governed by a military lieutenant: a proposal that emptied the government-in-exile supported by Piero Strozzi of any meaning.

In September 1556, the Duke of Alba, Viceroy of Naples, received orders to launch a threatening military offensive against the Church State, which had allied itself with Henry II. This initiative was answered in January 1557 by the descent into Italy of French troops commanded by Duke Francis of Guise, which raised the hopes of the Sienese exiles. However, the task of the Duke of Guise was only to protect the territorial integrity of the Papal States and, therefore, his soldiers never trespassed into the Duchy of Tuscany. The local tactical successes of Blaise de Montluc, assisted by Captain Moretto Calabrese and the brothers Mario and Carlo Sforza di Santa Fiora, did not change the situation.

With the fall of Porto Ercole at the hands of the Florentines, the last anti-Spanish bulwark, the long negotiations with Philip II of Habsburg began to define the fate of the State of Siena. Moreover, concerned about possible retaliation on the Duchy of Milan and the Kingdom of Naples, the new King of Spain decided to agree to Cosimo I's request for compensation. The first step was the Treaty of London of 29 May 1557, stipulated there because Philip II was the husband of Maria Tudor known as the Bloody and concluded directly between the King of Spain and Jacopo VI Appiani of AragonLord of Piombino. With this agreement, Philip II reserved the right to build one or more fortresses on the Island of Elba, on sites of his choice.

The text of the subsequent Treaty of Florence, more precisely known as the Treaty of Brussels, where the agreement was signed by the King of Spain on 3 July 1557, was drafted taking into account the premises contained in the Treaty of London and sanctioned the establishment of the State of the Tuscan Presidia The city and the State of Siena became the fiefdom of Cosimo I and his direct successors until the extinction of the dynasty, and then returned to Spain, but Philip II reserved the ports of Orbetello, Talamone, Porto Ercole, Porto Santo Stefano and Monte Argentario for the Spanish Monarchy, to be administered by the viceroys of Naples. Although he had obtained the Marsiliana estate as a gift, the Florentine Duke was to return Piombino and the Island of Elba to the Appiani, retaining only Portoferraio and the surrounding lands within a radius of two miles as a feud. Cosimo I renounced all claims against the Spanish Crown and the Appiani, pledging to contribute one third to the costs of defence, provisions and ammunition for the ports, while the King promised military aid of 4,000 infantrymen and 400 cavalrymen to drive the last French forces out of Tuscany. A perpetual alliance between the Florentine Duke and the Spanish Monarchy was also envisaged: on the one hand, Philip II undertook to support Florence, in the event of armed aggression, with 10,000 infantrymen, 400 men-at-arms and 600 cavalrymen; on the other hand, Cosimo I was to provide Spain with 4,000 infantrymen and 400 cavalrymen in the event of attacks against the Kingdom of Naples or the Duchy of Milan. The Duke of Florence was also to grant the Sienese their own government and magistracy. Finally, Cosimo I also accepted a secret act, according to which he could only allow his descendants to marry in marriages agreeable to the Spanish Crown.

During the negotiations, the Duke of Florence had tried to avoid the dismemberment of the State of Siena, emphasising both how such a fact would have damaged his own prestige and the difficulty he would have found himself in - not being able to dispose of the main military ports of the lower Maremma - in providing the King of Spain with the support

5.4/ Recto della Carta corografica della Toscana (Recto of the Chorographic map of Tuscany) by Giuseppe Rosaccio. Dating: 1662. Archivio di Stato di Firenze (Florence State Archives). Archival collection: ASFi, Carte nautiche, 20. Catalogue ID #148498. Su concessione del Ministero della cultura / Archivio di Stato di Firenze (by courtesy of the Italian Ministry of Culture / Florence State Archives).

of his galleys. Philip II, however, was immovable, since he considered maritime fortresses necessary to support Spanish supremacy in the Tyrrhenian Sea, so much so that some time before he had considered the hypothesis of an investiture in favour of Carlo Carafa, nephew of Paul IV. As already mentioned, the coastal area not assigned to Cosimo I went to constitute the State of the Presidia, subject to the rule of the Viceroy of Naples, but the legal titles underpinning the power of the Iberian monarchy remained divided. The Neapolitan area, in fact, came under the hereditary succession of Ferdinand II the Catholic, while this strip of the Tuscan coast retained its legal nature as imperial land, in the same way as the remaining part of the Sienese State.

Thus it was that on 19 July 1557, the army of Florence entered the city of Siena. Although Cosimo I was preparing a table for negotiationswith Blaise De Montluc, who had no more reason to defend Montalcino after the truce of Vaucelles, on 19 July, the same day as the Florentine occupation of the Sienese capital, Henry II of Valois sent the French leader an official decree annexing the Republic of Siena withdrawn at

Montalcino to the Kingdom of France. However, the situation of the government-in-exile was so dramatic that many were thinking of transferring it to Grosseto. Montluc tendered his resignation and Cosimo I continued negotiations with Francesco d'Este, facilitated by the fact that in those very days the Florentine Duke had given his daughter Lucrezia in marriage to Alfonso d'Este, hereditary prince of the Duchy of Ferrara. Francesco d'Este made no effort to favour Montalcino and the Sienese rebels, not even when Talamone and Castiglion della Pescaia were taken from the French by a Spanish fleet. His only diplomatic effort, however, foiled by Cosimo I, was to induce Alfonso d'Este to offer 350,000 scudi to the King of France in exchange for the annexation of the Republic of Siena withdrawn from Montalcino to the Duchy of Ferrara.
meantimethe Spaniards won a great victory in Flanders at St. Quentin, while the French only managed to partially redress the balance in 1558, when they conquered Calais, which had remained in the hands of the English, at that point allies of Philip II, since the Hundred Years' War. On 7 February 1559, the first phase of the fall of Montalcino began, in which the French army began to evacuate Tuscany, despite the fact that the Sienese rebels were trying to negotiate directly with the King of Spain in order not to subject themselves to Cosimo I. Since Philip II was now bound by the Treaty of Brussels to respect the Duke of Florence's demands, those diplomatic attempts only had the effect of delaying the total surrender of Montalcino. On 2 August 1559, the French troops embarked on thirteen galleys in the roadstead of Vada and so Montalcino surrendered definitively on 4 August.
Given the disastrous situation, both Philip II of Habsburg and Henry II of Valois took an interest in putting an end to the war started by their parents, thus stipulating the Peace of Cateau-Cambrésis between 2 and 3 April 1559. With this treaty, France definitively renounced all its territorial ambitions in Italy, returning Corsica to the State of Genoa and the territories of Savoy and Piedmont (with the exception of Saluzzo) to the leader of the Battle of San Quentin, Emanuele Filiberto. The French were allowed to temporarily occupy Calais and the localities of the Seine, already under English rule, committing themselves to return those territories eight years later to England upon payment of 800,000 gold crowns. Together with the imposition of the territorial subdivision already implemented by Charles V, the Spanish took over the undisputed hegemony over Italy. The Spanish dominion on the Peninsula was therefore determined with the following configuration: the Kingdoms of Naples, Sicily and Sardinia, each ruled by a viceroy; the Duchy of Milan, ruled by a governor; the State of the Tuscan Principalities, extrapolated from the Republic of Siena and defined by special treaties concluded with the Lords of Piombino and the Medici, Dukes of Tuscany. All the main Italian principalities were thus placed under Spanish hegemony, even those that could proclaim themselves independent, such as the Medici, elevated in 1570 to the rank of Grand Duchy of Tuscany[33].

5.6 The State of the Presidia in the Age of the Spanish Viceroys

During the period of subjugation to Spain, the Presidium State was involved in a series of historical events - such as the Thirty Years' War - that strongly influenced its extension, politics and socio-economic system.

5.6.1 Early years of development and expansion of the Presidium State

In the first years of the existence of the Tuscan Presidio State, the political class established in its government was incapable of adequately developing its autonomy and organising itself efficiently. This is why Philip II entrusted the government of the Presidiosto his ally Cosimo I de' Medici, ordering that all the Spanish commanders of Orbetello, Talamone, Porto Ercole and also those stationed at the garrison of Piombino obey the Duke of Florence. Realising the urgency of consolidating the new state through the construction of a defensive system of fortresses and towers, the King of Spain chose Cosimo I as he was an expert in this field and had the best military architects of the time.
The Florentine Duke took advantage of this privileged position to take Castiglione della Pescaia and the Island of Giglio from Don Indico Piccolomini, Marquis of Capestrano and Duke of Amalfi as well as an enemy of Florence and Spain, but he had to validate his conquests by having his consort, donna Eleonora di Toledo, pay a sum of 30,000 scudi in favour of the legitimate owner.
On 5 September 1560, a naval battle took place in the waters of Porto Santo Stefano between three Tuscan galleys commanded by Piero Machiavelli and a fleet of sixteen Turkish

5.5/ Pianta dello Stato dei Presidi della Toscana (Map of the State of the Presidi of Tuscany). Hypothetical dating: 1700-1750. Archivio di Stato di Firenze (Florence State Archives). Archival collection: ASFi, Piante dello Scrittoio delle Fortezze e Fabbriche, 63. Catalogue ID #15569. Su concessione del Ministero della cultura / Archivio di Stato di Firenze (by courtesy of the Italian Ministry of Culture / Florence State Archives).

galleys

The first Viceroy of Naples to actually take charge of the State of the Presidi, perhaps at the explicit request of Philip II, was Don Perafan de Ribera, Duke of Alcalà. After a visit to thePresidioshe had barracks built in 1569 in Orbetello, Porto Ercole and Talamone and then sent a larger contingent of troops there than those sent up to then

On 28 September 1589, Alessandro I d'Appiano, lord of Piombino, was killed, apparently the victim of a conspiracy hatched by Don Felix de Aragona, who commanded the Spanish troops stationed there, a conspiracy orchestrated with the approval and complicity of Donna Isabella Mendoza, the victim's wife. TheSpanish governor immediately took possession of the Seignory, albeit in the name of Philip II, provoking the reactions of the Grand Duke of Tuscany and the Emperor of Austria Ferdinand I of Habsburg until, in 1591, Iacopo VII became lord of Piombino, who was officially invested as an imperial prince in 1594. However, he died in 1600, causing a succession struggle.

Later, Tuscany was invaded by a mercenary company led by Alfonso Piccolomini, Duke of Montemarciano. On this occasion, Cosimo I suspected that Spain had provided military aid to Piccolomini's contingent through the State of the Presidia.

In May 1592Presidios were invaded by locusts, especially the territory of Talamone.

In 1596 Count Olivarez, Viceroy of Naples, overturned some strict orders of the Governor then in office in the Stato dei Presidi, allowing all its inhabitants to hunt freely throughout the Argentario promontory and to go around armed, justifying this dangerous measure with the threats of the Turks and thieves infesting the Maremma.

A few years later Philip III of Habsburg, who succeeded Philip II, decided to make use of the clause in the Treaty of London of 1557 that allowed the Spanish Crown to build one or more localities on the Island of Elba, to fortify them as part of the Presidio State. The international geopolitical situation was in fact becoming more complicated and, at the same time, diplomatic relations with the Grand Duchy of Tuscany were no longer as friendly as they had been at the time of Cosimo I de' Medici. The new King of Spain therefore ordered that a large fortress be built at Porto Longone, which would have many uses: to serve as a shelter in the event of new pirate raids of Turkish origin; to prevent any French or imperial offensive resumption; to act as a counterweight to the Medici fortress at Portoferraio; to serve as a military base with which to consolidate Spanish hegemony in central Italy and, in particular, on the Papal States. Therefore, on 8 May 1602, a Spanish naval team arrived at Porto Longone with the materials and specialised workers for the imposing work, designed by Don Garcia de Toledo. Theoretically, the construction was supposed to be called 'Fort Benaventano', in the name of the viceroy of Naples then in charge, but work took much longer under the rule of Juan Alfonso Pimentel de Herrera, Count of Benavente, so the work was simply christened Fort Porto Longone.

It was also under the viceroyalty of the Count of Beneavente that, on the initiative of Governor Don Nuño Orejón, the port of call at Porto Santo Stefano was upgraded. According to Pietro Fanciulli, these construction works did not correspond to the renewal of the site as a settlement, but rather to the building of warehouses for goods unloaded from ships too large to be moored at Porto Ercole, plus other facilities related to logistics. In addition to the warehouses for military supplies and provisions destined for Orbetello and Porto Ercole, the following were built: lodgings reserved for the officers and soldiers in charge of disembarking, transporting goods and storing them in the warehouses; temporary huts for seasonal fishermen, usually of southern and Catalan origin; and a chapel under the authority of the Governor of Orbetello and the jurisdiction of the Chaplain Major of Naples[34].

Also during that period, the State of the Tuscan Presidia interconnected with Piombino. In 1591, the very young Jacopo VII d'Appiano, still a pupil under the guardianship of his uncle Alfonso d'Appiano d'Aragona, became heir to the Seignory of Piombino, and then obtained its enfeoffment in 1594 together with the elevation to Principality by Emperor Rudolph II of Habsburg. The premature death of Jacopo VII in 1600, at only twenty-two years of age and without succession, caused the extinction of the sovereign line of the Appianiand thus a series of disputes between the pretenders to the title of prince

The matter was referred to the Emperor Ferdinand II of Habsburg, who invested three sons of Carlo Sforza d'Appiano, don Belisario, don Hannibal and don Orazio, on 29 October 1624, on condition that they achieve the subjugation of the King of Spain by paying a laudemy of 800,000 Rhine florins to the Imperial Chamber. Although the deadline for payment was then set for 1 August 1633 and then postponed to February 1634, the three investites were unable to pay this sum. The Emperor therefore had to declare the three d'Appiano brothers deprived of all rights to the feud and on 24 March 1634, in Naples, the extraordinary ambassadors of Ferdinand II and the Spanish King Philip IV of Habsburg invested Niccolò Ludovisi, former Prince of Verona and ally of the Spanish, with the Principality of Piombino. After taking charge of a laudemy of one million Rhine florins, to be paid to the Imperial Chamber in two instalments, on 20 May 1634 Niccolò Ludovisi took over the government of the Principality of Piombino, thus allowing the Spanish Crown to manage these territories (including the Promontory of the same name and the Island of Elba) as an extension of the Presidio State[35].

5.6.2 Involvement of the Presidium State in the Thirty Years' War

The initial and occasional reason for the conflict known as the Thirty Years' War was determined by a geopolitical framework characterised by unresolved religious conflicts. After the Peace of Cateau-Cambrésis, the core of Europe had split into two camps: on one side the Catholic states, on the other the Protestant states. In particular, the Protestant states believed that the dogmatic and absolutist principle of cuius regio eius religio, while not preventing the spread of Protestantism, did not allow for its large-scale expansion[36]. On the other hand, the Catholic states viewed the expansionist policy of the Habsburg emperors with concern. Thus, the Evangelical Union led by Elector Palatine Frederick V was formed in 1608 and, in 1609, the Catholic League supported by Spain and with Maximilian I of Wittelsbach as its leader.

Emperor Rudolf II of Habsburg in 1609 granted the Bohemian Protestants several freedoms, which were deliberately violated in the following decade by Ferdinand II of Habsburg, King of Bohemia, who even established a regime of persecution. The reaction of the Bohemians was so violent that on 23 May 1618, two imperial representatives, guilty of denying permission to build places of worship to a group of Protestant nobles, were thrown from a window of the royal castle: an episode remembered as the "defenestration of Prague". In 1619, the Bohemians then pitted the Calvinist Frederick V of the Palatinate-Simmern against Ferdinand II, who became emperor that same year. Thanks to the support of the Holy League, the Habsburg monarch defeated the dissenters at the Battle of White Mountain in 1620.

The Evangelical Union invoked the intervention of King Christian IV of Denmark, who was however defeated by the imperial troops in 1626-27, despite the support of the Netherlands and France, and then suffered the invasion of his own kingdom and had to give up the offensive with the Peace of Lübeck in 1629

King Gustav II Adolf of Sweden, supported by France, Brandenburg and Saxony, then intervened against the Holy Roman Empire. After some military successes, the king perished at the Battle ofLützen in 1632 and Sweden suffered defeat at Nördlingenin 1634

In 1635, Cardinal Richelieu's France, intent on breaking the Habsburg encirclement, entered the conflict directly by allying with Sweden and the Netherlands, declaring war on Spain and invading Valtellina.In its French period, the initially religious war took on a more openly political character and was characterised by diplomatic unscrupulousness, so that it is not surprising that Lutheran Sweden and Calvinist Holland were allied with Catholic France, while almost all the Protestant states of Europe were siding with the Empire, which was no less Catholic than France. Initially the Hispano-imperialists prevailed, but from 1640 onwards the Franco-Swedish prevailed.

In 1642 Cardinal Mazarin, who had succeeded Richelieu in French government affairs, planned to damage the prestige of Pope Urban VIII to prevent him from intervening in the final phase of the war. However, the Church State was already subject to a crisis caused by internal political events and the unbridled temporal ambitions of the Pontiff, who came from the Barberini family and was particularly prone to nepotism.

From 1641 to 1644, in fact, the Ecclesiastical State was engaged in the Castro War, provoked precisely by Urban VIII. After acquiring Ferrara and Urbino, setting himself against the will of Venice and Spain in order to satisfy his own family's princely ambitions,in October 1641 the Pontiff had the Duchy of Castro, ruled by the Farnese of the Duchy of Parma and Piacenza since the previous century, occupied by him thanks to the similarly nepotistic policy of Pope Paul III. Subsequently, Urban VIII excommunicated Prince Odoardo Farnese because he continued to protest without resigning himself to a fait accompli. The reaction to the occupation of Castro was of much greater proportions than the Pontiff had anticipated, because Venice, Florence, Modena and Richelieu's France sent considerable military aid to Odoardo Farnese. After unsuccessfully trying diplomatic ways, the Prince of Castro started his own military campaign and, during 1642, achieved a rapid series of successes by invading Romagna and occupying Imola, Faenza, Forlì, and even reaching Lake Trasimeno, despite the numerical inferiority of his army. After unsuccessful negotiations for a truce in the winter of 1642, hostilities resumed in the spring of 1643, ranging haphazardly from Umbria to Romagna, as each of Odoardo Farnese's allies conducted operations in their own way. Cardinal Mazarino proposed himself as mediator, but negotiations were only accelerated by a defeat inflicted by the Venetians on the papal soldiers, where Antonio Barberini, the Pontiff's nephew, was captured. With the peace of Ferrara of 31 March 1644 the Duchy of Castro was reconstituted under the Farnese, but the other Italian states that had participated in the conflict faced heavy consequences: in the Papal States, Umbria, part of Romagne and the territory of Ferrara had been devastated, the economy had been disrupted and the prestige of the Pope had been irreparably compromised; the weak military performance of the Venetians was interpreted by the Ottoman Empire as a sign of an opportunity to be exploited; the d'Este family only obtained the promise of a review of the case concerning their property lost with the devolution of Ferrara, fearing that they would abandon their traditional Spanish protection, although they did not yet seriously consider the hypothetical French protection.

On the death of Urban VIII, on 29 July 1644, geopolitical tensions re-emerged powerfully, as France and Spain directly intervened in the succession: the French would have wanted an ally of the Barberini family on the papal throne; the Spanish, on the other hand, succeeded in having an exponent of the Pamphili family, Innocent X, elected, towards whom Cardinal Mazarin had a personal aversion. Defeated, the Barberini family even had to take refuge in France, while Mazarin leaned towards an increasingly hostile policy against the Church State and Spain, acting in two ways: On the one hand, during 1645 he sent the Abbot of Saint Nicolas, Henry Arnauld, on a mission to the Peninsula to stir up the various Italian courts against the Spaniards and induce Innocent X to grant pardon to the Barberini and to recognise the secessions of Portugal and Catalonia from Spain; on the other hand, he planned military action against the Tuscan Presidium State to directly intimidate the Pope[37].

5.6.3 The siege of Orbetello

Cardinal Mazarin chose the Presidios as his target not only because of their strategic location, but also because they had been completely neglected by King Philip IV of Hapsburg of

Spain and his viceroy in Naples, Admiral Juan Alfonso Enriquez of Castile, had completely abandoned them to their own devices. Although the strongholds of the Presidio State were equipped with artillery, the few soldiers stationed there were malnourished, poorly paid and poorly equipped. Moreover, despite a leak of information by the Neapolitan fieldmaster Michele Pignatelli, who was imprisoned in France, both the Spanish Crown and the Viceroy of Naples misjudged the strategic picture by assuming that the French would attack Finale Ligure, another territory in Spanish hands and geographically closer to the enemy.

While Mazarin secretly gave the order to set up a fleet in February 1646, on the 11th of that same month a new viceroy was appointed in Naples, Don Rodrigo Ponze de Leon, Duke of Arcos, who on 20 March sent the general and master Carlo Della Grotta to Porto Ercole with reinforcements, ammunition and money. In March and April 1646, the French fleet was prepared with a subdivision into three squadrons, while in Liguria an expeditionary corps was set up headed by Prince Francesco Tommaso of Savoy, who later took on the coordination of the enterprise. In early May, the French fleet embarked its troops in Vado and on the 9th of the same month it reached the Saline del Fiume Albegna, halfway between Talamone and Porto Santo Stefano. On the same evening of the landing, having put the soldiers guarding the Saline Fortress to flight, Prince Thomas established his headquarters there, sending some of his landing troops to take Talamone and one of his infantry units to occupy the Spanish Fortress at Porto Santo Stefano. Realising the circumstances, General Della Gatta evacuated food and ammunition from Porto Ercole and concentrated all available forces in Orbetello, where he also armed the civilians. While the Savoy prince began his encirclement manoeuvre, the Duke of Arcos arranged for a land militia to be sent to Sessa to help the Presidios State and, at the same time, sent a corps of spoilers by sea, which was, however, dispersed by a French fleet, already deployed between Civitavecchia and Argentario to prevent any communication between the Presidios and Naples. However, on 17 May, Spanish ships arrived at Porto Ercole, which had not been occupied by the French, while Prince Thomas had already begun to request reinforcements from France on the 13th of the same month.

The struggle for the French to overrun the ditch at Orbetello dragged on until 7 June, when the Spanish managed to drive their enemies back outside the ditch. Prince Tommaso received the required reinforcements, but so did General Della Gatta, as a new Spanish fleet arrived at Porto Ercole on 12 June. Having circumnavigated the Argentario Promontory, on 13 June the Spanish fleet confronted the French fleet north of Tombolo di Giannella. In the evening, a storm forced the Spanish ships to take refuge in Porto Longone, while the French had to take sheltereven in Livorno and La Spezia

The French received reinforcements on 16 June, while for the Spanish, bombers, supplies and medical personnel arrived the next day. Although Prince Tommaso had blocked the passage to Orbetello by occupying the eastern end of the Tombolo di Feniglia, the Spanish managed to force the barrage and bring supplies into the city. TheSavoy princethen resumed bombarding Orbetello and conducting assaults against it

On 2 July, the besieged found themselves with little ammunition and without water or provisions Given the difficulties, the Viceroy appointedMarquis Caracciolo di Torrecuso as the new commander of all the Spanish and Neapolitan forces of thePresidios, but he was still in Naples. On 8 July, having received further reinforcements, Prince Tommaso subjected Orbetello to a violent bombardment and then ordered the Spanish to surrender the following day. General Della Gatta refused, although the arrival of Marquis Caracciolo at Porto Ercole had led to a quarrel over the command of the Spanish forces in the field. However, on 15 July, the Spanish put in place a coordinated operation: General Della Gatta simulated an offensive action from Orbetello, while Marquis Caracciolo forced the French blockade at Feniglia, and then reached Ansedonia to join the reinforcements sent by the Viceroy through the Papal States. While there was not even a blade of grass left in Orbetello to feed the besieged, Marquis Caracciolo marched towards the salt pans to fight with Prince Tommaso, but the latter had his camps destroyed and ordered a retreat from all positions above the Fort of the Saline. The French retreated by sea and the Savoy prince crossed Tuscany to take shelter in Piedmont. The Spanish and Neapolitans then reconquered Porto Santo Stefano, Talamone and the Saline d'Albegna[38].

5.6.4 The loss and reconquest of Porto Longone and the Principality of Piombino

5.6/ Plan de la Cote de Toscane depuis la Tour du Cinquale jusqu'a Civitavecchia (Map of the Tuscan Coast from the Cinquale Tower to Civitavecchia). Hypothetical dating: 1800-1814. Archivio di Stato di Firenze (Florence State Archives). Archival collection: ASFi, Piante dello Scrittoio delle Fortezze e Fabbriche, 5. Catalogue ID #15503. Su concessione del Ministero della cultura / Archivio di Stato di Firenze (by courtesy of the Italian Ministry of Culture / Florence State Archives).

Despite the defeat, Cardinal Mazarin immediately resumed the initiative and prepared a new, unpredictable attack on the Presidium State. The occupation of the chosen target on the island of Elba, Porto Longone, was not only directly aimed against Spain, but could be a key point in the conquest of Piombino. Since the Prince of Piombino Niccolò Ludovisi was a nephew of the Pope, this action would have been particularly effective in exerting pressure on the Church State. Moreover, the conquest of Porto Longone and the Principality of Piombino would have been a hindrance to Spain's maritime traffic and a threat to the Viceroyalty of Naples. The Cardinal therefore entrusted the command of the expedition to Marshals De La Milleraye and Du Plessis-Pralin.

Although the Duke of Arcos, Viceroy of Naples, had taken steps to reinforce the exhausted troops of the Presidium State and the Grand Duke of Tuscany had sent new troops to Portoferraio and Livorno, Porto Longone remained poorly protected by a small garrison. The French fleet divided into two contingents: one dropped anchor in the roadstead of Madiella, near Capo Stella; the other landed on the beach of Ortano, where the two commanders of the expedition also disembarked. On 28 September 1646, the two French squadrons met under the Fort of Longone, which could not have resisted for long. However, realising that the defence put up by the encircled garrison would delay the capitulation, General Du Plessis headed for Piombino, conquering it after just four days of siege.

After leaving 800 infantrymen and 400 cavalrymen at Piombino, Du Plessis returned to Porto Longone, where the siege was proving more difficult than anticipated. On 26 October 1646, however, the French blew up the walls of the fortress with a mine, giving the battle a decisive turn. The governor of Longone, Don Alfonzo Covello de Ribera, negotiated with the besiegers, then on 31 October 1646 the Spanish troops abandoned the stronghold and were led to Porto Ercole by two French vessels.Fort of Longone wasimmediately occupied by French troops commanded by Baron de Nouaylles.

The loss of Porto Longone caused serious damage to Spanish policy in Italy, as Spain lost a strategic port of call for maritime communication with the Neapolitan region, which now became an ideal base for the French in their strategy of pressure against the Ecclesiastical State and the Viceroyalty of Naples. Due to this unfavourable situation and urgent war expenses, the Duke of Arcos had to impose new duties, such as a tax on fruit, which provoked an immediate and violent popular uprising in Naples between 7 and 16 July 1647, led by the Amalfi fisherman Tommaso Aniello, better known as Masaniello. The killing of the ringleader by the classes most harmed by the uprising, i.e. the large bourgeoisie, led to the rehabilitation of Masaniello and the formation of the Republic of Naples, despite the arrival in port of a Spanish fleet commanded by Don John of Austria, son of King Philip IV of Habsburg.

While the Peace of Westphalia of 24 October 1648 put an end to the war between France and the Holy Roman Empire, the turmoil started by Masaniello was quelled with the rise of a new Spanish viceroy, don Junigo Velez de Guevara, Count of Oñate, who gathered the support of all the barons of the most eminent Neapolitan aristocracy between 1648 and 1649, to restore the order of the Viceroyalty in 1650. Philip IV then ordered Don Juan of Austria, the Count of Oñate and the governor of Milan, the Marquis of Caracena, to prepare the reconquest of Longone.

Thus, on 6 May 1650, Don Juan of Austria assembled an impressive fleet in the Gulf of Gaeta, including ships belonging to Cardinal Trivulzio, Viceroy of Sardinia, and Niccolò Ludovisi, who was interested in recovering the Principality of Piombino. The Spanish fleet set sail from Gaeta on 23 May, and one of its squadrons reached the island of Elba on the 25th of the same month. The Spanish also landed in the gulfs of Madiella and Ortano, only to discover that the defences of Porto Longone had been strengthened by the French and therefore had to prepare for a long siege. The other Spanish contingent, commanded by the Count of Conversano and accompanied by Niccolò Ludovisi's troops, besieged Piombino and recaptured it after a month. After a large part of the second squad reunited with the first under the Fort of Longone, the siege continued due to the Spanish reluctance to use artillery and explosives against the stronghold they had built. After attempting to take the fortress with a vigorous assault on the night of 14-15 July, Don Juan of Austria decided to resort to mines. After realising how desperate the situation was, the French troops threatened to mutiny in front of their commander, General Nouaylles, forcing him to negotiate with the Spanish. Therefore, on 15 August 1650, Baron Nouaylles and his soldiers left the Fort of Longone to embark on Spanish ships that would take them to the nearest French port.

The Presidios thus went through a period free of military threats between 1650 and 1707, strengthened by the Peace of the Pyrenees in 1659, which sanctioned the end of hostilities between Spain and France. Those years were characterised by an economic revival that was followed by a better standard of living for the population, disturbed however by the frequent plagues brought by the ships that docked in the ports of Argentario and Talamone. For this reason, in 1676 a Health Commissariat was set up in the State of the Presidi, divided into 'deputies' and 'ministers' in charge of overseeing the sanitary conditions of the territory. In 1657, the Spanish built Fort Focardo on the promontory opposite Fort Longone, both on the island of Elba.

During this historical period, the political and geographical integrity of the Presidium State was called into question before and during the war of devolution waged by the 'Sun King' Louis XIV, as the loyalty of the Grand Duke of Tuscany was disputed between the Holy Roman Empire, Spain and France. In fact, Grand Duke Cosimo III de' Medici received promises of great territorial rewards, even greater than the Tuscan Presidios, even going so far as to demand the title of King of Sardinia, making his claims on the basis of ancient possessions on the island by the Republic of Pisa. In 1691, Count Antonio Carafa descended on Milan, commanding Spanish troops, to impose a substantial monetary contribution on the Grand Duke of Tuscany. When Cosimo III threatened to form an alliance with the French in response to this request, the Spanish leader considerably reduced the sum to be demanded and hypothesised that it was much more desirable to consolidate and develop the ports of the State of the Presidia with a view to competing with the Medicean port of Livorno, which at the time had become one of the most important in the Mediterranean[39].

5.7 The State of the Presidi in the Age of Austrian Rule and in the Age of the Bourbon Rule

Charles II of Habsburg, the only male son of King Philip IV of Spain had no direct heirs. Both the Holy Roman Emperor Leopold I and the King of France, Louis XIV, could claim succession rights to the Spanish throne as they had married Maria Marguerite and Maria Theresa respectively, children of Philip IV. Louis XIV's position was even advantaged, as Cardinal Mazarin had arranged the marriage with Maria Theresa by negotiating a dowry in money so large that it could not even be covered by King Philip IV's finances, which is why the cancellation of this debt could have been a quid pro quo for the succession to the Spanish throne. In any case, the two

5.7/ Pianta di tutta la spiaggia del Mare Toscano da Bocca di Magra fino allo Stato Ecclesiastico (Map of the entire beach of the Tuscan Sea from Bocca di Magra to the State of the Church). Hypothetical dating: mid-19th century. Archivio di Stato di Firenze (Florence State Archives). Archival collection: ASFi, Miscellanea di Piante, 468. Catalogue ID #6158. Su concessione del Ministero della cultura / Archivio di Stato di Firenze (by courtesy of the Italian Ministry of Culture / Florence State Archives).

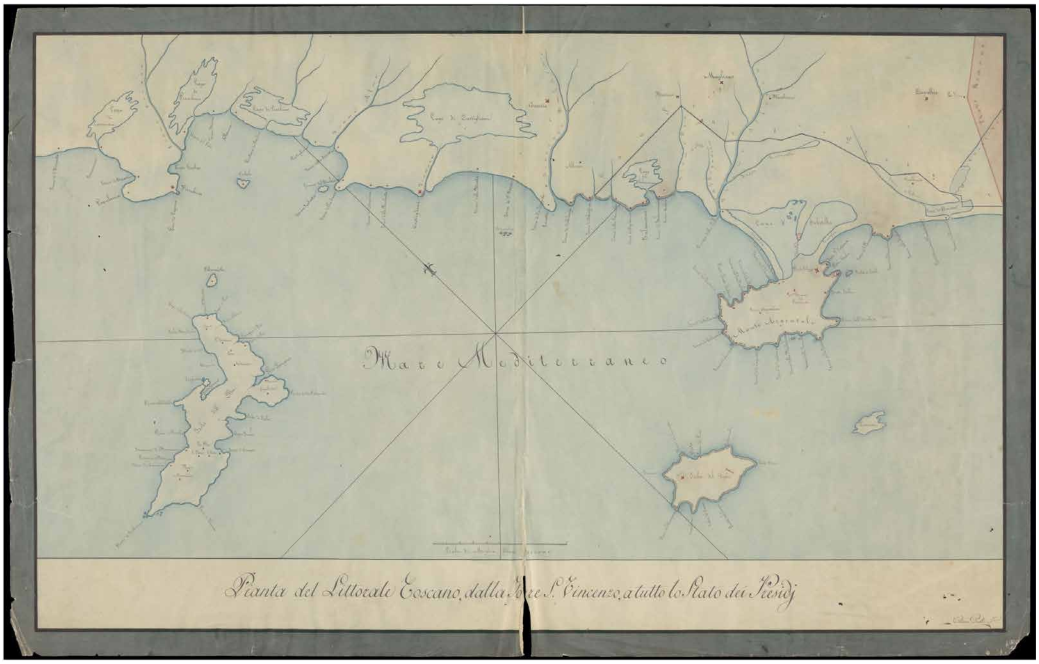

5.8/ Pianta del Littorale Toscano, dalla Torre S. Vincenzo, a tutto lo Stato dei Presidj (Map of the Tuscan coastline, from the Torre S. Vincenzo, to the entire State of the Presidi). Hypothetical dating: 1814-1824. Archivio di Stato di Firenze (Florence State Archives). Archival collection: ASFi, Piante dello Scrittoio delle Fortezze e Fabbriche, 6. Catalogue ID #15504. Su concessione del Ministero della cultura / Archivio di Stato di Firenze (by courtesy of the Italian Ministry of Culture / Florence State Archives).

5.9/ Pianta geometrica del territorio adiacente alle dogane di Port'Ercole, Porto S.Stefano, Torre delle Saline (Geometrical plan of the territory adjacent to the customs posts of Port'Ercole, Porto S. Stefano, Torre delle Saline). Hypothetical dating: 1830-1835. Archivio di Stato di Firenze (Florence State Archives). Archival collection: ASFi, Miscellanea di Piante, 289n. Catalogue ID #5746. Su concessione del Ministero della cultura / Archivio di Stato di Firenze (by courtesy of the Italian Ministry of Culture / Florence State Archives).

sovereigns claimed the throne for their descendants. Leopold I wanted to place his second son, Archduke Charles of Habsburg, on the Spanish throne; Louis XIV made claims for his grandson Philip of Anjou.

In the meantime, Charles II had first nominated Prince Ferdinand Joseph, son of the Elector of Bavaria and a daughter of Emperor Leopold I, as his successor, but the latter died prematurely and forced the King of Spain to establish an order of succession, according to the following sequence: Philip of Anjou; the Duke of Berry, Charles; the Archduke Charles of Habsburg, Victor Amadeus II of Savoy.

Immediately after the death of Charles II on 1 November 1700, Louis XIV forcibly installed his nephew Philip of Anjou on the Spanish throne, thus triggering a conflict that saw Austria and England on one side; France, Spain, Bavaria, Portugal and Savoy on the other. The War of the Spanish Succession lasted from 1701 to 17014 and is usually analysed in three phases.

The first phase, from 1701 to 1703, saw the Bourbons in the lead In 1702 Louis XIV suggested to his nephew Philip of Anjou to make a diplomatic trip to Sicily, Naples and the Presidium State. In this way the French secured the neutrality of Pope Clement XI and the sympathy of the Grand Duke of Tuscany, Cosimo III dei Medici. After Naples, Philip's journey

Luca Martelli

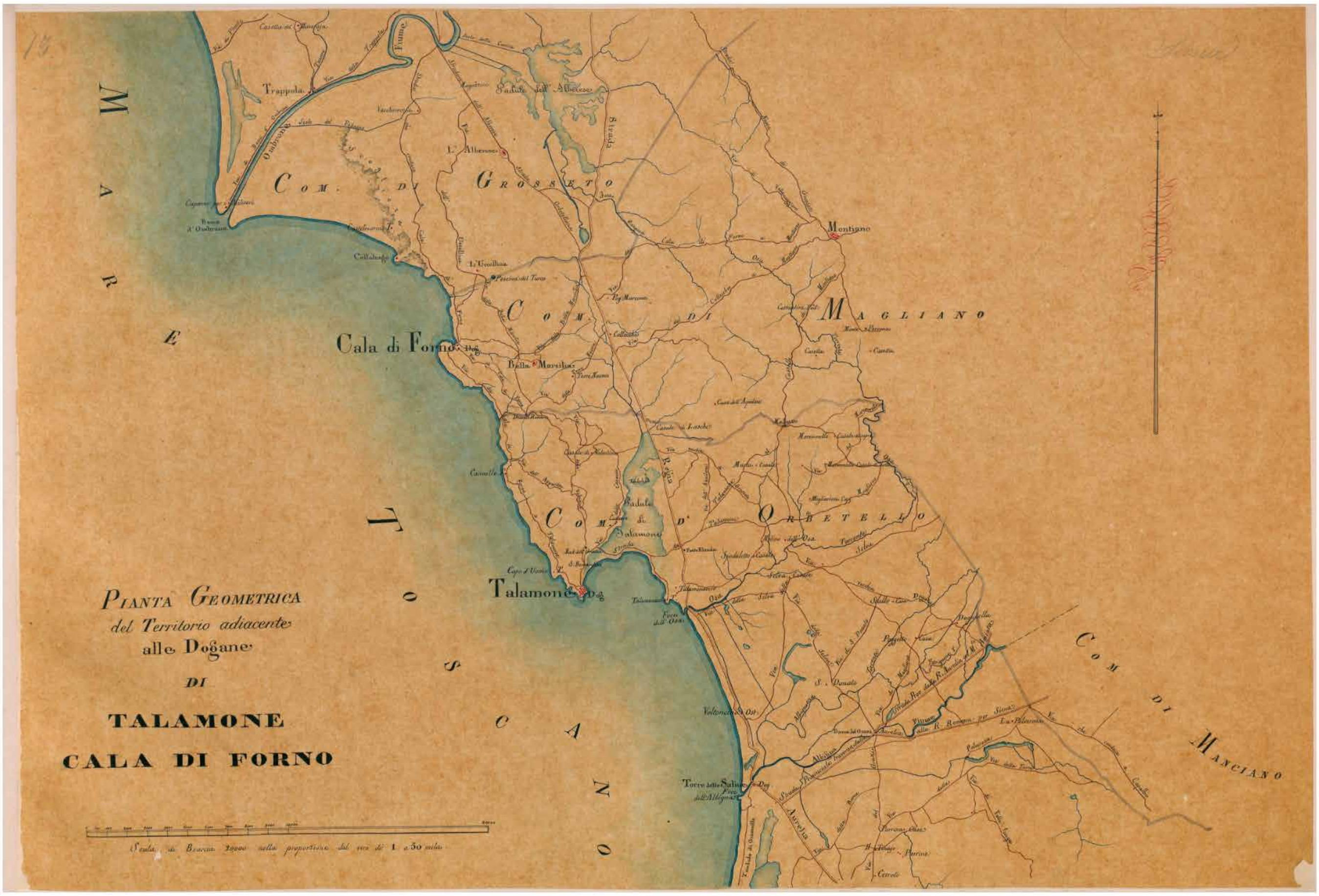

5.10/ Pianta geometrica del territorio adiacente alle dogane di Talamone, Cala di Forno (Geometric plan of the territory adjacent to the customs posts of Talamone, Cala di Forno). Hypothetical dating: 1830-1835. Archivio di Stato di Firenze (Florence State Archives). Archival collection: ASFi, Miscellanea di Piante, 289o. Catalogue ID #5758. Su concessione del Ministero della cultura / Archivio di Stato di Firenze (by courtesy of the Italian Ministry of Culture / Florence State Archives).

touched on Porto Santo Stefano, Portoferraio and Livorno.

In the second phase, from 1704 to 1709, the Bourbons suffered political defeats and military defeats, as in the battles of Ramillies in Belgium and Turin). In 1704, the English landed in Barcelona and Catalan separatists acclaimed the Austrian pretender, Archduke Charles of Habsburg. After defeating French forces in Piedmont and Lombardy, Prince Eugene of Savoy, as commander of the Imperial forces, sent an expeditionary force against the Viceroyalty of Naples in 1707, which routed the troops of the Prince of Castiglione, the Duke of Bicaccia and Nicola Pignatelli at Garigliano. On 3 July, the Imperials entered Capua and the viceroy, the Marquis of Villena, took refuge in the fortress of Gaeta. Thus it was that on 7 July the Imperials took possession of the Viceroyalty of Naples, while the first Austrian viceroy, Count Martinitz, took office. In 1708, the new viceroy sent a military contingent to conquer the Presidio State. It found no resistance in Orbetello, since Governor Bartolomeo Specovera and Auditor General Ferdinando Alvare had already recognised Charles III of Habsburg as the successor to Charles II of Spain. However, the new general of the Spanish fortresses in Italy, Francesco Pinelli, consolidated the fortresses of Porto Ercole, counting on the fact that the imperial armies of General Wetzeel did not have sufficient forces to conquer them. The

5.11/ Pianta geometrica del territorio adiacente alla dogana di Piombino (Geometric plan of the territory adjacent to the customs posts of Piombino). Hypothetical dating: 1825-1830. Archivio di Stato di Firenze (Florence State Archives). Archival collection: ASFi, Miscellanea di Piante, 286a. Catalogue ID #5689. Su concessione del Ministero della cultura / Archivio di Stato di Firenze (by courtesy of the Italian Ministry of Culture / Florence State Archives).

Austrian troops therefore limited themselves to garrisoning Orbetello and making sporadic actions for the Argentario, thus managing to occupy Porto Ercole. In 1708, the Imperials conquered Fort Focardo on Elba, but suffered a setback by failing in their attempt to conquer Fort Longone and were driven off the island with the arrival of French and Spanish reinforcements. Meanwhile, the new viceroy of Naples, Count Daun, ordered the siege of Porto Ercole. To carry out the task, the imperial governor of Orbetello, Count Alfredo Dietrichstein, recruited volunteers from among the inhabitants of the capital of the Stato dei Presìdi, who organised sorties. The Spanish responded by bombarding Orbetello and launching a number of offensive actions against the town. However, not only did the townspeople put up an effective resistance, they even launched a violent counter-offensive on 1 December 1709, and even occupied Talamone, which until then was still in Spanish hands. A peculiar stalemate was thus created in the Presidio State: the Imperials were stationed in Orbetello, Porto Santo Stefano and Talamone; the Spanish remained in Porto Ercole and Porto Longone.

Like the Spaniards, the Austrians also recognised the administrative autonomy of the Presidi State while keeping it under the rule of the viceroys of Naples.

In the third phase, from 1710 to 1714, a series of events led to negotiations. England and Holland withdrew from the war, while Archduke Charles had inherited the imperial crown, thus losing interest in obtaining the Crown of Spain. In 1711, imperial troops descended into Tuscany from Lunigiana to station themselves in the Maremma awaiting artillery that they were to receive from Naples, in order to attack Porto Ercole and Porto Longone, still in Spanish hands. This actually resulted in the conquest of Porto Ercole alone on 22 March, for a victory of demonstration and prestige, aimed at gaining a diplomatic advantage in view of the surrender negotiations in the European geopolitical framework.

Following the treaties of Utrecht in 1713 and Rastadt in 1714, therefore, Philip of Anjou was recognised as King of Spain and was crowned as Philip V.

Spain lost Belgium, Gibraltar, Minorca, several colonies and all Italian territories. Of the latter, Sicily went to the Savoy, resulting in the establishment of the Savoy Kingdom, while all other dominions passed to Austria, including the Presidios Between 1733 and 1738, the War of Polish Succession took place, the end of which was sanctioned by the Treaty of Vienna. On that occasion, the state of the Tuscan Presidia passed to the Bourbons of the Kingdom of the Two Sicilies. With the extinction of the Medici family, the rest of Tuscany passed under the Habsburg-Lorraine dynasty. During the sixty years of Bourbon rule, the Presìdi became practically a welfare state, where all the inhabitants were state employees of a bureaucratic administration in the civil, religious, judicial and military branches. In fact, in addition to the slow and inexorable decay of the fortified structures, the number of soldiers was excessive compared to the needs at that time. All this idle military force was enrolled among the State's citizens from birth and was maintained by the King of Naples through monthly subsidies. This situation, in addition to dissipating the economic resources of the territory and preventing the development and exploitation of environmental resources, severely limited the development of economic and cultural activities.

On 22 November 1801, the Tuscan Presidium State was annexed to the Kingdom of Etruria, a satellite state of Napoleonic France[40].

Notes

1 Fanciulli 1999, pp. 53, 76-87; Istituto dell'Enciclopedia Italiana Treccani, 1935; Mori, Scaramella 1935; Regione Toscana 2015a, pp. 8-13; Regione Toscana 2015b, pp. 8-11.

2 Maioli 2015, p. 26.

3 Regione Toscana 2015a, pp. 28-33; Mori, Solari, Scaramella, 1932.

4 Regione Toscana 2015a, pp. 28-33; Repetti 1841, pp. 290-296.

5 Regione Toscana 2015b, pp. 8, 20-26; Repetti 1841, pp. 677-678.

6 Maioli 2015, pp. 26-27; Regione Toscana 2015b, pp. 20-26, 28-33.

7 Maioli 2015, pp. 290-291.

8 Repetti 1841, p. 674.

9 Maioli 2015, pp. 290-292; Regione Toscana 2015b, pp. 20-26; 28-33.

10 Gazzetta ufficiale della Repubblica Italiana No. 227 of 20 August 1980, Part I, pp. 6986-6987; Maioli 2015, pp. 290-295, 304-305; Regione Toscana 2015b, pp. 28-33; Repetti 1841, pp. 678-679.

11 The terms 'open waters' or 'free waters' are used to identify areas of varying depths where no islets or sandbanks are present. In the case of the Orbetello Lagoon, they can reach a maximum depth of about 2 m with a salinity similar to that of the sea (3.7 ‰), cf. Maioli 2015, p. 295.

12 Gazzetta ufficiale della Repubblica Italiana No. 227 of 20 August 1980, Part I, pp. 6987-6988; Maioli 2015, pp. 290-295, 304-305; Regione Toscana 2015b, pp. 20-26, 28-33; Repetti 1841, pp. 678-679.

13 Della Monaca, Roselli, Tosi 1996, pp. 152-153; Repetti 1841, p. 677.

14 Regione Toscana 2015b, pp. 8, 20-26; Repetti 1833, pp. 127-128; Repetti 1841, pp. 677-680.

15 Regione Toscana 2015b, pp. 20-26, 28-33; Repetti 1833, pp. 127-128; Repetti 1835, pp. 592-599; Repetti 1841, pp. 677-680.

16 Regione Toscana 2015a, pp. 8, 20-21; Repetti 1835, pp. 583-605; Repetti 1841, pp. 609-610.

17 Regione Toscana 2015a, pp. 20-21, 28-33; Repetti 1835, pp. 583-605; Repetti 1841, pp. 609-610.

18 Regione Toscana 2015a, pp. 20-21, 28-33.

19 Giroldini 2010, p. 13; Mori 1935; Mori, Scaramella 1935; Regione Toscana 2015a, pp. 8, 20-21; Repetti 1841, p. 268, 290-296.

20 Regione Toscana 2015a, pp. 20-21, 28-33.

21 Regione Toscana 2015a, p. 9-10; Regione Toscana

2015b, p. 9; Uggeri 1979, p. 38.
22 Regione Toscana 2015a, p. 9-10; Regione Toscana 2015b, p. 9; Uggeri 1979, p. 39.
23 Regione Toscana 2015a, pp. 9-10; Regione Toscana 2015b, p. 9; Uggeri 1979, pp. 39-42.
24 Regione Toscana 2015a, pp. 9-10; Regione Toscana 2015b, p. 9; Uggeri 1979, pp. 42-43.
25 Maioli 2015, pp. 32, 35-36; Regione Toscana 2015a, p. 10; Regione Toscana 2015b, pp. 9-10; Uggeri 1979, pp. 44-45.
26 Maioli 2015, pp. 32, 35-57, 168-169; Regione Toscana 2015a, p. 10; Regione Toscana 2015b, p. 10; Uggeri 1979, pp. 45-51.
27 Maioli 2015, pp. 32-33, 60, 91, 93, 171-172; Regione Toscana 2015a, p. 10; Regione Toscana 2015b, pp. 10-11; Uggeri 1979, pp. 51-53.
28 Maioli 2015, pp. 32-33, 60-61, 72-73, 93, 172-173; Regione Toscana 2015a, p. 10-11; Regione Toscana 2015b, pp. 10-11; Uggeri 1979, pp. 51-53.
29 Caciagli 1971, p. 2; Maioli 2015, pp. 176-177.
30 Caciagli 1971, pp. 4-9; Maioli 2015, pp. 176-177.

31 Cf. Responsum XIX, nos. 28-31 in Deciani 1579, p. 173; Marrara 1979, p. 65.
32 Caciagli 1971, pp. 13-23; Maioli 2015, pp. 176-177; Marrara 1979, pp. 65-69; Mori, Solari, Scaramella 1932.
33 Caciagli 1971, pp. 9-11; 23-30; Marrara 1979, pp. 65-70.
34 Caciagli 1971, pp. 54-57; Fanciulli 1999, pp. 255-256.
35 Mori, Scaramella 1935; Mori, Solari, Scaramella 1932; Repetti 1841, pp. 285-286.
36 The formula of cuius regio eius religio derived from the conclusions reached with the Peace of Augsburg of 3 October 1555, desired by Charles V of Habsburg and constituting the first official recognition of the Protestant Reformation. With this principle, subjects were obliged to observe the religion of their prince, who instead enjoyed freedom of choice over his own confession. An influential element was the fact that, in the event of a change to the Protestant faith, a prince could arrogate to himself the right to forfeit all assets enjoyed by the Catholic Church in the territories of his principality until 1552. Most princely conversions of the time were stimulated by this very right. Cf. Caciagli 1979, p. 118.
37 Caciagli 1979, pp. 118-121; Istituto dell'Enciclopedia Italiana Treccani 2011a; Istituto dell'Enciclopedia Italiana Treccani 2011b.
38 Caciagli 1979, pp. 121-127.
39 Caciagli 1979, pp. 57-62; 116; 129-136.
40 Caciagli 1979, pp. 137-143.

Sintesi

Lo Stato dei Presìdi toscani si estese su diversi ambiti territoriali non contigui, i quali possono essere grossomodo individuati come quattro zone: l'Agro orbetellano, il Promontorio dell'Argentario, l'ex distretto di Porto Longone sull'Isola d'Elba e l'area dell'ex Principato di Piombino. Si tratta di quattro contesti ambientali distinti, le cui caratteristiche individuali hanno influenzato lo sviluppo del sistema insediativo poi assorbito dallo Stato dei Presìdi.

La presenza di insediamenti capannicoli di orizzonte appenninico lungo i Tomboli di Feniglia e Giannella (gli istmi che collegano il Monte Argentario con l'Agro orbetellano) attesta che questi ultimi si erano già formati e consolidati nel secondo millennio a.C. Nel periodo protovillanoviano tutte le zone costiere si spopolarono improvvisamente, probabilmente a causa di minacce provenienti dal mare: gli insediamenti si concentrarono così in posizioni d'altura spesso già abitate ma, a quel punto, divenute privilegiate in quanto naturalmente arroccate e quindi più sicure. Questo fenomeno si tradusse nella comparsa dei castellieri, insediamenti su rilievi le cui difese venivano potenziate con opere di fortificazione e ravvivando gli scoscendimenti con più cerchie concentriche di mura costruite a secco con tecnica megalitica.

Con lo sviluppo della civiltà etrusca, nella bassa Maremma scomparirono tutti i castellieri e uno dei centri di maggiore attrazione oltre a Vulci divenne una città lagunare corrispondente all'attuale Orbetello. Quest'insediamento non era visibile dalle navi passanti per il Mar Tirreno ed era quasi innaccessibile per via di terra, garantendo ad essa sicurezza.

A partire dall'età del Ferro avanzata iniziò una progressiva antropizzazione del territorio, mentre prese avvio una den-

sificazione degli insediamenti attorno ai nuclei primitivi di Marsiliana, Orbetello e Pescia.

La fondazione della colonia romana di Cosa condizionò fortemente l'Agro orbetellano. Essa costituiva un presidio di cittadini romani, estranei alla popolazione del territorio vulcente e i cui interessi erano catalizzati da una fascia di terreno agricolo centuriato piuttosto limitata localizzata subito all'esterno della città. In quanto avamposto romano, Cosa ebbe una certa importanza al momento della conquista dell'Etruria, ma iniziò rapidamente la propria decadenza dalla metà del II secolo a.C. La pace all'interno dello Stato romano e la prosperità delle piantagioni favorirono il decentramento degli insediamenti, che verso l'ultimo quarto del II secolo a.C. cominciarono ad espandersi su tutte le piane fertili e su tutte le coste, ricalcando quanto avvenuto durante l'età del Bronzo. Tuttavia, nel corso dell'Impero, questa fortunata situazione di libera espansione degli insediamenti in posizioni amene ma esposte e quindi poco protette volse al termine.

Nel corso dell'alto Medioevo sopravvissero pochissimi siti, per i quali non è neanche possibile escludere che la frequentazione fosse occasionale e limitata nel tempo.

Tra l'alto e il basso Medioevo, tutto il territorio fu dominio ecclesiastico, prima della basilica romana dei Santi Marcellino e Pietro presso il Monte Argentario, poi dell'abbazia romana delle Tre Fontane nel territorio cosano e dell'abbazia amiatina di San Salvatore, presso Talamone.

Nel secolo XIII queste terre divennero feudi degli Aldobrandeschi, i quali edificarono fortezze nei punti chiave del territorio, ripercorrendo quanto accaduto in epoca protostorica.

Nel frattempo, il tasso di criminalità ad Ansedonia divenne così alto che nel 1329 venne distrutta dai Senesi. Nel 1337 venne distrutta anche Talamone, per poi essere ricostruita dai Senesi nel 1357.

Il 30 maggio 1554, l'imperatore Carlo V d'Asburgo cancellò ogni privilegio concesso dai suoi predecessori alla Repubblica di Siena e la dichiarò ricaduta sotto la piena autorità del Sacro Romano Impero, attribuendone il relativo distretto al figlio Filippo.

Il 3 luglio 1557, dopo l'abdicazione di Carlo V, il re di Spagna Filippo II attribuì Siena ed il suo territorio a Cosimo dei Medici. Da tale infeudazione restarono però espressamente esclusi Porto Ercole, Porto Santo Stefano, Orbetello, Talamone e il Monte Argentario. Le proteste con le quali il Duca di Firenze tentò di evitare lo smembramento dei territori senesi furono vane poiché Filippo II, al pari di suo padre, era conscio del valore strategico di quelle fortezze marittime per la supremazia spagnola nel Mar Tirreno.

La spartizione decretata nel 1557, però, potè relizzarsi appieno soltanto dopo il ritiro delle truppe francesi conseguente al trattato di Cateau-Cambrèsis, nonché dopo la resa della Repubblica di Siena riparata a Montalcino, avvenuta il 31 luglio 1559. Questo nuovo assetto politico-giuridico della Toscana meridionale venne poi a consolidarsi definitivamente con le ratifiche degli imperatori asburgici Ferdinando I e Massimiliano II. Quando la lotta fra la Spagna e l'Islam si spostò ad Est verso il Tirreno, Talamone, Porto Ercole e Orbetello acquistarono improvvisamente un'importanza ben diversa da quella avuta sino ad allora. Da semplici scali economici divennero basi militari e strategiche, sia per scopi di difesa contro i Turchi e i Barbareschi, sia per esercitare una funzione di controllo sul Granducato di Toscana e lo Stato della Chiesa.

Luca Martelli

6. Integration of Synthetic Aperture Radar remote-sensing and other survey techniques

6.1 Role of radar remote-sensing within integrated survey operations

With regard to the integrated survey operations concerning the Spanish Fortress of Porto Santo Stefano, in the municipality of Monte Argentario and Talamone Town Walls in the municipality of Orbetello, two possible uses for radar remote-sensing were identified, both connected to the technique of Synthetic Aperture Radar Tomography (TomoSAR):

- the introduction of data regarding the average displacement velocities, along the Line of Sight (LOS) of selected satellite radars, of certain points in the urban areas studied;
- a modest contribution to the refinement of point clouds concerning the urban contexts of the sites chosen for the integrated surveys and acquired using standard techniques. In this case we are not referring to point clouds on an architectural scale obtained with laser scanner instruments or with Structure from Motion (SfM) photomodelling, but to point clouds on an urban scale with a lower density, such as those obtainable with a LIght Detection And Ranging (LIDAR) sensor mounted on an aerial platform or with a Total Station.

We initially decided to generate two tomographic point clouds, one for the site of Porto Santo Stefano and one for the site of Talamone, from a set of radar scans covering the portion of Tuscan coastline between Alberese and Burano. This first tomographic processing of the two point clouds used the NASADEM data as an external source of topographical information of the scene. NASADEM is a public domain Digital Elevation Model (DEM) with a ground resolution of 30m. We then obtained from the Deutsches Zentrum für Luft- und Raumfahrt e.V. (DLR) data regarding the same area of interest, which is from a DEM derived from observations of the TanDEM-X mission and that had 12 m ground resolution. We reiterated the process with this data as a source of topographical information of the scene, in order to be able to compare the results with those obtained from NASADEM. In total, we therefore obtained four tomographic clouds, two per case study.

6.1.1 Programming the tomographic cloud generation process

Thanks to the advice of Dr. Gianfranco Fornaro and Dr. Simona Verde of the Institute for Electromagnetic Sensing of the Environment of the National Research Council (Istituto per il Rilevamento Elettromagnetico dell'Ambiente del Consiglio Nazionale delle Ricerche – IREA-CNR), we planned a workflow for the generation of clouds from TomoSAR, divided into the following phases:

1. Selection and collection of 160 radar images from the COSMO-SkyMed (COnstellation of small Satellites for the Mediterranean basin Observation) satellite mission of Italian Space Agency (Agenzia Spaziale Italiana – ASI)[1] in Stripmap acquisition mode, acquired in succession and characterised by the lowest possible temporal separation.
2. An initial tomographic processing, by IREA-CNR, of the 160 COSMO-SkyMed products using the NASADEM [2]public domain Digital Elevation Model (DEM), with a ground resolution of 30 m.
3. The request and collection of DEM data from the TanDEM-X mission of the Deutsches Zentrum für Luft- und Raumfahrt e.V. (DLR)[3], having a ground resolution of 12 m.
4. A second, finer tomographic processing, by IREA-CNR, of the 160 COSMO-SkyMed products, using TanDEM-X data. The finer resolution of this DEM allows a reduction in the margin of error in the positioning of targets identified by the tomographic cloud.

6.2 The tomographic processing

In order to allow the delivery of the data by ASI and DLR and,

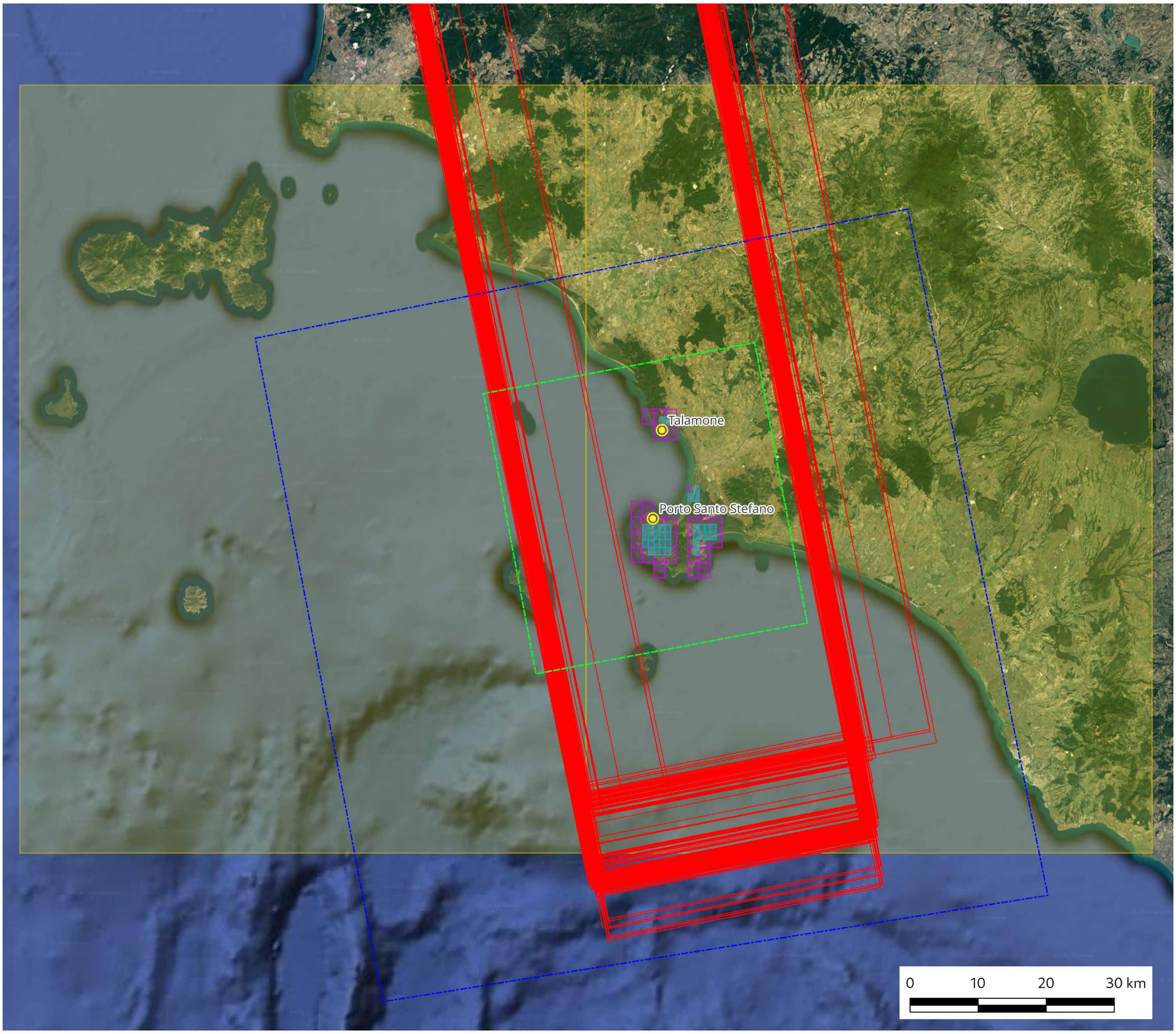

6.1/ Map based on Google Maps™, showing the case study sites (yellow dots), the coarse area of interest (blue square), the fine area of interest (green) and the areas related to the collected satellite radar data. The COSMO-SkyMed radar scan strips are highlighted in red. The DEM data tablets of the TanDEM-X mission are highlighted by beige rectangles. Source: Agenzia Spaziale Italiana, 2022. Products processed by Luca Martelli under a license of the Italian Space Agency (ASI); Original COSMO-SkyMed Products - ©ASI - (2012-2017); Deutsches Zentrum für Luft- und Raumfahrt e.V., 2006. © DLR <2023>. Google™ and Google Maps™ are trademarks of Google LLC and this thesis is not endorsed by or affiliated with Google in any way.

at the same time, to be able to establish an exchange channel between the Department of History, Design and Restoration of Architecture (Dipartimento di Storia, Disegno e Restauro dell'Architettura – DSDRA) of the Sapienza University and IREA-CNR, a computer server was set up.
Below we describe the various phases of the tomographic processing and the results achieved.

6.2.1 Selection and collection of 160 radar images from the COSMO-SkyMed mission

In November 2022, with the support of IREA-CNR, through a comparison with the acceleration maps of Synthetic Aperture Radar (SAR) data from the Environmental Satellite (Envisat) and European Remote-Sensing satellite (ERS) missions accessible from the Italian Ministry of the Environment's National Geoportal, it was determined that the best possible radar illumination for the Porto Santo Stefano and Talamone sites was that given by ascending orbital passages.
With the advice of Dr. Verde, between March and May 2022 we identified 160 products in the COSMO-SkyMed mission catalogue that frame the stretch of Tuscan coastline between (approximately) Alberese and Burano from ascending passages. At that time, the COSMO-SkyMed mission had four first-generation satellites (fig. 6.2) and two second-generation satellites, all in polar orbit and equipped with X-band SAR. However, in that period, the area of interest had only been scanned by the first-generation satellites.
The succession of selected scans, all belonging to the ascending orbital tract H4-01, begins with the acquisition of 17 July 2012 and ends with that of 6 August 2022, for an observation time interval of approximately ten years (Figs. 6.3, 6.4). In addition to the degree of updating of the radar images, this succession was also determined by the degree of temporal separation ΔT between one product and the next, which had to be limited above a value of -100. With the chosen sequence of images, the minimum value achieved was ΔT=-80.
In May 2022, a request was then submitted to the ASI for the delivery of the 160 selected COSMO-SkyMed products. An agreement was then signed in July 2022 between DSDRA of Sapienza University, IREA-CNR and ASI for the delivery and use of the radar images (fig. 6.5). The transmission of COSMO-SkyMed products from ASI to DSDRA of Sapienza University took place from July to September 2022. A copy of the radar images was sent to IREA-CNR on 16 September 2022.

6.2.2 First tomographic processing of 160 COSMO-SkyMed products using NASADEM data

Between September 2022 and April 2023, Dr. Verde and Dr. Diego Reale of IREA-CNR performed processing with four-dimensional TomoSAR techniques on the stack of 160 radar images. NASADEM, which is in the public domain and has a ground resolution of 30 m, was used as the DEM data source. NASADEM is the result of a scan performed during the Shuttle Topography Radar Mission (SRTM) in February 2000, which was subsequently supplemented by numerous additional interferometric acquisitions.
The processing consisted of a first phase at a territorial scale over the entire extent of each COSMO-SkyMed product, followed by a second phase at an urban scale framing the sites of the Spanish Fortress of Porto Santo Stefano and Talamone Town Walls[4].
From a material point of view, the result of the processing are two spreadsheets in .csv format: one concerning the Porto Santo Stefano site and one concerning the Talamone site. In addition to containing the georeferenced position (in WGS84) of each persistent backscatterer identified in the two areas of interest, the spreadsheets also report the average speed of di-

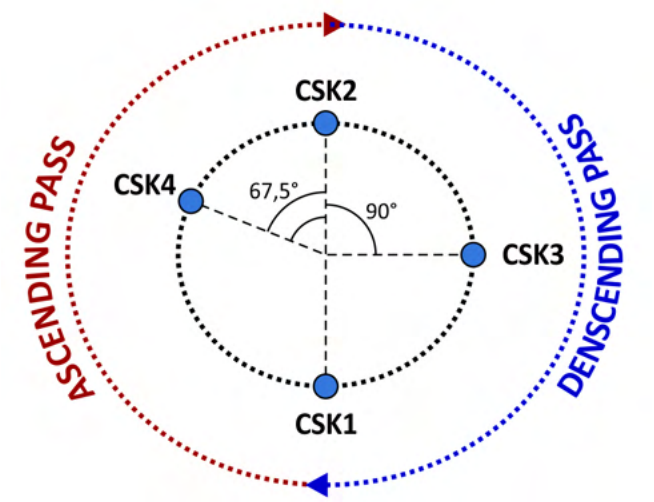

6.2/ Diagram of COSMO-SkyMed first generation constellation, in polar orbit. Source: Battagliere, Virelli 2019.

DATE AND HOUR OF SCAN	CATEGORY CODE	DATE	DECORRELATION		ORDER N.	PRODUCT ID.	FOLDER NUMBER
2012-07-17 at 04:54:08 UTC	309198	2012-07-17	-16		1726414	1316589	1726414-1316589
2012-08-02 at 04:54:00 UTC	310815	2012-08-02	-16		1747745	1319148	1747745-1319148
2012-08-18 at 04:53:50 UTC	310816	2012-08-18	-48		1747745	1319138	1747745-1319138
2012-10-05 at 04:53:30 UTC	310817	2012-10-05	-16		1747745	1319149	1747745-1319149
2012-10-21 at 04:53:23 UTC	310818	2012-10-21	-16		1747745	1319144	1747745-1319144
2012-11-06 at 04:53:15 UTC	310819	2012-11-06	-56		1747745	1319279	1747745-1319279
2013-01-01 at 04:52:46 UTC	310820	2013-01-01	-40		1747745	1319274	1747745-1319274
2013-02-10 at 04:52:30 UTC	310821	2013-02-10	-16		1747745	1319145	1747745-1319145
2013-02-26 at 04:52:21 UTC	310822	2013-02-26	-16		1747745	1319131	1747745-1319131
2013-03-14 at 04:52:15 UTC	310823	2013-03-14	-16		1747745	1319151	1747745-1319151
2013-03-30 at 04:52:10 UTC	310824	2013-03-30	-16		1747745	1319141	1747745-1319141
2013-04-15 at 04:52:01 UTC	310825	2013-04-15	-32		1747745	1319250	1747745-1319250
2013-05-17 at 04:51:48 UTC	310826	2013-05-17	-16		1747745	1319146	1747745-1319146
2013-06-02 at 04:51:41 UTC	310827	2013-06-02	-16		1747745	1319140	1747745-1319140
2013-06-18 at 04:51:35 UTC	310828	2013-06-18	-16		1747745	1319150	1747745-1319150
2013-07-04 at 04:51:28 UTC	310829	2013-07-04	-16		1747745	1319120	1747745-1319120
2013-07-20 at 04:51:20 UTC	310899	2013-07-20	-16		1747793	1319503	1747793-1319503
2013-08-05 at 04:51:16 UTC	310900	2013-08-05	-32		1747793	1319507	1747793-1319507
2013-09-06 at 04:51:05 UTC	310901	2013-09-06	-16		1747793	1319509	1747793-1319509
2013-09-22 at 04:51:00 UTC	310902	2013-09-22	-16		1747793	1319505	1747793-1319505
2013-10-08 at 04:50:54 UTC	310903	2013-10-08	-16		1747793	1319463	1747793-1319463
2013-10-24 at 04:50:49 UTC	310904	2013-10-24	-16		1747793	1319482	1747793-1319482
2013-11-09 at 04:50:41 UTC	310905	2013-11-09	-16		1747793	1319496	1747793-1319496
2013-11-25 at 04:50:34 UTC	310906	2013-11-25	-16		1747793	1319457	1747793-1319457
2013-12-11 at 04:50:30 UTC	310907	2013-12-11	-16		1747793	1319459	1747793-1319459
2013-12-27 at 04:50:25 UTC	310908	2013-12-27	-24		1747793	1319516	1747793-1319516
2014-01-20 at 04:50:16 UTC	310909	2014-01-20	-32		1747793	1319506	1747793-1319506
2014-02-21 at 04:50:05 UTC	310910	2014-02-21	-16		1747793	1319580	1747793-1319580
2014-03-09 at 04:49:57 UTC	310911	2014-03-09	-24		1747793	1319502	1747793-1319502
2014-04-02 at 04:49:54 UTC	310912	2014-04-02	-16		1747793	1319499	1747793-1319499
2014-04-18 at 04:49:53 UTC	310913	2014-04-18	-16		1747793	1319504	1747793-1319504
2014-05-04 at 04:49:48 UTC	311198	2014-05-04	-32		1769602	1322192	1769602-1322192
2014-06-05 at 04:49:40 UTC	311199	2014-06-05	-16		1769602	1322300	1769602-1322300
2014-06-21 at 04:49:31 UTC	311200	2014-06-21	-48		1769602	1322222	1769602-1322222
2014-08-08 at 04:49:19 UTC	311201	2014-08-08	-16		1769602	1322341	1769602-1322341
2014-08-24 at 04:49:16 UTC	311202	2014-08-24	-16		1769602	1322295	1769602-1322295
2014-09-09 at 04:49:13 UTC	311203	2014-09-09	-16		1769602	1322367	1769602-1322367
2014-09-25 at 04:49:09 UTC	311204	2014-09-25	-32		1769602	1322370	1769602-1322370
2014-10-27 at 04:49:04 UTC	311205	2014-10-27	-16		1769602	1322221	1769602-1322221
2014-11-12 at 04:49:02 UTC	311206	2014-11-12	-48		1769602	1322223	1769602-1322223
2014-12-30 at 04:48:51 UTC	311207	2014-12-30	-8		1769602	1322305	1769602-1322305
2015-01-07 at 04:48:48 UTC	311208	2015-01-07	-16		1769602	1322237	1769602-1322237
2015-01-23 at 04:48:45 UTC	311209	2015-01-23	-16		1769602	1322214	1769602-1322214
2015-02-08 at 04:48:43 UTC	311210	2015-02-08	-16		1769602	1322238	1769602-1322238
2015-02-24 at 04:48:42 UTC	311211	2015-02-24	-16		1769602	1322340	1769602-1322340
2015-03-12 at 04:48:39 UTC	311212	2015-03-12	-32		1769602	1322403	1769602-1322403
2015-04-13 at 04:48:33 UTC	311264	2015-04-13	-32		1769615	1323226	1769615-1323226
2015-05-15 at 04:48:29 UTC	311265	2015-05-15	-16		1769615	1323225	1769615-1323225
2015-05-31 at 04:48:28 UTC	311266	2015-05-31	-16		1769615	1323218	1769615-1323218
2015-06-16 at 04:48:27 UTC	311267	2015-06-16	-16		1769615	1323312	1769615-1323312
2015-07-02 at 04:48:22 UTC	311268	2015-07-02	-64		1769615	1323220	1769615-1323220
2015-09-04 at 04:48:18 UTC	311269	2015-09-04	-16		1769615	1323206	1769615-1323206
2015-09-20 at 04:48:19 UTC	311270	2015-09-20	-16		1769615	1323250	1769615-1323250
2015-10-06 at 04:48:18 UTC	311271	2015-10-06	-16		1769615	1323209	1769615-1323209
2015-10-22 at 04:48:16 UTC	311272	2015-10-22	-16		1769615	1323215	1769615-1323215
2015-11-07 at 04:48:15 UTC	311273	2015-11-07	-32		1769615	1323219	1769615-1323219
2015-12-09 at 04:48:10 UTC	311274	2015-12-09	-16		1769615	1323228	1769615-1323228
2015-12-25 at 04:48:05 UTC	311275	2015-12-25	-16		1769615	1323212	1769615-1323212
2016-01-10 at 04:48:05 UTC	311276	2016-01-10	-16		1769615	1323233	1769615-1323233
2016-01-26 at 04:48:00 UTC	311277	2016-01-26	-16		1769615	1323203	1769615-1323203
2016-02-11 at 04:47:56 UTC	311278	2016-02-11	-16		1769615	1323208	1769615-1323208
2016-02-27 at 04:47:53 UTC	311523	2016-02-27	-16		1769683	1323862	1769683-1323862
2016-03-14 at 04:47:49 UTC	311524	2016-03-14	-16		1769683	1323882	1769683-1323882
2016-03-30 at 04:47:44 UTC	311525	2016-03-30	-16		1769683	1324003	1769683-1324003
2016-04-15 at 04:47:41 UTC	311604	2016-04-15	-16	#	1778532	1324712	1778532-1324712
2016-05-01 at 04:47:33 UTC	311605	2016-05-01	-16	#	1778532	1324715	1778532-1324715
2016-05-17 at 04:47:29 UTC	311528	2016-05-17	-16		1769683	1323863	1769683-1323863
2016-06-02 at 04:47:23 UTC	311529	2016-06-02	-16		1769683	1323865	1769683-1323865
2016-06-18 at 04:47:12 UTC	311530	2016-06-18	-16		1769683	1324028	1769683-1324028
2016-07-04 at 04:47:08 UTC	311531	2016-07-04	-16		1769683	1323914	1769683-1323914
2016-07-20 at 04:47:02 UTC	311532	2016-07-20	-16		1769683	1323915	1769683-1323915
2016-08-05 at 04:46:53 UTC	311533	2016-08-05	-16		1769683	1324004	1769683-1324004
2016-08-21 at 04:46:50 UTC	311534	2016-08-21	-16		1769683	1323866	1769683-1323866
2016-09-06 at 04:46:44 UTC	311535	2016-09-06	-16		1769683	1324371	1769683-1324371
2016-09-22 at 04:46:39 UTC	311536	2016-09-22	-16		1769683	1323883	1769683-1323883
2016-10-08 at 04:46:35 UTC	311537	2016-10-08	-16		1769683	1323970	1769683-1323970
2016-10-24 at 04:46:27 UTC	311636	2016-10-24	-16		1778549	1325092	1778549-1325092
2016-11-09 at 04:46:26 UTC	311637	2016-11-09	-32		1778549	1325129	1778549-1325129
2016-12-11 at 04:46:13 UTC	311638	2016-12-11	-16		1778549	1325104	1778549-1325104
2016-12-27 at 04:46:08 UTC	311639	2016-12-27	-16		1778549	1325096	1778549-1325096
2017-01-12 at 04:46:03 UTC	311640	2017-01-12	-16		1778549	1325132	1778549-1325132
2017-01-28 at 04:45:56 UTC	311641	2017-01-28	-16		1778549	1325138	1778549-1325138
2017-02-13 at 04:45:51 UTC	311642	2017-02-13	-16		1778549	1325133	1778549-1325133
2017-03-01 at 04:45:49 UTC	311643	2017-03-01	-16		1778549	1325099	1778549-1325099
2017-03-17 at 04:45:45 UTC	311644	2017-03-17	-32		1778549	1325128	1778549-1325128
2017-04-18 at 04:45:37 UTC	311645	2017-04-18	-16		1778549	1325094	1778549-1325094
2017-05-04 at 04:45:34 UTC	311646	2017-05-04	-16		1778549	1325100	1778549-1325100
2017-05-20 at 04:45:28 UTC	311647	2017-05-20	-16		1778549	1325136	1778549-1325136
2017-06-05 at 04:45:27 UTC	311648	2017-06-05	-16		1778549	1325103	1778549-1325103
2017-06-21 at 04:45:25 UTC	311649	2017-06-21	-16		1778549	1325139	1778549-1325139
2017-07-07 at 04:45:22 UTC	311650	2017-07-07	-16		1778549	1325098	1778549-1325098

6.3/ List of the first 91 COSMO-SkyMed products used for tomographic processing. Scans performed from 17 July 2012 to 7 July 2017. Source: Agenzia Spaziale Italiana, 2022. Products processed by Luca Martelli under a license of the Italian Space Agency (ASI); Original COSMO-SkyMed Products - ©ASI - (2012-2017).

DATE AND HOUR OF SCAN	CATEGORY CODE	DATE	DECORRELATION	ORDER N.	PRODUCT ID.	FOLDER NUMBER
2017-07-23 at 04:45:23 UTC	312119	2017-07-23	-16	1778579	1326905	1778579-1326905
2017-08-08 at 04:45:22 UTC	312120	2017-08-08	-16	1778579	1326790	1778579-1326790
2017-08-24 at 04:45:22 UTC	312121	2017-08-24	-32	1778579	1326743	1778579-1326743
2017-09-25 at 04:45:24 UTC	312122	2017-09-25	-16	1778579	1326762	1778579-1326762
2017-10-11 at 04:45:23 UTC	312123	2017-10-11	-16	1778579	1327046	1778579-1327046
2017-10-27 at 04:45:27 UTC	312124	2017-10-27	-16	1778579	1326967	1778579-1326967
2017-11-12 at 04:45:29 UTC	312125	2017-11-12	-16	1778579	1326767	1778579-1326767
2017-11-28 at 04:45:27 UTC	312126	2017-11-28	-16	1778579	1326798	1778579-1326798
2017-12-14 at 04:45:28 UTC	312127	2017-12-14	-16	1778579	1326830	1778579-1326830
2017-12-30 at 04:45:31 UTC	312128	2017-12-30	-16	1778579	1327401	1778579-1327401
2018-01-15 at 04:45:31 UTC	312129	2018-01-15	-32	1778579	1326754	1778579-1326754
2018-02-16 at 04:45:29 UTC	312130	2018-02-16	-16	1778579	1326744	1778579-1326744
2018-03-04 at 04:45:34 UTC	312131	2018-03-04	-16	1778579	1326885	1778579-1326885
2018-03-20 at 04:45:38 UTC	312132	2018-03-20	-16	1778579	1326876	1778579-1326876
2018-04-05 at 04:45:39 UTC	312133	2018-04-05	-16	1778579	1326906	1778579-1326906
2018-04-21 at 04:45:38 UTC	312483	2018-04-21	-16	1778772	1328069	1778772-1328069
2018-05-07 at 04:45:43 UTC	312484	2018-05-07	-16	1778772	1328072	1778772-1328072
2018-05-23 at 04:45:46 UTC	312485	2018-05-23	-16	1778772	1328134	1778772-1328134
2018-06-08 at 04:45:46 UTC	312486	2018-06-08	-16	1778772	1328172	1778772-1328172
2018-06-24 at 04:45:49 UTC	312487	2018-06-24	-16	1778772	1328108	1778772-1328108
2018-07-10 at 04:45:54 UTC	312488	2018-07-10	-16	1778772	1328140	1778772-1328140
2018-07-26 at 04:45:50 UTC	312489	2018-07-26	-16	1778772	1328170	1778772-1328170
2018-08-11 at 04:45:51 UTC	312490	2018-08-11	-16	1778772	1328088	1778772-1328088
2018-08-27 at 04:45:53 UTC	312491	2018-08-27	-16	1778772	1328089	1778772-1328089
2018-09-12 at 04:45:55 UTC	312492	2018-09-12	-16	1778772	1328107	1778772-1328107
2018-09-28 at 04:45:56 UTC	312493	2018-09-28	-16	1778772	1328194	1778772-1328194
2018-10-14 at 04:45:57 UTC	312494	2018-10-14	-16	1778772	1328178	1778772-1328178
2018-10-30 at 04:45:59 UTC	312495	2018-10-30	-32	1778772	1328169	1778772-1328169
2018-12-01 at 04:45:57 UTC	312496	2018-12-01	-16	1778772	1328070	1778772-1328070
2018-12-17 at 04:45:59 UTC	312497	2018-12-17	-16	1778772	1328099	1778772-1328099
2019-01-02 at 04:45:57 UTC	313022	2019-01-02	-16	1778787	1328777	1778787-1328777
2019-01-18 at 04:45:57 UTC	313023	2019-01-18	-16	1778787	1328856	1778787-1328856
2019-02-03 at 04:45:58 UTC	313024	2019-02-03	-16	1778787	1328828	1778787-1328828
2019-02-19 at 04:45:59 UTC	313025	2019-02-19	-16	1778787	1328809	1778787-1328809
2019-03-07 at 04:45:58 UTC	313026	2019-03-07	-32	1778787	1328806	1778787-1328806
2019-04-08 at 04:46:01 UTC	313027	2019-04-08	-16	1778787	1328776	1778787-1328776
2019-04-24 at 04:46:04 UTC	313028	2019-04-24	-32	1778787	1328788	1778787-1328788
2019-05-26 at 04:46:05 UTC	313029	2019-05-26	-16	1778787	1328817	1778787-1328817
2019-06-11 at 04:46:05 UTC	313030	2019-06-11	-32	1778787	1328843	1778787-1328843
2019-07-13 at 04:46:08 UTC	313031	2019-07-13	-16	1778787	1328767	1778787-1328767
2019-07-29 at 04:46:06 UTC	313032	2019-07-29	-16	1778787	1328763	1778787-1328763
2019-08-14 at 04:46:08 UTC	313033	2019-08-14	-32	1778787	1328798	1778787-1328798
2019-09-15 at 04:46:13 UTC	313034	2019-09-15	-64	1778787	1328880	1778787-1328880
2019-11-18 at 04:46:23 UTC	313035	2019-11-18	-16	1778787	1328832	1778787-1328832
2019-12-04 at 04:46:22 UTC	313036	2019-12-04	-32	1778787	1328861	1778787-1328861
2020-01-05 at 04:46:14 UTC	313085	2020-01-05	-16	1778821	1329611	1778821-1329611
2020-01-21 at 04:46:14 UTC	313086	2020-01-21	-32	1778821	1329605	1778821-1329605
2020-02-22 at 04:46:14 UTC	313087	2020-02-22	-16	1778821	1329593	1778821-1329593
2020-03-09 at 04:46:11 UTC	313088	2020-03-09	-16	1778821	1329591	1778821-1329591
2020-03-25 at 04:46:15 UTC	313089	2020-03-25	-16	1778821	1329610	1778821-1329610
2020-04-10 at 04:46:17 UTC	313090	2020-04-10	-48	1778821	1329613	1778821-1329613
2020-05-28 at 04:46:17 UTC	313091	2020-05-28	-32	1778821	1329578	1778821-1329578
2020-06-29 at 04:46:13 UTC	313092	2020-06-29	-16	1778821	1329603	1778821-1329603
2020-07-15 at 04:46:09 UTC	313093	2020-07-15	-64	1778821	1329584	1778821-1329584
2020-09-17 at 04:46:04 UTC	313094	2020-09-17	-32	1778821	1329589	1778821-1329589
2020-10-19 at 04:46:08 UTC	313095	2020-10-19	-16	1778821	1329598	1778821-1329598
2020-11-04 at 04:46:06 UTC	313096	2020-11-04	-32	1778821	1329581	1778821-1329581
2020-12-06 at 04:46:05 UTC	313097	2020-12-06	-32	1778821	1329606	1778821-1329606
2021-01-07 at 04:46:01 UTC	313098	2021-01-07	-64	1778821	1329609	1778821-1329609
2021-03-12 at 04:45:59 UTC	313099	2021-03-12	-64	1778821	1329607	1778821-1329607
2021-05-15 at 04:46:02 UTC	313100	2021-05-15	-32	1778821	1329586	1778821-1329586
2021-06-16 at 04:46:03 UTC	313101	2021-06-16	-32	1778821	1329577	1778821-1329577
2021-07-18 at 04:46:03 UTC	318278	2021-07-18	-80	1824240	1423199	1824240-1423199
2021-10-06 at 04:46:11 UTC	318284	2021-10-06	-32	1824240	1423203	1824240-1423203
2021-11-07 at 04:46:16 UTC	318280	2021-11-07	-64	1824240	1417911	1824240-1417911
2022-01-10 at 04:46:10 UTC	318281	2022-01-10		1824240	1423204	1824240-1423204
2022-03-31 at 04:46:07 UTC	318282	2022-03-31		1824240	1423201	1824240-1423201
2022-06-03 at 04:46:07 UTC	318283	2022-06-03		1824240	1423202	1824240-1423202
2022-08-06 at 04:46:08 UTC	318284	2022-08-06		1824240	1423200	1824240-1423200

6.4/ List of the last 69 COSMO-SkyMed products used for tomographic processing. Scans performed from 23 July 2017 to 6 August 2022. Source: Agenzia Spaziale Italiana, 2022. Products processed by Luca Martelli under a license of the Italian Space Agency (ASI); Original COSMO-SkyMed Products - ©ASI - (2017-2022).7)

splacement of the individual targets along the average Line of Sight (LOS) of the various scans and the displacement detected during each scan with respect to the reference position. In addition to enabling the generation of a three-dimensional point cloud of the remotely sensed targets, therefore, each spreadsheet allows the average displacement velocity of these elements in centimetres per year to be represented with a colour map and time series diagrams on the displacements along the line of sight of the scanning radars to be produced5 (fig. 6.6).

6.2.3 Requesting and collecting TanDEM-X data

Among the TanDEM-X mission products made available to scientific institutions by the DLR is a DEM with global coverage and 12 m ground resolution. The TanDEM-X mission consists of the coupling of a first SAR satellite called TerraSAR-X with a second satellite with similar characteristics, called TanDEM-X, in order to create a single-pass interfe-

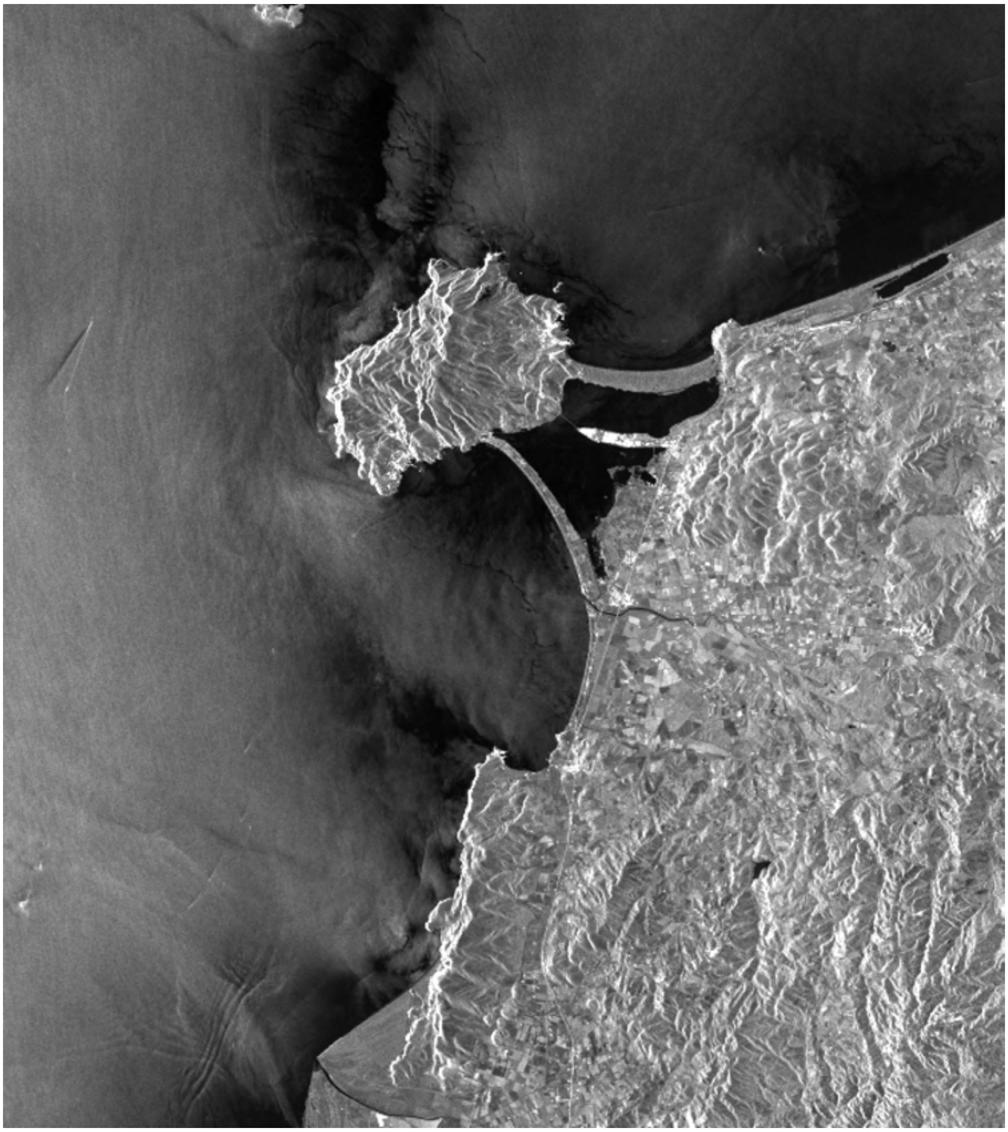

6.5/ Preview of the file CSKS1_SCS_B_HI_01_H_RA_SF_20120717045411_20120717045418.h5, radar image acquired on 17 July 2012 by the COSMO-SkyMed 1 satellite's X-band SAR. The product in this caseis mirrored due to the reading order of the radar data set in the display programme. Source: Agenzia Spaziale Italiana, 2022. Product processed by Luca Martelli under a license of the Italian Space Agency (ASI); Original COSMO-SkyMed Product - ©ASI - (2012).

rometer system for the generation of DEM with global coverage using Differential Interferometric Synthetic Aperture Radar (DInSAR)6.
In order to obtain a qualitative improvement in tomographic processing, therefore, in March 2023 we requested a DEM tile covering the stretch of Tuscan coastline between Alberese and Burano. The tile in question, with identifier TDM-DEM-12m:/dims_op_pl_dfd_XXXXB0000393155076492/dims_op_pl_dfd_//TDM.DEM.DEM and delivered in May 2023, is the result of scans that took place between 7 February 2011 and 16 April 2014. When compared with the NASADEM data, therefore, the TanDEM-X data are not only at a better resolution but, usually, also more up-to-date.

6.2.4 Second tomographic processing of 160 COSMO-SkyMed products using TanDEM-X data

Between May 2023 and July 2023, IREA-CNR then conducted a second tomographic processing of the radar images

6.6/ Three-dimensional point cloud in Google Earth™ environment, obtained by processing 160 COSMOSkyMed radar images with NASADEM data. Porto Santo Stefano site. Products processed by Luca Martelli, Diego Reale, and Simona Verde under a license of the Italian Space Agency (ASI); Original COSMO-SkyMed Products - ©ASI - (2012-2017); Google™ and Google Earth™ are trademarks of Google LLC and this thesis is not endorsed by or affiliated with Google in any way; United States Geological Survey, National Aeronautics and Space Administration 2020.

6.7/ Three-dimensional point cloud in Google Earth™ environment, obtained by processing 160 COSMOSkyMed radar images with NASADEM data. Talamone site. Products processed by Luca Martelli, Diego Reale, and Simona Verde under a license of the Italian Space Agency (ASI); Original COSMO-SkyMed Products - ©ASI - (2012-2017); Google™ and Google Earth™ are trademarks of Google LLC and this thesis is not endorsed by or affiliated with Google in any way; United States Geological Survey, National Aeronautics and Space Administration 2020.

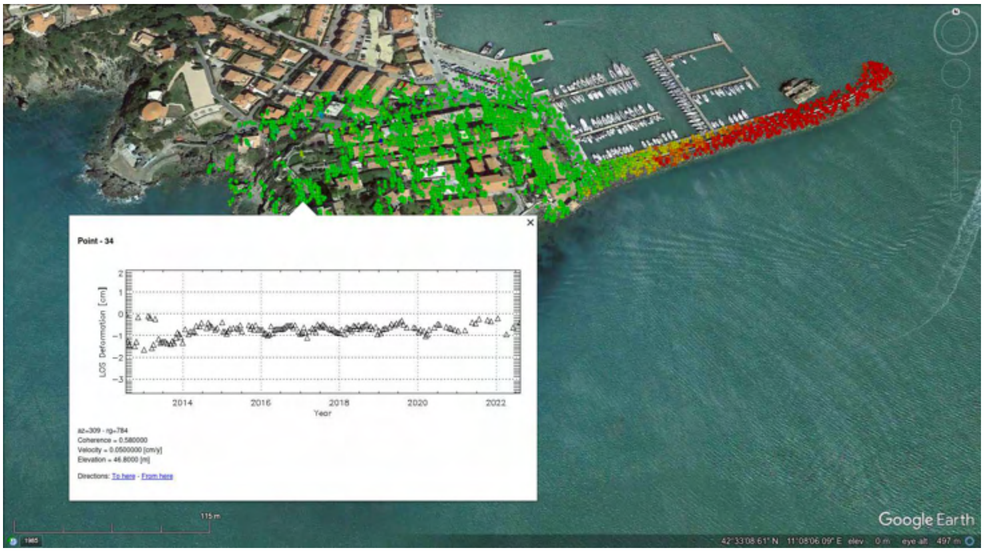

6.8/ Three-dimensional point clouds in Google Earth™ environment, obtained by processing 160 COSMOSkyMed radar images with NASA-DEM data. Talamone site with a diagram of the time series of the displacements of a target belonging to the Fortress. Source: Agenzia Spaziale Italiana, 2022. Products processed by Luca Martelli, Diego Reale, and Simona Verde under a license of the Italian Space Agency (ASI); Original COSMO-SkyMed Products - ©ASI - (2012-2017); Google™ and Google Earth™ are trademarks of Google LLC and this thesis is not endorsed by or affiliated with Google in any way; United States Geological Survey, National Aeronautics and Space Administration 2020.

provided by ASI in the summer of 2022. Improvements were already observed in the first processing phase at territorial scale, where we could observe greater continuity in the phase level of the signals (fig. 6.7).

Two other spreadsheets in .csv format were then obtained: one concerning the Spanish Fortress of Porto Santo Stefano and one concerning Talamone Town Walls.

Compared to the processing with NASADEM data, although a greater number of targets detected in the tomographic clouds obtained with the integration of TanDEM-X data was generally observed, as far as the western side of the Talamone Town Walls is concerned, there were fewer backscatterers detected (fig. 6.8). The reason for this anomaly is probably due to the fact that the pair of satellites of the TanDEM-X mission had sensed the area of Talamone just twice during the observation time (from February 2011 to April 2014), while the area of Porto Santo Stefano was sensed four times (fig. 6.9). As far as the area of Talamone is concerned, it is possible that one of NASADEM recent upgrades with acquisitions by other sensors may have resulted into finer quality data than those available from the TanDEM-X mission. In any case, the improvement on Porto Santo Stefano tomographic cloud is evident.

6.3 Integration of tomographic clouds with point clouds obtained from other surveying techniques

In order to obtain up-to-date models of the topographical configurations of the sites under study, data from the Extraordinary Environmental Remote Sensing Plan 2009 (Piano Straordinario di Telerilevamento – PST-A 2009), consisting of Digital Terrain Models (DTM) of Porto Santo Stefano and Talamone, together with point clouds obtained from LIDAR scans from sensors on aircraft that generated them, were requested from the Ministry of the National Geoportal of the Italian Ministry of the Environment. All these data have a ground resolution of 2m. Specifically, for Porto Santo Stefano, data from tile C42441110_0202 and C42421112_0202 were acquired, while for Talamone, data from tile C42541112_0202 were used.

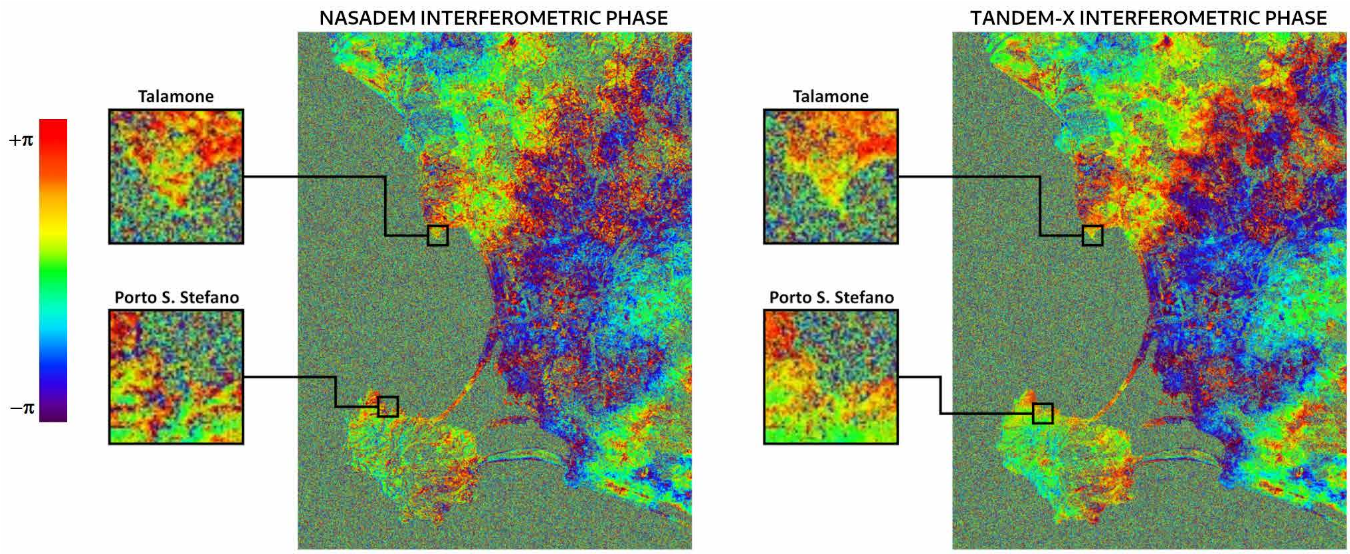

6.9/ Comparison of the interferometric phases of tomographic processing with NASADEM and tomographic processing with TanDEM-X at spatial scale. The latter appears to have a more regular fringe distribution than the former. Source: Agenzia Spaziale Italiana, 2022. Products processed by Luca Martelli,Diego Reale, and Simona Verde under a license of the Italian Space Agency (ASI); Original COSMOSkyMed Products - ©ASI - (2012-2017); Deutsches Zentrum für Luft- und Raumfahrt e.V., 2006. © DLR <2023>.

In order to be integrated with the data collected at the architectural scale (point clouds from laser scanners, point clouds from SfM photomodelling, topographic campaigns with total stations) the point clouds from the 2009 PST-A were then converted from the ETRF2000 geographic coordinate system with ellipsoid height (EPSG code: 6706) to the ETRF2000 map coordinate system with geoid height (EPSG code: 6707), through the application of the ITALGEO2005 geoid model and GK2 grids no. 342 and no. 352 (valid for 1:50,000 scale sheets) of the Geographic Institute of Italian Army (Istituto Geografico Militare – IGM), through ConveRgo software developed by the Permanent Committee for Geographic Systems of the Interregional Centre for Geographic and Statistical Information Systems (Comitato Permanente dei Sistemi Geografici del Centro Interregionale per I Sistemi Informatici Geografici e Statistici – CISIS-CPSG).

In parallel, IREA-CNR prepared a cartographic coordinate version of the two pairs of tomographic clouds.

In this way, it was possible to easily integrate the tomographic and LIDAR point clouds in the CloudCompare environment, since the data were all georeferenced. The smaller tomographic clouds were embedded onto those of the Italian Ministry of the Environment.

$$R_1(\alpha) = \begin{bmatrix} \cos(\alpha) & -\sin(\alpha) & 0 \\ \sin(\alpha) & \cos(\alpha) & 0 \\ 0 & 0 & 1 \end{bmatrix}$$

$$R_2(\beta) = \begin{bmatrix} \cos(\beta) & 0 & -\sin(\beta) \\ 0 & 1 & 0 \\ \sin(\beta) & 0 & \cos(\beta) \end{bmatrix} \quad (6.1)$$

$$R_3(\gamma) = \begin{bmatrix} 1 & 0 & 0 \\ 0 & \cos(\gamma) & -\sin(\gamma) \\ 0 & \sin(\gamma) & \cos(\gamma) \end{bmatrix}$$

tation parameters R1(α), R2(β), R3(γ), rotations around each of the three axes, with ϕ=(α, β, γ)T. The three rotation parameters are defined in Expression (6.1).

Notes

1. Battagliere, Virelli 2019, pp. 7-8.
2. United States Geological Survey, National Aeronautics and Space Administration 2020.

6.10/ Three-dimensional point clouds in Google Earth™ environment, obtained by processing 160 COSMOSkyMed radar images with DEM data from the TanDEM-X mission. Porto Santo Stefano site. Source: Agenzia Spaziale Italiana, 2022. Products processed by Luca Martelli, Diego Reale,and Simona Verde under a license of the Italian Space Agency (ASI); Original COSMO-SkyMed Products - ©ASI - (2012-2017); Deutsches Zentrum für Luft- und Raumfahrt e.V., 2006. © DLR <2023>. Google™ and Google Earth™ are trademarks of Google LLC and this thesis is not endorsed by or affiliated with Google in any way.

6.11/ Three-dimensional point clouds in Google Earth™ environment, obtained by processing 160 COSMOSkyMed radar images with DEM data from the TanDEM-X mission. Talamone site. Source: Agenzia Spaziale Italiana, 2022. Products processed by Luca Martelli, Diego Reale,and Simona Verde under a license of the Italian Space Agency (ASI); Original COSMO-SkyMed Products - ©ASI - (2012-2017); Deutsches Zentrum für Luft- und Raumfahrt e.V., 2006. © DLR <2023>. Google™ and Google Earth™ are trademarks of Google LLC and this thesis is not endorsed by or affiliated with Google in any way.

Luca Martelli

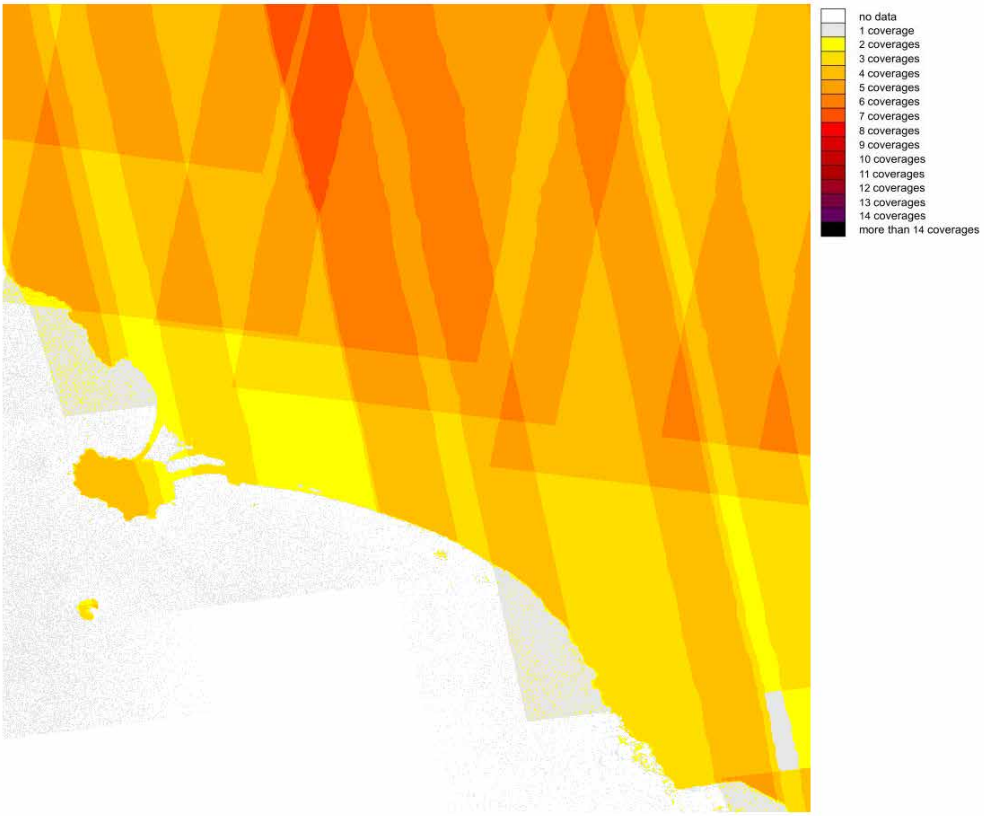

6.12/ Diagram of the number of single-pass scans carried out by the satellites of the TanDEM-X mission for the production of the TDM-DEM-12m tablet:/dims_op_pl_dfd_XXXXB0000393155076492/dims_op_pl_dfd_//TDM.DEM.DEM. Note that only two scans were carried out on the coast near Talamone, while Porto Santo Stefano was scanned four times. Fonte: Deutsches Zentrum für Luft- und Raumfahrt e.V., 2006. © DLR <2023>.

3. Wessel, Rizzoli, Fritz, Busche, Krieger, Buckreuss 2018, pp. 11-29.
4. Fornaro, Serafino 2006, pp. 3497-3504.
5. Fornaro, Reale, Serafino 2008, pp. 477-478.
6. Wessel, Rizzoli, Fritz, Busche, Krieger, Buckreuss 2018, pp. 11-12.
7. Watson 2006, pp. 386-389.

Sintesi

In merito alle operazioni di rilievo integrato riguardanti la Fortezza spagnola di Porto Santo Stefano e la Cinta muraria di Talamone, sono stati individuati due possibili usi per il telerilevamento radar, entrambi connessi alla tecnica della tomografia radar ad apertura sintetica:

- l'introduzione di dati riguardanti le velocità degli spostamenti medi, lungo la linea di mira dei radar satellitari scelti, di alcuni punti degli ambiti urbani studiati;
- un modesto contributo al raffittamento delle nuvole di punti riguardanti i contesti urbani dei temi scelti per i rilievi integrati e ottenute con tecniche standard. In questo caso non ci stiamo riferendo alle nuvole di punti a scala architettonica ottenute con strumenti scanner laser o con fotomodellazione Structure from Motion (SfM), ma a nuvole di punti a scala urbana con minore densità, come quelle ottenibili con da sensore LIght Detection And Ranging (LIDAR) montato su piattaforma aerea o con una stazione totale.

Grazie alla consulenza del dott. Gianfranco Fornaro e della dott.ssa Simona Verde dell'Istituto per il Rilevamento Elettromagnetico dell'Ambiente (IREA-CNR), abbiamo pianificato un percorso per la generazione delle nuvole da tomografia radar ad apertura sintetica, articolato nelle seguenti fasi:

- selezione e raccolta di 160 immagini radar della missione satellitare COSMO-SkyMed (COnstellation of small Satellites for the Mediterranean basin Observation) dell'Agenzia Spaziale Italiana (ASI) in modalità di scansione

Stripmap, acquisiti in successione e caratterizzati dalla minor decorrelazione temporale possibile;

- una prima elaborazione tomografica, da parte dell'IREA-CNR, dei 160 prodotti COSMO-SkyMed mediante impiego del Digital Elevation Model (DEM) di dominio pubblico NASADEM, avente una risoluzione a terra di 30 m.
- la richiesta e la raccolta dei dati DEM della missione TanDEM-X del Deutsches Zentrum für Luft- und Raumfahrt e.V. (DLR), avente una risoluzione a terra di 12 m;
- una seconda elaborazione tomografica più rifinita, da parte dell'IREA-CNR, dei 160 prodotti COSMO-SkyMed, mediante impiego dei dati TanDEM-X. La risoluzione più fine di tale DEM consente una riduzione del margine d'errore nel posizionamento dei bersagli individuati dalla nuvola tomografica.

Dal punto di vista materiale, il risultato delle prime due elaborazioni con NASADEM sono due fogli di calcolo in formato .csv: uno relativo al sito di Porto Santo Stefano e uno riguardante il sito di Talamone. Oltre a contenere la posizione georiferita (nel riferimento WGS84) di ogni elemento retrodiffondente persistente individuato nelle due aree di interesse, i fogli di calcolo riportano anche la velocità media di spostamento dei singoli bersagli lungo la linea di mira media delle varie scansioni e lo spostamento rilevato durante ogni scansione rispetto alla posizione di riferimento.

Oltre a consentire la generazione di una nuvola di punti tridimensionale dei bersagli telerilevati, quindi, ciascun foglio di calcolo permette di rappresentare con una mappa di colori la velocità media di spostamento di tali elementi in centimetri per anno e di produrre diagrammi delle serie temporali sugli spostamenti lungo la linea di mira dei radar di scansione in scansione.

Al fine di ottenere dei modelli aggiornati delle configurazioni topografiche dei siti oggetto di studio, sono stati richiesti dal Geoportale Nazionale del Ministero dell'Ambiente, cosistenti in dei Digital Terrain Models (DTM) di Porto Santo Stefano e di Talamone, assieme alle nuvole di punti ottenute da scansioni LIDAR da sensore su aeromobile che li hanno generati. Le nuvole di punti del Geoportale Nazionale sono state convertite da un sistema in coordinate geografiche a un sistema in coordinate cartografiche. Parallelamente, l'IREA-CNR ha predisposto una versione in coordinate cartografiche delle due coppie di nuvole tomografiche.

In questo modo è stato possibile integrare facilmente le nuvole di punti tomografiche e le nuvole di punti LIDAR in ambiente CloudCompare, poichè si è trattato di dati tutti georeferenziati. Le nuvole tomografiche, di estensione più contenuta, sono state innestate su quelle del Ministero dell'Ambiente.

L'allineamento con i dati non georeferenziati, consistenti in nuvole di punti da scanner laser e poligonali ottenute con battute topografiche con stazione totale, ha richiesto l'applicazione della trasformazione di Helmert a sette parametri, attivabile sempre in ambiente CloudCompare attraverso un apposito comando.

Luca Martelli

7. The Spanish Fortress of Porto Santo Stefano

7.1 The environmental context and historical events

The first settlement on the site of today's Porto Santo Stefano arose in Roman times, in an area affected by the economic activities of the Domizi Enobarbi family, which became influential when one of its members became cosole in 461. They owned a villa with a tuna fishery and cetaria in Santa Libertata. Thereafter, the place experienced a long period of decadence until the 16th century. During the period of domination by the Republic of Siena, in fact, it was not possible to fortify the inlet of Porto Santo Stefano because it was surrounded by many hills. For this reason, the town was more exposed to pirate raids, which put the inhabitants to flight and thus caused the abandonment of the tuna fisheries. A new attempt to establish a permanent settlement was only repeated at the beginning of the 17th century, but about another hundred years had to pass before a new settlement could arise and begin to develop on the northern slope of Monte Argentario. In fact, the economic and commercial development of the area remained blocked until the construction of the Fortress, which finally guaranteed the necessary protection for the local population.

However, from the 15th century on, the area became part of the dominions of the Republic of Siena and, as established following the capitulations of 1414, its government took energetic measures to defend Porto Santo Stefano, the Valle del Cocomero and Santa Liberata from pirate raids. In 1415, the three Sienese officers in charge of governing Agro orbetellano informed the Priors of Siena that some influential citizens of the lagoon village were willing to bear the cost of a tower at Porto Santo Stefano, including the cost of maintaining the guard. A few decades later, in 1440, the Commune ordered the construction of a fortress on Monte Argentario, to be built with the collaboration of the inhabitants of Orbetello, in order to warn the population of the arrival of thugs and also to signal the Saline and Talamone. This was probably the Argentiera Tower, erected two years later on the remains

7.1/ Photograph of the front facade of the Spanish Fortress from Piazza del Governatore.

7.2/ Photo of the Spanish Fortress from the south corner from Via Giardino Borselli.

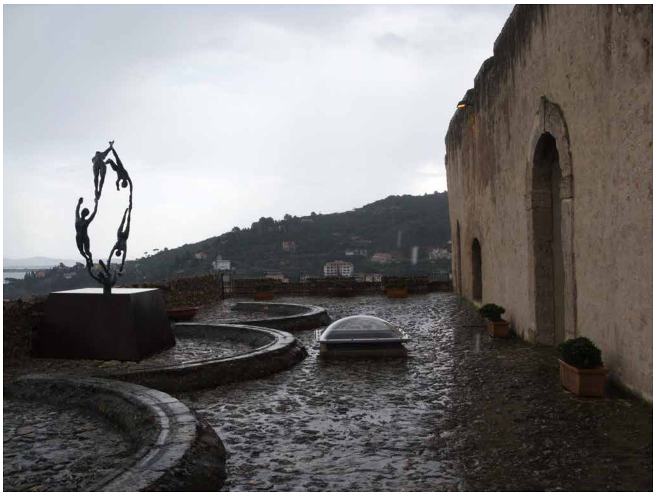

7.3/ Photo of the terrace of the Spanish Fortress, overlooking the sea.

of the ancient Castello Argentaro. It was a small settlement of a mining or agricultural nature, referred to in some 13th century documents concerning acts of succession of the Aldebrandeschi or the confirmation of the emphyteusis of the Agro orbetellano granted to them by the Abbey of the Tre Fontane.In fact, the main reason why the local population fortified these territories was the incursions of the Turks. After sacking the Island of Elba in 1544, Kayreddin Barbarossa headed towards the Maremma, where he first attacked Talamone, and then set Porto Ercole as his new target. The Sienese turned to Cosimo I de' Medici, who immediately sent a contingent. This relief did not arrive in time to save the village, but prevented the Ottomans from besieging Orbetello. With the death of the pirate Kayreddin in 1574, the Tuscan coast was free of his raids, so the troops were dismissed, while the commissioners and commander Don Giovanni De Luna returned to Siena after ordering Talamone and Porto Ercole to be fortified. Some prominent members of society of the time supported the project and commissioner Alessandro Guglielmi led the operations, on which he sent regular reports to the Bailiff. The Republic also ordered that fortresses and posterns sold to private individuals should revert to the State and that only those that were necessary should be fortified. Thus, the number of fortresses was reduced from 25 to 12. The Spanish were then allowed to settle in Talamone, Orbetello and Porto Ercole as long as these remained loyal to the Republic and were fortified using the revenues from the Marsiliana estate. With these funds, Porto Santo Stefano and Grosseto were also to be fortified, again under the leadership of Commissioner Alessandro Guglielmi, who was now acting under the directives of Don Diego de Hurtado de Mendoza. This information from 1547 is the first news about the building of the Fortress of Porto Santo Stefano, but it was probably just a planning intention that did not materialise.

Since the State of the Presidia was of great importance to Spain, as a valid support point for maritime connections with the Viceroyalty of Naples and a strategic element in the control of the Papal States and the Duchy of Tuscany, King Philip II was concerned about reinforcing its defence works immediately after its establishment. In addition to planning the construction of forts, he sent Don Pedro de Toledo with the task of executing a project, probably compiled by Don Perofan de Ribera, for the construction of coastal watchtowers. However, in the years immediately after the constitution of the Presidium State, no particular attention was paid to Porto Santo Stefano, since in 1560 there was still debate on the potential of the port of call to become a settlement with the name of 'Filippopoli', 'Filippica' or 'Filippiana' in honour of King Philip II, as well as on the advisability of erecting a fortification there. In 1572, a tower already existed in Porto Santo Stefano to defend the coast, together with that of Calvello, but its dimensions were small. For this reason, it was deemed appropriate to build another one on the point known as Capo San Giovanni. It remains a matter of debate, however, whether the tower of Santo Stefano meant the tower known as Lividonia or the Punta, or whether this artefact stood on the same spot where the Fortress of Porto Santo Stefano now stands. In any case, the two towers can be seen depicted in the map painted by Ignazio Danti between 1580 and 1583, preserved in the Vatican Galleries. In fact, the map shows the Towers of Santa Liberata, Calvello, Santo Stefano and Livivonia in the northern sector of the Argentario Promontory. The ancient Torre dell'Argentiera, however, does not appear there, at that time already in a state of neglect and ruin.

From 1603, ruling in Naples as Viceroy for Philip III was Don Juan Pimentel, Count of Benavente, who set Egidio Nuño Orejón, a Spanish captain, as the new Governor of the State of Presidia. He had warehouses built in Porto Santo Stefano

7.4/ Alignment of the first 48 point clouds from laser scanners in the JRC Reconstructor environment. Representation of the Fortress as seen from the north-east.
7.5/ 7.4/ Alignment of the first 48 point clouds from laser scanners in the JRC Reconstructor environment. Representation of the Fortress as seen from the north-west.

to store supplies and provisions for the garrisons of Orbetello and Porto Ercole. At the time, in fact, ships too large to dock at Porto Ercole were taken to Porto Santo Stefano to unload their goods. On that occasion, therefore, the Governor started the construction of accommodation for the officers and soldiers in charge of disembarking, transporting supplies and storing them in the warehouses. Seasonal fishermen of southern and Catalan origin were also present, but their dwellings were not made of masonry, but consisted of temporary huts that served only for the fishing season. A chapel was also built for these officers and soldiers, subject to the authority of the Presidio and, for the spiritual part, to the jurisdiction of the Military Ordinary, i.e. the Chaplain Major of Naples.

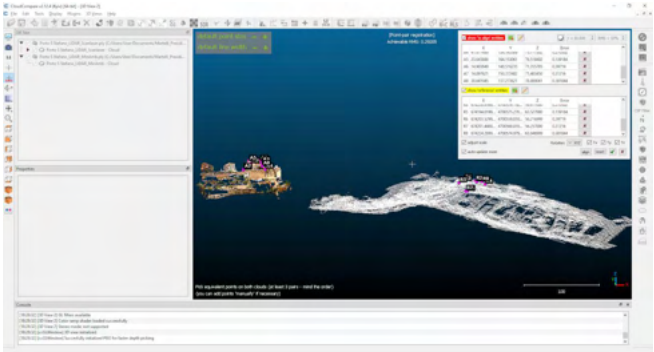

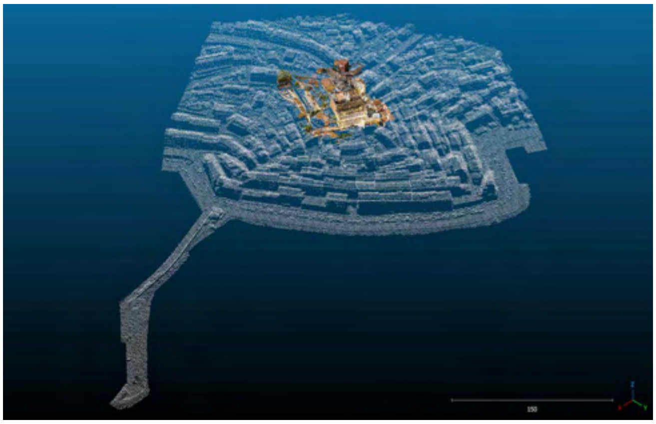

7.6/ Alignment and nesting of the point cloud of the Spanish Fortress obtained from laser scanners into the LIDAR cloud of the Ministry of Environment and Energy, via Helmert transformation in CloudCompare environment. Source: Ministero dell'Ambiente e dell'Energia – Italian Ministry of Environment and Energy / licensed under the CC BY-SA 3.0 IT (https://creativecommons.org/licenses/by/3.0/it/deed.it) / Creative Commons – Attribuzione - Condividi allo stesso modo Italia (CC BY-SA 3.0 IT).
7.7/ The point cloud of the Spanish Fortress, obtained from laser scanners (coloured), aligned and nested into the LIDAR cloud of the Ministry of Environment and Energy (white), in CloudCompare environment.
Source: Ministero dell'Ambiente e dell'Energia – Italian Ministry of Environment and Energy / licensed under CC BY-SA 3.0 IT (https://creativecommons.org/licenses/by/3.0/it/deed.it) / Creative Commons – Attribuzione - Condividi allo stesso modo Italia (CC BY-SA 3.0 IT).

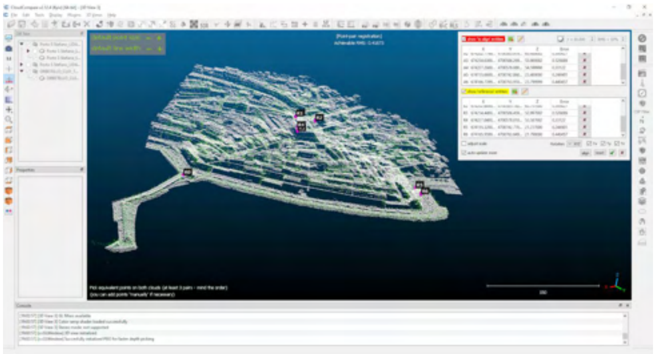

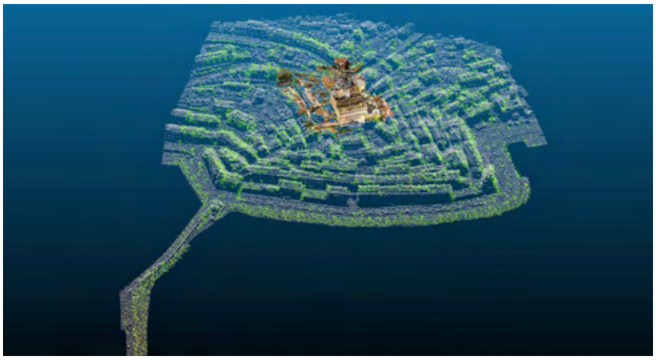

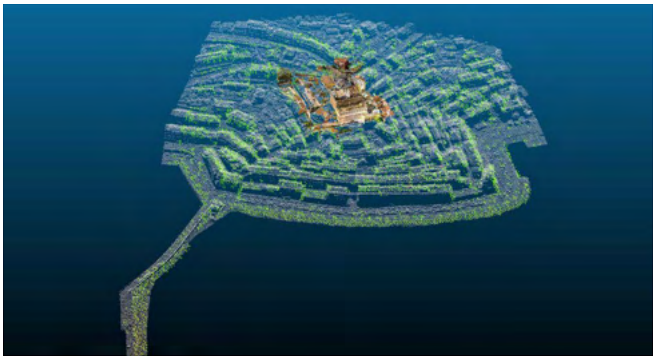

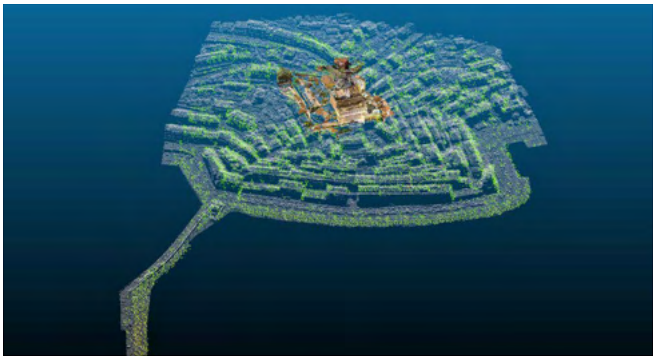

7.8/ Ministry of the Environment's LIDAR cloud and the tomographic cloud obtained with NASADEM data, before alignment in CloudCompare environment. Source: Agenzia Spaziale Italiana, 2022. Products processed by Luca Martelli, Diego Reale, and Simona Verde under a license of the Italian Space Agency (ASI); Original COSMO-SkyMed Products - ©ASI - (2012-2017); Ministero dell'Ambiente e dell'Energia – Italian Ministry of Environment and Energy / licensed under CC BY-SA 3.0 IT (https://creativecommons.org/licenses/by/3.0/it/deed.it) / Creative Commons – Attribuzione - Condividi allo stesso modo Italia (CC BY-SA 3.0 IT).

7.9/ Alignment in CloudCompare environment between the laser scan cloud (coloured), the Ministry of the Environment's LIDAR cloud (white) and the tomographic cloud obtained with NASADEM data (from green to orange). Source: Agenzia Spaziale Italiana, 2022. Products processed by Luca Martelli, Diego Reale, and Simona Verde under a license of the Italian Space Agency (ASI); Original COSMO-SkyMed Products - ©ASI - (2012-2017); Ministero dell'Ambiente e dell'Energia – Italian Ministry of Environment and Energy / licensed under CC BY-SA 3.0 IT (https://creativecommons.org/licenses/by/3.0/it/deed.it) / Creative Commons – Attribuzione - Condividi allo stesso modo Italia (CC BY-SA 3.0 IT).

7.10/ Alignment in CloudCompare environment between the laser scan cloud (coloured), the Ministry of theEnvironment's LIDAR cloud (white) and the tomographic cloud obtained with TanDEM-X data (from greento orange). Source: Agenzia Spaziale Italiana, 2022. Products processed by Luca Martelli, Diego Reale, and Simona Verde under a license of the Italian Space Agency (ASI); Original COSMO-SkyMed Products - ©ASI - (2012-2017); Deutsches Zentrum für Luft- und Raumfahrt e.V., 2006. © DLR <2023>. Ministero dell'Ambiente e dell'Energia – Italian Ministry of Environment and Energy / licensed under CC BY-SA 3.0 IT (https://creativecommons.org/licenses/by/3.0/it/deed.it) / Creative Commons – Attribuzione - Condividi allo stesso modo Italia (CC BY-SA 3.0 IT).

7.11/ Direct comparison by superposition between the tomographic cloud from NASADEM data (yellow) and the tomographic cloud from TanDEM-X data (magenta), both nested on the LIDAR cloud of the Italian Ministry of the Environment. Source: Agenzia Spaziale Italiana, 2022. Products processed by Luca Martelli, Diego Reale, and Simona Verde under a license of the Italian Space Agency (ASI); Original COSMO-SkyMed Products - ©ASI - (2012-2017); Deutsches Zentrum für Luft- und Raumfahrt e.V., 2006. © DLR <2023>. Ministero dell'Ambiente e dell'Energia – Italian Ministry of Environment and Energy / licensed under CC BY-SA 3.0 IT (https://creativecommons.org/licenses/by/3.0/it/deed.it) / Creative Commons – Attribuzione - Condividi allo stesso modo Italia (CC BY-SA 3.0 IT).

When the State of the Presidio came under the jurisdiction of the Bourbons of Naples, a visit to the territory was carried out starting in 1734 by Field Marshal Don Carlos Blom, who then drew up an accurate description of the various strongholds from a military, economic and demographic point of view, including Porto Santo Stefano and specifying that the latter was based on an essentially agricultural economy.

Between 1853 and 1885, there was a considerable growth of the urban centre By 1890, the built front towards the sea had advanced, while in 1903, the higher land had been occupied, although the space surrounding the Fortress was still free[1].

7.2 The Construction of the Fortress

The Governor of the State of the Presidia for the period between 1605 and 1617, Egidio Nuño Orejón, ordered the start of work on the fortress. The building work took many years and in fact, on 6 July 1622, the military engineer Pedro Alvarez, sent from Naples to inspect the Presidia, wrote to the Spanish Court expressing concern about the completion of the building, given the danger of Turkish incursions that were forcing the population to emigrate to Orbetello. Work, albeit of a minor nature, continued until 1636, at least according to another document that mentions the intention to build transverse brick defence bulkheads in several areas of the fort. This was certainly a type of yellow-brick characteristic of all local constructions in the 17th century. The sentry boxes, parapet finishes and lintels of the embrasures were also made with this type of brick. During restoration work between 1980 and 1998, carried out by the Soprintendenza per i Beni Ambientali e Architettonici for the provinces of Siena and Grossetoa faint trace of four sentry boxes appeared in the south-eastern corner, where two bricks stand to mark the demolished construction, which previously rested on the stone pavement. In any case, Porto Santo Stefano finally had a fortification that, though modest, was a deterrent to corsairs.

The building stands on the highest hillock in the centre of the town and the town developed around this siteIt has a square plan measuring 35 × 35 m. The cubic mass is formed by a scarped basement, within which the cisterns are located. Six rooms, originally used for the garrison, are developed in the body immediately above, around a courtyard connected to the lower cisterns by a well. The six rooms, with barrel vaults, are arranged three by three on two sides of the courtyard, from which they are accessed directly through stone-framed doors. On this floor, the volumetry does not occupy the entire area covered by the building, but recedes on the sea side to make room for a terrace, which was originally covered by a lime wainscot, steeply sloping outwards. Later, this terrace was raised about 50 cm and covered with coarse paving, in order to accommodate cannon emplacements. In the 19th century, there was a further intervention, with the laying of three semi-circles of stone to allow the rotation of the wheels of the more modern cannon barrels. In total, there were five cannons in the fortress and they were evidently placed according to the following arrangement: three on the terrace of the first floor, as suggested by the stone semicircles; two on the terrace of the second floor, where they were located at the muzzle-loaders. Two covered cordoned ramps, with arched entrances,provide access to the upper floor, where originally there were only two small volumes separated from the courtyard and located near the side facing the square. The two rooms inside the two bodies served as a lookout and ammunition storage respectively.

Confirming the period of construction, which took place under the Presidio State and shortly before the development of the built-up area of Porto Santo Stefano, the Fortress presents the Spanish typological characteristics found in other defensive works on the coast,especially in the Buranaccio Tower, located on the edge of Lake Burano. These peculiarities are also common to the numerous coastal towers in the Amalfi region, built since the time of Charles V of Habsburg. Crowning the levels of the terraces are large counter-scarp corbels, surmounted by merlons and interspersed with machicolations, in order to maximise the effectiveness of the lead defences. While the machicolations are strongly accentuated in height and width, the barbicans are of robust dimensions. These proportions are typically Spanish and profoundly different from the slender corbels found in 13th-14th century fortifications or castles. During the recent restoration, supervised by the Soprintendenza per i Beni Ambientali e Architettonici for the provinces of Siena and Grosseto, the patrol walkway was freed of superfetations, which is still legible on the inside.

The outer faces of the fortress walls are scarped, with a coordinated inclination with respect to the proportions of the machicolations. The masonry face of the escarpment basement was built in recours of approximately 50-70 cm in height, finely levelled by a layer of lime sloping outwards, so as to facilitate the possible escape of water from the cisterns. On the south side is the access to the floor of the spaces originally dedicated to the soldiers' quarters. A ramp leads to the former drawbridge, now replaced by a brick one. Above the gate there are still gaps for the bolzoni, controlled by a winch placed on the upper walkway. Above the two volumes of the second floor is a further walkway, also located along the south side and reached by a third ramp. In correspondence with this latter walkway are two rows of slits staggered at two different heights. With this expedient, two soldiers could shoot side by side at the same time, one standing and the other on his knees, so that the powder coming out of the guns would not harm their neighbour.

In 1739, Field Marshal Don Carlos Blom visited the Fortress of St. Stephen and produced an accurate description, in which he informed his superiors about the defensive possibilities of the defensive structure and the resources allocated there. He wrote that the building had a governor, five iron artillery pieces of different calibre and a detachment of forty men with their officers. Since the building gave excellent guarantees of defence in terms of both solidity and armament, it was possible to increase the garrison to sixty men with corresponding officers.At the beginning of the 19th century, the fortress was the port's only means of defence, especially against pirate attacks, so it was still maintained in a good state. In the vicinity of the building were vegetable gardens for the sustenance of the garrison it housed. A room with an oven and a gabled roof had also been added, completely independent of the two aforementioned volumes on the upper floor. However, the second floor was severely tampered with by the transformations carried out in the 20th century. Also in the 19th century, a series of maintenance works were carried out on the Fortress, well documented in a report sent by architect Giuseppe Ciulli to the director of the Department of Royal Factories, Cambray Digny. In fact, the architect Ciulli worked in the Maremma and left several of his expert reports, such as those for many fortresses in the Agro orbetellano and the one on the Rocca Pisana on the Island of Giglio. According to this report, the work consisted of resurfacing the floors, whitewashing three of the six rooms facing the courtyard, and repairing a door and a window. The architect Ciulli wrote again to Director Digny on 10 May 1824, pointing out that there was heavy dampness caused by the silting up of one of the two ramps leading to the second floor. He then proposed emptying the vaulted space and restoring the original situation, considering this to be the simplest and most economical solution. On 16 February of the same year, Ciulli asked for a slab above the vault of the armaments store and two mortar stone platforms for the upper battery, like those on the floor below, which had already been built in 1820. Furthermore, although the Military Department required a wall to be built against the entrance staircase, the architect opposed this for safety reasons and instead proposed installing a wooden wall so that it could be removed if necessary. On 11 September 1827, after discovering infiltrations in the room used as a powder magazine, due to the cannons on the terrace above, architect Ciulli proposed placing a stone slab on top of the room and opening a second slit in the wall overlooking the terrace. In the same report, the technician excluded that the reason for the dampness could be the proximity of the 'place of convenience'. In his report of 31 October 1827, the architect called for the following operations: demolishing and reconstructing part of the courtyard pavement; repairing the wall of the first battery, making holes in it for the drainage of water and reconstructing 120 fathoms of concrete; resurfacing one of the ramps leading to the second battery (an operation that can still be identified today thanks to the difference in the material used). In addition, Ciulli again laid the pavement above the second terrace.

In 1842, the Fortezza changed its use from barracks to 'Uffizio di sanità' (health office).

In the context of Porto Santo Stefano, the fortified structure is considered an artefact of particular aesthetic originality and, in principle, it has maintained its original typology. However, it has some structural anomalies that are totally alien to it, such as the two very recently built volumes, which occupy the terrace on the second floor in such an incisive manner that they can no longer be demolished. On the south façade, there were two voids above the corner brackets, possibly previously occupied by garrets but now filled in badly by a wall structure placed as a mere completion. Originally, the ramp for access to the fortress was not cordoned off but stepped and, on the left, was flanked by a retaining wall forming a

ravelin with a double acute angle.
As already mentioned, restoration work began in 1980 under the Soprintendenza per i Beni Ambientali e Architettonici for the provinces of Siena and Grosseto, completed in 1998. Beccatelli and merloni were the objects of intervention because they were unsafe and overhanging the public street. The consolidation of the corbels took place by inserting threaded metal bars and cement pours inside them. On this occasion, it emerged that only a few merlons retained their original, massive and rounded shape bordered by a row of bricks arranged in a knife-edge pattern. From these elements, it was deduced that the rear patrol walkway had been filled with earth in later times and then covered with a stone pavement. In addition to distorting the structure of the aforementioned walkway, this filling prevented rainwater from flowing freely from the appropriate outlets, causing infiltration and thus predictable static disruption in the structures below. The first-floor terrace had also been covered with a layer of earth to which a terracotta covering was then applied, thus concealing the original stone flooring and the semi-circles for the rotation of the cannon barrels around a pivot. Each pin was placed near the retaining wall of the terrace, in correspondence and in axis with a terracotta half-moon, placed above this wall and having the function of containing the oscillation of the cannon mouth. The greatest source of danger to public safety was the damaged lintels of the embrasures. They have been internally pivoted and consolidated, although not all of them retain the characteristic wedge-cut central stone as in an arch key. Some of these lintels have even been replaced with reinforced concrete, on which the Soprintendenza had to intervene to prevent further deterioration. Other tampering with exposed reinforced concrete was present on the covers of the parapets of the access ramp and on the corners of the south façade, where recent infill work can be seen on the machicolations, highlighted after the restoration with a more closed and smoothed plaster than the neighbouring parts of the wall face. During work on the outer face of the fortress, the Superintendency's technicians found numerous cannon balls fired from ships at anchor in the bay. It was the side of the fortress facing the sea that was most riddled and, in fact, its masonry was noticeably uneven. Before proceeding with the re-plastering, an accurate survey of the holes caused by the bullets was carried out, so that their trajectory could be reconstructed. In the inner courtyard, the original lime-beaten paving and the channels, connected to various wells, to channel rainwater into the cistern were brought to light. On the upper terrace, now irreversibly covered for the most part by the two aforementioned volumes, the various floorings have been left legible: the original beaten lime; the overlapping stone cladding; the overlapping knife-laid terracotta, according to a herringbone pattern. The north-east corner, subject to an angular lesion that caused it to slide downwards, was consolidated by inserting three IPE 220 beams embedded in the flooring, with iron tie-rods and blocked in such a way as to restore continuity to the masonry, as well as to support the perilous external cornice. As for the six rooms on the entrance floor, formerly reserved for the garrison's quarters, their original lime plaster was found, still partially preserved under the recently installed plaster. The rooms of the two superfetations on the upper floor, although largely built in recent times, have been preserved as it would have been very difficult to recover the original wall fabric, now irreparably compromised. The flat roofs of these two volumes were thickened and waterproofed with a double sheath, protected by an overlying non-wall draining layer made of pieces of stone, so that the final appearance would not clash with the colours of the fortress's wall faces. The system of large cisterns, located at the basement and accessible from an entrance on the south side, at a level below the square in front of the fortress, was mezzanine and converted into an exhibition space, which is currently underused[2].

7.3 Summary of data collected through remote sensing and databases

With regard to the urban context of the Spanish Fortress of Porto Santo Stefanowe collected the following data obtained by remote sensing:

- the Digital Terrain Model (DTM) of tile C42441110_0202 of the Extraordinary Plan for Environmental Remote Sensing 2009 (PST-A 2009), as well as the point cloud from which it was derived. Both products are the result of a scan with an aircraft-mounted LIDAR sensor;
- the Digital Terrain Model (DTM) of tile C42421112_0202 of the Extraordinary Environmental Remote Sensing Plan 2009 (PST-A 2009), as well as the point cloud from

which it was derived. Both products are the result of an aircraft-mounted LIDAR sensor scan ;
- the tomographic point cloud processed by IREA-CNR on the basis of the 160 COSMO-SkyMed products and the NASADEM Digital Terrain Model (DEM);
- the tomographic point cloud processed by IREA-CNR on the basis of the 160 COSMO-SkyMed products and the TanDEM-X DEM.

In addition, we downloaded sheet 03J24 of the 1:2000 Regional Technical Map of Tuscany, drawn up in 1998, in both .tiff and .dxf format, in order to use it as a cartographic basis for updating.

7.4. Report on in situ survey campaigns

Below is a report on the in situ survey campaigns carried out for the Spanish Fortress in Porto Santo Stefano.

7.4.1. Initial Approach to the Case Study and Preliminary Site Survey

In March and April 2022 we collected bibliographic sources on Porto Santo Stefano and the Spanish Fortress in order to form an initial picture of the site's environmental characteristics and built heritage, as well as to set up a first draft of the survey strategies to be adopted. This also made it possible to plan a preliminary survey coordinated with that of Talamone. Both surveys were in fact carried out on 8 May 2022.

the Spanish Fortress took place from 15:00 to 17:30 and covered the exterior, the entrance floor and the upper floor. These two levels are used as museum spaces and are the responsibility of the Pro Loco di Porto Santo Stefano, and can therefore be visited at certain times. The basement level, on the other hand, is the competence of the Monte Argentario municipality and can only be visited with permission. During the patrol, we acquired photographic documentation with a Canon PowerShot G9 compact digital camera.

On 21 June 2022 we carried out a further inspection, from 10.00 to 12.00, during which we took further photographs using the same camera. During the second inspection, a strong deformation of the intrados of the roof slab of the eastern superstructure on the upper floor was noticed, which was particularly evident by observing the cracking of the plaster at the joists and the east-facing perimeter wall (Fig. 7.12).

The original 12 MP digital frames are 4000 × 3000 px in size and were taken at: focal length of 7.40 mm; ISO 80; capture speed 1/800 s; aperture of f/4.0.

During the inspection we had the opportunity to view the graphs of the survey carried out before the 1980-1998 restoration works by the Soprintendenza per i Beni Ambientali e Architettonici for the provinces of Siena and Grosseto. From these graphs we were able to derive eidostypes to plan subsequent operations.

7.4.2 Laser scanner survey campaign

The survey campaigns with terrestrial LIDAR were carried out with a FARO Focus M70 3D laser scanner.

The interior of the Spanish Fortress can only be visited at certain times of the year and at certain times. This resulted in a staggering of the survey beats with rather long time intervals between each campaign.

The first instrumental survey campaign took place between 27 and 30 June 2022. The first day (from 9:00 a.m. to 6:00 p.m.) was dedicated to scanning the south façade, the interior rooms (with the exception of four rooms closed to the public) and the terrace on the entrance level, the terrace on the upper floor and the roofs. After requesting authorisation from the Municipality of Monte Argentario, the morning of the second day saw the scans of the cisterns on the basement floor. On the morning of the third day, from 6 a.m. until 12 noon, scans

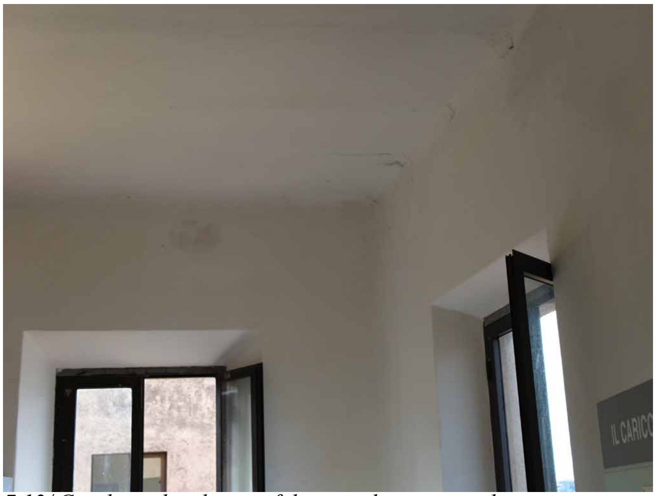

7.12/ Cracks in the plaster of the intrados joists in the eastern superstructure, caused by deformation of the roof slab.

were carried out of the exteriors on the west, north and east sides of the Fortezza. Thus, 48 scans were carried out on the first beat.

The presence of several installations on the second floor necessitated the preparation of a second special survey campaign, which took place between 19 and 21 September 2022. On this occasion, room scans were carried out inside the superfetations on the upper floor, in the rooms on the first floor that had not been surveyed during the first survey (a staff bathroom, an electrical panel room, a storeroom and one of the six main rooms, which was closed due to floor subsidence). Further scans of the terrace on the entrance floor were also carried out. Thus, 21 scans were carried out during the second beat.

On the morning of 7 June 2023, a third survey was carried out from 10 a.m. to 12 noon, during which additional scans were taken on the entrance level with regard to the terrace and the staff toilet. On the occasion of this last beat, 2 scans were carried out.

The total number of scans carried out amounted to 71.

7.5 Processing and integration of acquired data

We now present the procedure followed to process and integrate the data acquired through remote sensing and in situ survey operations.

7.5.1 Alignment of clouds acquired with laser scanners

Due to the time intervals between campaigns, the processing and alignment of the scans were restricted accordingly.

In July, August and September 2022, the alignments and processing of the 48 point clouds acquired during the first survey campaign were carried out.

From October 2022 to May 2023, the 21point clouds acquired during the second survey campaignadded to the generated digital model

June 2023, following the last 3 additional scans, it was possible to align all 71clouds and thus complete the digital model

All import, alignment and subsampling operations were performed with theJRC 3D Reconstructor software The processing consisted of a first phase of importing the scans and refining the associated point clouds, a second phase of pre-alignment, a third phase of fine alignment and a fourth phase of subsampling.

In the first phase, the programme automatically refined each point cloud obtained from each imported scan and removed inconsistent data.

In the second phase, we pre-aligned every two clouds to form a closed loop of scans that correctly determined the outer lateral surface of the Rock. In each pre-alignment operation, we ensured that the maximum acceptable error threshold of 3 cm was not exceeded.

In the third phase, we applied the Iterative Closest Point (ICP) algorithm every two clouds in order to perform a fine alignment. Here we ensured that the maximum acceptable error threshold of 0.5 mm was not exceeded in each fine alignment operation. This permissible error threshold is linked to the fact that the model resulting from the laser scanner scans was primarily intended for graphic restitution at an architectural scale.

In the fourth phase, we subjected each point cloud to subsampling. The quantity of points constituting each cloud was in fact surplus to requirements, and the surplus points would not have brought any benefit to the representation, instead risking slowing down the performance of the computer used in the processing. For

this reason, we decided to sub-sample each cloud in proportion to its location: the clouds derived from the scans of exteriors from the streets were subsampled by a factor of 2, so their number of points was halved; the clouds derived from the scans of exteriors within the perimeter of the Fortress itself, such as the terraces, were subsampled by a factor of 4 (their number of points thus became a quarter of what it was at the beginning); the clouds derived from the interior scans were subsampled by a factor of 8, so their number of points became one eighth of their initial consistency.

The 71 clouds were then merged into a single file saved in .ply format, with a 'Binary Little Indian' save mode, with a 'double' co-ordinate format and obviously incorporating the colour of the points.

7.5.2 Integration of point clouds

The purpose of the integration operation was to align point clouds obtained with different techniques and at different scales of representation, in order to derive a sufficiently detailed model of an urban area on which information regarding the mechanics of its structures could also be reported. The materials to be intergrated were therefore the following:

- the ones of tiles C42441110_0202 and C42421112_0202 of PST-A 2009, consisting of LIDAR data acquired by the Ministry of the Environment through an aircraft-mounted sensor. Since this is the largest point cloud, it was used as the input basis for all the others;
- the one derived from the union of the 71 laser scanner acquisitions;
- the tomographic point cloud processed by IREA-CNR on the basis of the 160 COSMO-SkyMed products and NASADEM data;
- the tomographic point cloud processed by IREA-CNR based on the 160 COSMO-SkyMed products and TanDEM-X data.

We therefore aligned the clouds listed above with the CloudCompare programme, keeping the errors below a maximum error threshold of 30 cm. This permissible error threshold is related to the fact that the model resulting from the integration of the point clouds was primarily intended for graphic restitution at an urban scale.

7.6. Graphical Representation of Data and Results

Using the alignment process, we obtained a virtual three-dimensional model on an urban scale. From this model we obtained graphical returns to the section profiles, where the targets identified by the COSMO-Skymed mission satellite radars and selected by the 3D SAR Tomography process applied by IREA-CNR were highlighted with coloured dots. The colour of each of the targets represents the estimated average velocity for the corresponding backscattering element with reference to the ten-year time interval covered by the 160 selected COSMO-Skymed products. As with the tomographic point clouds seen in Chapter 3, the average velocity shown in these profiles is the average of the estimated values of the displacements along the line of sight of the radar sensorin the time series

addition to these cross-sectional profiles, anupdated planimetry was renderedby superimposing, through GIS, contour lines obtained from the DTM of tiles C42441110_0202 and C42421112_0202 of the 2009 PST-A, the Regional Technical Map of Tuscany and satellite photographs.

From a direct comparison with the photographs taken during the survey of 21 June 2022, the deformation of the roof slab of the eastern elevation of the Fortezza is explicitly highlighted by the targets recorded by the COSMO-SkyMed sensors and selected by the tomographic processing, which were represented as points in the tomographic clouds and section profiles. For each target, the average velocity along the line of sight of the satellites was respectively represented with a colour, according to a scale ranging from blue (for the displacement component in the direction towards the sensor) to red (for the displacement component in the opposite direction to the sensor).

Notes

1. Della Monaca, Roselli, Tosi [dopo il 1993], 1-10; Maioli Urbini 1990, 61-78, 82.
2. Della Monaca, Roselli, Tosi [dopo il 1993], 1-10; Maioli Urbini 1990, 61-78, 82.
3. Ministero dell'Ambiente e della Tutela del Territorio e del Mare, 2017.
4. Gexcel, 2023.
5. CloudCompare 2023.

Sintesi

Tra i primi insediamenti degni di nota sviluppatisi nell'attuale sito di Porto Santo Stefano, ne sorse uno in epoca romana, in una zona di grande interesse per la famiglia dei Domizi Enobarbi. Questo nucleo attraversò poi un lungo periodo di decadenza che si estese fino al XVII, ossia prima del suo sviluppo commerciale. Tra le principali cause di queste condizioni precarie vi era il fatto che l'insenatura di Porto Santo Stefano sia circondata da molti colli, impedendo così qualsiasi tentativo di fortificazione anteriore allo sviluppo delle armi a polvere da sparo. I locali si trovavano pertanto esposti continuamente alle incursioni piratesche, in particolare quelle dei corsari ottomani.

Durante l'esistenza dello Stato dei Presìdi toscani le prime strutture stabili presenti sul sito furono dei magazzini militari, poiché lo scalo di Porto Santo Stefano era adibito all'attracco delle navi troppo grandi per Porto Ercole e allo sbarco delle loro merci. In seguito, la Fortezza spagnola fu costruita su iniziativa di Egidio Nuñez Orejon, governatore dello Stato dei Presìdi tra il 1605 e il 1617. La massa della Fortezza è formata da un basamento scarpato di pianta quadrata, all'interno del quale erano ubicate delle cisterne. È possibile accedere a queste cisterne dal lato ovest della costruzione, passando sotto la rampa di accesso principale ed entrando da una posta sul lato sud. L'ingresso principale alla fortezza è rialzato rispetto al piano stradale e avviene per mezzo di una rampa cordonata che originariamente aveva dei gradini e un ponte levatoio (sono rimasti i fori per relativi i bolzoni sul prospetto meridionale dell'edificio). Dal portone principale si accede a un cortile posto esattamente sopra la cisterna centrale del piano inferiore. Sui lati interni orientale e occidentale del cortile si affacciano sei stanze voltate a botte, tre per ognuno dei due sopraccitati lati e segnalate da porte incorniciate da elementi in pietra. Originariamente, questi sei locali erano adibiti alla guarnigione. A questo piano la costruzione non occupa tutta l'area coperta, ma arretra sul lato verso il mare, lasciando spazio a una terrazza accessibile dal lato settentrionale del cortile interno. In origine, la terrazza aveva un rivestimento in battuto di calce inclinato in modo pronunciato verso l'esterno, per favorire lo scolo delle acque ma, successivamente, venne ricoperta con uno strato di terra spesso circa 50 centimetri, al quale venne sovrapposta una pavimentazione in pietrame. Al di sopra del tutto vennero collocate le postazioni per tre cannoni. Queste sedi per le artiglierie vennero successivamente risistemate nel XIX secolo con la posa in opera di semicerchi in pietra, destinati alla rotazione delle ruote degli affusti presenti nei cannoni di concezione moderna. L'accesso al piano superiore è possibile solo mediante due rampe cordonate (una delle quali fu interrata e poi ripristinata durante il XIX secolo). Originariamente, la terrazza del livello superiore ospitava altre due postazioni per cannoni e due piccoli volumi con le rispettive stanze. Una era dedicata alla vedetta, l'altra era un deposito di munizioni. Oggi la maggior parte della terrazza superiore è occupata da due grandi superfetazioni, le quali hanno irrimediabilmente compromesso l'aspetto originario della Fortezza e impediscono il ritrovamento dei paramenti murari originari.

Le operazioni di rilevamento sono state anticipate da un sopralluogo preliminare eseguito il giorno 8 maggio 2022, in occasione del quale venne effettuata una prima campagna fotografica. Il 21 giugno 2022 è stato effettuato un secondo sopralluogo, dove si è provveduto ad ampliare la documentazione fotografica. In quell'occasione è stata notata una forte deformazione all'intradosso del solaio di copertura della superfetazione orientale, al piano superiore.

Tra il 27 giugno 2022 e il 30 giugno 2022 è stata condotta la prima campagna con scanner laser terrestre, in occasione della quale sono state acquisite 48 nuvole di punti tra ambienti interni (sotterranei, piano della terrazza, piano superiore, coperture) ed esterni (prospetti e terrazze).

Tra il 19 settembre 2022 e il 21 settembre 2022 è stata effettuata una seconda campagna con scanner laser terrestre, con l'acquisizione di altre 21 nuvole di punti.

Tra il 6 giugno 2023 e l'8 giugno 2023 è stata condotta una terza campagna con laser scanner terrestre, dove sono state effettuate altre 2 acquisizioni, raggiungendo così un totale di 71 scansioni.

Parallelamente allo svolgimento delle campagne, le nuvole sono state allineate tramite impiego del software JRC Reconstructor, prima con applicazione di un preallineamento manuale e poi mediante impiego di un algoritmo Iterative Closest Point (ICP), raggiungendo una soglia di errore medio inferiore ai 3 mm.

La nuvola di punti della Fortezza, ottenuta tramite scanner laser e allineata tramite JRC Reconstructor, è stata poi allineata alle nuvole LIDAR (LIght Detection And Ranging) delle tavolette C42441110_0202 e C42421112_0202 Piano Straordinario di Telerilevamento Ambientale 2009 (PST-A 2009) del Ministero dell'Ambiente Italiano, usando la trasformazione di Helmert. Lo stesso comando è stato poi usato per allineare alle nuvole del Ministero dell'Ambiente le nuvole di punti elaborate dall'Istituto per il Rilevamento Elettromagnetico dell'Ambiente del Consiglio Nazionale delle Ricerche (IREA-CNR) con le tecniche di tomografia radar ad apertura sintetica a quattro dimensioni, sia quella con dati NASADEM che quelle con dati TanDEM-X.

Dalla sovrapposizione di questi dati sono stati restituiti dei profili in sezione della Fortezza spagnola e del suo contesto urbano in Porto Santo Stefano, dove sono stati riportati i bersagli individuati dalle elaborazioni tomografiche lungo il piano di sezione.

Da una comparazione diretta con le fotografie scattate durante il sopralluogo del 21 giugno 2022, la deformazione del solaio di copertura della supefetazione orientale della Fortezza risulta evidenziata esplicitamente dai bersagli registrati dai sensori COSMO-SkyMed e selezionati dall'elaborazione tomografica, i quali sono stati rappresentati come punti nelle nuvole tomografiche e nei profili di sezione. Per ogni bersaglio, la velocità media lungo la linea di mira dei satelliti è stata rispettivamente rappresentata con un colore, secondo una scala che va dal blu (per la componente di spostamento nella direzione verso il sensore) al rosso (per la componente di spostamento nella direzione opposta rispetto al sensore).

7.13/ Planimetry of the urban context of Porto Santo Stefano in the surrondings of the Spanish fortress. The topography has been updated thanks to the Digital Terrain Model (DTM) of tile C42441110_0202 and tile C42421112_0202 of the Extraordinary Plan for Environmental Remote Sensing 2009 (PST-A 2009). Ministero dell'Ambiente e dell'Energia – Italian Ministry of Environment and Energy / licensed under CC BY-SA 3.0 IT (https://creativecommons.org/licenses/by/3.0/it/deed.it) / Creative Commons – Attribuzione - Condividi allo stesso modo Italia (CC BY-SA 3.0 IT).

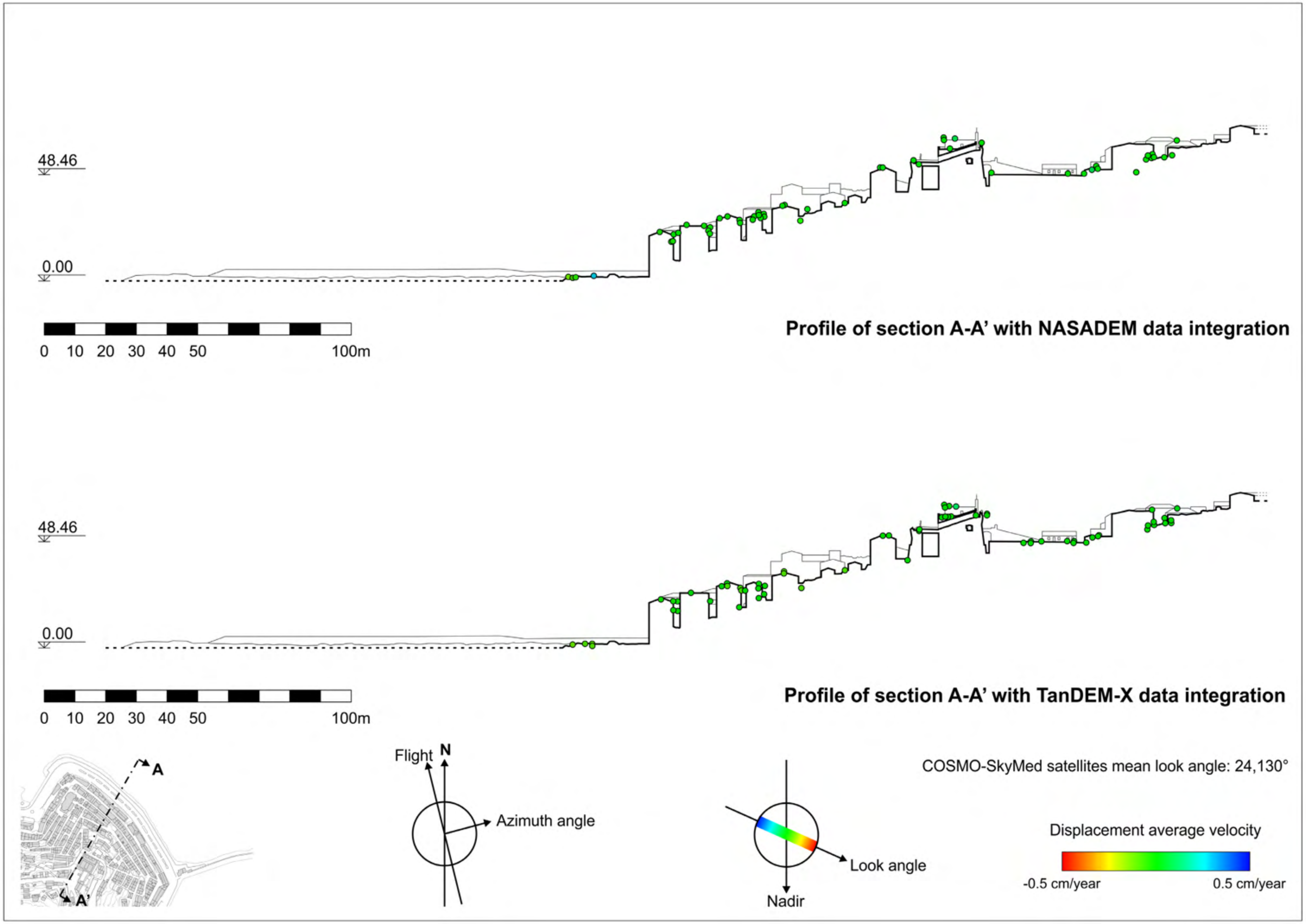

7.14/ Profile of section A-A' of the urban context of Porto Santo Stefano around the Spanish Fortress. Moving targets during observation are highlighted with coloured dots.

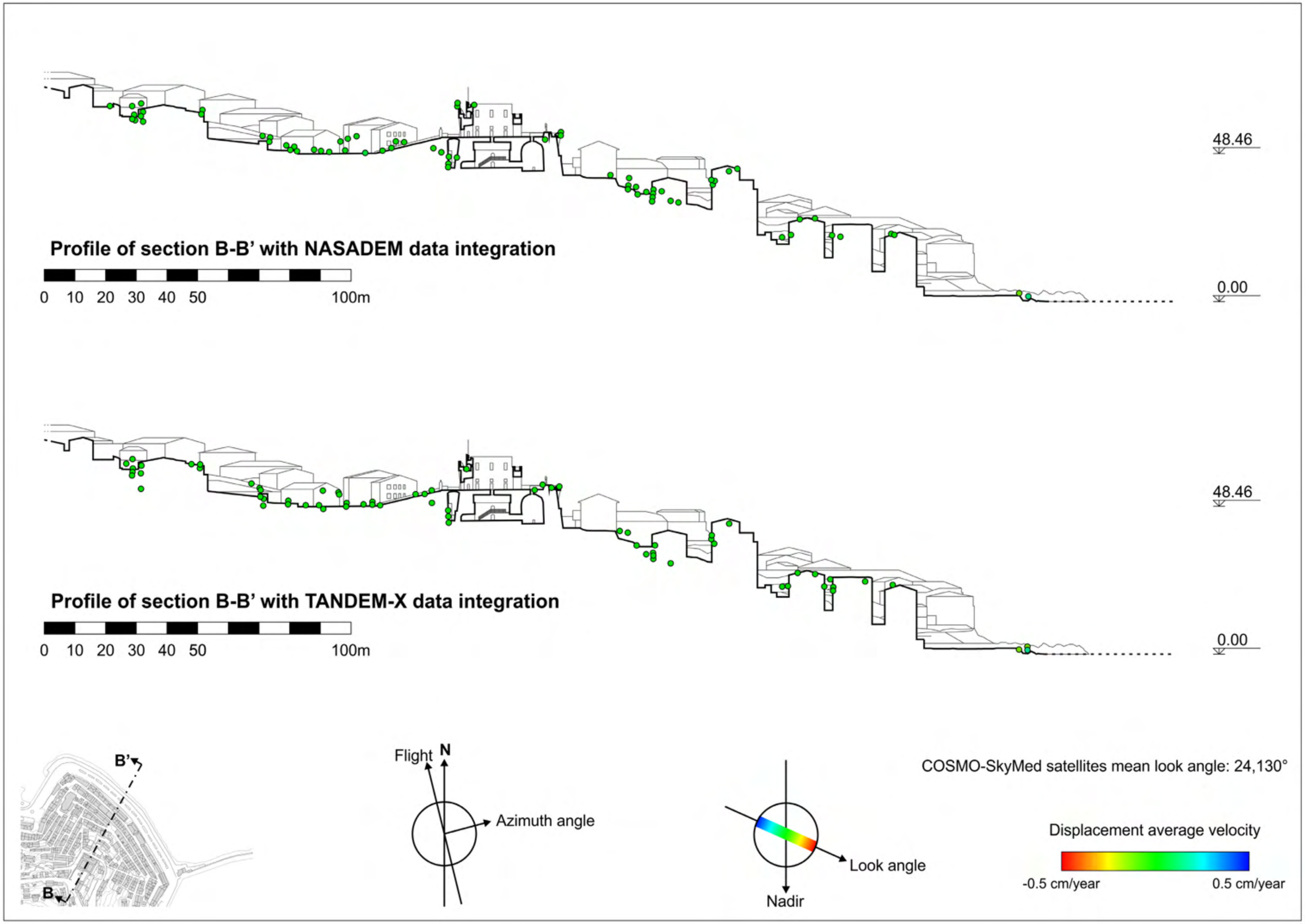

7.15/ Profile of section B-B' of the urban context of Porto Santo Stefano around the Spanish Fortress. Moving targets during observation are highlighted with coloured dots.

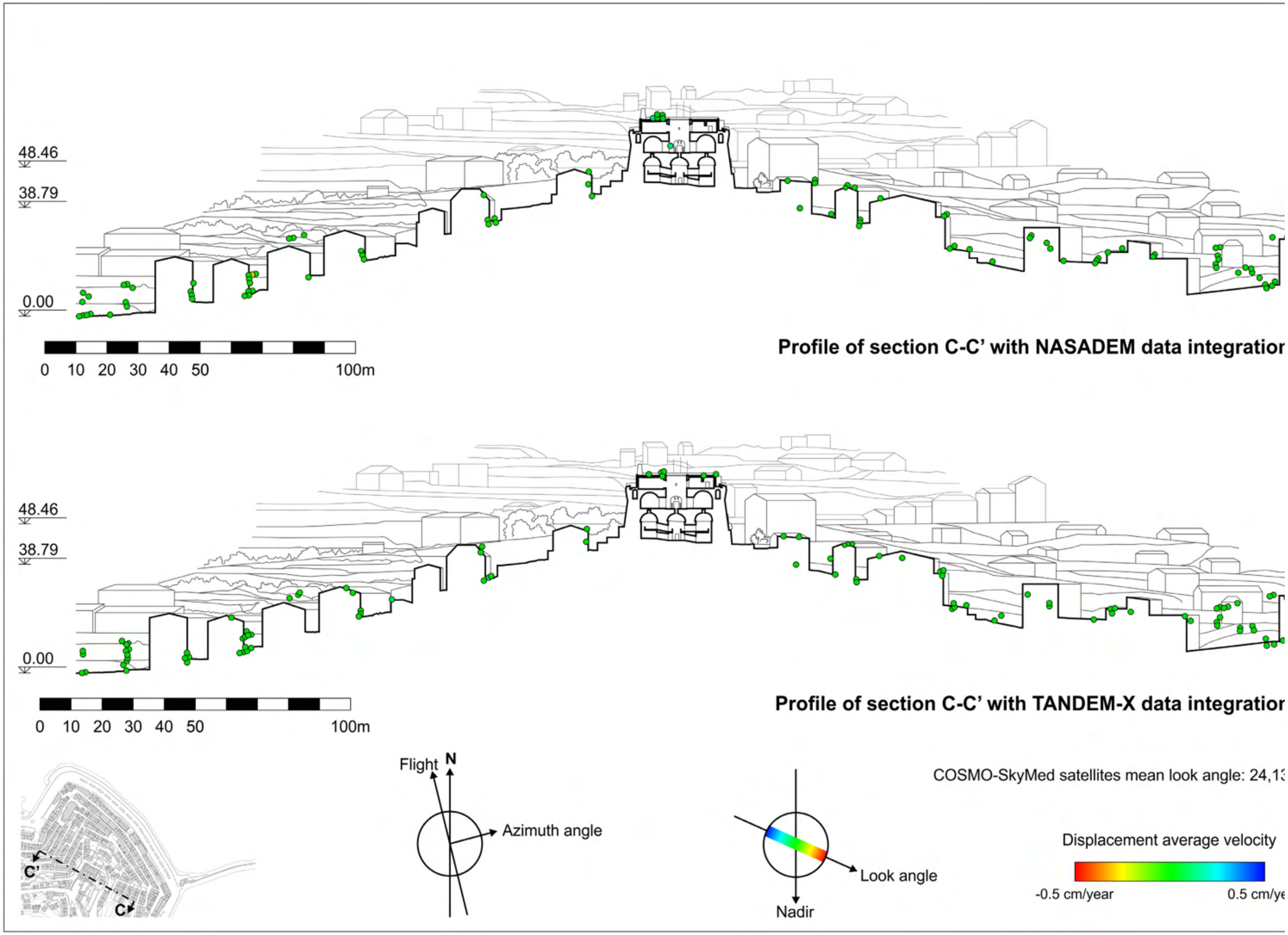

7.16/ Profile of section C-C' of the urban context of Porto Santo Stefano around the Spanish Fortress. Moving targets during observation are highlighted with coloured dots.

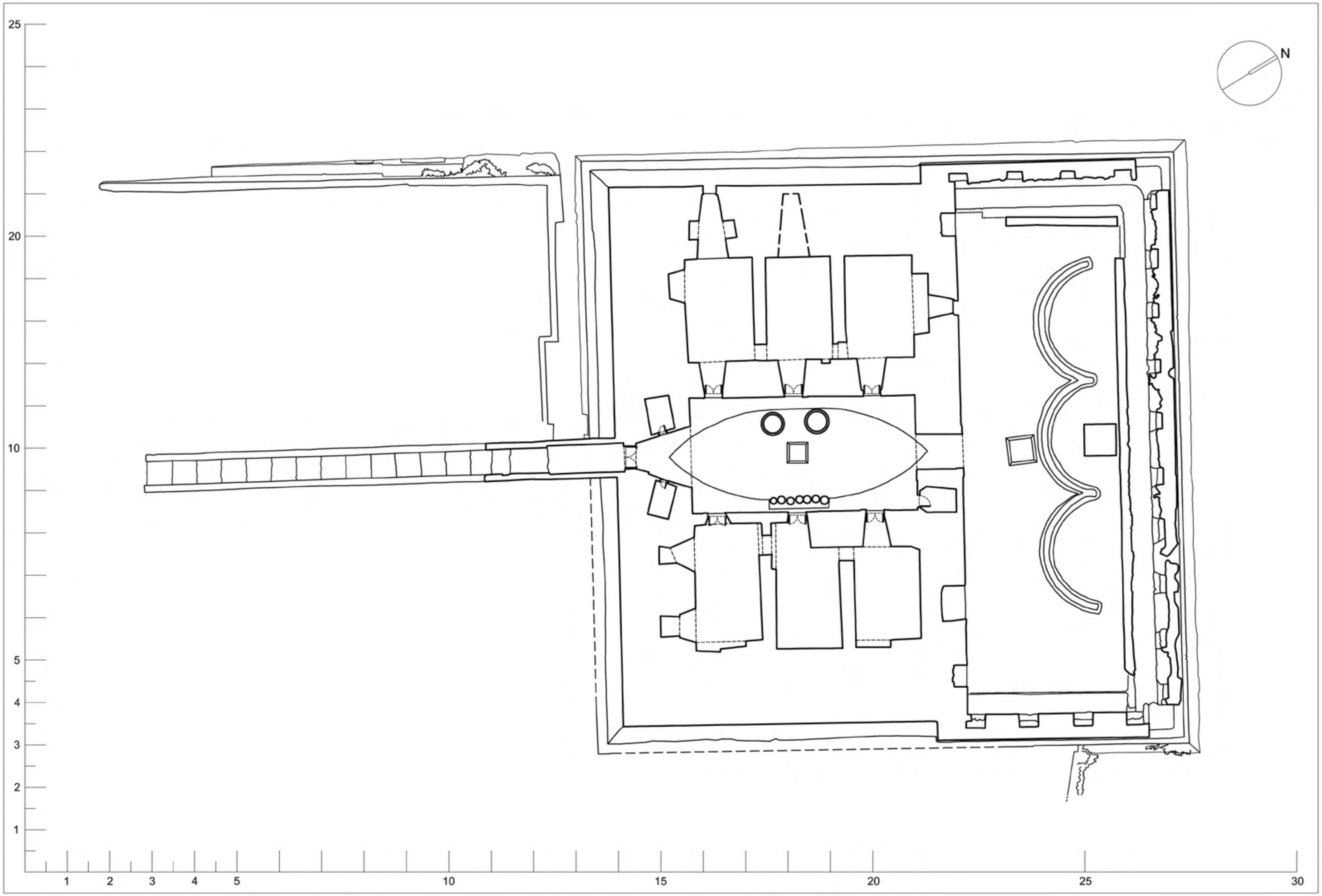

7.17/ Plan of the main entrance floor (48.46 metres above sea level).

8. The City Walls and the Fortress of Talamone

8.1 The environmental context and historical events

The defensive complex of Talamone stands on the western end of a wide inlet, open to the sea to the south, but close to the Argentario Promontory.

During the various epochs, this natural harbour protected from sea storms had mainly poor luck, despite some periods of great traffic. Some factors that negatively influenced the development of the town were of human origin, such as the constant wars and raids to which it was subjected. Other causes, on the other hand, were very much related to the environment, such as malaria from the surrounding marshy land, which caused depopulation that was countered by periodic, in some cases politically planned, immigrations. Also linked to the environmental context are the reduction of the seabed due to silting up and the erosion of the rocky coastline, phenomena that are still strongly present today.

As already mentioned in Chapter 5, in the arch of the Gulf of Talamone, near the mouth of the River Osa, there are traces of several settlements that have succeeded one another throughout history but, in any case, have some relationship with the present urban centre. Fragmentary finds on the Talamonaccio hill attest to the presence of a settlement during the Late Bronze Age and Villanovan Age (11th-7th century B.C.). The ancient settlement of the Etruscan port of Tèlamon and later the Roman mansio of Telamone stood to the east of the present town, between the small hill of Bengodi and the hillock of Talamonaccio, towards the Osa. The construction of the temple at the summit of the Talamonaccio hill, as part of the Etruscan city of Tèlamon, dates back to the first half of the 4th century BC. At that time, Tèlamonalready had a necropolis and a port

After conquering Etruria in 280 B.C., the Romans founded the colony of Cosa in 273 B.C., which also exerted its influence on Tèlamon. In 225 B.C. the Battle of Talamone took place, in which the Romans won over the Gauls. In 144 B.C., the Romans extended the Via Aurelia north of the Forum

8.1/ The town of Talamone as seen from the pier to the east.

8.2/ The northern side of the Talamone Walls, with Porta Garibaldi.

Aurelii (at today's Montalto di Castro), reaching the mansio of Telamone. During the second quarter of the 2nd century B.C., the temple of Talamonaccio was renovated and decorated with the fictile pediment representing 'The Seven against Thebes', which shows stylistic and technical similarities to the terracotta of Temple D at Cosa. However, in the context of the war between Marius and Sulla, in 82 BC the mansio of Telamon was destroyed and the temple of Talamonaccio burnt down. Also during the 1st century B.C., a Roman villa was built at the Madonna delle Grazie locality, constituting the future pole of 'Talamone vecchio'.

In the 1st century A.D., a phase of depopulation and decadence of the Talamone area began due to malaria, and in 412 A.D. the Visigoths devastated the Via Aurelia, destroying its bridges over the Albegna, Osa and Ombrone Rivers.

In the 6th century B.C., the Longobards settled on the hill of Talamonaccio in correspondence with the current location of Capo Marta and in continuity with the pre-existing Tèlamon and the mansio of Telamone. In 756, the Lombard king Rachis ordered the foundation of a Priory or Cell with a hospital for poor wayfarers in the vicinity of the River Osa, probably in the locality known today as Spedaletto, in the area of Talamone.

In January 921, the abbey of San Salvatore al Monte Amiata granted the priest Anso, who lived in the vico di Capo Marta, some goods of the Amiata monastery located in that very vico, in return for an annual fee. On 23 December 995, Marquis Ugo of Tuscany, of the Aldobrandeschi family, donated the Osa baths to the Abbey of San Salvatore al Monte Amiata, stipulating the deed in loco Marta, in the territory of Sovana. In 1154, Ildebrandino Maria, head of the Aldobrandeschi, sold the port of Talamone to the monks of the Abbey of Amiata, who on 22 June 1243 also became owners of the Valentina estate, further north. However, on 30 April 1251, the maritime ports of Talamone and Porto Ercole were granted to the Florentines by Guglielmo Aldobrandeschi, who did not care about previous agreements. In 1274, the Aldobrandeschi Committee was divided between the counts Ildebrandino di Guglielmo di Sovana and Ildebrandino di Bonifazio di Santafiora. Collecchio and Marta with Talamone were thus inherited by Ildebrandino di Bonifazio.

On 15 April 1303, the monks of the Abbey of San Salvatore al Monte Amiata formalised their intention to sell Talamone and Castiglione d'Orcia, occupied by the Aldobrandeschi, so in May of the same year, Abbot Ranieri went to Siena to negotiate the sale. On 25 July, the abbot signed a

8.3/ The south facade of the Fortress of Talamone.

lease agreement with Count Ildebrandino Novello di Santa Fiora regarding the Valentina estate in Collecchio. The terms of the agreement provided for a 29-year lease and a compensation of 50 cortonesi liras. The fact that the Valentina estate was an appurtenance of Collecchio indirectly attests to the non-existence of a stable fortified settlement with its own territory near the port of Talamone, which was probably still dependent on the vico di Capo Marta. Between 10 and 12 September, the Municipality of Siena approved the purchase of Talamone with the Valentina and Castiglione d'Orcia for a payment of 9,000 gold florins. Thus, on 22 September, Mino d'Orlando took possession of the port of Talamone on behalf of the Sienese Republic.

In May 1304, it was established that every two months the Podestà of Siena had to ask the Consiglio della Campana, the city's major decision-making body, to deliberate on the work to be done on the Talamone port: consequently, on 8 December of the same year, work on the port and fortifications was established. The project was drawn up in a plan, a copy of which was included in the Black Kaleffo, one of the Sienese registers of contracts preserved today in the Siena State Archives. This copy, which has come down to us today, was probably taken from a larger drawing. The dating of the plan can be set between a post-quem date - the already mentioned resolution of 8 December 1304 - and an ante-quem date, i.e. the start of work on the Fortress, which had already begun in

April 1305 under the direction of Mino Chiocciola. Although in 1304 a colony of Sienese citizens, led by Battista Gigli, had already taken up residence at Talamone, the land was only assigned on 19 March 1306. The drawing can therefore be dated between the end of 1304 and the early months of 1305, since in the planning cycle of the works, the Fortress was a fundamental element, to be realised as soon as possible. However, the plan of the Black Caliph was put on parchment and made official in 1306.

As already mentioned, therefore, in 1305, the construction of the Keep and the landing stage was begun. In addition, work was begun on the walls, the layout of the new settlement and the road network connecting with Siena. Building plots were also assigned in the castrum, i.e. the area surrounded by the walls. As mentioned above, on 19 March 1306, all the works to be carried out in the castrumand the division of the territory surrounding Talamone into one hundred farms wereresolved, which were assigned to the assignees of the building plots within the walls. On 28 May of the same year, the port and the Keep were completed, of which the castellan Pietro di Filippo took possession. On 10 June the tax delle Saline di Talamone was put up for sale for five years, approving the pacts and planning a detailed list of plots of land of different characteristics and sizes, so as to ensure a certain variety in cultivation. These plots were located between Talamone, Talamone Vecchio, the Collecchio, the Via Senese and the Via Grossetana, lined up in parallel rows and connected by new roads bordering the marsh and the Saline. In addition to the new axial thorn roads, there were secondary roads orthogonal to them. The allocation of these lands was by lottery and followed a precise plan to colonise the area.

On 8 September 1307, the New Salt Statutes were issued regulating the production of Grosseto and Talamone, establishing that a Salt Customs was to be located in the latter to facilitate communication routes with Siena. In addition, a new, easier road was built in the plain area that connected with the capital of the Republic, without having to pass through Grosseto and thus in total independence. On 21 December 1308, a further allotment of land was held in the area of Marta and the plain of Magliano, in addition to the previous one. On 12 August 1309, it was decided to send a bailiff of three men to Talamone to inspect the port and report on the progress of the work, and on the same day, the Council of the Campana approved new measures for the populating of the town and the maintenance of the port, salt pans and roads. On 8 October, new works were planned, including: the completion of the church; the munition of the Keep; the improvement of the town hall; the construction of a wooden wharf to facilitate the loading and unloading of goods and a lighthouse to ensure greater safety for ships; and the building of a new road between Talamone and Castelfranco di Paganico, constructing a stone bridge over the River Ombrone.

On 17 August 1311, a commercial treaty was stipulated between Florence and Siena on the use of the port of Talamone, thanks to which Florentine merchants could move from Porto Pisano to Talamone and transport their goods along the new road to Paganico, then from Paganico to Siena and Florence. In 1312, following the descent of Henry VII of Luxembourg into Tuscany, Talamone was treacherously conquered by pro-imperial Sienese exiles, allied with the Pisans and the Aldobrandeschi of Santa Fiora. After two years in Ghibelline hands, the town was recaptured by the Sienese on 5 October 1314: the town celebrated by lighting bonfires on the Mignanelli Tower, the bell tower of the cathedral and the Palazzo del Podestà. In 1320 Talamone was attacked by Genoese exiles under the pretext of revenge on Siena for having sent armed people to help King Robert of Naples, their enemy. The Genoese exiles occupied the town, plundered the grain they had just landed and slaughtered the few inhabitants there. On 3 November of that same year, the Council of Campana approved measures to encourage the population of Talamone and new taxes. At the beginning of 1321, the penalties imposed on 92 Sienese citizens, guilty of not having built their houses, as promised when the land in Talamone was assigned, or of having built them but not having gone to live there, were extended. Consistently, on 9 December 1323, the Council of the Campana resolved exemptions for ten years for allottees of plots and farms who had decided to settle in Talamone.

In May 1327, the Duke of Calabria preferred Talamone and Grosseto to Porto Pisano for the landing of his troops.After a brief occupation of Talamone by the Aragonese fleet in September 1328, on the following 19 October, the Duke of Calabria's viacario, Albertaccio Vicedomini, proposed to rent the castle, port and pastures of Talamone, as they had already been damaged several times due to the difficulties encountered during the defence. During the month of May 1337, the borders between the territory of Talamone and those of Magliano and Collecchio were established. The unfavourable environmental conditions (the unhealthy climate, malaria) and the constant attacks convinced the Sienese to hand over the port of Talamone to Messer Tedigi del Fiesco, from Genoa, but the latter had no intention of residing there and did not fulfil the obligations he had undertaken. The Florentines, at war with Pisa, renewed pacts with the Sienese for the use of the port of call and only returned to use Porto Pisano after the end of the 'war of Lucca'. On 7 May 1339, Talamone with the port and district were leased to the exiled Genoese Giannotto di Manfredi del Fiesco, Count of Lavagna, but the following year the lease was cancelled. In 1355 the Government of the Nine fell in Siena, replaced between March and May by the Government of the Twelve, i.e. twelve representatives of the people flanked by twelve nobles.

In 1356, the Pisans imposed a new tax for the defence of Porto Pisano without exempting the Florentine merchants, contrary to what had previously been agreed. The Florentine merchants refused to pay this tax and, consequently, their goods were seized. To remedy the situation, on 8 July of the same year the Florentines approved new agreements to be proposed to the Sienese and elected the magistracy of the 'Dieci del mare' (Ten of the Sea), and then sent Francesco Falconetti to Siena as ambassador. In August, a ten-year treaty was then signed between Siena and Florence for the use of the port of Talamone by Florentine merchants. According to the agreement, the construction of quays and docks, the maintenance and supervision of the road routes were the responsibility of Siena. Thus, in early November, the Florentine and other foreign merchants abandoned Porto Pisano and moved to Talamone. However, the retaliation of the Pisans was not long in coming and on 6 November the Commune of Siena had to send an ambassador to Florence to ask for military aid against the Republic of Pisa. On 5 January 1357, the wages of the labourers working in Talamone for the Commune of Siena were established and, on the 25th of the same month, the Council of the Campana resolved to start the construction of the Fondaco and new houses for the harbour, also managing to allocate 1,000 florins as the first funds for the work. The Fondaco, which was large, was to be built inside the walls, so as to be protected. Above it was the granary and the overseer's residence. However, Pisa's reprisals had not subsided and at the beginning of July several Pisan galleys entered the port of Talamone to hinder its activities and destroy the salt pans. In any case, during the course of the year, the leadership of the new magistracy of the 'Consoli del Mare' energetically continued work in the town: on the port, the Keep, the church and the houses. In the meantime, the Council of the Campana continued with its policies to encourage the colonisation of Talamone: on 4 December 1360, various concessions were deliberated for those who would go to live there; on 22 October 1361, numerous provisions were approved to encourage the repopulation of the Maremma and of Talamone in particular, including tax exemptions, concessions of plots of cultivable land and contributions to the artisans who would settle in the town.

Between June 1362 and August 1364, a war between Florence and Pisa took place, forcing most of the local population to abandon the territory. With the end of the conflict, in 1365 the Pisans managed to regain the trust of the Florentine merchants regarding the use of Porto Pisano. In order to prevent the abandonment of Talamone, the Sienese sent formal requests to Florence, managing to renew the ten-year agreement with the Florentines in 1366, which was also extended to the other merchants.

incentives adopted by the Republic of Siena to promote the colonisation of the Maremma did not succeed in containing the demographic and productive crisis: in the Council of the Campana of 12 October 1370, complaints were made regarding the depopulation of Grosseto, Magliano and Talamone (in the latter there were only eight men left) and the abandonment of crops, and then measures were adopted in this regardin 1376, it was decided to lease the revenues and taxes of those three Maremma settlements

Talamone was sacked twice by the army of Pisa, the second time also with the interference of the Prior of Pisa, friar Jacopo dei Gerosolimitani, who allowed the knights to occupy the nearby convent of San Rabano before the attack. In 1377, the port of call was in fact occupied by Pietro Gambacorta's soldiers, until Pietro Piccolomini sent militia to the Maremma, then imprisoned the Prior and sold the knights' possessions. Irritated, Pope Gregory XI sent papal troops to help the Pisans and they occupied Talamone in turn. In order to regain the port, the Commune of Siena then decided to arm a small army with the funds obtained from the sale of the Templars' possessions. In 1378, the castellare della Marta, on the hillock of Talamonaccio, was destroyed during a battle. With the death of Gregory XI on 27 March of that year and the election of Urban VI to the papal throne, the Sienese Republic was able to put an end to hostilities. At the beginning of 1379, the Sienese regained possession of the port of call after paying the newly elected Pope a substantial sum. On 28 March of that same year, an agreement was stipulated between the Commune and a colony of Catalans living in Pisa for the exploitation of the port of Talamone for a period of ten years. At the same time, the Sienese took charge of the maintenance of the wharf and possibly of extending it to a depth of 12 palms of water. The Catalans were also allowed to have their own loggia in Siena. Finally, the taxes established in the treaty with the Florentines in 1356 were halved.

On 12 January 1386, the Council of the Bell entered into a five-year lease contract with Salvestro Balzetti, representative of a trading company. The trading company would maintain an armed guard of 35 men in Talamone, while the Council would pay an annual rent of 850 gold florins. On 26 March 1397, it was decided to rent the Talamone guard again, but not the proceeds.

On 22 January 1398 tax payers of Talamone were subject were halved. Further tax relief occurred on 26 January of the following year, when all the taxes that had to be paid by merchants in Talamone were lowered to the level of those paid by Catalan settlers. On 14 February 1399, the Council of the Campana planned a series of initiatives for the improvement of the Sienese settlements in the Maremma and for the functioning of the Talamone port of call, calculating that 1,800 florins a year were spent on the armed surveillance of the latter. During the same year, the growing competition from the port of Piombino had begun to negatively affect Talamone's activities. However, in 1404, the Sienese took advantage of the Florentine army's occupation of Livorno to undertake new operations to make Talamone more attractive to merchants. On 16 October 1405, the Council of the Campana allocated 100 florins for the rebuilding of a wharf in the port, so that ships of at least 25 fathoms could dock there. On 26 October immediately afterwards, a number of citizens were commissioned to take care of the port's reinforcement works. On 7 February 1406, the construction ex novo of another wharf was ordered, with a budget of 1,000 florins. The conquest of Pisa by Florence that same year caused the Florentine merchants to move from the catchment area of Talamone to that of Porto Pisano, prompting the Sienese to plan further improvements. On 20 April 1407, extensive works on the fortress were planned, entrusted to master Meo Neri known as Canicchio, his brother Guccio and Giorgio di Angelo da Siena. In the same year, Domenico di Sano di Pietro worked on behalf of the Commune on five marble building elements for the Keep di Talamone, for a fee of 16 florins.

In 1410, the ships of the Genoese and Ladislaus I of Anjou-Durazzo, King of Naples,attacked Talamone and made it capitulate. The Sienese, allied with the Florentines, completely regained possession of the port on 17 December, after two months of attempted reconquest.

On 22 December 1411, the Sienese citizens in charge of the surveillance and maintenance of Talamone and its fortress were ordered to provide for the restoration of the walls, with a fine of one hundred gold florins in the event of non-compliance. On 23 January 1412, the Bell Council entrusted the execution of the work to ten citizens, later reduced to only five. Also in the same year, new measures were adopted for the security of the port and the surveillance of the goods stored there. The following 12 March, the Municipality presented a request to the Genoese Republic for the lifting of the ban on the port of Talamone.

In 1414, after the death of King Ladislaus I, Siena bought the territories of the Agro cosano, including Orbetello and Monte Argentario, for 8,000 gold florins. In this way, the Sienese Republic increased the number of ports at its disposal and, consequently, its commercial power, but, at the same time, Talamone essentially became a subordinate port of call to Orbetello. In May 1416, in fact, new regulations were approved for Orbetello and Talamone. For the latter, in particular, a bailiff was elected with 2,640 florins as annual funds, less than the 3,000 florins previously allocated by the municipality. This amount was earmarked for the construction of houses, salaries of public officials and troops, and contributions for the inhabitants, 44 at the time. In 1420, these funds were even reduced to only 1,000 florins.

In 1430, the cadastre or inventory of the real estate owned respectively by the Sienese Republic and the Church in the territory of Talamone was compiled. Within the City Walls there were many empty lots and 25 houses belonging to the municipality, which also owned plots concentrated in what is now Fonteblanda, on the Magliano Plain and at the mouth of the Osa. On 14 December 1436, new conventions were stipulated with the Catalan colonists, who intended to transfer their trade from Pisa to Talamone.

The development of alternative landings on the Maremma coastline, such as those near the Agro Cosano, caused a new phase of progressive abandonment of Talamone, which the Municipality of Siena tried to remedy with a series of maintenance and reinforcement works. In 1441, new works were planned for the fortress, the port and the walls. The Lombard master Giovanni Maffiuoli, hired to work on the ravelin, was paid an advance of 50 florins on 3 December 1442, to which was added a payment of 900 lire made between January and June 1443. The following 26 November, 100 florins were then paid to the master Giovanni da Como, who had taken care of the restoration of the city walls. On 10 February 1449, master Tommaso da Como was commissioned to build four houses and a ravelin at least one arm's width wide. On 17 September 1451, the Council of the Campana allocated a total of 800 florins for the purpose of providing a suitable reception in Talamone for Emperor Frederick III of Habsburg and his consort Eleanor of Aviz: 500 florins for the festivities and 300 for the renovation of the buildings. However, the following year, the sovereigns arrived in Siena without passing through the port of Talamone.

In 1453 there were disputes over the taxes regarding Talamone, so on 2 June the Consiglio della Campana appointed a bailiff to update the relative amounts, which were substantially increased.

On 13 June 1456, work on the ravelin by master Tommaso da Como was paid for. This structure can be identified today as the advanced fortified post protecting the entrance to the harbour, which was badly rebuilt after the bombing of World War II. Also in the year 1456, new initiatives for the repopulation of Talamone were approved on 5 July and 30 December. These were followed by facilities, approved on 8 January 1460, for merchants who would arm galleys in the port and open new fondachi in the town.

Between 1465 and 1467, restoration work on the fortified works of Talamone took place, overseen by Elia Mattei, a master from Como. These works included repairs to the fortress and the restoration of a breach in the walls. Through a new contract stipulated in 1468 with Giovanni Albini and Pietro di Giovanni, both residents of Talamone of Lombard origin, work was carried out on the City Walls and the tower of San Leonardo. The year 1469 saw extensive planning for work on the Orbetello and Talamone slipways. For the latter in particular, further work was planned on 23 January, including work on the walls carried out the following year. On 6 July 1470, other works were scheduled to be carried out at the Castellano di Talamone, which were followed by the General Council's resolution of 1 January 1473 to have another fifteen new houses built at the expense of the Republic.

In 1476, a plague decimated the town's population and some of the survivors emigrated to safety. Further damage was caused by King Ferdinand of Aragon's Neapolitan militia, placed in the Maremma to winter and fight the Florentines. The miserable conditions in which the population of Talamone found themselves were described in 1477 by the Sienese commissioners Santi di Bartolomeo and Giovanni Di Antonio Neri in a letter.

On 18 December1480, new incentives were deliberated to encourage the repopulation of the town, but in the following years its defensive structures were already practically crumbling, despite the repeated interventions carried out previously. In fact, on 31 March 1483, multiple reports were made on the poor condition of the Fortress (which had two towers to be repaired), the city walls, the battlements and the ravelin. Furthermore, on 6 August 1484, commissioner Bartolomeo Palazesi notified in a letter the perilous state of the tower of Santa Lucia.

On 2 December 1494, King Charles VIII of Valois of France entered Siena and, in order not to alienate it, the Republic was willing to hand over Talamone, Porto Ercole and Porto Santo Stefano to him However, this offer came to nothing. The interrelation between Porto Ercole and Talamone returned in a number of subsequent resolutions: on 13 March 1497, the taxes (taxes) on the two ports were lowered; on 14 February 1500, the revenues of both ports were sold for ten years to Alessandro di Galgano Bichi, in exchange for 4,500 florins; again in 1500, concessions for the two maritime centres were approved.

Between September and October 1503, further work on the city walls was paid for. In 1524, however, the population of Orbetello forwarded a request to the Commune of Siena for the walls of Talamone to be restored again, as they had even collapsed in some places. In the same year, work was also carried out on the wharf and jetties of the port.

In 1526, Talamone, Orbetello and Porto Ercole were occupied by the fleet of the Genoese admiral Andrea Doria on behalf of Pope Clement VII. However, Talamone was quickly reconquered by its own inhabitants.

In 1528, a letter from Captain Matteo di Giovanni reported the instability of the rampart works built a few years earlier in Talamone. This statement was confirmed in 1530, since not only were the walls in a poor state at the time, but even a bulwark towards the marina was half-destroyed.This state of dilapidation of the city walls was again recorded in the report written by Baldassarre Peruzzi in 1532, following his inspections in the ports of the Maremma on behalf of the Sienese Republic. In particular, he stated that the walls of Talamone were sufficiently battered to be easily climbed by the Turks and the Moors and therefore recommended that the defensive structures be strengthened and raised. Five years later, the report by Pietro Paolo Gallerani, commissioner of the Maremma, denouncedthat the settlement's walls were still shattered

All these close visits were a consequence of concern over the alliance between the King of France François I of Valois and Suleiman I, Sultan and Pasha of the Ottoman Empire, viewed with aversion by Spain, the Holy Roman Empire and consequently by Siena as their ally.In 1537, in fact, the Turkish fleet of Admiral Kayreddin the Redbeard sailed into the Strait of Messina, heralding the Ottomans' intention to conduct their raids in the Tyrrhenian Sea. So it was that in 1538, on the advice of Emperor Charles V and for fear of the Turkish army, the Sienese began fortification works at Talamone and in the other ports of the Republic. Between 1542 and 1544, work was carried out in Orbetello, Porto Ercole and Talamone, probably based on a design by Anton Maria di Paolo Lari, known as 'il Tozzo', a pupil and successor of Baldassarre Peruzzi. As for Talamone, work began on 31 December 1543. However, these works were thwarted by the assault of 10 June 1544 by Kayreddin's ships, which briefly conquered and occupied Porto Ercole and Talamone.

In 1545, following the looting by Kayreddin's soldiers, the community of Talamone sent ambassadors to Siena, asking for measures to repair the fortifications, as well as tiles and timber to rebuild the roofs of the houses. The Commune of Siena was thus forced to intervene and, in 1546, the commissioner of Orbetello, Ludovico Piccolomini, commissioned Pietro Catteneo, the great expert in military architecture, to inspect the defences of Talamone and supervise the necessary restoration work, while the execution of the work was entrusted to Antonio Parmigiano. This work also included the addition of a round tower a little to the north of the fortress, at the point where the escape door

probably existed. A probable fact related to military art, but not proven, is that the truncated tower that still exists today in the north-west section of the walls, i.e. a large angled slit cut into the barbette, i.e. the embankment intended for an open cannon, may also date back to this work. In any case, the end of the work supervised by Pietro Cattaneo was communicated to the Commune of Siena in a letter dated 24 April 1548.

At the end of the war of Siena that began in 1552, the capital and the territories of the Republic were annexed to the Duchy of Tuscany on 25 November 1558, but the King of Spain, Philip II, reserved possession of the entire coastal strip between Argentario, Orbetello and Talamone, which went to constitute the State of the Tuscan Presidios. With the new geopolitical framework, the governor of the Garrison of Orbetello also had jurisdiction over that of Talamone, while the Community was autonomous as far as civil administration was concerned. In the first years under the new State, the territory pertaining to the port, although not vast, offered sufficient income for the sustenance of its few inhabitants. Following an inspection of the Presidios, of which he was governor on behalf of the Spanish Monarchy, the Viceroy of Naples Don Perafan de Ribera ordered the reinforcement of its defences and garrisons in 1569. However, after the annexation, the recovery of Talamone was slow, if at all, and very little work was carried out there.

The oldest cartographic document on Talamone, after the foundation plan hypothetically datable between 1304 and 1305, is another plan dated 8 November 1595, limited to the defensive works. In it, the walkway connecting the fortress to the sea fortification still appears, which has now become part of the edge of the settlement due to landslides. According to the planat that time, the central gate was walled up, possibly for security reasons

On 9 May 1646, in the context of the Thirty Years' War, the

French occupied Talamone. On that occasion, they considered further consolidating the village anda plan for the modernisation of its defences and the construction of two ramparts facing land. However, these plans were not realised. On 15 July, during the retreat, the French army made scorched earth of Talamone, destroying everything they could. The devastation was such that it caused further depopulation and the abandonment of the surrounding countryside, where only the convent of San Bernardino existed, which was suppressed by Pope Innocent X on 22 October 1652.

Like other communities in the Stato dei Presìdi, the population of Talamone could no longer bear and overcome the economic difficulties alone. The local magistrates hypothesised that uniting their resources with those of the more developed and productive village of Orbetello would be beneficial to both sides. On 26 March 1678, mayor Elia Serra presented a request for the aggregation of Talamone to Orbetello at the offices of the Audienza Generale. As the only condition, he asked for the rights and privileges enjoyed by the citizens of Talamone up to that time to be maintained. After a long bureaucratic process, which also involved the Marquis De los Vélez, Viceroy of Naples, the request was granted and put into practice on 6 November. However, from March 1682, the introductory expressions in the minutes of Orbetello's council meetings no longer referred to Talamone, suggesting a separation between the two communities after barely three and a half years. In 1704, a plaque currently walled on the house in Via Garibaldi 1 was engraved in memory of the restoration of the prison by praetor Emanuele Galeano.

During 1709, in the context of the War of the Spanish Succession, soldiers from France and Spain plundered Talamone.

In his brief Report on the Presidios, sent to Naples from Orbetello on 17 January 1736, the Duke of Montemar wrote that Talamone's revenues were only 260 Roman scudi. An insignificant figure compared to the 4,000 Neapolitan ducats collected by the citizens of Orbetello. In the following year's more extensive and detailed report, the Duke of Montemar confirmed Talamone's weak economy, recording that his revenues ranged from 300 to 400 scudi, barely enough to pay the salaries and emoluments of the magistrates, officials and other Community employees. Also in 1737, repairs to the city walls were improvised in fear of Turkish attacks.

In his report of 1739, General Carlos Blom, governor of Orbetello, described the poor demographic and economic conditions of the port of Talamone, which had become chronic. There were only 29 families in the entire area, totalling 102 people, of whom 38 were military personnel. The port was underused, as there were no sailors and the locals did not own their own boats.Grape and wheat harvests were poor, as the fields had been semi-abandoned since the French occupation in 1646 and there were insufficient labourers. The water supply was low, as there were only two cisterns in the town and the nearest spring was three miles away. From a strategic point of view, General Blom also considered the garrison of Talamone to be weak, believing the strengthening of the site's fortifications, proposed on several occasions, to be unjustified. He assumed that fifty soldiers would be sufficient to defend the land from the Moors' landing. In any case, in an attempt to improve socio-economic conditions, General Blom easily granted entry to the Presidio State and citizenship to foreigners, especially those from neighbouring states. Thus, in 1740, the mayor and magistrates of Talamone petitioned the king to grant Corsican immigrants a licence to become citizens of the village.

However, by 1751, Talamone's defences were in ruins. In 1782, the Abbé de Saint-Non gave an account of the state of misery and abandonment of the town, later confirmed by Peter Leopold's report drawn up in 1787, in which he described the port as an unhealthy and dilapidated place, inhabited by 400 healthy people and 10 invalids, infested by bandits and fugitives.

On 22 November 1801, the Presidio State was united to the Kingdom of Etruria and its conditions were documented by Filippo Giannetti in a report written that same year.

With the Congress of Vienna, in 1815 the Stato dei Presìdi passed to the Grand Duchy of Tuscany and with it, of course, also Orbetello and Talamone Under the rule of the Habsburg-Lorraine of Tuscany, the village was subject to various interventions: in 1816 the Fortress and the City Walls were restored and a sentry box was built at the battery of Sant'Antonio, which was located near the port; in 1820 the main gate of the Fortress was rebuilt and the rebuilding of the Via Aurelia was begun (work completed in 1831); in 1824, further work was carried out on the Fortress and the surveyor Luigi Baglini registered the town in the Catasto Leopoldino; in 1826, further work was carried out on the Fortress and on the guardhouse at the town gate; a gate was rebuilt at the entrance to the town in 1827.

From 1828 onwards, Talamone was affected by other works, especially on the Fortress: that same year a platform was built at the entrance to the Keep; this was followed by work on the prison and the cistern in 1833; in 1838 work was carried out on the Keep tower. Between 1839 and 1842, another building site was opened at the borough. Thanks to these interventions, the Fortress was still in service when Giuseppe Garibaldi landed at Talamone with the 'Mille' on 7 May 1860. In 1861, the Grosseto-Orbetello railway line was completed and with it the Talamone railway station.

In 1877, excavations on the Talamonaccio hill by Marquis Carlo Strozzi and Francesco Vivarelli, the owner of the estate, brought to light various finds. Among the finds near the tower were those constituting the so-called 'Ripostiglio Strozzi'. Between 1887 and 1892, construction work for a military complex was carried out on the Talamonaccio hillock. Among the planned buildings were a barracks, a powder magazine and some warehouses. During the work, numerous finds, remains of tombs and a complex of small bronze reproductions of weapons and working tools were discovered, forming the 'Ripostiglio del Genio Militare' (Military Engineers' Storehouse). In addition, a cistern with the first group of clay fragments from the pediment of the temple of Talamonaccio came to light. During the works, the Torre Vecchia was destroyed. In September 1888, the archaeological discoveries attracted the commissioner for the monuments of Etruria and Umbria, Gian Francesco Gamurrini, to visit.

In 1893, the Ministry of Agriculture published a call for tenders to promote reclamation and agricultural development works in the Maremma. Knight Jader Vivarelli presented the project to reclaim the San Giuseppe estate, which was approved. In the same year, the reclamation of the vast Talamone marsh began. In 1898, Cavaliere Vivarelli drew up a progress report on the reclamation. Knight Vivarelli died in 1904 and his remains were transferred to the homonymous mausoleum built by architect Lorenzo Porciatti in 1906, in the Talamone cemetery.

Work on the reclamation continued after his death, and in 1907, during excavations for the construction of a collector to the north of the hill of Bengodi, an ancient fountain with an aqueduct was found. Between 1915 and 1916, the western collector was extended and levelled. During the construction of a waterworks to the north of the Bengodi hill, artefacts dating back to the 6th-5th century B.C. were discovered, probably connected to the ancient port. The reclamation works were completed in the 1930s.

In the wartime context of the Second World War, the port of Talamone was bombed by the Americans on 13 March 1944. In May of the same year, German soldiers systematically destroyed almost all the buildings in Talamone, except the Fortress and the City Walls. Post-war reconstruction largely respected the ancient street alignments, but the small church of Santa Croce was not rebuilt.

Between 1962 and 1969further excavation campaigns were carried out on the hillock of Talamonaccio, which made it possible to survey the layout of the temple and reconstruct its fictile pediment with greater accuracy. Between 1971 and 1981, the Fortress di Talamone passed from the heritage of the Ministry of Finance to that of the Ministry of Education and was restored[1].

8.2 Main buildings

We now present notes on the main artefacts that have been part of Talamone's urban layout throughout its existence.

8.2.1 The original Sienese project

In the contents of the plan of the Black Kaleffo, hypothetically datable between late 1304 and early 1305, no reference is made to pre-existing buildings and all buildings and spaces are treated equally. It is therefore impossible to establish with certainty what the layout of the earlier fortified settlement was. The only conceivable conjecture is that the sector of empty lots delimited by four parallel streets and comprised between the church square and the fortress derived from an earlier residential area, dilapidated and arranged in terraces as in the nearby port centre of Castiglione alla Pescaia. However, this block of lots depicted in the drawing is not reflected in the realisation.

There are considerable differences between the plan and the realised layout, which can be summed up in the insertion of the axis between the church and the fortress on the line of the fourth row of houses, starting from the gate. This resulted in the elimination of this row, also taking into account the squares. The first assignment of the lots must have been prior

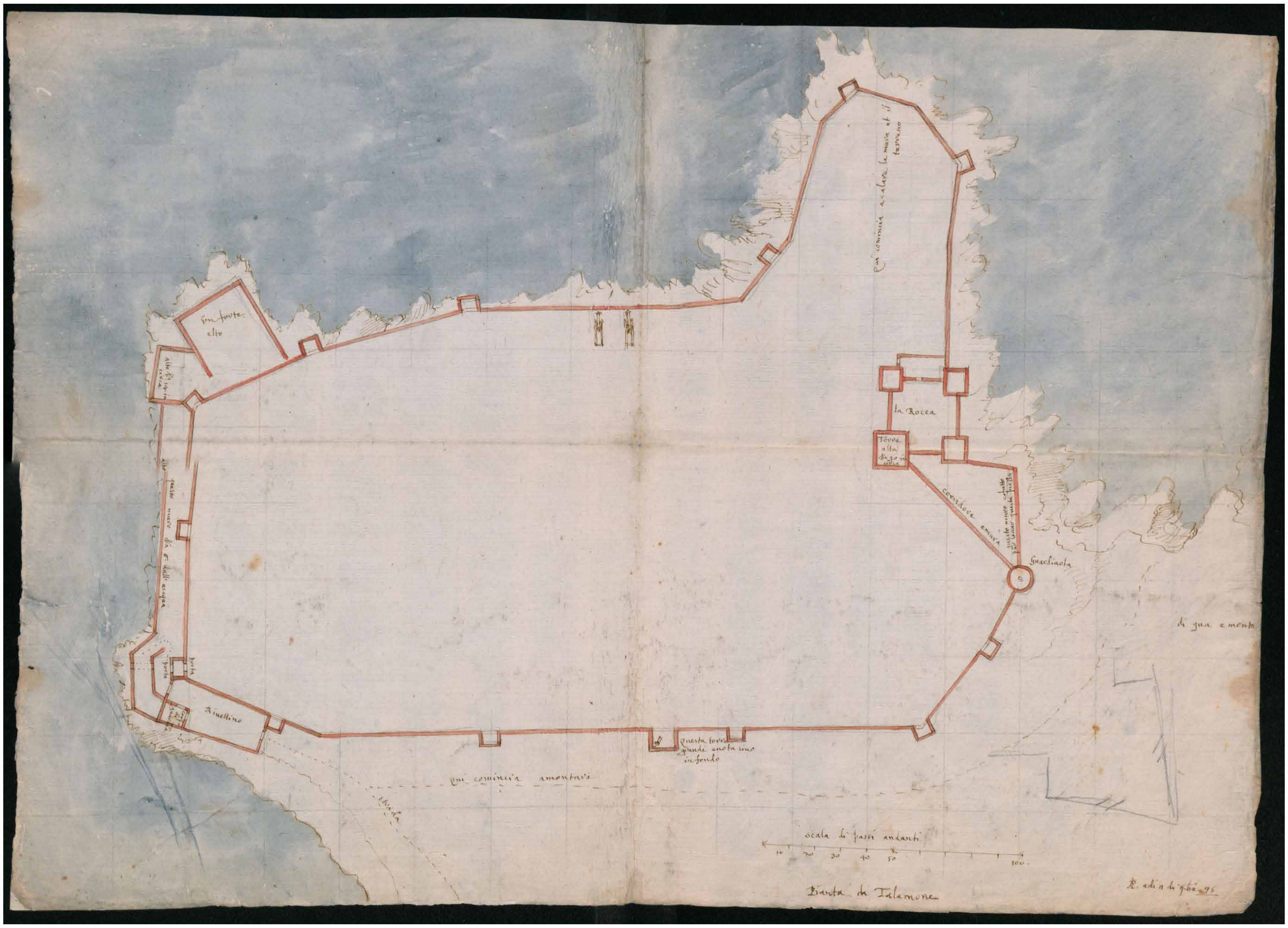

8.4/ Pianta di Talamone (Map of Talamone). Dating: 8th of September 1595. Archivio di Stato di Firenze (Florence State Archives). Archival collection: ASFi, Miscellanea Medicea, 93/III. Catalogue ID #16193. Su concessione del Ministero della cultura / Archivio di Stato di Firenze (by courtesy of the Italian Ministry of Culture / Florence State Archives).

to the start of work on the church and, given the alignment between the two main buildings and the spatial incompatibility between the last assigned lots - marked with the numbers 48 and 49 - and the Keep, probably also prior to the building site of the Fortress itself. In fact, lot 49 is even partially encroached upon by the Keep. This last observation would rule out the possibility that the present Fortress predates the Sienese project and provides a reason for the 'correction' of the layout proposed in a resolution of the Municipality on 19 March 1306. However, the dating of the original nucleus of the Keep is still controversial today and considered only addressable with appropriate archaeological investigations.

It can be deduced from the expenditure registers, outgoings and various provisions of the Republic that a fortress already existed in the area of Talamone before it was purchased by the Sienese Discordant conjectures have been made on the location of the fortress and port before the Sienese project.
Enrico Guidoni and Laura Pieroni, for instance, argue that the Aldobrandesque fortress was located in a hypothetical area that can be defined as Talamone Vecchio, situated in the north-west part of the bay, where the remains of the Roman villa are still presentthe disappeared walls of Talamone Vecchio, defined as 'Murum de civitatis', would therefore correspond in some ancient ruins such as the 'cantina sub justa volta de

Talamone' (later named in the land register of 1430) and other remains indicated as muros. This conjecture is also supported by the fact that the castrum of the Sienese project could never have been called civitas. In addition, the hypothesis would motivate the collection of stones organised in 1357 at an imprecisely identified set of walls in the area of Talamone, which would be absurd if referred to the walls of the present village, still to be fortified and restored, but perfectly consistent if referred instead to the recovery of building materials from the Talamone Vecchio remains. These ruins would therefore correspond to the port that was the subject of the contract between the Commune of Florence and Guglielmo Aldobrandeschi, stipulated in 1251, in which the count undertook to make the port functional and safe by constructing buildings and fortifications, later only partially realised. This hypothetical location of the pre-existing fortress would call into question the exact location of the Aldobrandeschi port, no longer corresponding to the site of today's port of Talamone but to the Roman landing place of Santa Francesca.

For Astorre Baglioni, however, the original keep and harbour were located in the same area where the Sienese fortress and harbour were built. The original keep would even date back to the Longobard period, only to become the object of frequent renovations and interventions ex novo throughout history.

According to the archaeologist Otto Wilhelm von Vacano, however, the Aldobrandesque fortress stood instead of the present one and the port of call was located to the northwest of it, in the Baia delle Donne. This conjecture takes into account the tower building that, in the plan of the Sienese project included in the Black Kaleffo, was planned in front of the north-western curve of the city walls. This was a slender tower with a circular plan, a forepart to perhaps house a spiral staircase. This vertical connecting element would have connected the plane of the base of the walls and the western edge of the cliff, located at a higher level, on which the settlement and the fortress actually stand. It would therefore have been a shortcut or escape gate to the sea or even to the Monti dell'Uccellina, ideally completing the Sienese 'canon' that normally provided for the construction of three gates for each urban centre. Despite the presence of its remains on the site, there is no trace of this artefact in documents, except in the cadastral registration of 1824, in the reinforced form already given to it by Antonio Parmigiano. The building, which has partially disappeared, was located outside the fortifications, protected at the back by the walls and the cliff sloping down towards the bay, facing a defence wall of its own with two projecting corner towers, which connects the cliff to the walled enclosure of the present-day village, thus forming a large convex arch. According to Von Vacano, these fortification works predate the Sienese project. The German archaeologist goes further and hypothesises that the section of the walled enclosure between the port and Baia delle Donne plus, perhaps, another small section beyond the sea gate, could be the walls of theslipway in poor condition mentioned in the 1251 contract. As appears in the plan of the Sienese project, therefore, the antemurale of the lower fortress would have been connected to the walls from the beginning. With the construction of the Sienese Keep, the Aldobrandesque one would have lost its function and would have been destroyed, probably to reuse the building materials. According to this hypothesis, therefore, no relocation took place, but if the upper fortress had been built before the arrival of the Sienese, the lower fortress and its relationship with the former would again have to be questioned. The Aldobrandesque keep would correspond to the Upper Fortress and the Lower Fortress would be a fortification to defend the small harbour that was probably located in the Baia delle Donne.

In any case, it is certain that the Republic of Siena did not abandon the Aldobrandeschi harbour but expanded it with ambitious projects and large investments of resources Written sources tend to validate Von Vacano's hypothesis since, at the Council of the Campana meeting of 8 December 1303, it was decided to proceed with the enlargement of Talamone, to strengthen the pre-existing harbour walls and erect new ones, as well as to subject the old fortress to a complete overhaul.

Another town-planning variation, introduced after the drafting of the Black Kaleffo plan, was determined by the secondary route connecting the church and the primary transversal road, which connects the port gate with the minor fortress. This secondary route still has the function of facilitating access from the port to the village's main square, where, in addition to the church, the municipal house was also built. This route could be dated to 1306, the year the final layout was built.

As pointed out by Guidoni and Pieroni, notwithstanding the poor environmental conditions, particularly those of a geotechnical nature, it is sufficiently clear that the Sienese did not intend to build oversized works detached from the reality of the time, but rather a port centre of modest dimensions but well protected. The functionality and defensive characteristics of the settlement of Talamone are very similar to those of the port of Castiglione della Pescaia, which belonged to the Pisan political sphere. Evidently, both port centres should also have exercised a surveillance role of the new maritime border between the two Republics[2].

8.2.2 The Fortress

As already stated, the Fortress in its complete form is datable to a period subsequent to the Black Kaleffo plan, since it occupies an area in the design already parcelled out or in any case not planned for its new destination. To this consideration one must add that the buffer area around the Keep could not reasonably have been less than 50-60 feet, or 15-20 m.

The analysis of the architectural layout and the metrological characteristics show a singular clarity of layout, a remarkable geometric rationality for the time of design and a perfect coherence between the parts. Therefore, the artefact is the result of a very accurate design and an agile and controlled execution of works in every part. The fortress is quadrilateral with angular towers and its layout is typically medieval, while its structure is made of stone with vertically oriented facings.

Therectangular plan can be inserted into a grid of squares, which constitutes a metrological guide for various geometric characteristics of the artefact: the main walls; the corner towers; the thickness of the walls; the dimensions of the courtyard. The sides of the basic square module yield measurements of 2 × 2 feet - 60 cm - or square arm. In effect, however, the design is governed by a double module, thus corresponding to a square of approximately 120 × 120 cm, i.e. with one side measuring one 'passetto' (Italian unit of measurement prior to the metric system). The main tower on the northern corner corresponds perfectly to the module but, compared to the rest of the building, is offset by half a module - 2 feet - in both directions. This is due to several needs: to contain the inward projection of its masonry, which is much less in the other three corner towers due to the notching; to symmetrically balance its sides inserted in the curtain walls; to allow for a greater outward projection of its masonry, further reinforced by the prominence of the basement. These necessities are obviously a consequence of its greater size compared to the other towers, corresponding to two modules (i.e. approximately 240 cm) entailing a greater wall thickness (5 feet instead of 4 feet), as well as a greater height already highlighted in the plan of the Black Kaleff. These characteristics are also determined by function, as the main tower had to fulfil refuge tasks that the other shield towers, i.e. open on the inside, could not support.

Some of the rooms on the ground floor were intended for the garrison, while the large inner room served as a storeroom for food reserves and as a war depot. There is a large cistern in the courtyard that ensured a reserve of water, which was especially necessary in cases of siege. In addition, three sides of the courtyard are currently occupied by buildings leaning against the inner walls. At the top of the courtyard, two rounded stone corbels protrude internally, which probably overhung the original entrance to the building.

Compared to the plan, the elevations are much less indicative of the original construction intentions, as they have been subjected to continuous cycles of destruction and rebuilding since the early years of their existence

In the plan of the Black Kaleffo, the fortress is represented with four towers, one of which is the largest, as in the realisation. It faces the keep inland, as it was believed with certainty that the attackers would first occupy the settlement and then attack from there. Chronicles from the 14th and 15th centuries confirm this trend.

The escape gate on Baia delle Donne is depicted as a smaller construction on the western corner of the city walls, symmetrically positioned with respect to the Port Gate and equipped with a very high tower. The drawing of 1304-1305 and the map of 1595 also depict a fortified walkway on the edge of the allotment, corresponding to the wall that still exists today. This walkway or elevated escape corridor probably entered the fortress at the arched gateway located on the northern side of the artefact, flush with themain tower. This path can be interpreted as an important element that has been present since the beginning of the Keep's existence. As we have already mentioned, the Fortress today stands almost on the edge of the overhang, whereas in the project drawing it appears noticeably inside the fortified wall that ran along the edge. Marine erosion and the resulting landslides led to a situation where, at a certain point, the supporting wall of the walkway assumed the role of an external defensive wall. This led to the complete 16th-century restructuring of the defences at the escape gate, which in the drawing by Black Kaleffo appears well protected by the outer antemurale, the one studied by Von Vacano.

The fortress was surrounded on two sides by a second curtain wall, added at a later date than the original Sienese design and of which only the base now remains.

During the rule of the Hapsburg-Lorraine of Tuscany, the Fortress of Talamone underwent numerous interventions. Among the works carried out between 1825 and 1826, a place of convenience placed in the wall of a landing of the gunner's barracks, corresponding to a tile jutting in and out, was removed. Due to noxious fumes, it was replaced with a movable wooden pot, known as a 'pacchè'. Another intervention was the rebuilding of the vault and the window of the refectory, as at that time the rushes were exposed to dust brought by the wind. In 1830, the top of the fireplace in the kitchen, which was located to the left of the entrance to the fortress, had to be restored. The door to the armoury, which was adjacent to the kitchen and corresponded to the room that today faces the courtyard, was also bricked up and whitewashed. Since the 'places of convenience' were insufficient, the idea of using the large underground room, once joined to the cistern room, for this purpose was considered. However, this work was no longer carried out. In 1844, the refectory layout was rebuilt with fortification bricks and the drainage pipe of the water closet was directed into the courtyard sewer. In 1845, although it was claimed that the fortress was in a good state of repair, it was necessary to: plaster the ravelin wall; apply enamel - at the time a mixture of coccio-pesto and pozzolana - in the passages and the adjoining barracks room; plaster and whitewash the cistern; and redo the barracks' brickwork. In 1847, the cistern was cleaned from the summer rains and the quartermaster's quarters were repaired, as it was raining there. Then, in 1849, the roof and the eaves channels were repaired, which were supposed to let the water flow into the cistern.

As already mentioned, the last damage to the Fortress was caused during the retreat of the Germans during World War II, as the garrison was undermined when it was abandoned and the surrounding fortifications almost completely destroyed.

In 1971, the Fortress was reclassified from a barracks of the Guardia della Finanza and State property to a property in the historical-artistic-archaeological branch of the public domain, as it was in need of urgent restoration In addition to being in a poor state of preservation and in a precarious static condition, it had undergone transformations due to its last use, which had altered its characteristics.Therefore, the restorations conducted by the Superintendence for Environmental and Architectural Heritage for the provinces of Siena and Grosseto pursued the following purposes: static consolidation; restoration of the original features in relation to the recent alterations; structural investigation, conservation and usability of the complex. The interventions were divided into five phases: the first between 16 June and 12 October 1972; the second between 18 December 1972 and 25 June 1977; the third between 23 February 1978 and 22 November 1978; the fourth between 10 October 1979 and 7 December 1979; and the fifth between 19 September 1980 and 19 March 1981[3].

8.2.3 The City Walls and the urban layout within them

The planimetric scheme envisaged by the original Sienese project and realised with variations is extremely simple. It was different from the complex compositions of the contemporary Florentine villages, but also from the grandeur of the Sienese town of Paganico. It is a reticular layout contained in a rectangle of approximately 100 × 300 fathoms, thus formed by three square modules, 'enlarged' by the central street axis. In the drawing of the Black Khaleef, this rectangle is surrounded by roads on each side and the strategic area in front of the gate, in reality occupied by dwellings, remains free. The originally planned interior layout should have been totally independent of the defensive works, to which it should have conformed. However, even in its practical realisation it is characterised by a notable archaism in the rows of simple lots arranged on parallel streets, of different widths but the same depth. The only significant variant consists of the lots built along the central axis, almost all of which are rotated so as to have their façade on the street itself, giving it greater hierarchical dignity.

Basically, this is a simplified version of a type of regular layout widely common in 13th-century maritime Tuscany, more precisely in the Lucca and Pisa area. Typically, such a scheme is composed of a main axis and orthogonal streets delimiting the blocks, possibly cut by minor streets and composed of 'double' lots, i.e. houses with access on one side only

and separated by an internal drainage channel. The theoretical common plot is approximately 20 × 40 feet (6 × 12 m), but in Talamone these plots are located between two streets and therefore the width of the blocks is halved. From the earliest phases of construction, in fact, numerous variations are noted, always respecting the units of measurement, as found in most of the new foundations of the 13th-14th centuries. Taking into account these differences in the module, comparisons can be made with Ponsacco, Santa Croce nell'Arno, Castelfranco di Sotto and the new town of Massa Marittima.
Probably, of the 100 houses budgeted by the project - shaped in the name of a colonisation planned by precise policies and pre-calculated in its demographic consistency - only about half were actually built. We had already observed that the fourth row of lots starting from the central gate was sacrificed as early as 1305 in order to gain space for the church and the fortress. It is also probable that the removal of this row is attributable to the difficulties of settlement present from the earliest days of the Sienese settlement.
According to Enrico Guidoni and Laura Pieroni, the Sienese 're-foundation' of Roccalbegna, which began in 1296, would constitute an immediate precedent for Talamone, corresponding to a specific technical-constructive model. The settlement modules and building technique could therefore derive from it. This hypothesis has also been put forward in consideration of the fact that Roccalbegna represents the extreme stronghold of Talamone's hinterland. Situated almost at the summit of the Amiata, at the end of the road to Magliano, Roccalbegna was affected in 1298 by a restructuring of the defences and an urban plan aimed at its repopulation, as a frontier point. On the area between the Keep and the Pietra, a grid layout was imposed with parallel streets, delimiting simple rows of terraced houses, interspersed with cross streets. At the centre of this layout is the square square, dominated by the Church of Saints Peter and Paul. Characteristics of Roccalbegna such as its size, number of inhabitants and monumental conception are directly comparable with those of Talamone, so it is likely that the original plans for both settlements were developed by the same group of town planners and technicians.
For most of its extension, the City Walls can be considered coeval to the Fortress, with the exception of the later-period addition of the irregularly shaped ravelin and the circular keep, a probable remake of a pre-existing structure. This can be deduced from the face with a slightly scarped base, which then continues to the top with a vertical course. The wall circuit is interspersed with towers with a quadrilateral plan, suitable for a flanking defence from the ramparts and piombing from the top of the wall, with short-range white guns.
In the 1304-1305 plan, the double wall on the outside of the most exposed section of the borough, protecting the Port Gate, does not appear. It was evidently built later. The main gate is clearly the central one, which opens onto the longitudinal road and constitutes the axis of symmetry of the design, appearing large and equipped with a scarp. It corresponds to the current Porta Garibaldi, which opens onto a major tower with a base surmounted by a cordon. On this side, the town wall was protected by a moat and it must be assumed that a drawbridge was placed here.
The defensive configuration of the borough, which is elementary, is due to the fact that it predates the spread of firearms and was not particularly adapted to the needs of artillery, with the exception of the modification of the section towards the harbour, where a rampart with muzzle-holes, i.e. cannon emplacements, was built in a later period. On the part of the Sienese ruling class, the re-evaluation of investments that had proved unproductive led to a rethinking of priorities in military architecture. Firearms in fact made the Keep obsolete, which no longer appeared to be successfully defensible or at least capable of guaranteeing the same security as the new fortification techniques. As far as Talamone was concerned, therefore, the Fortress began to be neglected in favour of restoration and modernisation of the outer walls. This technological evolution, however, was the cause of the progressive reduction of the village's strategic role, since its distinctive strong point compared to other military strongholds on the Maremma coast resided precisely in the Keep. Inevitably, therefore, Talamone had to become part of a much larger territorial defence system, such as that of the Republic of Siena at the time of its dominion over Orbetello or that of the State of the Tuscan Presidios. In
fact, very little work was carried out during the existence of the Presidios. After its annexation, it took little time for Talamone to disappear politically and economically within a Presidio State dominated by various European powers, but still ruled by Orbetello, where much more modern and

effective defensive works existed. Given the economic and demographic collapse of the area, there was a progressive degradation of the walls.

With the passage under the rule of the Hapsburg-Lorraine of Tuscany, Talamone was again the object of attention by the authorities. In 1824, it was decided that the ramparts (i.e. the embankments) near the fortress should be paved with rows of stone, as the pre-existing wooden floor did not facilitate the manoeuvre of the cannons, but in 1828 this intervention had not yet been carried out. We do not know where exactly this battery was located, but it was presumably located near the entrance, so that the guns could also be turned inland. In 1825, a new sentry box was built, located at the entrance to the village, on the opposite side of the road from the town wall, in order to guard and possibly barricade access. During 1826, it was found that the wooden gate at the entrance to Talamone, made in 1819, needed to be rebuilt because it was ruined by the passage of cars and carts, so it was decided to make a more durable iron one.

In 1827, it was noted that the walls had been ruined in several places due to the war. The restoration work was entrusted to the architect Giuseppe Ciulli and the Department of the Royal Factories charged the expense to the municipal administration, by virtue of the Motu Proprio of 24 March 1783 (notified on 11 April 1783), according to which the maintenance of the walls was the responsibility of the respective communities as they were considered indispensable elements for the citizenship. The forts, on the other hand, were considered the property of the Regie Fabbriche, as they were necessary for the defence of the State. The disruptions identified on that occasion consisted of: a metre of wall that had collapsed in the area known as Campaniglia, near the Fortress; sections of masonry near what is now Porta Garibaldi; the sections that had collapsed around the Porta Senese, affected by real breaches that allowed brigands to enter at night, as well as in many other places. In addition to these portions of the city walls that needed to be restored, repointed and curled, there was the fact that the military guard at the garrison gate was exposed to falling graves due to the obsolescence of the limestone. In 1828, repairs were made to the masonry at the guardhouse at the entrance to Talamone and the pipes of the cistern were redone. In 1831, work was carried out to rebuild a section of retaining wall under the harbour battery, where two stone platforms were placed. A gate was also installed to separate this place from the public square. In 1840, the cantonment of one of the towers on the falsabraca section (i.e. the outer and lower doubling of the walls) was reported as unsafe. In 1841, the fixtures of an unspecified vault used as a shelter for artillery shafts were rebuilt. It was speculated that it might have been an element of the large fondaco del borgo or one of the masonry vaulted structures near the troniera north of the Fortress, which still exist.

During the most recent restoration work, carried out by the Soprintendenza per i Beni Ambientali e Architettonici for the provinces of Siena and Grosseto between 1994 and 2001,the poor stability of the ground, which Baldassarre Peruzzi had denounced at the time, was once again discovered. In order to secure the City Walls on the sides facing the sea, cantilevered structures were put in place to release the septa from the rock below, requiring the intervention of the Grosseto Fire Brigade.

Another intervention concerned the 14th-century wall structure in the port area, which was founded on stable ground but had instabilities caused by neglect and much tampering. Moreover,in the 16th century, the structure had been filled with earth to adapt the wall to the evolution of military art, as indicated by the presence of archers and arquebusiers in the lower part and cannon emplacements in the upper part. During the restoration, micropilling and additions of stone material were carried out at the points that required it, in order to restore consistency to the masonry. The various openings were highlighted without annulling the evolution of the architectural organism over the centuries, i.e. without removing the earth. The surface finish of the artefact was executed with a mortar mix of lime and coarse aggregates, studying the composition of the original.

Another area of intervention was on the section beginning where the access called Porta di Santa Lucia or Porta Senese originally existed. The cause of the septum's disruption was precisely the loss of the original continuity, so the Superintendence intervened by means of core drilling, inserting metal bars and mortar pours inside, and then adding stone material where necessary. During the surface finishing operation, the Superintendency had the original part differentiated from the elevation of a later period. The latter, built with smaller and less polished material, was left completely covered by plaster.

During the restoration, lightning rods were installed, complying with the relevant regulations and especially in view of the location of the artefacts on the coast.The round tower, which had already partly collapsed in 1967, is currently turned outwards. Unfortunately, today's heavy tampering of the curtain wall by private individuals compromises the legibility of the whole[4].

8.2.4 The fondaco

The building, now destroyed, is mentioned in official documents as a fondaco, as a building or as a fondaco in the archival sources relating to the work of 1357 and as a warehouse in the cadastre of 1824. It also appears explicitly in the 1430 cadastre and in the 18th century survey. This grandiose construction stood internally on about half of the eastern straight stretch of the wall. It consisted of a single chamber about 20 fathoms wide (similar width to that of the church) and with an average length of about 70 fathoms, as it had its back side sloping at the corner of the walls, defended by a tower. The chamber was divided into nine bays by eight round arches and was only about 12 fathoms high. Being so low, the fondaco was totally invisible from the sea, since it was hidden by the city walls and overlooked by the rear 'granary' building, with which it was probably in direct communication.

In any case, both the written cadastre of 1430 and the 18th-century survey describe the fondaco as part of a larger and more complex building complex, including: a large three-storey communal building towards the Porta del Porto; a narrow wing towards the interior, also three storeys high and useful for counteracting the thrust of the fondaco's arches; a cistern; and a system of external fortifications, probably identifiable with the Torre di Santa Lucia Thus, the architectural organism was not only a warehouse but also a fortification, a granary and a palace for the residence of the 'fondacaro' and other Sienese officials.

Probably the entire complex, while taking into account constraints and pre-existing features such as the gate, walls and cemetery, was built ex novo before 1357 and then underwent partial renovations in that year. Documents show that it was built in a great hurry, with a major investment of materials and economic and human resources. Numerous movements of technicians and workers with Siena are recorded, as well as a large movement of timber and bricks from Paganico, Magliano and Collecchio, as well as stones recovered and processed from the archaeological ruins of Marta (Talamonaccio) and Talamone Vecchio.

According to the text of the trade agreement drawn up on 28 March 1379 between the Republic of Siena and a colony of Catalans for the use of the port of Talamone, it appears that even then the fondaco was in a very poor condition, and had been stripped of its fixtures and roofing, probably due to looting and abandonment[5].

8.2.5 The Church of Santa Maria Assunta

The original place of worship, built in the location provided by the Black Kaleffo plan, was mostly destroyed during the Second World War. The remains have deeply affected the appearance of today's church, which has been almost completely rebuilt. Only the bell tower could probably preserve part of the historical fabric.

Most of the buildings in the old town centre were demolished during the war and then badly rebuilt. Buildings showing simple local typological features throughout history are few and small[6].

8.2.6 The Board of Health and the wharf

In the 19th century the Sanitary Officers, in addition to the task of safeguarding public health in times of epidemic emergency, exercised control over goods and correspondence, and were therefore stationed in all maritime ports.

In 1837, there was a need to expand the Talamone Sanitary Office, located near the Fortino di Sant'Antonio, near the port. The extension, which was unrealised, should have included: a room for the Deputy; a parlour; a small room to perfume the papers, i.e. to subject them to sanitary inspection and treatment by placing them on a gridiron with embers; a room for the guard. Although unrealised, the project to extend the Sanitary Office later had further developments.

In the meantime, the pier was extended, because lances, even the smallest ones, could not approach it. A sentry box was also built for the harbour guard post and iron bells were placed for the ships.

In 1838, a fireplace was built in the guard room of the existing Health Office. In addition, the pole for the Royal Coat of Arms was placed on the building, the quay was paved and benches were placed.

An 1846 correspondence shows that a small fort, complete with chapel, existed on the port of Talamone, a short distance from the now demolished Porta di Santa Lucia. That place was designated as the site for the new Ufficio di Sanità, which had not yet been built in the 1837 project. The new project included the demolition of the blockhouse and the anti-port to recover the stone materials and make room for the square. Next to the space occupied by the anti-port would have been built the 'contumacious room' (i.e. the quarantine room) and, above this, the observation square. In this version of the project, the new Sanitary Office included: a parlour; an office for the Sanitary Deputy; a room for the scenting of papers; a room for the guards and the offices of the Merchant Marine, which were to be located above the old chapel and above the old guardhouse. An annotation suggests that the piers under the pier would have been of ancient origin. The old chapel had a bell tower, perhaps a sail-shaped one, built alongside the gate battery, which had two platforms. The bell was used both to signal the arrival of a vessel in the harbour and to wake up the troops. Evidently, this project was not realised either, because the present bastion rebuilt after the wartime destruction occupies the place of the Fortino di Sant'Antonio and follows its course[7].

8.2.7 Water supply works

The water supply improved considerably under the rule of the Habsburg-Lorraine of Tuscany. In 1836, repairs were made to the San Bernardino spring. In 1837, the need to supply boats with drinking water was recognised, and therefore various solutions were examined. The San Bernardino Fountain contained little water, so the idea was to resort to the Fonte Lunga, near the port. It had two very rich springs that could be suitably channelled. It was also considered to restore the ancient cistern under the town square[8].

8.3 Summary of data collected through remote sensing and databases

With regard to the Talamone site, we collected the following data from remote sensing:

- the Digital Terrain Model (DTM) of tablet C42541112_0202 of the Extraordinary Plan for Environmental Remote Sensing 2009 (PST-A 2009), taken from an aircraft-mounted LIDAR sensor;
- the point cloud of tablet C42541112_0202 of the 2009 Extraordinary Environmental Remote Sensing Plan (PST-A 2009), obtained from an aircraft-mounted LIDAR sensor;
- the tomographic point cloud processed by IREA-CNR on the basis of the 160 COSMO-SkyMed products and the NASADEM Digital Terrain Model (DEM);
- the tomographic point cloud processed by IREA-CNR on the basis of the 160 COSMO-SkyMed products and the TanDEM-X DEM.

In addition, we downloaded sheet 31905 of the 1:2000 Regional Technical Map of Tuscany, drawn up in 1987, in both .tiff and .dxf format, in order to use it as a cartographic basis for updating.

8.4 Report on in situ survey campaigns

The following is a report on the in situ survey campaigns carried out for the Fortress and the Talamone City Walls.

8.4.1 First Approaches to the Case Study and Preliminary Site Survey

In March and April 2022 we collected bibliographic sources on Talamone and its Fortress in order to form an initial picture of the site's environmental characteristics and built heritage, as well as to set up a first draft of the survey strategies to be adopted. This also made it possible to plan a preliminary survey coordinated with that of Porto Santo Stefano. Both surveys were in fact carried out on 8 May 2022.

The inspection in Talamone took place from 9.30 a.m. to 12.30 p.m. and mainly concerned the sides of the City Walls on the harbour (southern side), Via Cala di Forno (eastern side), under Via dei Mille (western side), the Fortress, Via della Fortezza and Piazza Garibaldi. During the survey, we acquired photographic documentation with a Canon PowerShot G9 compact digital camera, focusing in particular on Via Cala di Forno and the Fortress. The original 12 MP digital stills have dimensions 4000 ×3000 px and were taken with: focal length of 7.40 mm; ISO 80; capture speed 1/800 s; aperture of f/4.0.

Subsequently, in May 2022, a comparison was made between the following records:

- photographic material from the Gori Archive, in particular a photo of the Fortress taken in 1952 from the nor-

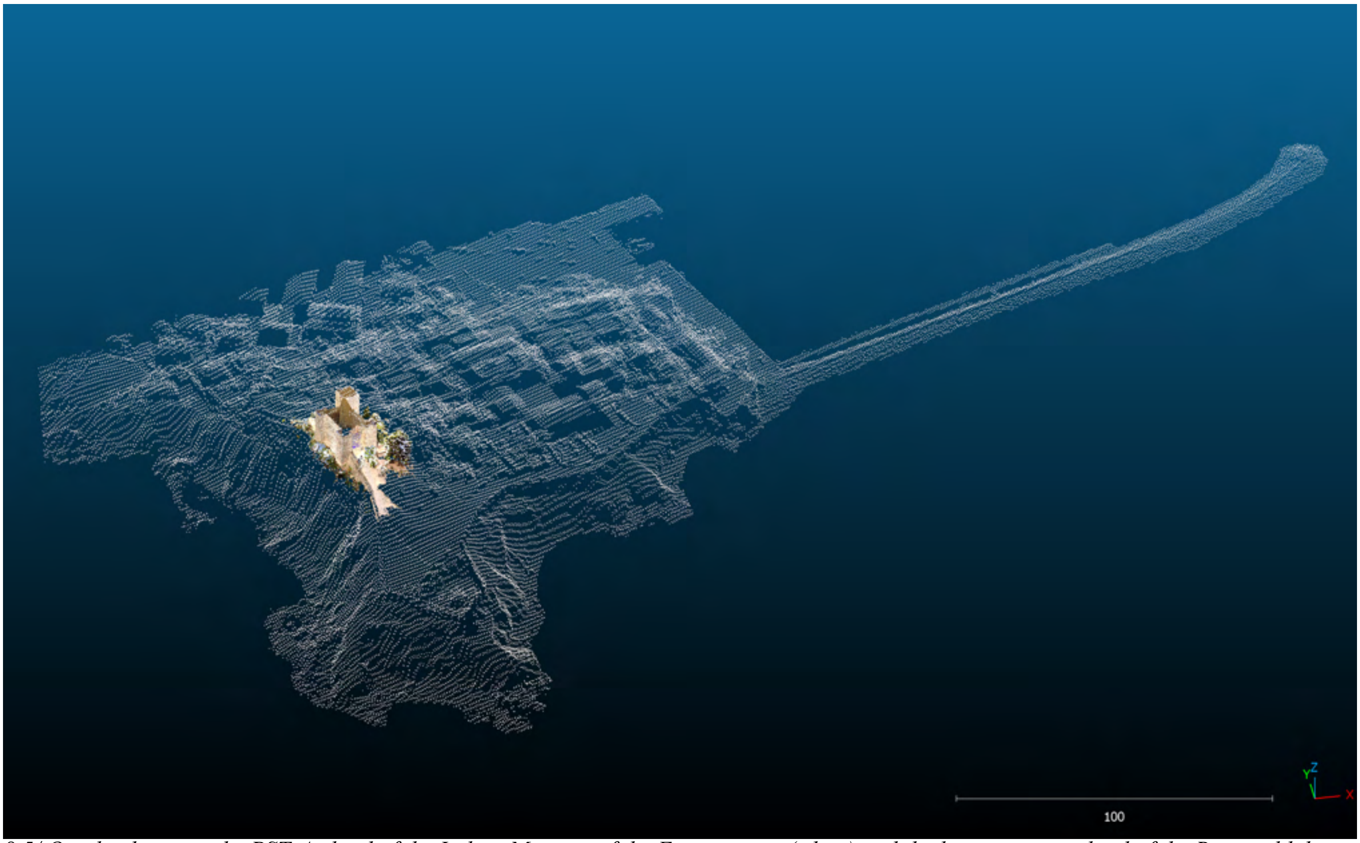

8.5/ Overlay between the PST-A cloud of the Italian Ministry of the Environment (white) and the laser scanner cloud of the Rocca aldobrandesca (coloured). Source: Ministero dell'Ambiente e dell'Energia – Italian Ministry of Environment and Energy / licensed under CC BY-SA 3.0 IT (https://creativecommons.org/licenses/by/3.0/it/deed.it) / Creative Commons – Attribuzione - Condividi allo stesso modo Italia (CC BY-SA 3.0 IT).

th-west, framing the overhang over the Baia delle Donne;
- Sheet 31905 of the 1:2000 Regional Technical Map of Tuscany, drawn up in 1987;
- satellite photographs available via Geographic Information System (GIS);
- the photographic material we took in situ on 8 May 2022.

From the comparison, the erosion phenomenon repeatedly reported over the centuries and already mentioned several times in this Chapter was evident, and was also confirmed by the addition of a steel parapet in recent years for safety reasons. The area where erosion is most easily detectable is at the base of the western side of the Fortress, having been significantly reduced compared to what is indicated on the Regional Technical Map. This poses a serious risk to the integrity of the artefact in the medium term.

8.4.2 Laser scanner survey campaign

The FARO Focus M70 3D laser scanner survey campaign took place on 19 September 2022, from 14:00 to 17:00. It covered the exterior of the fortress, collecting a total of 8 scans (approximately one for each side and each corner, so that they could be aligned as easily as possible), saved in the device's native file format (.fls).

The device was able to scan almost all the sides of the artefact, except for the upper corners of the crowns of towers and septa, which are difficult to reach by the sensor's laser beam. The instrument used is without Global Positioning System (GPS) tracking.

8.7/ Point cloud of Talamone Fortress, generated by eight laser scanner acquisitions.

8.4.3 Survey campaigns with video cameras mounted on drones

The planning of instrumented surveying with Unmanned Aerial Systems (UAS) equipped with video cameras required the study of the relevant international and national regulations, in particular:

- the Commission Delegated Regulation (EU) 2019/945 of 12 March 2019 on unmanned aircraft systems and on third-country operators of unmanned aircraft systems;
- the Commission Implementing Regulation (EU) 2019/947 of 24 May 2019 on the rules and procedures for the operation of unmanned aircraft (Text with EEA relevance.);
- the 1a Edition of the UAS-IT Regulations, published on 04/01/2021 by Disposition DG 01/2021 of the Italian Civil Aviation Authority (Ente Nazionale per l'Aviazione Civile - ENAC);
- Circular ATM-09 (Air Traffic Management Series) dated 24/05/2019 "Remotely piloted aircraft. Criteria for the use of airspace' by ENAC.

The Open Sub A1/A3 category drone
licence, obtained on 28 May 2023, was necessary in order to respect the privacy of persons not involved in surveying operations and for proper planning of campaigns, in compliance with the relevant regulations.

The instrumental survey with drones equipped with video cameras mounted on directional gimbals was planned with the aim of shooting video footage, from which photograms were then extracted for use in a Structure from Motion (SfM) photomodelling process.

8.8/ Fleet of drones (a Mavic DJ Mini Pro 2 and a Mavic DJ Mini Pro 3) with cameras for the survey of Talamone Town Walls by means of Structure from Motion photomodelling.

8.9/ Mavic DJ Mini Pro 3 drone in flight, while recording a video of Talamone Fortress North facade.

The fleet of drones used consisted of two UAS: a Mavic Dj Mini Pro 2 and a Mavic Dj Mini Pro 3. Both Unmanned Aerial Vehicles (UAVs) have a mass of less than 249 g respectively and therefore fall into the Open A1/A3 category, according to the classification of the European Union Aviation Safety Agency (EASA). As far as the cameras of the two instruments are concerned, their data are briefly outlined below:

- The sensor of the Mavic Dj Mini Pro 2 is a 1/2.3" CMOS of 12 MP effective, with 4K resolution (3840 × 2160 px) and recording format to .mp4 files;

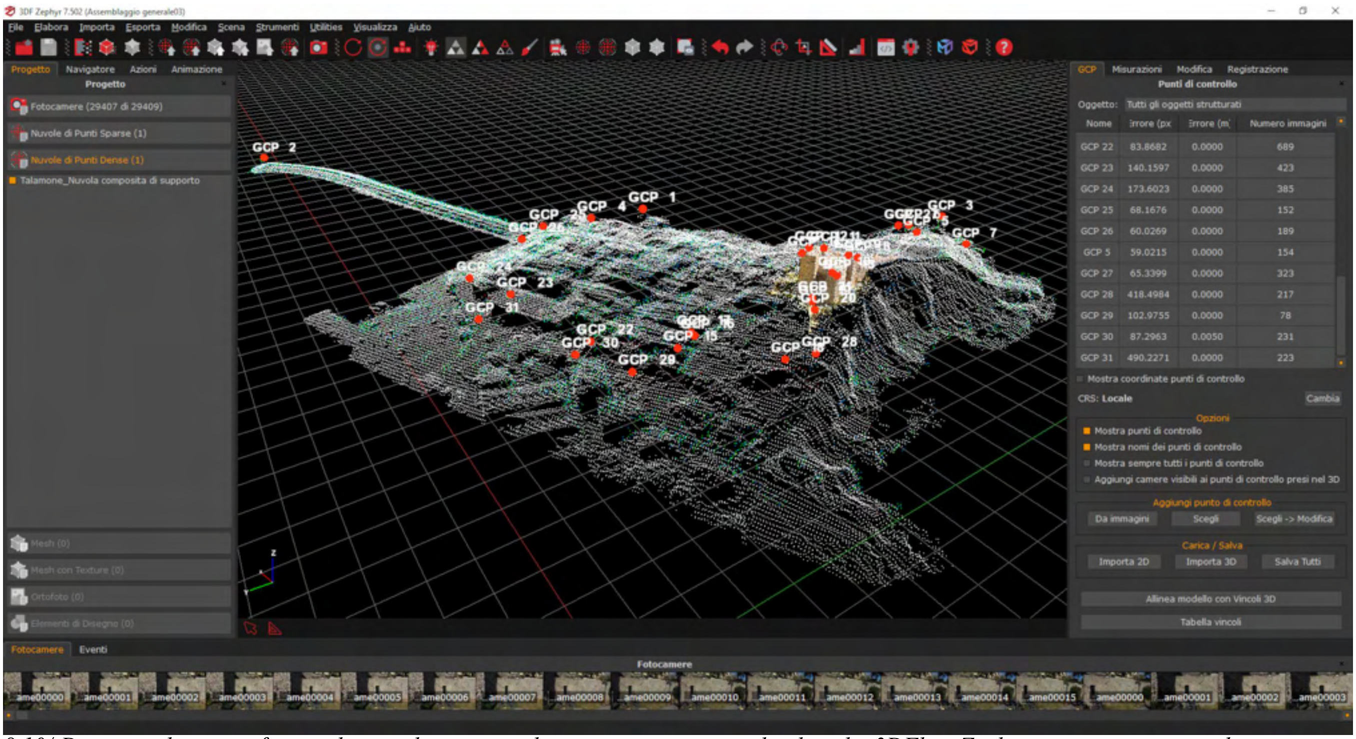

8.10/ Direct application of ground control points on the composite support cloud in the 3DFlow Zephyr environment, in order to correct and optimise the alignment of the cameras calculated by the programme from each clip. Source: Agenzia Spaziale Italiana, 2022. Products processed by Luca Martelli, Diego Reale, and Simona Verde under a license of the Italian Space Agency (ASI); Original COSMO-SkyMed Products - ©ASI - (2012-2017); Deutsches Zentrum für Luft- und Raumfahrt e.V., 2006. © DLR <2023>. Ministero dell'Ambiente e dell'Energia – Italian Ministry of Environment and Energy / licensed under CC BY-SA 3.0 IT (https://creativecommons.org/licenses/by/3.0/it/deed.it) / Creative Commons – Attribuzione - Condividi allo stesso modo Italia (CC BY-SA 3.0 IT).

- The sensor of the Mavic Dj Mini Pro 3 is a 1/1.3-inch CMOS with 48 MP effective resolution, 4K resolution (3840 × 2160 px) and .mp4 file recording format.

The first filming campaign (constituting the DA Series) was carried out on 12 April 2023 from 9:00 a.m. to 6:00 p.m., in relatively good weather conditions, but with difficulties caused by the strong wind on the coast. On that occasion we used both drones of the fleet to record footage of the following areas:

- the southern sides of the city walls from the pier to the park near the lighthouse, along the Viale dei Mille;
- the western sides of the city walls from the park near the lighthouse to the trunk north of the fortress;
- the fortress, especially from the south, west and north sides and from above.

The second filming campaign (constituting the DB Series) was conducted on 13 April 2023 from 09:00 to 11:00, again in acceptable weather conditions, but with strong currents near the coast. Also on this occasion, we used both drones of the fleet to record videos of the following areas:

- the section of the city walls behind the round tower, facing the Baia delle Donne;
- the northern sides of the city walls from above and from the north side of the fortress to the pier along Via Cala di Forno.

The third filming campaign (constituting the DC Series) took place on 17 May 2023 from 9.30 am to 4 pm. The weather conditions were unstable but there was less wind than on previous occasions. At the same time, a topographic survey with a total station was also carried out. On this occasion, only the Mavic Dj Mini Pro 3 drone could be used to film the following areas:

8.10/ Dense cloud of Talamone Town Walls and the Aldobrandeschi Fortress, obtained by means of Structure from Motion photomodelling in the 3DFlow Zephyr environment and superimposed on the supporting composite cloud. The composite cloud consists of: the laser scanner cloud of the Rocca aldobrandesca (coloured); the PST-A cloud of the Italian Ministry of the Environment (white); the tomographic cloud with NASADEM data (yellow); the tomographic cloud with TanDEM-X data (magenta); the topographic cloud obtained through Total Station (red). Source: Agenzia Spaziale Italiana, 2022. Products processed by Luca Martelli, Diego Reale, and Simona Verde under a license of the Italian Space Agency (ASI); Original COSMO-SkyMed Products - ©ASI - (2012-2017); Deutsches Zentrum für Luft- und Raumfahrt e.V., 2006. © DLR <2023>. Ministero dell'Ambiente e dell'Energia – Italian Ministry of Environment and Energy / licensed under CC BY-SA 3.0 IT (https://creativecommons.org/licenses/by/3.0/it/deed.it) / Creative Commons – Attribuzione - Condividi allo stesso modo Italia (CC BY-SA 3.0 IT).

- the lighthouse area south of the fortress;
- the eastern side of the fortress;
- the walkway from the north side of the fortress to the troniera;
- some northern sections of the city walls along Via Cala di Forno;
- the eastern section of the city walls, on the harbour.

The fourth filming campaign (constituting the DD Series) was carried out on 7 June 2023 from 9.30 a.m. to 1 p.m., in stable weather conditions and with less wind than the first two times. On that occasion, we used both drones of the fleet to shoot supplementary footage for the following areas, which had already been filmed previously:

- the lighthouse area south of the fortress;
- some northern sections of the city walls along Via Cala di Forno.

Although both UAS are equipped with a built-in GPS instrument, it is not sufficient to reconstruct the exact position of the camera's viewpoint at the time of filming, as it only serves the purpose of aerial navigation and positioning of the UAV.

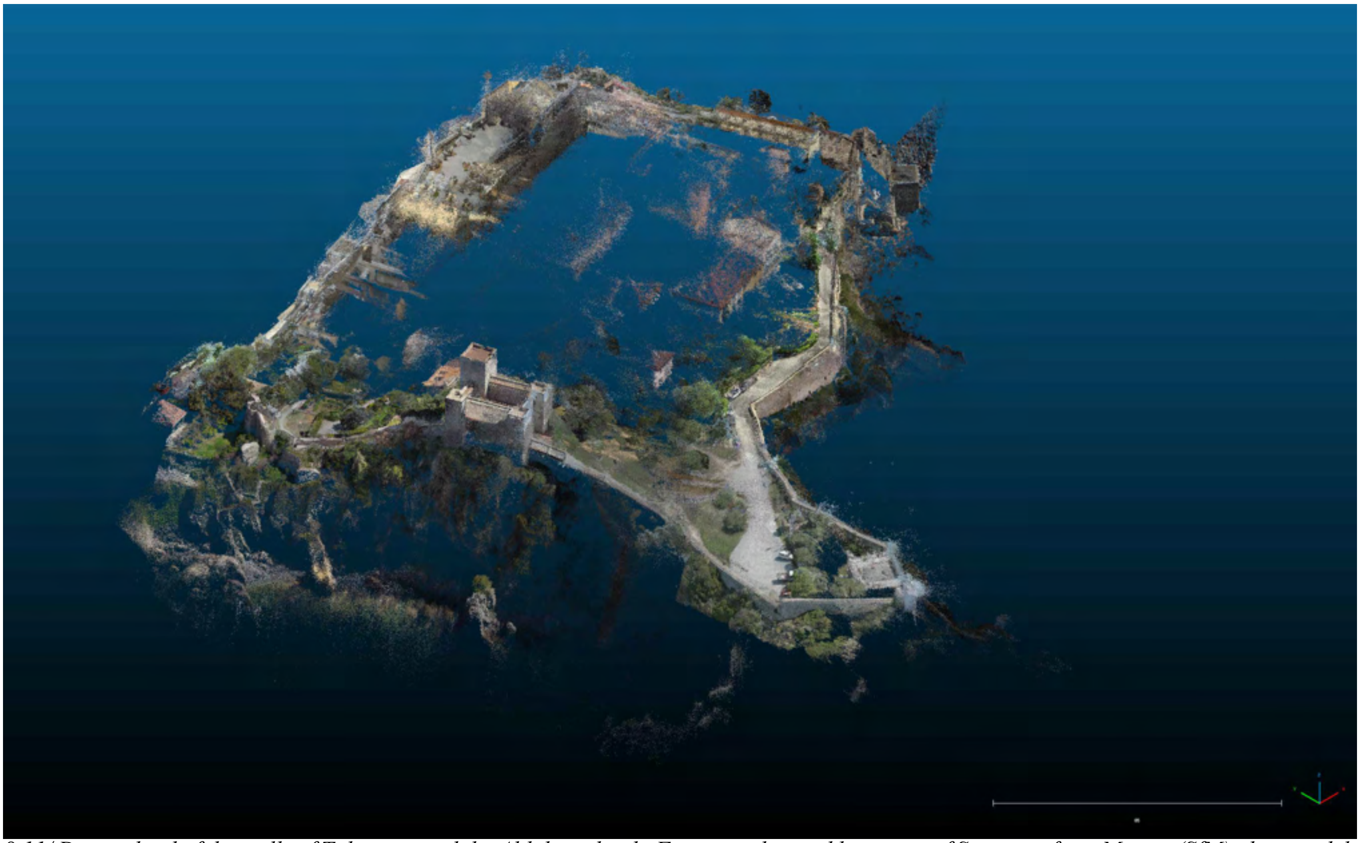

8.11/ Dense cloud of the walls of Talamone and the Aldobrandeschi Fortress, obtained by means of Structure from Motion (SfM) photomodelling in 3DFlow Zephyr environment. Source: Agenzia Spaziale Italiana, 2022. Products processed by Luca Martelli, Diego Reale, and Simona Verde under a license of the Italian Space Agency (ASI); Original COSMO-SkyMed Products - ©ASI - (2012-2017); Deutsches Zentrum für Luft- und Raumfahrt e.V., 2006. © DLR <2023>. Ministero dell'Ambiente e dell'Energia – Italian Ministry of Environment and Energy / licensed under CC BY-SA 3.0 IT (https://creativecommons.org/licenses/by/3.0/it/deed.it) / Creative Commons – Attribuzione - Condividi allo stesso modo Italia (CC BY-SA 3.0 IT).

8.4.4 Topographic survey campaign with total station

Given the impossibility of geolocalising the frames extracted from the UAV footage, we planned to acquire another part of the scalar data needed to guide the SfM photomodelling process with a topographic survey. We also decided to perform this operation in order to have a non-massive, personally acquired metric feedback, to be used for the purpose of verifying the accuracy of the remotely sensed data (both those of the 2009 PST-A and the tomographic clouds processed by IREA-CNR).

As already mentioned, the topographic campaign was conducted from 9:30 a.m. to 1:00 p.m. on 17 May 2023, using a Leica TCR 730 total stationwithout a GPS instrument and a prism.

A total of 135 points were acquired, of which 15 stations made up a closed polygonal. The polygonal in question starts from the top of a stepped ramp between the southern coast and Viale dei Mille (Station 100), and then points near the lighthouse park (Station 200) to the west, then goes around the Fortress from the east side to the north side (Station 300, Station 400, Station 500) and arrives between the circular-based tower and the troniera (Station 600). At this point, a station was placed in Via di Cala di Forno (Station 700), with a drop in height downwards of approximately 11 m and leaving the city walls, so that three more stations (Station 800, Station 900, Station 1000) could continue along the road towards the port. From there, a station was placed in the harbour car park (Station 1100), then running along the eastern side of the City Walls (Station 1200, Station 1300) and placing the last station about halfway along the southern pier (Station 1400), at a sufficient distance to avoid obstructions in the closing collimation with Station 100.

8.4.5 Survey campaign with hand-held video camera

As a supplement to the footage recorded with the drones, we carried out additional filming with a Sony AX33 4K hand-held video camera, equipped with a motion stabiliser and a 1/2.3" CMOS sensor with an effective 8.29 MP, with 4K resolution (3840 x 2160 px) and a recording format on .mp4 files. These recordings were useful for shooting footage inside the city walls, in areas where the use of a drone would have been more difficult due to the narrow road sections between individual buildings.

The first ground-based filming campaign(constituting the VE series) took place on 9 July 2023, from 10:00 to 15:00 in stable weather conditions. On that occasion, the following sectors were filmed:

- the trunk to the north of the fortress, from a closer viewpoint and avoiding the obstruction of the view by trees;
- the northern walkway of the fortress from a closer viewpoint and in both directions;
- the north-eastern corner of the fortress, from a closer viewpoint and avoiding, again, the occlusion of the view by nearby trees.

The second shooting campaign from the ground (constituting the VF series) took place on 16 July 2023, from 8:30 a.m. to 12:30 p.m. under stable weather conditions. On that occasion, the following sectors were filmed:

- the northern section of the City Walls along Via Cala di Forno, in both directions, as far as Porta del Porto;
- the inner side of the city walls from the Port Gate to Piazza IV Novembre;
- the inner side of the city walls along the entire Via dei Mille, in both directions.

8.5 Processing and integration of acquired data

We now present the procedure followed to process and integrate the data acquired through remote sensing and in situ survey operations.

8.5.1 Alignment of the clouds acquired with laser scanners

In October 2023, the eight scans of the Rock were processed and aligned with the JRC 3D Reconstructor software. The processing consisted of a first phase of importing the scans and refining the associated point clouds, a second phase of pre-alignment, a third phase of fine alignment and a fourth phase of subsampling.

In the first phase, the programme automatically refined each point cloud obtained from each imported scan and removed inconsistent data.

In the second phase, we pre-aligned every two clouds to form a closed loop of scans that correctly determined the outer lateral surface of the Rock. In each pre-alignment operation, we ensured that the maximum acceptable error threshold of 3 cm was not exceeded.

In the third phase, we applied the Iterative Closest Point (ICP) algorithm every two clouds in order to perform a fine alignment. Here we ensured that the maximum acceptable error threshold of 0.5 mm was not exceeded in each fine alignment operation. This permissible error threshold is linked to the fact that the model resulting from the laser scanner scans was primarily intended for graphic restitution at an architectural scale.

In the fourth phase, we subjected each point cloud to subsampling. The quantity of points constituting each cloud was in fact surplus to requirements and the surplus points would not have brought any benefit to the representation, instead risking slowing down the performance of the computer used in the processing. For this reason, we decided to subsample each cloud uniformly by a factor of 2, i.e. by halving the number of points.

The 8 clouds were then merged into a single file saved in .ply format, with a 'Binary Little Indian' save mode, with a 'double' co-ordinate format and obviously incorporating the colour of the points.

8.5.2 Import of the polygon obtained from the topographic survey

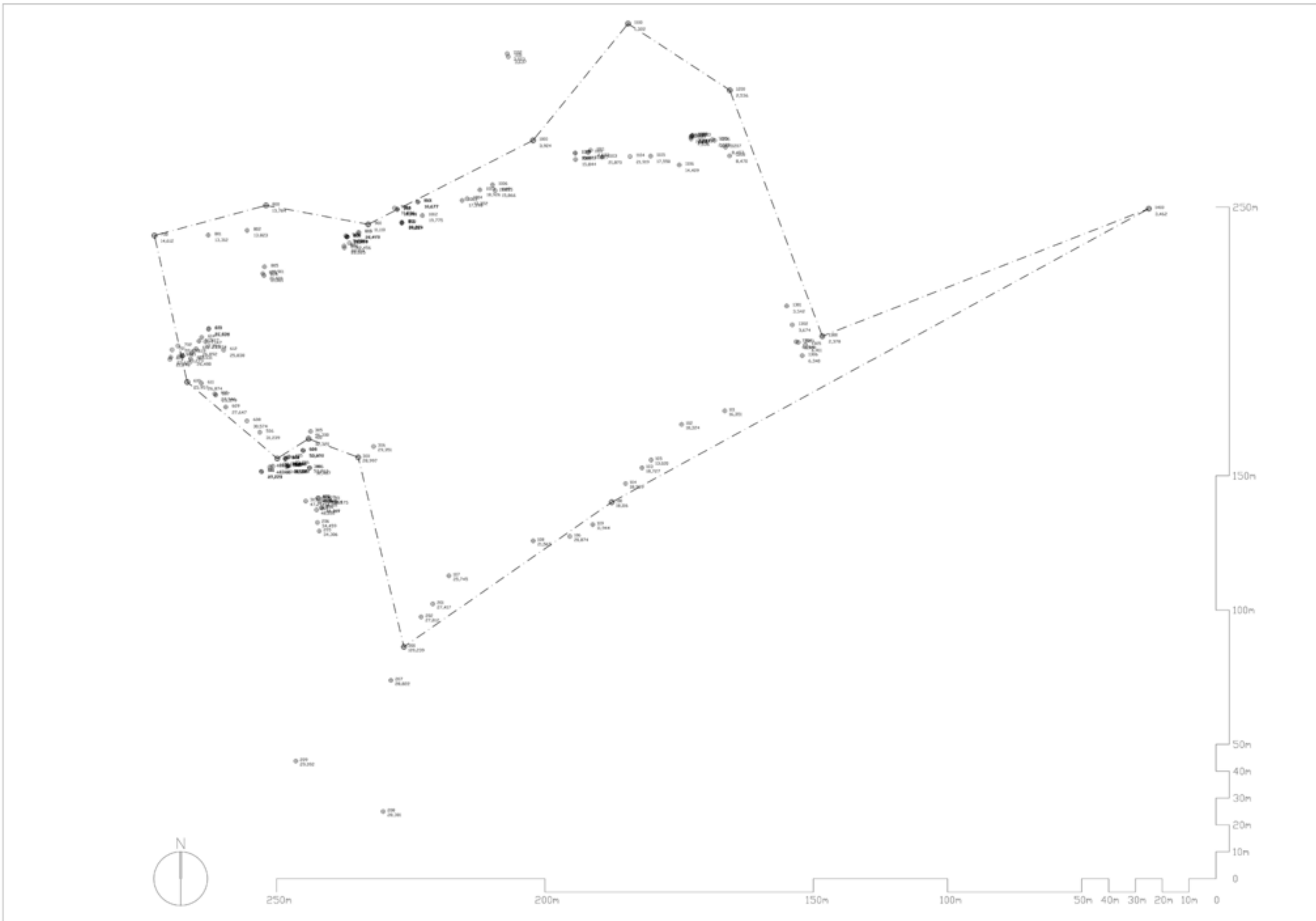

8.12/ Plan of the topographic survey of Talamone Town Walls, executed with a closed polygonal shape.

The points measured topographically with the Leica TCR 730 total stationwere imported onto the computer in a file in native .idx format, using the Leica WinDriver software
Subsequently, the .idx file was converted to .xyz formatboth so that it could be inspected with the Leica Survey Office programme and also so that it could be integrated with the point clouds acquired with the other surveying techniques. From the .xyz file, a version in .dxf format was also saved for the Autodesk Autocad software for the graphic restitution phase.

8.5.3 First integration for photomodelling purposes

In order to guide the SfM photomodelling process towards a reliable result, it is necessary to provide the program with reliable scalar data by entering Ground Control Points (GCPs) with known coordinates in its spatial reference system. Once the coordinates of the GCPs have been entered, they can be manually located on the frames that the programme will process to derive the three-dimensional digital model of the surface of the scene being filmed.
For this case study, we decided to derive the scalar data for the photomodelling programme from an auxiliary point cloud. This auxiliary cloud was derived from the union of the following point clouds:

- that of tablet C42541112_0202 of PST-A 2009, consisting of LIDAR data acquired by the Ministry of the Environment through an aircraft-mounted sensor. Since this is the largest point cloud, it was used as the input basis for all the others;

8.13/ The Leica TCR 730 Total Station used in the topographic survey.

- the one obtained from the union of the 8 laser scanner acquisitions;
- the polygon obtained by topographic surveying with total station;
- the tomographic point cloud processed by IREA-CNR on the basis of the 160 COSMO-SkyMed products and NASADEM data;
- the tomographic point cloud processed by IREA-CNR based on the 160 COSMO-SkyMed products and TanDEM-X data.

We then aligned the clouds listed above with the CloudCompare programme, keeping the errors below a maximum error threshold of 30 cm. This permissible error threshold is related to the fact that the model resulting from the integration of the point clouds was primarily intended for graphic restitution at an urban scale.

8.5.4 Structure from Motion photomodelling

In preparation for the extraction of the frames for the SfM process, the .mp4 films divided into 6 series (DA, DB, DC, DD, VE, VF) respectively corresponding to the 6 campaigns were cut and edited with the Losslesscut programme. The purpose of this operation was to eliminate the minutes in which the survey objects had not been framed and to facilitate the workflow of the photomodelling software.

The films thus recomposed were imported into the SfM 3DFlow Zephyr photomodelling programme, which automatically extracted the frames considered suitable for the three-dimensional reconstruction procedure of the surfaces filmed with the video cameras. Among the criteria for this automatic image selection, the most important were the overlap between frames and the focus (to avoid blurry photos). The images were then saved in .jpg format and grouped into 22 areas to be reconstructed individually and then merged.

We then imported the auxiliary point cloud of the entire area to be surveyed into the 3DFlow Zephyr environment. By applying the SfM process to each individual frame group for each of the 22 scopes, we obtained 22 sparse point clouds. Each of these sparse clouds was then realigned with the auxiliary point cloud of the entire area to be surveyed, each time finding an appropriate number of GCPs in the latter. In this assembly phase we introduced a total of 247 GCPs.

Having aligned the sparse clouds, we had the software construct the dense point clouds.

8.5.5 Second integration for restitution purposes

The three-dimensional model obtained through SfM photomodelling of the entire surveyed area was then imported into the CloudCompare environment and aligned in turn with the auxiliary point cloud.

Here too, we kept the alignment errors below themaximum error threshold of 30 cm, as this last integration operation was aimed at the graphic restitution at urban scale.

8.5.6 Graphical Representation of data and Results

Similarly to what we have already seen in the case study of the Spanish Fortress of Porto Santo Stefano, we obtained a virtual three-dimensional model on an urban scale using the integration procedure explained above. From this model we obtained graphical returns to the section profiles, where the targets identified by the COSMO-Skymed mission's satellite radars and selected by the 3D SAR Tomography process applied by IREA-CNR were highlighted with coloured dots. The colour of each of the targets represents the estimated average velocity for the corresponding backscattering element with reference to the ten-year time interval covered by the 160 selected COSMO-Skymed products. As with the tomographic point clouds seen in Chapter 3, the average velocity

shown in these profiles is the average of the estimated values of the displacements along the line of sight of the radar sensor in the time series
addition to these cross-sectional profiles, anupdated planimetry was returnedsuperimposition, through GIS, of contour lines obtained from the DTM of tablet C42541112_0202 of the 2009 PST-A, the Regional Technical Map of Tuscany and satellite photos.
With the integration of three-dimensional models from LIDAR scanning and SfM photomodelling, it was also possible to carry out the graphic restitution of the plan of the roofs and external elevations of the Fortress.

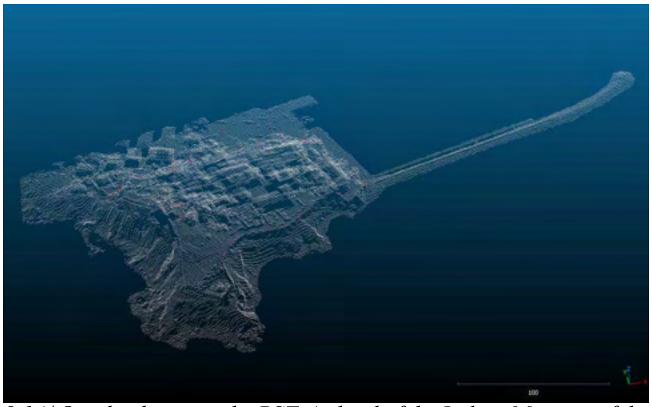

8.14/ Overlay between the PST-A cloud of the Italian Ministry of the Environment (white) and the topographic point cloud acquired with Total Station (red). Source: Ministero dell'Ambiente e dell'Energia – Italian Ministry of Environment and Energy / licensed under CC BY-SA 3.0 IT (https://creativecommons.org/licenses/by/3.0/it/deed.it) / Creative Commons – Attribuzione - Condividi allo stesso modo Italia (CC BY-SA 3.0 IT).

Notes

1 Fanciulli 1999, pp. 251-254; Guidoni, Pieroni 1994, pp. 14, 20-24, 38-40; Istituto Italiano dei Castelli 2011; Maioli 2015, pp. 65-69, 72-76, 81-82; Scoppola 1984, p. 43-58; Sordini 2000, pp. 89-91.
2 Guidoni, Pieroni 1994, pp. 9-10, 14, 20-24; Sordini 2000, pp. 89-91.
3 Guidoni, Pieroni 1994, pp. 9-10, 14, 20-24; Maioli 2015, pp. 77-78, 82-84, 93; Scoppola 1984, p. 43.
4 Guidoni, Pieroni 1994, pp. 9-10, 14, 20-24; Istituto Italiano dei Castelli 2020; Maioli 2015, pp. 77-78, 82-84, 93.
5 Guidoni, Pieroni 1994, p. 23.
6 Guidoni, Pieroni 1994, pp. 9-10, 14, 20-24; Maioli 2015, p. 85.
7 Maioli 2015, pp. 79-81.
8 Maioli 2015, p. 81.

Sintesi

All'epoca del passaggio di proprietà dall'Abbazia di San Salvatore di Monte Amiata alla Repubblica Senese, Talamone era già stata dotata dai conti Aldobrandeschi di mura e di cassero, caduti però tutti in rovina. Se il cassero antecedente la venuta dei Senesi sia poi andato a costituire il nucleo della Rocca di Talamone o meno è ancora oggi oggetto di dibattito. Ad ogni modo nel progetto originario Senese, databile nel 1304-1305 ed esposto al pubblico nel 1306, la Rocca e la chiesa erano i poli di uno degli assi viari principali. Talamone entrò ben presto in uno stato di decadimento cronico, dovuto a cause sia ambientali sia di origine umana. Per quanto riguarda le cause naturali, oltre alla malaria dovuta alle paludi circostanti che vennero bonificate solo nella prima metà del Novecento, la costa nei dintorni del porto è ancora oggi soggetta a fenomeni di erosione, le quali hanno continuamente accelerato i dissesti geologici delle opere di fortificazione e reso effimeri la maggior parte degli interventi di restauro fino all'Epoca contemporanea. Per quanto concerne le cause umane dello stato di precarietà di Talamone, innanzitutto vi fu la graduale ma sempre più schiacciante concorrenza di altri porti d partire dal 1414. In secondo luogo vi erano anche delle carenze difensive che emersero soprattutto con le scorrerie dei corsari sareceni del 1536, nel contesto del conflitto tra l'imperatore Carlo V del Sacro Romano Impero e l'alleanza costituita dal re di Francia Francesco I di Valois e l'imperatore ottomano Solimano I il Magnifico. Si susseguirono altri interventi di restauro tra 1541 e il 1546, sempre infruttuosi. Il passaggio di Talamone allo Stato dei Presìdi nel 1557 non migliorò particolarmente la sua situazione, poiché lo scarso interesse nei confronti del suo porto non sembrava giustificare una manutenzione significativa e costante. A partire dal

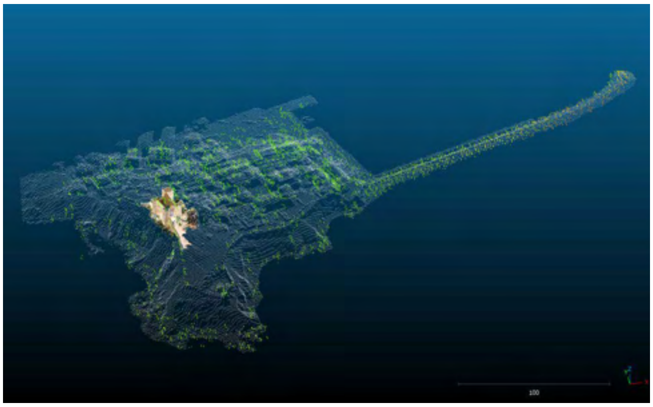

8.15/ Overlay between the laser scanner cloud of the Fortress (coloured), the PST-A cloud of the Italian Ministry of the Environment (white), and the tomographic cloud with NASADEM data (from green to red). Source: Agenzia Spaziale Italiana, 2022. Products processed by Luca Martelli, Diego Reale, and Simona Verde under a license of the Italian Space Agency (ASI); Original COSMO-SkyMed Products - ©ASI - (2012-2017); Ministero dell'Ambiente e dell'Energia – Italian Ministry of Environment and Energy / licensed under CC BY-SA 3.0 IT (https://creativecommons.org/licenses/by/3.0/it/deed.it) / Creative Commons – Attribuzione - Condividi allo stesso modo Italia (CC BY-SA 3.0 IT).

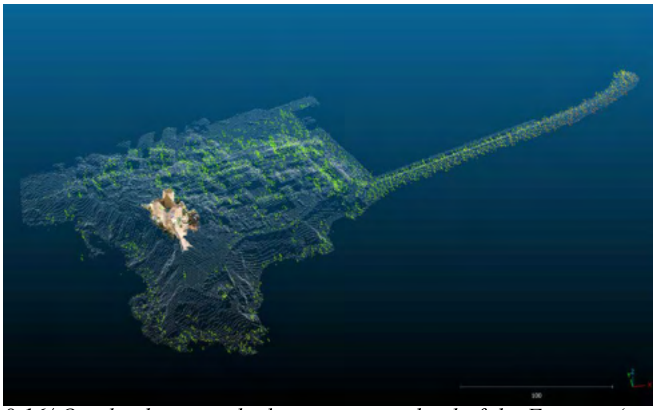

8.16/ Overlay between the laser scanner cloud of the Fortress (coloured), the PST-A cloud of the Italian Ministry of the Environment (white), and the tomographic cloud with TanDEM-X data (from green to red). Source: Agenzia Spaziale Italiana, 2022. Products processed by Luca Martelli, Diego Reale, and Simona Verde under a license of the Italian Space Agency (ASI); Original COSMO-SkyMed Products - ©ASI - (2012-2017); Deutsches Zentrum für Luft- und Raumfahrt e.V., 2006. © DLR <2023>. Ministero dell'Ambiente e dell'Energia – Italian Ministry of Environment and Energy / licensed under CC BY-SA 3.0 IT (https://creativecommons.org/licenses/by/3.0/it/deed.it) / Creative Commons – Attribuzione - Condividi allo stesso modo Italia (CC BY-SA 3.0 IT).

governo degli Asburgo-Lorena di Toscana, vennero eseguiti dei lavori di restauro che mantennero la struttura difensiva ancora in servizio all'arrivo di Garibaldi e dei Mille. Durante la Seconda Guerra Mondiale, i Tedeschi in ritirata causarono danni irreparabili minando la Rocca e le opere difensive limitrofe, coinvolgendo persino alcune abitazioni. Per quanto riguarda le attività di rilievo, dopo una prima ricognizione effettuata l'8 maggio 2022, con l'acquisizione di una documentazione fotografica, la prima campagna di rilevamento con laser scanner ha avuto luogo tra il 19 settembre 2022 e il 21 settembre 2022 concentrandosi sulle facciate esterne della Rocca. Per l'occasione è stato utilizzato un sensore FARO 3d Focus M70. Tra l'11 aprile e il 13 aprile 2023 ha avuto luogo una campagna con una flotta costituita da due droni: un Mavic Dj Mini Pro 2 e un Mavic Dj Mini Pro 3, provvisti di videocamera. Sono state eseguite diverse riprese aeree della Cinta muraria, con lo scopo di usare i fotogrammi estratti da tali filmati in un processo di elaborazione Structure from Motion (SfM). Il 17 maggio 2023 è seguito un rilevamento topografico con stazione totale accompagnato da una seconda campagna con il solo drone Mavic Dj Mini Pro 3. Tra il 6 giugno e l'8 giugno 2023 sono state eseguite ulteriori riprese della Rocca e della Cinta muraria con entrambi i droni della flotta. Il 9 luglio e il 16 luglio 2023 sono state eseguite delle riprese integrative con videocamera manuale Sony AX33 4K con stabilizzatore di movimento. Per la preparazione all'estrazione dei fotogrammi per il processo di SfM, i filmati acquisiti sono stati tagliati e montati con il programma freeware Losslesscut. Dai filmati sono stati ricavati degli spezzoni dove sono stati inquadrati solamente gli oggetti del rilievo, cioè le mura e la Rocca. In seguito, i filmati sono stati sottoposti a un primo processo SfM con il software 3DFlow Zephyr. La nuvola LIDAR della tavoletta C42541112_0202 del Piano Straordinario di Telerilevamento Ambientale 2009 (PST-A 2009) del Ministero dell'Ambiente italiano, le due nuvole tomografiche generate dall'Istituto per il Rilevamento Elettromagnetico dell'Ambiente (IREA-CNR) e la nuvola di punti ottenute con la stazione totale sono state allineate con il software CloudCompare e importate nell'ambiente 3DFlow Zephyr. In questo modo è stato possibile introdurre dati scalari nell'elaborazione attraverso l'individuazione di Ground Control Point direttamente sulla nuvola composita.

8.17/ Planimetry of the urban context of the Town Walls of Talamone. The topography has been updated thanks to the Digital Terrain Model (DTM) of tile C42541112_0202 of the Extraordinary Plan for Environmental Remote Sensing 2009 (PST-A 2009). Ministero dell'Ambiente e dell'Energia – Italian Ministry of Environment and Energy / licensed under CC BY-SA 3.0 IT (https://creativecommons.org/licenses/by/3.0/it/deed.it) / Creative Commons – Attribuzione - Condividi allo stesso modo Italia (CC BY-SA 3.0 IT).

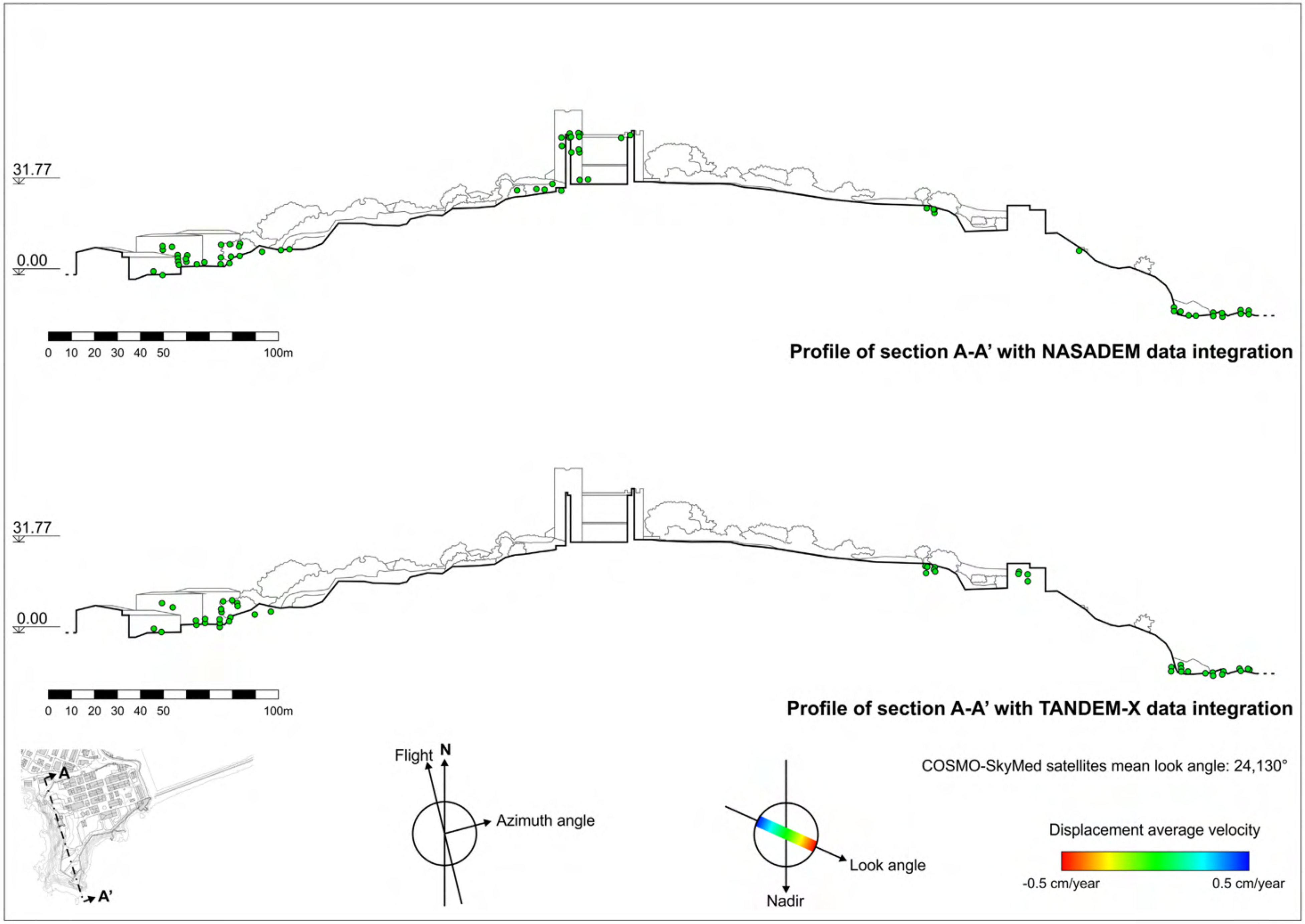

8.18/ Profile of section A-A' of the urban context of Talamone in the surroundings of the Fortress.

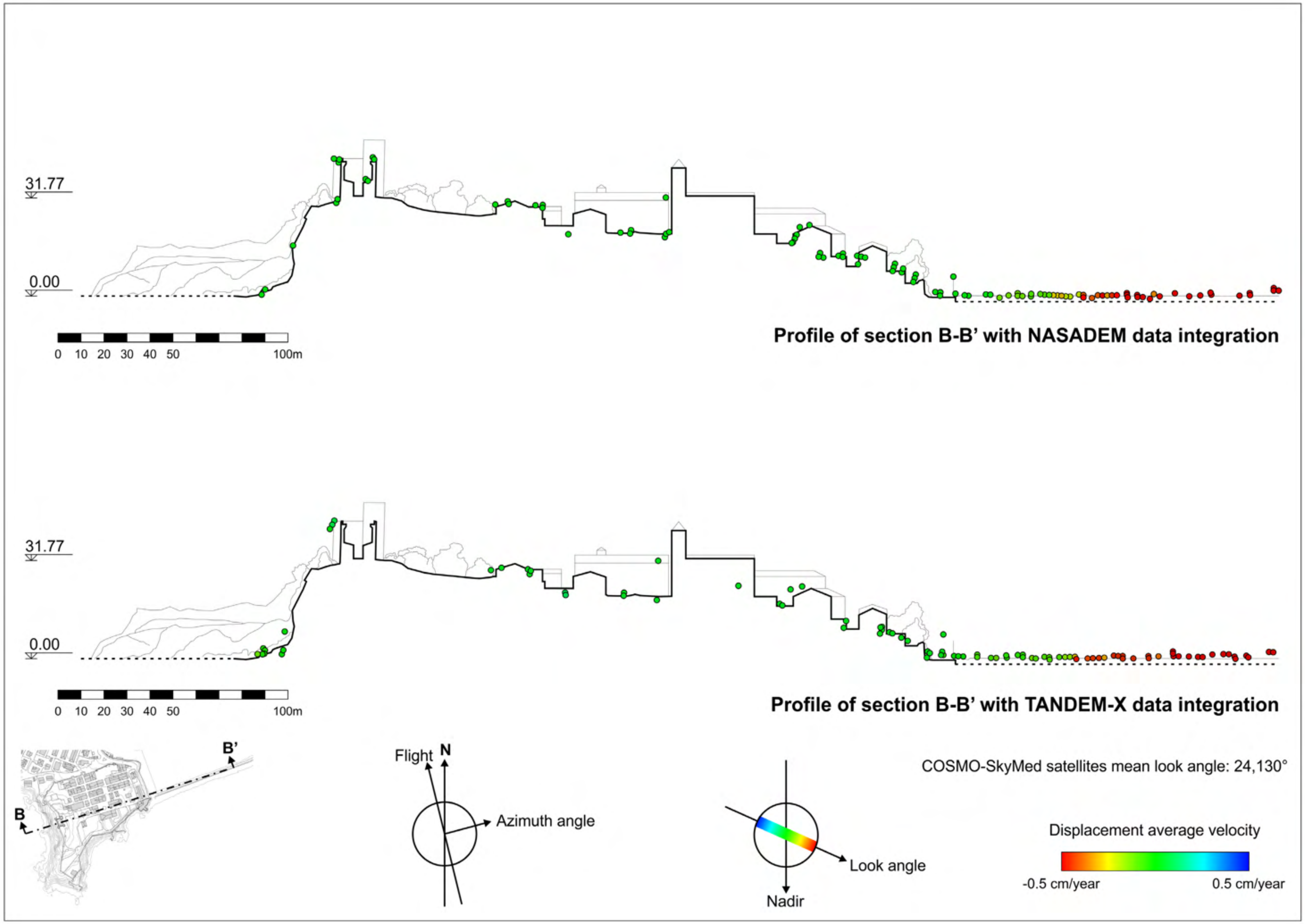

8.19/ Profile of section B-B' of the urban context of Talamone in the surroundings of the Fortress.

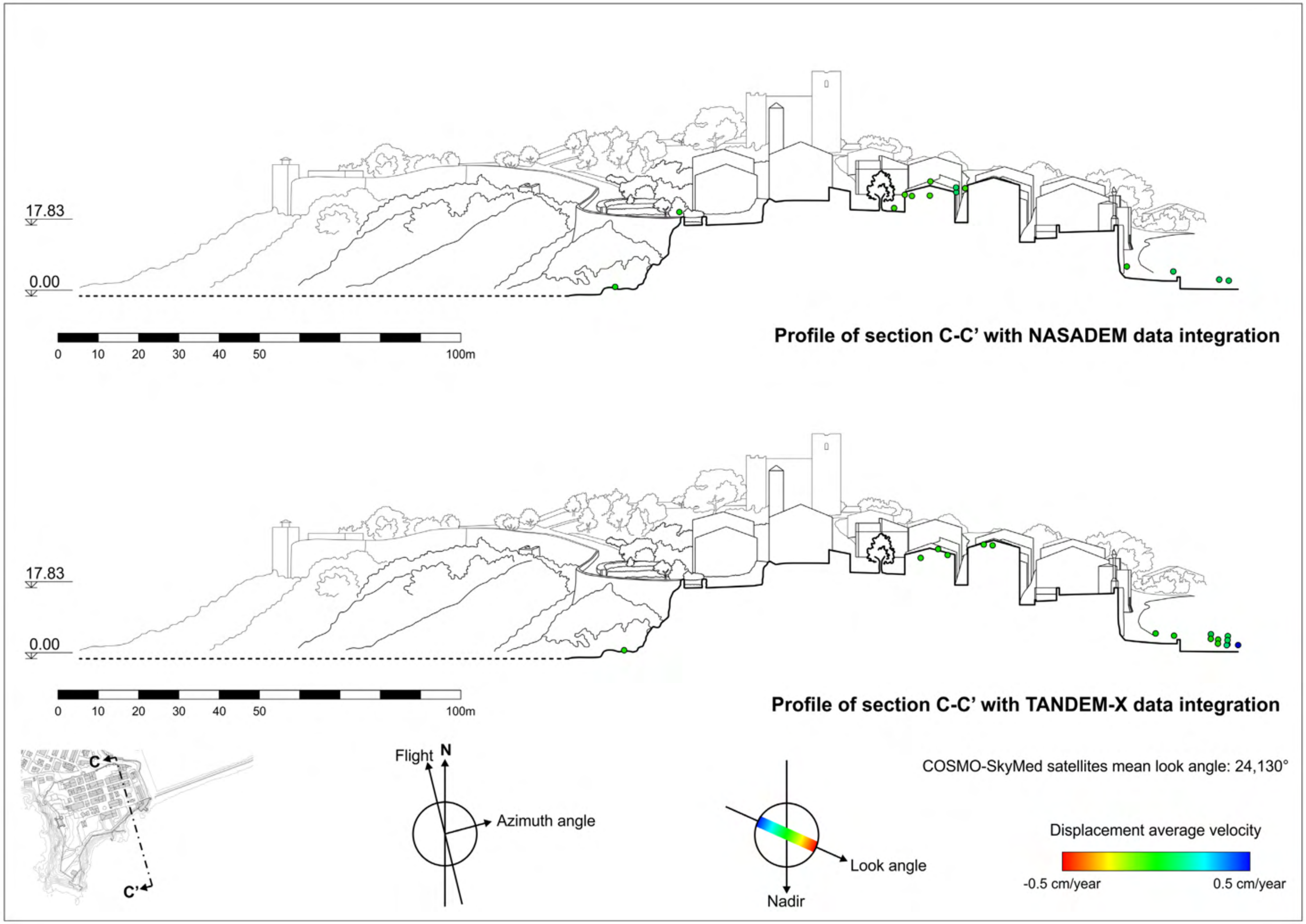

8.18/ Profile of section C-C' of the urban context of Talamone in the surroundings of the Fortress.

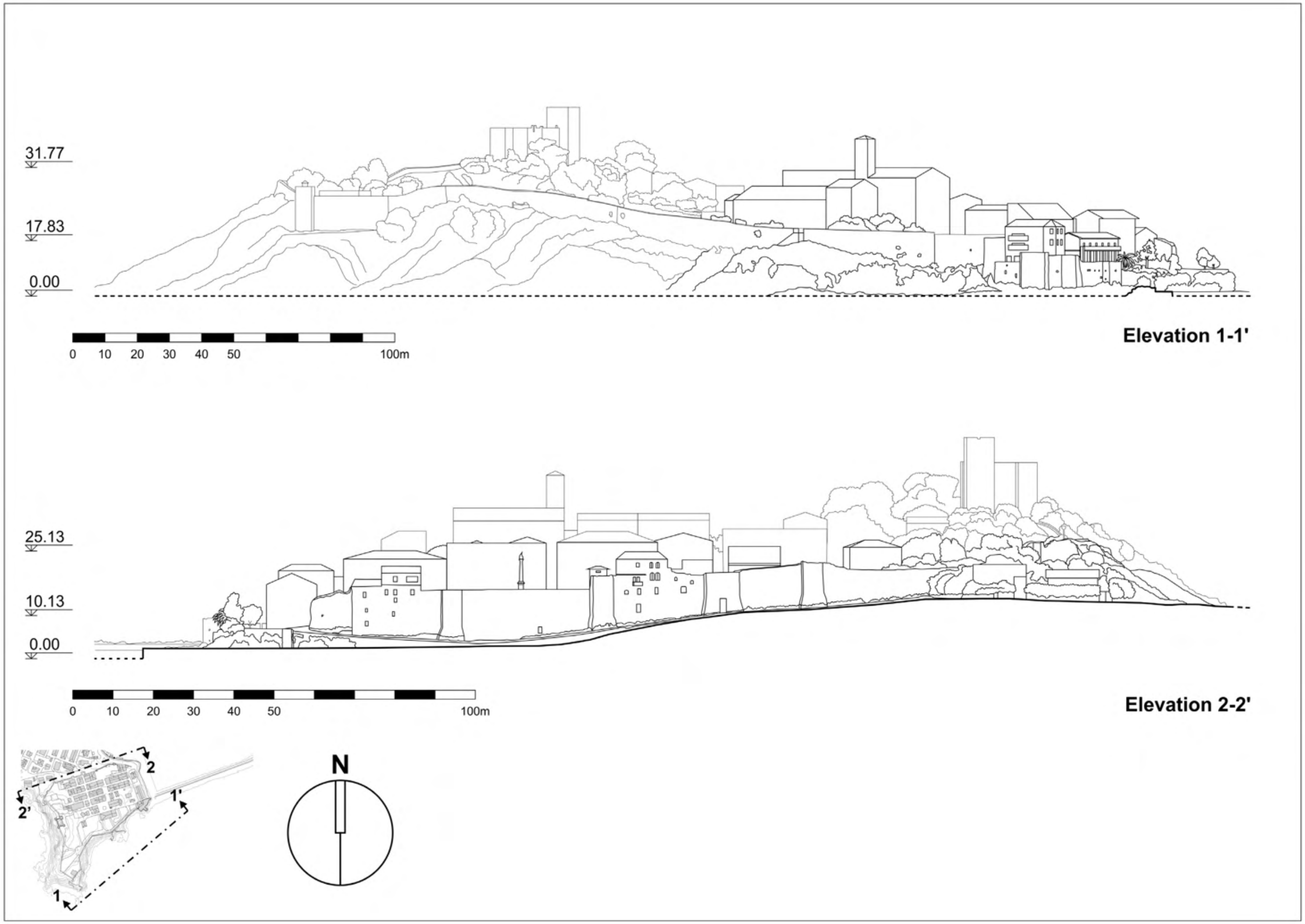

8.19/ Elevations 1-1' and 2-2' of the urban context of Talamone in the surroundings of the Fortress.

Luca Martelli

Conclusions

As far as the integrated survey of Architecture and Territory is concerned, remote-sensing with Synthetic Aperture Radar (SAR) presents a potential that is certainly still in the making, but which already manifests practical applications of considerable usefulness.

A first element to be taken into consideration is the free availability of these data for scientific institutions, even though this is often tied to a selection of requests from national and international space agencies. On the other hand, it should also be noted that data from older space missions (such as Sentinel, ERS, Envisat, etc. missions) are released to the public domain and can still constitute a useful source of data, at least in the preliminary remote-sensing stage. An ever-increasing availability of spatial information is also matched by a growing accessibility of the techniques that enable its processing, thanks to the dissemination and extensiveness of today's computer and telecommunication media. For example, until a few decades ago, processing with SAR interferometry was within the reach of a few specialised scientific institutes. Today, on the other hand, it is possible to equip many medium-capacity computers with special software packages (such as those in the MATLAB environment) in order to carry out this type of operation and derive, for example, a Digital Elevation Model (DEM) from a pair of radar images.

Secondly, it is important to bear in mind that since there are different radars set to diverse frequencies, these types of instruments can detect different aspects of the nature of a territory. What is opaque at one radar frequency, in particular vegetation and certain soil layers, may be transparent at another radar frequency. In Chapter 8, we had an example of this particular sensitivity. Satellite microwave radars were able to detect the column of the war memorial in Piazza IV Novembre in Talamone, while the airborne LIDAR sensor of the Extraordinary Remote Sensing Plan was unable to register its presence. Clearly, a fundamentally different detection capability compared to optical sensors corresponds to a radically different acquisition geometry. The geometric distortions (foreshortening, layover and radar shadows) and radiometric distortions described in Chapter 2 have already been the subject of study in the field of telecommunications engineering for many years, to the extent that effective means have already been developed to correct or at least mitigate them. However, both these anomalies and the geometric set-up that determines them are phenomena worthy, in our opinion, of becoming the subject of debate in the field of Representation and Spatial Geometry, since they pose a series of novel questions.

Another unseen aspect, as far as Architectural and Land Survey is concerned, is the relationship of these instruments with time. As discussed from a theoretical point of view in Chapter 4 and then appreciated from a practical point of view in Chapter 7, SAR interferometry and tomography make it possible to observe and measure (even) very small changes in buildings and territory. Thanks to the cyclic nature of satellite scans, it is possible to detect these changes in buildings even when they take place over very long time intervals (such as decades), thus expanding the detector's perceptive capabilities and giving him or her new measuring 'tools'. These time-series measurements can go beyond the kinematic configurations assumed by certain parts of the building (the backscatterers detected by radar), and even estimate elastic and thermal deformations through four- and five-dimensional tomography, thus colliding with the concept of Architectural and Land Survey as an open system of knowledge.

At the moment, of course, complex images obtained from radar scans and all products derived from them (such as tomographic point clouds) have considerable room for improvement over optical sensors, especially with regard to resolution. In the application cases addressed in Chapter 7 and Chapter 8, we were unable to use the radars of the COSMO-SkyMed mission at their maximum definition, associated with the Spotlight mode and consisting of a ground resolution of 1m. In our case, the best possible definition was that of the Stripmap Hi-Image mode, with a resolution of 3m. In any case, in addition to the continuous development of more and more high-performance sensors by national and international space agencies, there are already fee-based services capable of providing superior performances.

In parallel, another development frontier is represented by small-scale Unmanned Aerial Vehicles (UAVs) equipped with SAR. Currently, this new category of small-scale drones is moving from the experimental phase to on-demand production. Although expensive, UAV platforms are highly to be reckoned with when it comes to scanning with circular SAR and holographic SAR (i.e. the combination of SAR tomography with circular trajectories), as they would be an extremely cost-effective alternative to circular scanning by aircraft. This would give access to the best possible resolution of SAR at a relatively low cost, with the possibility of scanning buildings or architectural complexes at 360°.

To conclude then, the current level of versatility and accuracy of SARs is such that they have reached the dignity of other instrument surveying techniques. They can make a significant contribution within any integrated survey.

Sintesi

Per quanto riguarda il rilievo integrato dell'Architettura e del Territorio, il telerilevamento con radar ad apertura sintetica presenta delle potenzialità sicuramente ancora in divenire, ma che già manifestano delle applicazioni pratiche di utilità consistente.

Un primo elemento da prendere in considerazione è la disponibilità gratuita di questi dati per le istituzioni scientifiche, anche se spesso questa risulta vincolata a una selezione delle richieste da parte delle agenzie spaziali. D'altro canto, va pure notato che i dati delle missioni spaziali più vecchie vengono rilasciati al pubblico dominio e possono costituire comunque una fonte di dati utile, almeno in via di telerilevamento preliminare.

In secondo luogo, è importante tenere presente che, esistendo diversi radar impostati su frequenze differenti, questo tipo di strumenti consentono di rilevare aspetti differenti della natura di un territorio. Ciò che risulta opaco a una determinata frequenza radar, in particolare la vegetazione e certi strati di terreno, può risultare trasparente a un'altra frequenza radar.

Nel Capitolo 8, infatti, abbiamo avuto un esempio di questa particolare sensibilità. I radar a microonde satellitari sono stati in grado di rilevare la colonna del Monumento ai Caduti di Piazza IV Novembre a Talamone, mentre il sensore LIDAR aeromobile del Piano Straordinario di Telerilevamento non è stato in grado di registrarne la presenza.

Chiaramente, a un funzionamento sostanzialmente diverso nelle capacità di rilevamento rispetto ai sensori ottici corrisponde una geometria d'acquisizone radicalmente differente. Le distorsioni geometriche e radiometriche descritte nel Capitolo 2 sono già da molti anni oggetto di studio nell'ambito dell'Ingegneria delle Telecomunicazioni, tanto che sono già stati sviluppati mezzi efficaci per correggerle o, perlomeno, mitigarle. Tuttavia, sia queste anomalie sia l'assetto geometrico che le determina sono dei fenomeni meritevoli, a nostro avviso, di diventare oggetto di dibattito nel campo del Disegno e della Geometria spaziale, poiché pongono una serie di interrogativi inediti.

Un altro aspetto inedito, per quanto riguarda il Rilievo dell'Architettura e del Territorio, è il rapporto di questi strumenti con il tempo. Come discusso da un punto di vista teorico nel Capitolo 4 e poi apprezzato sotto il profilo pratico nel Capitolo 7, l'interferometria e la tomografia radar ad apertura sintetica consentono di osservare e misurare (anche) cambiamenti di entità molto piccola negli edifici e nel territorio. Queste misurazioni in serie temporali possono andare al di là delle configurazioni cinematiche assunte da alcune parti dell'edificio (gli elementi retrodiffondenti individuati dal radar), per poi addirittura stimare anche le deformazioni elastiche e termiche attraverso la tomografia a quattro e a cinque dimensioni, andando così a collimare con il concetto di Rilievo dell'Architettura e del Territorio come sistema aperto di conoscenze.

Al momento, ovviamente, le immagini complesse ottenute da scansioni radar e tutti i prodotti che ne derivano hanno dei notevoli margini di miglioramento rispetto ai sensori ottici, specialmente per quanto riguarda la risoluzione. Nei casi applicativi affrontati nel Capitolo 7 e nel Capitolo 8 non abbiamo potuto usufruire dei radar della missione COSMO-SkyMed alla loro definizione massima, associata alla modalità Spotlight e consistente in una risoluzione a terra di 1m. Nel nostro caso, la definizione migliore possibile era quella della modalità Stripmap Hi-Image, avente una risoluzione di 3m. In ogni caso, oltre al continuo sviluppo di sensori sempre più performanti da parte delle agenzie spaziali nazionali e inter-

nazionali, esistono già servizi a pagamento in grado di fornire prestazioni superiori.
Parallelamente, un'altra frontiera di sviluppo è quella rappresentata dagli Unmanned Aerial Vehicles (UAV) di piccola scala equipaggiati con radar ad apertura sintetica. Attualmente, questa nuova categoria di droni dalle dimensioni contenute sta infatti passando dalla fase sperimentale a quella della produzione su richiesta. Sebbene costose, le piattaforme UAV sono da tenere altamente in considerazione per quanto riguarda le scansioni con radar ad apertura sintetica circolare e il radar ad apertura sintetica olografico (cioè la combinazione della tomografia radar ad apertura sintetica con le traiettorie circolari), in quanto rappresenterebbero un'alternativa estremamente economica alle scansioni circolari effettuate da aeromobile.
L'attuale livello di versatilità e accuratezza dei radar ad apertura sintetica è tale da aver raggiunto la dignità di altre tecniche di rilievo strumentale, permettendo un apporto significativo all'interno di qualsiasi rilievo integrato.

Bibliography

Bibliography

Ager Thomas P., 2013. An Introduction to Synthetic Aperture Radar Imaging. *Oceanography*, 2, 2013, 26, pp. 20-33.

Alpers Werner, Melsheimer Christian, 2004. Rainfall. In Jackson Christopher R., Apel John R. (ed.) *Synthetic Aperture Radar: Marine User's Manual*. Washington, DC: U.S. Department of Commerce, National Oceanic and Atmospheric Administration, 2004, pp. 355-371.

Anceschi Giovanni, 1992. *L'oggetto della raffigurazione*. Milano: ETAS libri, 1992, 256 pp.

Battagliere Maria Libera, Virelli Maria, 2019. *COSMO-SkyMed Mission and Products Description. ASI-CSM-PMG-NT-001. 8 July 2019. Issue 3.* Rome: Agenzia Spaziale Italiana, 2019, 151 pp.

Bonanno Lucia, 2007. Problemi di conoscenza/soluzioni di rilievo. In Chiavoni Emanuela, Paolini Priscilla (ed.) *Metodi e tecniche integrate di rilevamento per la realizzazione di modelli virtuali dell'architettura della citta: ricerca COFIN 2004* / coordinatore nazionale Mario Docci. Roma: Gangemi, 2007, pp. 195-200.

Bueti Serafina, 1998. Lo Stato dei Presidi caposaldo strategico e militare del Regno di Napoli (1557-1801). In *Per la storia del Mezzogiorno medievale e moderno: studi in memoria di Jole Mazzoleni. Vol. 2.* Roma: Ministero per i beni culturali e ambientali. Ufficio centrale per i beni archivistici, 1998, 516 pp.

Caciagli Giuseppe, 1971. *Lo Stato dei Presìdi.* Firenze: Istituto Geografico Militare, 1971, 180 pp.

Chen Zhanye, Zeng Zhiqiang, Fu Dongning, Huang Yan, Li Qiang, Zhang Xin, Wan Jun, 2023. Back-Projection Imaging for Synthetic Aperture Radar with Topography Occlusion. *Remote Sensing,* 15, 2023, 3, 726.

Crary Jonathan, 2013. *Le tecniche dell'osservatore: visione e modernità nel XIX secolo*. Torino: Einaudi, 2013, 181 pp. Traduzione di Luca Acquarelli. Ed. orig. T*echniques of the Observer. On Vision and Modernity in the Nineteenth Century. Cambridge,* MA: Massachussetts Institute of Technology, 1990.

Cundari Cesare, 2013. *Il rilievo architettonico: ragioni, fondamenti, applicazioni.* Roma: Aracne, Kappa, 2013, 571 pp.

Dainelli Niccolò, 2011. *Telerilevamento: manuale teorico-pratico per l'elaborazione delle immagini digitali*. Palermo: D. Flaccovio, 2011, 245 pp.

Deciani Tiberio, 1579. *Responsa. Vol. III.* Venetiis: Hieronymum & Ioannem Zenarios, 1579, 723 pp.

Della Monaca Gualtiero, Roselli Domenico, Tosi Giuseppe, [after 1993]. *La Fortezza spagnola e il sistema difensivo di Porto S. Stefano (secoli XVI-XIX).* Monte Argentario: Editrice Libreria Massimi, [after 1993], 35 pp.

Della Monaca Gualtiero, Roselli Domenico, Tosi Giuseppe, 1996. *Fortezze e torri costiere dell'Argentario, Giglio e Giannutri. Cronaca. Storia. Aspetti architettonici*. Pitigliano: Laurum Editrice, 1996, 244 pp.

Docci Mario, Maestri Diego, 2006. *Manuale di rilevamento architettonico e urbano.* Roma: Laterza, 2006, 348 pp.

Docci Mario, Migliari Riccardo, 1992. *Scienza della rappresentazione: fondamenti e applicazioni della geometria descrittiva.* Roma: NIS, 1992, 620 pp.

Döring Björn J., Schmidt Kersten, Jirousek Matthias, Rudolf Daniel, Reimann Jens, Raab Sebastian, Antony John Walter, Schwerdt Marco, 2013. Hierarchical Bayesian Data Analysis in Radiometric SAR System Calibration: A Case Study on Transponder Calibration with RADARSAT-2 Data. *Remote Sensing*, 5, 2013, 12, pp. 6667-6690.

Emery William J., Camps Adriano, 2017. *Introduction to Satellite Remote Sensing: Atmosphere, Ocean and Land Applications.* Amsterdam: Elsevier, 2017, 856 pp.

Fanciulli Pietro, 1999. *Storia documentaria dei reali presidios di toscana. Lo Stato dei Presidi nelle carte degli archivi spagnoli e italiani. Oltre trecento documenti inediti degli archivi spagnoli (Simancas, Escorial, Madrid) e italiani (Firenze, Napoli, Roma, Orbetello). Vol. 1: Introduzione alla lettura dei documenti. Struttura organizzativa dello Stato dei Presidi nella società del tempo*. Pitigliano: Laurum, 1999, 380 pp.

Farr Tom G., 1993. Radar Interactions With Geologic Surfaces. In Ford John P., Plaut Jeffrey J., Weitz Catherine M., Farr Tom G., Senske David A., Stofan Ellen R., Michaels Gregory, Parker Timothy J. (ed.) *Guide to Magellan Image Interpretation (JPL Publication 93-24)*. Pasadena, CA: National Aeronautics and Space Administration, Jet Propulsion Laboratory, California Institute of Technology, 1993, pp. 45-56.

Ferretti Alessandro., Monti-Guarnieri Andrea, Prati Claudio, Rocca, Fabio, Massonnet, Didier, 2007. *InSAR Principles: Guidelines for SAR Interferometry Processing and Interpretation.* Noordwijk: ESA Publications, TM-19, 2007, 250 pp.

Ford John P., Blom Ronald G., Crisp Joy A., Elachi Charles, Farr Tom G., Saunders R. Stephen, Theilig Eilene E., Wall Stephen D., Yewell Susan B., 1989. *Spaceborne radar observations: a guide for Magellan radar-image analysis (JPL Publication 89-41).* Pasadena, CA: National Aeronautics and Space Administration, Jet Propulsion Laboratory, California Institute of Technology, 1989, pp. 132.

Fornaro Gianfranco, 2013. Tomographic SAR. In In Weiss Matthias (ed.) *Radar and SAR Systems for Airborne and Space-based Surveillance and Reconnaissance: STO Educational Notes EN-SET-191*. Brussels: NATO/STO, 2013, pp. 8 - 1-8 - 16.

Fornaro Gianfranco, Lombardini Fabrizio, Pauciullo Antonio, Reale Diego, Viviani Federico, 2014 Tomographic Processing of Interferometric SAR Data: Developments, applications, and future research perspectives. *IEEE Signal Processing Magazine,* 31, 2014, 4, pp. 41-50.

Fornaro Gianfranco, Pauciullo Antonio, Reale Diego, Verde Simona, 2014. Multilook SAR Tomography for 3-D Reconstruction and Monitoring of Single Structures Applied to COSMO-SKYMED Data. *IEEE Journal of Selected Topics in Applied Earth Observations and Remote Sensing,* 7, 2014, 7, pp. 2776-2785.

Fornaro Gianfranco, Reale Diego, Serafino Francesco, 2008. 4D SAR Focusing: A Tool for Improved Imaging and Monitoring of Urban Areas. In *IGARSS 2008 - 2008 IEEE International Geoscience and Remote Sensing Symposium (Boston, MA, 7-11 July 2008).* Piscataway, NJ: IEEE, 2008, pp. V - 475-V - 478.

Fornaro Gianfranco, Reale Diego, Verde Simona, 2013. Bridge Thermal Dilation Monitoring With Millimeter Sensitivity via Multidimensional SAR Imaging. *IEEE Geoscience and Remote Sensing Letters,* 10, 2013, 4, pp. 677-681.

Fornaro Gianfranco, Serafino Francesco, 2006. Imaging of Single and Double Scatterers in Urban Areas via SAR Tomography. *IEEE Transactions on Geoscience and Remote Sensing*, 44, 2006, 12, pp. 3497-3505.

Freeman Anthony, Durden Stephen L., 1998. A three-component scattering model for polarimetric SAR data. *IEEE Transactions on Geoscience and Remote Sensing,* 36, 1998, 3, pp. 963-973.

Freeman Anthony, Zink Manfred, Caro Ed, Moreira Alberto, Veilleux Louise, Werner Marian, 2019. The legacy of the SIR-C/X-SAR radar system: 25 years on. *Remote Sensing of Environment*, 231, 2019, 111255.

Gazzetta ufficiale della Repubblica Italiana n. 227 del 20 agosto 1980, Parte I, pp. 6986-6988.

Giroldini Pierluigi, 2010. *La pianura di Piombino in età antica: dinamiche di controllo e organizzazione territoriale* [doctoral thesis]. Firenze: Università degli Studi di Firenze, 2010, 205 pp.

Guidoni Enrico, Pieroni Laura, 1994. Talamone. Firenze: Giunta Regionale Toscana. Roma: Bonsignori, 1994, 78 pp.
Gunce Hamit Beran, San Bekir Taner, 2018. Measuring Earthquake-Induced Deformation in the South of Halabjah (Sarpol-e-Zahab) Using Sentinel-1 Data on November 12, 2017. *Proceedings* 2, 2018, 7: 346.

Holt Benjamin, 2004. SAR Imaging of the Ocean Surface. In Jackson Christopher R., Apel John R. (ed.) *Synthetic Aperture Radar: Marine User's Manual.* Washington, DC: U.S. Department of Commerce, National Oceanic and Atmospheric Administration, 2004, pp. 25-90.

Imperatore Pasquale, Di Martino Gerardo, 2023. SAR Radiometric Calibration Based on Differential Geometry: From Theory to Experimentation on SAOCOM Imagery. *Remote Sensing*, 15, 2023, 5: 1286.

Jiao Yanan, Zhang Fengli, Liu Xiaochen, Wang Qi, Huang Qiqi, Huang Zhiwei, 2023. Preliminary Evaluation of Geometric Positioning Accuracy of C-SAR Images Based on Automatic Corner Reflectors. *Remote Sensing*, 15, 2023, 19: 4744.

Jin Zhihong, Bea Robert G., Sharples Malcom, 2002. Failure Analysis of Texas Tower No. 4. In *2002 Offshore Technology Conference (Houston, 6-9 May 2002)*. Richardson, TX: Offshore Technology Conference, 2002, OTC 14193.

Jones Cathleen E., Holt Benjamin, 2018. Experimental L-Band Airborne SAR for Oil Spill Response at Sea and in Coastal Waters. *Sensors*, 18, 2018, 2, 641.

Kavoulaki Elisa, Psaroudaki Angeliki, Politaki Elpida, Lortal Gaëlle, Katsaveli Elisavet, Pangalou Matina, Pouli Paraskevi, Demadis Kostas, Grammatikakis Giannis, Eriksson Eva Marie, Soldovieri Francesco, Padeletti Giuseppina, 2017. *Deliverable D8.1. Description of the site and detailed end-users requirements and definition of the logistics for the monitoring system at Heraklion* [technical report]. HERACLES: HEritage Resilience Against CLimate Events on Site. European Commission: Horizon 2020.

Keydel Wolfgang, 1992. Basic Principles of SAR. In Keydel Wolfgang (ed.) *Fundamentals and Special Problems of Synthetic Aperture Radar (SAR): AGARD Lecture Series 182.* Laughton: Specialised Printing Services Limited, 1992, pp. 1 - 1-1 - 13.

Killinger Dennis K., 2014. Lidar (light detection and ranging). In Matthieu Baudelet (ed.). *Laser Spectroscopy for Sensing.* Sawston, Cambridge: Woodhead Publishing, 2014, pp. 292-312.

Lasaponara Rosa, Masini Nicola, Pecci Antonio, Perciante Felice, Pozzi Escot Denise, Rizzo Enzo, Scavone Manuela, Sileo Maria, 2016. Qualitative evaluation of COSMO SkyMed in the detection of earthen archaeological remains: The case of Pachamacac (Peru). *Journal of Cultural Heritage*, 23, 2017, pp. 55-62.

Long David, Ulaby Fawwaz T., 2014. *Microwave Radar And Radiometric Remote Sensing*. Ann Arbor, MI: University of Michigan Press, 2014, pp. 1116.

Luzi Guido, Crosetto Michele, Fernández Enric, 2017. Radar Interferometry for Monitoring the Vibration Characteristics of Buildings and Civil Structures: Recent Case Studies in Spain. *Sensors*, 17, 2017, 4, 669.

Maioli Nicoletta, 2015. *Orbetello. Storia, arte, ambiente e territorio. Il centro storico e le mura, il Novecento e l'industria, i palazzi e i casali, Talamone e l'archeologia, l'evoluzione del costruito e lo spettacolo della natura*. Firenze: Nardini, 2015, 313 pp.

Maioli Urbini Nicoletta, 1990. Forte Stella a Monte Argentario e la Fortezza Spagnola di Porto Santo Stefano: due diverse soluzioni tecniche nell'ambito della stessa funzione. *Bollettino d'arte del Ministero della pubblica istruzione.* Direzione generale delle antichità e belle arti. 75, 1990, 6, 51, pp. 61-88.

Marrara Danilo, 1979. La fine della «libertà» senese e la nascita dello Stato dei Presìdi. In Ferretti Roberto (ed.) *Aspetti e problemi di storia dello Stato dei Presìdi in Maremma*. Grosseto: La Poligrafica, 1979, pp. 65-70.

Masotti Biggiogero Giuseppina, 1980. *Lezioni di geometria proiettiva.* Milano: Masson, 1980, 246 pp.

Meyer Franz, 2019. Spaceborne Synthetic Aperture Radar: Principles, Data Access, and Basic Processing Techniques, 2019. In Flores-Anderson Africa Ixmucane, Herndon Kelsey E., Thapa Rajesh Bahadur, Cherrington Emil (ed.). *The Synthetic Aperture Radar (SAR) Handbook: Comprehensive Methodologies for Forest Monitoring and Biomass Estimation.* Huntsville, AL: SERVIR Global Science Coordination Office, 2019, pp. 21-62.

Miccoli Ilaria, 2019. *Applicazioni di telerilevamento da piattaforma aerea e satellitare per l'Archeologia: immagini multitemporali ad alta risoluzione per la conoscenza e il monitoraggio dell'area urbana di Falerii Novi (VT) e del territorio circostante* [doctoral thesis]. Viterbo: Università degli Studi della Tuscia di Viterbo, 2019, 256 pp.

Moreira Alberto, Prats-Iraola Pau, Younis Marwan, Krieger Gerhard, Hajnsek Irena, Papathanassiou Konstantinos P., 2013. A tutorial on synthetic aperture radar. *IEEE Geoscience and Remote Sensing Magazine,* 1, 2013, 1, pp. 6-43.

Ottl Herwig, 1992. The real aperture antenna of SAR, a key element for performance. In Keydel Wolfgang (ed.) *Fundamentals and Special Problems of Synthetic Aperture Radar (SAR): AGARD Lecture Series 182*. Laughton: Specialised Printing Services Limited, 1992, pp. 4 - 1-4 - 8.

Peng Wenshu, Huang Xuri, Wang Zegen, 2023. Coseismic Deformation and Fault Inversion of the 2017 Jiuzhaigou Ms 7.0 Earthquake: Constraints from Steerable Pyramid and InSAR Observations. *Remote Sensing*, 15, 2023, 1: 222.

Persico, Raffaele, Colica Emanuele, Zappatore Tiziana, Giardino Claudio, D'Amico Sebastiano, 2022. Ground-Penetrating Radar and Photogrammetric Investigation on Prehistoric Tumuli at Parabita (Lecce, Italy) Performed with an Unconventional Use of the Position Markers. *Remote Sensing*, 14, 2022, 5, 1280.

Pinotti Andrea, Somaini Antonio, 2016. *Cultura visuale: immagini, sguardi, media, dispositivi*. Torino: Einaudi, 2016. 290 pp.

Pizzurro Maria Rita, 2007. Dal "visibile" all'"invisibile". Un'esperienza di rilievo integrato. In Chiavoni Emanuela, Paolini Priscilla (ed.) *Metodi e tecniche integrate di rilevamento per la realizzazione di modelli virtuali dell'architettura della città: ricerca COFIN 2004* / coordinatore nazionale Mario Docci. Roma: Gangemi, pp. 222-227.

Ponce Octavio, Prats Pau, Scheiber Rolf, Reigber Andreas, Hajnsek Irena, Moreira Alberto, 2015. Polarimetric 3-D imaging with airborne holographic SAR tomography over glaciers. In 2*015 IEEE International Geoscience and Remote Sensing Symposium (IGARSS) (Milan, 26-31 July 2015).* Piscataway, NJ: IEEE, 2015, pp. 5280-5283.

Qu Junrong, Qiu Xiaolan, Wang Wei, Wang Zezhong, Lei Bin, Ding Chibiao, 2022. A Comparative Study on Classification Features between High-Resolution and Polarimetric SAR Images through Unsupervised Classification Methods. *Remote Sensing,* 14, 2022, 6, 1412.

Regione Toscana, 2015a. P*iano di indirizzo territoriale con valenza di piano paesaggistico. Scheda ambito di paesaggio 16. Colline Metallifere e Elba. Deliberazione di Consiglio regionale n. 37 del 27 marzo 2015.* Regione Toscana, Ministero dei beni e delle attività culturali e del turismo, 2015, 68 pp.

Regione Toscana, 2015b. *Piano di indirizzo territoriale con valenza di piano paesaggistico. Scheda ambito di paesaggio 20. Bassa Maremma e ripiani tufacei. Deliberazione di Consiglio regionale n. 37 del 27 marzo 2015.* Regione Toscana, Ministero dei beni e delle attività culturali e del turismo, 2015, 69 pp.

Reigber Andreas, Scheiber Rolf, Jäger Marc, Prats-Iraola Pau, Hajnsek Irena, Jagdhuber Thomas, Papathanassiou Konstantinos P., Nannini Matteo, Aguilera Esteban, Baumgartner Stefan, Nottensteiner Anton, Moreira Alberto, 2013. Very-High-Resolution Airborne Synthetic Aperture Radar Imaging:

Signal Processing and Applications. *Proceedings of the IEEE,* 101, 2013, 3, pp. 759-783.

Remondino Fabio, El-Hakim Sabry, 2006. Image-based 3D Modelling: A Review. *The Photogrammetric Record*, 21, 2006, 115, pp. 269-291.

Repetti Emanuele, 1833. *Dizionario geografico fisico storico della Toscana: contenente la descrizione di tutti i luoghi del Granducato, Ducato di Lucca Garfagnana e Lunigiana. 1: [A-C].* Firenze: A. Tofani, 1833, 842 pp.

Repetti Emanuele, 1835. *Dizionario geografico fisico storico della Toscana: contenente la descrizione di tutti i luoghi del Granducato, Ducato di Lucca Garfagnana e Lunigiana. 2: [D-L].* Firenze: A. Tofani, 1835, 955 pp.

Repetti Emanuele, 1841. *Dizionario geografico fisico storico della Toscana: contenente la descrizione di tutti i luoghi del Granducato, Ducato di Lucca Garfagnana e Lunigiana. 4: [P-R].* Firenze: Allegrini e Mazzoni, 1841, 844 pp.

Satalecka Konstancja, 2010. *Multimessenger studies of point-sources using the IceCube neutrino telescope and the MAGIC gamma-ray telescope* [doctoral thesis]. Berlin: Humboldt-Universität zu Berlin, 2010, 217 pp.

Schrank Helmut E., Evans Gary E., Davis Daniel, 1990. Reflector antennas. In Skolnik Merrill I. (ed.) *Radar handbook.* New York, NY: McGraw-Hill, pp. 6.1-6.30.

Schubert Adrian, Miranda Nuno, Geudtner Dirk, Small David, 2017. Sentinel-1A/B Combined Product Geolocation Accuracy. *Remote Sensing,* 9, 2017, 6: 607.

Scoppola Francesco, 1984. La rocca di Talamone. *Storia della città: rivista internazionale di storia urbana e territoriale*, 27, 1984, pp. 43-58.

Skolnik Merrill I., 1981. *Introduction to radar systems*. Auckland: McGraw-Hill, 1981, 581 pp.

Skolnik Merrill I., 1990. An introduction to radar. In Skolnik Merrill I. (ed.) *Radar handbook.* New York, NY: McGraw-Hill, 1990, pp. 1.1-1.21.

Sordini Beatrice, 2000. *Il porto della gente vana: lo scalo di Talamone tra il secolo XIII e il secolo XV.* Siena: Protagon editori toscani, 2000. 285 pp.

Stahoviak Carl C., 2019. An Instantaneous 3D Ego-Velocity Measurement Algorithm for Frequency Modulated Continuous Wave (FMCW) Doppler Radar Data [tesi di Laurea magistrale]. Boulder, CO: University of Colorado, 2019. 52 pp.
Strozzi Tazio, Werner Charles, Wiesmann Andreas, Wegmüller Urs, 2012. Topography Mapping With a Portable Real-Aperture Radar Interferometer. *IEEE Geoscience and Remote Sensing Letters,* 2, 9, 2012, pp. 277-281.

The Institute of Electrical and Electronics Engineers, 1976. IEEE Standard Letter Designations for Radar-Frequency Bands. *In IEEE Std 521-1976*. New York, NY: IEEE, 1976, pp. 1-8.

The Institute of Electrical and Electronics Engineers, 1984. IEEE Standard Letter Designations for Radar-Frequency Bands. In *IEEE Std 521-1984 (Revision of IEEE Std 521-1976).* New York, NY: IEEE, 1984, pp. 1-8.

The Institute of Electrical and Electronics Engineers, 2003. IEEE Standard Letter Designations for Radar-Frequency Bands. In *IEEE Std 521-2002 (Revision of IEEE Std 521-1984).* New York, NY: IEEE, 2003, pp. 1-10.

The Institute of Electrical and Electronics Engineers, 2020. IEEE Standard Letter Designations for Radar-Frequency Bands. In *IEEE Std 521-2019 (Revision of IEEE Std 521-2002)*. New York, NY: IEEE, 2020, pp. 1-15.

Uggeri Giovanni, 1979. Il popolamento del territorio cosano nell'antichità. In Ferretti Roberto (ed.) *Aspetti e problemi di storia dello Stato dei Presìdi in Maremma.* Grosseto: La Poligrafica, 1979, pp. 37-64.

Van Zyl Jakob, Kim Yunjin, 2011. *Synthetic Aperture Radar Polarimetry.* Hoboken, NJ: John Wiley & Sons, 2011, 2011, 288 pp.

Watson G. Alistair, 2006. Computing Helmert transformations. *Journal of Computational and Applied Mathematics*, 197, 2006, 2, pp. 387-394.

Werner Charles, Strozzi Tazio, Wiesmann Andreas, Wegmüller Urs, 2008. A Real-Aperture Radar for Ground-Based Differential Interferometry. In *IGARSS 2008 - 2008 IEEE International Geoscience and Remote Sensing Symposium (Boston, July 6-11 2008).* Piscataway, NJ: IEEE, 2008, pp. III - 210-III - 213.

Wessel Birgit, Rizzoli Paola, Fritz Thomas, Busche Thomas, Krieger Gerhard, Buckreuss Stefan, 2018. *TanDEM-X Ground Segment. DEM Products Specification Document. EOC – Earth Observation Center. TD-GS-PS-0021. Issue 3.2. Date: 07.05.2018.* Munich: Deutsches Zentrum für Luft- und Raumfahrt e.V., 2018, 49 pp.

Wu Baolong, Wang Haonan, Chen Jianlai, 2023. Feature Enhancement Using Multi-Baseline SAR Interferometry-Correlated Synthesis Images for Power Transmission Tower Detection in Mountain Layover Area. *Remote Sensing*, 15, 2023, 15: 3823.

Yu Kun, Zhu Shengqi, Lan Lan, Yang Biao, 2023. High-Resolution and Wide-Swath SAR Imaging with Space–Time Coding Array. *Remote Sensing*, 15, 2023, 9, 2465.

Zhang Yan, Li Zhengzheng, Cheong Boonleng, Cai Jingxiao, Ramesh Nepal, Suarez Hernan, Blake William, Andrews Joel, Yong Teoh, 2013. Optimized Radar Signal Processing for a Low-cost, Solid-State Airborne Radar. In *36th Conference on Radar Meteorology (Cooperative Institute for Research in Environmental Sciences at the University of Colorado, Boulder, 16-20 September 2013)*. Boston, MA: American Meteorological Society, 2013, 2B.1.

Siteography

3DFlow, 2023. 3DF Zephyr - Modelli 3D da foto. Software di fotogrammetria e scansione 3D. *3DFlow.* <https://www.3dflow.net/it/software-di-fotogrammetria-3df-zephyr/> Accessed on 25 August 2023.

Agenzia Spaziale Italiana, 2022. COSMO-SkyMed. Sistema duale per l'osservazione della Terra. *Agenzia Spaziale Italiana. Scienze della Terra.* <https://www.asi.it/scienze-della-terra/cosmo-skymed/>. Accessed on 16 May 2022.

CloudCompare, 2023. *CloudCompare 3D point cloud and mesh processing software - Open Source Project*. <https://www.cloudcompare.org/> Accessed on 25 August 2023.

Deutsches Zentrum für Luft- und Raumfahrt e.V. 2006. *TanDEM-X Science Service System.* <https://tandemx-science.dlr.de/>. Accessed on 15 March 2023.

European Incoherent Scatter Scientific Association, 2016. EISCAT Svalbard Radar. *EISCAT Scientific Association.* <https://eiscat.se/about/sites/eiscat-svalbard-radar/>. Accessed on 13 July 2023.

European Space Agency, 2012. Doppler Centroid Algorithms. *Sentinel Online*. <https://sentinels.copernicus.eu/web/sentinel/technical-guides/sentinel-1-sar/products-algorithms/level-1-algorithms/doppler-centroid-algorithms> Accessed on 25 August 2023.

Gallis Michael R., 2004. Animations for Physics and Astronomy Home Page. *PennState Schuylkill Physics and Astronomy Faculty.* <https://phys23p.sl.psu.edu/phys_anim/waves/indexer_waves.html>. Accessed on 13 July 2023.

Gexcel, 2023. JRC 3D Reconstructor. *Gexcel.* <https://gexcel.it/it/10-software/jrc-3d-reconstructor> Accessed on 25 August 2023.

Istituto dell’Enciclopedia Italiana Treccani, 1935. Porto Longone. *Enciclopedia Italiana*. Roma: Istituto dell’Enciclopedia Italiana Treccani, 1935, *ad vocem.* <https://www.treccani.it/enciclopedia/porto-longone_(Enciclopedia-Italiana)/>. Accessed on 25 August 2023.

Istituto dell’Enciclopedia Italiana Treccani, 1996. Depolarizzazione. *Dizionario delle Scienze Fisiche*. Roma: Istituto dell’Enciclopedia Italiana Treccani, 1996, *ad vocem.* <https://

www.treccani.it/enciclopedia/depolarizzazione_(Dizionario-delle-Scienze-Fisiche)/>. Accessed on 25 August 2023.

Istituto dell'Enciclopedia Italiana Treccani, 2011a. Guerra dei Trent'anni. Defenestrazione di Praga. Roma: Istituto dell'Enciclopedia Italiana Treccani, 2011, *ad vocem.* <https://www.treccani.it/enciclopedia/defenestrazione-di-praga_(Dizionario-di-Storia)/>. Accessed on 25 August 2023.

Istituto dell'Enciclopedia Italiana Treccani, 2011b. Guerra dei Trent'anni. *Dizionario di Storia.* Roma: Istituto dell'Enciclopedia Italiana Treccani, 2011, *ad vocem.* <https://www.treccani.it/enciclopedia/guerra-dei-trent-anni_(Dizionario-di-Storia)/>. Accessed on 25 August 2023.

Istituto dell'Enciclopedia Italiana Treccani, 2012. Georeferenziazione. *Lessico del XXI Secolo*. Roma: Istituto dell'Enciclopedia Italiana Treccani, 2012, vol. 1 (A-K), *ad vocem.* <https://www.treccani.it/enciclopedia/georeferenziazione_(Lessico-del-XXI-Secolo)/>. Accessed on 25 August 2023.

Istituto Italiano dei Castelli, 2020. Talamone Rocca e cinta muraria. *Istituto Italiano dei Castelli – Sezione Toscana.* <https://www.istitutocastelli-toscana.org/talamone-rocca-e-cinta-muraria/>. Accessed on 25 August 2023.

Istituto Italiano dei Castelli, 2021. Nomenclatura Castellana. *Istituto Italiano dei Castelli.* <http://www.istitutoitalianocastelli.it/nomenclatura-castellana/>. Accessed on 25 August 2023.

Japan Aerospace Exploration Agency, 1997. Polarimetric observation by PALSAR. Earth-graphy. *All about JAXA's Earth Observations.* <https://www.eorc.jaxa.jp/ALOS/en/img_up/pal_polarization.htm>. Accessed on 25 August 2023.

Meyer Franz, 2022. AlaskaX SAR-401. Synthetic Aperture Radar: Hazards. *EdX.* <https://learning.edx.org/course/course-v1:AlaskaX+SAR-401+3T2021>. Accessed on 31 July 2022.

Ministero dell'Ambiente e della Tutela del Territorio e del Mare, 2015. Telerilevamento ambientale della Guardia Costiera. *Natura Italia*. <https://www.naturaitalia.it/apriParagrafiArticoloSezioneMenu.do?paragrafo=1&idArticolo=263>. Accessed on 13 July 2023.

Ministero dell'Ambiente e della Tutela del Territorio e del Mare, 2017. *Geoportale nazionale.* <http://www.pcn.minambiente.it/mattm/>. Accessed on 16 November 2022.

Mori Attilio, 1935. Piombino, Promontorio di. *Enciclopedia Italiana.* Roma: Istituto dell'Enciclopedia Italiana Treccani, 1935, *ad vocem.* <https://www.treccani.it/enciclopedia/promontorio-di-piombino_(Enciclopedia-Italiana)/>. Accessed on 25 August 2023.

Mori Attilio, Scaramella Gino, 1935. Piombino. *Enciclopedia Italiana.* Roma: Istituto dell'Enciclopedia Italiana Treccani, 1935, *ad vocem.* <https://www.treccani.it/enciclopedia/piombino_(Enciclopedia-Italiana)/>. Accessed on 25 August 2023.

Mori Attilio, Solari Arturo, Scaramella Gino, 1932. Elba. *Enciclopedia Italiana.* Roma: Istituto dell'Enciclopedia Italiana Treccani, 1932, *ad vocem.* <https://www.treccani.it/enciclopedia/elba_(Enciclopedia-Italiana)/>. Accessed on 25 August 2023.

National Aeronautics and Space Administration, 1998. Photojournal. PIA01321: Onboard View - Space Shuttle Endeavour. *Jet Propulsion Laboratory. California Institute of Technology.* <http://photojournal.jpl.nasa.gov/catalog/PIA01321>. Accessed on 13 July 2023.

National Aeronautics and Space Administration, 2013a. *MCoRDS Underwing Radar Antenna Array.* <https://www.nasa.gov/content/goddard/mcords-underwing-radar-antenna-array/>. Accessed on 13 July 2023.

National Aeronautics and Space Administration, 2013b. *MCoRDS Data Graph of Region Between Dome C and Vostok.* <https://www.nasa.gov/content/goddard/mcords-data-graph-of-region-between-dome-c-and-vostok/>. Accessed on 13 July 2023.

National Oceanic and Atmospheric Administration, 2019. *NOAA Photo Library.* <https://photolib.noaa.gov/Collections/

Coast-Geodetic-Survey/Other/emodule/1181/eitem/71311>. Accessed on 13 July 2023.

OpenTopoMap, 2023. OpenTopoMap - Topographische Karten aus OpenStreetMap. *opentopomap.org* <https://www.opentopomap.org >. Accessed on 25 August 2023.

Planetek Italia, 2022. Planetek Academy. *Earth Observation Learning.* <https://eolearning.planetek.it/>. Accessed on 07 May 2022.

Sandia National Laboratories, 2023a. Pathfinder Radar ISR & SAR Systems. SAR Imagery. *Sandia National Laboratories.* <https://www.sandia.gov/radar/pathfinder-radar-isr-and-synthetic-aperture-radar-sar-systems/archive-imagery/>. Accessed on 13 July 2023.

Sandia National Laboratories, 2023b. Pathfinder Radar ISR & SAR Systems. VideoSAR. *Sandia National Laboratories.* <https://www.sandia.gov/radar/pathfinder-radar-isr-and-synthetic-aperture-radar-sar-systems/video/>. Accessed on 25 August 2023.

United States Geological Survey, National Aeronautics and Space Administration, 2020. NASADEM_HGT v001. *NASADEM Merged DEM Global 1 arc second. Land Processes Distributed Active Archive Center (LP DAAC).* <https://lpdaac.usgs.gov/products/nasadem_hgtv001/>. Accessed on 25 August 2023.

Archival funds

ASFi, Archivio di Stato di Firenze (Florence State Archives).

Additional references

Rabchevsky George (ed.), 1984. *Multilingual dictionary of remote sensing and photogrammetry: English glossary and dictionary, equivalent terms in French, German, Italian, Portuguese, Spanish, Russian.* Falls Church, VA: American Society of Photogrammetry, 1984, 343 pp.

Acronyms

ASI Agenzia Spaziale Italiana.
Italian Space Agency

AVHRR Advanced Very-High-Resolution Radiometer

BC before Christ

COSMO-SkyMed COnstellation of small Satellites for the Mediterranean basin Observation

CW Continuous Waveforms

DC Doppler centroid

DEM Digital Elevation Model

DInSAR Differential Interferometry Synthetic Aperture Radar

DL Downlink

DLR Deutsches Zentrum für Luft- und Raumfahrt e.V.

DSDRA Dipartimento di Storia, Disegno e Restauro dell'Architettura.
Department of History, Representation and Restoration of Architecture
DTM Digital Terrain Model

EASA European Union Aviation Safety Agency

EIRP Equivalent Isotropic Radiated Power

ENAC Ente Nazionale Aviazione Civile.
Italian Civil Aviation Authority

Envisat Enviromental Satellite

ERS European Remote-Sensing satellite

ESA European Space Agency

FOV Field Of View
GEO GEostationary Orbit

GCP Ground Control Point

GIS Geographic Information System

GNSS Global Navigation Satellite System

GPS Global Positioning System

HEO Highly Elliptical Orbit

HF High-Frequency

HPBW Half Power Beam Width

ICP Iterative Closest Point

IEEE Institute of Electrical and Electronics Engineers

InSAR Interferometric Synthetic Aperture Radar

IREA-CNR Istituto per il Rilevamento Elettromagnetico dell'Ambiente del Consiglio Nazionale delle Ricerche.
Institute for Electromagnetic Sensing of the Environment of the National Research Council

ISAR Inverse Synthetic Aperture RADAR

ITU International Telecommunications Union

JAXA Japanese Aerospace eXploration Agency

JPL Jet Propulsion Laboratory

LEO Low Earth Orbit

LIDAR LIght Detection And Ranging

LOS Line Of Sight

MCoRDS Multichannel Coherent Radar Depth Sounder

MEO Medium Earth Orbit

MISR Multi-angle Imaging SpectroRadiometer

MM Mobile Mapping

MODIS MODerate resolution Imaging Spectroradiometer

MUSIC Multiple Signal Classification

NASA National Aeronautics and Space Administration

NESZ Noise Equivalent Sigma Zero

OTH Over-the-Horizon

PRF Pulse Repetition Frequency

PS Persistent Scatterers

PSI Persistent Scatterers Interferometry

PSF Point Spread Function

PST-A 2009 Not-Ordinary Plan of Remote Sensing ofEnvironment 2009

Radar RAdio Detection And Ranging

RAR Real Aperture RADAR

RCS RADAR Cross Section

RT Revisit Time

RTC Radiometric Terrain Correction

SAR Synthetic Aperture RADAR

SfM Structure from Motion

SLAR Side-Looking Aperture RADARs

SLC Single Look Complex

SNR Signal-to-Noise Ratio

SRTM Shuttle Radar Topography Mission

SVD Singular Value Decomposition

TomoSAR Tomographic Synthetic Aperture Radar

TOPS Terrain Observation by Progressive Scans

TDRSS Tracking and Data Relay Satellite System

UAS Unmanned Aerial Systems

UAV Unmanned Aerial Vehicles

UHF Ultra-High-Frequency

VHF Very-High-Frequency

WWF World Wide Fund for Nature

Aknowledgments

The research inherent in this thesis was developed with the use of the following products covered by intellectual property:

- 160 COSMO-SkyMed products of beam H4-01 from No. 309198 acquired on 2012-07-17 at 04:54:08 UTC to No. 318284 acquired on 2022-08-06 at 04:46:08 UTC; “COSMO-SkyMed Product - ©ASI - Agenzia Spaziale Italiana - (2012-2022). All Rights Reserved”.
- Tile TDM-DEM-12m:/dims_op_pl_dfd_XXXXB00000000393155076492/dims_op_pl_dfd_//TDM.DEM.DEM, archived on 2015-06-24T00:47:17.109Z. © DLR <2023>.
- Tile C42441110_0202, tile C42421112_0202, and tile C42541112_0202 from the Extraordinary Environmental Remote Sensing Plan 2009 (Piano Straordinario di Telerilevamento – PST-A 2009); Ministero dell'Ambiente e dell'Energia – Italian Ministry of Environment and Energy / licensed under CC BY-SA 3.0 IT (https://creativecommons.org/licenses/by/3.0/it/deed.it) / Creative Commons – Attribuzione - Condividi allo stesso modo Italia (CC BY-SA 3.0 IT).

Gratitudes

First of all, I would like to thank Dr. Gianfranco Fornaro and Dr. Simona Verde from the Institute for Electromagnetic Sensing of the Environment of the National Research Council (Istituto per il Rilevamento Elettromagnetico dell'Ambiente del Consiglio Nazionale delle Ricerche – IREA-CNR) for their advice and support. Without them, this thesis would never have been possible.
Within the Department of History, Representation, and Restoration of Architecture (Dipartimento di Storia, Disegno e Restauro dell'Architettura – DSDRA) of 'Sapienza' University, I sincerely thank Prof. Fabio Lanfranchi for his technical support and Prof. Laura Carnevali for guiding me through these three years of my PhD.
I also owe special thanks to my colleague Angela Moschetti, whose help enabled this work to become a reality.
Finally, I would like to thank my family for supporting me during difficult times, especially my brother Massimo.